Development of multidimensional spectroscopies to investigate transition metal dichalcogenide and lead halide perovskite semiconductors

By
Darien James Morrow

A dissertation submitted in partial fulfillment of
the requirements for the degree of

Doctor of Philosophy
(Chemistry)

at the
UNIVERSITY OF WISCONSIN - MADISON
2020

Date of final oral examination: May 15, 2020
This dissertation is approved by the following members of the Final Oral Committee:
John Wright (advisor), Professor, Analytical Chemistry
J.R. Schmidt, Professor, Physical Chemistry
Martin Zanni, Professor, Physical Chemistry
Deniz Yavuz, Professor, Atomic and Optical Physics

Tell all the truth but tell it slant —
Success in Circuit lies
Too bright for our infirm Delight
The Truth's superb surprise
As Lightning to the Children eased
With explanation kind
The Truth must dazzle gradually
Or every man be blind —

— Emily Dickinson

Contents

Acknowledgments

Earning a doctorate is a community effort. Family, friends, funders, mentors, colleagues—they all play a crucial role.

For two years of graduate school, I was supported by a generous fellowship from the Link Foundation. I have also been continuously supported by the Department of Energy, Office of Basic Energy Sciences, Division of Materials Sciences and Engineering, under award DE-FG02-09ER46664.

To the Open Source Software community: thank you for building superb tools which align with your ethics—even at a cost to your careers.

To my Wright Group colleagues who have all been both mentor and friend: thank you for your kindness, time, and trust. I have learned much from you all.

To Prof. John Wright: thank you for being a kind and thoughtful advisor over the last five years. You show immense faith in your graduate students which leads to a freedom for them to explore any idea they see fit. Many of the chapters in this dissertation are born out of curiosity which stemmed from graduate student freedom.

To Dan Kohler: thank you for being my perpetual coauthor. Many of the chapters in this dissertation have you to thank for their crucial insight. You are truly a fount of sound advice, deep spectroscopic insight, stability, and most importantly, hope.

To Blaise Thompson: you have been an essential mentor and a dear friend. You taught me much about ethics, programming, open source software, spectroscopy, and how to think well about a measurement. I hope Dan will continue to supply you with instant coffee in lieu of me.

To Kyle Czech: thank you for being feisty, eclectic, and for not being afraid to dismantle an OPA in order to realign it just-right.

To Nathan Neff-Mallon: thank you for helping me to see the many injustices which weave their way through science and society.

To Jonathan Handali: thank you for being a zen desk/lab mate even when I was perplexed by your sleep schedule.

To Natalía Spitha: thank you for all of the "bless you" Slack messages from the other office.

To Kyle Sunden: thank you for continually coming to my `Python` and `BASH` aid, but more impor-

tantly thank you for being so generous with your time for everyone in your life.

To Emily Kaufman: thank you for all of the conversations about hot takes, Taylor Swift, and wondering why we do the work we do.

To Jason Scheeler and David Lafayette: thank you for reminding me of the joys of mentorship and being willing to talk about Frisbee while aligning our laser table.

To Chris Roy: thank you for being the breadth of fresh air and rigor that I needed right at the end of graduate school.

To my defense committee: I thank each of you for either providing career advice or project-level insight at crucial times during graduate school.

To members of the Garand group: thank you for providing a mirthful, second home for me in graduate school.

To all of my colleagues on the third floor, especially Matt Hautzinger, Yuzhou Zhao, and Prof. Song Jin: thank you for all you have taught me about materials chemistry, the art of collaboration, and communication.

To my first semester Quantum Mechanics and Statistical Mechanics friends, Aurora Janes, Jessi Flach, Kaarin Evens, Kaitlyn Fischer, and Morgan Rea: thank you for existing in my life these last five years. I hope our random walks continue to cross.

To Alexander Moore: thank you for being my best of buds since day one of undergrad. I hope that one day some of my lasers meet some of your recycled plastics.

To my family: thank you for your love and support even when I was unable to explain why I spent so much of my time modeling how lasers interact with semiconductors.

To Kaitlyn: Thank you for the happiness and perspective you bring into my existence. Thank you for seeing the best in me, even when I cannot. I look forward to the next season of our life together.

Abstract

A system's ability to create new electric fields from intense, applied electric fields offers unique insight into the quantum mechanical structure and photoexcited dynamics of the system. This dissertation describes the development, application, and modeling of new multidimensional spectroscopies along with more mature ones to investigate transition metal dichalcogenide and lead halide perovskite semiconductors which show great promise for next-generation photovoltaics and optoelectronics.

First, we show that multidimensional triple sum-frequency (TSF) spectroscopy is susceptible to group and phase velocity mismatch artifacts when accomplished in a transmissive geometry with thick substrates. Using TSF in a reflective geometry, we interrogate the electronic structure of a MoS_2 thin film and experimentally confirm predictions of band nesting contributions to MoS_2's optical joint density of states. We then show that TSF, when preceded by a pump, can probe the ultrafast dynamics of MoS_2 and WS_2 microstructures without suffering from sensitivity losses due to low surface coverage like the more common transient-reflectance spectroscopy. This work is then extended to the regime of an intense, non-resonant pump, and we demonstrate the existence of the optical Stark effect in optical harmonic generation.

Next, we investigate questions relevant to material scientists. Transient-reflectance spectroscopy is employed to monitor ultrafast charge dynamics in WS_2-MoS_2 core-shell lateral heterostructures. After applying a Fresnel model to account for effects of the stratified substrate, we find no evidence for ultrafast charge transfer. We then use transient-transmittance and -reflectance spectroscopies to probe the hot carrier cooling and surface recombination dynamics of lead halide perovskites. Finally, we develop multidimensional harmonic generation as a probe of crystal symmetry, which is not susceptible to multiphoton photoluminescence artifacts.

Chapter 1 Introduction and background

Semiconductors, light, and light-semiconductor interactions are at the heart of many of the last century's greatest technological achievements. Modern computers rely on cheap, tiny chips built from semiconductors. Humans use these computers to communicate from city-to-city and from country-to-country at fantastically high speeds by converting electrical signals into photons via a semiconductor device. These photons then travel down vast lengths of glass fibers, and are finally turned back into electrical signals by semiconductor devices at the end of the fiber. These electrical signals are then eventually converted by a computer into stimuli which are sensed by a human. In short, semiconductors, light, and light-semiconductor interactions allow humans to video chat with their families even when separated by thousands of kilometers.

Many of the advances humans have made with semiconductors are due to advances made in their synthesis, purification, and characterization. The same is true of our recent advances with light: the laser has allowed humans to synthesize and use light that is spatially and energetically cohesive. It is in the spirit of understanding and characterizing semiconductors that I spent my time in graduate school implementing, accessing, and modeling new semiconductor measurement techniques built on recent advances in optical physics.

In this dissertation I detail advances made while exploring the interface between semiconductor physics and laser physics over the last five years. My research focused on using semiconductors to facilitate the interaction of multiple lasers and then using the observed strength of this interaction to make inferences about the semiconductor. There are three common threads which run through my work.

1. Multiple very fast bursts of laser light which have high instantaneous intensity. The short-temporal bursts of light allow me to reach high *peak* intensity while operating at low (integrated) power so as to not destroy samples by localized heating.
2. Control of the color of these intense bursts of light using a device called an optical parametric amplifier, OPA. This allows me to see how semiconductors respond to different colors of light.
3. Interrogation of semiconductors which are microns to millimeters wide but which are composed of nanometer thick layers. These thin layers act as confinement channels for electrons in the material.

The goal of this introductory chapter is to provide background information (and a small amount of motivation) to the rest of the dissertation with a casual tone. Most of the chapters which follow are self-contained, and attempt to convey my measurements and insights to experts in the fields I inhabit. Thus, they skip over many of the interesting underlying ideas of my work. At the end of this Introduction I will provide an overview of these chapters.

1.1 Semiconducting materials

When a large number of atoms form a solid, their atomic orbitals clump together and form bands from their original discrete energy levels. Figure 1.1 shows this clumping (hybridization) for the case of a quantum dot. The distribution of electrons in these bands is defined by the Fermi-Dirac distribution. Figure 1.2 shows this distribution for a few different types of band spacings ranging from a metal to an insulator. If the lowest antibonding (conduction) band is close to but not touching the highest bonding (valence) band, then the material is a semiconductor. The distance between the top of the valence band and the bottom of the conduction band is called the bandgap, E_g.

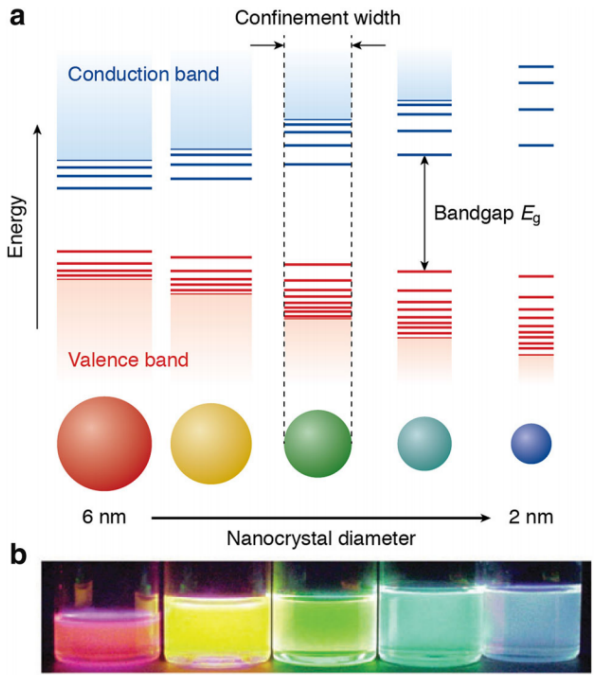

Figure 1.1: (a) Schematic representation of the quantum confinement effects: the bandgap (or HOMO-LUMO gap) of the semiconductor nanocrystal increases with decreasing size, while discrete energy levels arise at the band-edges. The energy separation between the band-edge levels also increases with decreasing size. (b) Photograph of five colloidal dispersions of CdSe QDs with different sizes, under excitation with a UV-lamp in the dark. The color of the photoluminescence changes from red to blue as the QD diameter is reduced from 6 to 2 nm. This figure is reproduced from ref.[1] and used under a CC-BY-4.0 license.

In the simplest case, absorption of light roughly follows the (joint) density of states of the material.

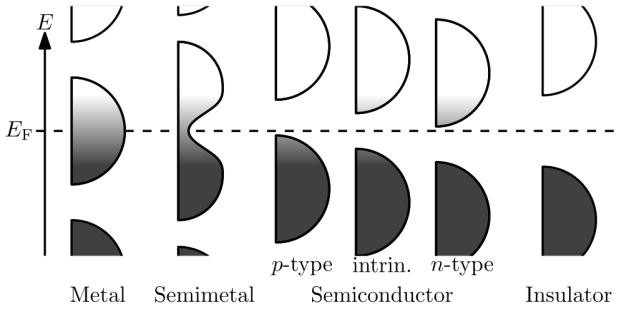

Figure 1.2: Filling of the electronic states in various types of materials at equilibrium. Here, height is energy while width is the density of available states for a certain energy in the material listed. The shade follows the Fermi-Dirac distribution (black = all states filled, white = no state filled). In metals and semimetals the Fermi level E_F lies inside at least one band. In insulators and semiconductors the Fermi level is inside a band gap; however, in semiconductors the bands are near enough to the Fermi level to be thermally populated with electrons or holes. This figure is in the public domain (CC0 license).

As shown in Figure 1.3 the generic density of states is different for bulk (3D) materials compared to atomically fine sheets, wires and dots. By changing the dimensionality of a system, the density of state can be fundamentally changed. The density of available states to excite an electron into cuts-on at the bandgap, and for a bulk material goes as the square-root of the photon energy in excess of the bandgap. Interrogating semiconductors with light would be quite boring if this square-root absorption spectrum were the whole story. In comparison, the absorption spectrum of a generic bulk semiconductor (Figure 1.4) is much richer than a square-root function.[1]

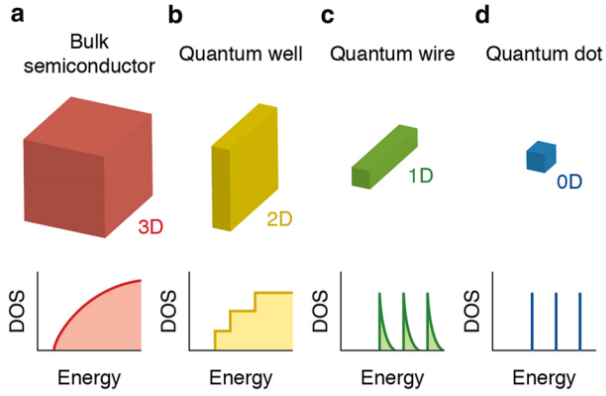

Figure 1.3: Schematic illustration of the energy level structure of a bulk semiconductor (a), and semiconductor nanostructures (b–d) with reduced dimensionality. DOS represents the density of electronic states. This figure is reproduced from ref.[1] and used under a CC-BY-4.0 license.

[1]In order to avoid confusion, note that Figure 1.4 and Figure 1.3 have their energy axes increasing in opposite directions.

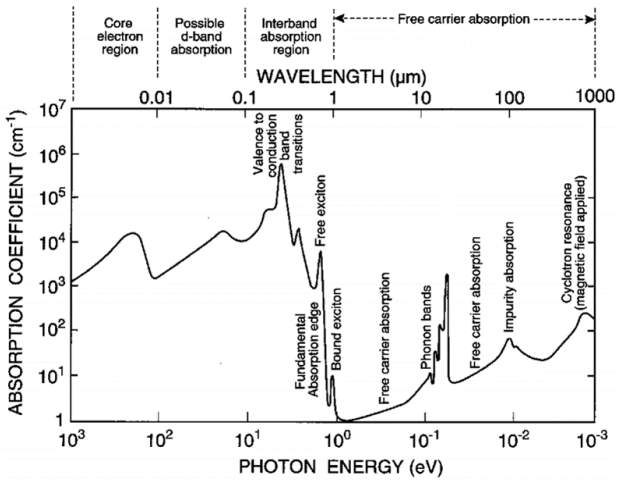

Figure 1.4: Absorption spectrum of a prototypical semiconductor showing a wide variety of optical processes. This figure is adapted from ref.[2].

Figure 1.4 shows the interband absorption in the visible region of the electromagnetic spectrum—the interband absorption is the part of the spectrum which will follow a square-root curve. At slightly lower energy than the interband absorption sharp excitonic peaks are present—we will talk about excitons in depth later in this chapter. At lower energy than the exciton are free carrier transitions which show a gradually increasing absorption as energy goes lower. These free carrier transitions are from electrons in the slightly filled conduction band being moved higher up in the conduction band by absorbing a photon. There are also distinct features due to phonons (particle-like lattice vibrations). At photon energies much higher than the bandgap are core-electron transitions from electrons which are tightly bound to their nuclei. Figure 1.4 highlights the many nuclear and electronic degrees of freedom which light of different colors can interact with in a semiconductor.

The spectroscopy community is actively researching how the nuclear and electronic degrees of freedom interact with each other. Current questions include: if an interband transition is excited, how does the excited semiconductor dissipate energy into phonon modes (i.e. heat up the semiconductor)? And, if a phonon mode is excited, how does that change the interband transition properties? Ultimately these are questions about "mode-coupling" which we will cover later in this chapter.

So far in our discussion of semiconductors we have thought of them like a big molecule with large clumps of electronic transitions. However, there is a crucial idea in semiconductor physics which

is not present from the molecular picture. A molecule's electron distribution around its nuclei is generally described in spatial coordinates (e.g. orbitals). But in a material which is functionally of infinite extent (compared to the size of a single atom), a differen picture is needed. If a material has periodically arranged nuclei, the Coulombic potential felt by the electrons attracted to these nuclei will also be periodic. Bloch's theorem says that in this system a good basis for describing the system's electrons are with wavefunctions (called Bloch waves) that go as

$$\psi_{n\mathbf{k}}(\mathbf{r}) = u_{n\mathbf{k}}(\mathbf{r}) \exp(i\mathbf{k} \cdot \mathbf{r}), \tag{1.1}$$

in which u has the same periodicity as the lattice, $\mathbf{r}$ is a spatial coordinate, $\mathbf{k}$ is the wavevector (momentum) of a plane wave, and n is a band index. Bloch's theorem says that each of these wavefunctions is an eigenstate of the periodic system; the energy eigenvalues, $E_n(\mathbf{k})$ are the energy bands which are collectively referred to as the *band structure*. These facts imply that the correct way to think about the possible electron distributions in a periodic system is indexed by the crystal momentum. An additional important fact is that the complete behavior of all these Bloch waves is completely described by momenta constrained within the primitive cell of the reciprocal lattice—the first Brillouin zone.

For the purpose of this dissertation, the primary need to consider the momentum description of electronic states in semiconductors is because of the restrictions it places on possible optical transitions. The absorption or emission of a photon is restricted by conservation of momentum and energy:

$$E_i + \hbar\omega = E_f \tag{1.2}$$

$$\mathbf{k}_i + \mathbf{q} = \mathbf{k}_f, \tag{1.3}$$

in which E_i and E_f are initial and final energy of an electron, $\mathbf{k}_i$ and $\mathbf{k}_f$ are the intial and final electron momentum, and $\hbar\omega$ and $\mathbf{q}$ are the photon's energy and momentum. Because a single photon has very little momentum compared to the momentum of an electron, when a photon is absorbed or emitted the electron's momentum does not noticeably change. These conservation requirements also imply that the photon energy must be greater than the material's bandgap to

induce an interband absorption.

If the top-most valence band and the bottom-most conduction band have extrema at the same **k**, then the semiconductor is known as a *direct band gap semiconductor*. Conversely, if the these bands do not have extrema at the same **k**, the semiconductor is known as an *indirect band gap semiconductor*. These two cases are illustrated in Figure 1.5. Absorption of a photon at the bandedge of an indirect gap semiconductor requires a secondary source of momentum—a lattice vibration (phonon) often supplies this momentum. Because absorption in an indirect gap semiconductor is a second-order process, the rate of photon absorption (related to the absorption coefficient) is much smaller than a direct gap semiconductor.

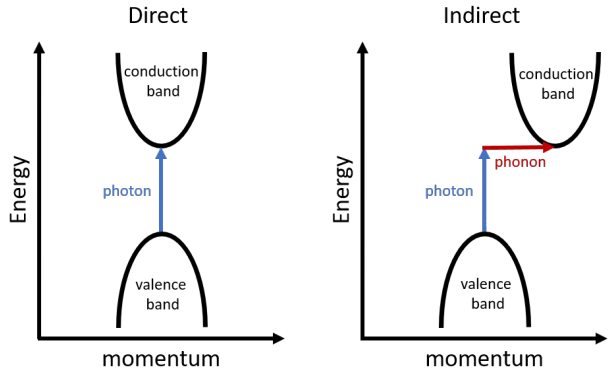

Figure 1.5: Direct and indirect band gap semiconductors. This representation assumes parabolic bands (effective-mass approximation).

Electrons excited into a band will eventually cool to the lowest point in the conduction band. A direct gap semiconductor will have appreciable interband fluorescence from these cooled electrons while an indirect gap semiconductor will not have appreciable fluorescence.

1.2 Transition metal dichalcogenides

Many chapters in this dissertation have transition metal dichalcogenides (TMDCs) as their material system of interest. TMDCs have the chemical formula of MX_2 with M being a transition metal and X being a chalcogen (see Figure 1.6a). I have primarily concentrated on MoS_2 and WS_2. MoS_2 is naturally occurring as the mineral molybdenite, has uses as a solid-state lubricant, and macroscopically has properties similar to graphite.

When MoS_2 and WS_2 are in a hexagonal phase (cf. Figure 1.6b,d) they are semiconductors. In other phases they have different properties, for instance when MoS_2 is in its trigonal phase (Figure 1.6c,e), it is a semimetal. Most of the TMDCs crystallize as layered compounds (cf. Figure 1.7a). Each TMDC layer is composed of sub-layers in which a metal layer is sandwiched by chalcogen layers. Within the plane, interatomic interactions are strong and covalent. However, between planes only weak, van der Waals forces exist. The layers therefore easily slip across each other, which is why molybdenite is a good lubricant. The layers can also be peeled away from each other using techniques like sonication or mechanical exfoliation based on tape (i.e. the "Scotch tape method" originally developed in the graphene community).

In 2010, the Heinz group discovered that MoS_2, when it is thinned-down to a monolayer, switches from an indirect bandgap semiconductor to a direct bandgap semiconductor.[6] The smoking-gun of this change is that monolayers have much brighter fluorescence than MoS_2 with two or more layers. Figure 1.7b shows the evolution of the MoS_2 bandstructure as the number of layers are decreased to unity and evidence the indirect to direct bandgap switch. The discovery of an atomically thin semiconductor sparked an intense research enterprise based on the idea/promise of ultra-thin, electronics made by stacking different TMDCs, graphene, and other 2D materials.[7]

Monolayer MX_2 has a hexagonal Brillouin zone (Figure 1.7c). The direct bandgap is at the K point. Due to large spin-orbit coupling, the time-reversal symmetry of the 6 K points is broken and 2 sets of 3 K points result. These two sets of K points have spin-split valence and conduction bands with the valence bands having a much larger degree of splitting than the conduction bands. The large valence band spin orbit splitting yields multiple transitions spaced hundreds of meV apart at

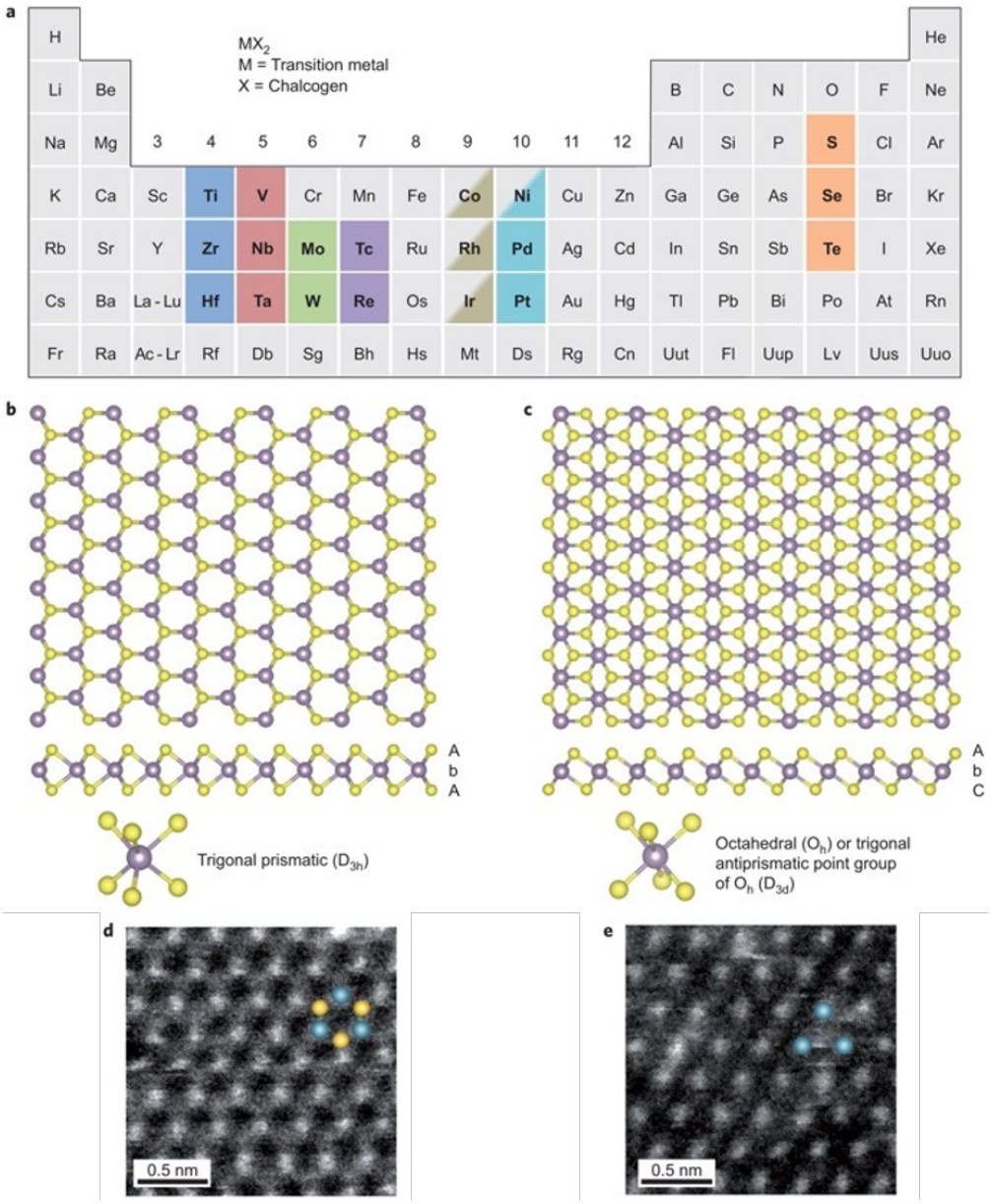

Figure 1.6: Overview of transition metal dichalcogenide structures. (a) About 40 different layered TMD compounds exist. The transition metals and the three chalcogen elements that predominantly crystallize in those layered structure are highlighted in the periodic table. Partial highlights for Co, Rh, Ir and Ni indicate that only some of the dichalcogenides form layered structures (b,c) c-Axis and [11-20] section view of single-layer TMD with trigonal prismatic (b) and octahedral (c) coordination. Atom color code: purple, metal; yellow, chalcogen. The labels AbA and AbC represent the stacking sequence where the upper- and lower-case letters represent chalcogen and metal elements, respectively. (d,e) Dark-field scanning transmission electron microscopy image of single-layer MoS_2 showing the contrast variation of 1H (d) and 1T (e) phases. Blue and yellow balls indicate Mo and S atoms, respectively. This figure is adapted from ref.[3] with the publisher's permission.

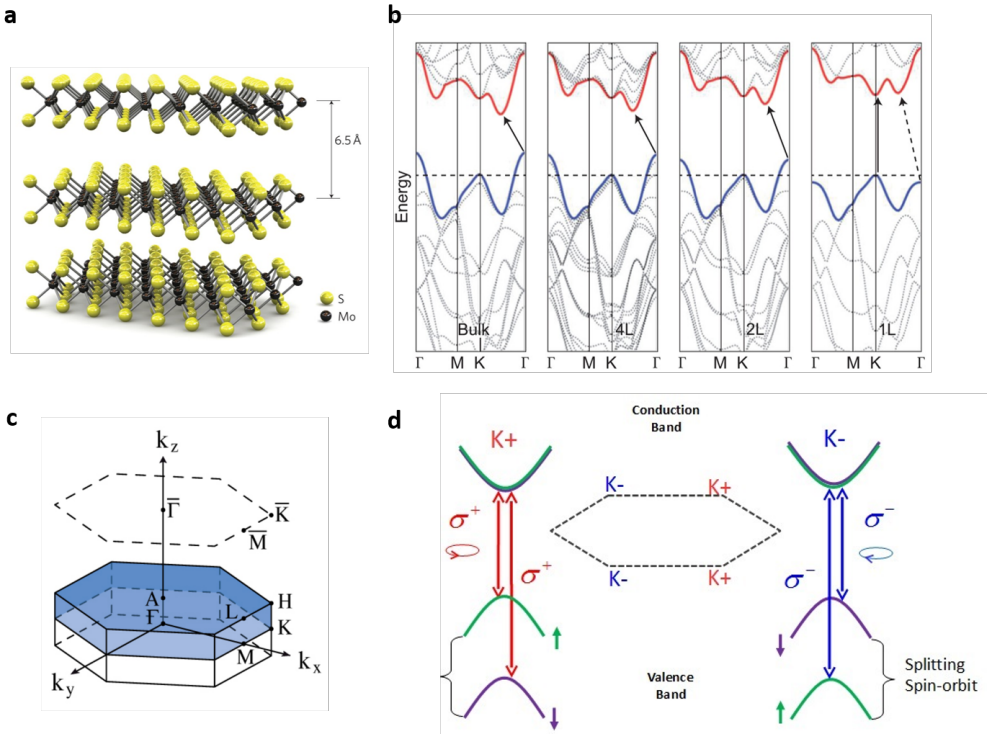

Figure 1.7: Overview of TMDC bandstructure. (a) 3D representation of the layered structure of MoS_2. (b) energy dispersion (energy versus wavevector k) in bulk, quadrilayer (4L), bilayer (2L) and monolayer (1L) MoS_2 from left to right. The horizontal dashed line represents the energy of a band maximum at the K point. The red and blue lines represent the conduction and valence band edges, respectively. The lowest energy transition (indicated by the solid arrows) is direct (vertical) only in the case of a single layer. Indirect transition in monolayer (dashed arrow in 1L plot) is greater in energy than the direct band edge transition (solid arrow). (c) hexagonal Brillouin zone of multilayer (solid lines) and the monolayer (dashed lines) TMDCs. (d) Representation of the opposite spin–orbit splitting of the valence band at the K and K' $(-K)$ points. The purple and green parabolas represent spin-orbit-split band maxima/minima, each of which is associated with a particular electron spin. The red and blue arrows show how each band has different selection rules for circularly polarized light. (a) Is derived with publisher's permission from ref. [4]. (b) is derived with publisher's permission from ref.[3]. (c) is derived from ref.[5] and used under a CC-BY-3.0 license (d) was created by Wikipedia user 3113Ian and is used under a CC-BY-SA-3.0 license from https://en.wikipedia.org/wiki/File:K_valley_TMDC_monolayer.jpg

the K points—the lower energy of these transitions is called "A" while the higher energy is called "B". As Figure 1.7d diagrams, the different sets of K points have opposite electron spin selection rules for the two valence bands. This fact has allowed researchers to selectively spin-polarize a specific K valley using circularly polarized lasers. Given that the entirety of this dissertation details experiments which used linearly polarized lasers, the specifics of the spin selection rules are not important here.[2]

While many research groups acquire monolayer TMDCs from bulk crystals using mechanical exfoliation, the work in this dissertation relies on bottom-up growth of TMDC structures. One strategy involves evaporation of a transition metal onto a substrate followed by gaseous chalcogenation which yields smooth, polycrystalline thin films. A different strategy involves chemical vapor deposition, CVD, or chemical vapor transport, CVT.[3] My collaborator Yuzhou Zhao developed a CVT method to effectively synthesize many interesting microstructure morphologies of TMDCs (see Figure 1.8).[8] Yuzhou uses gaseous water as a transport agent according to the following chemical equilibrium

$$\mathrm{WS}_{2(s)} + \mathrm{H_2O}_{(g)} \underset{T_{sub}}{\overset{1200^\circ\mathrm{C}}{\rightleftharpoons}} \mathrm{WO}_x(\mathrm{OH})_{y(g)} + \mathrm{H_2S}_{(g)}(+\mathrm{H}_{2(g)}) \tag{1.4}$$

in which a volatile $\mathrm{WO}_x(\mathrm{OH})_{y(g)}$ species is formed at high temperatures from $\mathrm{WS}_{2(s)}$. The tungsten oxide/hyroxide gaseous complex is subjected to a temperature gradient and then deposits on the substrate (held at cooler temperatures) as $\mathrm{WS}_{2(s)}$. The temperature at which the $\mathrm{WS}_{2(s)}$ is deposited effectively controls the type of microstructure which is grown (Figure 1.8b). Yuzhou is able to grow monolayers (Figure 1.8c,f), few layer stacks (Figure 1.8d,g), and screw dislocation pyramids (Figure 1.8e,h). Yuzhou can also grow heterostructures of two different TMDCs using a similar methodology.

[2]Linearly polarized light is an even mixture of left and right handed circularly polarized light.

[3]Interestingly, CVT is the process used in halogen lamps to replenish the tungsten filament after it self-ablates onto the walls of the bulb; a halogen, like iodine, serves as the transport agent.

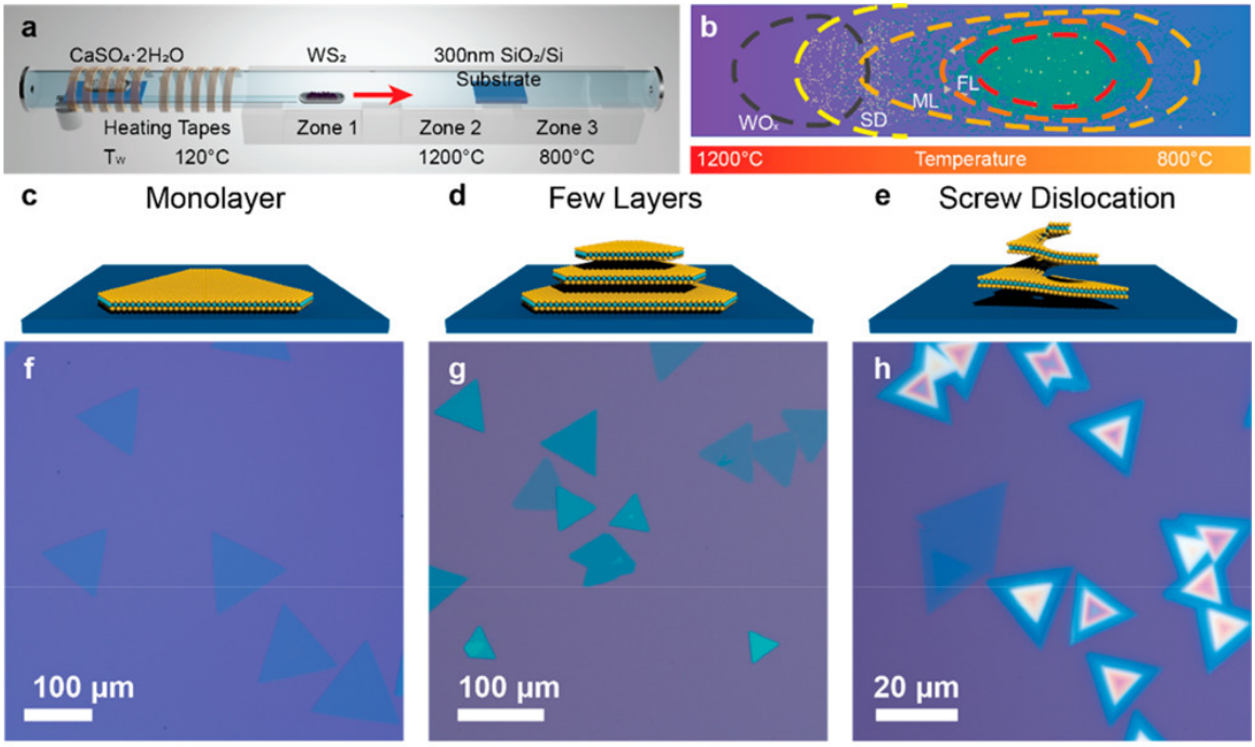

Figure 1.8: Overview of TMDC CVT growth methods developed by Yuzhou Zhao of the Prof. Song Jin group. (a) Schematic illustration of the experimental setup of WS_2 growth by water-assisted chemical vapor transport.(b) Schematic illustration of the representative spatial distribution of different WS_2 products on the 10 cm by 2 cm SiO_2/Si substrate: spiral nanoplates (SD, yellow), monolayer (ML, amber color), and few layers (FL, orange). The region enclosed by the black dashed circle is the major growth region of WOx byproduct. The schematic structures (c-e) and the optical microscopy images (f-h) of various WS_2 products: (c, f) monolayer, (d, g) few-layer nanoplate, (e, h) nanoplates with screw dislocations. This figure is adapted with publisher's permission from ref.[8].

1.3 Excitons

So far we have discussed the ability of light to excite an electron from a full valence band to an empty conduction band. Upon excitation, the electron leaves a positively charged "hole" from whence it came in the valence band. This hole is Coulombically attracted to the excited electron. When this Coulombic attraction is considered, it can be shown that bound states *below the conduction band* exist. These uncharged, bound states are called *excitons*.[4] When the effective radius (the Bohr radius) of an exciton is larger than the lattice spacing of its host semiconductor, it is called a Mott-Wannier exciton (Figure 1.9a); these excitons can move throughout the host material as a single particle. Excitons lead to strong, sharp optical transitions at energies below the band gap energy.

The Wannier equation, which is analogous to the Schrödinger equation of the hydrogen atom, describes the exciton eigenvalue problem. The solutions to the Wannier equation yields a set of bound excitons and a set of correlated (but not bound) electron-hole pairs. Some of these solutions are shown in Figure 1.9b. Just like dimensionality is important for the DOS of a semiconductor (Figure 1.3), it is also important for exciton transitions. The transition energies (referenced to the bandgap) for creation of bound excitons that look like the hydrogen s states are

$$E_\ell^{\mathrm{3D}} = -\frac{E_0}{\ell^2} \text{ with } \ell \in \mathbb{Z}^+ = \{1, 2, 3, \dots\} \tag{1.5}$$

$$E_\ell^{\mathrm{2D}} = -\frac{E_0}{(\ell + 1/2)^2} \text{ with } \ell \in \mathbb{Z}^* = \{0, 1, 2, \dots\}, \tag{1.6}$$

in which $E_0 = \frac{e^4 m_r}{2\varepsilon_0^2 \hbar^2}$ is the exciton Rydberg energy with reduced mass m_r. These bound excitons form an infinite collection which seamlessly meets with the continuum at the bandgap. The difference in energy between the bandgap and the first exciton transition is the *binding energy*, E_b, which is E_0 in 3D and $4E_0$ in 2D. So 2D systems have their first exciton better separated from the continuum by a factor of 4 more than 3D systems. An example of what an absorption

[4] As I write this, physicist Philip Anderson's death is reported in *Science*.[9] Anderson was a champion of emergent phenomena (of which excitons are an example).[10] Excitons are simply formed quasi-particles, but their behavior can be far more complex and different than their constituent electrons and lattice holes. One such example is that excitons, unlike their Fermionic constructors, are Bosons and can thus condense into a Bose-Einstein Condensate which is categorically not possible for electrons.[11]

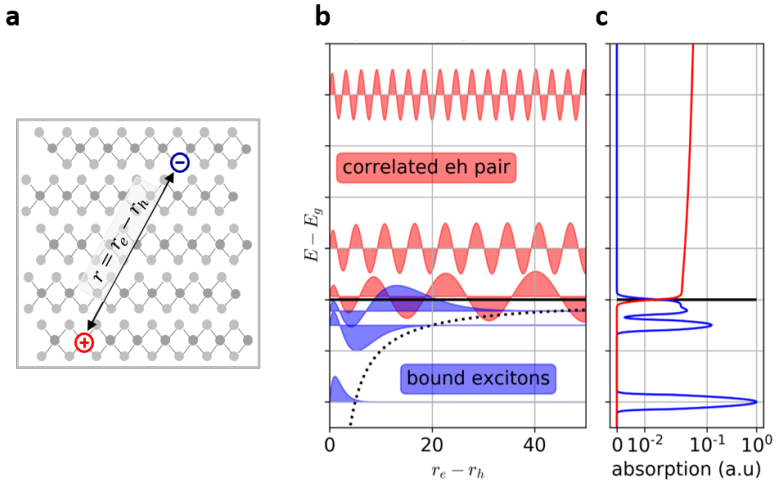

Figure 1.9: Excitonic wavefunctions. (a) schematic of Mott-Wannier exciton in a periodic lattice. (b) schematic of the radial wavefunction of an electron-hole pair after excitation in a direct gap semiconductor. The Coulomb potential is shown as a black, dotted line. Observe how the wavefunction are modified as they extend over the Coulomb potential well, this modification leads to the "Sommerfeld factor" which modifies the absorption spectrum. (c) the corresponding absorption spectrum with contributions from the bound (blue) and unbound (red) components. (a) is heavily adapted from ref.[12] with permission from the corresponding author and publisher. (b) and (c) were originally created by my colleague Dan Kohler—see `git.chem.wisc.edu/dkohler/background-semiconductor-optics` for the source code.

spectrum of an excitonic system would look like at cryogenic temperatures is shown in Figure 1.10. Note how only the first few excitonic transitions are apparent before their lineshapes congest each other. At room temperature, usually only the first transition is distinguishable. Also note that the continuum absorption is no longer a step-function or square-root curve as diagramed in Figure 1.3—the Coulomb potential modifies the unbound transitions. This modification of the DOS is called *Sommerfeld enhancement*.

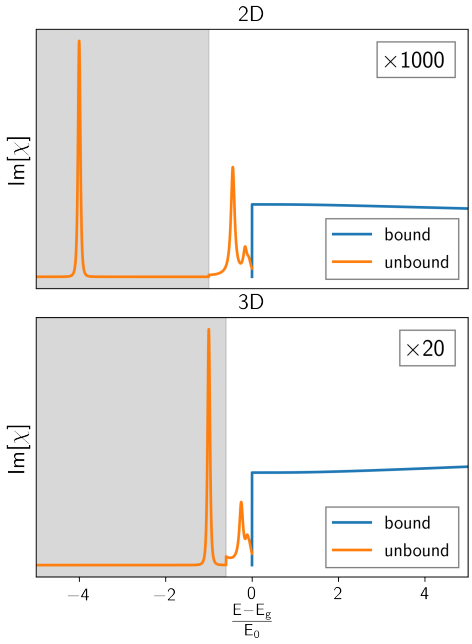

Figure 1.10: Excitonic Rydberg series and continuum absorption in normalized coordinates for 2D and 3D systems. The first excitonic transition is artificially suppressed. The Lorentzian broadening function for the Rydberg series has $\Gamma = E_0/20$.

Excitons in TMDCs like MoS_2 and WS_2 monolayers have extremely large binding energies (on the order of 0.5 eV) so more than just the first transition may be observed. Unlike 3D excitons in a bulk material, the Coulomb interaction binding the electron and hole together in monolayer TMDCs is spatially inhomogeneous. The dielectric environment outside of the monolayer is far less polarizable than the environment within the plane (see Figure 1.11a) which leads to the exciton series being modified. This type of effect leads to the dielectric environment outside of the material having significant influence on the excitons within the material.[13] The excitons in monolayer TMDCs also have rich spatial structure. For instance, Figure 1.11c shows the electron distribution of the first

exciton peak present in MoS_2's absorption spectrum. Conversely, an exciton peak present ~ 0.7 eV higher in the absorption spectrum has its electron distribution shown in Figure 1.11d—this exciton has a much tighter spatial distribution in some directions.

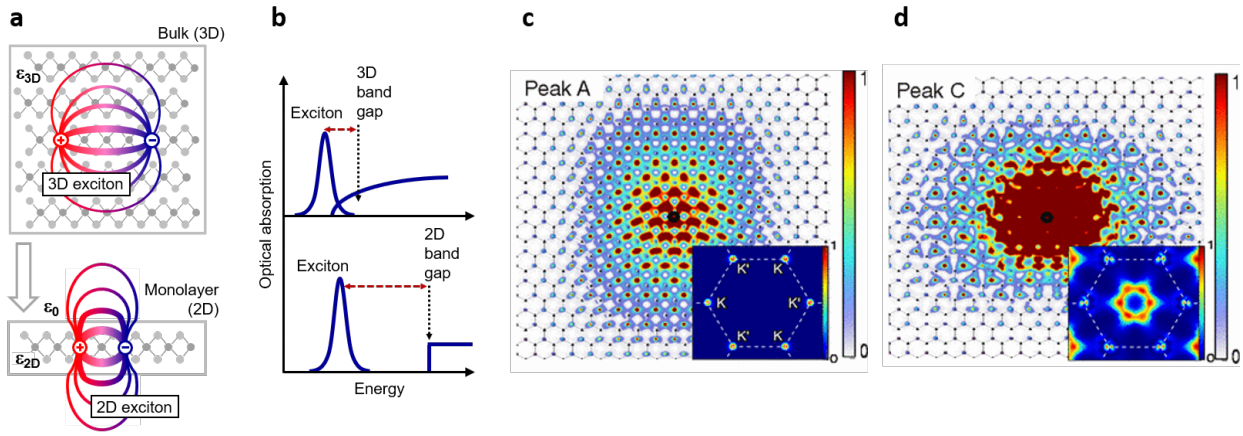

Figure 1.11: Excitons in TMDCs. (a) Real-space representation of electrons and holes bound into excitons for the three-dimensional bulk and a quasi-two-dimensional monolayer. The changes in the dielectric environment are indicated schematically by different dielectric constants ε_{3D} and ε_{2D} and by the vacuum permittivity ε_0. (b) Impact of the dimensionality on the electronic and excitonic properties, schematically represented by optical absorption. The transition from 3D to 2D is expected to lead to an increase of both the band gap and the exciton binding energy (indicated by the dashed red line). The excited excitonic states and Coulomb correction for the continuum absorption have been omitted for clarity. (c, d) Exciton corresponding to the A and C features of the absorption spectrum shown in real space and in k space (inset) and calculated using the GW-Bethe-Salpeter equation. The real-space plot is the modulus squared of the exciton wave function projected onto the plane with the hole (black circle) fixed near a Mo atom. Mo atoms are purple squares, and sulfur atoms are green triangles. (a,b) are reproduced from ref.[12] while (c,d) are adapted from ref.[14] both with permission from the publisher.

1.4 Nonlinear spectroscopy

So far in this Introduction we have considered what the absorption spectrum of specific material systems look like. We have seen that the absorption spectrum gives insights into the electronic and vibrational structure of the system. An absorption measurement is an example of a *linear* spectroscopy—a method which depends linearly on applied field strength. In this section, I will introduce nonlinear spectroscopies. As the name implies, these methods depend on the the response of the material system scaling nonlinearly with applied field strength.

When an electric field, E, passes through a material, it creates a polarization, P.[5] This polarization, if it is oscillating in time, can emit new electric fields. For linear optics, the polarization depends linearly on electric field strength

$$P = \epsilon_0 \chi^{(1)} E, \tag{1.7}$$

in which $\chi^{(1)}$ is the linear susceptibility and ϵ_0 is the permittivity of free space. If the polarization instead depends nonlinearly on the electric field strength, we can express the polarization as a power series in E

$$P = \epsilon_0 \left[\chi^{(1)} E + \chi^{(2)} E^2 + \chi^{(3)} E^3 + \cdots \right]. \tag{1.8}$$

$\chi^{(n)}$ is known as the n-th order optical susceptibility. In general, $\chi^{(n)}$ are tensors and $\chi^{(2n)} \neq 0$ only when the material system lacks inversion symmetry.

Much of this dissertation is concerned with the following processes: second harmonic generation, SHG, third harmonic generation, THG, sum-frequency generation, SFG, and triple-sum-frequency, TSF. These processes are diagrammed in Figure 1.12 which shows how multiple electric fields can impinge on a material and cause a new electric field of a different, new frequency to radiate from the material.

In order to understand how these processes arise from a mathematical perspective, we will consider

[5] P is the dipole moment per unit volume.

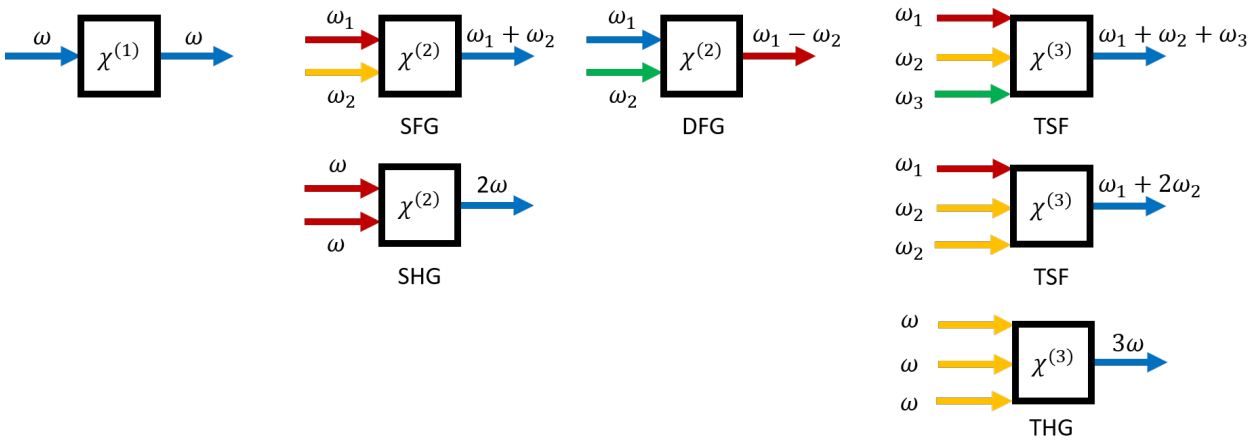

Figure 1.12: Mixing processes. The ability of a material to efficiently mix electric fields of various frequencies is a unique fingerprint of the material. Crucially, the output can be a different color and direction than the inputs.

the case of SHG and SFG. Consider a plane-wave form for the incident electric field with two frequency components $\{\omega_1, \omega_2\}$ and wavevectors $\{\mathbf{k}_1, \mathbf{k}_2\}$

$$\tilde{E}(t) = \frac{E}{2}\left[\exp\left[i(\mathbf{k}_1 \cdot \mathbf{r} - \omega_1 t)\right] + \exp\left[i(\mathbf{k}_2 \cdot \mathbf{r} - \omega_2 t)\right]\right] + \text{c.c.} \tag{1.9}$$

If only one of these frequency components were present, then $\tilde{E}(t)$ would be a simple, monochromatic cosine wave. Substitution of Equation 1.9 into Equation 1.8 yields (keeping only terms up to second order)

$$\begin{aligned}
\frac{P}{\epsilon_0} = &+ \chi^{(1)}\tilde{E}(t) \\
&+ \chi^{(2)}E^2 \exp\left[i(((\mathbf{k}_1 + \mathbf{k}_2)\cdot\mathbf{r} - (\omega_1 + \omega_2)\,t)\right] + \text{c.c.} \\
&+ \frac{\chi^{(2)}E^2}{2}\left\{\exp\left[i\,(\mathbf{k}_1 \cdot \mathbf{r} - 2\omega_1 t)\right] + \exp\left[i\,(\mathbf{k}_2 \cdot \mathbf{r} - 2\omega_2 t)\right]\right\} + \text{c.c.} \\
&+ \chi^{(2)}E^2 \exp\left[i\,((\mathbf{k}_1 - \mathbf{k}_2)\cdot\mathbf{r} - (\omega_1 - \omega_2)\,t)\right] + \text{c.c.} \\
&+ 2\chi^{(2)}E^2,
\end{aligned} \tag{1.10}$$

where complex-conjugation is on a line-by-line basis. The first line of Equation 1.10 is the linear interaction of the electric field, the second line corresponds to SFG, the third line to SHG of each fundamental, the fourth line to DFG, and the fifth line to optical rectification, OR. All of these processes happen simultaneously. Note that the different processes come out in different

directions as identified by the wavevector contributions.[6] These output directions are diagrammed in Figure 1.13a.

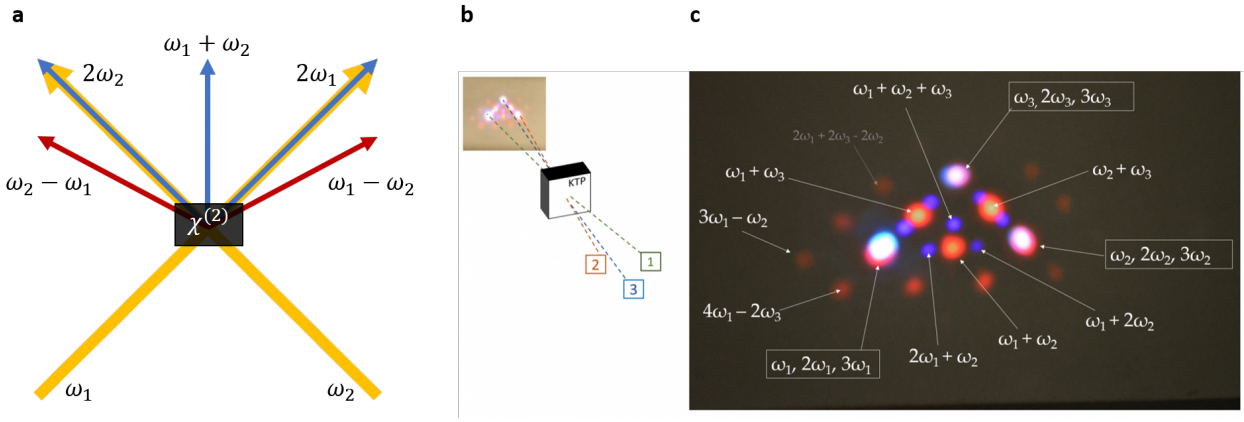

Figure 1.13: Spatial output of mixing processes. (a) Three-wave mixing projected onto z-x plane. (b,c) Many-order mixing in KTP. (b) Schematic of mixing process shown in (c). (c) Cell phone camera image of many-wave mixing after the KTP crystal imaged onto a white-card (y-x plane). Input lasers are set to 0.95 eV (1300 nm). (b,c) were annotated by Natalía Spitha. The photograph was acquired by Blaise Thompson and myself.

The same mathematical strategy as used to construct Equation 1.10 may be used to construct a third order polarization with three input waves. The equation is cumbersome (so it is not shown here), but seeing it in the lab is breathtaking. Figure 1.13c shows second, third, and higher order processes all exiting a KTP crystal and imaged on a card. The input lasers form the saturated vertices of the inner triangle. SFG (red) processes are at the midpoints of the triangle's edges. TSF (purple) is in the center of the triangle.

As is evidenced by absorption spectra having structure and not merely being flat, Equation 1.10 is hiding important details—the material's electric field frequency dependent response is encoded in χ. The frequency domain form of Equation 1.10 should actually have variants of $\chi^{(2)}$ depending on the process under consideration. The prefactors should be

- $\chi^{(2)}\left(-(\omega_1+\omega_2), \omega_1, \omega_2\right)$ for SFG,
- $\chi^{(2)}\left(-2\omega_1, \omega_1\right)$ and $\chi^{(2)}\left(-2\omega_2, \omega_2\right)$ for SHG,
- $\chi^{(2)}\left(-(\omega_1-\omega_2), \omega_1, \omega_2\right)$ and $\chi^{(2)}\left(-(\omega_2-\omega_1), \omega_1, \omega_2\right)$ for DFG,

[6] If the two input electric fields are propagating colinearly and incident normal to the mixing medium, then all of the processes will be spatially overlapped with each other.

- and finally $\chi^{(2)}(0, \omega_1)$ and $\chi^{(2)}(0, \omega_2)$ for OR.

These susceptibilities are written not only to emphasize their functional dependence on the input frequencies, but also to notate which output process is being considered. This frequency dependence is important because while nonlinear processes are useful for technological applications like frequency conversion of a laser (e.g. green laser pointers generally use SHG to convert a near-IR laser into 532 nm light), there is also rich quantum mechanical information encoded in the susceptibilities as a function of frequencies. Multiple electric field interactions are needed to form a nonlinear polarization—these multiple interactions may be facilitated by multiple quantum mechanical states.

In general, the material's electronic and vibrational structure may be assessed by observing how large of a polarization is built-up in the material for a given set of excitation conditions. When the frequency difference between states matches the driving laser frequency, the created material polarization is large, thus relative state energies may be measured. The strength of the polarization also depends on the transition moment between states which can give insight into the spatial overlap of states. The Wright group has spent decades making spectroscopies which leverage these facts to learn about molecular systems.

1.4.1 Triple sum-frequency spectroscopy

Much of this dissertation revolves around TSF and its degenerate analog, THG. At the time that I started graduate school, all of the TSF work had been accomplished on solution-phase molecular systems[15, 16, 17] or on carbon monoxide on a ruthenium surface.[18] Since I started graduate school, more work has been published on TSF by the Wright group and the Bonn group at the Max Planck Institute.[19, 20, 21, 22] All of these works are interested in using TSF to measure mixed vibrational-electronic coupling. TSF has been touted as a "resonance-IR" analog in that it has vibrational and electronic state sensitivity like resonance-Raman, but it uses IR transitions and not Raman transitions.[17]

Figure 1.14 shows a cartoon calculation of how multidimensional TSF can be used as an analytical

tool to see if a solution has only one or multiple species in it. If a system has coupled vibrational and electronic states, then TSF can adjudicate among the species in a mixture by telling if some vibrational modes are only coupled to some electronic transitions in one type of molecule while other vibrational modes are coupled to other electronic states in a different molecule. In this way, TSF is envisioned as a useful analytical tool.

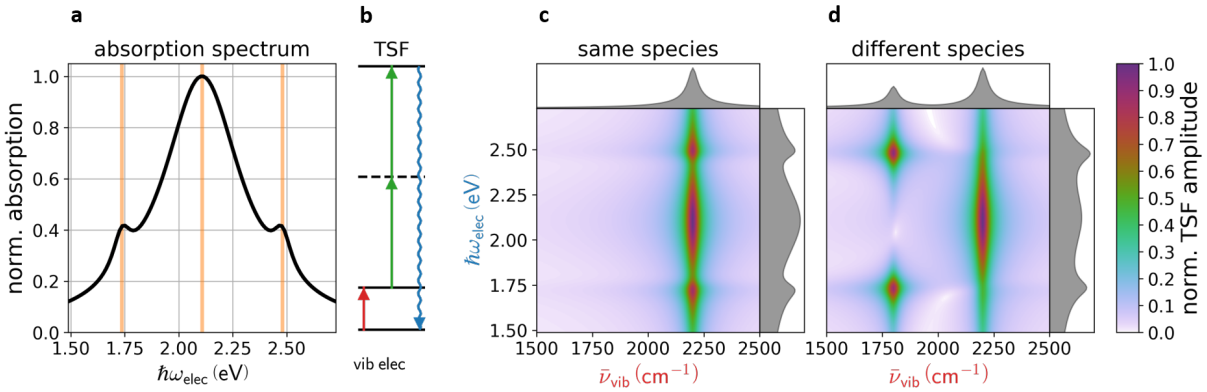

Figure 1.14: Schematic of TSF's ability to interrogate a complex mixture. (a) simulated absorption spectrum of a mixture in which it is not known if there is one or two components. (b) two color TSF WMEL: the first interaction creates a vibrational coherence and the next two interactions create an electronic coherence which then radiates. (c) the TSF spectrum expected if there is only one species in the solution—one vibrational state couples to three electronic states. (d) the TSF spectrum expected if there are two species in the solution—one vibrational state couples to two electronic states and another vibrational states couples to a single electronic state.

I originally hypothesized that TSF ought to be able to interrogate the electronic structure of semiconductors. Specifically, TSF can measure the energy difference of four different bands (integrated across crystal momentum). This measurement would be analogous to measuring a multidimensional joint density of states. The critical points in this multidimensional joint density of states would yield large TSF intensities (Figure 1.15b,c). This use of TSF would be an all-optical method in comparison to techniques like angle resolved photoemission spectroscopy (ARPES) and its excited-state variant time-resolved-ARPES (TR-ARPES) which can measure momentum resolved bandstructures of materials, but require ultra-high vacuums, deep-UV or X-Ray sources, and hemispherical electron detectors.[23] In order to access the bandstructure of materials like TMDCs using TSF, a very large tuneable laser bandwidth is needed.

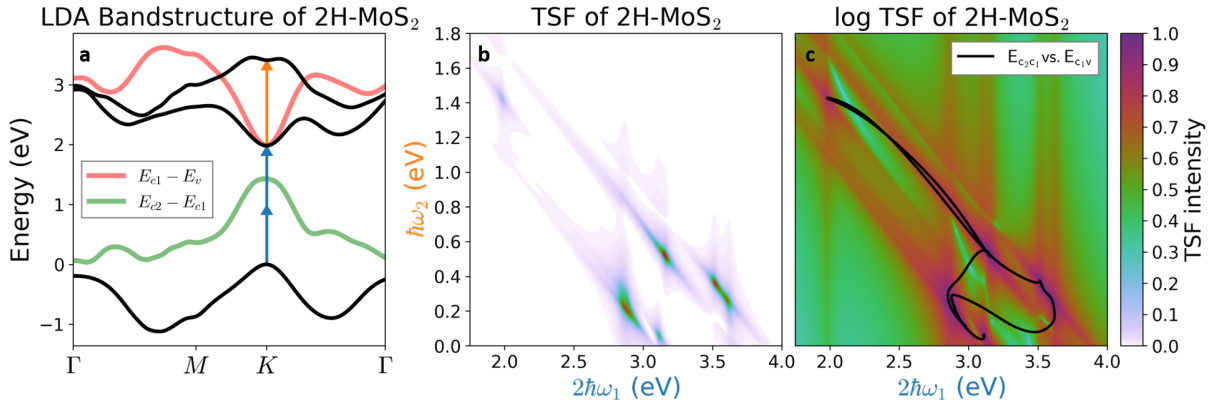

Figure 1.15: Schematic of TSF's ability to interrogate a semiconductor. (a) LDA bandstructure (no SOC) of MoS_2 showing the highest valence band and the lowest two conduction bands. The energy difference between the valence and first conduction band (red) and between the two conduction bands (green) are also shown. (b,c) Two color TSF spectrum calculated assuming that dipole moments are not momentum dependent. Regions of high intensity correspond to joint critical points in $E_{c_2c_1}$ and E_{c_1v}.

1.4.2 Pump-probe spectroscopy

Photoexcited semiconductors form the basis for photovoltaics like solar cells and the sensors in cameras. The processes and timescales that occur for a photo excitation in a semiconductor span many orders of magnitude (see Figure 1.16). The fastest cameras available do not have sufficient time resolution to watch processes like carrier thermalization and carrier-carrier scattering happen. Instead, optical scientists have developed a set of techniques called *pump-probe* spectroscopy. These techniques rely on ultra-short bursts of light to first pump (excite) the system and then probe the system some time later. The temporal length of the pulses dictates the shortest timescale able to be resolved by the pump-probe method. To this end, pulses shorter than 10 fs are now common in ultrafast chemistry/physics labs.

Figure 1.17 shows the basics of a common variant of pump-probe spectroscopy: transient transmittance (absorbance). A narrowband pump excites the sample. Then some time later (controlled by a mechanical delay stage),[7] a probe pulse with intensity $I_0(\hbar\omega)$ passes through the sample. The

[7]The pump and probe often originate at the same source. The mechanical delay stage causes the pump and probe to traverse different amounts of space and therefore arrive at the sample at different times.

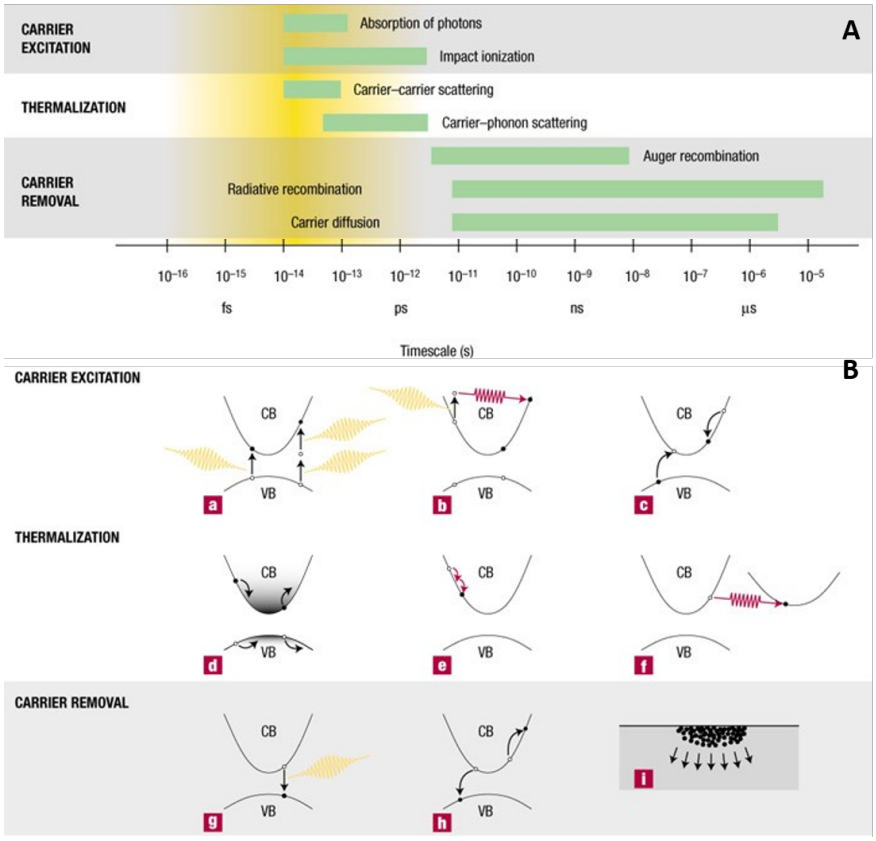

Figure 1.16: (A) Timescales of various electron and lattice processes in laser-excited solids. Each green bar represents an approximate range of characteristic times over a range of carrier densities from 10^{17} to 10^{22} cm^{-3}. The yellow highlighted region shows the common lengths of optical pulses used to interrogate semiconductors (B) Electron and lattice excitation and relaxation processes in a laser-excited direct gap semiconductor. CB is the conduction band and VB the valence band. (a) Multiphoton absorption. (b) Free-carrier absorption. (c) Impact ionization. (d) Carrier redistribution before scattering. (e) Carrier–carrier scattering. (f) Carrier–phonon scattering. (g) Radiative recombination. (h) Auger recombination. (i) Diffusion of excited carriers. This figure is adapted from ref.[24] with the publisher's permission. Note, ref.[24] adapted their figure from ref.[25].

sample's ability to absorb some of the broadband probe light is measured, $I(\hbar\omega)$. The absorbance is given by Beer's law

$$A(\hbar\omega) = \log\left(\frac{I_0(\hbar\omega)}{I(\hbar\omega)}\right). \tag{1.11}$$

Next, the pump pulse is blocked by an optical chopper, and the probe absorption is again measured with the change in absorbance being calculated by

$$\Delta A = A_{\text{pumped}} - A_{\text{unpumped}} \tag{1.12}$$

$$= \log\left(\frac{I_{\text{unpumped}}}{I_{\text{pumped}}}\right). \tag{1.13}$$

By changing the pump-probe time delay, the pump color, the pump intensity, etc the dynamics and energetics of a system may be quantified.

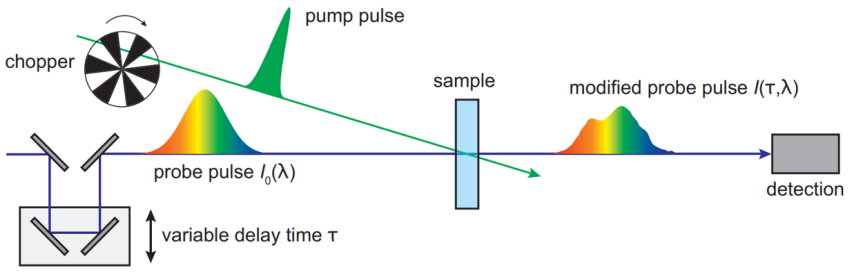

Figure 1.17: Schematic representation of a pump–probe experiment to measure photoinduced dynamics. In the transient absorption technique, an optical pump pulse excites the sample whereas a temporally delayed probe pulse measures the pump-induced change in the sample's absorbance. The wavelength-dependent intensity of the probe spectra is measured with and without the pump interaction. This figure is reproduced from ref.[26] and used under a CC-BY-NC-ND license.

When using pump-probe methods, we are interested in how a material's electronic or nuclear states are evolving as a function of time or other variables. However, we are not able to directly assess these states. Instead, we measure their evolution indirectly by observing how a sample's transmittance or reflectance are changed by photoexcitation. Consider the first row of Figure 1.18 which shows how an absorbance spectrum might change upon excitation of a material. Many pump-probe measurements can only measure differences in a material's spectrum—the second row of Figure 1.18. Decreases, shifts, and broadening of an absorption feature are all due to underlying changes in a material's electronic structure. However, extreme caution must be taken in connecting the thing

which may be observed (changes in a transmittance spectrum) with dynamical mechanisms of the semiconductor: Pauli blocking, band gap renormalization, carrier-carrier scattering, etc.

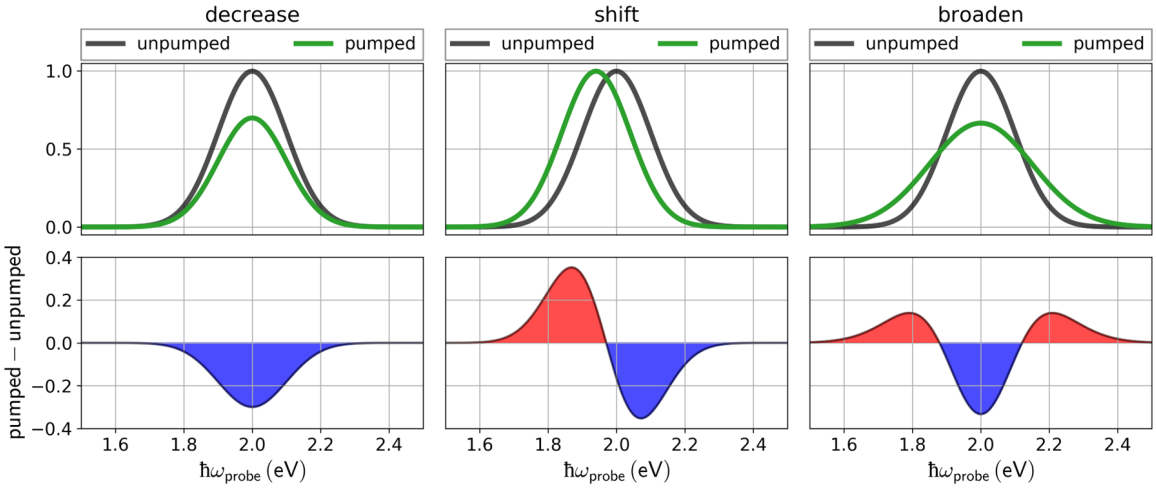

Figure 1.18: Calculated examples of pump-induced spectrum changes. Top row shows pumped and unpumped Gaussian spectra for decrease in oscillator strength, shift in entire spectrum, and broadening of spectrum. Bottom row shows the difference between the pumped and unpumped spectrum.

Some of the work in this dissertation uses transient-reflectance spectroscopy to watch carrier evolution. Other parts of this dissertation focus on developing *new* pump-probe methods in which the probe is not merely a photon being reflected or transmitted through the sample. Instead the probe in these new methods is a SHG or TSF probe. The primary idea is that the strength of TSF in measuring how multiple states are coupled together may be extended to measuring the photo-excited dynamics of these couplings.

1.5 OPAs and the laser table

Previously in this Introduction, I argued that methods like TSF can offer powerful insight into the quantum mechanical structure of materials. The utility of these methods relies on being able to scan the frequency of multiple lasers across transitions of interest. The experiments presented herein rely on two optical parametric amplifiers, OPAs, (TOPAS-C, Light Conversion). These OPAs utilize multiple stages of parametric processes to generate and amplify new colors of light.[27, 28] Specifically, the TOPAS-C accomplishes parametric down conversion (PDC) twice. This second-order nonlinear process is accomplished in β Barium Borate (BBO), is the opposite of SFG, and turns one photon into two lower energy photons. It follows the following frequency and momentum conservation rules

$$\hbar\omega_{\text{pump}} = \hbar\omega_{\text{signal}} + \hbar\omega_{\text{idler}} \tag{1.14}$$

$$\mathbf{k}_{\text{pump}} = \mathbf{k}_{\text{signal}} + \mathbf{k}_{\text{idler}} \tag{1.15}$$

in which by convention $\omega_{\text{pump}} > \omega_{\text{signal}} > \omega_{\text{idler}}$.[8] The TOPAS-C is specified by the manufacturer to be able to create signal frequencies from 0.77 eV to 1.08 eV and idler frequencies from 0.47 eV to 0.77 eV with a pump frequency of 1.55 eV. This basic tuning range does not define the absolute limits of the OPA, however. Signal, idler, and remaining pump photons can be mixed again in subsequent difference-frequency and sum-frequency crystals to produce scannable light from the mid-infrared to the ultra-violet. Figure 1.19 shows the ranges that are accessible using a TOPAS-C with up to two mixing stages after the original Signal and Idler generation. This ultra-broadband scannable range allows OPAs to be used in a diverse set of situations.

Figure 1.20 shows a block diagram of a TOPAS-C OPA. The OPA is pumped with an ultrafast 1.55 eV (800 nm) electric field from a Ti:sapphire amplifier. The pump is split into 3 parts. The first part is focused into a sapphire crystal and forms a white-light supercontinuum. The white light is stretched and chirped in time by passing through a thick ZnSe crystal. The near-IR component of the white light serves as a seed for PDC in crystal 1. This seed is mixed with part 2 of the

[8] Ensuring that the equality posited in Equation 1.15 is true is called "phase-matching".

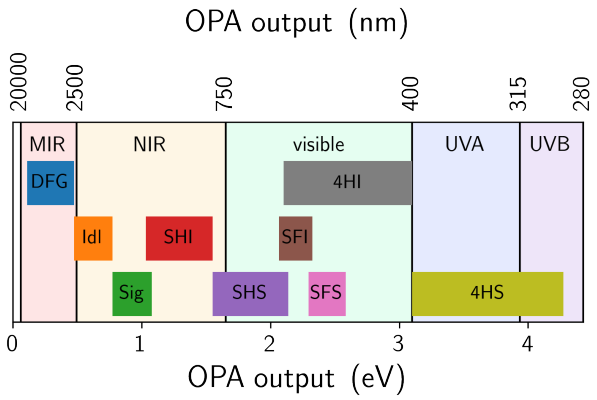

Figure 1.19: Tuning range of a Light Conversion TOPAS-C using many different nonlinear processes.

split pump; the desired color from crystal 1 is selected for by time gating (choosing which part of the chirped white light to amplify) and phase-matching (crystal angle). The near-IR output from crystal 1 is then mixed with the third, and largest part, of the split pump in crystal 2. In short, the color of the signal and idler output from the OPA may be tuned by changing crystal angles and time delays.

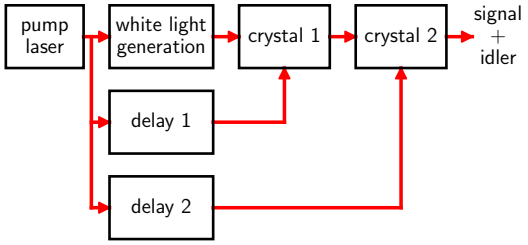

Figure 1.20: Block diagram of OPA showing laser beampaths.

Figure 1.21 diagrams how the two outputs of the OPAs progress through the rest of the laser table. Oftentimes additional filters and polarizers are placed between the mixer and delay stage to select for the correct process out of the OPA (e.g. selecting idler vs. signal).

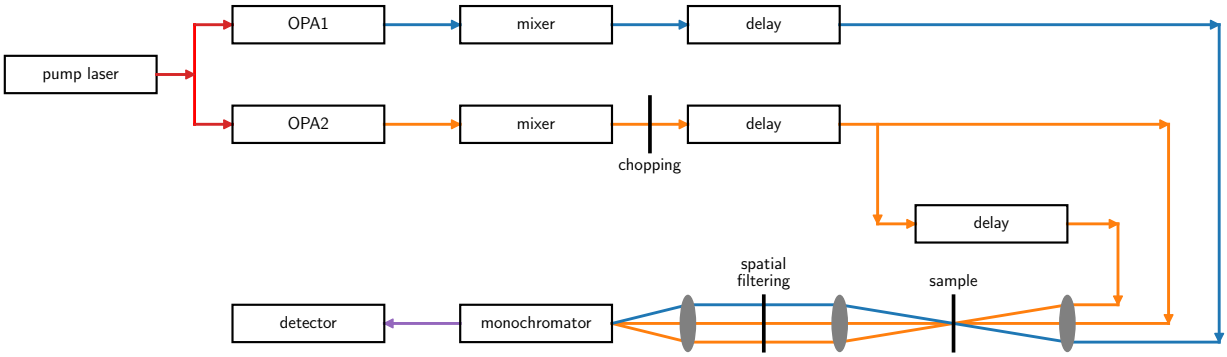

Figure 1.21: Schematic of laser table. Even though focusing optics are displayed as transmissive lenses, they are actually fully reflective focusing optics.

1.6 Overview of remaining chapters

When I joined the Wright group, I set out to investigate coherence transfer charge migration in TMDC vertical heterostructures (the Great White Whale of the Wright Group). I initially hypothesized that TSF would allow me to observe coherence transfer. At this time, TSF had only been accomplished in molecular systems. My goal was to extend TSF to semiconductors; so I set up experiments to observe TSF in a few layer thick MoS2 thin film using two near-IR lasers.

1.6.1 Chapter 2 overview

Instead of observing distinct cross-peaks as I changed the colors of the two lasers and observed the TSF output from the back of the sample, I observed drastic, fine fringes. Chapter 2 details our analysis of these fringes. Notably, this work did not provide any information about semiconductors because all of the TSF intensity that I observed was due to the half millimeter thick substrate that supported my nanometer thick film. The fringes are a manifestation of a now well-established phenomena: velocity-mismatch. TSF works by multiple (infra)red waves of light creating a disturbance (polarization) in the material which then emits a blue(r) wave of light. The efficiency of the TSF process is determined by how much energy the red wave can impart into the blue wave. For most materials (including my substrate) red light waves travel faster than blue light waves. For

TSF, this means that the intense red wave cannot efficiently feed a contiguous blue wave. Instead, as the red wave travels through the material it keeps starting new blue waves, which never are fed long enough by the red wave to become large in amplitude. Eventually these blue waves all exit the material and hit the detector, where they interfere with each other (as waves do). The net constructive or destructive interference of these blue waves determines if I detect any TSF. Importantly, the balance between construction and destruction is determined by the color of the input lasers.

After some sophomore-level electromagnetism mathematics, an analytic model presented itself. It became clear that using substrates thicker than a few microns would always lead to fringes, which would obscure the semiconductor response I sought. Given that semiconductor samples do not generally levitate, I proposed to use a backwards-propagating experimental geometry for future measurements. In a backwards-propagating (reflective) geometry, the only part of the sample/substrate that contributes to the measured signal is that which is on the order of the wavelength of light. This is advantageous for two reasons:

1. the sampled depth is not enough to cause velocity-mismatch fringes,
2. and the resonant signal from the thin semiconductor sample (low number density) is not overpowered by the nonresonant background signal from the substrate (high number density).

1.6.2 Chapter 3 overview

When switching to a backwards propagating geometry, I realized that the driving laser could not only reflect off of the front of the sample/substrate but also reflect off of the back of the substrate. This backwards propagating fundamental would lead to substrate contributions again. Therefore, I had a MoS_2 polycrystalline thin film grown on a prism substrate. This curious substrate geometry causes any TSF fed by the backwards propagating fundamental to exit the front face of the sample at the same angle as the desired semiconductor TSF, but at a slightly different spatial location. Serendipitously, the pathlength of this substrate TSF is long enough such that all of the mismatch fringes are tightly packed together and a few tricks with monochromator settings makes the fringes inconsequential to the measurement.

When I finally achieved TSF off of MoS_2, the 2D spectra had some broad peaks and a large antidiagonal trough. Neither the peak positions nor the existence of the trough made sense to me. After using the substrate TSF to correct for my instrument's OPA frequency dependent response, the broad peaks were no longer present, however the trough persisted. By using different OPA tuning ranges I was also able to resolve the spin-orbit split A and B resonances which presented as antidiagonal lines.

It became clear to us that our lasers were not able to couple more than two quantum states together. Our complicated TSF spectroscopy was singly resonant and presumably accessing the same states as absorption spectroscopy. So, we built a model to compare our TSF results to absorption and second harmonic generation (SHG) measurements. Because absorption, SHG, and TSF all have different scaling rules for transition moments and joint density of states, we were able to extract them from our measurements. Our results conclusively show that the "C" feature seen in the MoS_2 absorption spectrum is not exclusively due to an excitonic transition, but instead is due to a phenomena called band nesting.

1.6.3 Chapter 4 overview

Chapter 4 extends the work of Chapter 3 to the measurement of carrier *dynamics* by developing pump-TSF-probe spectroscopy. By preceding the TSF pulse sequence with a pump, TSF is able to probe an excited semiconductor. We demonstrate pump-TSF-probe on both MoS_2 and WS_2 thin films and spiral nanostructures. We compare the pump-TSF-probe results to transient-reflectance (TR) measurements on the same samples. Pump-TSF-probe and TR recover the same changes in quantum states. However, we found that TR suffers in sensitivity when surface coverage is low, but pump-TSF-probe does not. In short, pump-TSF-probe may be useful when working with samples of diverse morphology and low surface coverage.

Chapters 3 and 4 show that TSF and pump-TSF-probe are viable methods in semiconductors. However, I did not have the laser table tuning bandwidth needed to couple multiple bands together. The PMT I used in my work does not have a blue-enough response explore the frequency ranges that Figure 1.15 predicts we will need for TMDCs. I believe TSF has a bright future in semiconductor

science. Demonstration of its utility will require a careful choice of semiconductor with multiple bands accessible by near-IR lasers, or switching detection to a microchannel plate detector based system.

1.6.4 Chapter 5 overview

While both accomplishing the work presented in Chapter 4 and working on side projects, it became apparent to me that pump and probe scatter is a major issue when working with micro-structured semiconductors. This pump scatter can saturate the dynamic range of a measurement (c.f. ref.[29]) or obscure important features in the data set (c.f. ref.[30]). A dual-chopping routine can remove some pump scatter problems, but a dual chopping routine does not remove amplitude-level interference and fails if the detector is saturated. I hypothesized that combining a multiphoton absorption excitation with THG or SHG (optical harmonic generation, OHG) probing would solve the scatter problem. All lasers would be in the near-IR—a color range that the PMT used for detecting the OHG output is not able to observe.

An aspect of a two-photon-absorption pump which I had not considered involved the affects of the high laser intensities needed to build up a population. These high intensities caused the excitonic resonance to blueshift via the Optical Stark Effect. However, the normal blueshift of the Optical Stark Effect could not explain many of our observations. Chapter 5 shows a new manifestation of the Stark Effect, brought forth by photon exchange between the pump and probe fundamental fields, can produce strong modulations of the OHG signal and is thus promising for applications. We develop a model built on perturbation theory to explain our results. We also look at many different WS_2 morphologies to see if sample morphology influences the observed response. We find that morphology influences the competition between the Optical Stark Effect and multiphoton absorption processes.

1.6.5 Chapter 6 overview

The previous chapters are primarily focused on developing new spectroscopies and using multilayer TMDCs as a model system. In this chapter we use a water vapor assisted chemical vapor transport synthesis to create monolayer WS_2-MoS_2 core-shell lateral heterostructures in a Si/SiO_2 substrate. Out-of-plane (vertical) heterostructures have been extensively characterized in the literature using ultrafast spectroscopies, however their in-plane (lateral) counterparts have not had their ultrafast dynamics and energetics characterized.

I set out to measure charge transfer dynamics across the 1D junction present in the lateral heterostructures. For a long time I was perplexed by the multidimensional transient-reflectance lineshapes I measured; in some cases these lineshapes were flipped compared to the data I acquired on MoS_2 thin films. However, I was eventually able to reconcile the lineshapes after implementing a Fresnel model which accounts for interference effects from the stratified substrate. Despite the supposed Type-II band alignment, I found no evidence of ultrafast charge separation or coupling between the MoS_2 and WS_2 structures.

1.6.6 Chapter 7 overview

Like the previous chapters, Chapter 7 shows nonlinear spectroscopy results on a layered material. However, instead of TMDCs, Chapter 7 looks at Ruddlesden-Popper (RP) lead halide perovskites quantum wells with various well thicknesses and spacer ligands. Scientists working with these materials often find that single-crystal X-Ray diffraction does not conclusively determine the symmetry group of their newly synthesized material. SHG measurements, which can determine if the material is centrosymmetric or not, are often paralyzed by a multiphoton photoluminescence background from the material.

In Chapter 7 I present a simple, multidimensional variation of the normal SHG measurement. By scanning and correlating both excitation and emission frequencies, we un-ambiguously assess whether a material supports SHG by examining if an emission feature scales as twice the excitation frequency. Measurements of a series of $n = 2$ and $n = 3$ RP perovskites reveal that, contrary to

previous belief, *n*-butylammonium (BA) RP perovskites display no SHG, thus they are centrosymmetric.

Chapter 2 Group- and phase-velocity-mismatch fringes in triple sum-frequency spectroscopy

This Chapter borrows extensively from Morrow, Kohler, and Wright [31]. The authors are:

1. *Darien J. Morrow*
2. *Daniel D. Kohler*
3. *John C. Wright*

2.1 Abstract

The effects of group and phase velocity mismatch are well-known in optical harmonic generation, but the non-degenerate cases remain unexplored. In this work we develop an analytic model which predicts velocity mismatch effects in non-degenerate triple sum-frequency mixing, TSF. We verify this model experimentally using two tunable, ultrafast, short-wave-IR lasers to demonstrate spectral fringes in the TSF output from a 500 μm thick sapphire plate. We find the spectral dependence of the TSF depends strongly on both the phase velocity and the group velocity differences between the input and output fields. We define practical strategies for mitigating the impact of velocity mismatches.

2.2 Introduction

Triple sum-frequency, TSF, generation is a multicolor four-wave mixing process in which the generated electric field has an output frequency defined by the sum of all three driving fields. TSF is the four-wave mixing extension of sum-frequency generation (SFG), a three-wave mixing, ladder-climbing process, and the multicolor extension of third-harmonic generation (THG). In TSF, three electric fields drive an oscillating nonlinear polarization which generates the measured TSF field as defined by the medium's susceptibility. This susceptibility is the sole source of analyte information. In TSF, the driving lasers' frequencies are scanned; when a driving field is resonant with a state, the susceptibility becomes large and the TSF intensity dramatically increases. Wright and coworkers are actively developing TSF as an analytical methodology which is sensitive to vibrational-electronic state coupling.[15, 16, 17, 32]

It is well known that spectroscopies which are defined by the sum of their driving frequencies and accomplished in normally dispersive samples cannot be phase-matched. This means that the emitted TSF field cannot maintain a cooperative phase relationship with the driven non-linear polarization for long distances because they travel with different velocities.[33, 34] Velocity mismatches cause the output to scale in a non-trivial way with sample length. Ultrafast pulses further complicate the situation because the different fields travel with different group velocities and can temporally walk away from each other.[35] For instance, in THG microscopy, group velocity effects lead to an unusual depth dependence that can be mistaken for surface selectivity.[35, 36] This non-trivial scaling between the non-linear polarization and the emitted field drastically complicates measurement of the susceptibility.

As a rule of thumb, velocity-matching effects are mitigated by minimizing the excitation region's length, L, but the thinness required to satisfy this rule of thumb ($L < 10\,\mu$m for the experiment explicated herein) can be structurally untenable. Structurally, thick windows or substrates are desirable for TSF spectroscopy (e.g. a thin film deposited on a thick substrate or a liquid sample sandwiched between two windows). In this work, we consider the response of a typical substrate in an ultrafast, non-resonant TSF experiment to demonstrate phase and group velocity effects.

We accomplish a 2-color TSF experiment with frequency $\omega_{\mathrm{TSF}} = \omega_1 + 2\omega_2$ and spatial phase $\vec{k}_{\mathrm{TSF}} = \vec{k}_1 + 2\vec{k}_2$. We find that long samples and broadband excitation pulses lead to characteristic modulations in the output spectra defined by velocity matching conditions. These modulations depend on excitation color and will obscure the analyte response unless strategies are used to mitigate the observed fringes. We define such strategies in the Discussion section. Our formalism and findings easily extend to all wave-mixing processes whose output frequency is the sum of their input frequencies.

2.3 Theory

In this section we solve the wave equation for TSF using pulsed excitation with finite bandwidth. Our derivation is informed by Angerer et al. [37]'s frequency domain derivation of ultrafast SHG and Boyd's[38] derivation of continuous wave (CW) SHG intensity. Our derivation neglects the transverse evolution of the wave equation; these effects are important in experiments that tightly focus or have large beam crossing angles.[39]

The formation of the TSF electric field, $E_4(z,\omega)$, through a dispersive medium is given by Maxwell's scalar wave equation (presented in the frequency domain and in the SI unit system)[38]:

$$\left[\frac{\partial^2}{\partial z^2} + k^2(\omega)\right] E_4 = \frac{\omega^2}{\epsilon_0 c^2} P_{\mathrm{NL}}, \tag{2.1}$$

in which ϵ_0 is the vacuum dielectric constant, c is the vacuum speed of light, P_{NL} is a non-linear polarization driven by the excitation fields, and $k(\omega)$ is the frequency-dependent spatial wavevector. For both the excitation pulses and the TSF output field, the spatial wavevector is described by a first-order Taylor expansion about the field's central frequency, ω_0:

$$\begin{aligned} k(\omega) &\approx k(\omega_0) + \left.\frac{\partial k}{\partial \omega}\right|_{\omega_0} (\omega - \omega_0) \\ &= v_p^{-1}\omega_0 + v_g^{-1}(\omega - \omega_0), \end{aligned} \tag{2.2}$$

where v_p and v_g are the phase and group velocity at ω_0, respectively. The phase velocity is related

to the refractive index, n, by $v_p = c/n$, and the group velocity is related to the phase velocity and refractive index by $v_g = v_p\left(1 + \frac{\omega}{n}\frac{\partial n}{\partial \omega}\right)$. Truncating the Taylor series after the first-order neglects effects like group velocity dispersion. We also neglect effects like self-phase modulation. These effects are small because we work with sufficiently short samples and weak driving fields.[1]

Our electric fields have Gaussian envelopes:

$$E_j(z,\omega;\omega_j) = A_j(z)\exp\left[ik_j(\omega)z\right]\exp\left[-\frac{(\omega-\omega_j)^2}{2\sigma_j^2}\right], \tag{2.3}$$

where ω_j is the spectral center, σ_j is the spectral bandwidth, $k_j(\omega)$ is $k(\omega)$ expanded such that $\omega_0 = \omega_j$, and $A_j(z)$ is the amplitude through the sample. As we shall show, an analytic solution to the wave equation results when we assume this form for both the driving excitation fields (E_1, E_2, and E_3) as well as the generated TSF field (E_4). Using this definition for our TSF field, and invoking the slowly varying envelope approximation $\left(\left|\frac{\partial^2 A_4(z)}{\partial z^2}\right| \ll \left|2ik_4(\omega)\frac{\partial A_4(z)}{\partial z}\right|\right)$ in order to disregard the second order derivative, Equation 2.1 becomes

$$\frac{\partial A_4(z)}{\partial z}\exp\left[ik_4(\omega)z\right]\exp\left[-\frac{(\omega-\omega_4)^2}{2\sigma_4^2}\right] = \frac{\omega^2}{2ik_4(\omega)\epsilon_0 c^2}P_{\mathrm{NL}}(z,\omega). \tag{2.4}$$

We now consider the form of the non-linear polarization. In the convention of Maker and Terhune [42], P_{NL} is given by

$$P_{\mathrm{NL}}(z,\omega_4 = \omega_1+\omega_2+\omega_3) = \epsilon_0\chi^{(3)}\left(\omega_4;\omega_1,\omega_2,\omega_3\right)E_1(\omega_1)E_2(\omega_2)E_3(\omega_3) \tag{2.5}$$

in which $\chi^{(3)}$ is the third-order susceptibility (we suppress all tensors in this derivation). Equation 2.5 neglects the buildup of polarization that can occur with resonant, impulsive excitation.[43]

[1] We consider the effects of disregarding $\left.\frac{\partial^2 k}{\partial \omega^2}\right|_{\omega_0}$ in our Taylor expansion by comparing the accrued pulse duration (chirp), $\delta t \approx \left.\frac{\partial^2 k}{\partial^2 \omega}\right|_{\omega_0}\Delta\omega \cdot L$, to the original pulse duration, $\Delta t \approx \frac{0.441\cdot 2}{\Delta\omega}$. For our sample and experimental conditions we find $\frac{\delta t}{\Delta t} \approx 0.1\%$. Additionally, we may consider the prominence of self-phase modulation for our experimental conditions. Siegman [40] notes that the length scale, L, over which self-phase modulation is significant goes as $L = \frac{\lambda}{2\pi I n_{2I}}$ where I is the intensity at the beam waist and n_{2I} is the nonlinear refractive index. Using our experimental parameters and Major et al. [41]'s value of $n_{2I} = 3\times 10^{-16}$ cm^2/W for $\lambda = 1300$ nm, we find that $L \approx 0.3$ cm, which is an order of magnitude longer than our sample. Given both of these calculations, second-order effects are much smaller than first-order effects given our pulse bandwidth and sample length. We think of the intensity of driving fields at which our work is accomplished as being sufficient to see generated third-order response against black, but not sufficient to observe third-order effects (self-phase modulation) in the driving fields.

It is applicable for this work since transparent materials lack visible and near-IR resonances.

To account for our finite pulse bandwidth, the non-linear polarization is the weighted average of all incident field components:

$$\begin{aligned} P_{\mathrm{NL}}(z,\omega_4) =& \epsilon_0 \iiint_{-\infty}^{+\infty} \chi^{(3)}\left(\omega_\alpha+\omega_\beta+\omega_\gamma;\omega_\alpha,\omega_\beta,\omega_\gamma,\right) \\ & \times E_1(z,\omega_\alpha;\omega_1)E_2(z,\omega_\beta;\omega_2)E_3(z,\omega_\gamma;\omega_3) \\ & \times \delta\left(\omega_4-\omega_\alpha-\omega_\beta-\omega_\gamma\right)\mathrm{d}\omega_\alpha\mathrm{d}\omega_\beta\mathrm{d}\omega_\gamma, \end{aligned} \tag{2.6}$$

in which δ is the Dirac delta distribution. Furthermore, since transparent materials have a pseudo-flat spectral response, $\chi^{(3)}$ is well-approximated as a constant and may be removed from the integral.

For this work, we assume all driving fields have the same bandwidth, $\sigma_j = \sigma$. Assuming $\chi^{(3)}$ is constant and approximating $k(\omega)$ with a first-order Taylor expansion, Equation 2.6 can be evaluated[2] as:

$$\begin{aligned} P_{\mathrm{NL}}(z,\omega) =& P(z)\exp\left[-\frac{\left(\omega-\omega_1-\omega_2-\omega_3\right)^2}{6\sigma^2}\right] \\ & \times \exp\left[iz\left(v_{p,1}^{-1}\omega_1+v_{p,2}^{-1}\omega_2+v_{p,3}^{-1}\omega_3\right)\right] \\ & \times \exp\left[\frac{iz}{3}\left(v_{g,1}^{-1}+v_{g,2}^{-1}+v_{g,3}^{-1}\right)\left(\omega-\omega_1-\omega_2-\omega_3\right)\right] \\ & \times \exp\left[\frac{\sigma^2z^2}{3}\left(v_{g,1}^{-1}v_{g,2}^{-1}+v_{g,1}^{-1}v_{g,3}^{-1}+v_{g,2}^{-1}v_{g,3}^{-1}-v_{g,1}^{-2}-v_{g,2}^{-2}-v_{g,3}^{-2}\right)\right] \end{aligned} \tag{2.7}$$

in which we defined the spatial amplitude term

$$P(z) \equiv \frac{2\pi\epsilon_0\sigma^2}{\sqrt{3}}\chi^{(3)}A_1(z)A_2(z)A_3(z). \tag{2.8}$$

Inspection of Equation 2.7 shows that the spectral bandwidth of the polarization is $\sqrt{3}$ larger than the driving fields and centered at the TSF frequency $\omega = \omega_1+\omega_2+\omega_3$. The last multiplier in Equation 2.7 depends on σ^2z^2 and the differences in group velocity among the driving pulses. By the Cauchy-Schwarz inequality, the exponent is always negative so that the multiplier is bounded

[2] We use the well-known relation $\int_{-\infty}^{\infty}\exp\left[-\left(ax^2+bx\right)\right]\mathrm{d}x = \sqrt{\frac{\pi}{a}}\exp\left[\frac{b^2}{4a}\right]$ to integrate Equation 2.7.

to $(0, 1]$. This term captures how group velocity differences cause the pulsed excitation beams to temporally walk off from each other. Such effects may become important in TSF using disparate driving frequencies. For simplicity, we approximate this term as unity, which is valid when all driving fields have sufficiently similar group velocities. Since we have assumed a non-resonant medium with a shallow focus, there is no depletion of the excitation fields so we approximate the amplitudes as constant: $P(z) = P$.

We now substitute Equation 2.7 into Equation 2.4. We assume the generated TSF field has the same spectral properties as P_{NL} ($\sigma_4 = \sqrt{3}\sigma$ and $\omega_4 = \omega_1 + \omega_2 + \omega_3$), and so Equation 2.4 simplifies to:

$$\frac{\partial A_4(z)}{\partial z} = P\frac{\omega^2}{2ik_4(\omega)\epsilon_0 c^2}\exp\left[iz\left(\Delta k + (\omega - \omega_4)\,\Delta v_g^{-1}\right)\right], \tag{2.9}$$

where the phase velocity mismatch, Δk, and the group velocity mismatch, Δv_g, are defined according to:

$$\Delta k \equiv v_{p,1}^{-1}\omega_1 + v_{p,2}^{-1}\omega_2 + v_{p,3}^{-1}\omega_3 - v_{p,4}^{-1}\omega_4, \tag{2.10}$$

$$\Delta v_g^{-1} \equiv \frac{v_{g,1}^{-1} + v_{g,2}^{-1} + v_{g,3}^{-1}}{3} - v_{g,4}^{-1}. \tag{2.11}$$

Integration of Equation 2.9 (from $z = 0$ to L) yields

$$A_4(L, \omega) = \frac{P\omega^2}{2k_4(\omega)\epsilon_0 c^2}\left(\frac{1 - \exp\left[iL\left(\Delta k + (\omega - \omega_4)\,\Delta v_g^{-1}\right)\right]}{\Delta k + (\omega - \omega_4)\,\Delta v_g^{-1}}\right), \tag{2.12}$$

where L is the sample path length. The total TSF field is then

$$E_4(L, \omega; \omega_4) = A_4(L, \omega)\exp\left[ik_4(\omega)L\right]\exp\left[-\frac{(\omega - \omega_4)^2}{6\sigma^2}\right]. \tag{2.13}$$

For intensity-level detection, $I_4 \propto |E_4|^2$, we arrive at the key equation for this work:

$$I_4(L, \omega) \propto I_1 I_2 I_3 L^2 \mathrm{sinc}^2\left[\frac{\left(\Delta k + (\omega - \omega_4)\,\Delta v_g^{-1}\right)L}{2}\right]\exp\left[-\frac{(\omega - \omega_4)^2}{3\sigma^2}\right]. \tag{2.14}$$

Equation 2.14 describes the expected TSF signal as L, Δk, and Δv_g^{-1} change. If there is no group velocity mismatch, $\Delta v_g^{-1} = 0$, or if we measure at the center of the output pulse, $\omega = \omega_4$,

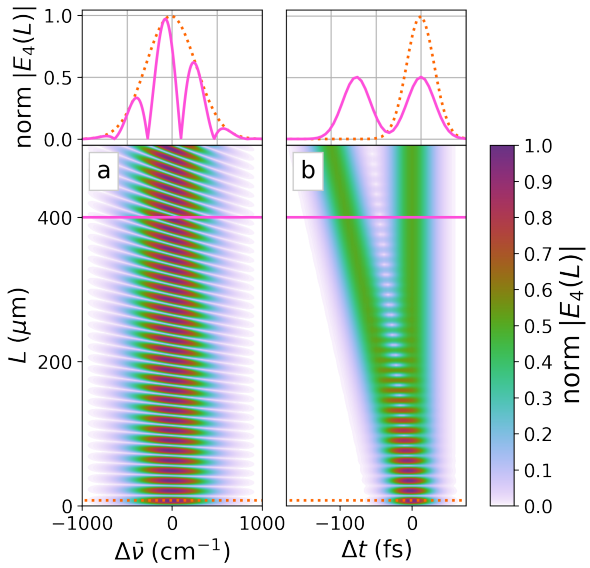

Figure 2.1: Pulsed excitation model for degenerate excitation ($\bar{\nu}_1 = \bar{\nu}_2 = \bar{\nu}_3 = 7700$ cm^{-1}) in sapphire with sample lengths up to 500 μm. (a) Frequency distribution of the output against sapphire sample length. The frequency axis is referenced to the TSF frequency center, $\omega_4 = \omega_1 + \omega_2 + \omega_3$. (b) The temporal envelope of the output against sapphire sample length. The time axis is referenced relative to when a TSF pulse which was generated at the front of the sample leaves the sample. In both plots, the small plots overhead show frequency/time cross-sections of $L = 10$ μm (dotted orange) and $L = 400$ μm (solid dark pink). The driving fields have width $\sigma = 160$ cm^{-1}.

then we recover the same ΔkL periodicity known in SHG and other processes.[38, 44, 45] Fringes defined by ΔkL will hereafter be called *phase mismatch fringes*. These are also referred to as Maker-Terhune-type oscillations.[45, 46] We note the expected intensity is periodically dependent on $\left(\Delta k + (\omega - \omega_4)\,\Delta v_g^{-1}\right) L$. Normally, minimizing ΔkL maximizes the output intensity, but for ultrafast pulses, the group velocity mismatch is also important. The $\left((\omega - \omega_4)\,\Delta v_g^{-1}\right) L$ term will result in periodicities of the spectrally resolved output for a given color combination of pulses (hereafter called *group mismatch fringes*). This spectral dependency on group velocity mismatch is known for SHG.[47, 48, 49, 50, 51]

To understand the consequences of this model, we calculate the electric field generated through a sapphire substrate as a function of sample length, L. We use the refractive index of sapphire as measured by Malitson [52]; for the range of excitation frequencies we survey, $|2\pi/\Delta k| \sim 15$ μm and

$|2\pi\Delta v_g| \sim 30$ μm/fs. Figure 2.1 shows the calculated TSF field that results over a range of different substrate lengths. By showing the range of substrate lengths, one can observe the "build-up" of TSF through the sample. The frequency-domain (Figure 2.1a) and time-domain (Figure 2.1b) representations of the TSF field provide different insights on the propagation. We explore both representations to give a thorough picture of the propagation effects.

As sample length increases, higher-order propagation effects are needed to explain the output. For the shortest path lengths ($L \ll \Delta k^{-1}$), phase mismatch and group velocity mismatch do not strongly influence the output and signal grows quadratically with L. Between the shortest path lengths and $\sim 50\mu$m, ($\Delta k^{-1} < L < \Delta v_g \Delta_t$), signal output modulates with phase mismatch fringes. The modulation only depends on the sample length. If CW driving lasers were in use, we would *only* see these phase mismatch fringes.

At path lengths longer than $\sim$ 50 μm, the pulsed nature of the propagation becomes essential to explain the evolution. In the frequency domain, these path lengths are large enough to resolve periodicities across the bandwidth of the TSF output. The fringes, which were horizontal at smaller path lengths, now accrue a tilt that gives them a mixed frequency/path length dependence. The accrued tilt is defined by the color dependence in Equation 2.14, which gives modulations in the frequency distribution. In the time domain (Figure 2.1b), the group velocity difference is large enough that the driving field walks off of the initial TSF polarization created at the front of the sample. In effect, this walkoff causes the Gaussian pulse to break into two distinct pulses separated by time $\Delta v_g L$. The delay corresponds to the TSF field created at the back of the sample exiting the sample sooner than the field created at the front of the sample. There is no TSF field in between the pulses because of symmetric, destructive interference of the phase mismatch fringes as previously seen in THG microscopy.[35, 36] Only electric fields generated at the sample edges contribute significantly to the observed output—electric fields generated at different planes in the sample interior are out of phase with each other and thus destructively interfere.[35] Others have observed and explained this type of separation in SHG.[53, 54, 46]

2.4 Experimental

An ultrafast oscillator (Spectra-Physics, Tsunami) seeds a regenerative amplifier (Spectra-Physics, Spitfire Pro XP) which creates ultrafast pulses ($\sim$ 35 fs) centered at 12500 cm^{-1} with a 1 kHz repetition rate. These pulses pump two optical parametric amplifiers, OPAs, (Light Conversion, TOPAS-C) which we label "OPA1" and "OPA2". The OPAs are operated in the 'signal' region for this experiment and their motors are tuned to maximize the smoothness of the OPA's tuning curve (see Figure 2.5a-d for OPA power curves and tuning tests). Their output, which we label ω_1 and ω_2, ranges from 6200 to 8700 cm^{-1}. A silicon wafer (0.4 mm thick) acts as a low-pass filter (cutoff: $\sim$8900 cm^{-1}) for removal of residual 12500 cm^{-1} pump light. A motorized (Newport, MFA-CC) retro-reflector defines the time delay, τ_{21}, between the two pulses. The relative delay of different colors of light caused by dispersion of transmissive optics is actively corrected by offsetting the τ_{21} set-point for each possible color combination. The offset is empirically defined by maximizing transmitted TSF signal—see Figure 2.5e,f for the measured offset. A spherical mirror (f = 1 m) focuses the two beams onto the sample (500 μm thick, double side polished sapphire) with each beam being 1° from surface normal (2° between beams). The width of the Gaussian mode at the sample position is $\sim$ 375 μm; incident pulse energies are $\sim$ 10 μJ (ω_2) and $\sim$ 1 μJ (ω_1) per pulse. The transmitted, spatially and temporally coherent output from the sample is spatially isolated in the $k_1 + 2k_2$ direction with an aperture, focused into a monochromator (HORIBA Jobin Yvon MicroHR, 140 mm focal length, with a 1200 nm blaze and 150 grooves per mm grating), and homodyne-detected (intensity level) with a thermoelectrically cooled PMT (Hamamatsu Photonics, H7422-20). This PMT has a responsivity which changes by a factor of $\sim$4 over the range of detected light. All collected TSF spectra are shown on the amplitude level (in post-processing we take the square root of the detected/recorded intensity). The acquisition software which controls all motors and records data is open source, written in Python, and available at http://github.com/wright-group/PyCMDS. The Python computing language and the NumPy, SciPy, and Matplotlib libraries were used to collect, analyze, and represent the data presented in this work.[55, 56, 57, 58]

2.5 Results

We have described and shown the oscillatory nature of the TSF output as a function of sample length. However, when using TSF as an analytical method, the sample/substrate length is generally constant while the carrier frequencies of the driving pulses are scanned across resonances. This scanning of carrier frequencies changes Δk and Δv_g^{-1} and can cause velocity mismatch fringes. In order to observe these effects we performed a TSF experiment using two tunable, ultrafast pulses where $\omega_{\mathrm{TSF}} = \omega_1 + 2\omega_2$ and $\vec{k}_{\mathrm{TSF}} = \vec{k}_1 + 2\vec{k}_2$. The pulses have a bandwidth of $\sigma \approx 160$ cm^{-1}. Figure 2.2 shows the normalized TSF magnitude as a function of the two excitation frequencies. Figure 2.2a,b show the experimental data with and without a tracking monochromator ($\omega = \omega_{\mathrm{measured}} = \omega_1 + 2\omega_2$), respectively.[3] Figure 2.2a displays deep periodicities along both axes. We are able to reproduce these periodicities with our model—see Figure 2.2c. With a tracking monochromator, all periodicities are exclusively due to the changing phase velocity mismatch, Δk, between the the TSF emission and polarization. Without a monochromator (Figure 2.2b), there are no fringes. We observe a peaked spectral profile which roughly follows the intensity profiles of our excitation lasers and detector spectral response function (much the same as the envelope of Figure 2.2a). In other words, for any combination of ω_1 and ω_2, TSF amplitude is created; however, the central frequency may not have appreciable amplitude due to phase mismatch effects.

In order to clarify the monochromator's role in the observation of spectral fringes, we scanned both ω_1 and ω_m for a set ω_2 frequency. The results are shown in Figure 2.3a. The total signal lies along the line $\omega_m - \omega_1 =$ constant, but modulations are present along this line. These modulations are the same as those observed in Figure 2.2a. Figure 2.3b shows the TSF amplitude as predicted by our model. All periodicities along the ω_m axis are due to the $(\omega - \omega_4)\Delta v_g^{-1}$ term in Equation 4.21 (group mismatch fringes). We note that there is a slight curvature in the periodicities as ω_1 changes; this curvature is due to the changes in group velocity of ω_1 and ω_4 not perfectly offsetting each other as ω_1 changes. Sapphire has fairly static group velocity differences between the excitation and emission frequencies explored in this work, so the curvature is slight.

[3] The spectra shown in Figure 2.2b was acquired with our monochromator/grating in "0th order mode" which effectively passed all colors to the detector as if it were a lossy mirror.

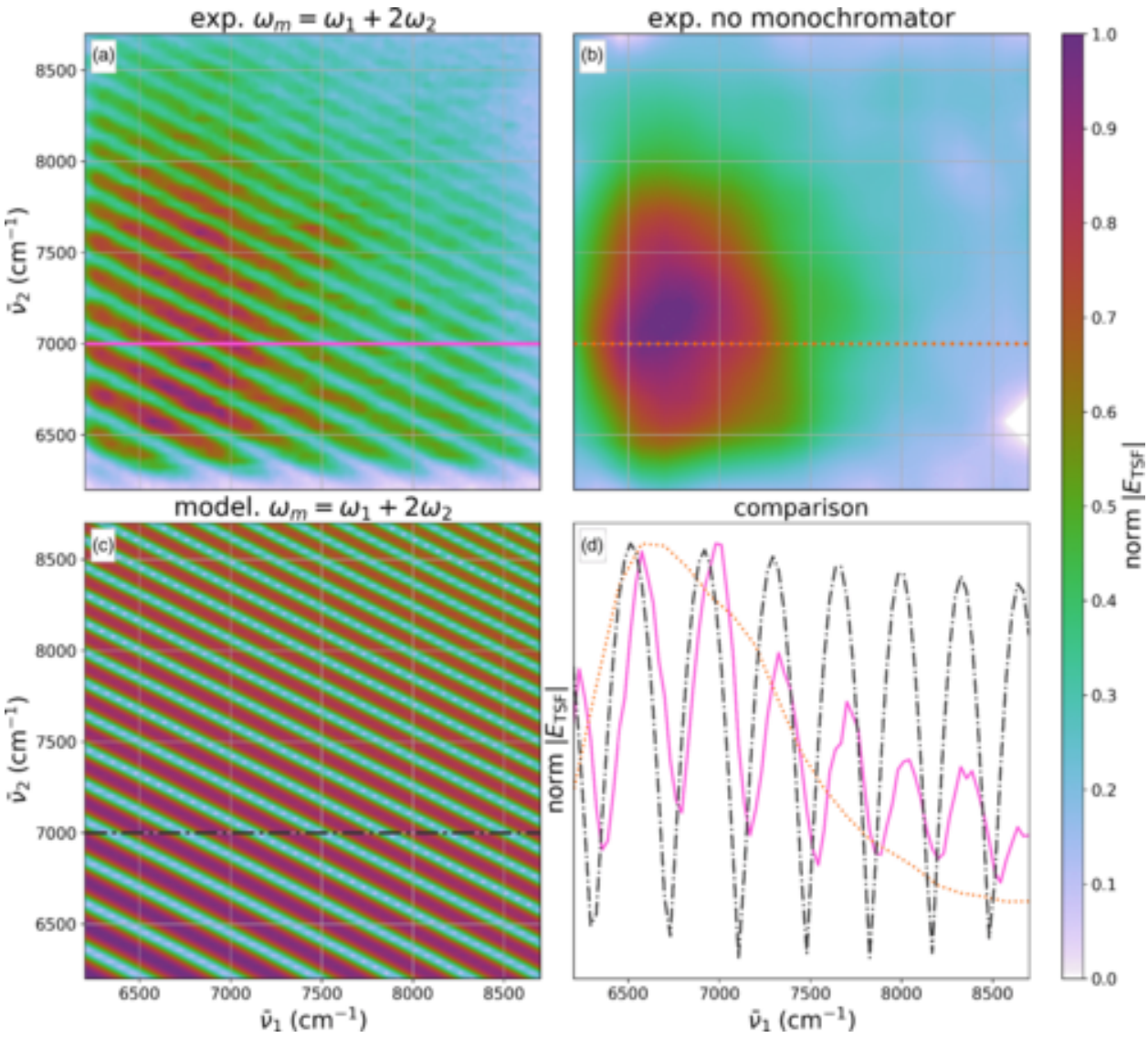

Figure 2.2: TSF amplitude at multiple combinations of pump colors—a juxtaposition between experiment and model. Experimental spectra (a and b) are represented as the square-root of the detected intensity. These spectra go to zero near the edges due to a lack of driving laser intensity—see powercurves in SI. We note that (b) has been lightly smoothed. (c) is our model's prediction assuming $\omega = \omega_1 + 2\omega_2$ with effectively no spectral bandwidth of resolution. (d) compares a color and linestyle coded trace from each of (a, b, and c).

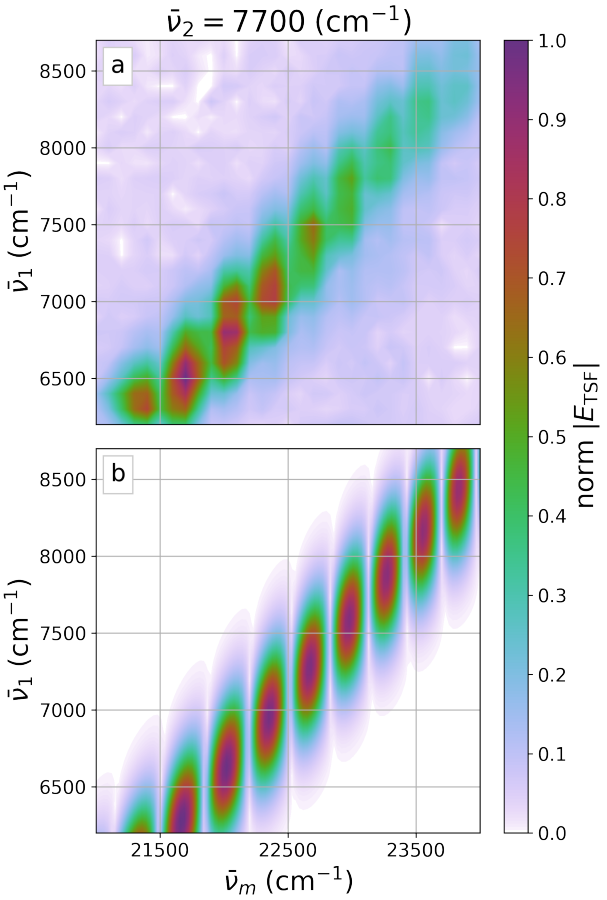

Figure 2.3: TSF amplitude for multiple combinations of pump and monochromator color. The experimental spectrum (a) is represented as the square-root of the detected intensity. Subplot (a) shows experiment while subplot (b) shows our model's prediction.

2.6 Discussion

Transparent materials are foundational components in optical sample cells because they are inactive as absorbers over spectral regions of interest. However, these materials do have substantial refractive indices. Consequently, they are bright in many non-linear experiments that are sensitive to both absorption and refraction and thus form a background signal that must be taken into account. By exploring the multidimensional TSF spectrum of sapphire, we have shown that TSF spectroscopy can have complex and significant backgrounds from transparent materials used as windows or substrates. Unlike window contributions in other non-linear spectroscopies (cf. Murdoch et al. [59]), window/substrate contributions to TSF are highly modulated in their output amplitude. These modulations can obscure analyte line shapes, especially when the modulation periodicity (Δv_g^{-1}) is comparable to the bandwidth of analyte features.

These potential complications can be avoided in a variety of ways. The most direct approach is to keep material path lengths short ($L < \frac{2\pi}{\Delta k + (\omega - \omega_4)\Delta v_g^{-1}}$), which prevents the formation of mismatch fringes entirely. This path length criterion is a modification of the CW standard of using samples thinner than $2\pi/|\Delta k|$. Figure 2.1 shows that sapphire samples and substrates thinner than ~ 10 μm fall within this standard. Additionally, for the ranges of frequencies explored in this experiment, $\Delta k \gg \sqrt{3}\sigma\Delta v_g^{-1}$ (greater by a factor of > 35) so just as in the CW case, Δk defines the critical dependence on length that the experimentalist must consider for these thin samples.

Sufficiently short material path lengths are often impractical because they are structurally weak. If thick sample cells are required, a reflective geometry can mitigate background effects. Reflected (epi) THG has an effective penetration depth of $\sim \lambda_{\text{fundamental}}/12$ which is $\sim$ 100 nm for our experiments. This small interaction distance is within the "thin sample" limit and therefore is not affected by mismatch effects. The small depth also keeps the amplitude of the background much smaller than the asymptotic limit, shown in Figure 2.1. In a similar vein, researchers doing coherent anti-Stokes Raman and transient grating spectroscopies have used reflective geometries to efficiently discriminate against background signal.[60, 61] We also note that some groups have already accomplished THG in a reflective geometry in order to mitigate absorptive losses and

focusing effects.[62, 63]

For another option, we note that mismatch fringes are only observed if the output field is spectrally resolved: if the spectral (angular frequency) resolution, R, is worse than $R \approx L\Delta v_g^{-1}$, then the fringes are washed out. Decreasing the resolution of a monochromator, using no monochromator (as in Figure 2.2b), or using sufficiently *long* material path lengths (large L) can all remove velocity mismatch effects. These are effectively a smoothing of Equation 2.14 with respect to ω because the monochromator is incapable of resolving the fast oscillations. Importantly, the decrease of output resolution may not affect the instrumental resolution as it pertains to $\chi^{(3)}$, because the bandwidth of the excitation fields already broadens the resolution.[43]

In light of our understanding of the TSF generation in non-resonant media, it is prudent to consider how resonant analytes will affect pulse propagation. Unlike the window/substrate materials we have studied here, input frequencies will be scanned about analyte resonances, which can introduce dramatic pulse distortions that require a higher-order (and complex-valued) expansion of Equation 2.2. This potentially makes analyte TSF polarizations much different from the normally dispersive case analyzed here, because dispersion can be anomalous and large, and absorption is strong.[64] These complications are avoidable in cases of small analyte loading. We note that it is common practice to keep analyte loading small enough (OD < 0.3) to avoid depletion of the pulse fields and the consequent spectral[65, 66] and temporal[67] signal distortions.

2.7 Conclusion

The use of tunable ultrafast excitation pulses in triple sum frequency spectroscopy requires extension of previous treatments of phase matching effects to include group velocity mismatches. The group velocity mismatch fringes appear as both periodic modulations in the frequency distribution of the output or changing temporal delays between the output beams created near the front and back surfaces of the sample. If a monochromator is used to isolate the triple sum frequency signal, there will be interference effects between the beams. These effects create fringes that are defined by $\left|\sin\left(\frac{(\Delta k+(\omega-\omega_4)\Delta v_g^{-1})L}{2}\right)\right|$ where the first and second terms of the argument describe the wave

vector (phase velocity) mismatch and group velocity mismatch, respectively. The fringes create modulations in multidimensional triple sum frequency spectra as the excitation or monochromator frequencies are scanned. The modulations can complicate and obscure spectral features in samples containing resonances. These effects can be minimized by using short samples or keeping the output resolution at or lower than the pulse bandwidth.

Supplementary Material

All data and the workup/representation/simulation script are available for download at http://dx.doi.org/10.17605/osf.io/emgta.

2.8 Appendix: Calculation of phase and group velocities

We use the following relations to calculate the phase and group velocity from refractive index data:

$$v_p(\omega) = \frac{c}{n(\omega)} \tag{2.15}$$

$$v_g(\omega) = \frac{c}{n(\omega) + \omega \frac{\partial n}{\partial \omega}}. \tag{2.16}$$

We use the refractive index of sapphire as measured by Malitson [52]. Our results are shown in Figure 2.4.

2.9 Appendix: OPA output characterization and correction

We characterize the OPA outputs using two principle metrics:

- Measuring the output power for each color with a thermopile (Newport, 407A).
- Measuring the output spectrum for a given set-point with a home-built InGaAs array detector (Sensor: Hamamatsu, G9494-256D) coupled to a monochromator/spectrograph.

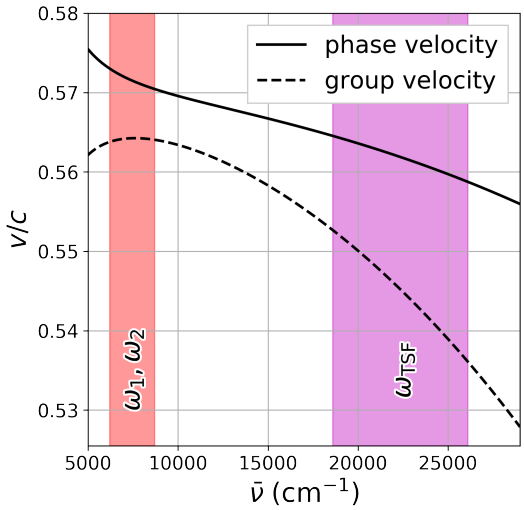

Figure 2.4: Phase and group velocities (v_p and v_g, respectively) in sapphire. Calculated from refractive index data measured by Malitson [52]. The salmon and magenta colored regions represent the experimental colors explored in this work by our pump lasers (labeled ω_1, ω_2) and TSF output (labeled ω_{TSF}), respectively.

In Figure 2.5a-d we show these metrics for both OPAs prior to collection of the data which is presented in the main article.

We correct for the color-dependent arrival times of incident pulses which we attribute to the dispersion of transmissive optics. The corrections that we apply control the arrival times of the driving pulses relative to each-other. The data we use to build our corrections are shown in Figure 2.5e,f. These data were acquired by performing TSF in a transmissive geometry while scanning both delay and set-point frequency for a given OPA with the other OPA set to 7700 cm^{-1}. Note how slight periodicities are present along the set-point axis—these are phase-mismatch fringes. We splined over these data and then actively offset pulses from each other for *every* pulse color combination. We did not take into account the effects of our silicon filter due to it being added to the system after corrections were applied.

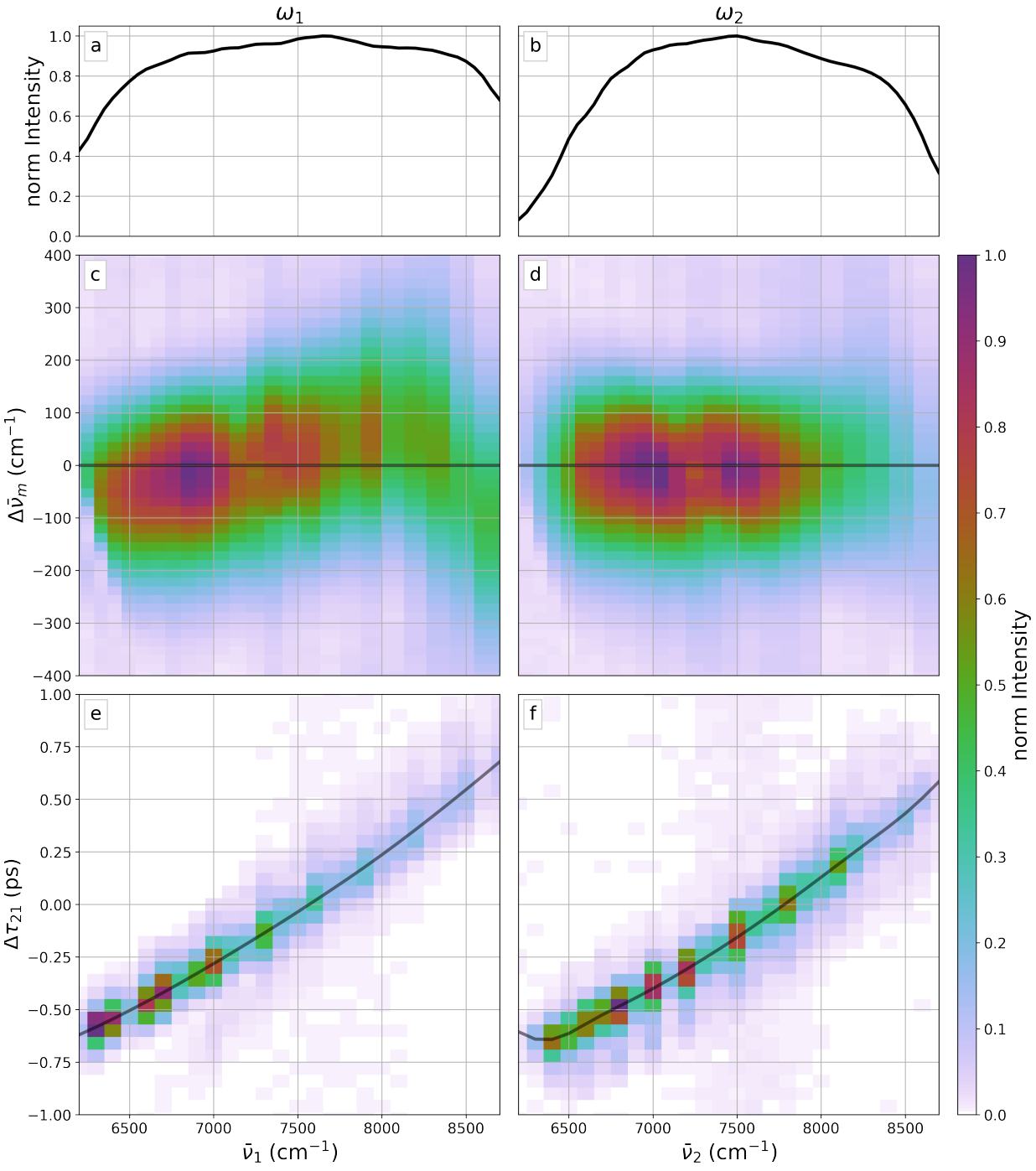

Figure 2.5: OPA output characterization and correction for different colors of pump light. The left hand column corresponds to ω_1 and the right hand column corresponds to ω_2. Subplots (a) and (b) were acquired by measuring the filtered NIR output of the OPAs with a thermopile [slight smoothing has been applied]. Subplots (c) and (d) were acquired using a monochromator and array detector to spectrally resolve the NIR output of each OPA. Subplots (e) and (f) were acquired by measuring the TSF output of sapphire in transmissive geometry with a PMT and scanning monochromator.

2.10 Appendix: Determination of pulse bandwidth

We determine our approximate pulse bandwidth by taking the data present in Figure 2.5d, summing/binning along set-point frequency and then fitting the result to a Gaussian function. We find our driving pulses to have a width, on the intensity level, of $\sigma_I = 112$ cm^{-1} which corresponds to an amplitude level width of $\sigma = \sqrt{2}\sigma_I = 160$ cm^{-1}.

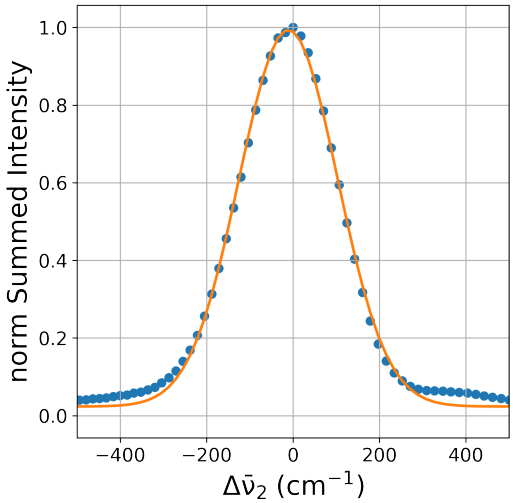

Figure 2.6: Determination of pulse bandwidth. Data is blue points while fit is orange line.

Chapter 3 Multidimensional Triple Sum-Frequency Spectroscopy of MoS_2 and Comparisons with Absorption and Second Harmonic Generation Spectroscopies

This Chapter borrows extensively from Morrow et al. [68]. The authors are:

1. *Darien J. Morrow*
2. *Daniel D. Kohler*
3. *Kyle J. Czech*
4. *John C. Wright*

3.1 Abstract

Triple sum-frequency (TSF) spectroscopy is a recently-developed methodology that enables collection of multidimensional spectra by resonantly exciting multiple quantum coherences of vibrational and electronic states. This work reports the first application of TSF to the electronic states of semiconductors. Two independently tunable ultrafast pulses excite the A, B, and C features of a MoS_2 thin film. The measured TSF spectrum differs markedly from absorption and second harmonic generation spectra. The differences arise because of the relative importance of transition moments and the joint density of states. We develop a simple model and globally fit the absorption and harmonic generation spectra to extract the joint density of states and the transition moments from these spectra. Our results validate previous assignments of the C feature to a large joint density of states created by band nesting.

3.2 Introduction

Coherent multidimensional spectroscopy (CMDS) is a useful tool for exploring the rich many-body physics of semiconductors.[69, 70] A new CMDS methodology is Triple Sum Frequency (TSF) spectroscopy. TSF is the non-degenerate analog of third harmonic generation (THG), and the four-wave mixing extension of three-wave mixing processes like sum-frequency generation and second harmonic generation (SHG).[19] TSF uses independently tunable ultrafast pulses to create coherences at increasingly higher frequencies while discriminating against transient populations. Scanning the multiple input pulse frequencies enables collection of a multidimensional spectrum. Cross peaks in the spectrum identify the dipole coupling between states. TSF has studied vibrational and electronic coupling in molecules.[15, 16, 17, 21] This work reports the first TSF spectroscopy of a semiconductor.

We investigate a polycrystalline MoS_2 thin film. Transition metal dichalcogenides (TMDCs), such as MoS_2, are layered semiconductors whose indirect bandgaps become direct in the monolayer limit.[6, 71] TMDCs exhibit strong spin-orbit coupling, high charge mobility, and have novel photonic capabilities.[72, 73, 74] The optical spectrum of MoS_2 is dominated by three features: A ($\hbar\omega_{\mathrm{A}} \approx 1.8$ eV), B ($\hbar\omega_{\mathrm{B}} \approx 1.95$ eV), and C ($\hbar\omega_{\mathrm{C}} \approx 2.7$ eV).[75, 76] A and B originate from high binding energy excitonic transitions between spin-orbit split bands.[75, 14, 77, 78, 79] The stronger C feature is predicted to arise from a large joint density of states (JDOS) due to band nesting across a large section of the Brillouin zone (BZ).[80, 81, 82, 83] As of yet, no direct, experimental verification of the large JDOS defining the C feature has been accomplished. In this work, we demonstrate how first, second, and third order spectroscopies can be used together to determine whether the prominence of a feature is due to a large transition dipole or a large transition degeneracy.

The spectroscopies considered here can be understood in the electric dipole approximation using perturbation theory.[38, 84] Briefly, an electric field (E) drives a polarization (P) in the material. The polarization is related to an oscillating coherence between two states. The polarization is expressed as an expansion in electric field and susceptibility (χ) order. Absorption, SHG, and TSF (THG) depend on $\chi^{(1)}$, $\chi^{(2)}$, and $\chi^{(3)}$, respectively. Absorption is proportional to Im $\left[\chi^{(1)}\right]$.

For very thin films (no interference or velocity-mismatch effects), SHG and TSF intensities are proportional to $\left|\chi^{(2)}\right|^2$ and $\left|\chi^{(3)}\right|^2$, respectively. All of the discussed spectroscopies detect state coupling through resonant enhancement. When the driving field is resonant with an interstate transition, χ is enhanced and the output intensity increases. In crystalline systems, interstate transitions are also subject to momentum conservation, which typically restricts interstate coupling to vertical transitions within the Brillouin zone (i.e. direct transitions).

Our work expands upon the extensive body of SHG and THG work on TMDCs[85, 86, 87, 88, 89, 90, 91, 92, 93, 94, 95, 96, 97, 98] by exploring the multidimensional frequency response. TSF and other CMDS spectroscopies that scan multiple driving field frequencies can identify multiresonant enhancement, whereby the driving fields resonate with more than one interstate transition.[99] Multiresonance selectively enhances coupled transitions and decongests dense spectra. In crystalline materials, multiresonant excitation is also subject to the momentum conservation mentioned earlier, so TSF can isolate multiple transitions from singular points in the Brillouin zone. Because of this selectivity, TSF is a potential method for mapping out band dispersion in crystals. With three independently tunable lasers, TSF can couple up to four states at a specific **k**-point together, so TSF could measure the dispersion of up to four bands. The present work is a step towards the goal of momentum-selective CMDS.

3.3 Experimental

Nonlinear measurements of thin films are often complicated by non-resonant substrate contributions which are mitigated by measuring the coherent output in the reflected instead of transmitted direction.[60, 61, 31, 100, 101] For our experiment, TSF measured in the reflected direction has an effective penetration depth of $\sim \lambda_{\text{fundamental}}/12 \sim 100$ nm; this small sampling length allows the resonant response from the thin film to be orders of magnitude more intense than the non-resonant response (see the appendix for more discussion). We prepared a 10 nm thick MoS_2 thin film by first evaporating Mo onto the fused silica substrate followed by sulfidation of the Mo.[61, 102] Our sample substrate is a fused silica prism so that back-reflected, non-resonant TSF exits the substrate traveling parallel to the desired TSF signal but shifted spatially. Sample geometry,

synthesis details, AFM measurements to determine film thickness, and a Raman spectrum are presented in the appendix.

For our TSF measurements, an ultrafast oscillator seeds a regenerative amplifier, creating pulses centered at 1.55 eV with a 1 kHz repetition rate. These pulses pump two optical parametric amplifiers (OPAs) which create tunable pulses of light from ~ 0.5 to ~ 1 eV with spectral width on the amplitude level of FWHM ≈ 46 meV. The two beams with frequencies ω_1 & ω_2 and wave vectors $\vec{k}_1$ & $\vec{k}_2$ are focused onto the sample. All beams are linearly polarized (S relative to sample) and coincident in time. The spatially coherent output with wave vector $-\left(\vec{k}_1 + 2\vec{k}_2\right)$ is isolated with an aperture (the negative signs correspond to the reflective direction), focused into a monochromator, and detected with a photomultiplier tube. The TSF intensity is linear in ω_1 fluence and quadratic in ω_2 fluence (see the appendix for details). The measured MoS_2 TSF spectrum is normalized by the measured TSF spectrum of the fused silica substrate in order to account for spectrally-dependent OPA output intensities and detector responsivity. The appendix contains additional experimental and calibration details. All raw data, workup scripts, and simulation scripts used in the creation of this work are permissively licensed and publicly available for reuse.[1] Our acquisition,[103] workup,[104] and modeling software are built on top of the open source, publicly available Scientific Python ecosystem.[56, 57, 58]

3.4 Experimental Results

Our main experimental result is a 2D TSF spectrum of a MoS_2 thin film (Figure 3.1). The TSF spectrum of MoS_2 has a simple structure, with all features running parallel to a line with slope of -1/2. This single variable dependence of our output intensity implies there is negligible multiresonant enhancement within our spectral window. Our spectral window specifically rules out optical coupling between the A and C features. If the A and C features were coupled we would see a peak that depends on two frequency conditions: $\hbar\omega_2 = \hbar\omega_A/2 \approx 0.9$ eV and $\hbar\omega_1 = \hbar\left(\omega_C - \omega_A\right) \approx 0.9$ eV. Note that A and C features are believed to originate from different regions of the Brillouin zone, so resonant enhancement is not expected.

[1] https://dx.doi.org/10.17605/OSF.IO/2WF6G

The slope of -1/2 implies that only the output frequency, $\omega_1 + 2\omega_2$, determines the resonant enhancement. The energy ladder diagram for such a resonant enhancement is shown in the Figure 3.1 inset (left). Peaks at output colors ∼1.85 & ∼2.0 eV are roughly consistent with three photon resonances with the A and B features, while a trough is present for output colors close to the C feature (∼ 2.7 eV). Curiously, we do not see contributions from two-photon resonances (energy level diagram Figure 3.1 inset, right), even when $2\omega_2$ or $\omega_1 + \omega_2$ traces over the A or B features. The two-photon resonances would manifest as horizontal or anti-diagonal (slope of -1) features in Figure 3.1. The lack of two-photon resonances was surprising to us given the large two-photon absorption cross-section of MoS_2.[105] We address this observation later.

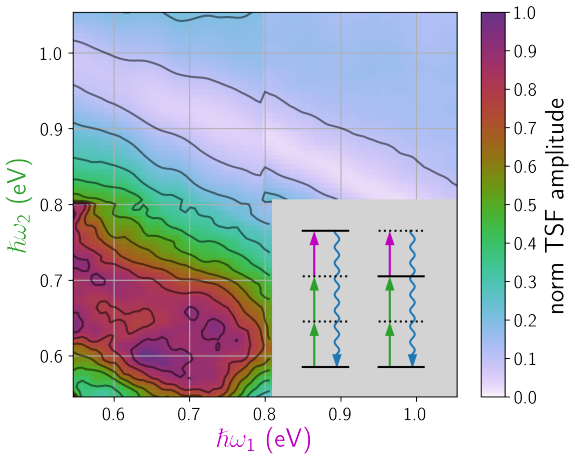

Figure 3.1: Normalized 2D TSF spectra of MoS_2. Inset diagrams processes where the third interaction is resonant with a state (left) and when the second interaction is resonant with a state (right). The measured output is represented by a wavy downward arrow. Note, the gray area of the inset was not experimentally explored.

Since the dominant spectral features in Figure 3.1 depend only on output color, we can generate a 1D THG spectrum by plotting the mean TSF amplitude for each output color. The THG spectrum is compared with other techniques in Figure 3.2. Due to the unconventional prism substrate, we were unable to acquire an absorption spectrum of the sample, but we did acquire a reflection contrast spectrum shown in Figure 3.2.[106, 107] The absorption spectrum presented in Czech et al. [61] and Figure 3.2 is of a sample prepared with similar conditions as our sample, but on a flat window substrate. The A and B feature peaks of the THG spectrum are blue-shifted compared to

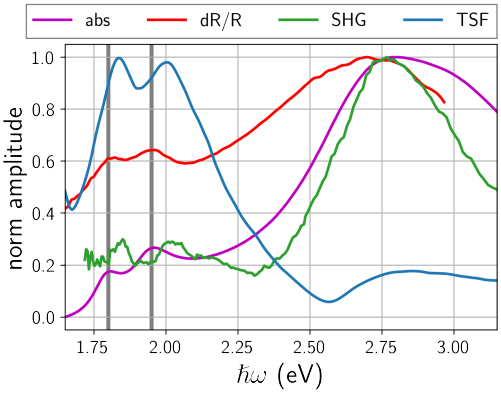

Figure 3.2: Normalized amplitude 1D spectra of MoS_2 thin films: absorption[61], SHG[92], reflection contrast (dR/R), and TSF (THG). The TSF spectrum is derived from Figure 3.1 as detailed in the main text. Vertical gray bars are guides to the eye set at 1.80 and 1.95 eV to demonstrate how SHG and TSF features are blue shifted from absorption and dR/R spectral peaks.

the absorption spectrum. Wang et al. [88] observed a similar blue shift when they measured the THG spectrum of MoS_2 around the A and B features. The C feature is dominant in the SHG[92] and absorption spectrum[61] while the A and B features are dominant in the THG spectrum. This observation is the main motivation for our analysis.

3.5 Theory

To explain why C dominates the absorption and SHG spectra but not the THG spectrum, we develop a simple model. To our knowledge, a unified model for comparing large dynamic-range absorption, SHG, and THG spectra of a semiconductor does not exist. Notable headway has been made to calculate SHG spectra[108] and write closed equations of motion[109] for semiconductors, but simple formalisms are lacking. Most simple formalisms (c.f. refs.[110, 111]) approximate the dipole as a constant with respect to both transition energy and lattice momentum. This constant dipole approximation breaks down above the bandgap, where the lattice momentum of transitions is significantly different from that of the bandgap transitions. As the lattice momentum changes, Bloch waves alter their bonding symmetries and intralattice character (cf. Padilha et al. [112]), which alters the transition dipole moments. Since the C feature is believed to originate from a

different region of the Brillouin Zone than the bandedge transitions, our theory requires both the dipole moment and JDOS to vary across our spectral range.

We develop our simple model by expanding the typical linear response formalism for direct transitions of semiconductors to include sum-frequency processes. In the case of $\chi^{(1)}$, simple theories exist for expanding the single oscillator case to bulk conditions. For more than one oscillator, the total susceptibility is the sum of individual susceptibilities. For a semiconductor system, this is a summation over all wave-vectors, $\{\mathbf{k}\}$ such that $\mathbf{k} \in \mathrm{BZ}$:

$$\chi^{(1)}\left(-\omega_1, \omega_1\right) = \sum_{a,g} \sum_{\mathbf{k}} \frac{\mu_{ga\mathbf{k}}^2}{\Delta_{ga\mathbf{k}}^1}, \tag{3.1}$$

where $\Delta_{ga\mathbf{k}}^1 = \omega_{ag\mathbf{k}} - \omega_1 - i\Gamma$ and Γ is a damping rate which accounts for the finite width of the optical transitions. It is common to replace the summation with a transition energy distribution function between conduction band x and valence band y, $J_{xy}(E)$,[2] such that

$$\chi^{(1)}(-\omega_1, \omega_1) \propto \int \frac{\mathrm{d}E}{E - \hbar\omega_1 - i\hbar\Gamma} \sum_{x,y} J_{xy}(E)\mu_{xy}(E)^2. \tag{3.2}$$

In crystals, $J_{xy}(E)$ is the JDOS. Note the dependence of the susceptibility on both $J_{xy}(E)$ and $\mu_{xy}(E)^2$. In the case that either the JDOS or the transition dipole are constant, spectroscopy techniques can be used to locate excitonic transitions or critical points in the JDOS. If the JDOS and transition dipole both vary, then traditional techniques fail.

The THG and SHG responses take the form of:

$$\chi^{(2)}\left(-\omega_{21}, \omega_1, \omega_2\right) = \mathcal{P} \sum_{b,a,g} \sum_{\mathbf{k}} \frac{\mu_{gb\mathbf{k}}\mu_{ba\mathbf{k}}\mu_{ag\mathbf{k}}}{\Delta_{gb\mathbf{k}}^{12}\Delta_{ga\mathbf{k}}^1} \tag{3.3}$$

$$\chi^{(3)}\left(-\omega_{321}, \omega_1, \omega_2, \omega_3\right) = \mathcal{P} \sum_{c,b,a,g} \sum_{\mathbf{k}} \frac{\mu_{gc\mathbf{k}}\mu_{cb\mathbf{k}}\mu_{ba\mathbf{k}}\mu_{ag\mathbf{k}}}{\Delta_{gc\mathbf{k}}^{123}\Delta_{gb\mathbf{k}}^{12}\Delta_{ga\mathbf{k}}^1}, \tag{3.4}$$

where c, b, a, and g are bands of the semiconductor. We have defined $\omega_{21} \equiv \omega_2 + \omega_1$ and $\omega_{321} \equiv \omega_3 + \omega_2 + \omega_1$. $\mathcal{P}$ is a permutation operator which accounts for all combinations of field-matter

[2] Equation 4.2, and all further theory developed, neglect indirect transitions. We find this a reasonable assumption since our multidimensional spectrum exhibited no cross-peaks between the K-point features (A and B) and the C band.

interactions. The additional detuning factors are defined by $\Delta^{123}_{gc\mathbf{k}} \equiv \omega_{cg\mathbf{k}} - \omega_{321} - i\Gamma$ and $\Delta^{12}_{gb\mathbf{k}} \equiv \omega_{bg\mathbf{k}} - \omega_{21} - i\Gamma$ in which ω_{ab} is the frequency difference between bands a and b at point $\mathbf{k}$ in the BZ. The JDOS formalism employed in Equation 3.15 can be abstracted to describe $\chi^{(2)}$ and $\chi^{(3)}$ with the introduction of multidimensional joint density functions. These joint densities depend not just on the energy difference between the initial and final states, but also on the energy differences between the intermediate states reached during the sum-frequency process. See the appendix for further details.

To simulate the spectra, the sum over bands in Equation 3.15-Equation 4.3 is truncated at three total bands: the valence band, v, the conduction band, c, and a third higher-energy band, b, (note: bands b and c are not to be confused with the B and C absorption spectrum features). The SHG and THG spectra are measured close to the direct bandgap, so transitions between c and v are key to describing the response. The b band is taken to be a much higher energy (6 eV) than the valence band. We define the transition strength of low-lying states (c and v) to this nondescript high-lying band with the parameter $\mu_{\mathrm{NR}}(\hbar\omega)$. We note that μ_{NR} is not formally a dipole, but instead contains all non-resonant transition factors involving band b (dipoles and degeneracies between c and b or v and b). While this is a improper parameterization of the actual band structure above the conduction band and below the valence band, its inclusion is crucial for reproducing details of our spectra, and the parameters offer insight into the role of virtual states in sum-frequency spectroscopies.

With this framework, we can now reason why THG, SHG, and absorption measurements are complementary for distinguishing degeneracy and dipole moments. The strength of absorption is proportional to μ^2_{cv} and J_{cv} (Equation 3.15). SHG signals will be due to the sequence $v \to b \to c$, which informs on the non-resonant band b. THG has sequences such as $v \to c \to v \to c$, which scale as μ^4_{cv} but are still linear in J_{cv}. On the other hand, THG can depend on state b and consequently depends on the same non-resonant features of SHG. THG and absorption give different scalings for transitions between c and v, but SHG is also needed to constrain the non-resonant transitions of THG involving band b.

3.6 Modeling

Figure 3.3 summarizes the fit of our model to experiment. Our simulation uses a discrete set of transition energies to approximate the integral of Equation 3.15. We employ 140 discrete energies spaced 20 meV apart with $\hbar\Gamma = 20$ meV, $\hbar\omega_{b_j} = 6$ eV, and $\hbar\Gamma_b = 500$ meV. Our strategy of a discretized set of transition energies is similar to the constrained variational analysis that is often employed to relate a material's reflection spectrum to its absorption or dielectric spectra.[113, 76, 114] As a function of transition energy, the model extracts the dipole strength of the $c \leftrightarrow v$ transitions, μ_{cv}; a weighting factor for transitions involving the non-resonant state, μ_{NR}; and the transition degeneracy, J_{cv}. See the appendix for further modeling details.

Figure 3.3a shows qualitative agreement between the model and experiment.[3] Our model does not assume a functional form for the JDOS or dipole spectra, so we can compare the response from an excitonic transition to that of an interband transition. The fitted parameters are shown in Figure 3.3b and Figure 3.3c; note that both μ_{cv} and μ_{NR} are peaked near the A and B features, while J_{cv} is minimized. As $\hbar\omega$ increases from the B feature, J_{cv} drastically increases while μ_{cv} and μ_{NR} both decrease—the increase in J_{cv} is analogous to the large JDOS attributed to band nesting by recent workers.[80, 81, 82] For comparison, in Figure 3.3c we plot the JDOS as recently calculated by Bieniek et al. [83] for monolayer MoS_2 within their tight-binding model. Both the extracted J_{cv} and the tight-binding, monolayer JDOS have a small value near the A and B features but form a peaked structure near the C feature. Because absorption, SHG, and THG spectra all scale linearly with J_{cv} but differently with transition dipole strength, the extracted structure of J_{cv} and μ_{cv} explains the glaring disparities between THG and the other two spectra. Our fitting procedure convincingly reproduces the large degeneracy of the C feature due to band-nesting.

To the red of the A feature, the JDOS and μ_{NR} increase while μ_{cv} decays to zero. We attribute this behavior to an artifact of our finite spectral range. Variational approaches are known to have difficulty with the edges of spectra.[116]

[3] After this work was published, another group published an SHG spectrum of MoS_2 which is significantly different than the one used in this work.[115] They use a good normalization scheme and their spectrum has much less noise in it compared to that of Trolle et al. [92] I am unsure how much the modeling results of this work would change if we used Stiehm et al. [115]'s monolayer SHG spectrum instead of Trolle et al. [92].

Though our fitting procedure examined only harmonic generation, our fits also explain the notable lack of two-photon resonances in the 2D TSF spectrum. Figure 3.3d shows a 2D TSF spectrum simulated from our fit parameters. The TSF features produced by our model are primarily three photon resonances which lie parallel to lines of constant output color. Some features from two-photon resonances (e.g. $v \rightarrow b \rightarrow c \rightarrow b$), such as the trough over the anti-diagonal line $\hbar(\omega_1+\omega_2) =$ 1.7 eV are visible but minor. The two-photon resonances that are prominent in the SHG spectra are suppressed because transitions involving b are severely detuned so sequences like $v \overset{\mu_{cv}}{\rightarrow} c \overset{\mu_{cv}}{\rightarrow} v \overset{\mu_{cv}}{\rightarrow} c$ dominate the output over sequences like $v \overset{\mu_{\mathrm{NR}}}{\rightarrow} b \overset{\mu_{\mathrm{NR}}}{\rightarrow} c \overset{\mu_{\mathrm{NR}}}{\rightarrow} b$. In the model, below the line $\hbar(\omega_1 + \omega_2) = 1.7$ eV, the dominant features come from coherence pathways like $v \rightarrow c \rightarrow b \rightarrow c$ or $v \rightarrow c \rightarrow v \rightarrow c$, in which the third excitation is resonant.

Our model fails to capture some features of the three optical measurements. For instance, the model shifts the position of A and B absorption features and undershoots the THG spectrum at energies above 2.7 eV. The model falsely attributes the nature of the deep trough seen in Figure 3.1 which runs along $\hbar(\omega_1 + 2\omega_2) \approx 2.56$ eV. Specifically, Figure 3.3d shows the dip of the simulated THG spectrum to be due to a two photon resonance running along $\hbar(\omega_1 + \omega_2) \approx 1.7$ eV; this resonance is not seen in Figure 3.1 which exclusively exhibits three photon resonances. A more complete fit would take into account our full 2D spectrum in order to distinguish between pathways with resonance enhancement from the second and third interaction. A more careful treatment of non-resonant transitions (μ_{NR}) may suppress these pathways. For instance, our model extracts a deep trough in μ_{NR} around 2.2-2.6 eV, yet we do not expect the non-resonant transition strength to have a strong dependence on our output color. Despite these shortcomings, our approach provides a robust characterization that informs on the interplay of dipole strength and state density on the linear and non-linear spectra of our sample.

3.7 Conclusions

In summary, we performed TSF measurements to explore the electronic structure of MoS_2 thin films. Our TSF measurements uncover a conspicuous difference between absorption, SHG, and TSF spectra: the C feature is prominent in absorption and SHG but not TSF. We address this

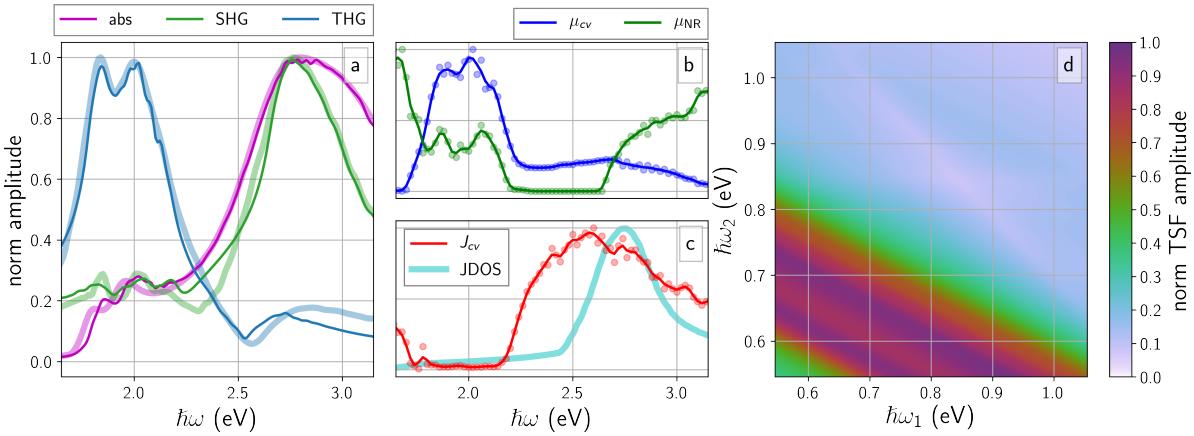

Figure 3.3: Variational model of optical spectroscopies. (a) normalized comparison of experiment (thick, translucent lines, absorption[61] and SHG[92]) and model (thin lines). (b) normalized model dipole parameters in experimentally explored range. (c) normalized model density, J_{cv}, and tight-binding optical JDOS from Bieniek et al. [83]. (d) normalized TSF spectrum as predicted by our model as fit to 1D experiments.

conundrum by extracting the spectrally dependent dipole and JDOS using all three spectra. We find the differences in the spectra arise because the C feature has a large JDOS and small dipole compared to the A and B features. We hope our measurements and analysis catalyze a renewed interest in elucidating the full spectral features of semiconductors by combining the results of many orders of complementary spectroscopies. Our measurements demonstrate the utility of non-linear, sum-frequency spectroscopies of semiconductor nanostructures over a wide range of excitation frequencies. In the future, our work can be extended and to examine the coupling of multiple transitions which originate at the same point in the BZ and thus elucidate how different conduction or valence bands interact with each other.

3.8 Appendix: Sample synthesis and substrate geometry

3.8.1 Mitigation of substrate response

In order to minimize non-resonant substrate contributions we collected our TSF spectra in a reflective geometry. The effective penetration depth of TSF in the reflective direction is estimated

by considering that appreciable intensity is only accrued when the forward and back-propagating driving fields are in spatial phase with each-other. The phase-mismatch between the forward and backward propagating waves is

$$\Delta k_{fb} = (k_1 + k_2 + k_3) - (-k_1 - k_2 - k_3) \tag{3.5}$$

$$= 6k_{\text{fundamental}} \tag{3.6}$$

$$= \frac{12\pi}{\lambda_{\text{fundamental}}} \tag{3.7}$$

in which we set $k_1 = k_2 = k_3 = k_{\text{fundamental}}$ for sake of simplicity and substituted $k_j = \frac{2\pi}{\lambda_j}$ in which λ_j is the medium of propagation dependent wavelength. Solving the nonlinear wave propagation problem (c.f. Morrow, Kohler, and Wright [31]) shows that the total output intensity is dependent on propagation length, L,

$$I(L) \propto L^2 \text{sinc}^2 \left[\frac{\Delta k L}{2}\right]. \tag{3.8}$$

The first node of Equation 3.8 happens at

$$\frac{\Delta k L}{2} = \frac{\pi}{2}. \tag{3.9}$$

Substituting Equation 3.7 into Equation 3.9 and solving for L yields

$$L = \frac{\lambda_{\text{fundamental}}}{12}. \tag{3.10}$$

Equation 3.10 gives an estimate for the effective penetration depth of backwards propagating TSF. For our experiments the penetration depth is on the order of 100 nm. So we sample 10 times more substrate than sample in this experiment, as opposed to the $\sim 10\,\mu$m of substrate sample in the transmissive geometry (predicted by similar calculations as above). Because, sample response is larger than substrate response by at least three orders of magnitude due to resonant enhancement (see below for measured intensities) our measurements of TSF in the reflected direction efficiently suppresses non-resonant background.

We collected spectra with an MoS_2 thin film on a conventional, flat substrate (reflective geometry). We found these TSF spectra to be strongly influenced by back-reflected, non-resonant substrate contributions. In order to further mitigate substrate contributions we deposited an MoS_2 thin film on a fused silica right-angle prism (ThorLabs) as shown in Figure 3.4a. Importantly, we only deposit MoS_2 on half of the prism face; we are thus able to measure the response of clean fused silica merely by translating the sample. We leverage our ability to measure TSF of clean fused silica when normalizing our MoS_2 spectra as detailed in Section 3.13.

Unlike the flat substrate, the prism back reflection is spatially distinct from the front face reflection. This is due to the added path length that takes place from beam folding. The light that is internally reflected can exit the prism at the original incident angle, but the light is shifted away from the initial excitation point—see Figure 3.4b for a sketch. One can iteratively apply the law's of reflection and refraction to calculate the output angle, θ_7, of the back-reflected beam from the input beam angle, θ_1,

$$\theta_7 = \arcsin\left[\frac{n_{\mathrm{FS}}}{n_{\mathrm{air}}}\sin\left[\arcsin\left[\frac{n_{\mathrm{air}}}{n_{\mathrm{FS}}}\sin\left[\theta_1\right]\right]\right]\right] \tag{3.11}$$

$$= \theta_1. \tag{3.12}$$

Hence, the back-reflected beam leaves the substrate at the same angle as the first reflection. The spatially shifted output was imaged with a camera in the far field (Figure 3.4c). Either the front- or back-reflected TSF could be isolated with a razor blade slid in front of the sample.

Our sample was mounted on an XYZ stage which allowed us to record TSF intensity for four different sample/imaging positions. We measured the response when we

1. excited MoS_2 and imaged the excitation spot;
2. excited MoS_2 and imaged the prism back-reflection;
3. excited just the fused silica substrate and imaged the excitation spot;
4. excited just the fused silica substrate and imaged the prism back-reflection.

The measured intensities were

1. $3 \times 10^9 \frac{\text{photons}}{\text{s}}$;
2. $8 \times 10^6 \frac{\text{photons}}{\text{s}}$;
3. no measurable intensity above noise;
4. $1 \times 10^6 \frac{\text{photons}}{\text{s}}$;

with $\hbar\omega_1 = \hbar\omega_2 \approx 0.71$ eV. Hence, in the standard geometry of our experiment we do not observe any substrate response.

We now briefly discuss velocity-mismatch fringes as discussed in Morrow, Kohler, and Wright [31]. The heuristics given in Morrow, Kohler, and Wright [31] say that short or long path lengths are able to mitigate mismatch fringes. In our case, the thin film is in the short length limit, while the substrate is in the long length limit. Hence, we do not observe mismatch fringes in our TSF spectra (c.f. Figure 3.8).

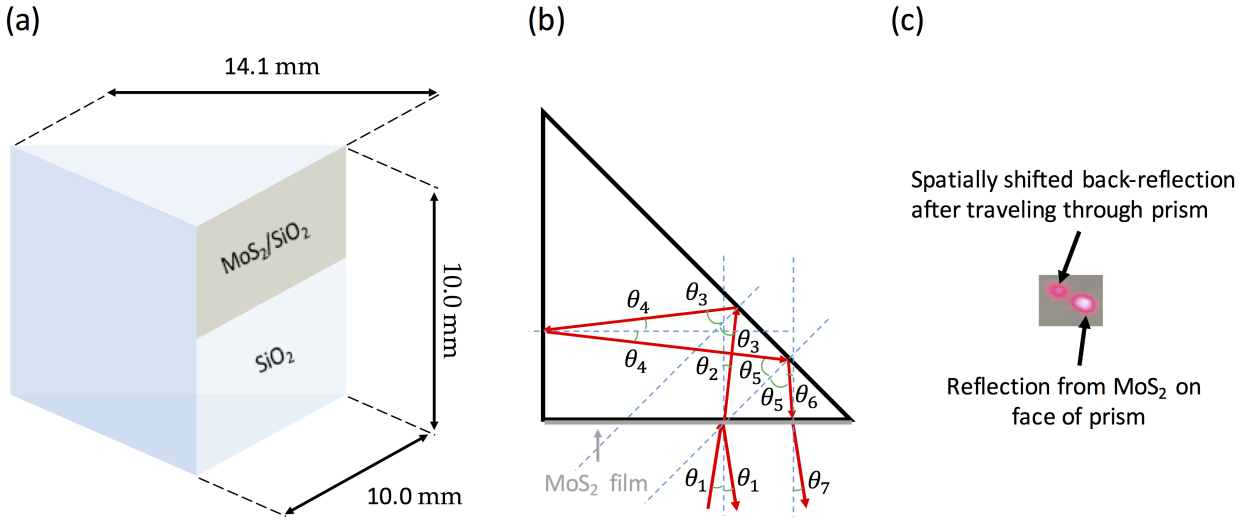

Figure 3.4: (a) Schematic of MoS_2 thin film deposited on a fused silica prism. (b) Top-down sketch of driving laser back-reflections inside of prism. (c) Photograph of visible laser reflecting off of prism and imaged on card in the far-field. Note, the sensor was saturated for the brightest spot.

3.8.2 Thin film synthesis

A description of our synthesis procedure is as follows:

1. A 2 nm amount of molybdenum metal (Kurt J. Lesker, 99.95%) was electron beam evaporated

onto half of a fused silica prism face. A shadow mask was used to selectively deposit the film on half of the face.

2. In a 1 inch CVD tube furnace purged with argon we sulfidized the molybdenum film with 500 mg of sulfur at 760 torr and 750 °C for 10 min.
3. After sulfidation, the half prism face with no MoS_2 was wiped clean.

3.9 Appendix: Raman spectra of MoS_2 thin film

A Thermo DXR Raman microscope was used to obtain the Raman spectra of our MoS_2 thin film on a fused silica prism. The microscope operates in reflective geometry. A 100 × 0.9NA focusing objective and a 2.0 mW 2.33 eV excitation source were used to collect Figure 3.5. The two observed resonances are the well known $E^1{}_{2g}$ and A_{1g} lattice modes. These resonances are known to be sensitive to layer number.[117] The red $E^1{}_{2g}$ resonance corresponds to in-plane vibrations of Mo and S atoms in which the S atoms move in the opposite direction of the Mo atoms for a given unit cell; conversely, the blue A_{1g} mode is an out-of-plane vibration with the S atoms moving opposite of each other.[118] Correlating our peak centers of 382.5 and 407.6 cm^{-1} to the series reported in Li et al. [117] and Lee et al. [119], our thin film has a many-layer/bulk-like Raman spectrum.

3.10 Appendix: Details concerning reflection contrast spectrum of MoS_2 thin film

The reflection contrast spectrum[106, 107] of our sample was acquired with an Ocean Optics USB-2000 spectrometer and phosphor-based LED source (JANSJÖ, IKEA). In order to obtain the reflection contrast spectrum we do the following:

1. Spatially filter LED source with pinhole to create a point source.
2. Collimate light, shine on sample, measure reflected light with spectrometer which has its own focusing optics.
3. Measure background spectra, $B(\omega)$ with LED source off.

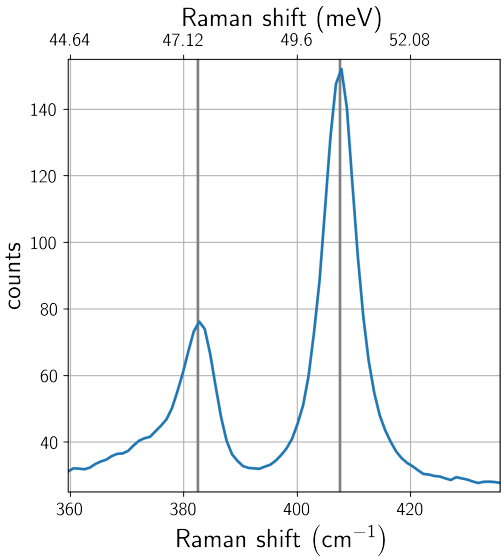

Figure 3.5: Raman spectra of MoS_2 thin film on a fused silica prism. The gray, vertical, guides to the eye are centered at 382.5 and 407.6 cm^{-1}.

4. Measure reflected source light off-of face of substrate. We call this quantity $R_{\text{substrate}}(\omega)$.
5. Measure reflected source light and off-of face of thin film on substrate. We call this quantity $R_{\text{sample}}(\omega)$. This step is accomplished by merely vertically translating the sample.
6. Calculate reflectance contrast spectra dR/R by

$$dR/R = \frac{(R_{\text{sample}}(\omega) - B(\omega)) - (R_{\text{substrate}}(\omega) - B(\omega))}{R_{\text{substrate}}(\omega) - B(\omega)} \tag{3.13}$$

$$= \frac{R_{\text{sample}}(\omega) - R_{\text{substrate}}(\omega)}{R_{\text{substrate}}(\omega) - B(\omega)} \tag{3.14}$$

3.11 Appendix: AFM measurements to determine MoS_2 film thickness

Tapping-mode atomic force microscopy (AFM) was performed with an Agilent 5500 AFM. Using laser ablation, we created a groove in the MoS_2 film so that the AFM tip could trace over the film and then onto the fused silica substrate and back onto the film again. The laser ablation was performed months before the AFM scan was acquired. We fabricated a sample holder in order to

hold the prism face with the MoS_2 parallel to the x-y plane of the AFM. An AFM scan along with two traces are shown in Figure 3.6. The randomly distributed large height specks are attributed to dust which accrued on the sample over many months of use. The AFM measurement indicates the thickness of our sample is on the order of 10 nm. The commonly reported thickness of individual layers of MoS_2 layers is 0.65 nm[119], so our sample is roughly 15 layers thick.

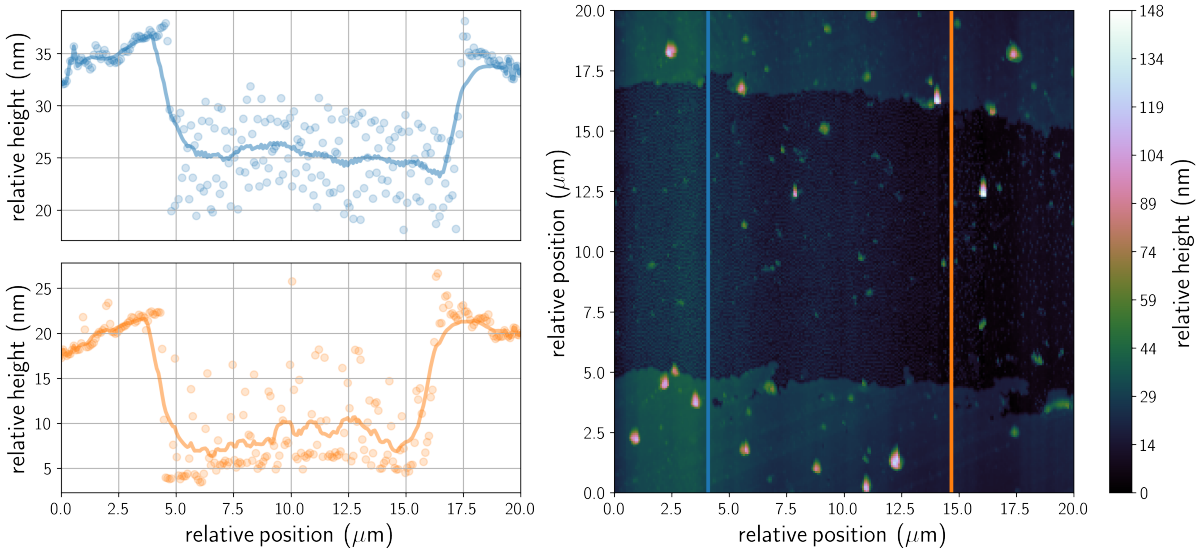

Figure 3.6: AFM of MoS_2 thin film on a fused silica prism. Traces (left) are representative slices through the full AFM image (right). Traces are color-coded to vertical overlines in the AFM image.

3.12 Appendix: Ultrafast spectrometer

3.12.1 Instrument overview

An ultrafast oscillator seeds a regenerative amplifier which creates ultrafast pulses ($\sim$ 40 fs) centered at 1.55 eV with a 1 kHz repetition rate. These pulses pump two optical parametric amplifiers (OPAs). The "idler" (0.48 - 0.77 eV) and "signal" (0.77 - 1.08 eV) outputs of the OPAs are selected using broadband polarizers and filtered with a silicon wafer (0.4 mm thick) acting as a low-pass absorption filter (cutoff: $\sim$ 1.1 eV). The spectral width of our pulses on the amplitude level is FWHM $\approx 46\,\mathrm{meV}$. The OPAs are tuned at several OPA colors to both maximize the output power and ensure good interpolation between tune points. The validation procedure for our OPA tuning is discussed in Section 3.12.3.

A motorized retro-reflector controls the delay, τ_{21}, between pulses E_1 and E_2. The dispersion of transmissive optics on the beam path makes the beam time-of-flight color-dependent. This color-dependent time-of-flight is actively corrected by offsetting the τ_{21} set-point for each possible color combination. The offset is empirically defined by maximizing TSF signal and loaded into the acquisition software. Figure 3.7 (bottom row) shows the result of this calibration. The validation procedure for our delay correction is discussed in Section 3.12.3.

A spherical mirror ($f = 1$ m) focuses the two beams onto the sample (2° between beams) with the optical axis $\sim$9° from surface normal. The beam waist of ω_1 at the sample is 0.3 mm while the waist of ω_2 is 0.4 mm; both beams have vertical polarization (s polarization relative to sample). The spatially and temporally coherent output from the sample is spatially isolated in the reflected $-\left(\vec{k}_1 + 2\vec{k}_2\right)$ direction with an aperture (in order to capture the desired $\omega_\Sigma = \omega_1 + 2\omega_2$ output), focused into a monochromator, and homodyne detected (intensity level) with a photomultiplier tube (PMT). As expected and shown in Figure 3.11, our TSF intensity is linear in ω_1 fluence and quadratic in ω_2 fluence. Our fluence dependence is unlike the saturated fluence dependence of high-harmonic generation seen by Liu et al. [120]—we are working in a regime of small perturbation. The acquisition software which controls all motors and records data is open source and written in

Python.[103]

3.12.2 Hardware

Below we specify the commercial models of various hardware we use to accomplish the TSF experiment.

- ultrafast oscillator: Spectra-Physics, Tsunami
- regenerative amplifier: Spectra-Physics, Spitfire Pro XP
- optical parametric amplifiers: Light Conversion, TOPAS-C
- motorized translation stages: Newport, MFA-CC
- monochromator: HORIBA Jobin Yvon MicroHR, 140 mm focal length
- monochromator gratings:
    1. "grating 1": 150 grooves/mm, 1200 nm blaze.
    2. "grating 2": 300 grooves/mm, 500 nm blaze.
- PMTs:
    1. "PMT 1": uncooled Hamamatsu 1P28A.
    2. "PMT 2": thermoelectrically cooled Hamamatsu H7422-20.
- Optical choppers: Thorlabs MC2000B and MC1000A

The three tuning OPA tuning range combinations explored in this work were not all accomplished back to back and with the exact same detection strategy (hence the importance of fused silica normalization). Below we describe the exact detection strategy used for each combination. Note, some experiments were performed with an optical chopping strategy to remove background contributions (none were detected).

- (ω_1, ω_2) = (signal, signal). Grating 1 was used in second order with PMT 1. No optical choppers in use.
- (ω_1, ω_2) = (idler, signal). Grating 1 was used in second order with PMT 1. No optical choppers in use.
- (ω_1, ω_2) = (idler, idler). Grating 2 was used in first order with PMT 2. Optical choppers in

use.

3.12.3 OPA characterization

Here we discuss the OPA output characteristics for the colors employed in this work. We used both signal and idler OPA output configurations for this work. Though both signal and idler are simultaneously produced in our OPAs, we use filters to select each individually. Figure 3.7 shows the results of our OPA color and time-of-flight properties after calibration. The rows of Figure 3.7 demonstrate the different calibration metrics used.

OPA output power

We measure the output power of OPAs with a thermopile (Spectra-Physics 407A). For this measurement, filters isolating signal or idler were *not* used, so the power spectrum is composed of the sum of both processes. The power spectra are shown in Figure 3.7, top row.

OPA output color

For each OPA set point assigned during the tuning procedure, we measure the OPA spectra (see second row of Figure 3.7). The idler spectra are collected with a scanning monochromator and a liquid nitrogen cooled InSb (Judson-Teledyne) detector; the signal spectra are measured with a home-built InGaAs array detector (Sensor: Hamamatsu G9494-256D) coupled to a monochromator acting as a spectrograph. The spectra are plotted relative to the set point color in Figure 3.7, second row.

OPA time-of-flight dispersion corrections

The third row of Figure 3.7 shows the delay dependence of TSF signal after the time-of-flight offsets have been applied. The delay dependence is monitored as either OPA1 is scanned with OPA2 kept constant (columns 1 and 3) or OPA2 is scanned with OPA1 kept constant (columns 2 and 4). In

both cases the monochromator tracks the output at $\omega_m = \omega_1 + 2\omega_2$. As OPA colors are scanned, the signals peak at our encoded zero delay value, demonstrating that the color-dependent offsets have been accurately measured and applied.

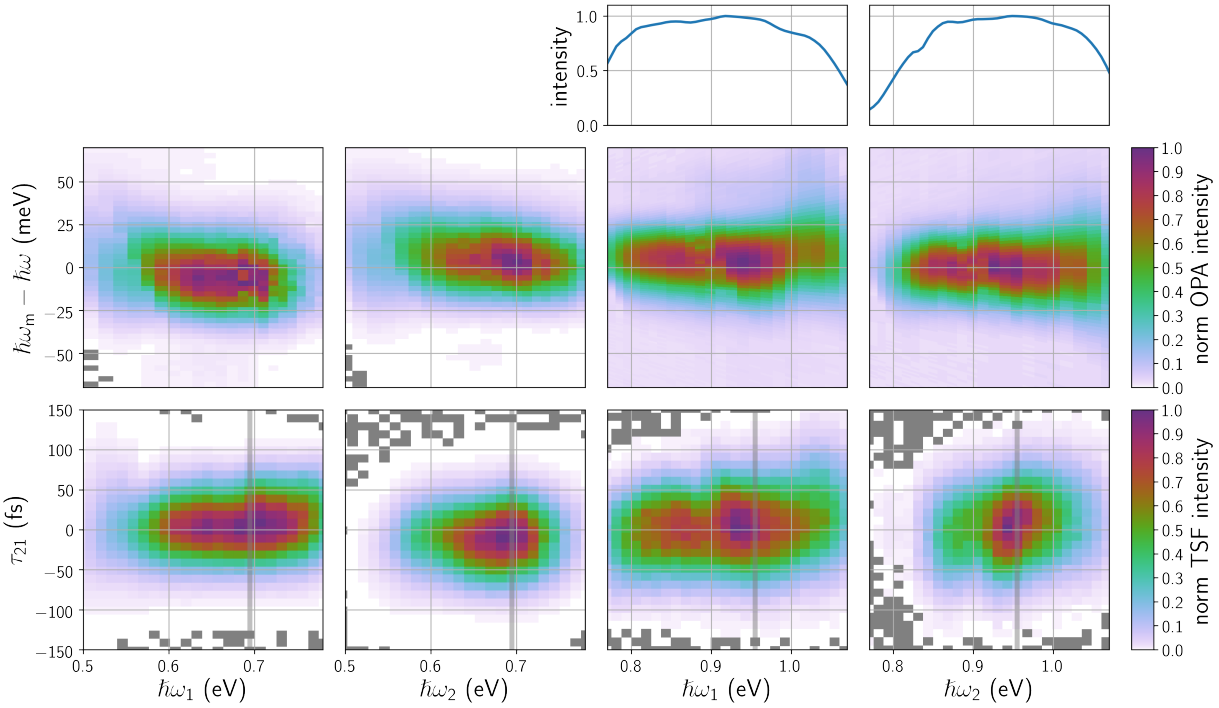

Figure 3.7: Calibration metrics of OPAs First row: OPA output power, as measured by a thermopile, plotted against OPA setpoint. Second row: OPA output spectrum (y-axis) vs. OPA setpoint (x-axis). Third row: time delay setpoint (with active co-setting) between OPA1 and OPA2 (y-axis) vs. OPA setpoint (x-axis) with the measured response (z-axis, colormap) being TSF intensity. The OPA which is not scanned has its setpoint shown with the vertical gray lines. The columns of this figure are as follows: OPA1 idler, OPA2 idler, OPA1 signal, and finally OPA2 signal. Gray pixels correspond to negative results which are expected to appear in the no-signal regions due to noise.

3.13 Appendix: Raw MoS_2 and fused silica TSF

The raw data used to generate the MoS_2 TSF spectrum in the main text is shown in Figure 3.8. The TSF spectrum of our MoS_2 thin film presented in the main text is built from six separately acquired 2D spectra. The six spectra come from three different combinations of the signal and idler

output processes: both OPAs using signal colors (SS), OPA1 using idler and OPA2 using signal (IS), and both OPAs using idler colors (II). For each of the three combinations, a MoS_2 TSF 2D spectrum was measured as well as a control spectrum from the fused silica substrate. The fused silica signals and MoS_2 signals could be interchanged by translating the sample position to change the surface region illuminated by the beams. Notably, the fused silica TSF beam is emitted from the prism at a slightly different angle than the MoS_2 TSF, so the collection optics had to be slightly realigned between these acquisitions. This change in angle arises because the TSF from the fused silica is not a surface generated signal, but is instead a back-reflection of the bulk TSF generation.

We take the back-reflected TSF spectra of the fused silica substrate as the "instrument response function" (IRF) of a given table alignment. This type of measurement is necessary due to the non-uniform power spectrum of our OPAs and the varying spectral responsivity of our detection apparatus. Importantly, the optical interaction length of the back-reflected measurement is sufficiently long that velocity mismatch fringes are not detectable.[31] Since the fused silica has no resonant features, the spectral structure observed in the second row of Figure 3.8 is due to spectral variations in our THG generation efficiency (e.g. spatial overlap of input beams, OPA power) and detection (e.g. detector responsivity).

In order to generate the MoS_2 spectra shown in the main text, we performed the following steps:

1. Convolve each of the six measured spectra with a small 2D Kaiser window (low-pass filtering).
2. Divide the measured MoS_2 spectrum by the fused silica spectrum.
3. Take the square root of the divided spectra to transform them from intensity to amplitude.
4. Scale the spectra to enforce a continuous boundary. The scaling factor was small and accounts for subtle changes in the THG generation from the different OPA output configurations.
5. Join the three divided spectra along the chosen boundaries.

3.14 Appendix: Monochromator scans

We characterize the TSF output of MoS_2 by choosing an OPA1 and OPA2 color and then scanning monochromator color and the delay between pulses. This type of measurement is analogous to a

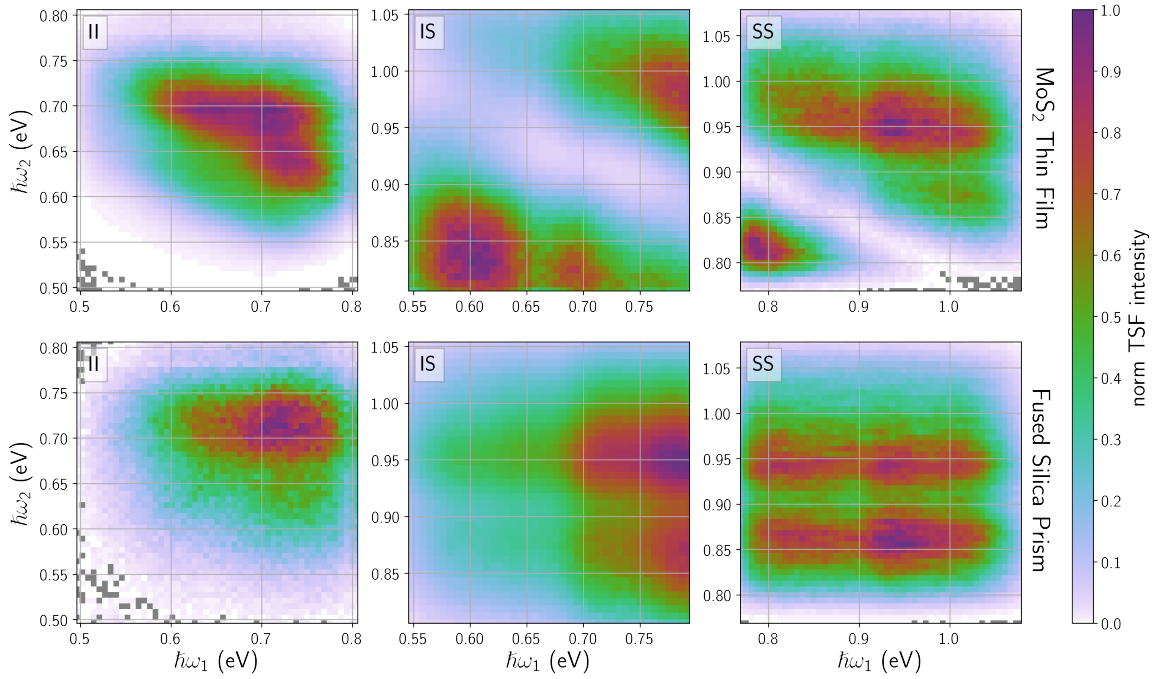

Figure 3.8: Measured, raw TSF intensity of MoS_2 thin film (top row) and its fused silica substrate (bottom row). The different columns, from left to right, correspond to (OPA1, OPA2) outputs being configured as (idler, idler); (idler, signal); and finally (signal, signal). The monochromator tracked the color $\omega_1 + 2\omega_2$. Gray pixels correspond to negative results which are expected to appear in the no-signal regions due to noise.

frequency-resolved optical gating (FROG) measurement. The TSF spectrum as a function of delay between pulses (as shown in Figure 3.9) is remarkably symmetric and smooth.

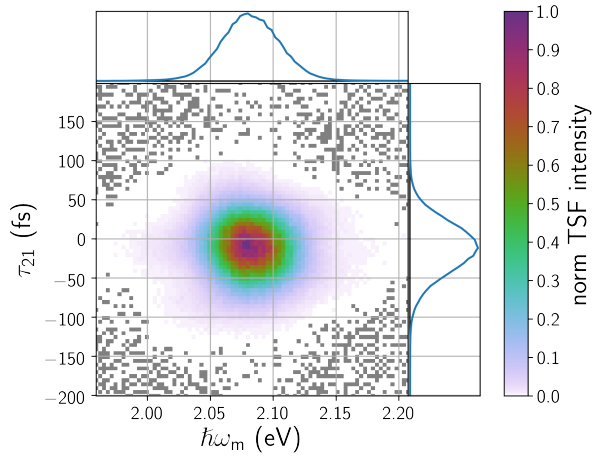

Figure 3.9: Delay setpoint between OPA1 and OPA2 (y-axis) vs. monochromator color (x-axis) with colormap being measured TSF intensity. Sideplots are bins of the dataset. $\omega_1 = \omega_2 = 0.694$eV. Gray pixels correspond to negative results which are expected to appear in the no-signal regions due to noise.

We also ensure that the output in the direction investigated in this paper, $-\left(\vec{k}_1 + 2\vec{k}_2\right)$ has the expected center frequency dependence on driving field colors. We expect the TSF output color to go as ω_1's frequency and twice ω_2's frequency. This is indeed what we observe (see Figure 3.10) in which the first row has a response with slope one and the second row has response with slope two.

3.15 Appendix: Fluence dependence of TSF

With $\hbar\omega_1 = 0.620$ eV and $\hbar\omega_2 = 0.868$ eV we measure the TSF intensity as a function of each individual beams' fluence (as shown in Figure 3.11). We measure the power of each beam at the sample position using a thermopile (Scientech, 360001) and correlate that power to the observed TSF intensity as measured by a PMT. Because we are watching frequency tripling in the output direction of $-\left(\vec{k}_1 + 2\vec{k}_2\right)$, we expect the measured TSF intensity for a given set of colors to go linearly with OPA1 fluence and quadratically with OPA2 fluence. This is the observed trend.

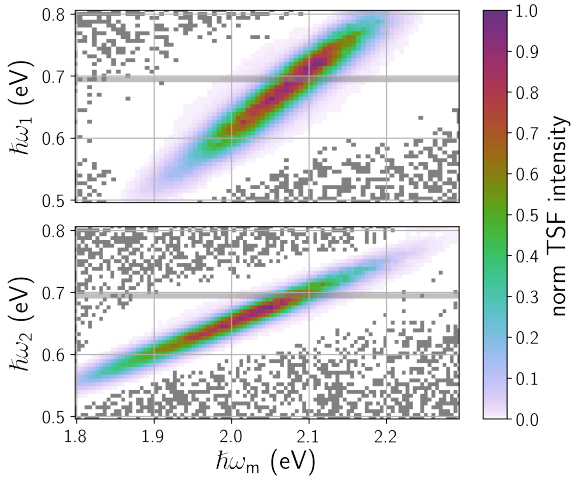

Figure 3.10: TSF spectrum (x-axis) as a function of OPA setpoint (y-axis). The frequency of the non-scanned OPA in each row is marked by the horizontal gray line. Gray pixels correspond to negative results which are expected to appear in the no-signal regions due to noise.

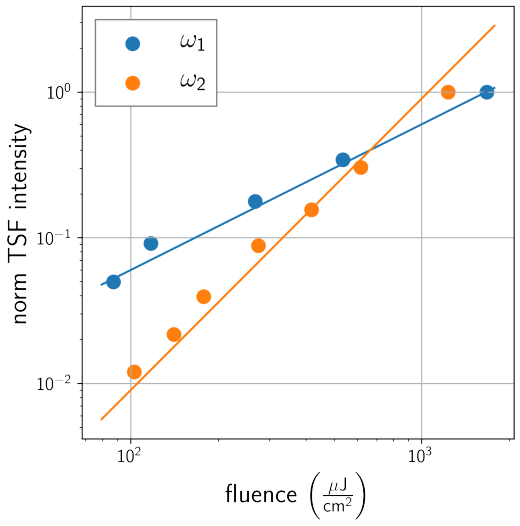

Figure 3.11: Log-log plot of measured TSF intensity as a function of beam fluence for both ω_1 (blue) and ω_2 (orange) having their fluence scanned. Lines are guide to the eye for linear (blue) and quadratic (orange) fluence dependence.

3.16 Appendix: Density of states and sum-frequency spectroscopies

In this section we sketch how to use the idea of a density of states in sum-frequency spectroscopies.

3.16.1 Univariate JDOS

We review the standard treatment of interband direct transitions in a semiconductor near resonance. The first order susceptibility of a semiconductor with a transition dipole, $\mu_{cv}(E)$, which varies slowly with respect to $\vec{k}$ across a set of filled valence, v, and empty conduction, c, bands is given by[121, 122]

$$\chi^{(1)}(\omega) \propto \int \frac{\mathrm{d}E}{E - \hbar\omega - i\hbar\Gamma(E)} \sum_{c,v} J_{cv}(E) \left|\mu_{cv}(E)\right|^2 . \tag{3.15}$$

Γ is a damping rate which accounts for the finite width of the optical transitions. J_{cv} is the joint density of states given by[111]

$$J_{cv}(E) = \frac{1}{(2\pi)^D} \int \delta\left(E_c(\vec{k}) - E_v(\vec{k}) - E\right) \mathrm{d}^3k \tag{3.16}$$

in which D is the dimensionality of the semiconductor. J_{cv} specifies how many optical transitions are available for a given photon energy. Equation 3.16 is usually calculated by integrating cuts, $S(E)$, of constant energy, $E = E_c - E_v$, across the BZ

$$J_{cv}(E) = \frac{1}{(2\pi)^D} \int_{S(E)} \frac{\mathrm{d}S}{\left|\nabla_k \left(E_c - E_v\right)\right|} \tag{3.17}$$

Points in the BZ where $\nabla_k \left(E_c - E_v\right) = 0$ are called critical points (CP) and define a large JDOS. One form of CP occurs when a conduction and valence band are parallel, $|\nabla_k E_c| \approx |\nabla_k E_v| > 0$, this phenomenon is called band nesting.

If all response in an explored frequency range comes from one set of valence and conduction bands,

or each region of frequency is dominated by one set of bands, then we may write Equation 3.15

$$\chi^{(1)}(\omega) \propto \int \frac{\mathrm{d}E}{E - \hbar\omega - i\hbar\Gamma(E)} J_{\text{eff}}(E) \left|\mu_{\text{eff}}(E)\right|^2 \tag{3.18}$$

By construction, Equation 3.18 phenomenologically accounts for excitonic transitions by emphasizing them in the structure of $\mu_{\text{eff}}(E)$.

3.16.2 Extension to sum-frequency spectroscopies

We now extend the JDOS formalism to SHG and THG. We start by writing the optical response of a semiconductor as a collection of transitions at distinct points, $\mathbf{k}$, in the Brillouin zone (BZ). The total response is the summation over the response from all points in the BZ. If multiple transitions occur, then multiple bands must be summed over. We write out all such transitions below for $\chi^{(1)}$, $\chi^{(2)}$, and $\chi^{(3)}$. For sake of compactness we introduce $\omega_{21} \equiv \omega_2 + \omega_1$ and $\omega_{321} \equiv \omega_3 + \omega_2 + \omega_1$; we also neglect proportionality constants.

$$\chi^{(1)}(-\omega_1, \omega_1) = \sum_{c,v} \sum_{\mathbf{k}} \frac{\mu_{vc}(\mathbf{k})\, \mu_{cv}(\mathbf{k})}{\omega_{cv}(\mathbf{k}) - \omega_1 - i\Gamma} \tag{3.19}$$

$$\chi^{(2)}(-\omega_{21}, \omega_1, \omega_2) = \mathcal{P} \sum_{b,a,v} \sum_{\mathbf{k}} \frac{\mu_{vb}(\mathbf{k})\, \mu_{ba}(\mathbf{k})\, \mu_{av}(\mathbf{k})}{[\omega_{bv}(\mathbf{k}) - \omega_{21} - i\Gamma]\,[\omega_{av}(\mathbf{k}) - \omega_1 - i\Gamma]} \tag{3.20}$$

$$\chi^{(3)}(-\omega_{321}, \omega_1, \omega_2, \omega_3) = \mathcal{P} \sum_{c,b,a,v} \sum_{\mathbf{k}} \frac{\mu_{vc}(\mathbf{k})\, \mu_{bc}(\mathbf{k})\, \mu_{ba}(\mathbf{k})\, \mu_{av}(\mathbf{k})}{[\omega_{cv}(\mathbf{k}) - \omega_{321} - i\Gamma]\,[\omega_{bv}(\mathbf{k}) - \omega_{21} - i\Gamma]\,[\omega_{av}(\mathbf{k}) - \omega_1 - i\Gamma]} \tag{3.21}$$

such that $\mathbf{k} \in \text{BZ}$, c, b, a, and v are bands of the semiconductor, and Γ is a damping rate which accounts for the finite width of the optical transitions. $\mathcal{P}$ is a permutation operator which accounts for all possible combinations of field-matter interactions.

We wish to sum over frequency, rather than momentum. We approximate transition dipoles to be a function of transition frequency: $\mu(\mathbf{k}) \to \mu(\omega)$. To replace the summation over $\mathbf{k}$ accurately, we must count the degeneracy of $\mathbf{k}$. To this end, we define $J_{cv}(\Omega) \equiv |\{\mathbf{k} : \omega_{cv}(\mathbf{k}) = \Omega\}|$ in which $|A|$

represents the size of set A. $J_{cv}(\Omega)$ is the number of transitions with resonance at Ω (the joint density of states). $\chi^{(1)}$ can now be written as

$$\chi^{(1)}\left(-\omega_1,\omega_1\right)=\sum_{cv}\sum_{\Omega_1}J_{cv}\left(\Omega_1\right)\frac{\mu_{vc}\left(\Omega_1\right)\mu_{cv}\left(\Omega_1\right)}{\Omega_1-\omega_1-i\Gamma}. \tag{3.22}$$

For spectroscopies with more than one driving frequency, we must define multivariate joint densities to perform a sum over energy:

$$J'_{bav}(\Omega_2,\Omega_1)\equiv\left|\left\{\mathbf{k}:\omega_{ba}=\Omega_2,\omega_{av}=\Omega_1\right\}\right| \tag{3.23}$$

$$J''_{cbav}(\Omega_3,\Omega_2,\Omega_1)\equiv\left|\left\{\mathbf{k}:\omega_{cb}=\Omega_3,\omega_{ba}=\Omega_2,\omega_{av}=\Omega_1\right\}\right|. \tag{3.24}$$

$J'_{ijk}\left(\Omega_2,\Omega_1\right)$ and $J''_{ijk\ell}\left(\Omega_3,\Omega_2,\Omega_1\right)$ count how many points in the BZ have bands i, j, k, and ℓ with transitions at frequencies of Ω_1 Ω_2 and Ω_3 (referenced in energy to the starting state). The second nonlinear susceptibility is

$$\chi^{(2)}\left(-\omega_\Sigma,\omega_1,\omega_2\right)=\mathcal{P}\sum_{b,a,v}\sum_{\Omega_2,\Omega_1}J'_{bav}\left(\Omega_2,\Omega_1\right)J_{av}\left(\Omega_1\right)\frac{\mu_{vb}\left(\Omega_2+\Omega_1\right)\mu_{ba}\left(\Omega_2\right)\mu_{av}\left(\Omega_1\right)}{\left[\Omega_2+\Omega_1-\omega_{21}-i\Gamma\right]\left[\Omega_1-\omega_1-i\Gamma\right]} \tag{3.25}$$

The third nonlinear susceptibility is

$$\begin{aligned}\chi^{(3)}\left(-\omega_\Sigma,\omega_1,\omega_2,\omega_3\right)=\mathcal{P}\sum_{cbav}\sum_{\Omega_3\Omega_2\Omega_1}&J''_{cbav}\left(\Omega_3,\Omega_2,\Omega_1\right)J'_{bav}\left(\Omega_2,\Omega_1\right)J_{av}\left(\Omega_1\right)\\&\times\frac{\mu_{vc}\left(\Omega_3+\Omega_2+\Omega_1\right)\mu_{cb}\left(\Omega_3\right)\mu_{ba}\left(\Omega_2\right)\mu_{av}\left(\Omega_1\right)}{\left[\Omega_3+\Omega_2+\Omega_1-\omega_{321}-i\Gamma\right]\left[\Omega_2+\Omega_1-\omega_{21}-i\Gamma\right]\left[\Omega_1-\omega_1-i\Gamma\right]}.\end{aligned} \tag{3.26}$$

We have thus shown how to extend the concept of a density of transitions from linear spectroscopies to nonlinear spectroscopies.

3.17 Appendix: Model implementation and fitting

3.17.1 Three band approximation

We now show the explicit equations, derived from Equation 3.22, Equation 3.25, and Equation 3.26, that we employed to calculate and extract the JDOS and dipole. As mentioned in the main Article, we consider a model system of three bands: valence band v, conduction band c, and a higher energy b band. All resonant transitions occur from the bands c and v. Band b is an ad hoc inclusion to account for the non-resonant transitions from all other bands; it's energy is defined as 6 eV above the valence band. Since band b is non-physical, we do not distinguish between JDOS factor and dipole enhancement for transitions involving b, and instead combine both terms as the parameter μ_{NR}.

With these simplifications, Equation 3.25 simplifies to

$$\chi^{(2)}\left(-\omega_{\Sigma},\omega_{1},\omega_{2}\right)=\mathcal{P}\mathcal{P}'\sum_{\Omega}J_{cv}\left(\Omega\right)\frac{\mu_{\mathrm{NR}}\left(\Omega\right)\mu_{\mathrm{NR}}\left(\Omega\right)\mu_{cv}\left(\Omega\right)}{\mathcal{D}\left(\omega_{21}\right)\left[\Omega-\omega_{1}-i\Gamma\right]}, \tag{3.27}$$

in which $\mathcal{D}\left(\omega\right)\equiv\Omega_{bv}-\omega-i\Gamma_{b}$ is the resonance denominator for band b. The permutation operator $\mathcal{P}'$ accounts for all permutations of all bands, while the first permutation operator $\mathcal{P}$ accounts for all permutations of driving frequencies.

The form of $\chi^{(3)}$ is a bit more complicated to write out because there are many permutations of resonant and non-resonant interactions. For sake of simplicity we only present only the pathway $v\rightarrow c\rightarrow b\rightarrow c\rightarrow v$ and account for all other pathways by permutation operations in actual calculations. We rewrite Equation 3.26 as

$$\chi^{(3)}\left(-\omega_{\Sigma},\omega_{1},\omega_{2},\omega_{3}\right)=\mathcal{P}\mathcal{P}'\sum_{\Omega}J_{cv}\left(\Omega\right)\frac{\mu_{cv}\left(\Omega\right)\mu_{\mathrm{NR}}\left(\Omega\right)\mu_{\mathrm{NR}}\left(\Omega\right)\mu_{cv}\left(\Omega\right)}{\left[\Omega-\omega_{321}-i\Gamma\right]\mathcal{D}\left(\omega_{21}\right)\left[\Omega-\omega_{1}-i\Gamma\right]}. \tag{3.28}$$

$\chi^{(1)}$ is rewritten from Equation 3.22:

$$\chi^{(1)}\left(-\omega_1, \omega_1\right) = \sum_{\Omega} J_{cv}\left(\Omega\right) \frac{\mu_{vc}\left(\Omega\right) \mu_{cv}\left(\Omega\right)}{\Omega - \omega_1 - i\Gamma}, \tag{3.29}$$

which is the discrete, two-band analog of Equation 3.15.

3.17.2 Simulation details

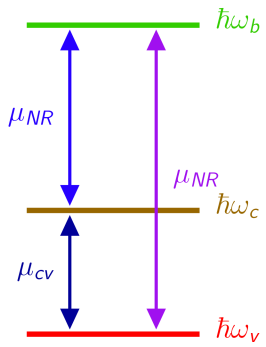

Figure 3.12: Schematic of a single state, c, in our model. This figure diagrams how c is connected to a high-lying state, b, and the ground (valence band) state, v, by transition dipoles.

In order to implement our model, we space each state by 20 meV between 1.1 and 3.9 eV (140 points). We arbitrarily impose $\hbar\Gamma = 20$ meV while the upper state is characterized by $\hbar\omega_b = 6$ eV and $\hbar\Gamma_b = 0.5$ eV. We then simultaneously fit the absorption, SHG, and THG spectra of MoS_2 by varying each state's μ_{cv}, μ_{NR}, and J_{cv} (420 parameters in total). The Levenberg-Marquardt algorithm is used to solve the least squares problem; the three individual spectra are equally weighted in the cost function by interpolating each onto the same grid (10 meV spacing). We impose smoothly decaying boundaries on all spectra outside of their experimentally explored regions in an attempt to minimize boundary problems. We extensively, randomly perturb our starting guesses to ensure convergence to a suitable minimum in the vast parameter space—we present the average

of five fits each with randomly perturbed initial guesses.

Chapter 4 Triple sum frequency pump-probe spectroscopy of transition metal dichalcogenides

This Chapter borrows extensively from Morrow et al. [123]. The authors are:

1. *Darien J. Morrow*
2. *Daniel D. Kohler*
3. *Yuzhou Zhao*
4. *Song Jin*
5. *John C. Wright*

4.1 Abstract

Triple sum-frequency (TSF) spectroscopy measures multidimensional spectra by resonantly exciting multiple quantum coherences of vibrational and electronic states. In this work we demonstrate pump-TSF-probe spectroscopy in which a pump excites a sample and some time later three additional electric fields generate a probe field which is measured. We demonstrate pump-TSF-probe spectroscopy on polycrystalline, smooth, thin films and spiral nanostructures of both MoS_2 and WS_2. The pump-TSF-probe spectra are qualitatively similar to the more conventional transient-reflectance spectra. While transient-reflectance sensitivity suffers under low surface coverage, pump-TSF-probe sensitivity is independent of the sample coverage and nanostructure morphologies. Our results demonstrate that pump-TSF-probe is a valuable methodology for studying microscopic material systems.

4.2 Introduction

Pump-probe spectroscopy is a ubiquitous methodology for investigating the dynamics and energetics of excited systems on sub-picosecond time scales. In a pump-probe experiment, a pump excites the system of interest and a probe interrogates the evolved system at a later time, T. The differences in the probe signal with and without the pump inform on system evolution. Most analytical merits of a pump-probe experiment, such as sensitivity and selectivity, are determined by the choice of a specific probe methodology, of which there are many.[124, 125, 126, 127, 128, 129, 130, 131, 132, 133] The development of Coherent Multidimensional Spectroscopy (CMDS) offers promising possibilities for new probes because CMDS methods can have increased selectivity compared to conventional methods.[99, 32, 134, 135, 136, 137, 138] CMDS uses multiple optical interactions to create a multiple quantum coherence within the material whose optical emission is measured. The ability/requirement to couple multiple quantum states together leads to the selectivity inherent within CMDS. By preceding a CMDS pulse sequence by a pump, the selectivity of CMDS can be leveraged as a probe in a "pump-CMDS-probe" measurement.[139, 125, 126, 129, 140] In this chapter we introduce triple sum-frequency (TSF) spectroscopy as a new fully-coherent probe for material systems by measuring the pump-induced TSF response of model semiconductor systems: transition metal dichalcogenides (TMDCs).

TSF spectroscopy uses three electric fields, E_1, E_2, and E_3, to create coherences at increasingly higher energies. These coherences cooperatively emit a new electric field with frequency $\omega_{\text{out}} = \omega_1+\omega_2+\omega_3$ in a direction defined by phase-matching. Scanning the multiple driving laser frequencies enables collection of a multidimensional spectrum whose cross-peaks identify dipole coupling among probed states. The selectivity of TSF is due to the increase in output intensity achieved when the driving fields are resonant with one or more states; multiple resonance conditions can act as a spectral fingerprint of an analyte.[19] TSF has been used to investigate vibrational and electronic coupling in molecules,[20, 15, 16, 17, 22, 18] and recently, TSF has revealed the electronic states of MoS_2 and the mixed-vibrational-electronic coupling of organic-inorganic perovskites.[68, 21] We believe TSF is a promising probe methodology for several reasons: TSF offers complementary information compared to standard techniques like reflection and absorption;[68] TSF is usable

across many different sample morphologies; multiresonant TSF can examine interactions between multiple electronic and/or vibrational states; and pump-TSF-probe is easily extended to microscopy due to the groundwork already laid for multiphoton microscopy.[141, 142, 143]

In this chapter, we use MoS_2 and WS_2 as model systems to demonstrate some of the capabilities of pump-TSF-probe spectroscopy. MoS_2 and WS_2 are well-studied, layered semiconductors in the TMDC family.[6] The bandedge optical spectrum of MoS_2 has two excitonic features labeled A ($\hbar\omega_A \approx 1.8$ eV) and B ($\hbar\omega_B \approx 1.95$ eV) while WS_2 is dominated near the bandedge by a single excitonic feature labeled A ($\hbar\omega_A \approx 2$ eV). These features originate from high binding energy excitonic transitions between spin-orbit split bands (cf. absorption spectrum of MoS_2 and inset diagram in Figure 4.1).[144, 75, 14, 77, 78, 79] The present work expands upon our previous work on the unpumped TSF response of MoS_2,[68] the extensive body of harmonic generation work on TMDCs (cf. the review by Autere et al. [145] and references therein), and the innovative pump-second-harmonic-generation probe work accomplished on semiconductors.[146, 147, 148, 149, 150, 151, 152, 153]

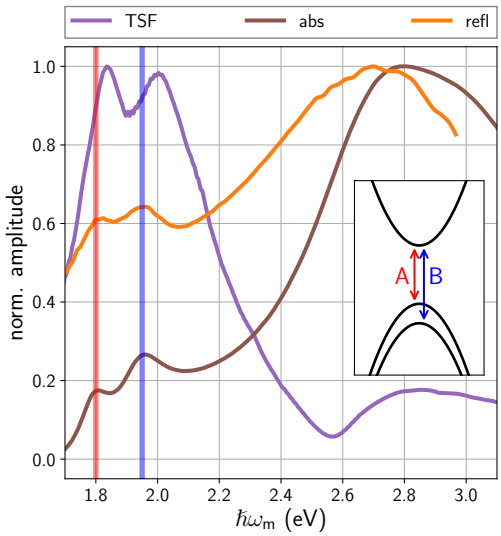

Figure 4.1: Normalized amplitude 1D spectra of MoS_2 thin films. The absorption measurement was originally shown in Czech et al. [61]. The TSF and reflection contrast measurements were originally shown in Morrow et al. [68]. Vertical bars are guides to the eyes set at 1.80 and 1.95 eV. The inset is a cartoon of the band dispersion of MoS_2 about the K point. Only the valence bands are shown as spin-orbit-split because the splitting of the conduction bands is generally too small to be observed for MoS_2.

In our previous work on the unpumped TSF response of MoS_2 we noted important differences between the non-linear TSF probe and conventional linear probes, such as absorption or reflection.[68] One important difference is the scaling with transition dipole, μ, and state density, J: TSF intensity scales as $\mu^8 J^2$, while absorption and reflection scale as $\mu^2 J$. The steep scaling of TSF with transition dipole compared to state density depresses continuum signals and enhances large dipole transitions. The dipole scaling of other CMDS techniques has enabled the measurement of protein structure against large backgrounds when conventional absorption measurements fail.[154, 155] The ability of TSF to isolate large dipole transitions is highlighted in Figure 4.1 for the example of MoS_2. The absorption and reflection spectra of the MoS_2 thin film are dominated by higher energy transitions with large joint density of states and low transition moments. Conversely, the TSF spectrum (in this case $\omega_1 = \omega_2 = \omega_3 = \omega_{\text{out}}/3$, a third harmonic generation, THG, spectrum) is dominated by the large transition dipole A and B excitonic transitions.

Another important difference between TSF and linear probes is the nature of backward propagating light. For linear probes, the amount of backward propagating light (reflection) depends not only on resonance, but also on refractive index mismatch, which can result in large background contributions, especially for samples with incomplete surface coverage, or rough morphologies. This limitation is important for optically thick samples, where reflection is the only viable linear probe. On the other hand, TSF is well-suited for a reflection geometry, where non-linear pulse propagation effects due to phase mismatch, group velocity mismatch, and absorption are negligible.[31] Furthermore, non-linear emission in the backwards direction is qualitatively different than the direct reflection of incident light, and the refractive index mismatch does not control the measured intensities.[156] For example, we have found that the ratio of reflected TSF emission from MoS_2 films to pure substrate TSF emission is beyond the dynamic range of our our experiment as determined by our analog-to-digital-converter (>65,000:1).[68] As a result, a TSF probe provides high contrast signal, resulting in better signal-to-noise, lower detection limits, and sensitivity to a variety of sample morphologies. This chapter highlights these advantages by examining different sample morphologies and surface coverage levels.

The structure of this chapter is as follows. In the Theory section we describe the pump-TSF-probe response and compare it to the familiar pump-reflection-probe method. In the Experimental section

we describe our spectrometer and our various TMDC samples. In the Results section we present our pump-TSF-probe measurements on TMDCs. We first examine how the multidimensional TSF spectrum is affected by an optical pump. We find that the multidimensional TSF spectrum can be fully described by the one-dimensional pump-THG-probe spectrum. We compare pump-THG-probe to pump-reflectance-probe spectroscopy and we demonstrate that the same pump-induced physics explains both spectra. We then compare the pump-TSF-probe of several TMDC samples that differ in morphology and composition, both demonstrating the versatility of pump-TSF-probe and revealing the strong dependence of morphology on several layer TMDC dynamics. Finally, we discuss how transient-TSF might be used in the future on other systems.

4.3 Theory

4.3.1 The linear and non-linear probe

In this section we present the correspondence between the reflectance and TSF of a material. We investigate the phenomenological, microscopic properties that are responsible for the susceptibility and also how the susceptibility dictates the electric field output. Readers interested in first-principle calculations of TMDC nonlinear susceptibility should consult refs.[157, 158, 159, 160, 161]. Our analysis uses standard perturbation theory.[38, 84] The material polarization, P, is expanded in orders of the electric field, E:

$$P = \epsilon_0 \left(\chi^{(1)} E + \chi^{(2)} E^2 + \chi^{(3)} E^3 + \cdots \right), \tag{4.1}$$

where $\chi^{(n)}$ is the n^{th}-order susceptibility and ϵ_0 is the permittivity of free space. The linear susceptibility, $\chi^{(1)}$, determines the response of linear spectroscopies such as absorption and reflection. The third-order susceptibility, $\chi^{(3)}$, determines the response of non-linear spectroscopies such as TSF.

Within the dipole approximation, $\chi^{(1)}$ is constructed from a sum over all initial and final states:

$$\chi^{(1)}\left(\omega_1\right) = \sum_{a,g} \frac{\mu_{ag}^2}{\Delta_{ag}^1}, \tag{4.2}$$

where $\Delta_{ag}^1 \equiv \omega_{ag} - \omega_1 - i\Gamma$, μ_{ag} and ω_{ag} are the transition dipole and frequency difference between states a and g, Γ is a damping rate which accounts for the finite width of the optical transitions, and ω_1 is the driving frequency. We see from Equation 4.2 that when the driving field is resonant ($\omega_1 = \omega_{ag}$), $\chi^{(1)}$ is large and the interaction with light is strong.

Like Equation 4.2, the TSF susceptibility is a sum over states, but we must consider three sequential excitations $g \to a \to b \to c$:

$$\chi^{(3)}\left(-\omega_{321}, \omega_1, \omega_2, \omega_3\right) = \mathcal{P} \sum_{c,b,a,g} \frac{\mu_{gc}\mu_{cb}\mu_{ba}\mu_{ag}}{\Delta_{gc}^{123}\Delta_{gb}^{12}\Delta_{ga}^1}, \tag{4.3}$$

$$\Delta_{ga}^1 \equiv \omega_{ag} - \omega_1 - i\Gamma,$$

$$\Delta_{gb}^{12} \equiv \omega_{bg} - \omega_{21} - i\Gamma,$$

$$\Delta_{gc}^{123} \equiv \omega_{cg} - \omega_{321} - i\Gamma,$$

$$\omega_{21} \equiv \omega_2 + \omega_1,$$

$$\omega_{321} \equiv \omega_3 + \omega_2 + \omega_1,$$

where $\mathcal{P}$ is a permutation operator which accounts for all combinations of field-matter interactions. If only the triple sum transition is resonant, we can approximate all other resonance (Δ) terms as constant and arrive at an expression similar to Equation 4.2:[68]

$$\chi^{(3)}(\omega_{123}) \propto \sum_{a,g} \frac{\mu_{ag}^4}{\Delta_{ag}^{123}}. \tag{4.4}$$

We now consider how the linear and third-order susceptibilities dictate the reflectance and TSF response, respectively. Both relations are formulated using Maxwell's equations via continuity relations (boundary conditions) between the incident, reflected, and transmitted fields. For ease of comparison, we will analyze the simple limit of an extremely thin film (thickness much less

than the wavelength of light) on a transparent substrate. We also restrict consideration to normal incidence. Including thickness and angular dependence is straightforward but needlessly complex for our intent of illustrating qualitative differences between methodologies. These conditions are reasonable for many of the samples and experiments we consider here.

With these conditions, the reflectance, R, is related to the thin film linear susceptibility, $\chi^{(1)}$, by[162, 114]

$$R \equiv \frac{I_{\text{reflected}}}{I_{\text{incident}}} = \frac{(1 - n_s - A)^2 + B^2}{(1 + n_s + A)^2 + B^2}, \tag{4.5}$$

in which n_s is the substrate refractive index,

$$A \equiv \frac{\omega_1 \ell}{c} \text{Im}\left[\chi^{(1)}\right], \tag{4.6}$$

$$B \equiv \frac{\omega_1 \ell}{c} \text{Re}\left[\chi^{(1)}\right], \tag{4.7}$$

ℓ is the film thickness (propagation length), and c is the speed of light in vacuum.

Expanding Equation 4.5 and keeping only terms linear in $\chi^{(1)}$, shows that the imaginary component of the thin film susceptibility is responsible for contrast from the substrate background:

$$R \approx \frac{(1 - n_s)^2 - 2(1 - n_s)A}{(1 + n_s)^2 + 2(1 + n_s)A}. \tag{4.8}$$

Equation 4.8 can be further simplified by Taylor expansion around $A = 0$:

$$R \approx R_0 \left(1 - \frac{2}{1 + n_s^2} A\right), \tag{4.9}$$

where $R_0 \equiv \frac{(1-n_s)^2}{(1+n_s)^2}$ is the reflectance of the substrate-air interface.

Equations 4.5-4.9 show that reflectance is largely determined by the substrate refractive index, which results in large background. As an example, consider properties appropriate for TMDC thin films encountered here: $\ell \sim 10$ nm and $n_s = 1.45$. Under the optimal conditions of resonant excitaton (excitation wavelength ~ 600 nm and $\chi^{(1)} = i$), $A \approx 0.1$ so the thin film gives a maximum contrast from the substrate of $(R - R_0)/R_0 \sim 0.4$. This level of background is typical for reflection

studies of TMDC samples.[163] Note that the contrast becomes considerably worse in the case of incomplete sample coverage, where the observed reflection amplitude would be a weighted average of the reflection coefficients. Rough samples introduce scattering which also distort resonance effects of specular reflection.

TSF emission, or non-linear frequency conversion in general, is qualitatively different from reflectance (or transmittance) because the TSF wave originates from inside the thin film. This difference brings two important consequences to the measured beam: (1) TSF emission is dark in regions where the thin film is not present, and (2) the continuity relations are acutely sensitive to the thin film non-linear polarization, rather than an incident field.[156] For the aforementioned thin film conditions, the TSF output intensity satisfies the proportionality

$$\frac{I_{\mathrm{TSF}}}{I_1 I_2 I_3} \propto \left|\chi^{(3)}\right|^2 (\omega\ell)^2, \tag{4.10}$$

where I_i is the intensity of the ith excitation field.[156] Unlike reflectance, thin film TSF emission obeys the same $\chi^{(3)}$ scaling as the thick film emission case,[15] where the film thickness is larger than or close to the wavelength of light, but phase mismatch effects are still small.

4.3.2 Pump-TSF-probe and TR spectroscopy

We now consider how the different nature of the reflectance and TSF probe result in different, yet similar, pump-probe measurements. For both linear and non-linear probes, we can describe the pump-induced susceptibility as a perturbation to the unpumped susceptibility:

$$\chi^{(n)}_{\mathrm{pumped}} = \chi^{(n)}_{\mathrm{unpumped}} + \mathrm{d}\chi^{(n)}, \tag{4.11}$$

where $\mathrm{d}\chi^{(n)} = \chi^{(n+2)} I_{\mathrm{pump}}$ is the small pump-induced perturbation. Pump-probe methodologies often look at relative changes in the probe:

$$\text{signal metric} = \frac{X_{\mathrm{pumped}} - X_{\mathrm{unpumped}}}{X_{\mathrm{unpumped}}} \tag{4.12}$$

in which X is the probed quantity. This normalization removes the probe intensity dependence from the signal.

Using reflectance as our probe (Equation 4.9) gives a transient response of

$$\frac{\Delta R}{R} \approx -\frac{R_0}{R}\frac{4\omega\ell}{(1+n_s^2)\,c}\mathrm{Im}\left[\mathrm{d}\chi^{(1)}\right]. \tag{4.13}$$

This expression shows that our signal metric scales as $\mathrm{Im}\left[\mathrm{d}\chi^{(1)}\right]$ which is the same as transient transmittance in a bulk sample (see Appendix 4.7.2 for a derivation). In other words, in the extremely thin film limit, transient reflectance will have lineshapes which are intuitive to those who are used to interpreting bulk transient transmittance (absorption) measurements. The intuitive correspondence between transient reflectance and transient transmittance spectroscopies will break down as $\frac{\omega_1\ell}{c}\left|\chi^{(1)}\right|$ increases—thick samples require a full Fresnel analysis to understand the transient reflectance lineshapes.

With TSF intensity as our probe, we use Equation 4.11 and Equation 4.10 to arrive at

$$\frac{\Delta I_{\mathrm{TSF}}}{I_{\mathrm{TSF}}} = \frac{\left|\mathrm{d}\chi^{(3)}\right|^2 + 2\left|\mathrm{d}\chi^{(3)}\right|\left|\chi^{(3)}\right|\cos(\mathrm{d}\theta)}{\left|\chi^{(3)}\right|^2}, \tag{4.14}$$

where we have used phasor representations of the susceptibilities: $\chi^{(3)} \equiv \left|\chi^{(3)}\right| e^{i\theta}$ and $\mathrm{d}\chi^{(3)} \equiv \left|\mathrm{d}\chi^{(3)}\right| e^{i(\theta+\mathrm{d}\theta)}$, in which θ can be dependent on probe frequency. If $\left|\mathrm{d}\chi^{(3)}\right| \ll \left|\chi^{(3)}\cos(\mathrm{d}\theta)\right|$ we can write

$$\frac{\Delta I_{\mathrm{TSF}}}{I_{\mathrm{TSF}}} \approx 2\frac{\left|\mathrm{d}\chi^{(3)}\right|}{\left|\chi^{(3)}\right|}\cos(\mathrm{d}\theta), \tag{4.15}$$

If the pump changes only the amplitude of $\chi^{(3)}$ ($\mathrm{d}\theta = 0, \pi$), the relative change in TSF intensity tracks the relative change in susceptibility. However, if the pump also changes the phase, the amplitude changes can be suppressed. Note that in the case of a $\pi/2$ phase shift, our assumption behind Equation 4.15 is invalid. It is important, then, to understand when $\cos(\mathrm{d}\theta)$ can be small. In general, θ changes rapidly near resonances; if pump induced changes shift or broaden a resonance to an extent similar to its linewidth, $\mathrm{d}\theta$ will strongly influence the pump-TSF-probe spectrum. In the absence of dramatic resonance changes, lineshapes will closely approximate $\mathrm{d}\chi^{(3)}/\chi^{(3)}$.

To anticipate the spectra of each technique, it is useful to consider the case of a single Lorentzian resonance perturbed by the pump. For a small perturbation to lineshape parameter $\lambda \in \{\Gamma, \omega_{ag}, \mu\}$, we can construct $\mathrm{d}\chi^{(n)}$ using the derivative

$$\mathrm{d}\chi^{(n)} = \frac{\partial \chi^{(n)}}{\partial \lambda} \mathrm{d}\lambda. \tag{4.16}$$

In the appendices we derive analytical expressions for the lineshapes expected from transient-TSF, transient-reflectance, and transient-transmittance spectroscopies in this single resonance limit. Numerically calculated spectra are shown in Figure 4.2 for three different types of perturbations:

- An increase in the transition dipole, $\mathrm{d}\mu > 0$. State-filling and Coulomb-screening lead to a decrease in exciton transition dipoles (opposite of change shown in the figure). Note that changes in state density will cause the same lineshape as transition dipole changes.
- An increase in the resonance frequency, $\mathrm{d}\omega_{ag} > 0$. Bandgap renormalization or Coulomb-screening can decrease or increase an exciton resonance freuquency.
- An increase in the dephasing rate, $\mathrm{d}\Gamma > 0$. Pump-excited carriers can scatter with probe excitations, causing the dephasing rate of a transition to increase.

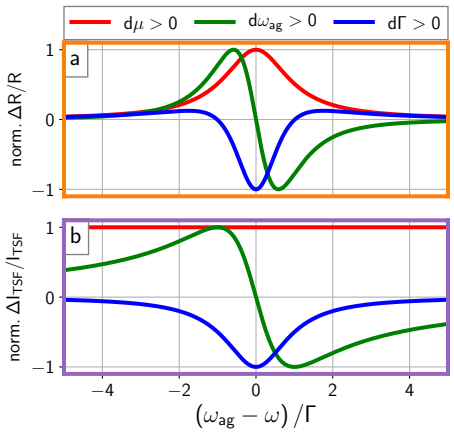

Figure 4.2: Calculated transient lineshapes for a single, complex Lorentzian resonance (see Appendices 4.7.1-4.7.2). (a) The transient-reflectance spectrum. (b) The transient-TSF spectrum. The spectra are produced by perturbing μ, ω_{ag}, or Γ by a factor of 10^{-5}.

The transient-reflectance spectra (see Figure 4.2a) are easily interpreted because changes in Im $\left[\chi^{(1)}\right]$

correlate with changes in absorptive cross-section (Equation 4.9). Interpretation of $\Delta R/R$ line shapes mirrors the traditional interpretation of differential transmission, $\Delta T/T$, for bulk samples obeying Beer's law. Increasing the dipole strength (red line) increases reflectance (positive $\Delta R/R$), with a line shape mirroring the unpumped transition. Resonance red-shifts (green line) increase reflectance to the red and decreases reflectance to the blue. Line shape broadening (blue line) decreases reflectance in the center of the resonance but increases reflectance on the wings.

The transient-TSF lineshapes (Figure 4.2b) have similar interpretations. Increases in transition dipole (red line) increases TSF (positive $\Delta I/I$). Unlike reflectance, the increase results in a constant $\Delta I/I$ offset. This is because the unpumped I_{TSF} lineshape has no background from substrate and so its lineshape is sharply peaked and matches that of ΔI. Line shape broadening (blue line) and blue-shifting (green line) again mirror the behavior of $-\Delta T/T$, but the $\Delta I/I$ line shapes are noticeably broader than $\Delta R/R$. Since TSF is sensitive not only to imaginary component, but also the dispersive real component of $\chi^{(3)}$ (Equation 4.15), the resulting lineshapes are intrinsically broader. In general, for the same dephasing rate, the transient-TSF lineshapes are broader than the transient-transmittance and transient-reflectance lineshapes.

4.4 Experimental

4.4.1 Ultrafast measurements

Our experimental setup uses an ultrafast oscillator seeding a regenerative amplifier (Spectra-Physics Tsunami and Spitfire Pro, respectively) to produce ∼35 fs pulses centered at 1.55 eV at a 1 kHz repetition rate. The amplifier output separates into three arms. Not all arms are used in every experiment. Two arms are optical parametric amplifiers (Light-Conversion TOPAS-C) which create tunable pulses of light from ∼0.5 to ∼2.1 eV with spectral width on the amplitude level of FWHM ≈ 46 meV, absorptive filters and wire grid polarizers are used to isolate light of the desired color.[1] The third arm frequency doubles the output of the amplifier to create pulses centered at

[1] A crucial filter for our TSF probe experiments is a 1000 nm longpass filter (ThorLabs FGL1000M) which ensures no visible light from secondary OPA processes reach the sample. Notably, double side polished silicon was not a suitable filter because it created non-negligible THG as well as lossy transmission.

3.1 eV in a β-barium-borate crystal. Each arm has its own mechanical delay stage and optical chopper. All pulses are then focused onto the sample with a 1 m focal length spherical mirror. The spatially coherent output (either the reflected probe or the triple sum of the probe) is isolated with an aperture in the reflected direction (sometimes referred to as an *epi* experiment), focused into a monochromator (Horiba Micro-HR) and detected with a thermoelectrically cooled photomultiplier tube (RCA C31034A). Figure 4.3 diagrams the focusing and collection geometry used in this work. A dual-chopping routine is used to isolate the desired differential signal.[164] The color-dependent time-of-flight for each arm is corrected by offsetting the mechanical delay stages for each combination of pump and probes colors. We use a reflective geometry for our TSF measurements in order to minimize phase-mismatch effects.[31, 100] Unless otherwise noted, the pump fluence in these measurements is $\sim$100 μJ/cm^2. In Appendix 4.10 we show that this pump fluence is sufficiently small such that higher-order non-linear pump-induced effects can be neglected. The visible probe beam for the reflectance-probe experiments has a fluence of $\sim$2 μJ/cm^2 while the NIR probe lasers for the TSF-probe experiments have a fluence of $\sim$1000 μJ/cm^2. All beams are hundreds of microns wide at the sample. All raw data, workup scripts, and simulation scripts used in the creation of this work are permissively licensed and publicly available for reuse.[165] Our acquisition[103] and workup[166] software are built on top of the open source, publicly available Scientific Python ecosystem.[56, 57, 58]

4.4.2 Sample preparation and characterization

Polycrystalline MoS_2 (WS_2) films were prepared by first e-beam evaporating 2 nm of Mo (W) onto a fused silica substrate and subsequent sulfidation in a tube furnace at 750 °C for 10 (30) minutes.[61] Note that this exact MoS_2 thin film sample was previously explored in Morrow et al. [68]. Following the methods detailed in Zhao and Jin [8], WS_2 (MoS_2) nanostructure samples on 300 nm SiO_2/Si substrates were prepared using water vapor assisted chemical vapor transport growth by heating 100 mg WS_2 (MoS_2) powder to 1200 °C at 800 torr in a tube furnace in which water vapor was produced by heating 1 g $CaSO_4{\cdot}2H_2O$ powder to 150 °C (120 °C) using heating tape wrapped around the tube furnace. 100 sccm argon was used as the carrier gas during the reaction.

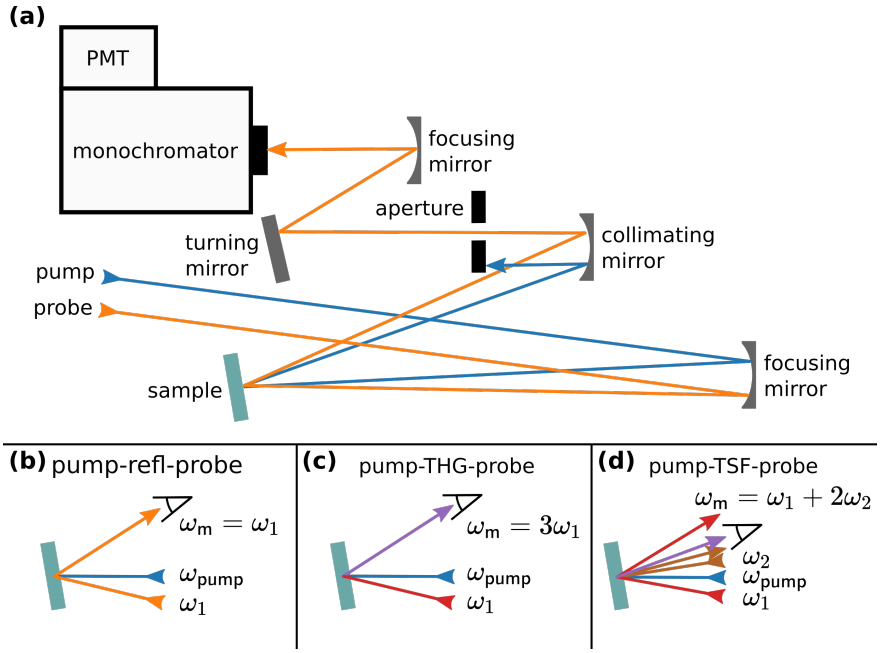

Figure 4.3: Overview of the pump-probe experiments in this work. (a) Schematic of the focusing and collection assembly (not to scale). The optical axis is $\sim 9°$ from the sample surface normal. "PMT": photomultiplier tube. Also shown are the three excitation geometries used in this work: (b) pump-reflection-probe, in which the specular probe (ω_1) reflection is measured, (c) pump-THG-probe, in which the third harmonic signal ($3\omega_1$) travels in the same direction as the fundamental incident probe, and (d) pump-TSF-probe, in which signal is isolated in the $2k_1 + k_2$ direction. The $\lhd$ symbol denotes the collected beam direction (isolated with an aperture). For sake of clarity, some reflections are not shown.

Figure 4.4 shows optical microscope (Olympus BX51M) images, atomic force microscope (Agilent 5500) data, and Raman spectra (LabRAM Aramis, Confocal Raman/PL Microscope, 2.33 eV excitation) of the samples. The Raman spectra show the common E^1_{2g} and A_{1g} modes seen in WS_2 and MoS_2 at the frequencies expected for many-layer to bulk morphologies.[119, 117, 167] The polycrystalline thin films (∼10 nm thick) are continuous, flat, and smooth samples that are much larger than the spot size of our lasers (see Figure 4.4a). Each MoS_2 nanostructure (Figure 4.4b) is a few microns wide and sparsely scattered across the substrate. The nanostructures exhibit a wide range of morphologies from screw-dislocation spirals to stacked plates. The WS_2 nanostructure (Figure 4.4c and d) is a single screw-dislocation spiral which is 84 nm (∼120 layers) thick and ∼150 μm wide. TMDC screw-dislocation spirals are known to have excellent optical harmonic generation abilities.[96, 168, 169, 170] Note that the perceived colors of the nanostructures in Figure 4.4b and Figure 4.4c are due to thin-film interference effects from the combination of the pyramid nanostructures, which have a large change in height across the structure, and the SiO_2/Si substrates; this class of effects have previously been explored for monolayers and nanostructures.[171, 172, 173]

4.5 Results and Discussion

4.5.1 MoS_2 thin film: transient-TSF

We first examine the effect of a pump on the multidimensional TSF spectrum, in which ω_1 and ω_2 are independently scanned. The output frequency of the TSF probe, $\omega_m = \omega_1 + 2\omega_2$, covers the range of the A and B excitons (1.65 - 2.25 eV). We explore this dependence with a MoS_2 thin film. In this film, the unpumped multidimensional spectra exhibit singly resonant features that depend only on the output triple sum frequency (e.g. Equation 4.4).[68] There are no cross peaks in the unpumped TSF spectrum because MoS_2 A and B excitons do not have the correct symmetry for our excitation beams to couple together. Like the unpumped spectrum, we found that the pump-TSF-probe spectra depends only on the triple sum frequency, regardless of pump-probe delay time. Pump-TSF-probe spectra of the MoS2 thin film at two different delays are shown in Figure 4.5 ($\hbar\omega_{\text{pump}} = 3.1$ eV). At both delay times, all features run along lines of constant output color (slope

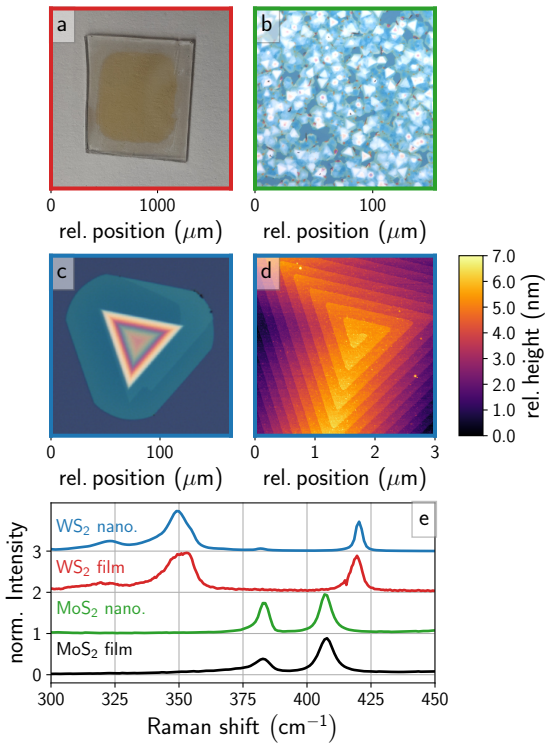

Figure 4.4: TMDC Sample characterization. (a) Photograph of the WS_2 film explored in this work. (b) Optical microscope image of the MoS_2 nanostructures explored in this work. (c) Optical microscope and (d) atomic force microscope image of the WS_2 nanostructure explored in this work. (e) Raman spectra of each sample; the maximum of each Raman spectrum is normalized to 1 and then offset for ease of comparison.

of -1/2). We explored the multidimensional probe spectra at other frequency and T combinations (output energies up to 3 eV and population times up to 100 ps); all features found are defined solely by the output color.

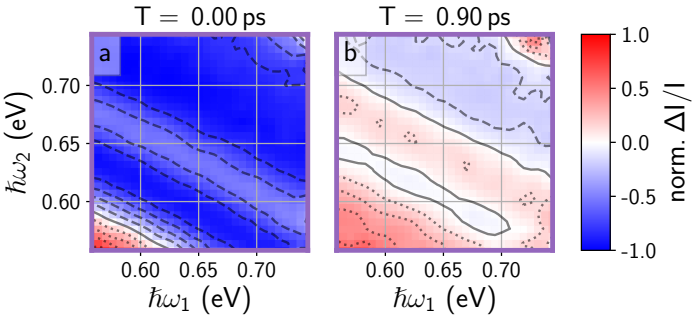

Figure 4.5: Pump-TSF-probe spectra of an MoS_2 thin film at 0 ps (a) and 0.90 ps (b) delay between pump and probe interactions. In both frames $\hbar\omega_{\text{pump}} = 3.1$ eV with a fluence of 120 μJ/cm^2, $\omega_m = \omega_1 + 2\omega_2$, and $\vec{k}_{\text{out}} = \vec{k}_1 + 2\vec{k}_2$.

Given the similarities in band structure, we expect this result to be general to all TMDCs. The simplicity of the TSF and pump-TSF-probe spectra motivate the use of Equation 4.4 and its associated pump-THG-probe analysis which was discussed in the Theory section. Since the output color seems to uniquely determine the observed spectra, we restrict ourselves to the case $\omega_1 = \omega_2 = \omega_m/3$ (pump-THG-probe) for the rest of this work. We will understand the lineshapes present in Figure 4.5 by understanding the lineshapes of the pump-THG-probe spectroscopy presented in the next section.

4.5.2 MoS_2 thin film: transient-THG and transient-reflectance

Here we consider the pump-reflectance-probe and the pump-TSF-probe side-by-side to understand the differing selectivities of both methods. We first compare both probe methodologies using a single pump color. Figure 4.6 shows both the pump-reflectance-probe (left) and the pump-TSF-probe (right) response of the MoS_2 thin film with pump excitation at the B exciton. Note that horizontal $3\omega_1$ slices through Figure 4.6b are almost equivalent to the diagonal, $\omega_1 = \omega_2$ slices of Figure 4.5; they differ only in the use of different pump colors.

The TR and pump-THG-probe responses of Figure 4.6 are qualitatively similar. Our analysis in the Theory section indicates that phenomena like shifting and broadening will lead to similar lineshapes between the two spectroscopies while state density and dipole decreases will look different between the two spectroscopies—so our observed response is likely due to shifting and broadening of the underlying excitonic resonances. In both spectra, the measured intensity at the A and B excitons decreases when the pump is on ($\Delta I/I < 0$). The intensity decreases dominate at $T = 0$, then decay over ∼500 fs to form spectra that undulate between positive and negative values. These undulating spectra persist for several picoseconds (data not shown).

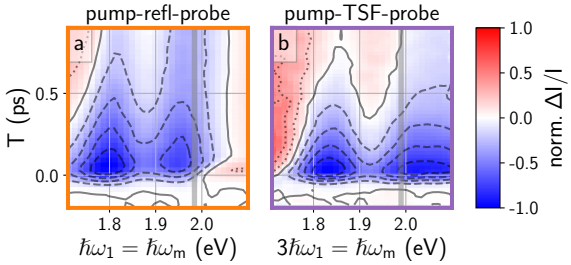

Figure 4.6: Comparison of transient-reflectance spectroscopy (a) to transient-TSF spectroscopy (b) for a MoS_2 thin film. In both frames $\hbar\omega_{\text{pump}} = 1.98$ eV, as indicated by the vertical gray line. Each plot has its own colormap extent, red (dotted contours) signifies $\Delta I/I > 0$, white (solid contour) signifies $\Delta I/I = 0$, and blue (dashed contours) signifies $\Delta I/I < 0$.

The minima of the transient-THG spectra are blue-shifted relative to the corresponding minima observed in the transient-reflectance spectrum, but roughly agree with the peak positions of the unpumped THG spectrum (Figure 4.1). The A and B peaks of the unpumped THG spectrum are blue-shifted by ∼50 meV compared to the absorption/reflection spectrum. We cannot explain why the maxima of the THG and absorption/reflection spectra are different by ∼50 meV, but we note that Wang et al. [88] also observed this same unexplained blue-shift in their THG measurements.

To understand the spectral and temporal information in Figure 4.6, we examine transients at fixed probe frequencies and spectra at fixed time delays in Figure 4.7. For both cases, we use simple models to ensure standard physical arguments can explain our observations. Specifically, we show that the behavior of both probes can be understood with the same underlying system changes.

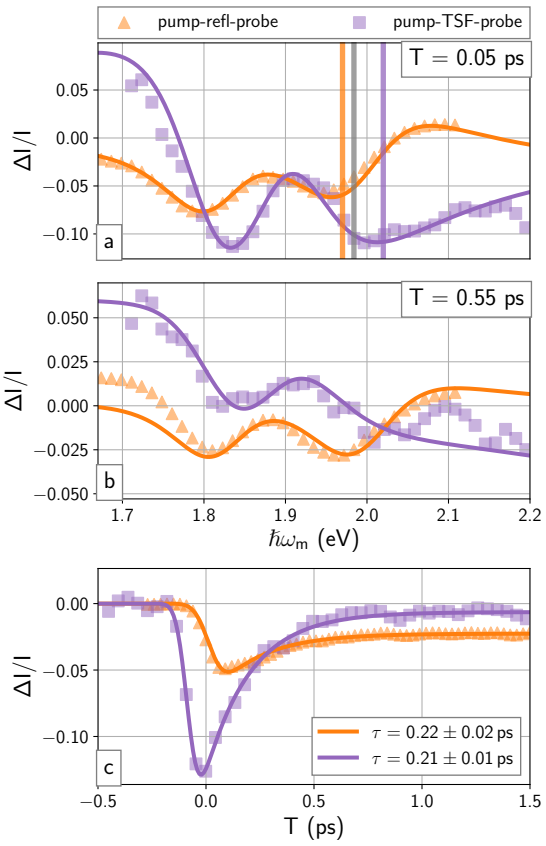

Figure 4.7: Comparison of spectral and temporal lineshapes with $\hbar\omega_{\text{pump}} = 1.98$ eV (gray vertical line). Spectral lineshapes in (a) and (b) are acquired with delay times of 0.05 and 0.55 ps, respectively. Dynamics in (c) are acquired at probe energies indicated by the vertical lines in (a) (1.97 and 2.02 eV for pump-refl-probe and pump-TSF-probe, respectively). Solid lines in each plot are calculated from the models described in the main text and Appendix 4.8.

We first consider the spectral slices. The technical details of the spectral lineshape model (results shown as solid lines in Figure 4.7a and Figure 4.7b) are discussed in Appendix 4.8. In both spectroscopies, the lineshape at $T \approx 0$ (Figure 4.7a) can be explained by a ∼10 meV redshift, slight broadening, and slight amplitude decreases of the A and B resonances. In order to describe the pump-TSF-probe lineshape in Figure 4.7b we incorporated an additional ESA background. We attribute the additional ESA to excitation of near band edge carriers (conduction band electrons, valence band holes, or excitons) upon pump photoexcitation and subsequent relaxation. We attribute the redshift to carrier-induced bandgap renormalization (BGR), which was previously predicted and observed by many in monolayer TMDCs.[174, 131, 175, 176, 177, 178] The lineshape broadening upon excitation is common in semiconductors and has been previously observed by refs. [179, 180] in TMDCs. The amplitude decrease is likely due to state/band filling from the photocarriers.

A short time after excitation, $T = 0.55$ ps, the probe spectra change (Figure 4.7b): the line shapes are reproduced by a few meV redshift, no broadening, and no amplitude decrease. The simultaneous decrease in broadening, BGR, and state/band filling suggests that the majority of photocarriers have relaxed within several hundred femtoseconds, a curious dynamic that will be explored throughout this chapter. Importantly, the interpretation of both probe methodologies is consistent.

Dynamics were described by an exponential decay and a static offset:

$$\frac{\Delta I}{I}(T) = \left(A_0 \exp\left(-\frac{T}{\tau} \right) + A_1 \right) \Theta\left(T - t_0 \right), \tag{4.17}$$

in which Θ is the Heaviside step function. We convolve Equation 4.17 with an instrument response function, which we approximate as Gaussian. Results are shown as solid lines in Figure 4.7c). Like the spectral lineshapes, the dynamics of both probe methods are consistent (Table 4.1). The fast dynamic that changes the probe spectra in Figure 4.7a,b have a time constant of ∼200 fs.[2] Dynamics on this timescale have previously been attributed to several mechanisms, including carrier trapping,[181, 182, 183] carrier-carrier scattering,[179, 184] carrier-phonon scattering,[185, 186,

[2]Because these lineshapes are not merely caused by amplitude changes (J or μ), fitting different probe colors results in different decay rates, with τ up to 0.4 ps.

187] free-carrier screening effects,[180, 188] and exciton formation.[188] The longer dynamic in Figure 4.7c, which we treat as an offset, A_1, is common in single crystal ultrathin TMDC samples.[182, 188]

Table 4.1: Results from fitting Equation 4.17 to the dynamics shown in Figure 4.7b. FWHM = full width at half maximum of the instrument response function.

	pump-refl-probe	pump-TSF-probe
$\hbar\omega_m$ (eV)	1.97	2.02
τ (ps)	0.22 ± 0.02	0.21 ± 0.01
FWHM (ps)	0.125 ± 0.009	0.095 ± 0.006

Figure 4.8 shows the response from both TR and transient-THG spectroscopies for different combinations of pump and probe frequencies when $T = 50$ fs. Figure 4.8a is a very similar measurement to refs. [61, 189, 190, 191, 192, 193, 194, 195] where "traditional" coherent multidimensional spectroscopies were accomplished on TMDCs using a single electric field interaction as a probe; this measurement similarity is not the case for Figure 4.8b in which TSF acts as the probe with three electric field interactions. Nevertheless, both of our spectroscopies in Figure 4.8 have a similar dependence on the pump frequency—this can be seen by comparing vertical slices of Figure 4.8a and b (these horizontal slices are analogous to horizontal slices of Figure 4.6.).[3] The lineshapes of our two spectroscopies change smoothly as a function of $\hbar\omega_{\text{pump}}$—there are no distinct contributions from the A or B resonances along the pump axis. The lack of structure along the pump axis mirrors the results of transient grating measurements on a MoS_2 thin film.[61] The general insensitivity to pump color suggests band gap renormalization (BGR) is a large contributor to the pump-induced changes. BGR is determined by Coulomb interactions, which are less sensitive to the explicit electron and hole occupation than, for instance, Pauli blocking effects.

Conversely, small, but noticeable, dependencies on ω_{pump} suggest secondary contributions to the TR and transient-TSF spectra. For instance, when $\hbar\omega_{\text{pump}} \approx 1.8$ eV $\approx \hbar\omega_{\text{A}}$, the decreases in intensity at $\omega_{\text{out}} = \omega_A$, are $\sim 15\%$ larger than at $\omega_{\text{out}} = \omega_B$ for both TR and pump-TSF-probe. When $\hbar\omega_{\text{pump}} \approx \hbar\omega_{\text{B}}$, however, both A and B have similar decreases in intensity. We believe band/state filling (bleaching) can account for the observed asymmetries in the decreases in intensity. The MoS_2

[3]The decrease in $\Delta I/I$ at high pump frequencies in the TR experiment Figure 4.8a is likely caused by a decrease in the I_{pump} at those frequencies. The two spectra in Figure 4.8 were collected at different times and do not share the same pump intensity spectrum.

valence band is energetically split for different hole spins, but the conduction band is energetically degenerate for electron spins (cf. the inset in Figure 4.1). The A transition and B transition share neither valence nor conduction bands, so state/band filling is not shared between transitions. When the pump is resonant with the A transition, the bleach of the B transition is not direct and is expected to be smaller, in agreement with our measurements. Some bleaching is allowed through intervalley scattering, but valley depolarization measurements suggest these timescales are much longer than our pump probe delay time (50 fs) and is thus not significant.[196, 197, 198] When the pump is resonant with the B transition, it will also directly excite hot excitons or free electons/holes from the A band, which explains why the effects on the A and B transitions are similar for these pump colors. These observations are all consistent with line shape analysis of Figure 4.7a, in which redshifts (BGR) played a significant, but not complete, role in the line shape.

Guo et al. [195] also found asymmetries in the cross peaks of their multidimensional spectra of monolayer MoS_2 at 40 K. They attribute the asymmetric cross-peaks and their dynamics to be due to an exchange interaction between A and B excitons. This effect does not explain our results because the exchange interaction requires simultaneous populations of A and B excitons, which is not the case for $\omega_{\text{pump}} \approx \omega_A$.

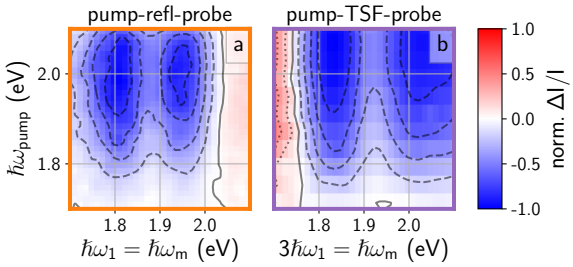

Figure 4.8: Comparison between transient-reflectance spectroscopy (a) and transient-TSF spectroscopy (b) of a MoS_2 thin film. In both frames $T = 50$ fs.

4.5.3 MoS_2 and WS_2 nanostructures

In this section we investigate the effects of sample morphology on pump-TSF-probe spectroscopy by comparing all the samples shown in Figure 4.4. We first compare spectra of the previously discussed

thin film with an ensemble of spiral nanostructures grown via a screw dislocation driven growth method (Figure 4.4b). The goal of this comparison is to broadly demonstrate that the spectra and dynamics observed with transient-TSF are sensitive to the specifics of sample morphology. We then compare the transient-TSF and TR response of both a WS_2 thin film and a single WS_2 screw-dislocation nanostructure.

Transient-THG of a MoS_2 thin film vs. nanostructures

Figure 4.9 shows the probe frequency vs. delay time response of the thin film (Figure 4.9a) and nanostructure (Figure 4.9b). Both spectra show similar spectral lineshapes near zero delay with decreases at the A and B features. The nanostructures spectrum (Figure 4.9b) demonstrate narrower peaks and greater increase in TSF intensity to the red of the A exciton resonance compared to the thin film (Figure 4.9a). The nanostructures exhibiting narrower features indicates that the thin film has more structural inhomogeneity. While both samples show similar lineshapes at $T = 0$, they exhibit drastically different dynamics.

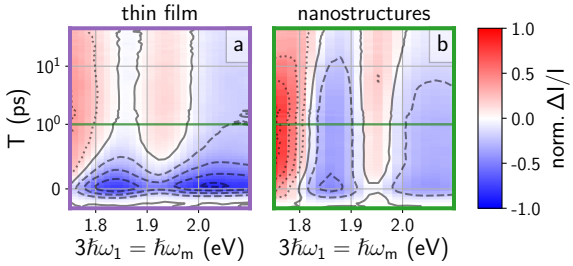

Figure 4.9: Pump-TSF-probe spectra of a MoS_2 thin film (a) and a MoS_2 spiral nanostructure ensemble (b). The temporal axis has linear scaling until 1 ps (horizontal green line) and then logarithmic scaling until the end (50 ps). In both frames $\hbar\omega_{\text{pump}} = 3.1$ eV with a fluence of 120 μJ/cm^2.

Figure 4.10 shows a single temporal trace through the data shown in Figure 4.9 for each sample morphology. The thin lines are the measured data and the thick lines are fits using Equation 4.17. We recover exponential decay time constants of 0.34 ± 0.02 ps for the thin film and 12.7 ± 0.8 ps for the nanostructures. The morphology strongly affects dynamics. We speculate that the dramatic

differences in timescales are related to the density of grain boundaries, which can affect carrier scattering, recombination, and/or trapping.[181] The grain size of the thin film is on the order of 100 nm^2 while that of the nanostructures is on the order of 10-100 μm^2. We believe that carrier trapping or defect assisted annihilation is the main source of dynamics in Figure 4.10; a carrier once it has been trapped/annihilated is not able to efficiently screen the electron-hole Coulomb interaction, so BGR is lessened and the observed differential response is decreased.

There is a low amplitude, rapid dynamic present for each sample in Figure 4.10 that is not captured by our single exponential fit; we attribute this rapid dynamic to hot carriers (the carriers have ~ 1 eV excess energy upon photoexcitation) cooling to form excitons.[188, 180] In TMDCs, hot carriers bleach excitonic transitions more effectively than excitons; so a hot carrier cooling will reduce the bleach observed at the A and B transitions.[199, 188, 180] Taken together, we believe defect/grain-boundary assisted quenching of carriers along with hot carrier cooling can explain the dynamics observed in Figure 4.9 and Figure 4.10.

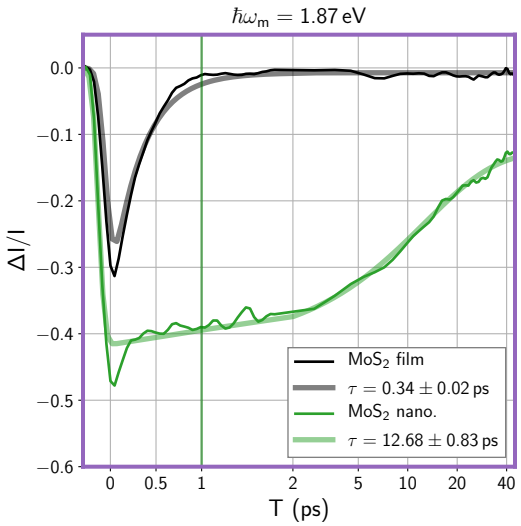

Figure 4.10: Pump-TSF-probe of a MoS_2 thin film and an ensemble of spiral nanostructures. The temporal axis has linear scaling until 1 ps (green line) and then logarithmic scaling until the end (50 ps). This figure displays 1D slices out of Figure 4.9 in which the pump is set to $\hbar\omega_{\text{pump}} = 3.1$ eV while the probe is set to $3\hbar\omega_1 = \hbar\omega_m = 1.87$ eV .

Unified description of pump induced dynamics in MoS_2

Our measurements support the following description of carrier dynamics in multilayer MoS_2. The pump creates electrons (holes) in the valence (conduction) band and excitons. These carriers affect the optical transitions that a probe observes. At $T = 0$, the excited carriers screen the electron-hole Coulomb interaction causing BGR and lowering exciton transition energy. The excited carriers also scatter with each other leading to faster dephasing rates and therefore broadening of the exciton transition. The excited carriers can also Pauli-block the bandedge transitions leading to a small decrease in transition amplitude.

After photoexcitation, the carriers are rapidly annihilated, trapped, or scattered to other momentum points (recall that few-layer MoS_2 is an indirect semiconductor). The exact timescale for this relaxation depends on extrinsic properties such as defects: for our polycrystalline thin film the timescale is hundreds of femtoseconds, while for nanostructures the timescale is roughly ten picoseconds. An electron and hole, once annihilated or trapped, does not scatter or Pauli-block transitions, so the probe sees the original exciton linewidth and transition amplitude. Importantly, a trapped carrier or an indirect exciton can still screen the electron-hole Coulomb interaction,[200, 201] so a long-lived redshift of the exciton transition is commensurate with residual BGR caused by trapped/indirect carriers. The $T = 0.55$ ps spectrum shown in Figure 4.7b represents this residual BGR.

Transient-THG vs. transient-reflectance for WS_2 thin film vs. single nanostructure

To further investigate the abilities of pump-TSF-probe, we performed pump-TSF-probe and pump-reflectance-probe experiments on two different morphologies of WS_2: a thin film on a fused silica substrate (photo shown in Figure 4.4a), and a single, isolated, spiral nanostructure grown on a 300 nm SiO_2 on Si substrate (optical microscope and atomic force microscope characterization shown in Figure 4.4c, and Figure 4.4b, respectively). Our probe beam area is small compared to the area of the thin film, but much larger than the single nanostructure.

In Figure 4.11 we use a NIR pump to drive mid-gap or 2-photon transitions and probe the A exciton

transition of WS_2. Appendix 4.9 describes experiments on our MoS_2 thin film which demonstrate our ability to drive mid-gap transitions with a NIR pump. The full spectra and a discussion of these NIR pump measurements will be the subject of another publication. The unpumped THG spectra of the thin film and nanostructure are shown in Figure 4.11a, and the differential spectra ($T = 120$ fs) for each morphology are shown in Figure 4.11b. In both cases, the thin film exhibits a broader and redder A feature than the nanostructure—structural inhomogeneity from the small grain size of the polycrystalline film likely causes the increased linewidth of the thin film. The differing amount of spectral inhomogeneity causes the transient-reflectance and transient-TSF spectra between the two samples to look slightly different.

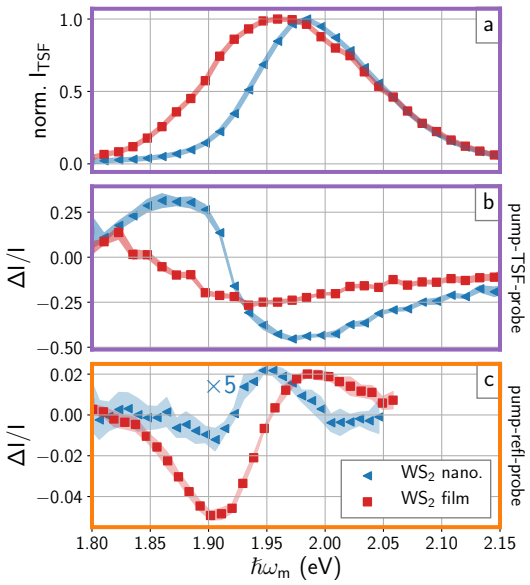

Figure 4.11: Comparison of pump-TSF-probe and pump-reflectance-probe for two morphologies of WS_2: a thin film and a single, ∼150 μm wide spiral nanostructure. (a) normalized TSF spectrum for each sample, these spectra are not normalized for the frequency dependent intensity of the probe OPA. (b) pump-TSF-probe spectra for each sample. (c) pump-refl-probe spectra for each sample. In (b) and (c) the sub-band edge pump has frequency of $\hbar\omega_{pump} = 1.054$ eV and a fluence of ∼7000 $\mu J/cm^2$. All spectra were acquired for the same number of laser shots. Each spectra is composed of 7 spectra averaged together at $T \approx 0.12$ ps. (b) and (c) each show the standard deviation of the averaged spectra for each sample morphology as a filled spread around the average.

While the transient-TSF spectra from both the thin film and the single nanostructure are comperable in signal strength, the same is not true for transient-reflectance measurements. Figure

4.11c shows that the nanostructure signifcantly reduces the transient reflectance signal ($\sim 5\times$ less signal). This is largely due to the indiscriminate nature of reflectivity (Equations 4.5—4.9): since the bare substrate has a substantial reflectivity and covers a large portion of the illumination area, a correspondingly large portion of the reflected probe does not represent the nanostructure. As a result, the relative changes in reflectivity of the nanostructure is diminished. Furthermore, reflected light from bare substrate interferes with reflected light of the nanostructure signals, significantly complicating comparisons between the spectra of the two structures.

In contrast, TSF emission is strongly dependent on resonance enhancement and dipole strength (Equations 4.3 and 4.10). These dependencies strongly suppress both glass substrates (no resonant enhancement) and bulk semiconductor substrates (small dipoles for resonant transitions). As a result, our TSF probe is virtually background free, with contrast similar to that of fluorescence imaging.

4.6 Outlook and Conclusion

Using the examples of MoS_2 and WS_2, this work shows that pump-TSF-probe spectroscopy can elucidate the dynamics and energetics of photoexcited semiconductor thin films and nanostructures. We demonstrated that this new spectroscopy (specifically the degenerate case of pump-TSF-probe, pump-THG-probe) is complementary to the more mature spectroscopy, transient-reflectance. While pump-THG-probe and transient-reflectance have different dependencies on variables like transition dipole strength and state density, we showed that the two spectroscopies can be understood in tandem from the same underlying excited-state physics. These differences in dependencies allow pump-TSF-probe to offer a complementary view on excited state physics, which in some cases will be more definitive than a transient-reflectance measurement. We found that transient-TSF is robust to extrinsic nanocrystal properties, such as size and surface coverage, that dramatically affect transient-reflectance spectra. This robustness allowed us to measure the transient-TSF spectrum of nanostructures much smaller than the excitation spot size, while at the same time maintaining a high signal-to-noise ratio. We predict that with pump-TSF-probe spectroscopy, researchers can avoid the reflectance artifacts which have complicated recent ultrafast work (cf. refs [202, 203])

because the measured TSF and pump-TSF-probe intensities are easily connected to the sample's susceptibility.

Previous studies have shown that TSF can be used to measure coupling between states.[20, 21] Isolating cross peaks is a strategy not explored in this work that could further increase the selectivity of pump-TSF-probe spectroscopy in the future. We believe that samples with states/bands of the correct symmetry would yield insightful dynamical coupling information. For instance, since TSF can measure the energy separations of up to four states, it could resolve how bands change their dispersion upon photo-excitation. Crucially, unlike other multidimensional probes which are not fully-coherent,[139, 125, 129, 140] TSF is not susceptible to population relaxations during the multiple electric field interactions, it is therefore a more direct probe of the underlying quantum states.

Another area that could benefit from the proof-of-concept measurements in this work is multiphoton microscopy. Multiphoton microscopy uses a diverse set of techniques, including THG/TSF,[141, 142, 143] to predominantly measure biologically relevant samples. These multiphoton microscopies could easily incorporate a pump and a delay stage in order to measure spatially resolved dynamics.

Supplementary Material

All data and the workup/representation/simulation scripts used to generate the figures in this work are available for download at http://dx.doi.org/10.17605/OSF.IO/UMSXC.

4.7 Appendix: Single resonance simulations of pump-probe responses

Here we examine the spectra produced by small changes in a system described by one Lorentzian resonance. We assume the system changes are small (Equation 4.16).

4.7.1 Pump-THG-probe

The single resonance third-order susceptibility is given by

$$\chi^{(3)} = \frac{\mu^4}{\omega_{ag} - \omega_{321} - i\Gamma}. \tag{4.18}$$

The parital derivatives of Equation 4.18 are

$$\frac{\partial \chi^{(3)}}{\partial \mu} = \frac{4\mu^3}{\omega_{ag} - \omega_{321} - i\Gamma} \tag{4.19}$$

$$\frac{\partial \chi^{(3)}}{\partial \Gamma} = i\frac{\mu^4}{(\omega_{ag} - \omega_{321} - i\Gamma)^2} \tag{4.20}$$

$$\frac{\partial \chi^{(3)}}{\partial \omega_{ag}} = -\frac{\mu^4}{(\omega_{ag} - \omega_{321} - i\Gamma)^2} \tag{4.21}$$

Using Equation 4.12 and Equation 4.16 we can calculate the change in TSF intensity due to a perturbation:

$$\frac{\Delta I}{I} = \left| 1 + \frac{1}{\chi^{(3)}} \frac{\partial \chi^{(3)}}{\partial \lambda} \mathrm{d}\lambda \right|^2 - 1 \tag{4.22a}$$

$$\approx 2\mathrm{Re}\left[\frac{1}{\chi^{(3)}} \frac{\partial \chi^{(3)}}{\partial \lambda} \right] \mathrm{d}\lambda, \tag{4.22b}$$

where in Equation 4.22b we used the fact that the perturbation is small, $\mathrm{d}\chi^{(3)} \ll \chi^{(3)}$ (Equation 4.22b is equivalent to Equation 4.15). Combining Equations 4.18 - 4.22b, we have

$$\frac{\Delta I}{I} \approx 8\frac{\mathrm{d}\mu}{\mu} \qquad \lambda = \mu \tag{4.23}$$

$$\frac{\Delta I}{I} \approx -\frac{2\Gamma}{(\omega_{ag} - \omega_{321})^2 + \Gamma^2}\mathrm{d}\Gamma \quad \left(\propto \mathrm{Im}\left[\chi^{(3)}\right]\right) \qquad \lambda = \Gamma \tag{4.24}$$

$$\frac{\Delta I}{I} \approx -\frac{2\left(\omega_{ag} - \omega_{321}\right)}{(\omega_{ag} - \omega_{321})^2 + \Gamma^2}\mathrm{d}\omega_{ag} \quad \left(\propto \mathrm{Re}\left[\chi^{(3)}\right]\right) \qquad \lambda = \omega_{ag}. \tag{4.25}$$

This is the desired result which was discussed in the main text (Figure 4.2).

4.7.2 Appendix: Transient transmittance and transient reflectance

The single resonance linear susceptibility is given by

$$\chi^{(1)} = \frac{\mu^2}{\omega_{ag} - \omega - i\Gamma}. \tag{4.26}$$

The partial derivatives are

$$\frac{\partial \chi^{(1)}}{\partial \mu} = \frac{2\mu}{\omega_{ag} - \omega - i\Gamma} \quad \left(\propto \chi^{(1)}\right) \tag{4.27}$$

$$\frac{\partial \chi^{(1)}}{\partial \Gamma} = i\frac{\mu^2}{(\omega_{ag} - \omega - i\Gamma)^2} \quad \left(\propto i\frac{\mathrm{d}}{\mathrm{d}\omega}\chi^{(1)}\right) \tag{4.28}$$

$$\frac{\partial \chi^{(1)}}{\partial \omega_{ag}} = -\frac{\mu^2}{(\omega_{ag} - \omega - i\Gamma)^2} \tag{4.29}$$

Using Equation 4.12 and the thin film limit Equation 4.13, the differential reflectivity for a small change in parameter λ is

$$\frac{\Delta R}{R} = -\frac{R_0}{R}\frac{4\omega\ell}{(1+n_s^2)\,c}\mathrm{Im}\left[\frac{\partial \chi^{(1)}}{\partial \lambda}\mathrm{d}\lambda\right]. \tag{4.30}$$

Since the quantity $\frac{R_0}{R}\frac{4\omega\ell}{(1+n_s^2)c}$ is relatively insensitive to frequency, the differential reflectance lineshape can be inferred by examining the imaginary projections of Equations 4.27-4.29. The lineshape for $\lambda = \mu$ corresponds to the imaginary component of the original Lorentzian lineshape. The lineshape for $\lambda = \Gamma$ corresponds to the first derivative lineshape of the real (dispersive) part of the resonance. The lineshape for $\lambda = \omega_{ag}$ corresponds to the first derivative lineshape of the original Lorentzian.

Finally, note that for transmission that obeys Beer's law ($I = I_0 \exp(-\alpha\ell)$ with $\alpha \equiv \frac{\omega}{cn}\mathrm{Im}\left[\chi^{(1)}\right]$, where n is the refractive index of the volume), the expression for small differential signal differs

from Equation 4.30 only by prefactors:

$$\frac{\Delta T}{T} = \frac{\exp\left(-\alpha_{\text{pumped}}\ell\right) - \exp\left(-\alpha_{\text{unpumped}}\ell\right)}{\exp\left(-\alpha_{\text{unpumped}}\ell\right)} \tag{4.31}$$

$$\approx -\ell\left(\alpha_{\text{pumped}} - \alpha_{\text{unpumped}}\right) \tag{4.32}$$

$$= -\frac{\omega\ell}{nc}\text{Im}\left[\frac{\partial\chi^{(1)}}{\partial\lambda}\text{d}\lambda\right] \tag{4.33}$$

$$= \frac{R}{R_0}\frac{1+n_s^2}{4n}\frac{\Delta R}{R}, \tag{4.34}$$

so $\Delta T/T$ and $\Delta R/R$ are proportional to the extent that R, n, and n_s are frequency invariant. Therefore the transient reflection lineshapes of Figure 4.2a can be interpreted as the absorption cross section lineshape changes seen in $\Delta T/T$ measurements.

4.8 Appendix: Lineshape modeling

In this appendix we describe our simple model for building the spectral lineshapes shown in Figure 4.7. The general implementation is:

1. For both spectroscopies construct an unexcited $\chi^{(n)}$ spectrum from a sum of oscillators.
2. Calculate the unexcited reflectance or TSF spectrum from $\chi^{(1)}$ and $\chi^{(3)}$, respectively.
3. Create a $\chi^{(n)\prime}$ spectrum to perturb the central frequencies, linewidths, and amplitudes of the oscillators used to construct $\chi^{(n)}$.
4. Calculate the excited reflectance or TSF spectrum from $\chi^{(1)\prime}$ and $\chi^{(3)\prime}$, respectively.
5. Use Equation 4.12 to calculate $\frac{\Delta I}{I}$ for both spectroscopies.
6. Iterate through previous steps to fit observed lineshapes.

We choose to use complex, Lorentzian oscillators to construct our spectra:

$$\chi^{(n)} = \sum_{j=1}\sqrt{\frac{\Gamma_j}{\pi}}\frac{A_j}{E_{0,j} - \hbar\omega_m - i\Gamma_j} \tag{4.35}$$

in which $j = 1$ and $j = 2$ are the A and B transitions, and the other oscillators are high-lying

non-resonant transitions. To create $\chi^{(n)\prime}$ we replace $\Gamma_j \rightarrow \Gamma_j + \Delta\Gamma_j$, $E_{0,j} \rightarrow E_{0,j} + \Delta E_{0,j}$, and $A_j \rightarrow (1 - \%\text{ decrease})A_j$. ESA-like additional transitions are incorporated by adding a phased offset to $\chi^{(n)\prime}$; the pump-TSF-probe spectrum in Figure 4.7b has a slight offset with phase described by $\exp[i\theta]$ with $\theta = 1$ radian. Table 4.2 codifies the parameters we found, by hand, to give acceptable fits to the data shown in Figure 4.7.

We construct a TSF spectrum by merely calculating the square magnitude of $\chi^{(3)}$ as indicated by Equation 4.10. We construct a reflectance spectrum by converting $\chi^{(1)}$ to a complex refractive index, $\bar{n}$ and then using a Fresnel-coefficient-like analysis, specifically as discussed in Anders [204], which takes into account the influence of multiple reflections and the substrate. This treatment is slightly more holistic than merely using Equation 4.5 because it takes into account the finite thickness of the sample (while the derivation of Equation 4.5 assumes a delta function sample). R is calculated using

$$R = \left| \frac{\bar{r}_1 + \bar{r}_2 \exp[-i\phi_1]}{1 + \bar{r}_1\bar{r}_2 \exp[-i\phi_1]} \right|^2 \tag{4.36}$$

$$\bar{r}_1 = \frac{\bar{n}_0 - \bar{n}_1}{\bar{n}_0 + \bar{n}_1} \tag{4.37}$$

$$\bar{r}_2 = \frac{\bar{n}_1 - \bar{n}_2}{\bar{n}_1 + \bar{n}_2} \tag{4.38}$$

$$\phi_1 = \frac{4\pi\ell\bar{n}_1}{\lambda} \tag{4.39}$$

in which $\bar{n}_0$ is the refractive index of air, $\bar{n}_1$ is the constructed refractive index of the MoS_2 thin film with thickness ℓ, $\bar{n}_2$ is the refractive index of the fused silica substrate, and λ is the vacuum wavelength of the interrogating electric field.

Table 4.2: Parameters used to produce the lineshapes shown in Figure 4.7.Note that the model in Figure 4.7b for pump-TSF-probe has a slight offset with phase described by $\exp[i\theta]$ with $\theta =$ 1 radian and amplitude of 1% of the maximum feature.

transition	E_0 (eV)	ΔE_0 (eV)	Γ (eV)	$\Delta\Gamma$ (eV)	relative A	% A decrease
transient reflectance model $T = 0.05$ **ps**						
A	1.807	-0.01	0.1	0.002	1	2
B	1.98	-0.009	0.12	0.005	1.1	2
	2.7	-0.008	0.25	0	4	5
	3.2	0	0.25	0	8	0
	6	0	0.25	0	40	0
transient reflectance model $T = 0.55$ **ps**						
A	1.807	-0.005	0.1	0	1	2
B	1.98	-0.005	0.12	0	1.1	2
	2.7	0	0.25	0	4	5
	3.2	0	0.25	0	8	0
	6	0	0.25	0	40	0
transient TSF model $T = 0.05$ **ps**						
A	1.81	-0.012	0.085	0.005	1	2
B	1.95	-0.009	0.1	0.005	0.91	2
transient TSF model $T = 0.55$ **ps**						
A	1.81	-0.003	0.085	0	1	0
B	1.95	-0.002	0.1	0	0.91	0

4.9 Appendix: Sub-bandgap pump, reflectance probe of a MoS_2 thin film

TMCDs have weak but finite absorption well below the bandgap.[205] To investigate this sub-band edge response, we tuned our pump to NIR colors, using fluence an order of magnitude higher than the visible pump. The effects of this sub-band edge pump on the band-edge reflectance spectrum are shown in Figure 4.12. We observe similar spectral and temporal lineshapes for both the visible and NIR pump, indicating the NIR pump generates photocarriers in a similar manner to a visible pump.

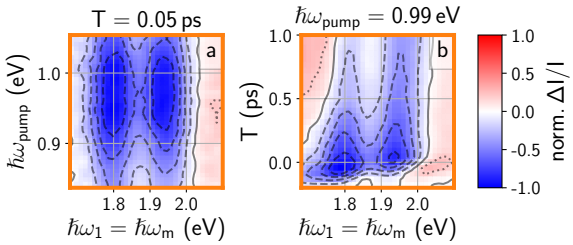

Figure 4.12: Transient-reflectance spectroscopy on a MoS_2 thin film with a NIR pump. (a) shows the transient-reflectance spectrum for different combinations of pump and probe frequencies for $T = 50$ fs. This spectrum is not normalized for the frequency dependence of the pump laser intensity. (b) shows the measured dynamics for different probe colors with $\hbar\omega_{\text{pump}} = 0.99$ eV

Given the strong two-photon absorption in TMDCS,[105, 206, 207, 208, 209] it is possible that the signals in Figure 4.12 arise from two-photon absorption of sub-bandgap light. To identify the presence of two-photon transitions, we examined the fluence scaling. Figure 4.13 shows the TR signal scaling for the sub-bandgap pump (orange down-pointing triangles). We observe linear scaling of the probe metric with respect to the NIR pump fluence. This linear scaling is commensurate with the work of Völzer et al. [210] who observe linear response in bulk MoS_2 up to a pump fluence of $\sim$200 μJ/cm^2. These observations rule out two-photon absorption as the dominant contribution to Figure 4.12. Instead, it is likely that our NIR pump excites electrons/holes to/from midgap states that have small optical cross-sections. Midgap states exist in synthetically grown MoS_2 and are generally attributed to sulfur vacancies and edge defects.[181, 211, 212, 213, 214, 215, 216]

We believe mid-gap excitations can induce BGR and band-filling in a manner similar to direct, allowed transitions, which explains the similarity in lineshape between visible and NIR pumps (compare Figure 4.8a with Figure 4.12a or Figure 4.6a with Figure 4.12b). The insensitivity to pump wavelength reflects the large dispersion of mid-gap states and their transitions to valence and conduction bands.

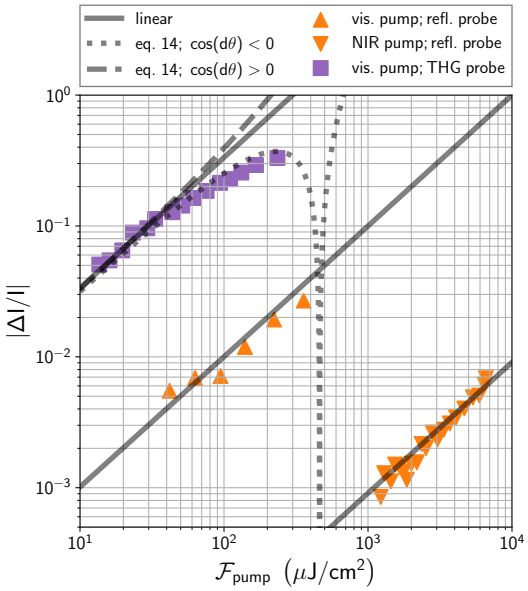

Figure 4.13: Comparison of transient-reflectance spectroscopy (orange) to transient-TSF spectroscopy (violet) pump fluence scaling for a MoS_2 thin film. The y-axis is maximum extent of the bleach measured (near $T = 0$). The pump and probe combinations are as follows: (▲, $\hbar\omega_1 = \hbar\omega_m = \hbar\omega_{\text{pump}} = 1.98$ eV); (▼, $\hbar\omega_1 = \hbar\omega_m = 1.98$ eV, $\hbar\omega_{\text{pump}} = 0.99$ eV); and (■, $3\hbar\omega_1 = \hbar\omega_m = 2.05$ eV, $\hbar\omega_{\text{pump}} = 1.98$ eV). Gray solid lines show linear scaling to guide the eye. The gray dotted line is a fit of Equation 4.14 to the THG probe data. Also shown is an example of Equation 4.14 for the case of constructive interference (dashed line).

4.10 Appendix: Pump-fluence dependence of pump-TSF-probe

Here we investigate the scaling of pump-TSF-probe signal with respect to pump fluence. Figure 4.13 shows the fluence dependence of $|\Delta I_{\text{TSF}}|/I_{\text{TSF}}$ when pumping and probing near the B exciton resonance (purple squares), and compares the response to pump-reflection-probe pumping and probing the same resonance (orange up-pointing triangles).

The $|\Delta I_{\text{TSF}}|/I_{\text{TSF}}$ shows sublinear behavior at higher fluences (> 50 μJ/cm^2). Since the reflec-

tion probe exhibits linear response for far higher pump fluences than the onset of THG sublinear scaling, we cannot attribute the sublinear trend to traditional explanations like band saturation or many-body effects caused by the pump interaction. Rather, we attribute this unique power dependence to the competition between quadratic scaling, difference intensity signal, $\left|\mathrm{d}\chi^{(3)}\right|^2$, and the linear scaling, heterodyne signal, $\left|\chi^{(3)}\right|\left|\mathrm{d}\chi^{(3)}\right|\cos(\mathrm{d}\theta)$ (cf. Equation 4.14). For low pump fluence, $\mathrm{d}\chi^{(3)} \ll \chi^{(3)}$ so $|\Delta I_{\mathrm{TSF}}|/I_{\mathrm{TSF}}$ scales linearly. As the pump fluence is increased to the point where $|\Delta I_{\mathrm{TSF}}|/I_{\mathrm{TSF}} \sim 1$, the intensity level differential signal becomes similar to the heterodyne signal, so the quadratic term becomes important. The observed power scaling in this regime depends on the sign of $\cos(\mathrm{d}\theta)$, which can be inferred by the sign of ΔI in the linear fluence regime. When $\cos(\mathrm{d}\theta) > 0$ (and $\Delta I > 0$ for low fluence), the quadratic terms adds to the linear term and superlinear scaling is observed (as simulated in Figure 4.13, hashed line). When $\cos(\mathrm{d}\theta) < 0$ (and $\Delta I < 0$ for low fluence, as is the case in Figure 4.13), the quadratic term and linear scaling terms destructively interfere and sublinear scaling is observed (as simulated in Figure 4.13, dotted line). Note that the Equation 4.14 fit of our pump-TSF-probe fluence data recovers the phase and amplitude of $\chi^{(5)} = \mathrm{d}\chi^{(3)}/\mathcal{F}_{\mathrm{pump}}$: we find that $\left|\chi^{(5)}\right| / \left|\chi^{(3)}\right| = 0.003$ cm$^2/\mu$J and $\cos(\mathrm{d}\theta) = -0.6$.

Theoretically, a similar power scaling competition as Equation 4.14 can occur in linear probe experiments if $\mathrm{d}\chi^{(1)}$ becomes large enough, but this regime is uncommon because in linear experiments the unpumped probe (reflection or transmission) is usually more intense, so higher-order pump processes often contribute before this onset. For example in Figure 4.13, a pump-fluence of $\sim$100 μJ/cm^2 produces only a $\sim$ 1% change in reflectivity, while under the same conditions the TSF intensity changes by $\sim$ 20%.

To reiterate, the pump-TSF-probe fluence scaling is both non-linear and well-understood; the trend is *not* due to higher-order non-linear effects (e.g. $\chi^{(7)}$). The pump fluence trends observed here are well-described by a fluence-independent absorption cross-section for the pump. Note that the lineshape simulations in Figure 4.2 assume linear scaling of pump fluence. Our main results were acquired at a pump fluence of $\sim$100 μJ/cm^2 which is in the regime of nonlinear scaling of $|\Delta I_{\mathrm{TSF}}|/I_{\mathrm{TSF}}$ with pump fluence. Importantly, the lineshape fitting of our data (Figure 4.7) accounts for the possible nonlinear scaling of $|\Delta I_{\mathrm{TSF}}|/I_{\mathrm{TSF}}$ with pump fluence because Equation 4.12 is explicitly used in our model. If we had used Equation 4.15 in our analysis this nonlinear pump

scaling would not have been taken into account.

Chapter 5 The Optical Stark Effect in optical harmonic generation

This Chapter borrows extensively from a manuscript to be submitted. The authors are:

1. *Darien J. Morrow*
2. *Daniel D. Kohler*
3. *Yuzhou Zhao*
4. *Jason M. Scheeler*
5. *Song Jin*
6. *John C. Wright*

5.1 Abstract

An applied field can modulate optical signals by resonance shifting via the Stark Effect. The Optical Stark Effect (OSE) uses ultrafast light in the transparency region of a material to shift resonances with speeds limited by the pulse duration or system coherence. In this Chapter we investigate the OSE of resonant optical harmonic generation (OHG) signals from the ground state exciton transition of WS_2. We use multidimensional pump-probe spectroscopy, where our probe is second- or third-harmonic emission, to investigate the OSE. We find large Stark shifts, commensurate with the large optical susceptibility commonly seen with WS_2 excitons, but we also find the behavior to be more complex than simple OSE treatments predict. We show how a new manifestation of the Stark Effect, brought forth by photon exchange between the pump and OHG fundamental fields, can produce strong modulations of the OHG signal and is thus promising for applications. We also investigate the effect of sample morphology, which affects competing multiphoton absorption processes.

5.2 Introduction

Optical harmonic generation (OHG) occurs when an AC electric field, E, of frequency ω, drives a non-linear polarization that coherently radiates new electric fields at the harmonics of the original frequency, $\{2\omega, 3\omega, \dots\}$, see Figure 5.1a.[217, 45] OHG emission efficiency is often controlled by phase-matching,[45] crystal orientation,[85] thickness, applied DC electric and magnetic fields,[218, 219, 220, 221] or by having frequency components resonant with excitonic transitions.[93] Optical harmonic generation can be especially strong in few-layer transition metal dichalcogenides (TMDCs).[85, 86, 88, 93]

Optical gating is a way to control OHG on the ultrafast timescales that may suit photonics applications like optical modulators.[222] Ultrafast optical gating in OHG has been previously achieved through induced currents.[223] Herein we explore the Optical Stark Effect (OSE) as another potential optical gating method. In the OSE, a non-resonant optical field (the pump) coherently drives a system, creating photon dressed states which hybridize with the system's original eigenstates, shifting their energies (Figure 5.1b).[224, 225, 226, 38] The change in transition energy due to the pump is

$$\Delta E = \frac{|\mu_{ab}|^2 \left\langle \mathcal{E}^2 \right\rangle}{E_0 - \hbar\omega_{\text{pump}}}, \tag{5.1}$$

in which $\left\langle \mathcal{E}^2 \right\rangle$ is the time-averaged electric field amplitude, which is proportional to the pump intensity, μ_{ab} is the transition dipole between states a and b, and $E_0 \equiv E_b - E_a$ is the equilibrium transition energy. When the pump is detuned below the transition resonance, the hybridized states repel and the OSE manifests as a blue-shift of the resonance, which adiabatically follows the pump's envelope. The OSE blue shift is well-known in semiconductors, but it is typically observed via a weak, resonant electric field probe.[227, 228, 229] The OSE is also expected to modulate resonant harmonic generation,[230] but no experimental demonstration is apparent.

In this Chapter we test the application of the OSE to OHG by exploring IR pump, harmonic probe spectroscopy of a TMDC: WS_2. TMDCs exhibit a strong OSE due to large exciton transition dipoles and intrinsic quantum confinement.[231, 232, 233, 234, 235, 236, 237, 238] We find that

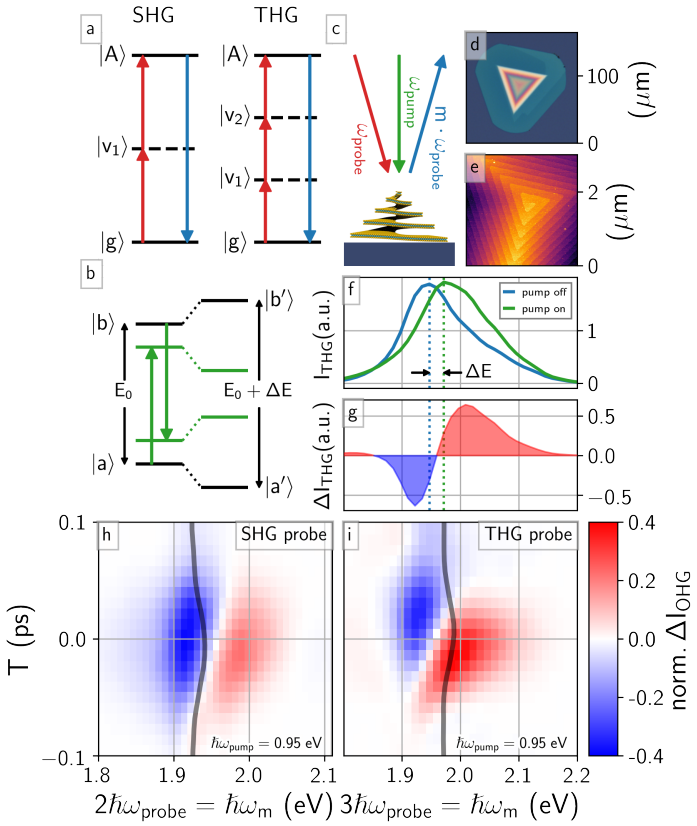

Figure 5.1: Overview of optical harmonic generation and the optical Stark effect. (a) Energy level diagrams showing how a probe (red) creates an A exciton coherence which then emits at a frequency (blue) which is a harmonic of the probe. (b) Non-resonant optical Stark effect in which a pump (green) drives the $a \leftrightarrow b$ transition which results in photon-dressed states with energy $E_0 + \Delta E$. (c) Cartoon of experimental geometry. (d) Optical micrograph of WS_2 screw-dislocation pyramid on Si/SiO_2 explored in the main text. (e) Atomic force microscope image of sample that is ~ 120 layers thick. (f) THG spectrum of WS_2 pyramid with NIR pump on and off. (g) difference between THG spectra in (f). (h,i) Difference between unpumped and pumped harmonic generation spectrum for different pump-probe time delays, T. Both plots share the colormap with red (blue) being an increase (decrease) in harmonic generation upon pump excitation. The thick black lines are the center-of-mass of the pumped harmonic generation spectrum. The pump frequency is $\hbar\omega = 0.95$ eV.

the OSE energy shifts are strong for OHG, with resonance shift rates in excess of 2 meV per $\frac{\text{V}}{\text{nm}}$ of applied optical field. The precise sensitivity of the OSE depends on morphology factors such as uniformity and thickness. Morphology also affects the prominence of incoherent pump interactions such as multiphoton absorption, which compete with the OSE. In addition to the well-known OSE blue shift, we find the OHG process incurs novel hybridization between the pump and fundamental probe fields. When the pump and the probe fundamental have similar frequencies, quantum interference of the pump and probe photons strongly modulate the efficiency of OHG. By tuning the pump frequency about the probe fundamental, the interference can either greatly suppress or enhance OHG. This pump-induced modulation of harmonic generation is an example of quantum interference,[239] similar to the photocurrent control using interference of multiple multiphoton absorption processes.[240, 241, 242]

5.3 Results and Discussion

Our experiments use two ultrafast optical parametric amplifiers (OPAs) to generate linearly polarized pump and probe electric fields ($\sim$ 50 fs FWHM) (additional experimental details are available in the Appendices). We measure the second harmonic generation (SHG) or third harmonic generation (THG) of the probe beam in the reflective direction (Figure 5.1c) from a single WS_2 ($E_0 \approx 2$ eV) screw-dislocation spiral (84 nm tall, Figure 5.1d,e) on a Si/SiO_2 substrate. Though this work surveys many morphologies, the TMDC screw dislocation spiral is highlighted in the main text due to its bright SHG and THG.[96, 169, 168] Figure 5.1f shows the A exciton THG resonance of the spiral (blue line). When a non-resonant pump (0.95 eV) is applied, the resonance blue-shifts (Figure 5.1f, green line), yielding an asymmetric difference lineshape (Figure 5.1g).

To investigate pump-OHG-probe, we explore the OHG dependence on the pump and probe frequency, relative arrival time, and fluence. We look at changes in OHG intensity relative to the peak OHG of the unpumped spectrum:

$$\text{norm. } \Delta I \equiv \frac{I_{\text{OHG, pumped}} - I_{\text{OHG, unpumped}}}{\max\{I_{\text{OHG, unpumped}}\}}. \tag{5.2}$$

The conventional pump-probe metric, in which signal is normalized by the probe *spectrum* (i.e. $\Delta I/I$),[123] is relinquished here because it over-emphasizes small changes at the wings of the OHG resonance, where the probe is weak. Figures 5.1h(i) shows the pump-SHG(THG)-probe signal according to Equation 5.2 as the probe color and pump-probe delay are scanned. The pump blue-shifts both SHG and THG with a time dependence that roughly follows the pump-pulse envelope as the relative time delay between the pump and probe, T, is scanned. There is an appreciable signal at latent probe delays ($T \geq 0.05$ ps), suggesting that the pump induces system dissipation, such as pump absorption, that contribute to the signal.

Figure 5.2 shows the THG dependence on pump frequency $\hbar\omega_{\text{pump}}$, probe frequency $\hbar\omega_{\text{probe}}$, and pump-probe time delay T. When the probe arrives before the pump ($T < 0$), THG is enhanced near the resonance ($\Delta I > 0$). When pulses are overlapped, $T \approx 0$, the probe spectra (horizontal slices) is dispersive, which is consistent with blue-shifting of the exciton resonance. When the probe is delayed by times greater than the pulse duration ($T > 50$ fs), response is observed only when $2\hbar\omega_{\text{pump}} > E_0$, indicating that the pump is dissipating energy via two photon absorption (2PA). The effects of this absorption remain longer than the 10s of picoseconds experimentally accessible by our instrument (data shown in Appendices).

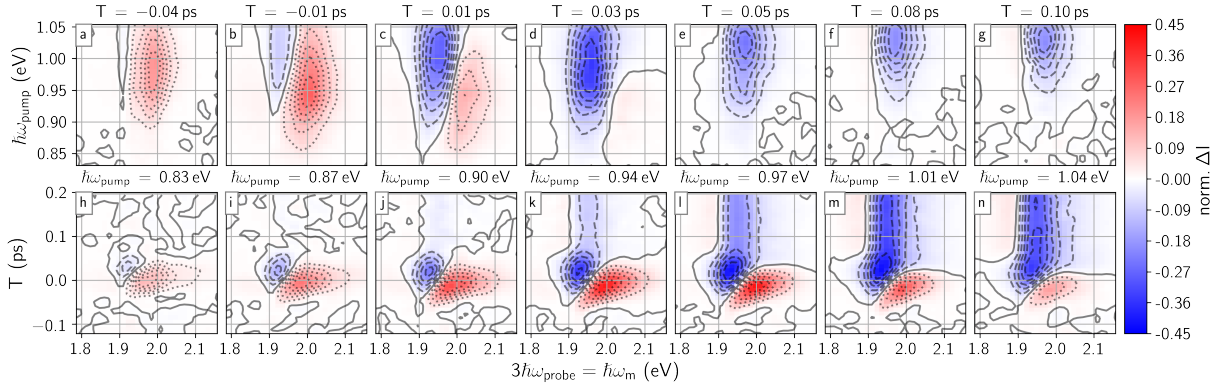

Figure 5.2: Effects of pump frequency, probe frequency, and pump-probe time delay on WS_2 THG spectrum. The first row shows pump frequency vs. probe frequency for seven time delays (noted in subfigure title). The second row shows time delay vs. probe frequency for seven pump frequencies (noted in subfigure title). The colormap is shared across all frames with contour lines locally normalized. $\mathcal{F}_{\text{pump}} \approx 3000 \frac{\mu\text{J}}{\text{cm}^2}$.

Some of the pump-OHG-probe behaviors shown in Figure 5.2 run counter to expectations of the

conventional OSE. For example, the probe line shapes (horizontal slices of Figure 5.2) are not strictly antisymmetric, contrary to expectations of a resonance shift.[228, 243, 244] The balance of the positive (red) and negative (blue) lobe is unequal and depends on the pump color, and the dominant lobe differs between SHG (stronger negative) and THG (stronger positive) probes under the same pump excitation (cf. Figures 5.1h and i). Furthermore, the probe spectrum is strongly non-symmetric about $T = 0$ (see Figure 5.2h-n) which is counter to the expectation of adiabatic following of the pulse envelope. These unusual behaviors cannot be explained by the incoherent population contributions because these contributions are negligible for many pump colors (Figure 5.2h-j).

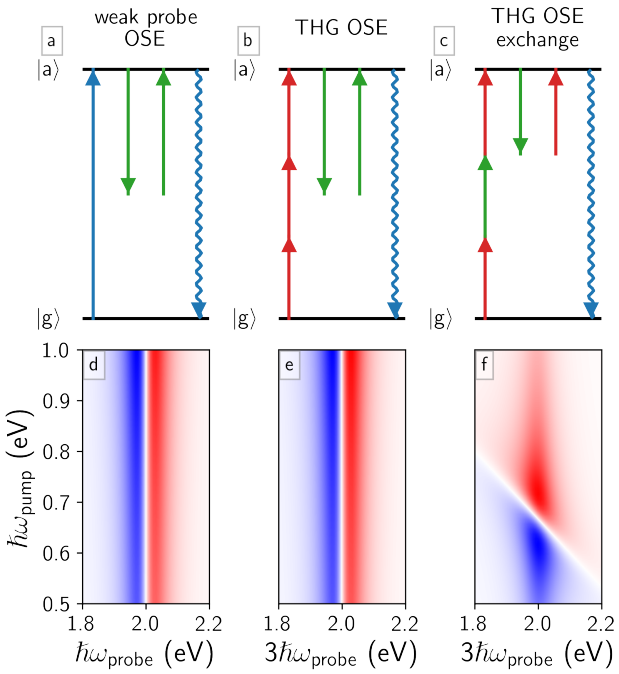

Figure 5.3: (a-c) Wave-mixing energy level (WMEL, [245]) diagrams used to represent the OSE. Straight arrows represent interactions of the input fields with the detuned pump (green), probe fundamental (red), and resonant weak field probe (blue). The wavy blue arrow represents the emission of the field to be measured. Time flows from left to right. (d-f) Perturbative response expected from pathways in (a-c) with $\hbar\omega_{ag} = 2$ eV and $\hbar\Gamma = 0.05$ eV. In order to emulate a transient absorption experiment, (d) shows the imaginary projection of the third-order susceptibility. (e) is the first and (f) is the second term of Equation 5.3.

To understand the differences between the conventional OSE and its manifestation in harmonic generation, we employed the well-known perturbative expansion technique to a two-level system.[246,

38] This expansion technique determines the non-linear response through a series of time-ordered linear interactions with the pump and probe. Figure 5.3a shows this technique's diagrammatic representation of the OSE in a transient absorption/reflection measurement. The perturbative technique representation differs from Figure 5.1b in that it does not explicitly solve for the hybridized states; it does, however, explicitly treat the probe polarization. As a consequence, the extension of the perturbative method to OHG is trivial, though cumbersome. We provide a thorough walk-through of our treatment in the appendices. Although we focus on THG, the underlying effects are general to OHG.

The perturbative treatment recovers the OSE analogue for our experiment (THG OSE, Figure 5.3b), in which the third harmonic polarization is generated and the pump subsequently drives the system. An additional process arises, however, due to the similar frequencies of the pump and probe fundamental. When the probe fundamental and the pump have similar frequencies, they become indistinguishable, so their roles in harmonic generation and dressing the system can exchange. A new pathway results where a triple-sum frequency (TSF,[68] $2\omega_{\text{probe}} + \omega_{\text{pump}}$) polarization is dressed by both the probe and pump fields (THG OSE exchange, Figure 5.3c). This manifestation of the OSE is unique to harmonic generation because in the weak probe case, degeneracy of the pump and probe frequencies implies the pump is at resonance, where incoherent excitation (carrier populations) or strong field Rabi cycling effects will dominate.

In general, calculation of the OHG OSE and OHG OSE exchange line shape are complicated and time-dependent (see the appendices). The line shapes are simplified, however, if pulse durations, Δ_t, are assumed to be much longer than the system's coherent dynamics, $T_2 = \Gamma^{-1}$.[43] At $T = 0$, the signal for n-th harmonic generation of a two-level system can be approximated by:

$$\text{norm. } \Delta I = \left| \frac{\Gamma \mu_{ag} E_2}{\Delta_{ag}^{(\text{OHG})}} \right|^2 \text{Re} \left[\frac{x}{\Delta_{ag}^{(\text{OHG})}} + \frac{ny}{\Delta_{ag}^{(\text{exch})}} \right], \tag{5.3}$$

in which Γ is the dephasing rate, resonance enhancement is determined by:

$$\Delta_{ag}^{(\text{OHG})} \equiv \hbar(\omega_{ag} - n\omega_{\text{probe}} - i\Gamma), \tag{5.4}$$

$$\Delta_{ag}^{(\text{exch})} \equiv \hbar(\omega_{ag} - (n-1)\omega_{\text{probe}} - \omega_{\text{pump}} - i\Gamma), \tag{5.5}$$

and the quantities $x \equiv -\hbar^{-1}(n\omega_{\text{probe}} - \omega_{\text{pump}} - i/\Delta_t)^{-1}$ and $y \equiv -\hbar^{-1}((n-1)\omega_{\text{probe}} + i/\Delta_t)^{-1}$ are attenuation factors due to non-resonance. For a strongly detuned pump, x and y are relatively insensitive to pump and probe frequency, approximately equal in magnitude, and primarily real in character. The first term inside the real operator of Equation 5.3 represents THG OSE, while the second term represents THG OSE exchange.

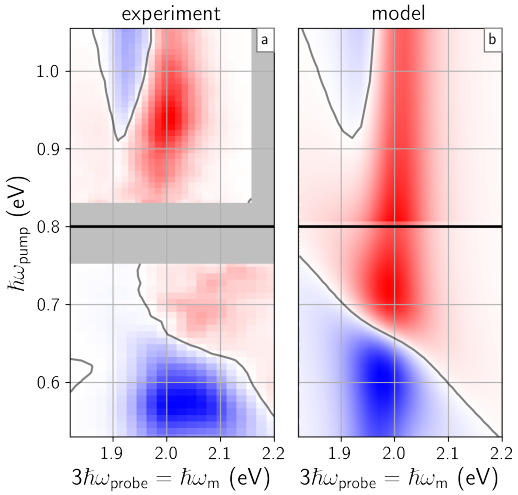

Figure 5.4: Comparison between experiment and perturbative expansion model of the OSE for THG including finite pulse effects ($\hbar\omega_{ag} = 1.98$ eV, $\hbar\Gamma = 36$ meV $\Rightarrow T_2 = 18$ fs, and $\Delta_t = 50$ fs.). Experimental data are for $T = -0.01$ ps. The upper and lower sections of (a) and (b), as demarcated by the horizontal, black lines, each have their own colormap extent with red (blue) being an increase (decrease) in harmonic generation upon pump excitation. The gray section in (a) was not explored due to experimental constraints. Data in (a) were normalized along the pump axis by the frequency-dependent pump intensity.

Figure 5.4 plots a simulation of pump-THG-probe and compares it with experiment. The simulation uses a numerical integration technique to account for a small pump-probe delay,[43, 247, 248] which is qualitatively similar to Equation 5.3. The simulation agrees well with experiment and the line shape can be understood as follows. When pump and probe frequencies differ greatly (e.g. $\hbar\omega_{\text{pump}} \approx 1$ eV), the THG OSE effect is clearly resolved, and a blue shift along the probe axis is observed. Near pump-probe degeneracy, however, the exchange pathway is prevalent, and a blue-shift normal to the $\omega_{\text{pump}} = \omega_{ag} - 2\omega_{\text{probe}}$ TSF resonance is seen. Importantly, the blue shift from the exchange pathway enhances THG for pump frequencies greater than degeneracy and suppresses THG with pump frequencies less than degeneracy. This observation explains the spectral asymmetry of the observed OHG OSE (Figure 5.1h).

Dissipative coupling of the pump, through absorption, competes with the coherent OSE and provides a THG modulation that is long-lived. Multiphoton absorption has potential applications in analytical studies as a way to reduce scatter,[123] but its prominence affects the application of the OSE in devices, so here it is a parameter to minimize. Figure B.3a-c shows how THG changes for different pump fluences, $\mathcal{F}_{\text{pump}}$, ranging from 500 to 7000 $\frac{\mu\text{J}}{\text{cm}^2}$ (or, for our 50 fs pulse, electric field amplitudes ranging from roughly 1 to 20 $\frac{\text{V}}{\text{nm}}$). As expected, both the pulse-overlap feature and the latent population response increase in prominence as pump fluence is increased; at the most intense pump fluence we instigated, we observed a 70% decrease in resonant THG. The resonance blueshift near $T = 0$ and the maximum of norm. ΔI both scale linearly with pump fluence (Figure B.3e,f), while the population response (Figure B.3g) scales as $\mathcal{F}_{\text{pump}}^{1.4}$. Two-photon absorption is supposed to scale as $\mathcal{F}_{\text{pump}}^{2}$; the discrepancy is not understood. Despite this discrepancy, we clearly see that dissipative coupling of the pump can be strongly suppressed by tuning the pump frequency below the 2PA threshold (cf. Figure 5.2).

We also accomplished multidimensional pump-THG-probe in a variety of WS_2 morphologies to explore the balance of absorptive and coherent processes. In all morphologies explored, we find that 2PA, which has an onset at $\omega_{\text{probe}} \approx \omega_{ag}/2$, is a moderate to strong contributor at fluences that strongly modulate the OSE, while 3-photon absorption (onset near $\omega_{\text{probe}} \approx \omega_{ag}/3$) is not. The exact balance between 2PA and the THG OSE depends on morphology—more crystalline samples exhibiting both narrower lineshapes and weaker absorption will favor THG OSE over 2PA. Because of 2PA, utilizing the SHG OSE exchange effect for optical modulation of SHG is not ideal, but the THG OSE exchange effect can be controlled without strong pump dissipation. Furthermore, we find the SHG resonance of our WS_2 pyramid is between a different, weaker transition than the THG resonance. Theoretically, the OHG OSE exchange process would also be viable for higher harmonics and should be sensitive to a wide variety of state symmetries through even vs. odd harmonic orders.[206, 93, 218] For high enough harmonics, however, our description will break down because the mechanism of harmonic generation becomes non-perturbative.[120, 249]

While our two-state model recovers the dominant features present at $T = 0$, our model does not fully account for the asymmetric dynamics about $T = 0$ (see the appendices). It is possible we miss these effects due to our lowest-order perturbation theory. The time behavior depends on

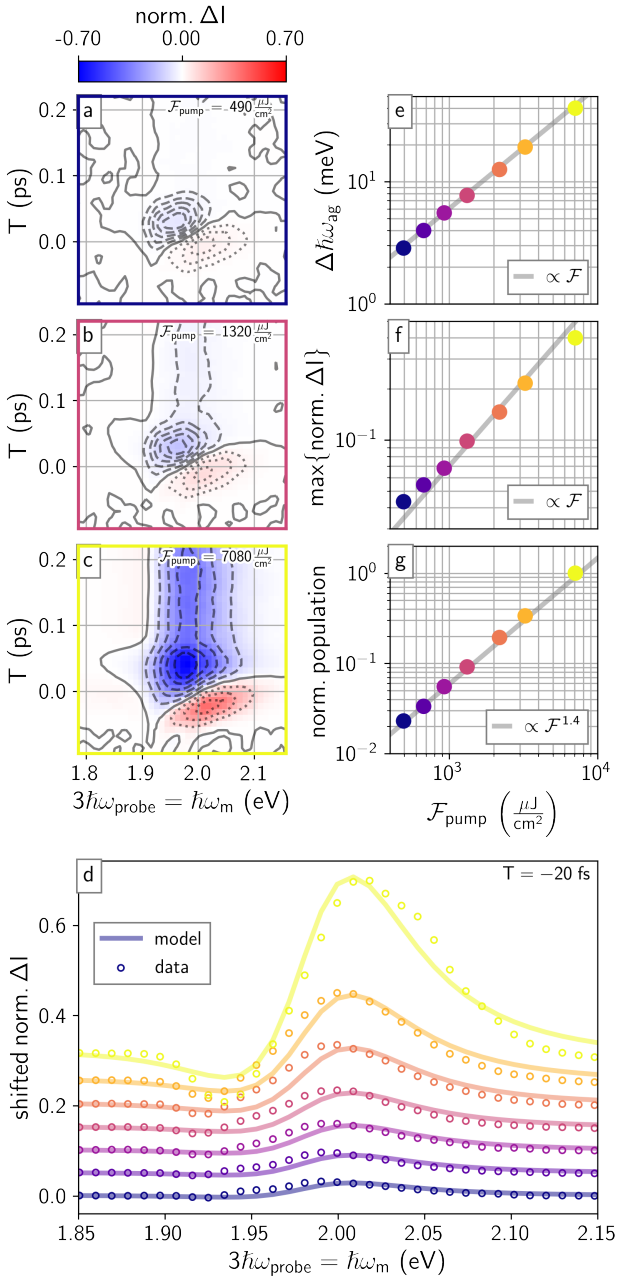

Figure 5.5: Effects of pump fluence and pump-probe time delay on WS_2 THG spectrum when $\hbar\omega_{\text{pump}} = 0.99$ eV. (a)-(c) Time delay vs. probe frequency for three pump fluences. The colormap is shared across all frames with contour lines locally normalized. (d) $T = 0$ slices (color-keyed dots) with lines showing the best fit of the data assuming the simple-shift model developed in the Appendices. (e) Fitted values of $\Delta\hbar\omega_{ag}$ vs. pump fluence showing a linear trend. (f) Maximum increase in THG vs. pump fluence showing a linear trend. (g) Population response (average absolute response after 0.1 ps) vs. pump fluence showing a $\mathcal{F}^{1.4}$ trend.

the morphology of the sample, which again suggests that multiphoton absorption pathways may contribute to the signal at pulse overlap. Our probe fundamental was strong enough to induce its own OSE. Treating these extra effects require a higher-order expansion or a non-perturbative technique[250], and accounting for these effects is a goal for future work.

5.4 Conclusions

In this work we showed that resonant harmonic generation in WS_2 is significantly altered by application of an intense, sub-bandedge pump. The pump field not only shifts the resonant transition in a manner similar to the traditional optical Stark effect with single photon probes, but the pump field can also exchange with the probe field which reveals a novel way to shift and modulate the intensity of harmonic output. We envision that this optical Stark effect may be useful for creating ultrafast, all-optical modulators.

5.5 Appendix: Synthesis of WS_2 samples

Following the methods detailed in Zhao and Jin [8], the WS_2 pyramid microstructure sample on a 300 nm SiO_2/Si substrate was prepared using water vapor assisted chemical vapor transport growth by heating 100 mg WS_2 powder to 1200 °C at 800 torr in a tube furnace in which water vapor was produced by heating 1 g $CaSO_4 \cdot 2H_2O$ powder to 150 °C using heating tape wrapped around the tube furnace. 100 sccm argon was used as the carrier gas during the reaction.

To grow monolayer and few-layer samples, the above procedure was followed except the $CaSO_4 \cdot 2H_2O$ powder was heated to 85 °C with heating tape.

Polycrystalline WS_2 films were prepared by first depositing 2 nm of W onto a fused silica substrate via e-beam evaporation and subsequently sulfidizing in a tube furnace at 750 °C for 30 minutes.[61]

Suitable samples were identified with an optical microscope (Olympus BX51M) and additionally characterized with an atomic force microscope (Agilent 5500), and a confocal Raman microscope (LabRAM Aramis).

5.6 Appendix: Description of ultrafast spectrometer

Our experimental setup uses an ultrafast oscillator seeding a regenerative amplifier (Spectra-Physics Tsunami and Spitfire Pro, respectively) to produce ∼35 fs pulses centered at 1.55 eV at a 1 kHz repetition rate. The amplifier pumps two optical parametric amplifiers (OPAs, Light-Conversion TOPAS-C) which create tunable pulses of light from ∼0.5 to ∼2.1 eV with spectral width on the amplitude level of FWHM ≈ 46 meV. Absorptive filters (ThorLabs FGL1000M) and broadband wire grid polarizers are used to isolate light of the desired color. Each OPA beamline has its own mechanical delay stage (Newport, MFA-CC), optical chopper (Thorlabs MC2000B and MC1000A), and motorized neutral density filter wheel (in-house motorization, Thorlabs NDC-100C-4M). All pulses are focused onto the sample with a 1 m focal length spherical mirror. The spatially coherent output (either the reflected probe or a harmonic of the probe) is isolated with an aperture in the reflected

direction (sometimes referred to as an *epi* experiment), focused into a monochromator (Horiba Micro-HR) and detected with a thermoelectrically cooled photomultiplier tube (RCA C31034A). A dual-chopping routine is used to isolate the desired differential signal.[164] The color-dependent time-of-flight for each OPA beamline is corrected by offsetting the mechanical delay stages for each combination of pump and probes colors. The offset is empirically determined by measuring the delay-dependent response of singly resonant sum-frequency or triple-sum-frequency generation directly on the WS_2 samples.[68, 123] All beams are hundreds of microns wide at the sample. All raw data, workup scripts, and simulation scripts used in the creation of this work are permissively licensed and publicly available for reuse at http://dx.doi.org/10.17605/OSF.IO/SNTPC. Our acquisition[103] and workup[166] software are built on top of the open source, publicly available Scientific Python ecosystem.[251, 57, 58]

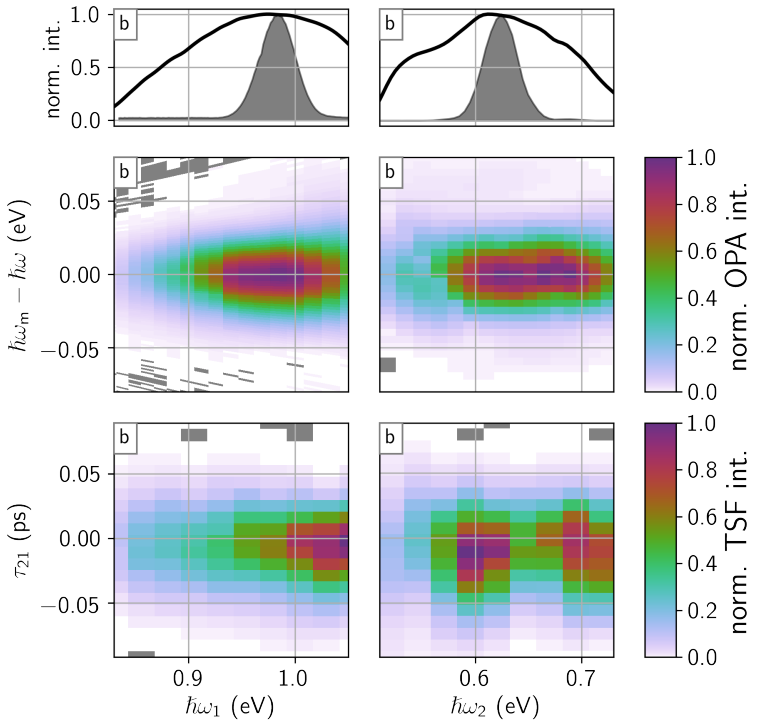

Figure 5.6: Demonstration of ultrafast spectrometer calibration. (a, b) OPA output power as measured by a thermopile, plotted against OPA setpoint. These variations in output power as a function of setpoint are not corrected for in the data presented in this work. Shaded features are the OPA spectra for a single setpoint (taken from slices of the second row). (c, d) OPA output spectrum vs. OPA setpoint after calibration. (c) was measured with an home-built InGaAs array detector (Sensor: Hamamatsu G9494-256D) while (d) was measured with a liquid nitrogen cooled InSb photodiode (Judson-Teledyne). (e, f) two-beam TSF in WS_2 in which the monochromator is set to track $\omega_m = \omega_1 + 2\omega_2$. In the (e) $\hbar\omega_2 = 0.66$ eV and in the (f) $\hbar\omega_1 = 0.95$ eV. In both (e) and (f) the TSF intensity peaks at $\tau_{21} = 0$ which indicates that the color-dependent time-of-flight offsets have been accurately measured and applied.

5.7 Appendix: The Semiclassical Stark Effect: theory

Here we overview several different treatments of the semiclassical Stark Effect and demonstrate their consistency. Common (non-perturbative) approaches to the Stark effect excel at their intuitive picture but are difficult to apply to experimental conditions.[224, 252] Our perturbative approaches are much easier to apply to experiments, but their connection to the dressed state view is less obvious. The derivations here focus on cases in which the pump field is significantly detuned from resonance, while the probe field is near resonance. For non-classical (quantized photon field) treatments, important when the photon field is weak, other approaches may be used.[253]

We present the semiclassical Stark Effect in three different ways. In Section 5.7.1 we derive a classic example of a two level system. The solution is non-perturbative and is valid when the fields are strong enough to induce Rabi cycling. The derivation examines changes to the wavefunction under a strong light field and explicitly solves for the hybridized dressed states that result. This derivation is pedagogical and relies heavily on Boyd's excellent treatment.[38] It falls short of fully describing the pump-probe experiment, which must address the probe field and its measurement.

In Section 5.7.2 we apply a perturbative treatment relying on Liouville pathways. This treatment directly connects to the measured observables in a pump-probe experiment in which the probe is a single photon (electric field interaction). In this treatment, the states are not formally dressed by the pump; the shift arises by considering how the pump modifies the probe susceptibility. Our treatment breaks down when the amplitude of Rabi cycling is large, so the validity depends on the extent to which the pump is weak and/or detuned.

Section 5.8 extends the perturbative treatment of Section 5.7.2 to a THG probe, which yields Liouville pathways and related equations important to our analysis.

5.7.1 Non-perturbative treatment of Dynamic Stark Effect

Consider a two level system with ground state $|a\rangle$ and another state $|b\rangle$. The states are orthonormal, $\langle m|n\rangle = \delta_{mn}$, and have no time dependence, $\frac{\partial}{\partial t}|m\rangle = 0$. The wave function of the system, Ψ, evolves

according to the Schrödinger equation

$$i\hbar\frac{\partial\Psi}{\partial t} = \hat{H}\Psi \tag{5.6}$$

with the Hamiltonian

$$\hat{H} = \hat{H}_0 + \hat{V}(t) \tag{5.7}$$

in which $\hat{H}_0$ is the Hamiltonian of the unperturbed system such that

$$\hat{H}_0 |m\rangle = E_m |m\rangle , \tag{5.8}$$

$$E_m = \hbar\omega_m \tag{5.9}$$

and $\hat{V}(t)$ is interaction between the system and an applied field. We treat the applied electric field classically

$$\hat{V}(t) = \hat{\mu}\tilde{E}(t), \tag{5.10}$$

$$\tilde{E}(t) \equiv E_0 \cos(\omega t) = \frac{E_0}{2}\left[\exp(-i\omega t) + \exp(i\omega t)\right] \tag{5.11}$$

with the dipole moment operator being $\hat{\mu} \equiv -e\hat{r}$.

The electric field mixes $|a\rangle$ and $|b\rangle$ to form the superposition

$$|\Psi(t)\rangle = C_a(t)\exp(-i\omega_a t)|a\rangle + C_b(t)\exp(-i\omega_b t)|b\rangle . \tag{5.12}$$

$C_m(t)\exp(-i\omega_m t)$ is the time evolution of the state m, and $|C_m(t)|^2$ is the probability that the system is in state m. To determine $C_m(t)$, we substitute Equation 5.12 into Equation 5.6:

$$\sum_{m\in\{a,b\}}\left[i\hbar\dot{C}_m(t) + E_m C_m(t)\right]\exp(-i\omega_m t)|m\rangle = \sum_{m\in\{a,b\}}\left[\hat{H}_0 + \hat{V}\right]C_m(t)\exp(-i\omega_m t)|m\rangle \tag{5.13}$$

in which we have used the product rule and the fact that $|m\rangle$ is time-invariant.[1] Projecting[2] Equation 5.13 onto the individual eigenstates yields two coupled rate equations

$$\begin{aligned}\dot{C}_a(t) &= -\frac{i}{\hbar}C_b(t)\exp\left[-i(\omega_b-\omega_a)t\right]\langle a|\hat{V}(t)|b\rangle \\ \dot{C}_b(t) &= -\frac{i}{\hbar}C_a(t)\exp\left[-i(\omega_a-\omega_b)t\right]\langle b|\hat{V}(t)|a\rangle.\end{aligned} \tag{5.14}$$

We now introduce the resonance frequency $\omega_{ba} \equiv \omega_b - \omega_a$ and note that

$$\langle a|\hat{V}(t)|b\rangle = \tilde{E}\langle a|\hat{\mu}|b\rangle = -\left[\frac{E_0}{2}\exp\left(-i\omega t\right) + \frac{{E_0}^*}{2}\exp\left(i\omega t\right)\right]\mu_{ab} \tag{5.15}$$

which yields

$$\begin{aligned}\dot{C}_a(t) &= \frac{i\mu_{ab}}{2\hbar}C_b(t)\left[E_0\exp\left(-i(\omega+\omega_{ba})t\right) + E_0^*\exp\left(i(\omega-\omega_{ba})t\right)\right] \\ \dot{C}_b(t) &= \frac{i\mu_{ba}}{2\hbar}C_a(t)\left[E_0\exp\left(-i(\omega-\omega_{ba})t\right) + E_0^*\exp\left(i(\omega+\omega_{ba})t\right)\right].\end{aligned} \tag{5.16}$$

The exponentials with arguments of $\omega + \omega_{ba}$ will oscillate much more rapidly than those with arguments of $\omega - \omega_{ba}$. We therefore make the *rotating wave approximation* (RWA) and disregard the rapidly oscillating terms while introducing the detuning factor $\Delta = \omega - \omega_{ba}$

$$\dot{C}_a(t) = \frac{i\mu_{ab}E_0^*}{2\hbar}C_b(t)\exp\left(i\Delta t\right) \tag{5.17}$$

$$\dot{C}_b(t) = \frac{i\mu_{ba}E_0}{2\hbar}C_a(t)\exp\left(-i\Delta t\right). \tag{5.18}$$

General solution of the two level system

To solve the coupled equations (Equation 5.17, Equation 5.18) we introduce a complex ansatz

$$C_a(t) = K\exp\left(-i\lambda t\right), \lambda \in \mathbb{R} \tag{5.19}$$

$$\implies \dot{C}_a(t) = -i\lambda K\exp\left(-i\lambda t\right) \tag{5.20}$$

[1] $\frac{\partial}{\partial t}\left[C_m(t)\exp\left(-i\omega_m t\right)|m\rangle\right] = \left[\dot{C}_m(t) - i\omega_m C_m(t)\right]\exp\left(-i\omega_m t\right)|m\rangle$

[2] To project onto state m, multiply Equation 5.13 by $\langle m|$.

which we substitute into Equation 5.17

$$-i\lambda K \exp\left(-i\lambda t\right) = \frac{i\mu_{ab}E_0^*}{2\hbar} C_b(t) \exp\left(i\Delta t\right) \tag{5.21}$$

$$\implies C_b(t) = \frac{-2\hbar\lambda K}{\mu_{ab}E_0^*} \exp\left(-i(\lambda+\Delta)t\right) \tag{5.22}$$

$$\implies \dot{C}_b(t) = \frac{i2\hbar\lambda K(\lambda+\Delta)}{\mu_{ab}E_0^*} \exp\left(-i(\lambda+\Delta)t\right). \tag{5.23}$$

We now substitute this form of $\dot{C}_b(t)$ into Equation 5.18 along with Equation 7.10

$$\frac{i2\hbar\lambda K(\lambda+\Delta)}{\mu_{ab}E_0^*} \exp\left(-i(\lambda+\Delta)t\right) = \frac{i\mu_{ba}E_0}{2\hbar} K \exp\left(-i\lambda t\right) \exp\left(-i\Delta t\right) \tag{5.24}$$

$$\implies \lambda(\lambda+\Delta) = \frac{\left|\mu_{ba}\right|^2 \left|E_0\right|^2}{4\hbar^2} \tag{5.25}$$

$$\implies \lambda_\pm = -\frac{\Delta}{2} \pm \frac{\sqrt{\Delta^2 + \frac{\left|\mu_{ba}\right|^2 \left|E_0\right|^2}{\hbar^2}}}{2} = -\frac{\Delta}{2} \pm \frac{\Omega'}{2} \tag{5.26}$$

in which we have introduced the *generalized Rabi frequency*

$$\Omega' \equiv \sqrt{|\Omega|^2 + \Delta^2} \tag{5.27}$$

in which the complex Rabi frequency is $\Omega \equiv \frac{\mu_{ba}E_0}{\hbar}$.

The general solutions for the probability amplitudes are then obtained by substituting Equation 5.26 into Equation 5.20

$$C_a(t) = \exp\left(\frac{i\Delta t}{2}\right)\left[K_+ \exp\left(\frac{-i\Omega' t}{2}\right) + K_- \exp\left(\frac{i\Omega' t}{2}\right)\right] \tag{5.28}$$

$$C_b(t) = \exp\left(\frac{-i\Delta t}{2}\right)\left[\frac{\Delta-\Omega'}{\Omega^*} K_+ \exp\left(\frac{-i\Omega' t}{2}\right) + \frac{\Delta+\Omega'}{\Omega^*} K_- \exp\left(\frac{i\Omega' t}{2}\right)\right] \tag{5.29}$$

in which Equation 5.29 was obtained by substituting the time derivative of Equation 5.28 into Equation 5.17. The coefficients $K_\pm$ are determined by the initial conditions of the system. For example, Boyd [38] explores the case where the system is initially in the ground state.

Without the pump field, the states evolve at their Bohr frequencies, ω_a and ω_b. With the pump field, the frequencies are augmented by both the strength of the field and its detuning.

Optical Transitions and the Stark Shift

Inspection of Equation 5.28 and Equation 5.29 shows that eigenstates $|a\rangle$ and $|b\rangle$ oscillate with characteristic frequencies given by the couplets $E_{a\pm}$ and $E_{b\pm}$, respectively:

$$E_{a\pm} = \omega_a - \frac{\Delta}{2} \pm \frac{\Omega'}{2} \tag{5.30a}$$

$$E_{b\pm} = \omega_b + \frac{\Delta}{2} \pm \frac{\Omega'}{2}. \tag{5.30b}$$

A probe will monitor transitions between the a and b manifolds. The observable transition frequencies are then

$$E_{b+} - E_{a+} = \omega_b + \frac{\Delta}{2} + \frac{\Omega'}{2} - \left(\omega_a - \frac{\Delta}{2} + \frac{\Omega'}{2}\right) = \omega_{ba} + \Delta = \omega \tag{5.31a}$$

$$E_{b+} - E_{a-} = \omega_b + \frac{\Delta}{2} + \frac{\Omega'}{2} - \left(\omega_a - \frac{\Delta}{2} - \frac{\Omega'}{2}\right) = \omega_{ba} + \Delta + \Omega' = \omega + \Omega' \tag{5.31b}$$

$$E_{b-} - E_{a+} = \omega_b + \frac{\Delta}{2} - \frac{\Omega'}{2} - \left(\omega_a - \frac{\Delta}{2} + \frac{\Omega'}{2}\right) = \omega_{ba} + \Delta - \Omega' = \omega - \Omega' \tag{5.31c}$$

$$E_{b-} - E_{a-} = \omega_b + \frac{\Delta}{2} - \frac{\Omega'}{2} - \left(\omega_a - \frac{\Delta}{2} - \frac{\Omega'}{2}\right) = \omega_{ba} + \Delta = \omega \tag{5.31d}$$

in which we have used the relation $\Delta = \omega - \omega_{ba}$. Thus three characteristic transition frequencies result: ω, $\omega - \Omega'$, $\omega + \Omega'$. This is known as the *Mollow triplet*.[254]

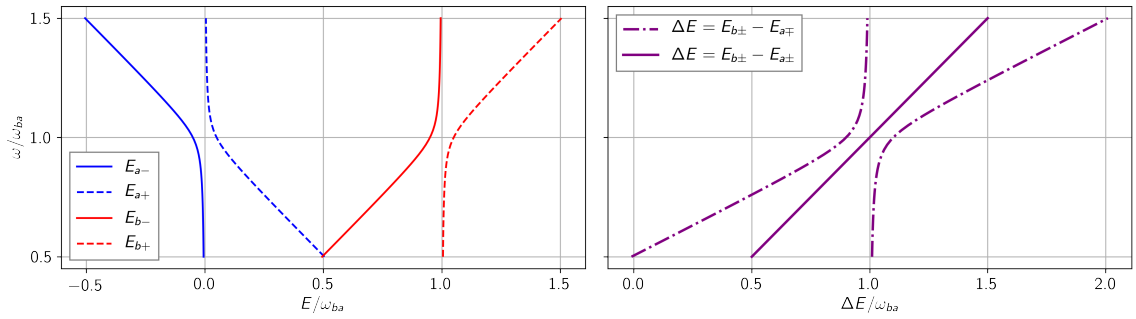

Figure 5.7: The effect of the applied field frequency, ω, on the system. The left plot shows how applied field controls the renormalized frequencies (Equation 5.30), and the right plot shows the resulting transition frequencies (Equation 5.31) In both plots, $\Omega = 0.1\omega_{ba}$.

The Stark shift is the difference between these new and the undressed transition frequencies:

$$\text{shift} \equiv \omega_{ba} - \left(\omega \pm \Omega'\right) \tag{5.32}$$

$$= -\Delta \mp \Omega' \tag{5.33}$$

$$= -\Delta \mp \Delta\sqrt{1 + \frac{\Omega^2}{\Delta^2}}. \tag{5.34}$$

Figure 5.7 shows how these energy levels and transitions change with input frequency. If we are in the large detuning limit, $\Delta \gg \Omega$, then we can expand $\sqrt{1 + \frac{\Omega^2}{\Delta^2}} \approx 1 + \frac{\Omega^2}{2\Delta^2}$ to yield

$$\text{frequency shift} \approx -\Delta \mp \Delta\left(1 + \frac{\Omega^2}{2\Delta^2}\right) \tag{5.35}$$

$$= \begin{cases} \frac{\Omega^2}{2\Delta} \\ -2\Delta - \frac{\Omega^2}{2\Delta}. \end{cases} \tag{5.36}$$

Again, since detuning is large, the transition frequency $-2\Delta - \frac{\Omega^2}{2\Delta}$ is far away from our observation window of $\sim \omega_{ba}$ and can be neglected. This leaves us with one transition frequency to consider:

$$\boxed{\text{frequency shift} = \frac{\Omega^2}{2\Delta} = \frac{\mu_{ba}^2 E_0^2}{2\hbar^2(\omega - \omega_{ba})},} \tag{5.37}$$

in which we see that the dynamic Stark effect scales as the transition dipole squared, the pump intensity, and inversely with pump/transition detuning.

5.7.2 Perturbative treatment: detuned pump, single photon probe

In this section we again consider a single mode system, but we explicitly include the probe electric field:

$$V(t) = \mu\left(\tilde{E}_{\text{pump}} + \tilde{E}_{\text{probe}}\right) \tag{5.38}$$

This treatment is based on a perturbative expansion of $V(t)$, truncated at third-order ($|E_{\text{pump}}|^2 E_{\text{probe}}$). This approach results in a set of Liouville pathways, each one describing a unique series of four

field-matter interactions that contributes to the output signal. An example of one of these pathways is[3]

$$gg \xrightarrow{1} ag \xrightarrow{\bar{2}} gg \xrightarrow{2} ag \rightarrow gg, \tag{5.39}$$

in which $\bar{2}$ represents a negative wave vector interaction from pulse 2. Within the RWA, positive wave vectors stimulate ket-side (bra-side) absorption or bra-side (ket-side) emission. The perturbative expansion technique is well-known and described elsewhere.[246, 255] Here we focus on assembling the set of Liouville pathways, isolating the members crucial for describing our domain of pump and probe frequencies, and then understanding their behavior through closed form expressions and simulations.

Relevant Liouville pathways

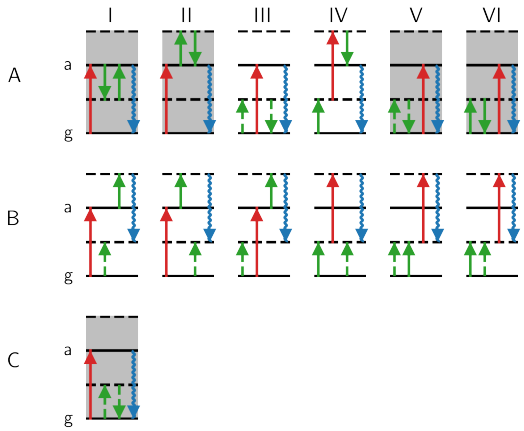

Figure 5.8: Some wave mixing energy level diagrams (WMELs) of the Liouville pathways for sub-resonant pump, resonant probe experiment. Time flows from left to right, the green arrows correspond to the pump, the red arrow is the probe, and the blue wavy arrow is the emission. Gray shaded WMELs highlight the doubly resonant pathways.

We must consider the pathways which could lead to signals at the phase-matching direction and output frequency imposed by our experiment. We then use the RWA and neglect pathways that are triply non-resonant. Figure 5.8 shows WMEL representations of all valid pathways, while Figure 5.9

[3]This expression uses a shorthand notation for density matrix elements: $ij = \rho_{ij} = |i\rangle\langle j|$.

diagrams these pathways by state indices; the probe is indexed to 1 and the pump is indexed to 2. The WMEL representations make it clear how detuning affects resonance, while the Liouville pathways focuses on the identity of the density matrix elements after each pulse interaction. Our analysis here focuses on WMEL representations.

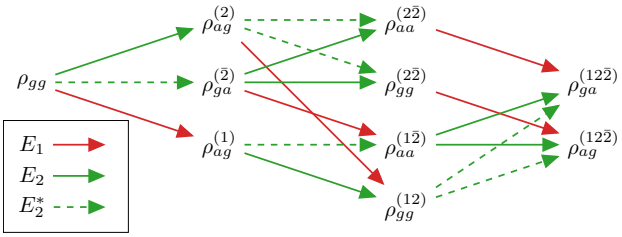

Figure 5.9: Liouville pathways for a non-resonant pump, resonant probe experiment. Green arrows correspond to the pump while red is the probe. The driven limit is assumed for dermining the wave mixing energies. Superscripts denote the field interactions which have occurred to create the density matrix element.

We now determine which of the allowed pathways are important for our case of a detuned pump. Since we are focused on a far-detuned pump pulse, we can neglect several (8) pathways, unshaded in Figure 5.8, because they are singly resonant when the pump is detuned; all remaining pathways are doubly resonant and deserve further consideration (Figure 5.8, shaded).

The doubly resonant pathways from time orderings V and VI have intrinsic interference that makes them negligible in this regime as well. Time-orderings V make an intermediate population through the process $gg \xrightarrow{\bar{2}} ag \xrightarrow{2} aa/gg$, while VI make a population via the conjugate route $gg \xrightarrow{2} ga \xrightarrow{\bar{2}} aa/gg$. The result of this pathway conjugation is well-known: the net population from a pump pulse scales as the imaginary component of the frequency response (absorption), rather than the complex resonance.[256] The imaginary component is much more sensitive to detuning than the real part ($\sim 1/\Delta^2$ vs. $\sim 1/\Delta$), and as a result our large pump detuning makes this contribution smaller than the other doubly resonant pathways (time orderings I and II). We will therefore neglect VA and VIA as well.

We have reduced our consideration to 3 WMELS: IA, IC, and IIA. IA and IC are mathematically equivalent pathways. Pathway IIA has the same resonance conditions as IA and IC, but opposite sign; it will destructively interfere with IA and IC. Given that pathway IIA introduces additional model parameters, but will only change the amplitude of the resulting lineshape, we will exclude

it from consideration.

In summary, we have shown how our experimental conditions restrict our analysis to the doubly resonant pathways of time-ordering I. We will now evaluate these Liouville pathways and connect them to the Stark effect.

Driven limit expressions

Here we evaluate the Liouville pathways using the "driven limit" equations, valid when the free-induction-decay (FID) of the system is shorter than the pulse-width of the driving fields, when excitation is non-resonant, or at $T = 0$.[43] In this derivation the ground state will be g and the excited state a.

For these expressions, we use a shorthand notation for resonance denominators. For a transition to a density matrix element, ij, driven by the series of laser interactions S, the resonance denominator, denoted, Δ_{ij}^{S}, is given by

$$\Delta_{ij}^{S} \equiv \hbar \left(\omega_{ij} - \omega_S - i\Gamma_{ij} \right). \tag{5.40}$$

Here S is a list denoting the linear combination of laser frequencies, ω_S, stimulating the transition. For example, $S = (1)$ means $\omega_S = \omega_1$ and $S = (112)$ means $\omega_S = 2\omega_1 + \omega_2$. A laser frequency is positively signed unless the laser index is barred, in which case the sign is negative (e.g. $S = (1\bar{2})$ means $\omega_S = \omega_1 - \omega_2$).

The first order susceptibility when no pump is present is simply

$$\chi^{(1)} = \frac{\mu_{ag}^2}{2\Delta_{ag}^{(1)}} \tag{5.41}$$

in which Γ is the dephasing rate, and ω_n is a (signed) electric field interaction frequency.[4] The

[4]The factor of $1/2$ originates from using the Euler representations of incident light, $\cos(x) = 1/2(\exp(-x)+\exp(x))$, we only keep one of the exponential terms when we are propagating.

third order susceptibility when the pump is present is

$$\chi^{(3)} = \frac{\mu_{ag}^2}{2\Delta_{ag}^{(1)}} \left(\frac{\mu_{ag}}{2\Delta_{gg}^{(1\bar{2})}} + \frac{\mu_{ag}}{2\Delta_{aa}^{(1\bar{2})}} \right) \frac{\mu_{ag}}{2\Delta_{ag}^{(1\bar{2}2)}} \tag{5.42}$$

$$= \left(\frac{\mu_{ag}}{2\Delta_{ag}^{(1)}} \right)^2 \left(\frac{\mu_{ag}^2}{2\Delta_{gg}^{(1\bar{2})}} + \frac{\mu_{ag}^2}{2\Delta_{aa}^{(1\bar{2})}} \right) \tag{5.43}$$

$$= \left(\chi^{(1)} \right)^2 \frac{1}{\Delta_{gg}^{(1\bar{2})}} \tag{5.44}$$

in which we have used the fact that $\Delta_{aa}^{(1\bar{2})} = \Delta_{gg}^{(1\bar{2})}$. Figure 5.10 plots Equation 5.44 in experimental coordinates. Since we have assumed the pump is non-resonant and the probe is near resonance, the 2D response shown in Figure 5.10 is valid only in certain frequency ranges (gray shaded). The other areas of the plot require consideration of other resonant processes, such as resonant absorption of the pump. This is the same regime considered to arrive at Equation 5.37. Note that in the valid regime, a dispersive lineshape is present along the probe axis for the imaginary projection of $\chi^{(3)}$. We will now connect this dispersive lineshape to shift in the resonance frequency.

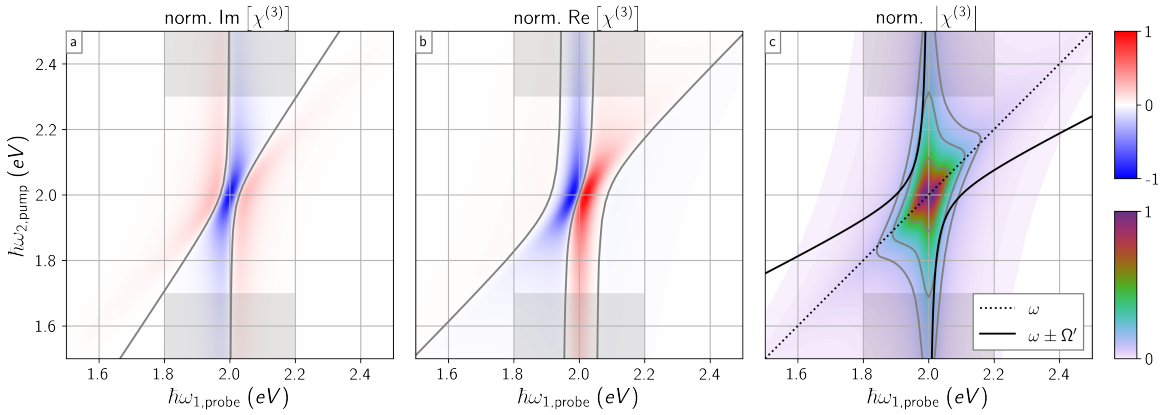

Figure 5.10: Plot of Equation 5.44 for $\hbar\omega_{ag} = 2$ eV and $\Gamma = 50$ meV. Contour lines in (a) and (b) are set at 0, while they are set to 0.1, .2, and .5 in (c). Black shaded boxes show the regime where this response describes the system completely. The thick black lines in (c) show the renormalized transition frequencies from Equation 5.31 for comparison.

It is the pump induced *change* in $\chi^{(1)}$ which is commonly measured

$$\mathrm{d}\chi^{(1)} = |E_2|^2 \chi^{(3)}. \tag{5.45}$$

To connect Equation 5.44 to the Stark Effect, we will compare it with a small shift ($\Delta\omega_{ag} \ll \Gamma$) of the susceptibility through the differential:

$$\mathrm{d}\chi^{(1)} \approx \frac{\partial\chi^{(1)}}{\partial\omega_{ag}}\Delta\omega_{ag}, \tag{5.46}$$

in which a positive (negative) $\Delta\omega$ corresponds to a blueshift (redshift).

Inspection of Equation 5.41 yields

$$\frac{\partial\chi^{(1)}}{\partial\omega_{ag}} = -\frac{2(\chi^{(1)})^2}{\mu_{ag}^2} \tag{5.47}$$

which upon substitution into Equation 5.46 yields

$$\mathrm{d}\chi^{(1)} = -\frac{2(\chi^{(1)})^2}{\mu_{ag}^2}\Delta\omega_{ag} \tag{5.48}$$

which upon further substitution of Equation 5.45 and rearranging yields

$$\Delta\omega_{ag} = -\frac{|E_2|^2\mu_{ag}^2\chi^{(3)}}{2(\chi^{(1)})^2}. \tag{5.49}$$

We substitute $\chi^{(3)}$ for the specific pathway considered in this section (Equation 5.44)

$$\Delta\omega_{ag} = -\frac{\mu_{ag}^2|E_2|^2}{2\Delta_{gg}^{(1\bar{2})}} \approx \frac{\mu_{ag}^2|E_2|^2}{2\hbar(\omega_1-\omega_2)} \tag{5.50}$$

in which the approximation $\Delta_{gg}^{(1\bar{2})} \approx \hbar(\omega_2-\omega_1)$ is valid for a significantly detuned pump. The prediction of Equation 5.50 is analogous to that predicted from the traditional wavefunction analysis of the weak-field Stark effect (Equation 5.37). In the traditional analysis, the frequency dependence goes as $1/(\omega_{ag}-\omega_2)$. Our analysis considers the effect of a driven system, so the free induction frequency of the traditional analysis (Section 5.7.1) does not apply. Nonetheless, since we consider the regime where $\omega_{ag} \approx \omega_1$, the differences are minute.

5.8 Appendix: Perturbative treatment: detuned pump, THG probe

We take a similar tact as the last section to derive an expression for the dynamic Stark shift with a THG probe (instead of a 1 photon probe). We first systematically compile a list of potential pathways, and then reduce that list to a handful of the most prominent pathways, based on resonance enhancement. With these pathways we then define expressions within the driven limit to simulate.

5.8.1 Relevant Liouville pathways

We first assemble the set of Liouville pathways that scale as $E_1^3|E_2|^2$. For our two-level system, we assume the a and g states are separated by roughly three photons of energy so that three photon absorption can be resonant with the a state. Compared to our four wave mixing analysis, the number of pathways is enormous: 5 interactions of three distinguishable pulses give 20 time orderings, each with $2^5 = 32$ possible wave mixing combinations (640 pathways). Four photon absorption is not considered here, though we note that such transitions are viable and important processes in certain Stark Effect experiments especially when interband absorption and biexciton states are isolated.[232, 238, 235, 257] Removing pathways containing antiresonant contributions reduces the number to 52, all of which are represented in Figure 5.11. Further, we identify only sixteen pathways as doubly resonant (shaded gray).

Of these sixteen doubly resonant pathways, only four represent unique paths of density matrix elements. Each unique path has four "copies" owing to the interchangeable role between the pump (2) and the probe fundamental (1). The four copies are all in adjacent columns. Of these four copies, one pathway uses all three probe photons to perform THG from g to a (purple box), while the other three use a pump interaction to perform TSF from g to a (gold boxes). The three TSF pathways are mathematically equivalent because they differ only in transitions between virtual states. The three TSF pathways will be important when $\omega_1 \approx \omega_2 \approx \omega_{ag}/3$, while only THG pathways are important when ω_1 and ω_2 differ greatly.

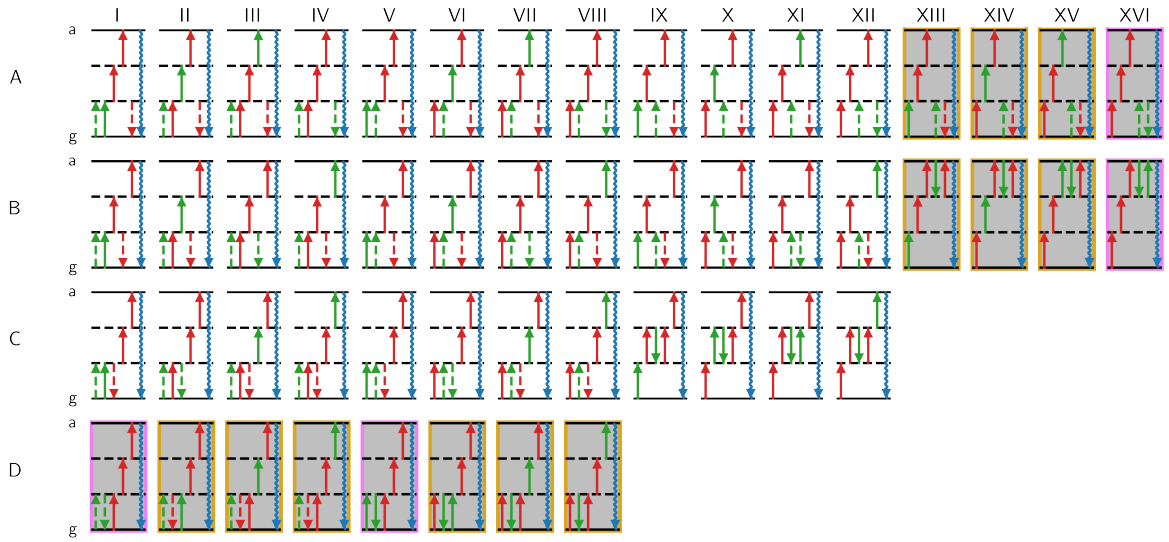

Figure 5.11: WMELs for a non-resonant pump, THG probe experiment. Gray shaded WMELs highlight the doubly resonant pathways. Purple outlines highlight conventional pathways where the probe stimulates THG, while gold outlines highlight the exchange pathways where pump and probe photons mix to stimulate TSF.

5.8.2 Driven limit expressions

We first define the THG output in the unpumped case. We will use the same resonance denominator notation introduced in Equation 5.40. The unpumped THG susceptibility is given by

$$\chi^{(3)}_{\text{THG}} = \frac{M_{ag}\mu_{ag}}{2\Delta^{(111)}_{ag}} \tag{5.51}$$

in which M_{ag} (μ_{ag}) is the effective THG (dipole) transition moment from the ground state, g, to the excited state, a. This THG formalism was successful in describing TMDCs previously.[68]

For the pumped case, we consider doubly resonant WMELs of Figure 5.11. We stratify the pathways into four sets, $\mathbb{A}$, $\mathbb{B}$, $\mathbb{C}$, and $\mathbb{D}$, that differ in their mechanism of 3-photon transition (111 vs. 112) and their remaining pathways can be separated into four unique contributions:

$\mathbb{A}$: **Pathways A-XVI and B-XVI**

$$gg \xrightarrow{111} ag \xrightarrow{\bar{2}} gg/aa \xrightarrow{2} ag \xrightarrow{\text{out}} gg \tag{5.52}$$

$$\mathbb{A} = \frac{M_{ag}\mu_{ag}^3}{8\Delta_{ag}^{(111)}\Delta_{ag}^{(111)}}\left(\frac{1}{\Delta_{gg}^{(11\bar{2})}} + \frac{1}{\Delta_{aa}^{(11\bar{2})}}\right) \tag{5.53}$$

$$= \chi_{\text{THG}}^{(3)}\frac{\mu_{ag}^2}{2\Delta_{ag}^{(111)}\Delta_{gg}^{(11\bar{2})}} = \left(\chi_{\text{THG}}^{(3)}\right)^2\frac{\mu_{ag}}{M_{ag}\Delta_{gg}^{(11\bar{2})}} \tag{5.54}$$

$\mathbb{B}$: **Pathways A-XIII—XV + B-XIII—XV**

$$gg \xrightarrow{112} ag \xrightarrow{\bar{2}} gg/aa \xrightarrow{1} ag \xrightarrow{\text{out}} gg \tag{5.55}$$

$$\begin{aligned}\mathbb{B} &= \frac{3M_{ag}\mu_{ag}^3}{8\Delta_{ag}^{(111)}\Delta_{ag}^{(112)}}\left(\frac{1}{\Delta_{gg}^{(11)}} + \frac{1}{\Delta_{aa}^{(11)}}\right) \\ &= \chi_{\text{THG}}^{(3)}\frac{3\mu_{ag}^2}{2\Delta_{ag}^{(112)}\Delta_{gg}^{(11)}}\end{aligned} \tag{5.56}$$

$\mathbb{C}$: **Pathways D-I + D-V**

$$gg \xrightarrow{2/\bar{2}} ag/ga \xrightarrow{\bar{2}/2} gg/aa \xrightarrow{111} ag \xrightarrow{\text{out}} gg \tag{5.57}$$

The pathways involving aa are not shown in Figure 5.11 because they have the same time-ordering and wave mixing combination as the pathway involving gg.

$$\begin{aligned}\mathbb{C} &= \frac{M_{ag}\mu_{ag}^3}{8\Delta_{ag}^{(111)}}\left(\frac{1}{\Delta_{gg}^{(2\bar{2})}} + \frac{1}{\Delta_{aa}^{(2\bar{2})}}\right)\left(\frac{1}{\Delta_{ag}^{(2)}} + \frac{1}{\Delta_{ga}^{(\bar{2})}}\right) \\ &= -\chi_{\text{THG}}^{(3)}\frac{\mu_{ag}^2}{\Gamma_{gg}}\text{Im}\left[\frac{1}{\Delta_{ag}^{(2)}}\right]\end{aligned} \tag{5.58}$$

$\mathbb{D}$: **Pathways D-II—IV + D-VI—VIII**

$$gg \xrightarrow{1/\bar{2}} ag/ga \xrightarrow{\bar{2}/1} gg/aa \xrightarrow{112} ag \xrightarrow{\text{out}} gg \tag{5.59}$$

The pathways involving aa are not shown in Figure 5.11 because they have the same time-ordering and wave mixing combination as the pathway involving gg.

$$\begin{aligned}\mathbb{D} &= \frac{3M_{ag}\mu_{ag}^3}{8\Delta_{ag}^{(111)}}\left(\frac{1}{\Delta_{gg}^{(1\bar{2})}}+\frac{1}{\Delta_{aa}^{(1\bar{2})}}\right)\left(\frac{1}{\Delta_{ag}^{(1)}}+\frac{1}{\Delta_{ga}^{(\bar{2})}}\right)\\ &= \chi_{\mathrm{THG}}^{(3)}\frac{3\mu_{ag}^2}{2\Delta_{gg}^{(1\bar{2})}}\left(\frac{1}{\Delta_{ag}^{(1)}}+\frac{1}{\Delta_{ga}^{(\bar{2})}}\right)\end{aligned} \tag{5.60}$$

The terms $\mathbb{A}$ and $\mathbb{B}$ represent fully coherent pathways and are analogous to the weak probe OSE effect (cf. Section 5.7.2). They differ in whether they entail a THG ($\mathbb{A}$) or a TSF ($\mathbb{B}$) transition. Terms $\mathbb{C}$ and $\mathbb{D}$ are partially coherent because they create a stationary polarization (after two interactions) and are sensitive to the incoherent amplitudes of the a and g states.

As an important implementation detail, we note that the pathways in expressions $\mathbb{C}$ and $\mathbb{D}$ feature resonant excitation of the aa/gg populations, which depend on the state lifetime $\Gamma_{gg} = \Gamma_{aa}$. The driven limit is inappropriate for resonant population creation because exciton lifetimes are typicaly much longer than the pulse duration that time gate the experiment; the instrument response function bandwidth is much broader than the resonance linewidth. In effect, the driven limit expressions above feature unrealistically narrow linewidths and strong peaks for these resonance. Following earlier work on this effect,[43] we correct this issue by simply replacing the population decay rate Γ_{gg} with the inverse of the pulse duration: $\Gamma_{gg} \to 1/\Delta_t \sim 1/50$ fs^{-1}). This procedure is followed for evaluation of all equations in this section.

The total response will be the sum of all four pathway groupings

$$\chi^{(5)} = \mathbb{A} + \mathbb{B} + \mathbb{C} + \mathbb{D}. \tag{5.61}$$

The measured intensity in the absence of the pump is:

$$I_{\mathrm{THG,unpumped}} \propto \left|\chi_{\mathrm{THG}}^{(3)}\right|^2 I_1^3, \tag{5.62}$$

and when pumped the intensity is

$$I_{\text{THG,pumped}} \propto \left|\chi^{(3)}_{\text{THG}} + \chi^{(5)}|E_2|^2\right|^2 I_1^3, \tag{5.63}$$

where the constant of proportionality is the same as Equation 5.62. The signal is given by

$$\begin{aligned}\text{norm. } \Delta I_{\text{THG}}(\omega_1) &\equiv \frac{I_{\text{THG, pumped}} - I_{\text{THG, unpumped}}}{\max\left\{I_{\text{THG, unpumped}}\right\}} &(5.64)\\ &= \frac{4\Gamma^2}{M_{ag}^2\mu_{ag}^2}\left(\left|\chi^{(3)}_{\text{THG}} + \chi^{(5)}|E_2|^2\right|^2 - \left|\chi^{(3)}_{\text{THG}}\right|^2\right), &(5.65)\end{aligned}$$

where in the second line we evaluated $\chi^{(3)}_{\text{THG}}$ at its maximum value: $\omega_1 = \omega_{ag}$. For the purpose of analytic equations, we assume the perturbation is small, $\chi^{(5)}|E_2|^2 \ll \chi^{(3)}_{\text{THG}}$, in which case a first-order Taylor expansion of Equation 5.65 yields

$$\text{norm. } \Delta I_{\text{THG}} = \frac{8\Gamma^2|E_2|^2}{M_{ag}^2\mu_{ag}^2}\text{Re}\left[\overline{\chi^{(3)}_{\text{THG}}} \times \chi^{(5)}\right] \tag{5.66}$$

Inserting Equations 5.54—5.61 into Equation 5.66 gives our closed-form expression for the response:

$$\begin{aligned}\text{norm. } \Delta I_{\text{THG}} = &\left|\frac{\Gamma\mu_{ag}E_2}{\Delta_{ag}^{(111)}}\right|^2 \\ &\times \text{Re}\left[\frac{1}{2\Delta_{ag}^{(111)}\Delta_{gg}^{(11\bar{1}\bar{2})}} + \frac{3}{2\Delta_{ag}^{(112)}\Delta_{gg}^{(11)}} - \frac{1}{\Gamma_{gg}}\text{Im}\left[\frac{1}{\Delta_{ag}^{(2)}}\right] + \frac{3}{2\Delta_{gg}^{(1\bar{2})}}\left(\frac{1}{\Delta_{ag}^{(1)}} + \frac{1}{\Delta_{ga}^{(\bar{2})}}\right)\right].\end{aligned} \tag{5.67}$$

Figure 5.12 shows 2D spectral response of all four terms, as well as their sum, for a pump-THG-probe experiment.

Justification: separation of coherent and partially coherent processes

In our two level system, the weights of all four contributions in $\chi^{(5)}$ are well-defined (see Equations 5.61 and 5.67). The fixed weighting belies the reality that the coherent pathways ($\mathbb{A}$ and $\mathbb{B}$) and the incoherent pathways ($\mathbb{C}$ and $\mathbb{D}$) have different non-resonant factors: the fully coherent

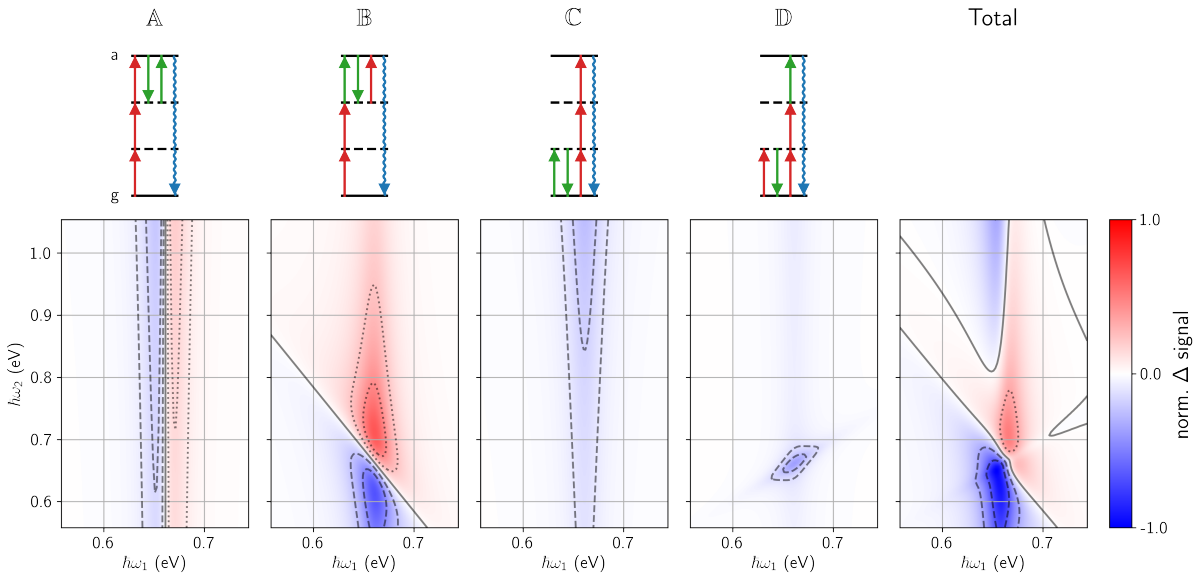

Figure 5.12: The 2D spectral response of Re $\left[\overline{\chi^{(3)}_{\mathrm{THG}}} \times \chi^{(5)}\right]$ (cf. Equation 5.66) for the different $\chi^{(5)}$ contributions and their sum (Equation 5.61). We have used $\hbar\Gamma = 50$ meV, $\hbar\omega_{ag} = 1.98$ eV, $\Gamma_{gg} \to 1/\Delta_t = 1/50$ fs^{-1}.

contributions depend on the real and imaginary components of a detuned resonance, e.g. $\Delta_{gg}^{(111\bar{2})}$, while the partially coherent contributions depend on the imaginary portion of detuned resonance (e.g. Im $\left[1/\Delta_{ag}^{(2)}\right]$). In real systems, inhomogeneous broadening and complex dephasing behaviors often disrupt the Lorentzian absorptive (imaginary) wing predicted by our simple system, while the behavior of the refractive (real) component is less sensitive to such effects. This behavior can be clearly seen by comparing the refractive behavior of various peaked absorption line shapes (Gaussian, Voigt, Lorentzian, etc.) using the Kramers-Kronig relations. This underscores our experimental observation that the weights vary with both fluence and morphology (see Section 5.12), sometimes to the extent that ℂ and 𝔻 contributions are negligible. For these reasons, our analysis in the paper treats these weights as independent and separates the coherent and partially coherent contributions.

Connection to conventional OSE

Here we verify that the pathways A-XVI and C-XVI are consistent with the conventional OSE. Like our perturbative treatment in Section 5.7.2, we show here that these pathways produce a spectral shift that has the same dependence as that predicted from the non-perturbative analysis. To this end, we restrict our consideration here to $\chi^{(5)} = \mathbb{A}$, which will dominate when ω_1 and ω_2 differ greatly. In analogy with Section 5.7.2, we consider a perturbative resonance shift of the probe, which can be written as:

$$\mathrm{d}\chi^{(3)}_{\mathrm{THG}} \equiv \frac{\partial \chi^{(3)}_{\mathrm{THG}}}{\partial \omega_{ag}} \Delta\omega_{ag}. \tag{5.68}$$

We can also evaluate the partial derivative using Equation 5.51:

$$\frac{\partial \chi^{(3)}_{\mathrm{THG}}}{\partial \omega_{ag}} = -\frac{2}{M_{ag}\mu_{ag}} \left(\chi^{(3)}_{\mathrm{THG}}\right)^2. \tag{5.69}$$

Setting $\mathrm{d}\chi^{(3)}_{\mathrm{THG}} = \mathbb{A}|E_2|^2$, we can form analogous relations to those with a linear probe for small shifts in resonance frequency:

$$\mathrm{d}\chi^{(3)}_{\mathrm{THG}} = -\frac{\mu_{ag}^2 |E_2|^2}{2\Delta^{(11\bar{1}\bar{2})}_{gg}} \frac{\partial \chi^{(3)}_{\mathrm{THG}}}{\partial \omega_{ag}} \tag{5.70}$$

$$\implies \Delta\omega_{ag} \approx \frac{\mu_{ag}^2 |E_2|^2}{2\hbar(3\omega_1 - \omega_2)}. \tag{5.71}$$

For completeness, we also explore the lineshape function for the traditional pump probe metric $\Delta I/I$. For a small shift in resonance frequency, the pump-THG-probe signal is given by

$$\frac{\Delta I_{\mathrm{THG}}}{I_{\mathrm{THG}}} = \left| 1 + \frac{\mathrm{d}\chi^{(3)}_{\mathrm{THG}}}{\chi^{(3)}_{\mathrm{THG}}} \right|^2 - 1 \tag{5.72}$$

$$\approx 2\mathrm{Re}\left[\frac{\mathrm{d}\chi^{(3)}_{\mathrm{THG}}}{\chi^{(3)}_{\mathrm{THG}}} \right] \tag{5.73}$$

$$= 2\Delta\omega_{ag}\mathrm{Re}\left[\frac{\partial \chi^{(3)}_{\mathrm{THG}}}{\partial \omega_{ag}} \frac{1}{\chi^{(3)}_{\mathrm{THG}}} \right] \tag{5.74}$$

$$= \frac{4\Delta\omega_{ag}}{M_{ag}\mu_{ag}} \mathrm{Re}\left[-\chi^{(3)}_{\mathrm{THG}} \right]. \tag{5.75}$$

Note that the lineshape of the spectral shift is slightly different from a transient absorption measurement. The lineshape differences was previously explored: it arises from differences in the non-pumped probe lineshapes, which interfere with the pumped lineshapes when measured.[123]

Abstraction of THG OSE to OHG OSE

The reformulation of expressions $\mathbb{A}$ (Equation 5.54) and $\mathbb{B}$ (Equation 5.56) for a harmonic of arbitrary order, n, is straightforward. First, we make the substitutions

$$3\omega_1 \to n\omega_1 \tag{5.76}$$

$$M_{ag} \to \mu_{ag}^{(n)} \tag{5.77}$$

$$\Delta_{ag}^{(111)} \to \Delta_{ag}^{(\mathrm{OHG})} = \omega_{ag} - n\omega_1 - i\Gamma \tag{5.78}$$

$$\Delta_{ag}^{(112)} \to \Delta_{ag}^{(\mathrm{exch})} = \omega_{ag} - (n-1)\omega_1 - \omega_2 - i\Gamma \tag{5.79}$$

$$\chi_{\mathrm{THG}}^{(3)} \to \chi_{\mathrm{OHG}}^{(n)} = \frac{\mu_{ag}^{(n)}\mu_{ag}}{2\Delta_{ag}^{(\mathrm{OHG})}} \tag{5.80}$$

For THG probe, the contribution $\mathbb{B}$ has three times the number of pathways than $\mathbb{A}$ (hence the factor of 3 in Equation 5.56), but the degeneracy is n-fold for nHG due to the number of ways pump and probe fields can mix to form $(n-1)\omega_1 + \omega_2$ SFG. The result is

$$\mathbb{A} = \frac{\chi_{\mathrm{OHG}}^{(n)}\mu_{ag}^2}{2\Delta_{ag}^{(\mathrm{OHG})}\left(\omega_2 - n\omega_1 - i/\Delta_t\right)} \tag{5.81}$$

$$\mathbb{B} = \frac{n\chi_{\mathrm{OHG}}^{(n)}\mu_{ag}^2}{2\Delta_{ag}^{(\mathrm{exch})}\left(-(n-1)\omega_1 - i/\Delta_t\right)} \tag{5.82}$$

From Equation 5.66, and using $\chi^{(n+2)} = \mathbb{A} + \mathbb{B}$, the signal is

$$\text{norm. } \Delta I_{\mathrm{OHG}} = \frac{8\Gamma^2|E_2|^2}{(\mu_{ag}^n)^2\mu_{ag}^2}\mathrm{Re}\left[\overline{\chi_{\mathrm{OHG}}^{(n)}} \times \chi^{(n+2)}\right] \tag{5.83}$$

substitution gives

$$\boxed{\text{norm. } \Delta I_{\text{OHG}} = \left|\frac{\Gamma\mu_{ag}E_2}{\Delta_{ag}^{(\text{OHG})}}\right|^2 \text{Re}\left[\frac{1}{2\Delta_{ag}^{(\text{OHG})}(\omega_2 - n\omega_1 - i/\Delta_t)} + \frac{n}{2\Delta_{ag}^{(\text{exch})}(-(n-1)\omega_1 - i/\Delta_t)}\right],} \tag{5.84}$$

which is the form used in the main text.

Fitting procedure and parameter extraction of Figure 4

We fit the measured probe spectra of Figure 4 using Equation 5.84 ($n = 3$) and optimizing least squares through three independent parameters: $|\mu_{ag}E_2|^2$, ω_{ag}, and Γ. We calculate $\Delta\omega_{ag}$ from $|\mu_{ag}E_2|^2$ using Equation 5.71 and approximating THG as resonant ($3\omega_1 \approx \omega_{ag}$): $\Delta\omega_{ag} = \frac{|\mu_{ag}E_2|^2}{2\hbar(\omega_{ag}-\omega_2)}$. We made the resonant THG approximation to arrive at a constant value of $\Delta\omega_{ag}$ for each probe spectrum; the chosen ω_1 value has only a weak effect on $\Delta\omega_{ag}$. The full equation is

$$\begin{aligned}\text{norm. } \Delta I_{\text{THG}}\left[\omega_1, \Delta\omega_{ag}; \omega_2, \omega_{ag}, \Gamma, \Delta_t\right] = (\hbar\Delta\omega_{ag})\,(\omega_{ag} - \omega_2)\left|\frac{\Gamma}{\Delta_{ag}^{(111)}}\right|^2 \\ \times \text{Re}\left[\frac{1}{\Delta_{ag}^{(111)}\,(\omega_2 - 3\omega_1 - i/\Delta_t)} + \frac{3}{\Delta_{ag}^{(112)}\,(-2\omega_1 - i/\Delta_t)}\right],\end{aligned} \tag{5.85}$$

in which $\Delta\omega_{ag}$ is fit as a function of pump fluence.

5.9 Appendix: Numerical Simulations of pump-THG-probe: Delay dependent line shapes

The line shapes of pump probe spectroscopy can be complicated when pump and probe beams are nearly overlapped in time, or when the probe pulse precedes the pump.[256, 258, 259, 260, 227] Since our experimental data shows dramatic changes in line shape with delay, it is important to understand the effect of time delay on our theoretical line shapes. To account for these effects,

we employ numerical integration of the Liouville pathways (5.52, 5.55, 5.57, 5.59) using software previously developed by our group.[43, 261]

The theoretical delay dependence is summarized by Figures 5.13 and 5.14. Figure 5.13 shows the numerical results when the contributions are $\chi^{(5)} = \mathbb{A}+\mathbb{B}$. Figure 5.13g is essentially the simulation result presented in the main text (Equation 5.84), but calculated without explicitly making the long pulse approximation. Note that the 2D spectra at slight negative delays capture the "kink" of the zero-signal contour around $2\omega_{\text{probe}} + \omega_{\text{pump}} \approx \omega_{ag}$ in the exprimental data.

Figure 5.14 shows the numerical results when the contributions are $\chi^{(5)} = \mathbb{A}+\mathbb{B}+\mathbb{C}+\mathbb{D}$. Including the incoherent pathways in Figure 5.14 is useful because one can surmise the dynamics induced by photon absorption, particularly for the pump energies near and above ∼1 eV. The numerical simulation assumes a single photon absorption pathway, however, so the the threshold energy of $\omega_{\text{pump}} = \omega_{ag}/2$ is not reproduced in this simulation, and population signals for lower pump energies.

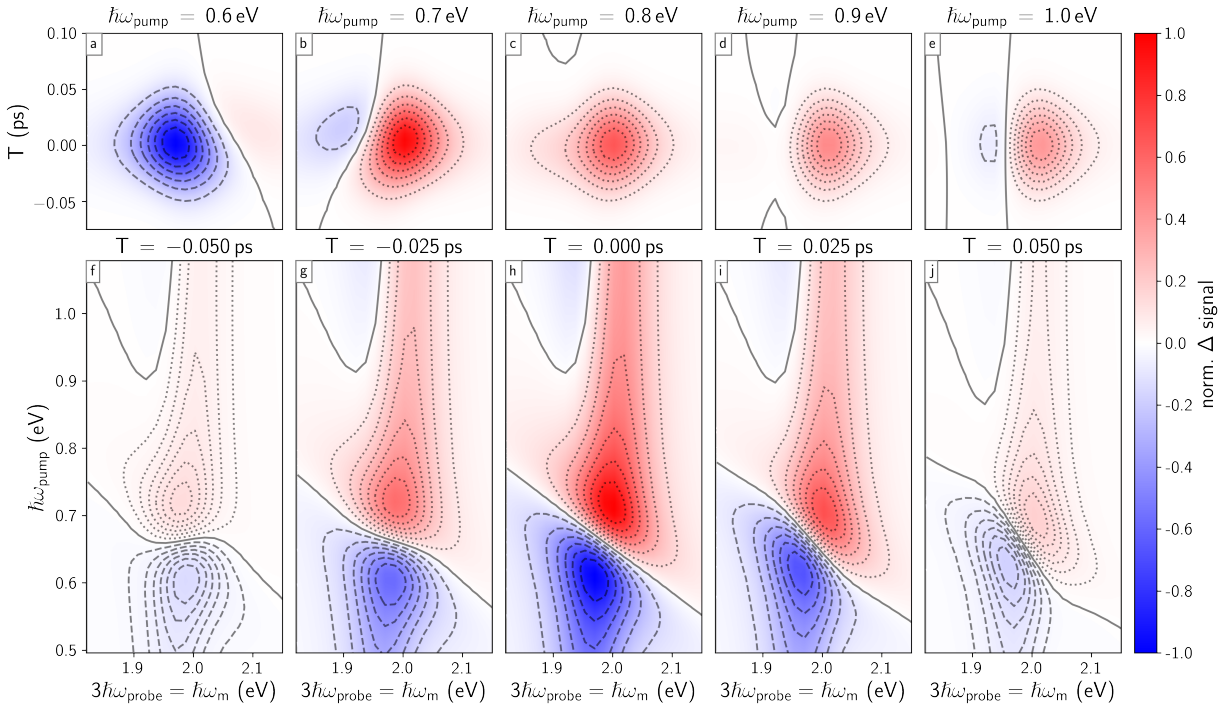

Figure 5.13: Results of numerically integrating the Liouville–von Neumann equation for $\chi^{(5)} = \mathbb{A}+\mathbb{B}$ with a 50 fs laser pulse, $\hbar\omega_{ag} = 1.98$ eV, and an 18 fs dephasing rate.

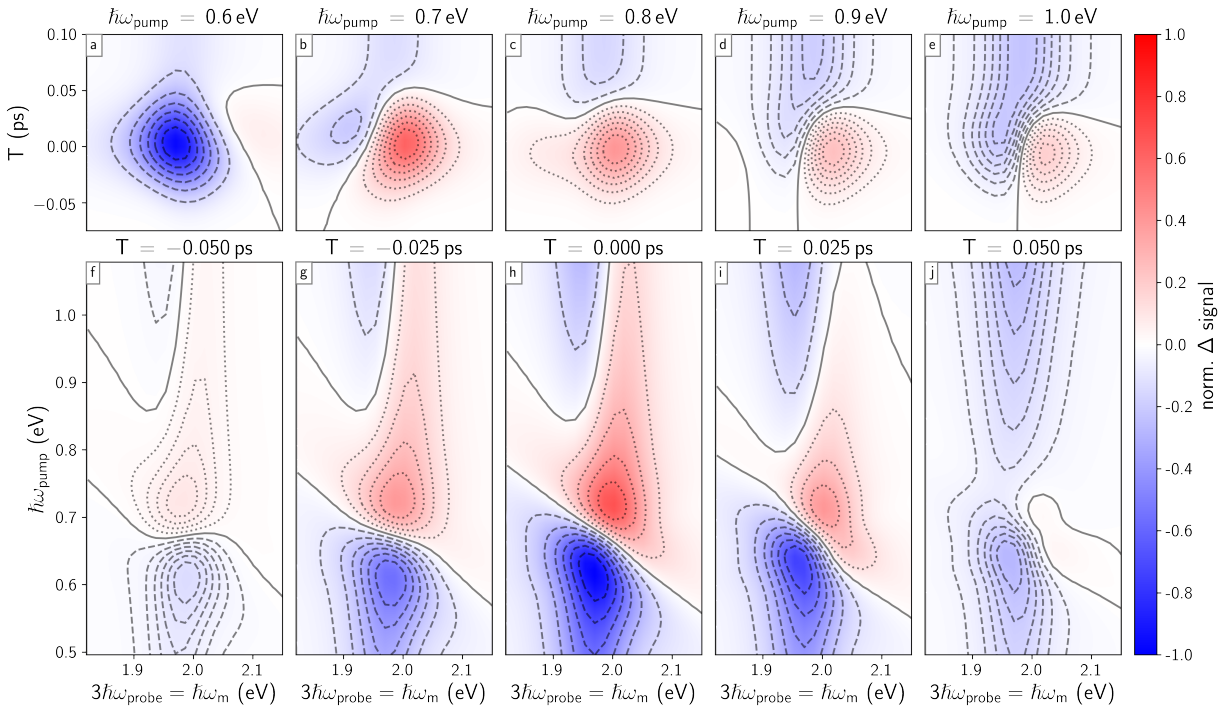

Figure 5.14: Results of numerically integrating the Liouville–von Neumann equation for $\chi^{(5)} = \mathbb{A} + \mathbb{B} + \mathbb{C} + \mathbb{D}$ with a 50 fs laser pulse, $\hbar\omega_{ag} = 1.98$ eV, and an 18 fs dephasing rate.

5.10 Appendix: Pump-SHG-probe

Here we present the 2D frequency response of pump-SHG-probe on the pyramid system. We show general agreement with our OSE theory. Furthermore, the results support the idea that the SHG probes a different state than that of THG. This is supported by two general observations:

1. The SHG resonance is ~ 30 meV shifted from the THG resonance, as seen in both pump-SHG-probe difference signals (Figure 5.15) and SHG (Figure 5.16), and
2. The SHG transition has a significantly smaller dipole moment, as measured by the fluence scaling of the OSE (cf. Figure 5.16i and j).

We do not have enough information to assign the SHG transition, but the energy shift is commensurate with trion states.[218]

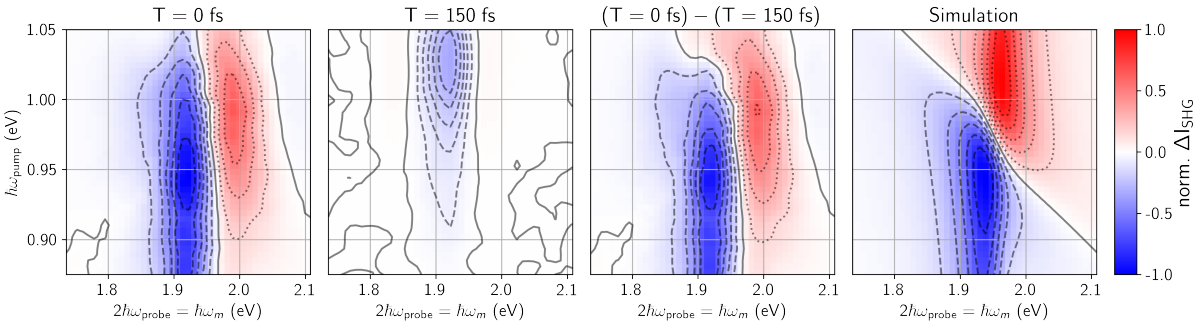

Figure 5.15: 2D frequency response of pump-SHG-probe on the WS_2 pyramid structure, and attempts to isolate the SHG OSE exchange signature. First column: $T = 0$ fs. Second column: $T = 150$ fs shows the persistent population due to pump excitation. Third column: Same as first column, but with the signals at $T = 150$ subtracted off to isolate the coherent spectrum. Fourth column: Pump-SHG-probe simulation using Equation 5.84 ($\Gamma = 40$ meV, $\hbar\omega_{ag} = 1.95$ eV).

Figure 5.15 shows our attempt to isolate the OSE effects in an SHG experiment. When the pump and probe are overlapped in time (first column), the spectra is influenced by both the coherent OSE and the incoherent absorption pathways, the latter of which can be partially isolated by introducing a delay between the pump and the probe (second column). With the pump and probe delayed, the signal shows an onset around $\hbar\omega_{\text{pump}} = 1$ eV, indicating the 2PA pathway is the

dominant absorption process. This absorption process isolated at $T = 150$ fs does not account for 2PA contributions that exchange pump and probe interactions (the 2PA analogue of the $\mathbb{D}$ contribution), which only occurs when pulses are temporally overlapped.

As a crude attempt to isolate the OSE 2D spectral response, we subtract incoherent 2PA contribution from the spectral signatures at temporal overlap (Figure 5.15, third column). The spectrum has qualitative agreement with the predictions of Equation 5.84 (fourth column). Importantly, this third column has the qualitative negative-positive cross-over behavior along the pump axis near $\omega_{\text{pump}} = \omega_{\text{probe}}$. Disagreement between the simulation and experiment can be attributed to several factors, including the imprecise nature of our OSE isolation and the unknown identity of the SHG probe resonance itself. Nonetheless, the level of agreement suggests our simple theory is a good starting point for explaining the pump-SHG-probe spectra.

5.11 Appendix: Nuances of SHG and THG probes of WS_2 pyramid

5.11.1 Probe induced Stark shifting

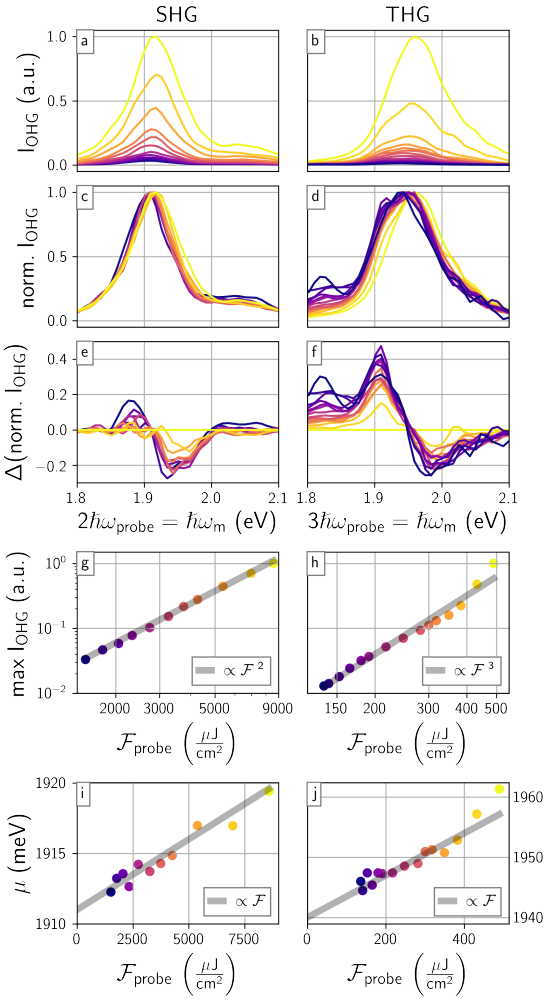

Figure 5.16: Self Stark shifting of SHG and THG probes. (a, b) SHG and THG spectra for various probe fluences. Each column has its fluence color coded to the markers in (i,j). (c, d) Same spectra as (a, b) but normalized to their maximum extent. (e, f) The difference between each spectra in (c, d) and the highest probe fluence spectrum (bright yellow line) in (c, d). (g, h) The maximum of each spectrum in (a, b) vs. probe fluence on a log-log scale. (i, j) The first moment (also known as center-of-mass or expectation value of $I_{\mathrm{XHG}}(\hbar\omega_m)$) of the spectra in (a, b) vs. probe fluence on a lin-log scale.

Figure 5.16 shows the dependence of SHG and THG on the fluence of the incident probe fundamental (no pump is used in this data). The first row shows the OHG spectrum for all fluences explored. The raw intensity of the OHG spectrum shows the steep intensity scaling of OHG. The SHG and THG signals obey the expected $\mathcal{F}^2$ and $\mathcal{F}^3$ scaling, respectively, as can be seen by plotting the peak SHG and THG signals against the applied fluence (fourth row).

Scaling the OHG spectra each to equal dynamic range (norm I_{OHG}, second row), however, reveals small changes in the spectrum. The changes can be amplified by subtracting a reference spectrum, which we take as the OHG spectrum at the highest fluence. The resulting spectra ($\Delta\,(\text{norm } I_{\mathrm{OHG}})$, third row) gives derivative line shapes corresponding to red-shifting from lower fluences (i.e. higher fluence induces a blue shift). This peak shift is indicative of the probe self-inducing the OSE. For both harmonic processes, the blueshift scales roughly linearly with fluence (fifth row).

The OSE behavior seen here has some differences with that of Figure 5 of the main text. Based on Figure 5.16, THG OSE susceptibility here ($\sim$ 10 meV per $250\frac{\mu\mathrm{J}}{\mathrm{cm}^2}$ applied field) is $\sim 5x$ stronger than that in the pump-THG-probe fluence study (Figure 5 of the paper), but a consistent definition of the shift must be used for a proper comparison; the paper adopts the definition of Equation 5.71, while here we adopt the empirical, center-of-mass defintion. A consistent definition will account for the difference in pump frequency and the different permutation symmetries (the fifth order effect here has two distinguishable fields instead of three). It should also be noted that, unlike Figure 5 of the main text, our theory predicts the line shapes of Figure 5.16e and f to be anti-symmetric. This can be shown by applying Equation 5.84 for the constraint $\omega_1 = \omega_2$ (diagonal slices of our 2D frequency space).

Figure 5.16i and j reveal important differences between the self-induced SHG OSE and the self-induced THG OSE. For one, the self-induced SHG OSE is much less ($\sim 40x$) susceptible to its incident fluence than the THG OSE is. Our model (Equation 5.84) predicts the integer of the harmonic, n, does not have a strong influence on the susceptibility, so the discrepancy cannot be explained by that. The most likely explanation is a different dipole moment between the two probes. Secondly, extrapolation of the linear OSE trend lines to negligible fluence levels shows that the native transition energies for SHG and THG are quite different (1911 meV vs. 1940 meV). This

strongly suggests SHG transitions are different from those stimulated by THG.

5.11.2 Sum-frequency processes between pump and probe

Figure 5.17 shows the existence of SFG ($\omega_{\text{out}} = \omega_{\text{probe}} + \omega_{\text{pump}}$) and TSF ($\omega_{\text{out}} = 2\omega_{\text{probe}} + \omega_{\text{pump}}$) processes which make there way past our spatial filter. In the case of the data presented in the main text, these processes are sufficiently far away from the measured output because the pump and probe electric fields are sufficiently different in frequency.

Figure 5.17 also demonstrate the presence of the pump induced Stark effect *within* the bandwidth of the probe pulse. In other words, within the frequencies present in the harmonic generation emission envelope for a single OPA setpoint, the blue frequencies see enhanced emission while the red frequencies see depressed emission upon application of the pump.

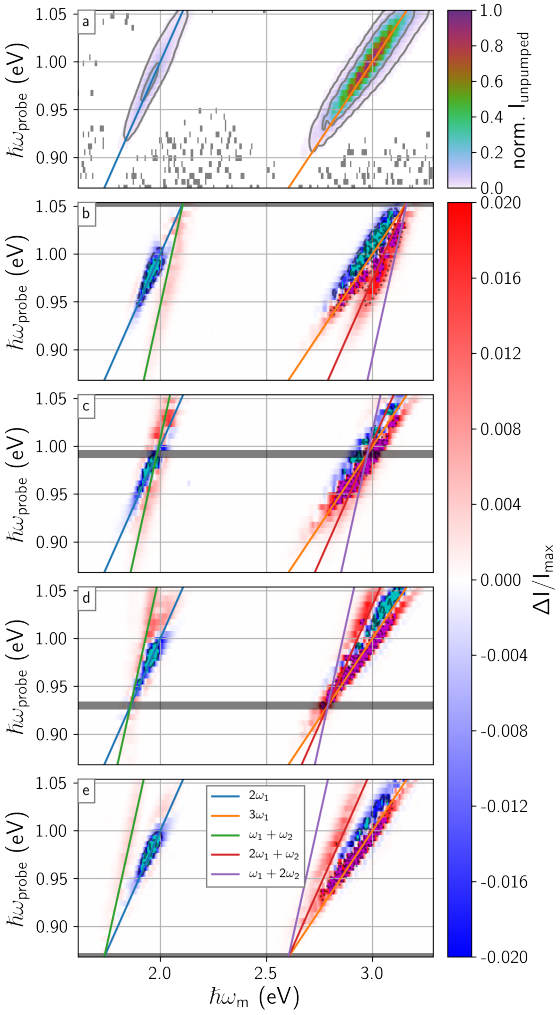

Figure 5.17: Demonstration of pump-probe sum-frequency processes. (a) Multidimensional harmonic generation from the WS_2 pyramid with no pump present. (b-e) Difference between pumped and unpumped emission. Pump frequency is indicated by thick, horizontal gray line. Colorbar is intentionally saturated to highlight small changes. Colored overlines show scaling of SHG, THG, SFG, and TSF processes (note, 1 is: probe, 2 is pump)

5.12 Appendix: Pump-THG-probe of various WS_2 morphologies

In this section we show the results of experiments in which we repeated many of the measurements shown in the main text, but with different WS_2 morphologies. Figure 5.18 shows the five samples investigated with the "pyramid" having been presented in the main text. The samples are:

- a single CVT grown WS_2 monolayer
- an ensemble of monolayer and few-layer CVT grown WS_2 triangles, 10-20 triangles fit inside the probe area of our lasers
- the screw-dislocation pyramid investigated in the main text
- a CVT grown "flower" WS_2 which exhibits a complex morphology
- a $\sim$10 nm thick polycrystalline WS_2 thin film on a fused silica substrate.

These particular samples were chosen to investigate if the measurements presented in the main text are robust to sample morphology. In general we find that the width and pitch of the dispersive, differential lineshape is heavily dependent on sample morphology (inhomogeneity). We also find that the polycrystalline thin film has a population response for all pump colors—we likely excited mid-gap or defect states via a one-photon absorption mechanism.

5.12.1 Multidimensional exploration of WS_2 morphologies

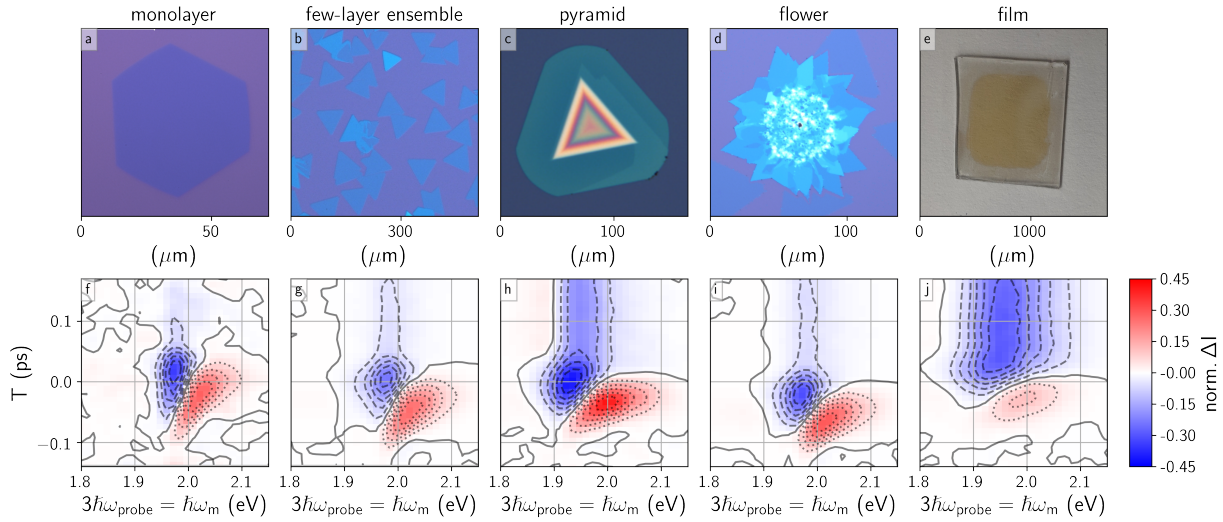

Figure 5.18: Response from different WS_2 morphologies. (a-e) Micrographs. (f-j) Time delay vs. probe frequency for each morphology with $\hbar\omega_{\text{pump}} = 0.96$ eV. Figure 5.19 shows additional data. The colormap is shared across all frames with contour lines locally normalized.

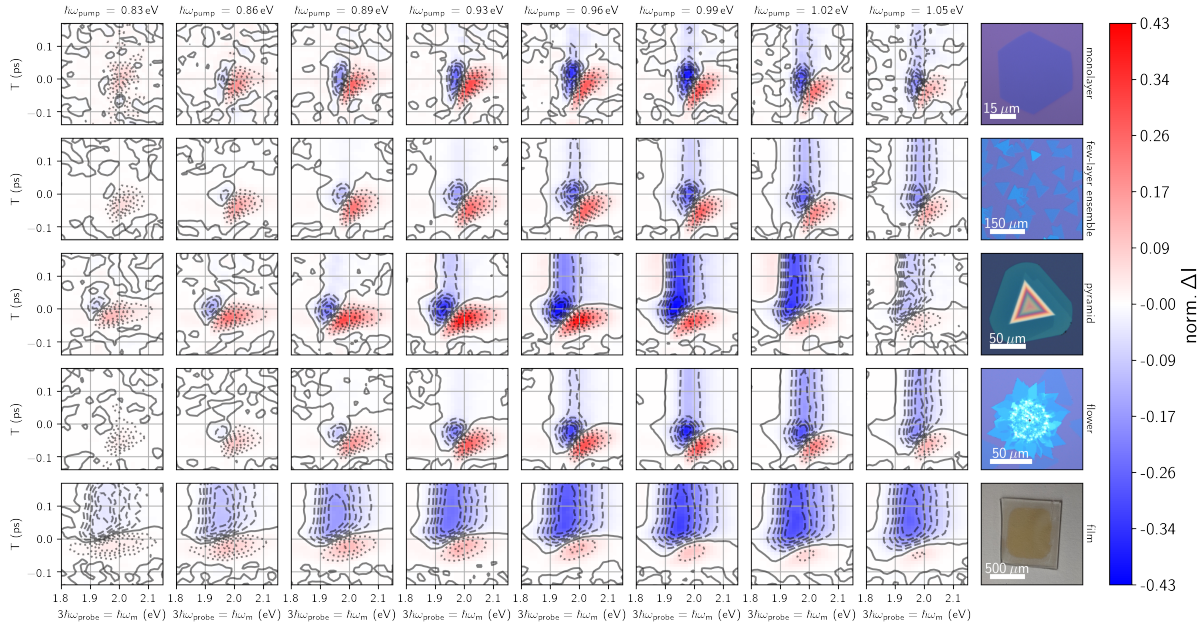

Figure 5.19: Time delay vs. probe frequency for seven pump frequencies (noted in first row subfigure titles) and five different sample morphologies. The colormap is shared across all frames with contour lines locally normalized.

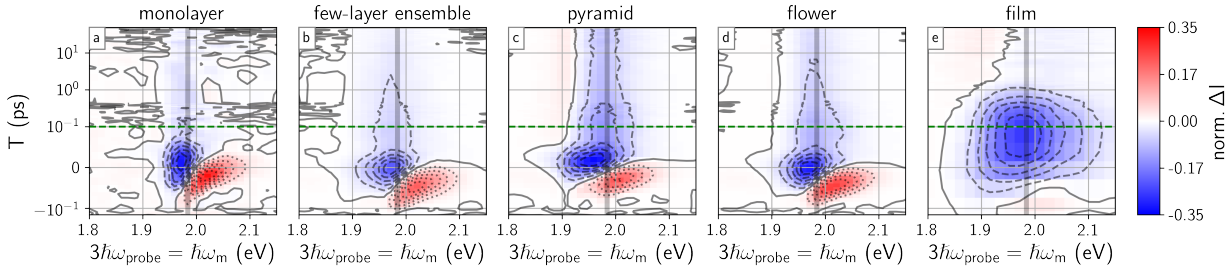

Figure 5.20: Time delay vs. probe frequency for five different sample morphologies with longer time delays than shown in Figure 5.19. The gray vertical line marks twice the pump frequency. The green, dashed line marks where the delay axis switches from linear to logarithmic scaling. The colormap is shared across all frames with contour lines locally normalized.

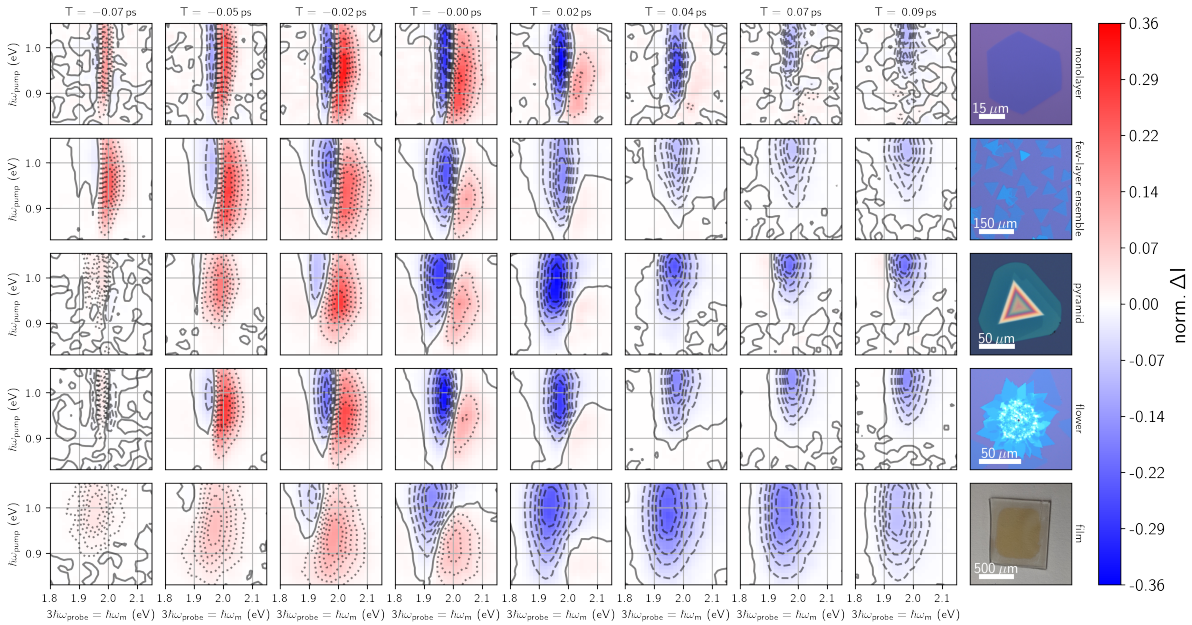

Figure 5.21: Pump frequency vs. probe frequency for eight time delays (noted in first row subfigure titles) and five different sample morphologies. The colormap is shared across all frames with contour lines locally normalized.

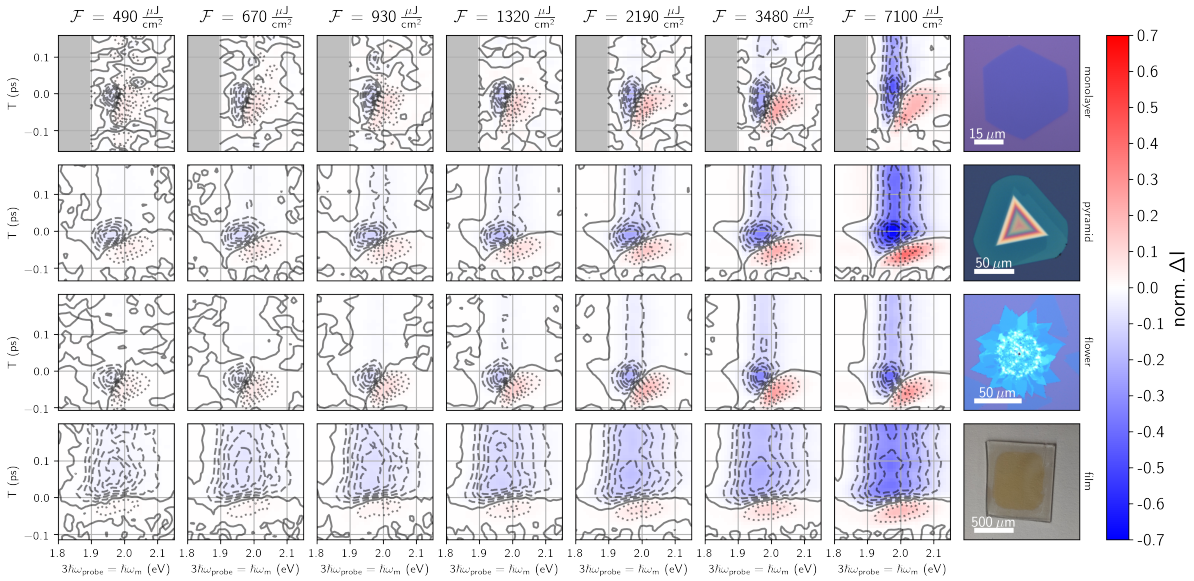

Figure 5.22: Time delay vs. probe frequency for seven pump fluences (noted in first row subfigure titles) and four different sample morphologies. In these measurments $\hbar\omega_{\text{pump}} = 0.99$ eV. The colormap is shared across all frames with contour lines locally normalized. Areas in gray and the few-layer ensemble sample were not experimentally investigated.

5.12.2 Decomposition of WS_2 morphology data

Figure 5.23 shows slices through the data presented in Figure 5.20. Figure 5.23a shows that after ∼0.1 ps, all samples other than the polycrystalline thin film exhibit uniform, gradual decay. Figure 5.23b shows that the polycrystalline thin film also has a much broader THG spectrum compared to the other samples with the monolayer having the narrowest peak.

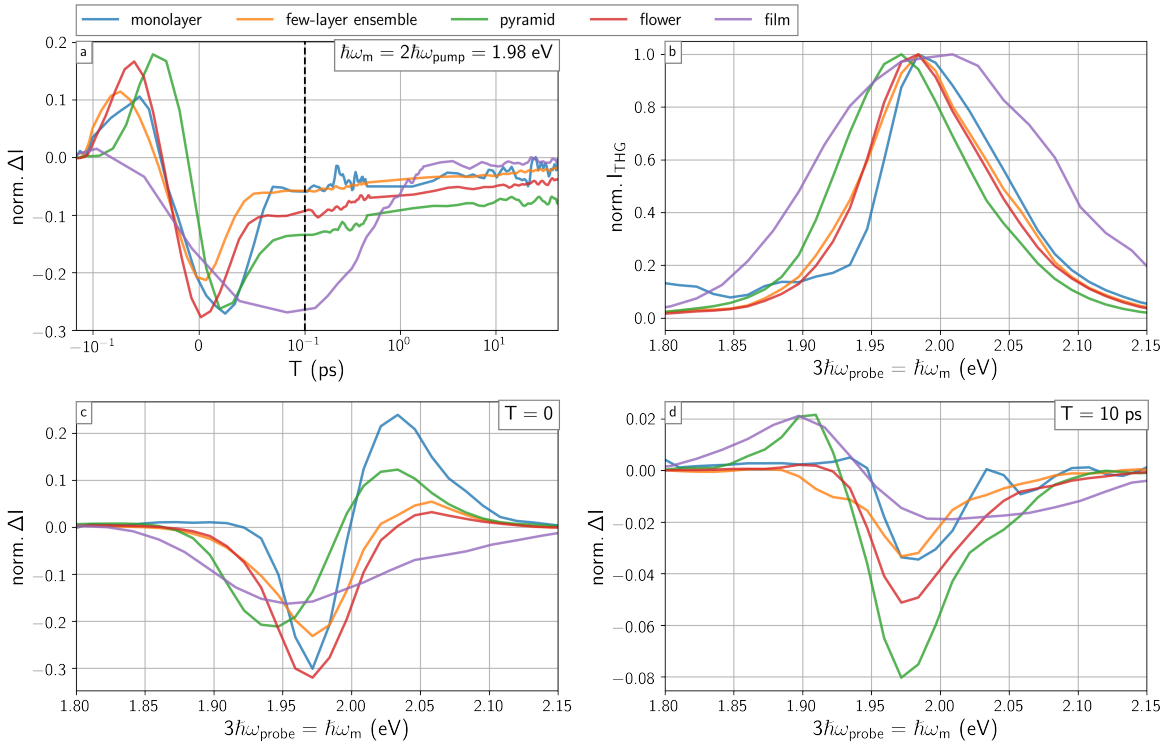

Figure 5.23: Response from different WS_2 morphologies; slices through the data shown in Figure 5.20. In (a) the black, dashed line marks where the delay axis switches from linear to logarithmic scaling.

Figure 5.24 shows a decomposition of the data originally shown in Figure 5.22. We arbitrarily define a "population metric", p as

$$\Delta I\left(\hbar\omega_m; T > 0.1 \text{ ps}, \mathcal{F}_{\text{pump}}\right) = p\left(\mathcal{F}_{\text{pump}}\right) \cdot \Delta I\left(\hbar\omega_m; T > 0.1 \text{ ps}, \mathcal{F}_{\text{pump, max}}\right), \tag{5.86}$$

and our "OSE metric" is simply the maximum extent of each 2D dataset:

$$\mathrm{OSE}\left(\mathcal{F}_{\mathrm{pump}}\right) = \max \Delta I\left(\hbar\omega_m, T; \mathcal{F}_{\mathrm{pump}}\right). \tag{5.87}$$

Except for saturation at the highest fluence, all samples display a roughly linear response for the OSE metric. This is as expected. The population response scaling is not as trivial. The polycrystalline thin film scales roughly linearly with fluence—this is to be expected if we are indeed exciting mid-gap and defect states via a single photon absorption mechanism. The monolayer response scales roughly quadratically with fluence—this is to be expected if true two-photon absorption is the excitation mechanism. The pyramid and the flower have scaling laws in-between that of the film and monolayer: $\mathcal{F}^{\sim 1.4}$.

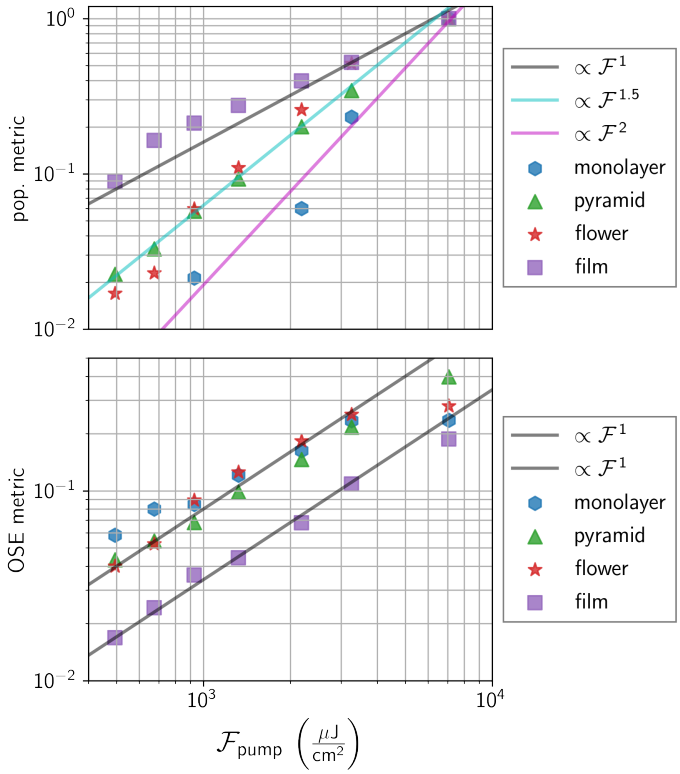

Figure 5.24: Response scaling with respect to pump fluence from different WS_2 morphologies. Metrics are defined by Equation 5.86 and Equation 5.87. Note that all scatter points at the maximum pump fluence are overlapped.

5.13 Appendix: Method comparison

Figure 5.25 shows the response from two different WS_2 samples, a screw-dislocation pyramid (Figure 5.18c) and a polycrystalline thin film (Figure 5.18e). Both a THG probe and a more-standard reflectance probe are used for the same pump colors and pump fluence. The probe beam is larger than the microstructure extent, but smaller than the extent of the thin film. A discussion on how to compare lineshapes from pump-THG-probe and pump-reflectance-probe experiments is given in ref.[123].

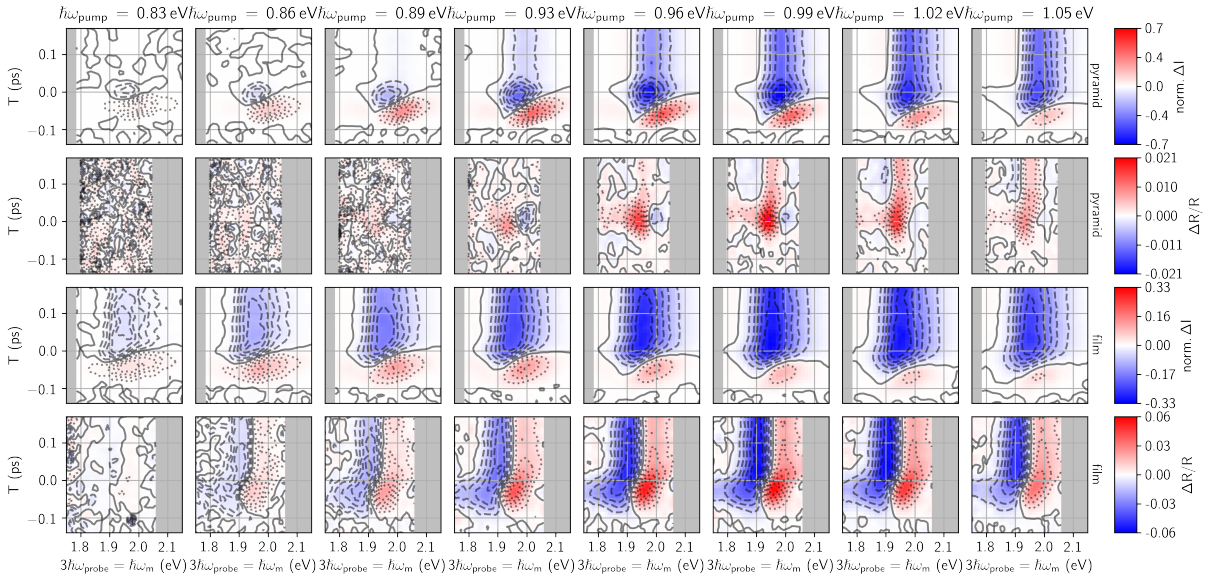

Figure 5.25: Comparison of transient-THG to transient-reflectance for a WS_2 screw-dislocation pyramid and polycrystalline thin film. First two rows show results from the same pyramid as the main text, the last two rows show results for a smooth, polycrystalline thin film. The first and third rows use a THG probe while the second and fourth rows use a single-photon reflectance probe. Given the low signal-to-noise present in the second row, we elected to use a high pump fluence in these measurements, 7000 $\mu J/cm^2$.

Chapter 6 Ultrafast, multidimensional pump-probe spectroscopy of atomically thin WS_2-MoS_2 lateral heterostructures

This Chapter borrows extensively from a manuscript to be submitted. The authors are:

1. *Darien J. Morrow*
2. *Daniel D. Kohler*
3. *Yuzhou Zhao*
4. *Jason M. Scheeler*
5. *Song Jin*
6. *John C. Wright*

6.1 Abstract

Heterostructures comprised of two-dimensional transition-metal dichalcogenides offer promise as both an exotic physics and modular electronics platform. Out-of-plane (vertical) heterostructures have been extensively characterized using ultrafast spectroscopies, however their in-plane (lateral) counterparts have not had their ultrafast dynamics and energetics characterized. In this work we use a water vapor assisted chemical vapor transport synthesis to create monolayer WS_2-MoS_2 core-shell lateral heterostructures. These heterostructures display a blue-shifted photoluminescence feature at the junction. To investigate the dynamics and energetics of the heterostructure, we use multidimensional transient-reflectance and transient second harmonic generation spectroscopies. These spectroscopies are sensitive to charge transfer across the interface and static buildup of fields. We develop an analytical lineshape model that disentangles the Fresnel interference effects, due to the stratified substrate, from the evolution of the heterostructure excitons. Our measurements of the heterostructure are largely consistent with that of isolated homostructures. Despite the supposed Type-II band alignment, our measurements find no evidence of ultrafast charge separation or coupling between the two structures. We discuss how the absence of junction signatures may be connected to unique aspects of these heterostructures, and how one may overcome these obstacles.

6.2 Introduction

Two-dimensional transition-metal dichalcogenide (TMDC) heterostructures are composed of atomically thin layers of MX_2 (M = Mo, W; X = S, Se, Te) which are direct gap semiconductors in the monolayer limit.[262, 144, 74, 6] Monolayer TMDCs exhibit strong light-matter interactions, significant electron-electron interactions, and exciton binding energies of hundreds of meV.[262, 144, 74, 6] The last decade has featured extensive work focused on creating and exploiting manually stacked van der Waals (vdW) heterostructures of dissimilar TMDCs.[7] These vdW heterostructures facilitate a vast array of exotic excitonic phenomena including exciton condensation,[263] exciton lasing,[264] and moiré excitons.[265, 266, 267, 268, 269, 270] vdW heterostrutures also display intriguing ultrafast dynamics and valley physics.[271, 272] Interlayer exciton formation and charge separation across the vdW interface have intrigued the community because the electron-hole separation happens on the femtosecond timescale and is electrically controllable.[273, 128, 274, 275] Interestingly, interlayer coupling is expected to be weak, so many different mechanisms of charge-transfer have been proposed which attempt to explain the fast transfer process.[276, 277, 278, 279, 280, 281]

It is also possible to create in-plane epitaxial heterojunctions (Figure 6.1a,b) via chemical vapor deposition (CVD) and transport (CVT) growth strategies.[282, 283, 284, 285, 286, 287, 288, 289, 290, 291, 292, 293, 8] These growth strategies offer immense electronic tunability by creating single crystal superlattices which have many atomically fine[282, 283, 284, 286, 287, 289, 290] or alloyed[285, 288] junctions. The one-dimensional, covalently bonded interface of atomically fine lateral heterojunctions offers an intriguing system for charge and energy transfer because they offer stronger intermaterial electronic coupling than vdW heterostructures.[294, 295] Indeed, flexible rectifiers and photovolatics have already been created from these in-plane heterojunctions.[296, 297] Despite this, to our knowledge, there is currently only one ultrafast study on lateral heterojunctions, which investigated exciton transfer of the type-I MoS_2-$MoSe_2$ junction.[298] This Article investigates monolayer WS_2-MoS_2 lateral heterostructures (Figure 6.1d shows an image of the sample). The bandedges at the K points of WS_2 and MoS_2 are staggered, forming a type-II heterojunction (Figure 6.1c), where electrons should flow to MoS_2 and holes should flow to WS_2.[299, 300]

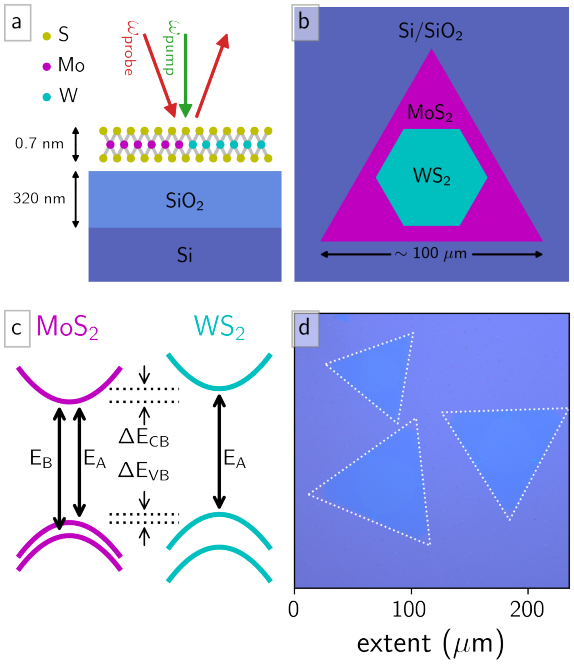

Figure 6.1: Overview of WS_2-MoS_2 lateral heterostructures. (a) Side-on sketch of single layer of WS_2-MoS_2 on SiO_2/Si substrate. Pump and probe beams for a transient reflectance experiment are shown. 0.7 nm thickness of monolayer is derived from Lee et al. [119], (b) Top-down sketch of lateral heterostructure. (c) Energy level diagrams of WS_2 and MoS_2 semiconductors.[299, 300] Free-carrier levels are not shown. (d) Optical microscope image of the three WS_2-MoS_2 lateral heterostructures simultaneously pumped and probed in the present work. For clarity, the outer edges of the heterostructures have been outlined by white, dashed lines.

In this work we use two ultrafast, optical pump-probe methods, transient-reflectance (TR) and transient second harmonic generation (TSHG), to excite and probe monolayer WS_2-MoS_2 lateral heterostructures (Figure 6.1d shows a sample image). Intriguingly, photoluminescence (PL) mapping shows bright, blue-shifted carrier recombination at the WS_2-MoS_2 junction. This junction behavior is not currently understood, but it naively suggests an intermaterial coupling which may be indicative of charge transfer occurring at the junction. Specifically, the blue-shifted PL could result from recombination of electrons originating from the WS_2 conduction band with holes originating from the MoS_2 valence band. To further investigate the junction, we extensively explore the dependence of TR and TSHG on pump frequency, probe frequency, pump-probe time delay, and pump fluence. We attempt to quantify the charge transfer dynamics across the one-dimensional junction as a function of the type and density of carriers injected by the optical pump. To do this, we developed a lineshape model to extract the excited-state response of WS_2 and MoS_2. A definitive observation of charge transfer would entail directly exciting MoS_2 (but not WS_2) and observing a modulation in the WS_2 exciton transition due to hole transfer from MoS_2's valence band to WS_2's valence band.[273] In the end, our pump-probe measurements do not detect any ultrafast charge transfer across the junction. As we discuss, the lack of charge transfer observation is likely related to the strong background signals from the homostructure areas far away from the junction. We now believe that pump-probe methods with high spatial resolution may be better for exploring these types of one-dimensional heterojunctions.

6.3 Experimental

6.3.1 Sample preparation and characterization

Monolayer WS_2-MoS_2 heterostructures were synthesized using a previously established water vapor-assisted chemical vapor transport method.[8] The reaction was conducted in a custom-built three zone tube furnace system equipped with pressure and gas flow controls. 100 mg WS_2 (Alfa Aesar) powder was placed in custom-made fused silica boat in the center of the first zone of the three-zone furnace, 100 mg MoS_2 (Alfa Aesar) powder was placed in a second fused silica boat 20 cm upstream

of WS_2, and the 300 nm SiO_2/Si substrate was placed between the second and the third zone with the polished side facing up. An alumina boat filled with approximately 1 g $CaSO_4{\cdot}2H_2O$ powder was placed on a holder at a position 35 cm upstream from the heating zone of the furnace. Heating tapes were used to heat the $CaSO_4{\cdot}2H_2O$ to provide water vapor. 100 sccm argon was used as the carrier gas, and the pressure was maintained at 800 torr to minimize the penetration of ambient moisture into the reactor.

The three-zone furnace was first preheated to 200 °C under 100 sccm argon for 30 min to drive off any moisture inside the tube. Then the second zone was heated to 1200 °C at a rate of 20 °C/min, and simultaneously the third zone was heated to 700 °C at the same rate. Once the furnace temperatures were reached, the heating tapes were used to heat up and maintain the $CaSO_4{\cdot}2H_2O$ around 110 °C for the first step WS_2 growth. After all the temperatures were stabilized, WS_2 precursor was pushed into the second zone by a magnet coupled positioner and a quartz rod to initiate the reaction. After WS_2 growth, the temperature of $CaSO_4{\cdot}2H_2O$ was lowered to ∼85 °C, then MoS_2 precursor was pushed into the second zone as WS_2 precursor was pushed out. The reaction went on for about 10 min for the first step WS_2 growth, and 10 min for the second step MoS_2 growth, after that the furnace was opened and rapidly cooled to ambient conditions. Monolayers were identified by their reflectance contrast against the substrate with an optical microscope (Olympus BX51M)—see Figure 6.1d for image. The intense photoluminescence from the individual structures (LabRAM Aramis, Confocal Raman/PL Microscope, 2.33 eV excitation) further confirms the monolayer nature of the heterostructures as well as the core-shell nature of the lateral heterostructures

6.3.2 Ultrafast measurements

Our spectrometer employs an ultrafast oscillator seeding a regenerative amplifier (Spectra-Physics Tsunami and Spitfire Pro, respectively) to produce ∼35 fs pulses centered at 1.55 eV at a 1 kHz repetition rate. The amplifier pumps two optical parametric amplifiers (OPAs, Light-Conversion TOPAS-C) which create tunable pulses of light from ∼0.75 to ∼2.1 eV with spectral width on the amplitude level of FWHM ≈ 46 meV. Absorptive filters (ThorLabs FGL1000M) and broadband wire

grid polarizers are used to isolate light of the desired color. Each arm has its own mechanical delay stage (Newport, MFA-CC), optical chopper (Thorlabs MC2000B and MC1000A), and motorized neutral density filter wheel (Thorlabs NDC-100C-4M). All pulses are focused onto the sample with a 1 m focal length spherical mirror ($\sim 2^\circ$ between beams) with the optical axis $\sim 9^\circ$ from the surface normal. The spatially coherent output (either the reflected probe or the second harmonic of the probe) is isolated with an aperture in the reflected direction, focused into a monochromator (Horiba Micro-HR) and detected with a thermoelectrically cooled photomultiplier tube (RCA C31034A). The OPA generating the probe beam and the monochromator scan their frequencies in unison to measure probe spectra. A dual-chopping routine is used to isolate the desired differential signal.[164] The color-dependent time-of-flight for each arm is corrected by offsetting the mechanical delay stages for each combination of pump and probe colors; offsets are empirically measured by non-resonant transient grating in CCl_4 for the TR experiments,[301, 61] or singly-resonant triple-sum-frequency generation in WS_2 for the TSHG experiments.[123, 68] The visible probe beam for the reflectance-probe experiments has a fluence of ~ 2 μJ/cm^2. All beams are hundreds of microns wide at the sample. Due to the size of our beams, we simultaneously interrogate all three monolayers shown in Figure 6.1d and do not individually interrogate either MoS_2 nor WS_2.All beams are s-polarized, with the exception of the TSHG pump, which is p-polarized so that pump scatter could be filtered with a polarizer setup before the monochromator input.

The TR experiments in this work were accomplished in a high-carrier fluence regime ranging from 20 to 300 μJ/cm^2. This excitation fluence regime corresponds to a range of 6.2×10^{13} to 9.3×10^{14} photons/cm^2 for 2 eV (620 nm) light. Our calculations indicate that $\sim$ 10% of incident photons are absorbed by the monolayers. Thus, our intense excitation creates carriers with density ranging from $\sim 6 \times 10^{12}$ to $\sim 1 \times 10^{14}$ carriers/cm^2. The exact carrier density will depend somewhat on the excitation color (due to a frequency dependent absorption spectrum and varying power spectrum of our OPA). At these fluences, carrier-carrier interactions should play a significant role because we are above the fluence at which biexcitons and exciton-exciton annihilation have been observed.[114, 302, 303, 304, 305, 306] However, we are likely below the carrier density where excitons are no longer bound (the Mott threshold).[175, 307] Our carrier density regime is similar to that explored by Ruppert et al. [308] on WS_2 monolayers.

All raw data, workup scripts, and simulation scripts used in the creation of this work are permissively licensed and publicly available for reuse.[309] Our acquisition[103] and workup[166] software are built on top of the open source, publicly available Scientific Python ecosystem.[57, 58, 251]

6.4 Modeling transient-reflectance spectra

Our heterostructure sample consists of a supersystem of a lateral heterostructure composed of two different monolayer materials both on the same ∼320 nm thick SiO_2 on Si substrate. This layered substrate (Figure 6.1a) lead to rich Fresnel effects in the measured reflectance spectrum.[173, 171, 172, 310, 311] It is thus imperative to model the reflectance spectrum of the stratified structure if the ultrafast changes in reflectance of the lateral heterostructure are to be understood. Due to substrate interference effects, we cannot assume (as is often done for transparent substrates like SiO_2) that changes in reflectance are merely due to changes in the absorptive component of the monolayers' refractive index.

6.4.1 Calculating the reflectance of a stratified sample

In order to understand how the heterostructure's resonances change upon photoexcition, we construct an unexcited permittivity spectrum by considering the results of Li et al. [76] and summing excitonic transitions

$$\varepsilon(\hbar\omega) = \varepsilon_{\text{back}} + \sum_j \frac{A_j}{\sqrt{\Gamma_j \pi}} \frac{1}{E_j - \hbar\omega - i\Gamma_j} \tag{6.1}$$

in which $\varepsilon_{\text{back}}$ is the structure-less background permittivity from high-lying states; A_j, Γ_j, and E_j are the amplitude, width, and center of the jth transition, respectively.[1] The complex refractive

[1] We chose a simple few-states model over excitonic models like the 2D Elliott model[312, 313, 314, 315, 316] because the binding energies of monolayer MoS_2 and WS_2 are hundreds of meV.[12, 317, 318] Therefore any continuum states and all but the lowest exciton transitions exist above the frequency range explored in our experiment. For such large binding energies and our frequency range, the Elliott model reduces to the single 1S exciton transition—a Lorentzian lineshape in our case. If necessary, inhomogeneous broadening may be accounted for with a Gaussian distribution of narrow Lorentzians around the individual excitonic features. Given the distribution of PL intensities and peak positions which we observe when mapping the sample (Figure 6.4), it is likely that our measured reflectance spectrum is significantly broadened by inhomogeneity. To minimize the number of free parameters, however, we

index is given by

$$\tilde{n}(\hbar\omega) = \sqrt{\varepsilon(\hbar\omega)}. \tag{6.2}$$

To calculate the multilayer net reflectance, R, we use a thin film interference model adapted from Anders [204] and also similarly implemented by refs.[171, 172, 173]. We assume a stratified system composed of 4 layers (air, MX_2, SiO_2, and Si) each with a complex-valued index of refraction, $\tilde{n}_m$, and thickness, d_m. For simplicity, we assume normal light incidence. The first and fourth layers—air and silicon, respectively–are of infinite extent so that the total system has three interfaces. The system is probed with light of vacuum wavelength, λ, first interacting with the 0th interface. The net multilayer reflection amplitude, r, is given by

$$r \equiv \frac{r_1 + r_2 e^{i\Delta_1} + r_3 e^{i(\Delta_1+\Delta_2)} + r_1 r_2 r_3 e^{i\Delta_2}}{1 + r_1 r_2 e^{i\Delta_1} + r_1 r_3 e^{i(\Delta_1+\Delta_2)} + r_2 r_3 e^{i\Delta_2}} \tag{6.3}$$

$$r_m \equiv \frac{\tilde{n}_{m-1} - \tilde{n}_m}{\tilde{n}_{m-1} + \tilde{n}_m} \tag{6.4}$$

$$\Delta_m \equiv \frac{4\pi \tilde{n}_m d_m}{\lambda} \tag{6.5}$$

where r_m is the reflection amplitude of the mth interface. The net reflectivity amplitude from a layered sample with different lateral components on the 1st layer (n_1) is given (in the far field) by a weighted sum of the net reflectance amplitudes of the individual components

$$r_{\text{total}} = \sum_j c_j r(n_1 = n_j). \tag{6.6}$$

In our specific case, the lateral components of the 1st layer are $j \in \{\text{air}, MoS_2, WS_2\}$. The individual c_j represent the fraction of illuminated area containing each lateral component. These c_j are estimated from the monolayers' area (Figure 6.1d) and the probe laser spot size; we set $c_{WS_2} = 0.2$, $c_{MoS_2} = 0.3$, and $c_{\text{air}} = 0.5$. The fraction of reflected light intensity, or reflectivity, is given by

$$R = |r_{\text{total}}|^2. \tag{6.7}$$

assume homogeneous lineshapes for all of our modeling.

Before considering TR spectra, it is useful to understand the consequences of our layered structure on the reflectivity. Nominal reflectivity acts as a local oscillator that interferes with the pump probe signal,[123] so understanding the reflectivity is important for understanding and simulating the transient-reflectance measurement. Refractive index values from refs.[319, 320] are used to calculate the reflectance for SiO_2 (n_2) and Si (n_3).

Figure 6.2a,b show the real and imaginary projections of the simulated complex permittivity for MoS_2 and WS_2. Figure 6.2c shows the simulated reflectivity spectra for the bare SiO_2/Si substrate (blue) and the sample containing area (with weighted c_js). The bare substrate has a large reflectivity, and its spectral behavior is dominated by a single cycle of etalon interference between the front (SiO_2) and back (Si) surfaces. The addition of the heterostructure modifies the reflectivity only slightly. Perhaps surprisingly, the monolayer *decreases* the reflectivity for most colors in our probe range. Furthermore, the excitonic resonances play a very minor role in the reflectivity spectrum, visible only as slight curvature changes to the broad, curved background created by interference within the SiO_2/Si substrate. TR measurements will therefore be heavily influenced by the substrate.

6.4.2 Calculating the transient-reflectance of a stratified sample

The TR spectra are calculated by

$$\frac{\Delta R}{R} \equiv \frac{R_{\text{pumped}} - R_{\text{unpumped}}}{R_{\text{unpumped}}}. \tag{6.8}$$

The R_{pumped} spectra are calculated by changing the A_j, Γ_j, and E_j composing each excitonic resonance and then re-evaluating Equation 6.7. Peak shifts can be attributed to a complex interplay between band gap renormalization and exciton binding energy reduction. Amplitude decreases can be attributed to Pauli blocking. Broadening can be attributed to increased carrier-carrier and carrier-phonon scattering.

A brief survey of the literature indicates that some authors explicitly account for the effects of SiO_2 and SiO_2/Si substrates on TR lineshapes,[321] while other authors mistakenly equate the two

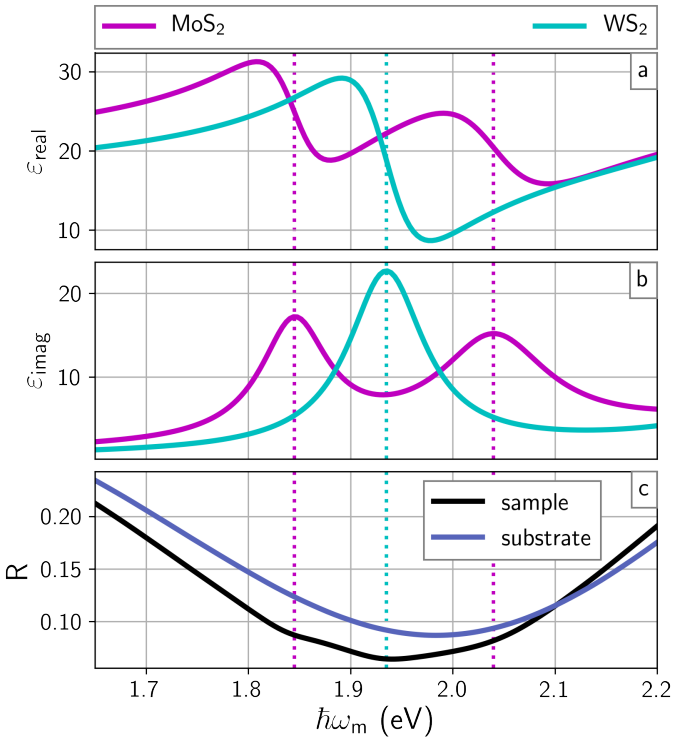

Figure 6.2: Model of permittivity and reflectance of WS_2-MoS_2 lateral heterostructure. (a) real component of permittivity for WS_2 and MoS_2. (b) imaginary (absorptive) component of the permittivity. (c) Reflectance of bare 320 nm thick SiO_2 on Si substrate and of monolayer lateral heterostructure on the same substrate. Dashed, colored, horizontal lines show the position of the lowest energy excitonic resonances.

substrate types.[322, 323] This mistake grossly changes the interpretation of pump probe signals. To highlight the importance of treating interference effects caused by stratified substrates, we show example monolayer MoS_2 TR spectra in Figure 6.3. Each column explores how a small perturbation to the excitonic resonances changes the imaginary part of the permittivity (top row), as well as how this change translates to reflectivity on different substrates (bottom row). Changes in exciton resonances can translate into a myriad of spectral shapes. The TR spectra for Si/SiO_2 substrates are completely different from that of pure SiO_2. The TR spectrum with the SiO_2 substrate is proportional to the transient-absorptance spectra ($\Delta\varepsilon_{\mathrm{imag}}$), a general relation for monolayers on thick transmissive substrates.[107, 123] The two spectra from $MoS_2/SiO_2/Si$ show almost no similarity to $\Delta\varepsilon_{\mathrm{imag}}$. Moreover the two SiO_2/Si lineshapes demonstrate a strong dependence on the precise thickness of the SiO_2 layer: peaks and troughs have their positions and relative magnitudes changed by the monolayer being on SiO_2/Si instead of SiO_2. This demonstrates the importance of accurate accounting of the substrate properties when considering TR spectra.

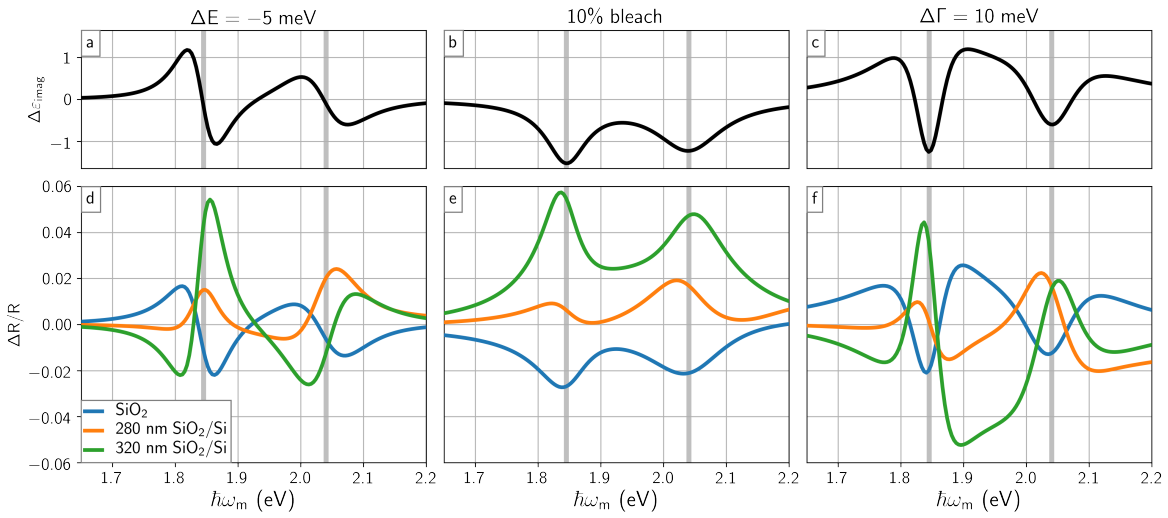

Figure 6.3: Comparison of monolayer MoS_2 TR lineshapes for different substrates. Lineshapes are calculated as described in the main text with the original dielectric and reflectance spectra shown in Figure 6.2. (a-c) $\Delta\varepsilon_{\text{imag}}$ spectra (analogous to transient-absorptance) for three different perturbations to both the A and B excitonic resonances of MoS_2 as noted in the subfigure titles. The perturbations shown in the three columns could be considered bandgap normalization, phase-space filling (Pauli blocking), and increased carrier-carrier or carrier-phonon scattering, respectively. (d-f) TR spectra for three different substrates: SiO_2 (blue), 280 nm SiO_2 on Si (orange), and 320 nm SiO_2 on Si (green). Transition energies of the original, unexcited A and B resonances are notated with vertical gray lines.

6.5 Results and Discussion

6.5.1 Photoluminescence mapping

Figure 6.4 shows confocal PL mapping of one of the three WS_2-MoS_2 lateral heterostructures examined. The spectra at each (x, y) point are fit to a weighted sum of three basis-set spectra (Figure 6.4d), Figure 6.4a-c show the amplitudes of the basis-set coefficients at each (x, y) point. This decomposition allows us to isolate PL emission contributions from MoS_2 (red), WS_2 (green), and the interface region (blue). As diagrammed in Figure 6.1b, the WS_2 core is roughly hexagonal while the MoS_2 shell forms an equilateral triangle. These shapes are determined by the growth kinetics of the individual materials.[324] Both WS_2 and MoS_2 exhibit enhanced emission at their edges. Similar edge enhancement has been previously observed and attributed to enhanced recombination at edge defects.[325, 326] Close inspection of the optical image (Figure 6.1d) of the sample shows cracks where the MoS_2 is thinnest, and comparison with Figure 6.4 shows there is a lack of PL at these crack locations.

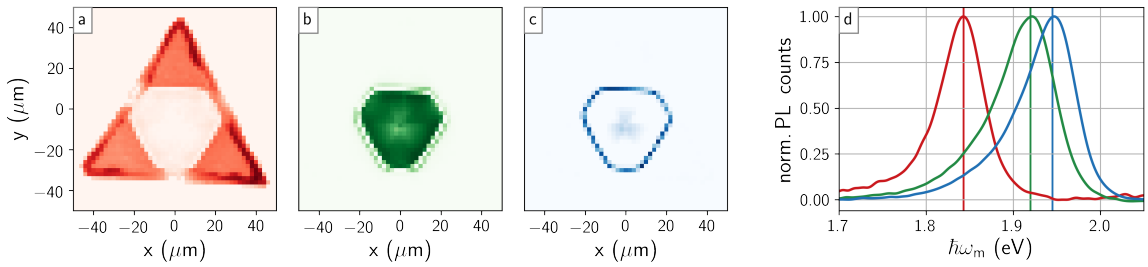

Figure 6.4: Confocal photoluminescence mapping of a single WS_2-MoS_2 lateral heterostructure excited with a 2.33 eV laser. Mapping data are decomposed via three basis spectra with slices through the 3D dataset presented in an appendix. (i, j, k) amplitudes of color-coded basis-elements shown in (l). (l) spectral basis elements used for fitting entire dataset. Colored vertical lines in (d) correspond to energies of 1.843 eV (red), 1.920 eV (green), and 1.945 eV (blue).

There is a trefoil shape imprinted within the PL map of the WS_2 core. Different regions of the WS_2 have different peak intensities and output spectra which cause the trefoil shape (see Figure 6.10 in the appendix for further representations). This trefoil shape has been previously observed and

attributed to heterogeneous defect distributions.[327]

Intriguingly, the interface between the WS_2 and MoS_2 has an unusual emission that is bluer than either WS_2 or MoS_2 emission. The resolution of our PL mapping measurement puts a $\sim$ 1 μm upper bound on the length scale of the blue emission region. The increased energy of the emission compared to the individual materials indicates that a traditional charge-transfer state is *not* present at the junction. Previously, other researchers observed interlayer low energy emission from the lowest conduction band to the highest valence band in vdW heterostructures.[328] In lateral heterostructures, the interfacial PL has been observed to be a broadened psuedo-combination of the two materials' PL,[285, 284] to be a gradual shift between the two PL peaks,[288] and in some samples to display a low energy emission.[284, 283] A high energy emission, presumably from the conduction band of WS_2 to the valence band of MoS_2 has not previously been observed in lateral TMDC heterostructures. While not well understood, this blue-shifted emission at the lateral junction evidences that noteworthy events occur at the interface between WS_2 and MoS_2. Future work should investigate this junction with increased spatial resolution (tip-enhanced PL is a natural choice given its $\sim$15 nm spatial resolution)[329] in order to determine the exact length scale in which the blue-shifted recombination occurs.

6.5.2 Multidimensional transient-reflectance

To investigate the ultrafast dynamics of WS_2-MoS_2 lateral heterostructures, we employ multidimensional TR spectroscopy. Unlike the confocal microscopy data shown in Figure 6.4 ($\sim$ 1 μm excitation/collection spot diameter), our TR spectrometer is built without a focusing objective and has a ($\sim$ 250 μm excitation/collection spot diameter). Our TR experiments simultaneously observe the WS_2 and MoS_2 response from the *three* lateral heterostructures shown in Figure 6.1d. In these TR measurements, we are attempting to observe hole transfer from MoS_2's valence band to WS_2's valence band. This will be most definitively observed by exciting the MoS_2 A exciton feature and watching for changes to the WS_2 A feature.

Figure 6.5 shows the response of the lateral heterostructures when pumped and probed with frequencies near the A and B excitonic features. Right after the A exciton of MoS_2 is excited, we

observe an increase in reflectance at the A $\left(\hbar\omega_{\mathrm{A,\ MoS_2}} = 1.845\ \mathrm{eV}\right)$ and B $\left(\hbar\omega_{\mathrm{B,\ MoS_2}} = 2.040\ \mathrm{eV}\right)$ exciton of MoS_2 and a small decrease in reflectance at the A exciton of WS_2 $\left(\hbar\omega_{\mathrm{A,\ WS_2}} = 1.935\ \mathrm{eV}\right)$. As the pump frequency is increased, the A exciton of WS_2 is excited and a corresponding increase in reflectance at the A exciton of WS_2 is observed. As the delay time increases, the differential features narrow and form a spectrum which oscillates between negative and positive changes to the reflectance. Other than at the cut-on frequency of the WS_2 A exciton, no abrupt features are observed along the pump-axis. This lack of structure along the pump axis is similar to what has been observed in transient-grating measurements on a MoS_2 thin film.[61] The signature of charge transfer that would be visible in Figure 6.5 is a change at the WS_2 A resonance when the MoS_2 A resonance is excited. We observe a decrease in reflectance at the WS_2 A energy when pumping at the MoS_2 A energy, which is our proposed signature of hole transfer. However, as evidenced by Figure 6.3, it is imperative to model the full reflectance lineshape to see if this decrease in reflectance is due to only the MoS_2 changing its spectrum or if it indeed due to hole transfer from MoS_2 to WS_2.

Comparing the response at the A exciton of WS_2 to the excitons of MoS_2 in Figure 6.5d-f indicates that WS_2 returns to equilibrium slightly faster than MoS_2. Figure 6.6 shows the same behavior for three different pump colors—WS_2's picosecond dynamics are faster than MoS_2's. The picosecond dynamics of TMDCs vary widely depending on growth method (defect density), substrate, thickness, and excitation density.[198, 304] One simple explanation for WS_2's faster decay than MoS_2 is that faster relaxation of carriers is facilitated by a higher defect density in WS_2 than MoS_2.

To understand how changes in the excitonic resonances are related to the measured TR spectra, we use the model explicated in Section 6.4. The parameter set for fitting each probe spectrum includes a peak shift, peak amplitude decrease, and peak broadening for each excitonic resonance.[308, 302, 180] Figure 6.7 shows the parameters which result from our fits. Figure 6.8 shows contour plots of the recapitulated experimental data—representative 1D spectra are shown in the appendices.

Figure 6.8 shows that our lineshape model can effectively reconstruct the experimental results. The ability to reconstruct our TR data using simple Lorentzian resonances allows us insight into the fundamental energetics and dynamics at play after photoexcitation. The MoS_2 and WS_2 A exciton

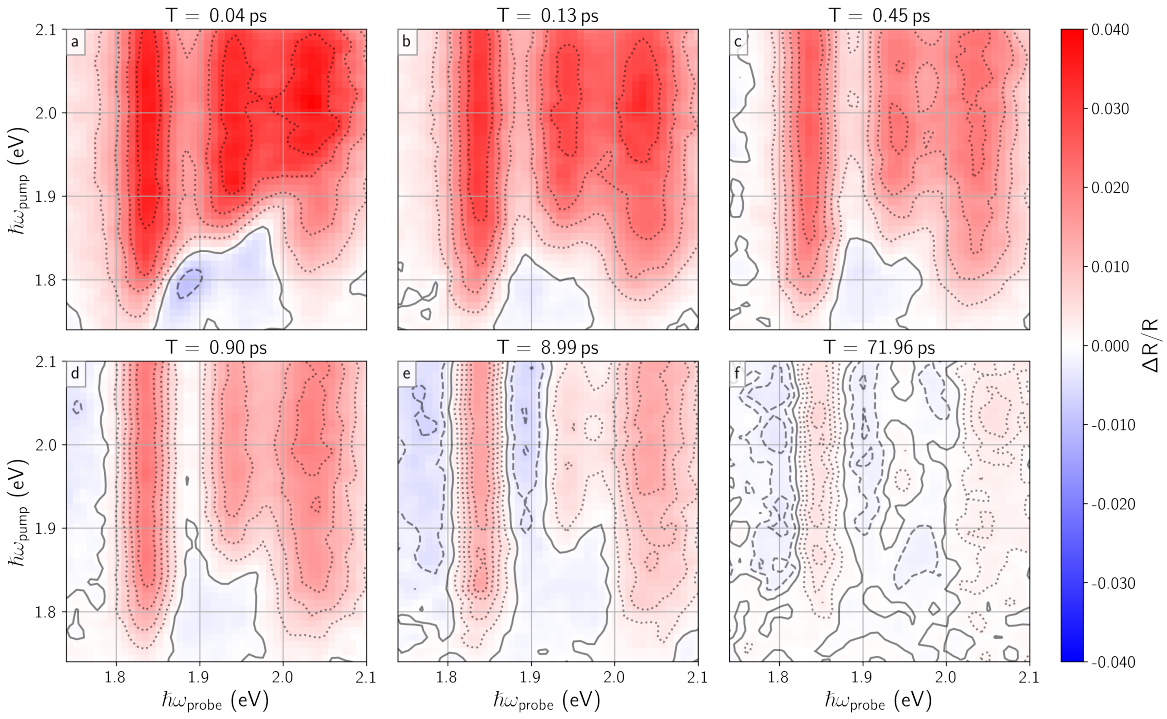

Figure 6.5: Pump frequency vs. probe frequency TR spectra of WS_2-MoS_2 lateral heterostructures with a pump fluence of $\sim 200\ \mu J/cm^2$. Time delay, T between pump and probe pulses is notated in the title of each subfigure. The colormap is shared across all subfigures with red (dotted contours) signifying $\Delta R/R > 0$, white (solid contour) signifying $\Delta R/R = 0$, and blue (dashed contours) signifying $\Delta R/R < 0$.

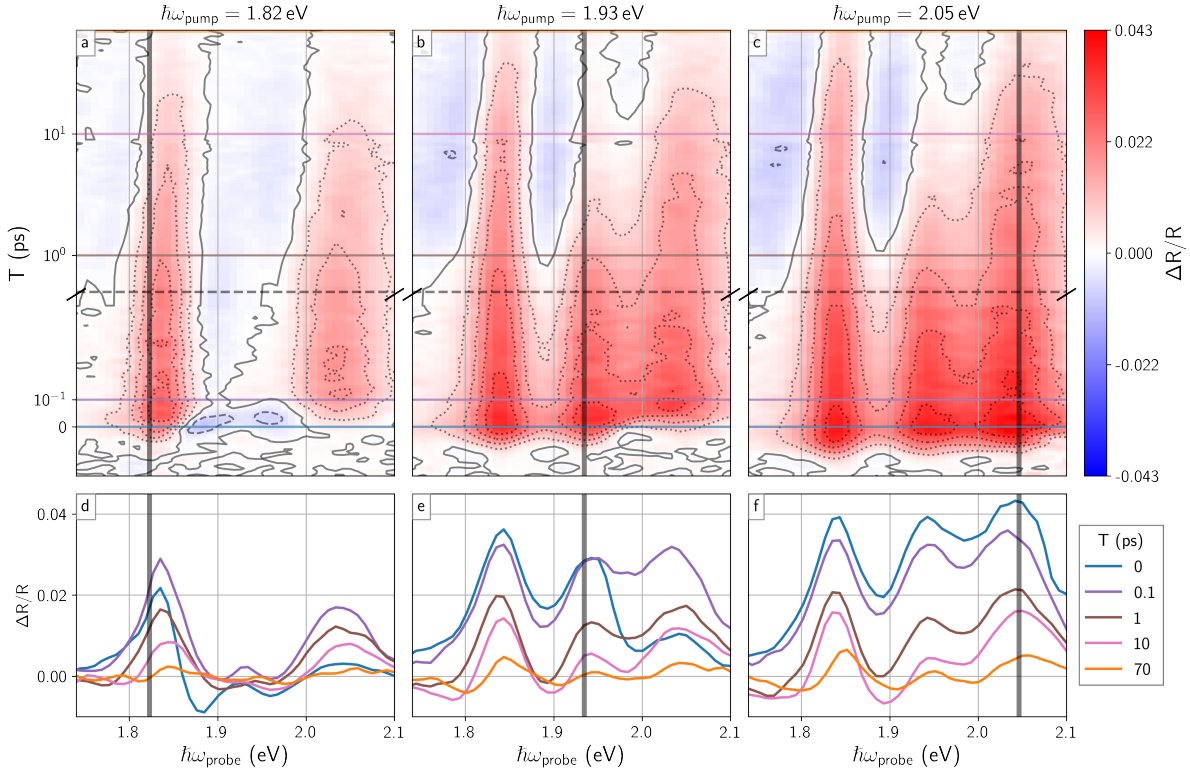

Figure 6.6: Time delay vs. probe frequency TR spectra of WS_2-MoS_2 lateral heterostructures with a pump fluence of $\sim 200\mu J/cm^2$. (a, b, c) Pump color is notated in the title of each subfigure and by gray vertical lines. The colormap is shared across all subfigures with red (dotted contours) signifying $\Delta R/R > 0$, white (solid contour) signifying $\Delta R/R = 0$, and blue (dashed contours) signifying $\Delta R/R < 0$. Delay axis (y) switches from linear to logarithmic scaling at $T = 0.5$ ps which is notated by the gray, dashed, horizontal line. (d, e, f) spectral slices at various delay times.

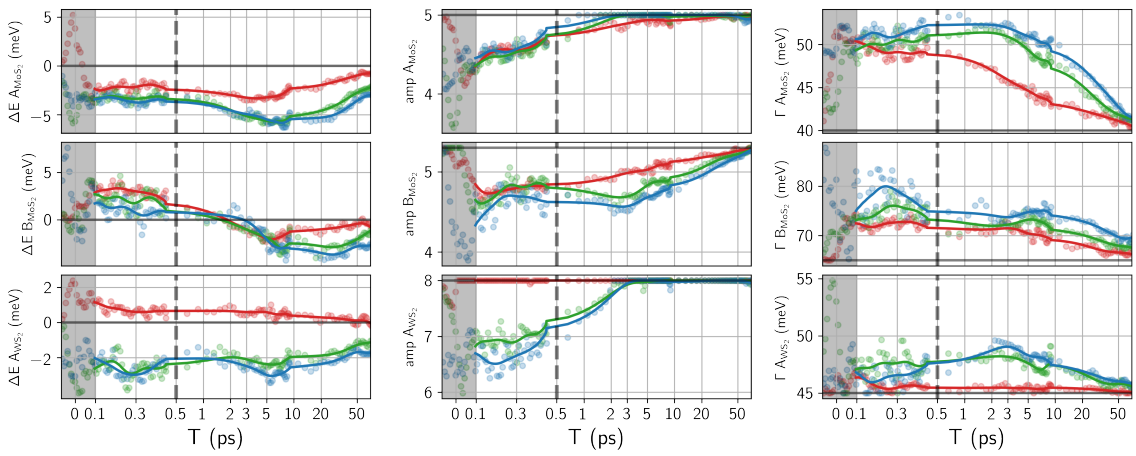

Figure 6.7: Temporal trends of nine parameter fit of Figure 6.6. Red, green, and blue markers correspond to pump frequencies of 1.82, 1.93, and 2.05 eV, respectively. The first column shows the shift in central frequency of the three excitonic resonances considered. The second column shows how these excitonic resonances decrease in transition amplitude after photoexcitation. The third column shows the broadening of the excitonic resonances after photoexcitation. Shaded gray area represents the pulse overlap region in which pump-probe-coupling effects can dominate the measured response—our model does not take these effects into account. Solid lines are representations of the parameters after Fourier smoothing with a Kaiser window. The cusps near 0.5 and 9 ps are due to data sets collected at slightly different times being concatenated together to explore the entire delay space.

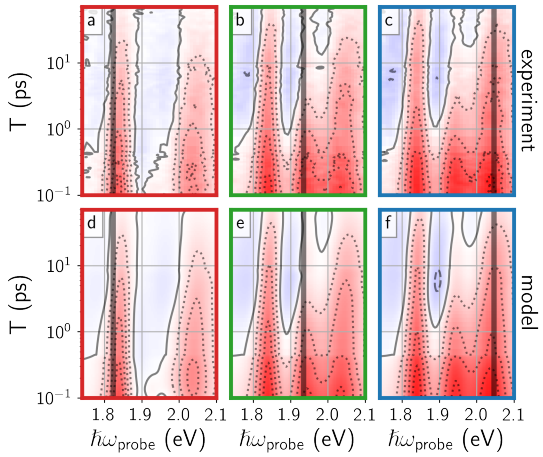

Figure 6.8: Recapitulation of data originally represented in Figure 6.6. The low-pass filtered parameters (solid lines) shown in Figure 6.7 are used to calculate the model spectrum (bottom row) for three different pump colors (notated by vertical lines).

amplitudes undergo the majority of their decay within the first 2 ps, after this the dominant remaining effects are broadening and shifting. On the same timescale that the MoS_2 and WS_2 A exciton amplitudes undergo the majority of their decay, the A and B MoS_2 excitons undergo a few meV additional redshift. The A exitons of MoS_2 and WS_2 also seem to have a build-up in their linewidth over a similar timescale. These results are in agreement with the report of Ruppert et al. [308] in which they observe non-radiative recombination and exciton-exciton annihilation on the few picosecond timescale. This recombination and annihilation results in extensive energy transfer to the TMDC lattice which must then cool over the 10-100 ps timescale. The hot lattice modifies the optical response through a temperature dependent band gap shift and enhanced carrier-phonon scattering.[308]

The evolution of the MoS_2 B resonance is different from the A exciton evolution of either material. This is because the MoS_2 B resonance parameters are likely taking into account more than just the exciton behaviors. Since the B resonance is near the MoS_2 A exciton's free-carrier bandedge, the B occupancy could artificially be accounting for changes in higher-lying states.

When the MoS_2 A exciton is directly pumped (red traces and markers), the WS_2 A exciton parameter do not show as significant modulation as for other pump conditions. Indeed, there is effectively no change in WS_2's amplitude upon excitation of the MoS_2 A exciton resonance. If there were extensive charge/energy transfer occurring, we would expect to see amplitude changes in WS_2 due to the transferred hole Pauli-blocking an excitonic excitation. We can further demonstrate this lack of charge transfer by recapitulating the data in which the MoS_2 A exciton is excited and requiring that the WS_2 A resonance remains static. The result of this fit is shown in Figure 6.9. The model (which has WS_2 not allowed to change) does an exceedingly good job at recreating the experiment after the first 100 fs. Any feature which is not captured before $\sim$100 fs is likely due to the AC Stark effect or other pump-probe electric field couplings which are not accounted for in our model.[256, 330, 259, 231, 234] Figure 6.9 demonstrates that changes in exclusively MoS_2 can account for the decrease in reflectance observed at WS_2 A exciton's center frequency after photoexcitation of MoS_2—no charge/energy transfer is needed to explain our experimental observations. This result highlights the need for careful lineshape modeling when multiple broad resonances are near each other.

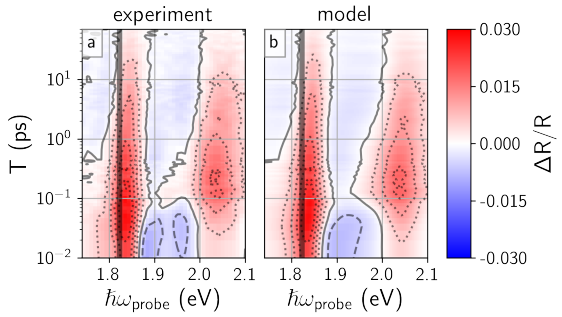

Figure 6.9: Recapitulation of data originally represented in Figure 6.6 in which the A exciton of MoS_2 is excited. The model does not include any excited state response from WS_2.

6.5.3 Transient-reflectance with varying pump fluence

Because the previous datasets were collected at such a high excitation density, it is prudent to examine the fluence dependent response of our system. The appendices have pump fluence dependent pump frequency vs. probe frequency data. The primary difference among the fluences is increased pump and probe resolution at lower fluences. For instance, at a pump fluence of 20 μJ/cm^2 the WS_2 A exciton feature is clearly resolved in both dimensions, which is not true for the pump fluence of 300 μJ/cm^2. Likewise, the appendices have delay time vs. probe frequency data with varying pump fluence. We do not observe significant changes as a function of pump fluence other than peak narrowing. We fit these data to the same model used to generate Figure 6.7. The parameters largely track those present in Figure 6.7 with increased fluence merely inducing a larger effect size.

6.5.4 Transient second harmonic generation

Because our TR measurements did not provide evidence for charge/energy transfer, we sought a technique which would have less substrate interference and enhanced sensitivity to events at the heterojunction. SHG is sensitive to charge accumulation and movement across interfaces.[331, 332, 333, 223, 334] We therefore accomplished TSHG measurements. We detail these measurements and results in the appendices. Our TSHG measure, like our TR measurements do not reveal any charge transfer.

6.5.5 Concerning a lack of observed ultrafast charge transfer

Given that our PL mapping indicates interesting junction physics, but our ultrafast measurements indicate no ultrafast charge transfer, it is imperative to understand why. Either no charge transfer is taking place, or we do not have the sensitivity to observe it. We believe the second case is likely true.

Our TR measurements indicate that excitons have an occupancy lifetime, τ, on the order of picoseconds (Figure 6.7). Measurements of the diffusion constant, D, of excitons in CVD grown WS_2 yield a values around 0.1 cm^2/s (10 nm^2/ps).[304] The diffusion length, $L_d = \sqrt{4D\tau}$, of an exciton is then ∼6 nm. Discounting local field effects, this implies that only excitons within 6 nm of either side of the junction will be able to have their constituent electrons and holes separated at the junction. If we model the WS_2 as a regular hexagon of inradius $r = 20$ μm and the MoS_2 as an equilateral triangle with edge length $a = 100$ μm then we find that the ∼6 nm on either side of the junction constitutes a belt which occupies an area of merely ∼1.6 μm^2. The whole heterostructure occupies an area of ∼4300 μm^2, so events which take place at the junction cover merely 0.04 % of the heterostructure area. This is an insignificant relative interaction region to observe changes within.[2]

In general we are unable to observe charge transfer due to dimension mismatch: a 1D junction is difficult to observe when confounded with the response from 2D base materials. This dimension mismatch is not the case for the now common vdW heterostructures which have both a 2D junction and 2D base materials. Conversely, high quality, exfoliated samples can have much longer diffusion lengths, for instance Kulig et al. [335] report $L_d = \sqrt{4D\tau} = \sqrt{4 \cdot 30 \frac{\text{nm}^2}{\text{ps}} \cdot 1100 \text{ ps}} \approx 360$ nm for monolayer, mechanically exfoliated WS_2. Thus, for high quality samples, diffusion lengths at least two orders of magnitude greater than which our sample supports can be expected. Increasing the homogeneity of the CVT grown samples considered in this work may lead to increased diffusion lengths and a greater amount of charge-transfer.

[2]The small relative interaction region is why we elected to use such high excitation densities in hopes of teasing out transfer.

6.6 Conclusion

In this work we attempted to observe charge transfer in a CVT grown WS_2-MoS_2 lateral heterostructure on a SiO_2/Si substrate using ultrafast, multidimensional TR and TSHG spectroscopies. After deconstructing the observed response into its constituent excitonic resonance modulations, we found no evidence supporting ultrafast charge transfer. When MoS_2 is photoexcited, we observe no transfer to WS_2. We believe our instrument does not have sufficient spatial resolution to isolate the heterojunction region from the homolayers. High spatial resolution ultrafast microscopes with a tunable pump may be able to isolate the junction region well enough to observe ultrafast charge transfer.[336, 337, 338, 339, 340]

6.7 Appendix: Confocal photoluminescence mapping

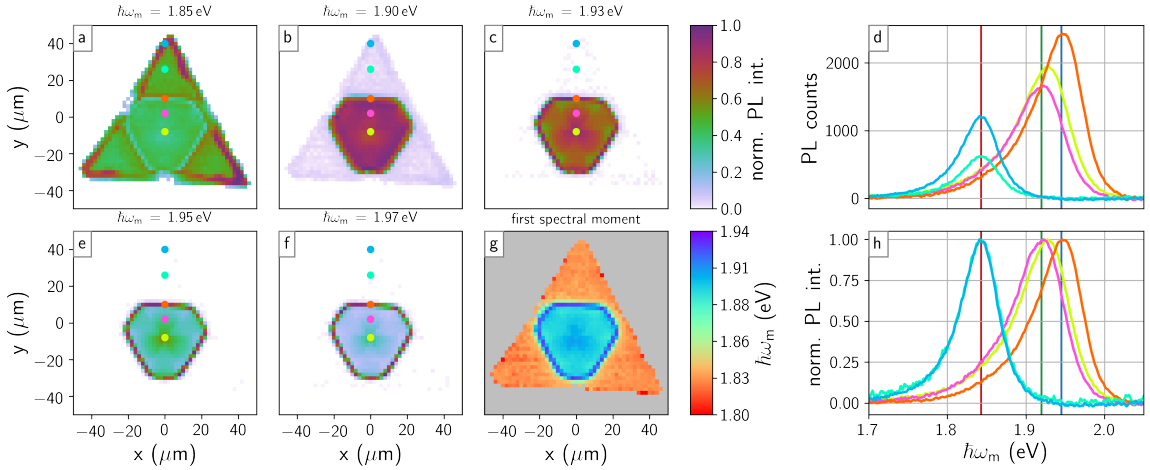

Figure 6.10: Confocal photoluminescence mapping of a single WS_2-MoS_2 lateral heterostructure excited with a 2.33 eV laser. (a, b, c, e, f) Normalized photoluminescence intensity at different emission colors (indicated in each subfigure's title). (d) Photoluminescence spectra at different spatial coordinates (color-coded to dots in (a, b, c, e, f)). (h) same data as (d) but normalized to the maximum of each spectra. These spectra highlight how MoS_2 has changes only in peak intensity (not peak position) while WS_2 has both peak position and intensity changes at different spots on the sample. (g) First spectral moment of entire dataset; gray pixels are masked due to low intensity. Colored vertical lines in (d,h) correspond to energies of 1.843 eV (red), 1.920 eV (green), and 1.945 eV (blue).

6.8 Appendix: Representative transient-reflectance slices/fits

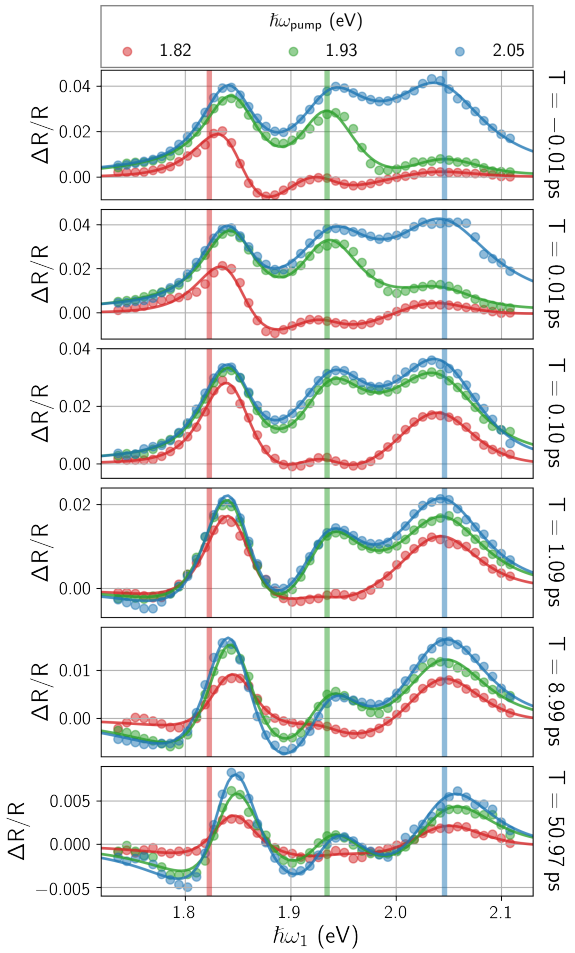

Figure 6.11: Spectra (solid lines) calculated for nine parameter fit of TR spectra at representative delay times. Red, green, and blue markers correspond to data collected at pump frequencies of 1.82, 1.93, and 2.05 eV, respectively. The fit parameters are shown in the main text.

6.9 Appendix: Pump fluence dependent transient-reflectance

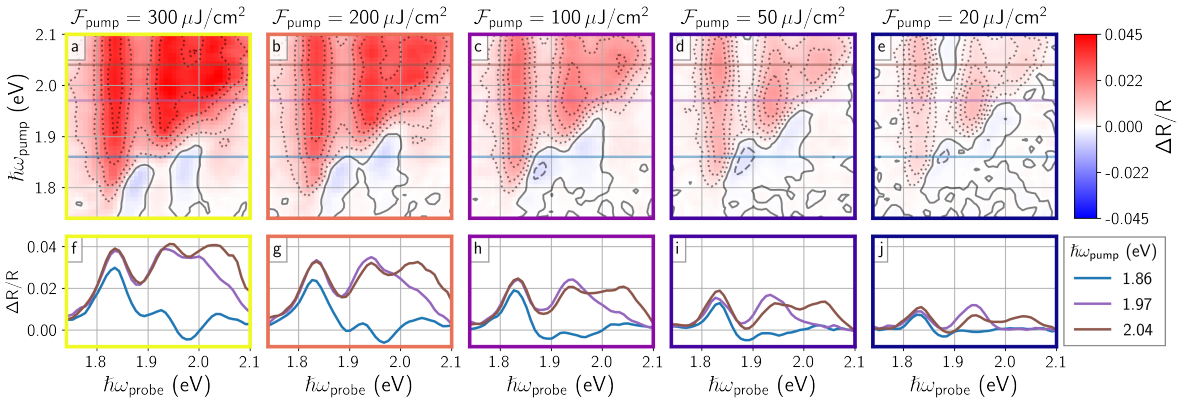

Figure 6.12: Pump frequency vs. probe frequency TR spectra of WS_2-MoS_2 lateral heterostructures at $T \approx 0$ for different pump fluences. Pump fluence is notated in the title of each subfigure. The colormap is shared across all subfigures with red (dotted contours) signifying $\Delta R/R > 0$, white (solid contour) signifying $\Delta R/R = 0$, and blue (dashed contours) signifying $\Delta R/R < 0$. $T \approx 0$. (f-j) spectral slices at various pump frequencies.

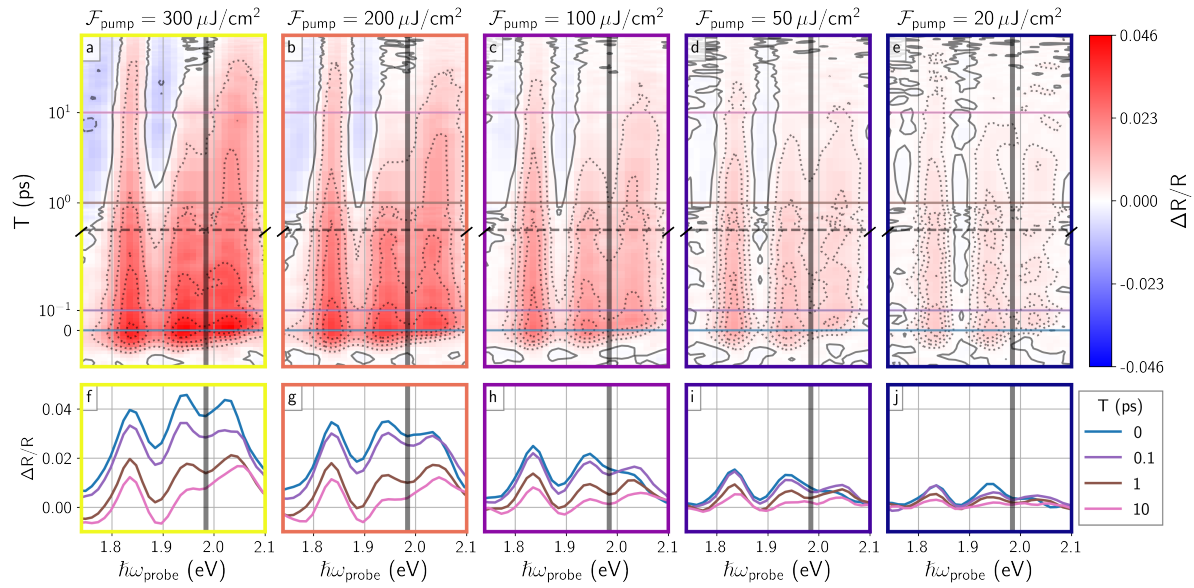

Figure 6.13: Time delay vs. probe frequency TR spectra of WS_2-MoS_2 lateral heterostructures at $\hbar\omega_{\text{pump}} = 1.98$ eV for different pump fluences. Pump fluence is notated in the title of each subfigure. The colormap is shared across all subfigures with red (dotted contours) signifying $\Delta R/R > 0$, white (solid contour) signifying $\Delta R/R = 0$, and blue (dashed contours) signifying $\Delta R/R < 0$. $T \approx 0$. Delay axis (y) switches from linear to logarithmic scaling at $T = 0.5$ ps which is notated by the gray, dashed, horizontal line. (f-j) spectral slices at various time delays.

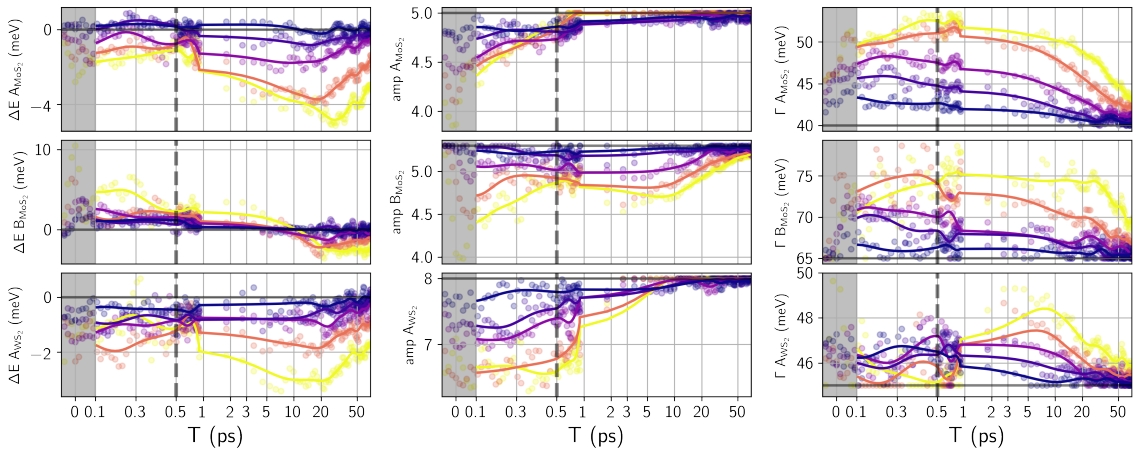

Figure 6.14: Temporal trends of nine parameter fit of Figure 6.13. The marker colors represent the pump fluence as color-coded to the spines of the subplots of Figure 6.13. The first column shows the shift in central frequency if the three excitonic resonances considered. The second column shows how these excitonic resonances decrease in transition amplitude after photoexcitation. The third column shows the broadening of the excitonic resonances after photoexcitation. Shaded gray area represents the pulse overlap region in which pump-probe-coupling effects can dominate the measured response—our model does not take these effects into account. Solid lines are representations of the parameters after being low-pass filtered through a Kaiser window. The cusps near 1 ps are due to data sets collected at slightly different times being concatenated together to explore the entire delay space.

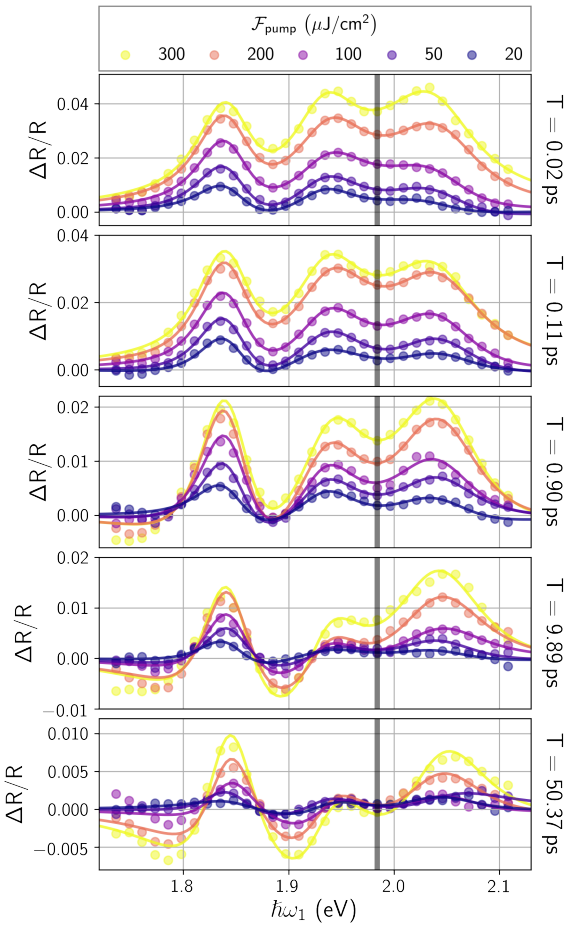

Figure 6.15: 9 parameter fit representative spectral slices of fluence dependent wigners. Data originally represented in Figure 6.13; fit parameters shown in Figure 6.14.

6.10 Appendix: Transient Second Harmonic Generation

Because our TR measurements did not provide evidence for charge/energy transfer, we sought a technique which would have less substrate interference and enhanced sensitivity to events at the heterojunction. TSHG has previously been reported as a probe of heterojunction dynamics.[331, 332, 333] Moreover, monolayer TMDCS are non-centrosymmetric and SHG active,[87, 86, 85, 341, 218, 92, 93, 115] and their SHG spectrum is enhanced when the excitation electric field has frequencies at half of the excitonic transitions' frequencies.[93, 115] So we attempted to observe charge transfer in our lateral heterojunctions using TSHG.

TSHG involves measuring how photoexcitation changes the SHG emission intensity from a sample. If charge transfer occurs at the WS_2-MoS_2 interface, a space-charge field, E_{sc}, will develop parallel to the sample surface. Past research has shown that this space-charge field which develops at a heterojunction can cause a change in the second order susceptibility

$$\chi^{(2)}_{\text{pumped}} = \chi^{(2)}_{\text{unpumped}} + \beta E^2_{sc}, \tag{6.9}$$

in which β is a complex number.[331, 332, 333] This change in susceptibility can cause a change in SHG output intensity[38]

$$I_{\text{SHG}} \propto \left|\chi^{(2)}\right|^2 I^2_{\text{probe}}. \tag{6.10}$$

Note that charge transfer can also cause a change in $\chi^{(2)}$ due to the same factors which influence $\chi^{(1)}$. Changes in linewidth, amplitude, and position of excitonic resonances will influence the transient harmonic generation spectra.[123] Figure 6.16 shows results of our TSHG measurement with our signal metric being

$$\frac{\Delta I}{I} \equiv \frac{I_{\text{SHG, pumped}} - I_{\text{SHG, unpumped}}}{I_{\text{SHG, unpumped}}}. \tag{6.11}$$

When the pump excites the MoS_2 A exciton, we observe a decrease in SHG intensity at the MoS_2

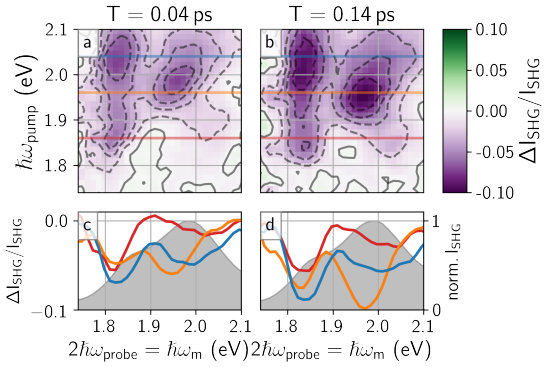

Figure 6.16: Pump frequency vs. probe frequency TSHG spectra of WS_2-MoS_2 lateral heterostructures with a pump fluence of $\sim 6\mu J/cm^2$. Time delay, T between pump and probe pulses is notated in the title of each subfigure. The probe fluence is $\sim$ 7000 $\mu J/cm^2$. Pump and probe are cross polarized. (c,d) spectral slices (left-hand y-axis) at various pump frequencies notated by horizontal lines in (a,b). Gray shaded region corresponds to the measured SHG spectrum (right-hand y-axis) of the heterostructures.

A and B exciton frequency. As the pump frequency is increased, we observe a loss of SHG intensity at the WS_2 A exciton. The loss of SHG intensity due to WS_2 being excited dwarfs the contribution from the MoS_2 B exciton. There are some changes in the maximum decrease in SHG intensity during the first 100 fs after photoexcitation (compare Figure 6.16a to Figure 6.16b). All of the features then decay away with time constants of $\sim$20 ps (data not shown). Crucially, we do not observe a change in SHG intensity at an output frequency correlated to the WS_2 A exciton when we excite the MoS_2 A exciton. In other words, upon photoexcitation of MoS_2, we do not observe a change in the WS_2 $\chi^{(2)}$ caused by a space-charge field or by changes in the excitonic resonances. We only observe changes in WS_2 $\chi^{(2)}$ when directly exciting WS_2. This lack of space-charge observation could be related to the high symmetry of the heterojunctions—an SHG electric field created at one junction could be destructively interfered with by an electric field from the junction across the heterostructure.

Chapter 7 Multidimensional Harmonic Generation Determines Halide Perovskite Crystal Symmetry: Disentangling Second Harmonic Generation from Multiphoton Photoluminescence

This Chapter borrows extensively from a work submitted for publication. The authors are:

1. *Darien J. Morrow*
2. *Matthew P. Hautzinger*
3. *David P. Lafayette II*
4. *Jason M. Scheeler*
5. *Lianna Dang*
6. *Meiying Leng*
7. *Daniel D. Kohler*
8. *Amelia M. Wheaton*
9. *Yongping Fu*
10. *Ilia A. Guzei*
11. *Jiang Tang*
12. *Song Jin*
13. *John C. Wright*

7.1 Abstract

Metal halide perovskites are an intriguing class of semiconductor materials being explored for their linear and non-linear optical, and potentially ferroelectric properties. In particular, layered two-dimensional Ruddlesden-Popper (RP) halide perovskites have shown ferroelectric properties. Optical second harmonic generation (SHG) is commonly used to screen for ferroelectric materials, however, SHG measurements of perovskites are complicated by their intense multiphoton photoluminescence (mPL) which can be mistaken for SHG signal. In this work, we introduce multidimensional harmonic generation as a method to eliminate the complications caused by mPL. By scanning and correlating both excitation and emission frequencies, we un-ambiguously assess whether a material supports SHG by examining if an emission feature scales as twice the excitation frequency. Careful multidimensional harmonic generation measurements of a series of $n = 2$ and $n = 3$ RP perovskites reveal that, contrary to previous belief, n-butylammonium (BA) RP perovskites display no SHG, thus they have inversion symmetry; but RP perovskites with phenylethylammonium (PEA) and 2-thiophenemethylammonium (TPMA) spacer cations display SHG. Multidimensional harmonic generation is also able to confirm the SHG and thus non-centrosymmetry of a recently reported ferroelectric RP perovskite even in the presence of an obscuring mPL background. This work establishes multidimensional harmonic generation as a definitive method to measure the SHG properties of materials and demonstrates that tuning organic cations can allow the design of new non-centrosymmetric or even ferroelectric RP perovskites.

7.2 Introduction

Ferroelectric materials lack inversion symmetry, exhibit an electric polarization with no applied field, and can have the direction of their polarization switched with the application of an electric field.[342, 343] Harnessing the innate crystal polarity of ferroelectric semiconductors in order to separate photoexcited electrons from their lattice holes to create a photocurrent without relying on judicious doping as in silicon solar cells is an exciting area of solar materials research.[342, 343] One such area of ferroelectric research involves metal halide perovskites, solution processable semiconductors with a wide range of optoelectronic applications including high efficiency solar cells.[344, 345, 346] There is much debate and controversy as to whether methylammonium (MA) lead iodide perovskite possesses ferroelectric domains, and it is not known if these domains contribute to the remarkable efficiency of $MAPbI_3$ solar cells.[347, 348, 349, 350, 351, 352, 353, 354, 355, 356] Two-dimensional (2D), Ruddlesden-Popper (RP) layered perovskites have emerged as an intriguing class of halide perovskites due to their quantum-well-like structure which allows for tunable optical properties and enhanced environmental stability compared to 3D lead halide perovskites,[357, 358] while still being easily processable into efficient solar cells.[359, 360]

RP perovskites have the general formula of $(RNH_3)_2(A)_{n\text{-}1}M_nX_{3n+1}$ in which RNH_3 is a long chain ammonium cation, including *n*-butylammonium (BA),[361] phenylethylammonium (PEA),[358] and 2-thiophenemethylammonium (TPMA);[362, 363] A is small, monovalent cation; M is a divalent metal cation (e.g. Pb^{2+}); X is a halide anion; and n is a positive integer. RNH_3 acts as a spatial and dielectric barrier between the inorganic layers consisting of corner-sharing $[MX_6]^{4-}$ octahedra, creating quantum wells that support large binding energy excitons with intense room-temperature PL.[364] The value of n controls the exciton binding energy and bandgap (both binding energy and bandgap decrease as n increases).[364] The identity of M, X and n largely determines the bandedge optical properties with the A and RNH_3 cations having a small influence.[365, 366] However, the size and shape of the RNH_3 spacer cation can impact the perovskite layers by templating the metal halide octahedral network's bonding.[365, 346, 367] Recently, ferroelectric layered perovskites have been reported, including the biaxial $(EA)_4Pb_3Br_{10}$ (EA = ethylammonium),[368] and diverse RP perovskites like $(BA)_2(FA)Pb_2Br_7$ (FA = formamidinium),[369] $(BA)_2CsPb_2Br_7$,[370]

$(BA)_2(EA)_2Pb_3I_{10}$,[371] and $(BZA)_2PbCl_4$ (BZA = benzylammonium).[372]

Notably, proving that a metal halide perovskite is ferroelectric can be an arduous task.[347, 348] A first step involves ensuring that a candidate material lacks inversion symmetry. Optical second harmonic generation (SHG) has commonly been employed to screen ferroelectric candidates as materials that are SHG active necessarily lack inversion symmetry.[38] Metal halide perovskites are known to efficiently support a wide variety of nonlinear optical phenomena[373] including SHG in special cases,[347, 372, 370, 368, 374, 375, 371, 367] third harmonic generation (THG),[376, 377] high-harmonic generation up to 13th harmonic,[378] and multiphoton photoluminescence (mPL).[379, 380, 381, 382] Figure 7.1a diagrams these phenomena. SHG and THG are spatially coherent processes with a directional output.[38, 84] SHG and THG are caused by an intense electric field driving a material polarization which then emits a new electric field with frequency components not found in the original field. The output frequencies and intensities of SHG and THG scale with the driving laser color, ω, and intensity, I, as

$$\omega_{\mathrm{SHG}} = 2\omega \qquad I_{\mathrm{SHG}} \propto \left|\chi^{(2)}\right|^2 I^2 \tag{7.1}$$

$$\omega_{\mathrm{THG}} = 3\omega \qquad I_{\mathrm{THG}} \propto \left|\chi^{(3)}\right|^2 I^3 \tag{7.2}$$

in which $\chi^{(m)}$ is the m^{th}-order susceptibility. Importantly, within the electric dipole approximation, if a material has inversion symmetry, then it is necessarily the case that $\chi^{(2)} = 0$.[44, 383] Thus, if a material supports SHG, the response is due either to a lack of bulk inversion symmetry, or the air-material interface which always lacks inversion symmetry. THG does not have this strict constraint and can occur in materials with inversion symmetry. These considerations imply that the presence of SHG can be a sensitive tool to probe whether a material is noncentrosymmetric.

However, as noted by Govinda et al. [384], the strong, broad mPL present in lead halide perovskites (c.f. refs.[379, 380, 381, 382]) can compete with weak SHG and lead to erroneous conclusions. In contrast to SHG and THG, mPL is caused by photons, usually with energy below the bandgap, undergoing multiphoton absorption to create hot carriers which then cool to the bandedge and isotropically fluoresce, just like carriers excited by normal, above-bandedge photon absorption.

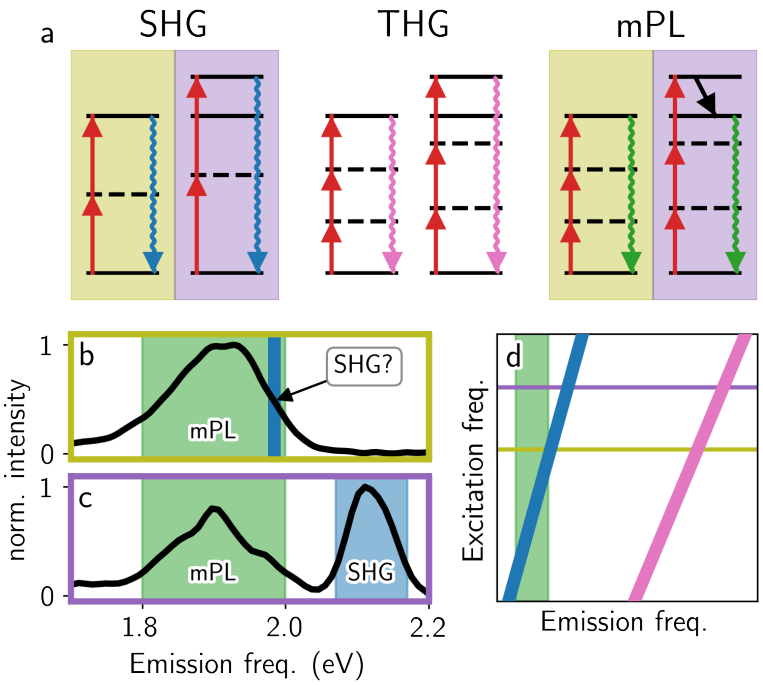

Figure 7.1: Comparison of various nonlinear optical processes, and methods to measure SHG. (a) energy level diagrams of SHG, THG, mPL. Arrows pointing up are the input laser, wavy arrows are emission, and diagonal arrows are cooling of hot carriers to a bandedge. Shadings are used to correlate the subfigures defining the different cases when the SHG and mPL have the same [yellow, see (b)] and different [lilac, see (c)] emission frequencies. (b) Measured emission spectrum from a 2D-RP perovskite when the expected SHG is within the band of mPL and no aperture is used to select against mPL—this spectrum corresponds to a conventional SHG measurement. (c) Same as (b) except the excitation laser is increased in frequency so the SHG output is moved outside the band of mPL and an aperture is used to select against mPL. (d) Diagram demonstrating how output frequency and input frequency can both be scanned to determine if a process is SHG (blue), THG (magenta), or mPL (green). Horizontal yellow and lilac lines indicate the cases shown in (b) and (c).

The output frequency and intensity of mPL will therefore be

$$\hbar\omega_{\mathrm{mPL}} \approx E_g \qquad\qquad I_{\mathrm{mPL}} \propto \chi^{(2j-1)} I^j \tag{7.3}$$

for E_g being the material's optical bandgap, j being the number of photons interacting in the multiphoton absorption process, and assuming no saturation effects or Stokes shift. Initially, we attempted to measure the SHG capabilities of a library of RP perovskites as part of a structure-property study. The broad, intense mPL from the perovskites swamped our initial (conventional) SHG measurement and obscured the weak SHG signals (see Figure 7.1b).[384]

Therefore, here we report a multidimensional harmonic generation method which relies on a tunable excitation laser, spatial filtering, and a spectrally resolved output to ensure that we can definitively determine whether a material supports SHG by correlating the excitation and emission frequencies. As illustrated in Figure 7.1d, we can confidently assess whether a material supports SHG (or THG) because SHG (THG) will have an emission frequency that scales as twice (thrice) the excitation frequency (Equation 7.1, blue line, for SHG and Equation 7.2, magenta line, for SHG), in contrast to the mPL emission frequency which is not dependent on excitation frequency (Equation 7.3, green band). In this way, mPL emission features cannot obscure the definitive assignment of SHG features regardless of the relative intensities or peak positions of mPL vs. SHG. We use this technique to conclusively determine the SHG responses of RP perovskites with different n values, spacer cations, and A-site cations, all of which have intense mPL, thus elucidating and clarifying their respective crystal symmetries.

7.3 Results and Discussion

7.3.1 2D RP Perovskites

In order to access the influence of the RNH_3 cation on the symmetry of the perovskite cage network, we synthesized millimeter-sized single crystals of the $n = 2$ and $n = 3$ variants of $(RNH_3)_2(MA)_{n\text{-}1}Pb_nI_{3n+1}$ with RNH_3 being one of BA, PEA, TPMA. Figure 7.2 shows the crys-

tal structures of our samples. Note that we have established the exact single-crystal structure of $(PEA)_2(MA)Pb_2I_7$ based on the data collected from a high quality crystal at 100 K. The synthesis details, optical micrographs (Figure 7.7), and powder X-ray diffraction patterns (Figure 7.8) confirming the phase purity of these compounds are all presented in the Appendix sections of this chapter.

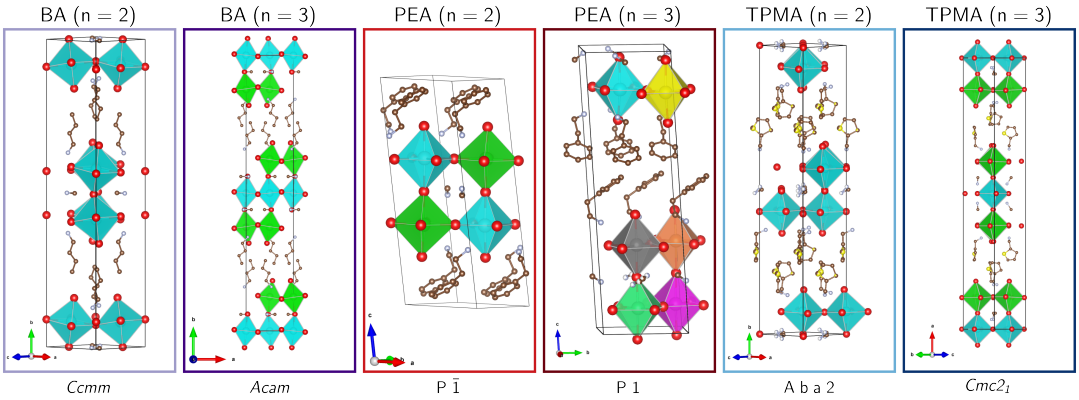

Figure 7.2: Crystal structures of the $n = 2$ and $n = 3$ $(RNH_3)_2(MA)_{n\text{-}1}Pb_nI_{3n+1}$ 2D-RP perovskites with BA,[361] PEA,[358] and TPMA[362, 363] spacer cations studied in this work. The PEA ($n = 2$) structure is a new structure reported here-in. Colored octahedra are $[PbI_6]^{4-}$, with different colors to highlight the different crystallographic sites of Pb; for instance, in BA $n = 3$, all blue are Pb1 and green are Pb2 corresponding to two different symmetry-independent crystallographic sites. The color scheme for the subfigure borders used in this figure will be used consistently throughout this work.

7.3.2 Multidimensional Harmonic Generation Measurements

To perform the multidimensional harmonic generation measurements, we use an ultrafast optical parametric amplifier (OPA) to generate tunable near-IR light. This light passes through a variable neutral density filter and is loosely focused onto the sample. We use a backscattering (reflective) geometry to collect SHG and THG in order to minimize absorption and phase-mismatch effects; this geometry only probes the first 100-200 nm of material.[31, 68] The SHG and THG are selected by an aperture, spectrally resolved with a monochromator, and detected with a photomultiplier tube. To intentionally measure PL and mPL, we remove the aperture and excite with 3.1 eV (400 nm) or

0.99 eV (1250 nm) light, respectively; note that the collection efficiency of our photoluminescence apparatus is very low compared to a traditional PL microscope because our long focal length collection mirror leads to a numerical aperture of merely ~ 0.05. Additional details about our multidimensional spectrometer are described in the appendices. Note that our methodology is similar to the shifted excitation difference technique used in the resonance and stimulated Raman community to remove fluorescence interference.[385, 386]

Our main spectroscopic results are shown in Figure 7.3, in which we measure the output intensity for six different samples as a function of both excitation OPA frequency, ω, and emission frequency, $\hbar\omega_{\mathrm{m}}$. The most consistent and prominent feature in all six spectra (right hand side) has an excitation/emission frequency dependence of $\hbar\omega_{\mathrm{m}} = 3\hbar\omega$. This feature is THG. The 2D-RP perovskites with PEA and TPMA spacer cations show a weaker but definitive feature which goes as $\hbar\omega_{\mathrm{m}} = 2\hbar\omega$. Note that this feature is SHG. Conversely, no SHG is observed for 2D-RP perovskites with BA spacer cations. Conclusive assignments of SHG and THG are not based merely on the presence or absence of an emission feature, but rather the scaling relationship of the emission features.

The width of the THG and SHG features along the $\hbar\omega_{\mathrm{m}}$ axis is determined by the frequency bandwidth of our ultrafast driving laser. When recording the data shown in Figure 7.3 we were not always able to fully reject mPL with our aperture. This mPL appears as broad features (upper left corner of each spectrum) whose emission frequency does not depend on the excitation frequency. The SHG and THG features exhibit structure which is not merely due to the non-uniform spectrum of our driving laser (Figure 7.9). Projections of the THG spectra corrected for the excitation laser power (Figure 7.10) demonstrate prominent peaks between $\hbar\omega_{\mathrm{m}} = 2.9{-}3.2$ eV—these enhancements are at significantly bluer frequencies compared to the enhancements at excitonic resonances observed by refs.[376, 377] in similar 2D-RP perovskites. Because the present work is focused on the *existence* of SHG in materials, we elect to not provide further discussion of the structure present in the SHG and THG spectra.

Furthermore, our assignments of SHG, THG, and mPL are confirmed by measuring each feature's output intensity scaling as a function of excitation laser fluence. The data presented in Figure 7.4

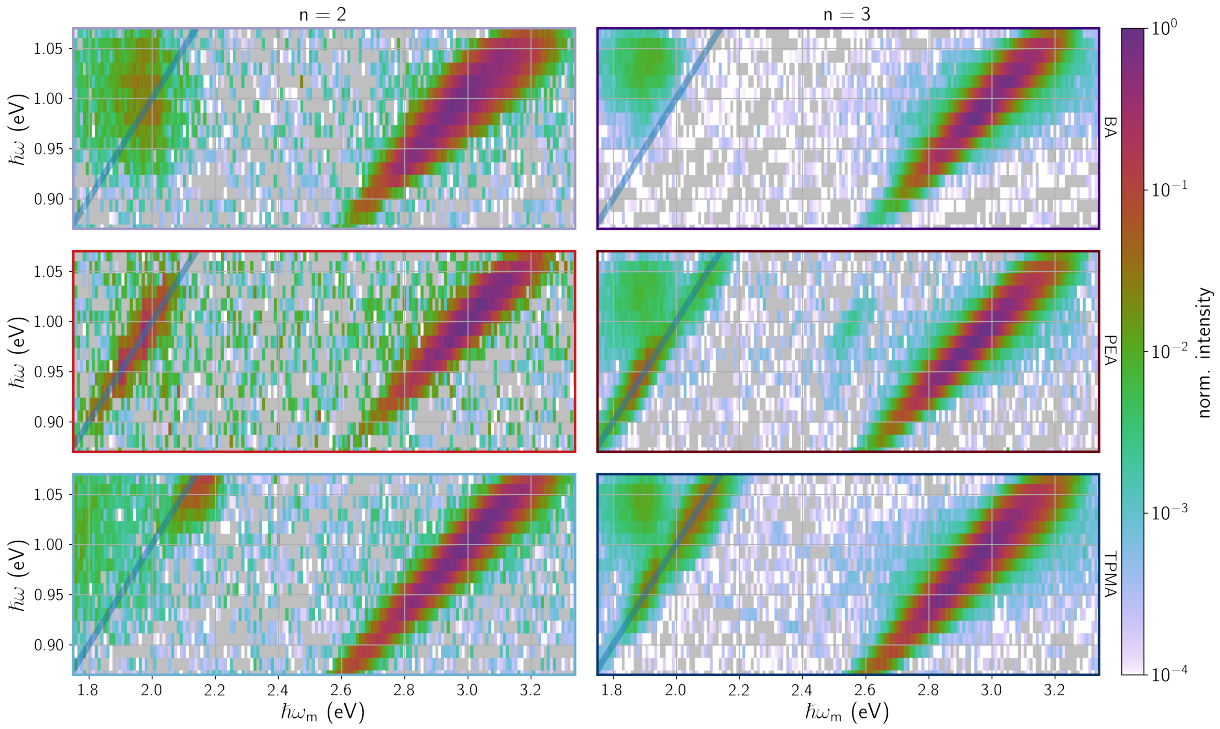

Figure 7.3: Multidimensional harmonic generation for six $(RNH_3)_2(MA)_{n\text{-}1}Pb_nI_{3n+1}$ 2D-RP perovskite samples. x-axis is monochromator setpoint (emission color), y-axis is excitation laser setpoint, and colormap (in logarithmic scale, shown on the right hand side) corresponds to measured output intensity. Columns and rows correspond to n and RNH_3 permutations, respectively. Blue overlines indicate the SHG emission frequency. The excitation laser has a smooth variation in its spectrum which is maximized at $\hbar\omega \approx 0.96$ eV with a fluence of $\sim$1400 μJ/cm^2—this variation is not corrected for in these spectra. Gray pixels indicate values which are negative and therefore unable to be represented on a logarithmic scale. These pixels characterize the noise floor of our measurement.

demonstrate the expected quadratic (Equation 7.1) and cubic (Equation 7.2) output intensity scaling for SHG and THG, respectively. Slight saturation is present at the highest fluences. The mPL feature has cubic or higher scaling which indicates that the photoluminescence is excited by a three or more photon process.

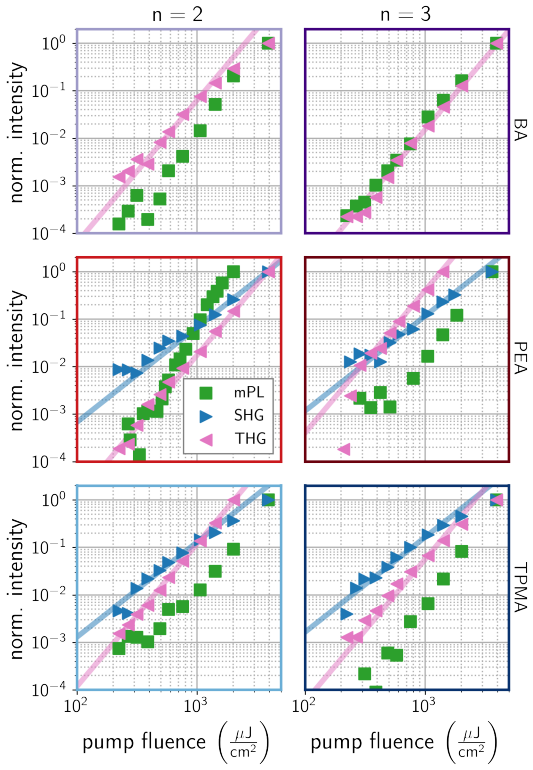

Figure 7.4: Scaling of the measured intensity as a function of pump fluence for SHG, THG, and mPL processes for various $(RNH_3)_2(MA)_{n\text{-}1}Pb_nI_{3n+1}$ 2D-RP perovskite samples. Straight lines are guides to the eye for quadratic (blue) and cubic (magenta) scaling. All measurements were performed with $\hbar\omega = 0.99$ eV except for the PEA $n = 2$, TPMA $n = 2$, and TPMA $n = 3$ SHG measurements which were performed with $\hbar\omega = 1.05$ eV. For SHG and THG, the monochromator was set to the second and third harmonics of the fundamental frequency, respectively, while for mPL the monochromator was set to the maximum of the mPL spectrum (see Figure 7.5 for spectra).

Because SHG is a second-order process, standard heuristics dictate that it will be brighter than third-order processes such as THG.[38, 387] However, the observed SHG intensity in all cases herein is at least an order of magnitude less than the THG intensity (ratios tabulated in Table 7.1 for the specific case of $\hbar\omega = 1.03$ eV). In the appendices we discuss and rule out various reasons why $I_{\text{THG}} \gg I_{\text{SHG}}$ and conclude that SHG is weaker than THG because the anharmonic potential felt

by the optically driven electrons is only weakly noncentrosymmetric.

Table 7.1: Summary of the space groups and spectroscopic characterization of the six 2D-RP perovskites. RNH_3 and n correspond to the chemical formula of $(RNH_3)_2(MA)_{n-1}Pb_nI_{3n+1}$. The peak values for photoluminescence correspond to the vertical bars shown in Figure 7.5. I_{SHG}/I_{THG} was determined from the data shown in Figure 7.3 for $\hbar\omega = 1.03$ (eV) with a fluence of ∼1400 $\mu J/cm^2$.

RNH_3	n	space group	mPL peak (eV)	PL peak (eV)	I_{SHG}/I_{THG}	SHG?
BA	2	orthorhombic *Cc*2*m* (at 293(2) K) (No. 40) Or *Ccmm*. Ref.[361]	1.98	2.12	< 0.001	no
BA	3	orthorhombic *C*2*cb* (at 293(2) K) (No. 41) Or *Acam*. Ref.[361]	1.875	2.00	< 0.001	no
PEA	2	P $\bar{1}$ (No. 2). Ref.[388] and this work	2.05	2.15	0.10	yes
PEA	3	P 1 (No. 1). Ref.[358]	1.91	1.98	0.02	yes
TPMA	2	orthorhombic A b a 2 (293 K) (No. 41). Ref.[362]	2.00	2.14	0.02	yes
TPMA	3	orthorhombic, $Cmc2_1$ (No. 36) 100 K and 296 K (no phase change). Ref.[363]	1.90	1.995	0.10	yes

7.3.3 Single- and multiphoton photoluminescence

Figure 7.5 shows the single and multiphoton excited photoluminescence spectra of each sample. The marked peak positions for each sample are summarized in Table 7.1. The PL spectra peak at ~ 1.99 eV (623 nm) and ~ 2.14 eV (579 nm) for the $n = 2$ and $n = 3$ variants, respectively. These values are similar to the ~ 2.01 eV and ~ 2.12 eV peaks previously reported for the $n = 2$ and $n = 3$ BA variants.[361] All of the mPL spectra peak positions are redshifted by ~ 0.1 eV from the PL peak positions. A similar redshift has been reported for 3D $(MA)PbI_3$ and BA 2D perovskites.[381, 382, 377] We attribute the redshift to a photon recycling effect.[381, 382] Multiphoton absorption can create excited carriers much deeper into a sample than single photon absorption. The deeper that carriers are excited in a sample, the more likely their photoluminescence will be reabsorbed to create other carriers. The Stokes-shift associated with the photoluminescence will lead to the reddest photons selectively being able to exit the sample. Notably, photon recycling may play a crucial role in the apparent long lifetimes of charge carriers in halide perovskites.[389]

7.3.4 Centrosymmetry of 2D-RP perovskites

The presence of SHG in RP perovskites made with PEA and TPMA spacer cations but not BA cations indicates that the bulky PEA and TPMA cations template different bonding in the inorganic lead iodide network. Single-crystal X-ray diffraction structures show that the TPMA $n = 2$,

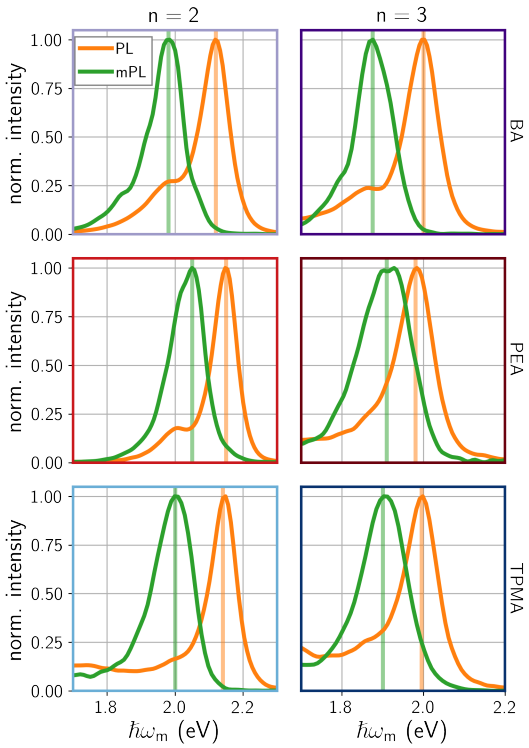

Figure 7.5: Normalized PL (3.1 eV excitation) and mPL (0.99 eV excitation) spectra for various $(RNH_3)_2(MA)_{n\text{-}1}Pb_nI_{3n+1}$ 2D-RP perovskite samples. Vertical lines correspond to approximate peak maxima and are recorded in Table 7.1.

TPMA $n = 3$, and PEA $n = 3$ 2D-RP perovskites have noncentrosymmetric space groups (see Table 7.1).[358, 362, 363] The previously reported SCXRD structure refinements of BA $n = 2$ and $n = 3$ 2D-RP perovskites showed that they could either be centrosymmetric or noncentrosymmetric space groups, but a weak SHG response, $I_{\mathrm{SHG}}/I_{\mathrm{THG}} \approx 0.01$, was measured with a single excitation color which was used as the basis to conclude that BA $n = 2$ and $n = 3$ are noncentrosymmetric.[361] Our multidimensional harmonic generation experiments did not reveal SHG in any of the BA $n = 2$ and $n = 3$ crystals we examined. We further quantify the limit of our ability to measure SHG (Figure 7.11) and find that our detection limit is three orders of magnitude lower than the limit needed to observe SHG at the previously reported SHG to THG ratio.[361] It is possible that local symmetry-breaking effects were at play which led to some weak SHG signal,[361] as noted by the authors. It is also possible that mPL photons from low energy "edge" states[390, 391] were measured and attributed to SHG. The lack of SHG in our multidimensional measurements on BA $n = 2$ and $n = 3$ crystals indicates that these crystal structures are better described as centrosymmetric in the *Ccmm* and *Acam* space groups, respectively, instead of the previously assigned space groups of *Cc2m* and *C2cb*.[361] The main difference between the centrosymmetric and non-centrosymmetric structures is whether the methylammonium cations are disordered or ordered, respectively.[361]

Based on previous SCXRD measurements, the PEA $n = 2$ structure is believed to be centrosymmetric.[388] However, this crystal structure (originally reported in 1991) was based on a partial structural model with incomplete organic cation atom positions, likely due to their high degree of disorder at the 298 K experiment temperature.[388] We therefore grew high-quality single crystals (see Figure 7.7) of the PEA $n = 2$ phase and carried out SCXRD analysis at 100 K. Our complete structural refinement yielded a centrosymmetric space group with a well-defined PEA cation disorder. A structural refinement was also attempted in a non-centrosymmetric group, however the same PEA cation disorder was observed and numerical indicators suggested a higher symmetry (centrosymmetric) space group. Since our structural refinement confirms the centrosymmetry of PEA $n = 2$, it is tempting to attribute the observed SHG from PEA $n = 2$ to surface effects or localized symmetry breaking domains. To investigate this contradiction between observing SHG and a centrosymmetric structure from SCXRD, we examined many PEA $n = 2$ crystals from different synthesis batches and observed SHG in all of them (data shown in Figure 7.12 and Figure 7.13).

Some samples displayed a greater SHG to THG ratio than others, indicating inhomogeneity among the crystals. In an attempt to mitigate local defects, we also grew PEA $n = 2$ using an alternative, slow, organic solvent based growth method.[358] The resultant crystals also supported SHG. We intentionally degraded PEA $n = 2$ crystals in a humidity chamber and observed significantly more mPL from the $n = 2$ phase and the emergence of mPL from the $n = 1$ phase that was formed upon degradation. Crucially, we did not observe a significant increase in SHG efficiency when a sample had its surface degraded. This observation suggests that surface effects are not the dominant contributor to such observed SHG.

Tentatively, PEA $n = 2$ samples display at least local noncentrosymmetry, which may be due to the disorder in the cations contributing to a noncentrosymmetric structure not observable in SCXRD measurements. The possibility of localized and spatially dependent SHG response could be investigated by future microscopy studies.[392] Other researchers have found the disordered nature of PEA $n = 1$ cations to be an important influence to breaking local degeneracy in the excitonic energy landscape of thin films.[393, 394, 395] Their observations, like ours, suggest the importance of RNH_3 cations in determining the symmetry of the electronic states of 2D-RP perovskites. Our multidimensional harmonic generation method could be extended in the future to measuring excited state symmetries (like those considered in refs.[393, 394, 395]) by the addition of an optical pump.[130, 123]

7.3.5 Harmonic generation in a ferroelectric 2D-RP perovskite

To further demonstrate the capability of multidimensional harmonic generation to discriminate against mPL, we grew a single crystal of $n = 3$ $(BA)_2(EA)_2Pb_3I_{10}$, which has recently been identified as a 2D-RP perovskite that is ferroelectric at room temperature.[371] As shown in Figure 7.6, this ferroelectric 2D-RP perovskite has intense mPL that could obfuscate a conventional SHG measurement. However, because we observe an unambiguous feature (highlighted by a blue line) whose output frequency tracks twice the input frequency, we can be assured that $(BA)_2(EA)_2Pb_3I_{10}$ is indeed SHG active, and thus non-centrosymmetric, and therefore possibly a ferroelectric material at room temperature. The confirmation that a 2D-RP perovskite with a butylammonium spacer

cation and ethylammonium A-site cation is non-centrosymmetric is especially of note because the analogous $(BA)_2(MA)_2Pb_3I_{10}$ RP perovskites with MA in the perovskite cage have been confirmed to be centrosymmetric (see results and discussion above). This observation indicates that small permutations in both the A-site and RNH_3 spacer cations can influence the inversion symmetry of the entire 2D-RP perovskite crystal structure.[367]

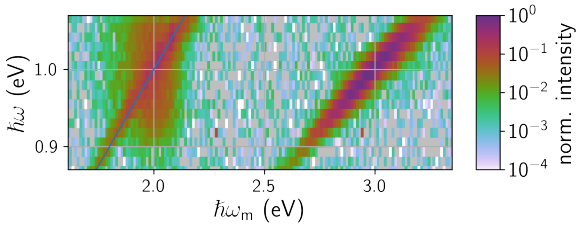

Figure 7.6: Multidimensional harmonic generation of a $(BA)_2(EA)_2Pb_3I_{10}$ single crystal. This compound is reported by Han et al. [371] to be ferroelectric at room temperature. The blue overline indicates the SHG emission frequency.

7.4 Conclusions

We have shown that multidimensional harmonic generation can be used to definitively measure and clarify the SHG and THG response of halide perovskite materials, even in the presence of a strong mPL background. By scanning and correlating both excitation and emission frequencies, we unambiguously assess whether a material supports SHG. This methodology is systematically applied to single crystals of seven 2D-RP perovskites with different spacer cations, n values, and A cations. The lack of SHG in $n = 2$ and $n = 3$ 2D-RP perovskites with BA spacer cations definitively indicates that these materials have a centrosymmetric crystal structure instead of the previously reported non-centrosymmetric structures based on inconclusive SHG measurements. Observation of SHG from $n = 2$ and $n = 3$ 2D-RP perovskites with PEA and TPMA spacer cations demonstrate that bulky, aromatic spacer cations can template the lead iodide network creating materials that lack inversion symmetry. There remains a contradiction between our SCXRD analysis that shows the $(PEA)_2(MA)Pb_2I_7$ crystal is centrosymmetric, and the observation of SHG. This contradiction

should be investigated by future microscopy studies.[392] We further showed that multidimensional harmonic generation confirms the noncentrosymmetry of the recently reported ferroelectric 2D-RP perovskite $(BA)_2(EA)_2Pb_3I_{10}$ even in the presence of bright mPL.[371] This work establishes multidimensional harmonic generation as a definitive technique to reveal the SHG properties of a material. Our results also demonstrate that subtle variations in A-site and RNH_3 spacer cations can be used to control the overall crystal symmetry of 2D-RP perovskites as strategies to engineer and design next generation ferroelectric photovoltaic materials.

7.5 Appendix: Sample preparation

7.5.1 Materials

All manipulations were conducted in air. All chemical were used without further purification and purchased from the following vendors:

- methylammonium iodide (MAI, greatcellsolar)
- phenylethylammonium iodide (PEAI, 98%, Sigma-Aldrich)
- ethylammonium iodide (EAI, Greatcellsolar)
- *n*-butylamine (99.5%, Sigma-Aldrich,)
- *n*-butylammonium iodide (BAI, Greatcellsolar)
- 2-thiophenemethylamine (96%, Sigma-Aldrich)
- lead (II) iodide (99.99%, TCI)
- lead (II) oxide (PbO, ACS reagent, >99.0%, Sigma-Aldrich)
- sodium iodide (NaI, Fisher Chemical)
- hydroiodic acid (HI) (57% w/w aqueous solution, stabilized with 1.5% hypophosphorous acid, Alfa Aesar)
- hypophosphorous acid (H_3PO_2) (50 wt. %, Sigma Aldrich)
- nitromethane (Sigma-Aldrich, ≥99.0%)
- acetone (Sigma-Aldrich, 99.8%, Extra Dry AcroSeal®)

7.5.2 Preparation of 2-thiophenemethylammonium iodide (TPMAI)

2-thiophenemethylammine (2 g) was added to 5 mL of isopropyl alcohol in a vial, and cooled to -78 °C in a dry ice and acetone bath. Slowly, 5 mL of concentrated HI was added, to yield a white powder which was collected by quickly filtering the solution before warming to room temperature over vacuum. Subsequently the powder was dried *in vacuo* at 7 mtorr overnight.

7.5.3 Growth of single crystals

To grow $(BA)_2(MA)Pb_2I_7$ single crystals, powders of PbO_2 (558 mg, 2.50 mmol) and MAI (198 mg, 1.25 mmol) were added into a vial with 3.75 mL of stabilized HI solution (57 wt % in H_2O) and 0.4 mL H_3PO_2. Subsequently, the vial was cooled to ∼0 °C and *n*-butylamine (161 μL, 1.63 mmol) was added dropwise via a micropipet. The solution was heated to 120 °C in an oil bath to completely dissolve all the solids. The vial was then slowly cooled initially to 80 °C, then room temperature over the course of 3 hours. Large single crystals of $(BA)_2(MA)Pb_2I_7$ were produced within hours.

To grow $(BA)_2(MA)_2Pb_3I_{10}$ single crystals, powders of PbO_2 (558 mg, 2.50 mmol) and MAI (265 mg, 1.67 mmol) were added into a vial with 3.75 mL of stabilized HI solution (57 wt % in H_2O) and 0.4 mL H_3PO_2. Subsequently, the vial was cooled to ∼0 °C and *n*-butylamine (107 μL, 1.08 mmol) was added dropwise via a micropipet. The solution was heated to 120 °C in an oil bath to completely dissolve all the solids. The vial was then slowly cooled initially to 80 °C, then room temperature over the course of 3 hours. Large single crystals of $(BA)_2(MA)_2Pb_3I_{10}$ were produced within hours. The growth procedure for BA RP perovskite crystals follows that reported by Paritmongkol et al. [396].

To grow $(PEA)_2(MA)Pb_2I_7$ single crystals, powders of PbO_2 (178 mg, 0.798 mmol), PEAI (50 mg, 0.20 mmol), and MAI (63 mg, 0.80 mmol) were added into a vial with 2.5 mL of stabilized HI solution (57 wt % in H_2O). The solution was heated to 120 °C in an oil bath to completely dissolve all the solids. The vial was then slowly cooled initially to 80 °C, then room temperature over the course of 3 hours. The mother liquor was allowed to sit undisturbed at room temperature

for several hours to yield flake-like single crystals.

To grow $(PEA)_2(MA)_2Pb_3I_{10}$ single crystals, powders of PbO_2 (178 mg, 0.798 mmol), PEAI (50 mg, 0.20 mmol), and MAI (84 mg, 0.53 mmol) were added into a vial with 2.5 mL of stabilized HI solution (57 wt % in H_2O). The solution was heated to 120 °C in an oil bath to completely dissolve all the solids. The vial was then slowly cooled initially to 80 °C, then room temperature over the course of 3 hours. The mother liquor was allowed to sit undisturbed at room temperature for several hours to yield flake-like single crystals. The growth procedure for PEA RP perovskite crystals in HI follows that reported by Chen et al. [397].

To grow $(TPMA)_2(MA)Pb_2I_7$ single crystals, powders of PbI_2 (369 mg, 0.800 mmol), TPMAI (48 mg, 0.38 mmol) and MAI (127 mg, 0.799 mmol) were dissolved in a vial with 2.0 mL of stabilized HI solution (57 wt % in H_2O). The solution was heated to 150 °C on a hot plate to completely dissolve all the solids. The vial was then left at room temperature. Large single crystals of $(TPMA)_2(MA)Pb_2I_7$ were produced within a few days.

To grow $(TPMA)_2(MA)_2Pb_3I_{10}$ single crystals, powders of PbI_2 (369 mg, 0.800 mmol), TPMAI (48 mg, 0.38 mmol) and MAI (223 mg, 1.40 mmol) were dissolved in a vial with 2.0 mL of stabilized HI solution (57 wt % in H_2O). The solution was heated to 150 °C on a hot plate to completely dissolve all the solids. The vial was then left at room temperature until cool, followed by storage in a 2 °C refrigerator. Large single crystals of $(TPMA)_2(MA)_2Pb_3I_{10}$ were produced within a few days.

To grow $(PEA)_2(MA)Pb_2I_7$ single crystals from an organic solvent, powders of PbI_2 (100 mg, 0.217 mmol), PEAI (54 mg, 2.2 mmol), MAI (17 mg, 1.1 mmol), and NaI (65 mg, 0.4336 mmol) were dissolved in 100 mL acetone and 50 mL of nitromethane by sonicating in a beaker. The yellow solution was then transferred into 16 x 100 mm test tubes (∼6 mL per tube), and left to evaporate for a week. Large, rectangular crystals grew in one week. This growth procedure for $(PEA)_2(MA)Pb_2I_7$ crystals from an organic solvent follows that reported by Smith et al. [358].

To grow $(BA)_2(EA)_2Pb_3I_{10}$ single crystals, powders of PbI_2 (1380 mg, 3.00 mmol), EAI (346 mg, 2.00 mmol), and BAI (175 mg, 0.870 mmol) were added into a vial with 4.5 mL of stabilized HI

solution (57 wt% in H_2O) and 0.5 mL of H_3PO_2. The solution was heated to 120 °C on a hot plate to completely dissolve all the solids. The solution was kept on a hot plate until ∼1/3 of the solution had evaporated, followed by a cool down to room temperature. Within 3 hours during the cooling process, large crystals precipitated from solution. This growth procedure follows that reported by Fu et al. [398].

7.5.4 Humidity treatment

Crystals of $(PEA)_2(MA)Pb_2I_7$ grown from HI were placed in a sealed container with a saturated solution of ammonium nitrate in DI water at the bottom. The lab temperature is between 20-25 °C providing conditions for relative humidity in the range of 64-67%. The crystals were only removed for periodic SHG measurements and imaging, then returned to the humidity chamber and resealed.

7.5.5 Appendix: Optical micrographs of RP perovskite crystals

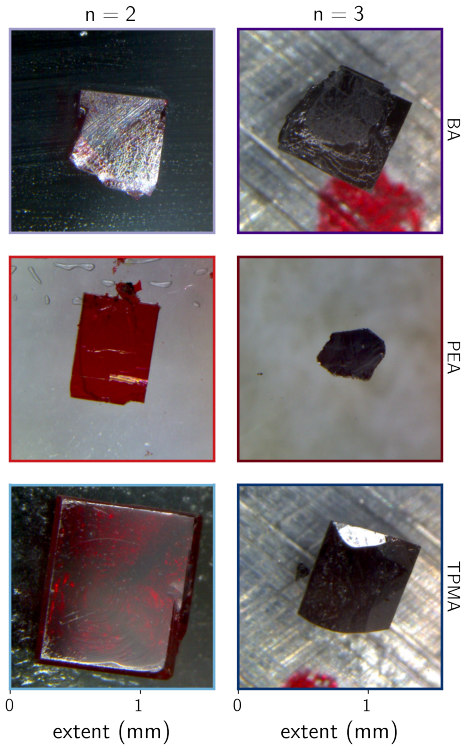

Figure 7.7: Optical micrographs of the six RP perovskite samples primarily explored in this work.

7.6 Appendix: Powder X-ray diffraction

PXRD patterns were collected on as-prepared samples on silicon wafer substrates using a Bruker D8 Advance Powder X-ray Diffractometer with Cu K_α radiation.

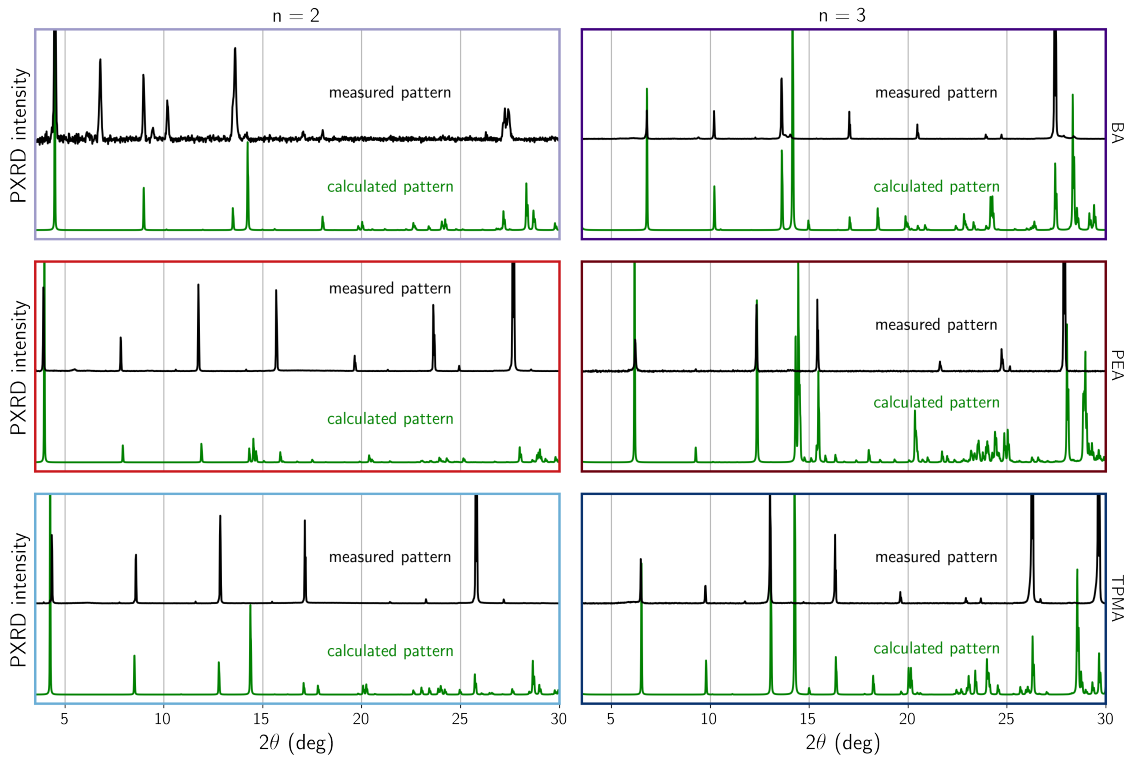

Figure 7.8: Experimental and calculated powder X-ray diffraction patterns for the six samples primarily explored in this work. The single scrystal structures used for the calculated patterns are taken from Stoumpos et al. [361] for BA $n = 2$ and $n = 3$, the present work's SCXRD analysis for PEA $n = 2$ (see next section), Smith et al. [358] for PEA $n = 3$, Zhu et al. [362] for TPMA $n = 2$, and Lai et al. [363] for TPMA $n = 3$.

7.7 Appendix: Single crystal X-ray diffraction of $(PEA)_2(MA)Pb_2I_7$

A red crystal with approximate dimensions of 0.03 x 0.02 x 0.005 mm^3 was selected under oil under ambient conditions and attached to the tip of a MiTeGen MicroMount©. The crystal was mounted in a stream of cold nitrogen at 100(1) K and centered in the X-ray beam by using a video camera.

The crystal evaluation and data collection were performed on a Bruker Quazar SMART APEXII diffractometer with Mo K_α (λ = 0.71073Å) radiation and the diffractometer to crystal distance of 4.96 cm.[399] The initial cell constants were obtained from three series of ω scans at different starting angles. Each series consisted of 12 frames collected at intervals of 0.5° in a 6° range about ω with an exposure time of 30 seconds per frame. The reflections were successfully indexed by an automated indexing routine built into the APEXII program suite. The final cell constants were calculated from a set of 3528 strong reflections from the actual data collection.

The data were collected by using a full sphere data collection routine to survey reciprocal space to the extent of a full sphere to a resolution of 0.68 Å. A total of 35179 data were harvested by collecting 4 sets of frames with 0.6° scans in ω and φ with exposure times of 90 sec per frame. These highly redundant datasets were corrected for Lorentz and polarization effects. The absorption correction was based on fitting a function to the empirical transmission surface as sampled by multiple equivalent measurements.[400]

The diffraction data were consistent with the space groups $P\bar{1}$ and $P1$. The E-statistics strongly suggested the centrosymmetric space group $P\bar{1}$ which yielded chemically reasonable and computationally stable results of refinement.[401, 402, 403, 404, 405, 406] A successful solution by direct methods provided most non-hydrogen atoms from the E-map. The remaining non-hydrogen atoms were located in an alternating series of least-squares cycles and difference Fourier maps. All non-hydrogen atoms (unless specified otherwise) were refined with anisotropic displacement coefficients. All hydrogen atoms were included in the structure factor calculation at idealized positions and were allowed to ride on the neighboring atoms with relative isotropic displacement coefficients.

The structure composition is $[C_6H_5CH_2CH_2NH_3]_2[CH_3NH_3][Pb_2I_7]$. The anions form two-dimensional

networks stacked in the [001] direction, with $[CH_3NH_3]^+$ cations in the perovskite cage and $[C_6H_5CH_2CH_2NH_3]^+$ cations between the layers. Atoms I2, I3, I4, and I5 exhibit positional disorder as a result of rotation of those atoms about the I1–Pb1 bond by an average of 25.8(4)°. The major disorder component has an occupancy of 87.54(9)%. These disordered iodide atoms were refined with atomic displacement parameter constraints. The $[C_6H_5CH_2CH_2NH_3]^+$ cations were each equally disordered across two positions. The non-hydrogen atoms of these cations were refined isotropically with geometric and atomic displacement parameter constraints and restraints.[407] The $[CH_3NH_3]^+$ cation was also equally disordered over two positions. The non-hydrogen atoms of this cation were refined isotropically with restraints and atomic displacement parameter constraints.

The final least-squares refinement of 163 parameters against 11201 data resulted in residuals R (based on F^2 for $I \geq 2\sigma$) and wR (based on F^2 for all data) of 0.0644 and 0.1411, respectively. The final difference Fourier map contains several peaks of residual electron density (ca. 2.9 $e^-/Å^3$) in the structure. These peaks are in chemically unreasonable positions and were considered noise.

The Crystallographic Information File (CIF) associated with this SCXRD analysis is available via the CCDC at www.ccdc.cam.ac.uk/data_request/cif with accession code 1978042.

Table 7.2: Complete crystal data and structure refinement of $(PEA)_2(MA)Pb_2I_7$ at 100 K.

Compound name	$(PEA)_2(MA)Pb_2I_7$
Empirical formula	$(C_6H_5(CH_2)_2NH_3)_2(CH_3NH_3)Pb_2I_7$
Formula weight	1579.12
Crystal system	triclinic
Space group	$P\bar{1}$ (no. 2)
a/Å; $\alpha/^\circ$	8.722(3); 97.604(16)
b/Å; $\beta/^\circ$	8.726(3); 93.482(11)
c/Å; $\gamma/^\circ$	22.533(8); 90.36(2)
Volume/Å^3	1696.6(10)
Z	2
Temperature (K)	100.01
ρ_{calc}, g/cm^3	3.091
Absorption Coefficient μ/mm^{-1}	16.29
F(000)	1376
2Θ range for data collection/$^\circ$	3.654 to 63.088
Index ranges	$-12 \leq h \leq 12$, $-12 \leq k \leq 112$, $-33 \leq l \leq 28$
Radiation	Mo Kα ($\lambda = 0.71073$)
Reflections collected	35179
Independent reflections	11201 [$R_{int} = 0.0817$, $R_{sigma} = 0.1148$]
Data/restraints/parameters	11201/11/163
Goodness-of-fit on F^2	1.014
Final R indexes [$I \geq 2\sigma$ (I)]	$R_1 = 0.0644$, $wR_2 = 0.1229$
Final R indexes [all data]	$R_1 = 0.1237$, $wR_2 = 0.1412$
Largest diff. peak/hole / e Å^{-3}	2.87/-4.22

7.8 Appendix: Description of the ultrafast spectrometer used for multidimensional harmonic generation measurements

An ultrafast oscillator seeding a regenerative amplifier (Spectra-Physics Tsunami and Spitfire Pro, respectively) produces ∼35 fs pulses centered at 1.55 eV at a 1 kHz repetition rate. The amplifier pumps an OPA (Light-Conversion TOPAS-C) operated in "signal mode", the output of the OPA is filtered by a 1000 nm longpass filter (ThorLabs FGL1000M). The fluence at the sample position is controlled by automated reflective neutral density filter wheels (ThorLabs NDC-100C-4M). The fluence spectrum of the OPA is shown in Figure 7.9 along with the spectrally resolved output of the OPA at a single setpoint. The filtered output of the OPA is focused onto a sample with a 1 m focal length spherical mirror at $\sim 9^\circ$ from surface-normal. The spatially coherent output in the reflective direction is collected with a 0.5 m focal length mirror, selected with an aperture, focused into a monochromator (Horiba Micro-HR), and detected with a thermoelectrically cooled PMT (RCA C31034A). The beam width at the sample is ∼300 μm. We do not correct for the color-dependent response of our PMT or monochromator in our measurements.

In order to collect photoluminescence, the aperture after the collecting mirror is removed. The excitation source for single-photon absorption photoluminescence is provided by doubling a small portion of the output of the regenerative amplifier using a β-barium-borate crystal to 3.1 eV. This 3.1 eV light is loosely focused onto the sample; the photoluminescence is collected with the same optics as the nonlinear processes.

Micrographs are obtained directly on the laser table by using a retractable microscope (Adafruit, "USB Microscope", Product ID: 636) whose field of view is centered with the excitation laser's focal point by imaging a pinhole that the laser passes through. The spatial extent of the field of view is estimated by imaging a pinhole with a known diameter.

All raw data, workup scripts, and simulation scripts used in the creation of this work are permissively licensed and publicly available for reuse at http://dx.doi.org/10.17605/OSF.IO/JN24U. Our acquisition[103] and workup[166] software are built on top of the open source, publicly available

Scientific Python ecosystem.[251, 57, 58]

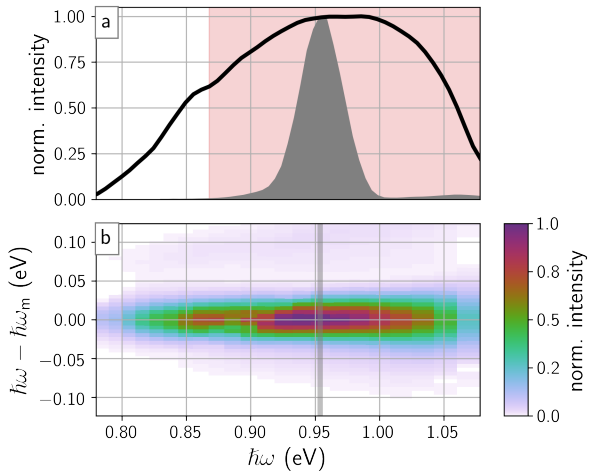

Figure 7.9: Characterization of OPA output. (a) OPA setpoint vs. output power as measured with a thermopile. Pink shaded region corresponds to the region principally used in this work. Shaded spectrum corresponds to the spectrum of the OPA at a setpoint of $\hbar\omega = 0.95$ eV. (b) OPA setpoint vs. differential monochromator setpoint as measured with an InSb photodiode cooled to 77 K.

7.9 Appendix: Projected THG spectra

Figure 7.10 shows a projection of the THG spectra onto the monochromator axis for the six RP perovskite samples. OPA power corrected spectra are also shown. Power correction is accomplished by first dividing the THG spectra along the pump laser axis by the cube of the (interpolated) powercurve shown in Figure 7.9a; the data are then collapsed onto the monochromator axis.

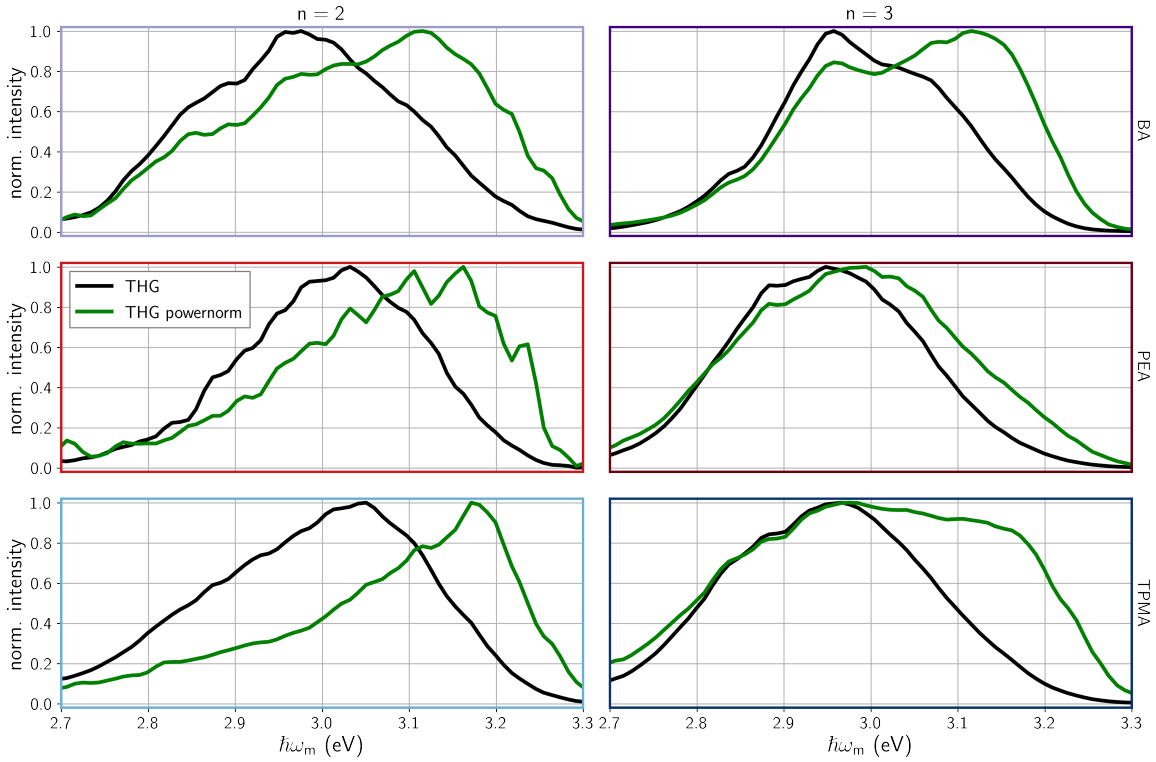

Figure 7.10: Projection of THG spectrum onto the monochromator axis for the 6 $(RNH_3)_2(MA)_{n\text{-}1}Pb_nI_{3n+1}$ RP perovskite samples primarily explored in this work (same data as those shown in Figure 3 of main text). Green curve is corrected for the frequency dependent variation of the pump intensity of the excitation laser.

7.10 Appendix: Quantification of the lack of SHG in $(BA)_2(MA)_2Pb_3I_{10}$

In this section we quantify our inability to observe SHG from a $(BA)_2(MA)_2Pb_3I_{10}$ sample. Figure 7.11 shows the spectrally resolved output from $(BA)_2(MA)_2Pb_3I_{10}$ with a 1.05 eV excitation laser. The noise floor (standard deviation of measured signal when no mPL, SHG, and THG are present) is more than 3 orders of magnitude below the measured THG response. By comparing the ratio of the noise-floor to the THG intensity, we find that the ratio of SHG/THG photons, were the SHG photons to exist, would have to be below 0.0004. Our results are in contrast to Stoumpos et al. [361] who measured a SHG/THG ratio of 0.01 for their $(BA)_2(MA)_2Pb_3I_{10}$ sample. Note that their measurement was performed with $\hbar\omega = 0.69$ eV and a fluence around 15000 μJ/cm^2, ten times more intense than our excitation laser. Larger fluences ought to *depress* their SHG/THG ratio compared to ours because SHG output intensity scales quadratically with driving laser intensity while THG output intensity scales cubically with driving laser intensity. According to their work, at our excitation fluence, we expect a SHG/THG ratio of 0.1. Instead we observe no SHG down to a factor of 0.0004 of the THG signal (as determined by our noise-floor).

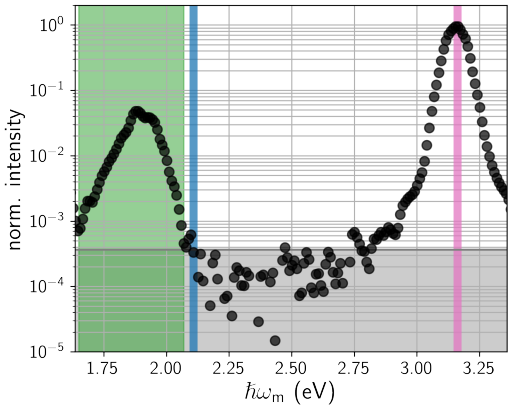

Figure 7.11: Output intensity spectrum for $(BA)_2(MA)_2Pb_3I_{10}$ with $\hbar\omega = 1.05$ eV. The y-axis is logarithmically scaled. Blue and magenta vertical lines notate where SHG and THG are expected to exist given the frequency of the excitation laser. Green vertical bar indicates mPL. Gray horizontal bar indicates values below the noise floor of our measurement.

7.11 Appendix: Further studies on $(PEA)_2(MA)Pb_2I_7$

In an attempt to understand why we observe SHG when the SCXRD analysis by Calabrese et al. [388] and us show that $(PEA)_2(MA)Pb_2I_7$ has a centrosymmetric space group, we measure the multidimensional harmonic generation spectrum of many different $(PEA)_2(MA)Pb_2I_7$ crystals and after different treatments.

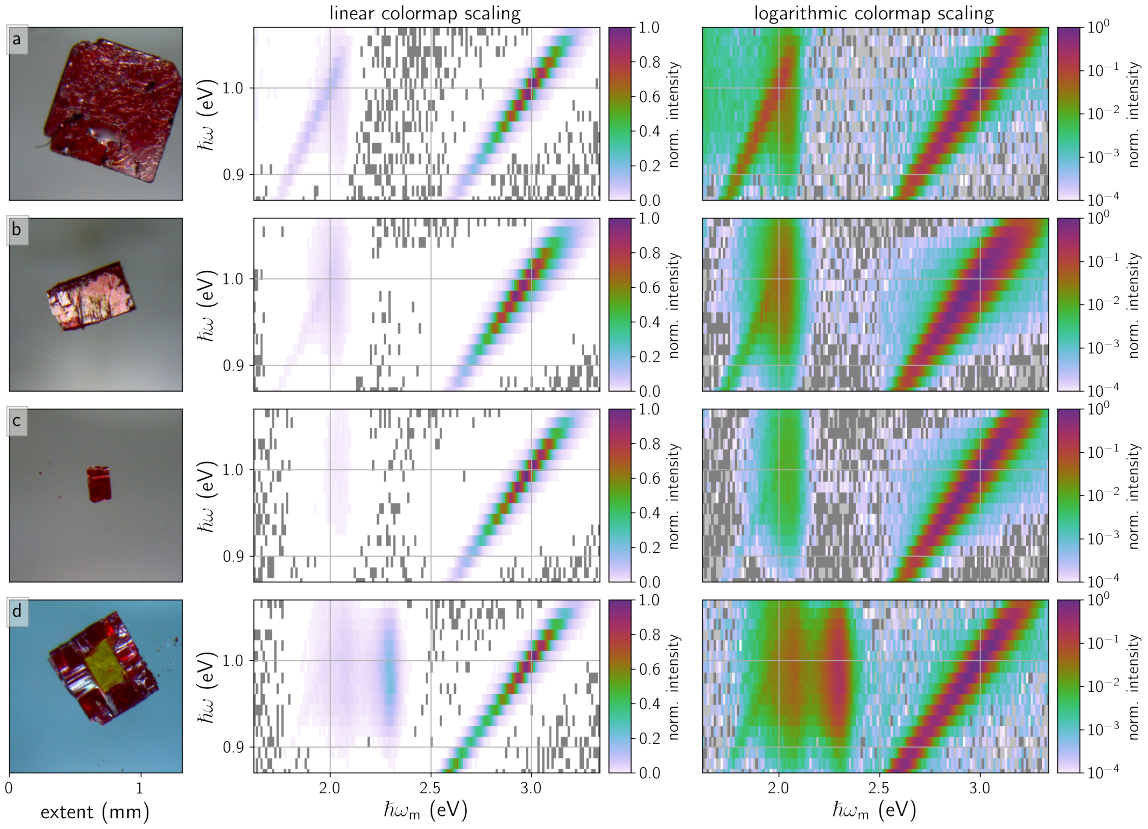

Figure 7.12: Multidimensional harmonic generation from multiple $(PEA)_2(MA)Pb_2I_7$ crystals. Second and third column have the colormap linearly and logarithmically scaled, respectively. (a) PEA $n = 2$ grown the same way as the sample presented in the main text. (b)-(c) PEA $n = 2$ crystals grown via a slow, organic solvent based growth method,[388] (d) same as (b)-(c) but with a serendipitously formed core-shell structure. The mPL from this sample can be compared to that of Figure 7.13c in which degredation causes a similar spectrum.

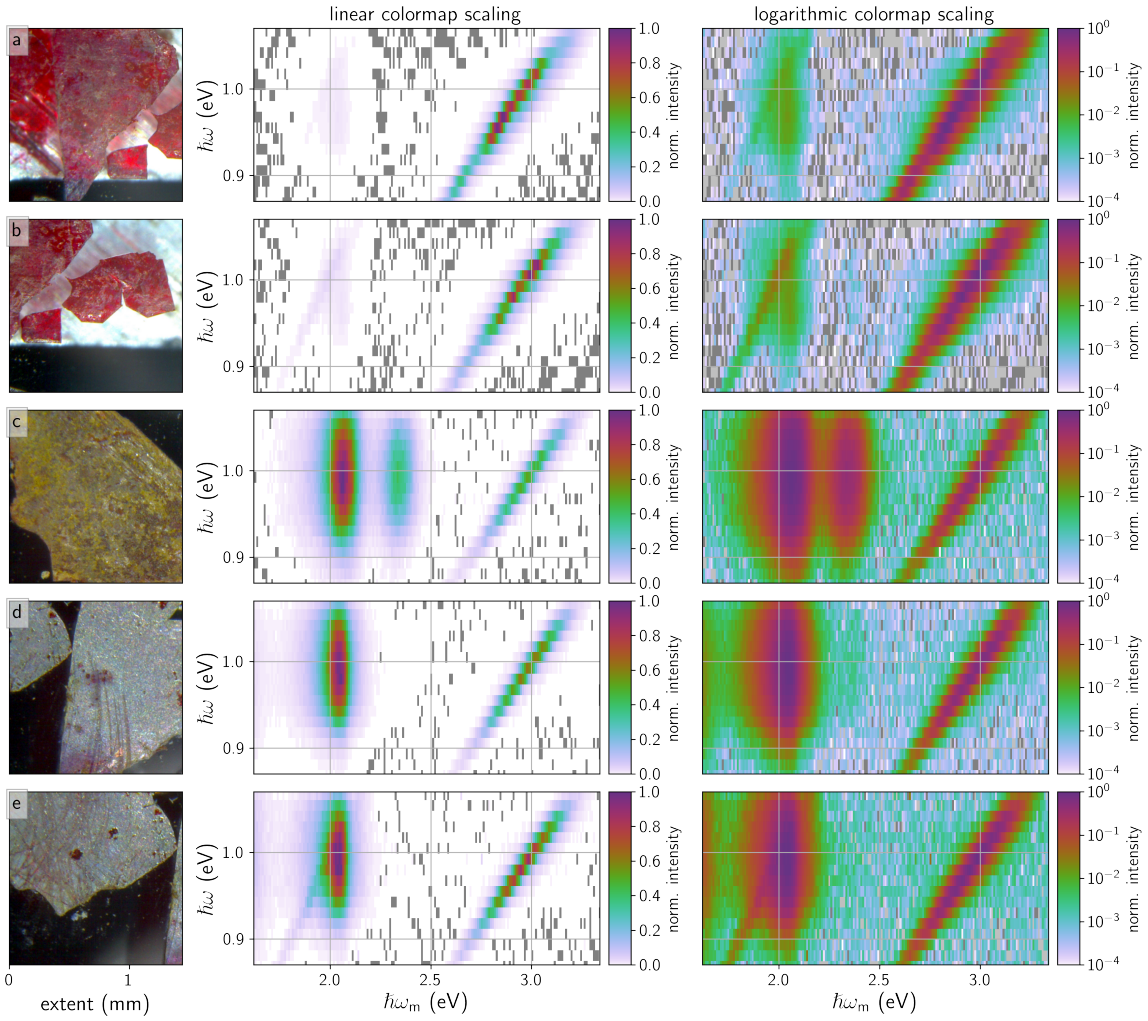

Figure 7.13: Multidimensional harmonic generation from multiple $(PEA)_2(MA)Pb_2I_7$ crystals after degradation. Second and third column have the colormap linearly and logarithmically scaled, respectively. (a)-(b) adjacent crystals which show different amounts of SHG. (c)-(e) crystals after degradation in a humidity chamber. (c) shows mPL and visual features of the $n = 1$ phase that was formed upon degradation. (d) is same crystal as (a), (e) looks visually similar to (d) but shows significantly more SHG. (c) and (d) do not have noticeable SHG above the intense mPL.

7.12 Appendix: Ferroelectric $(BA)_2(EA)_2Pb_3I_{10}$

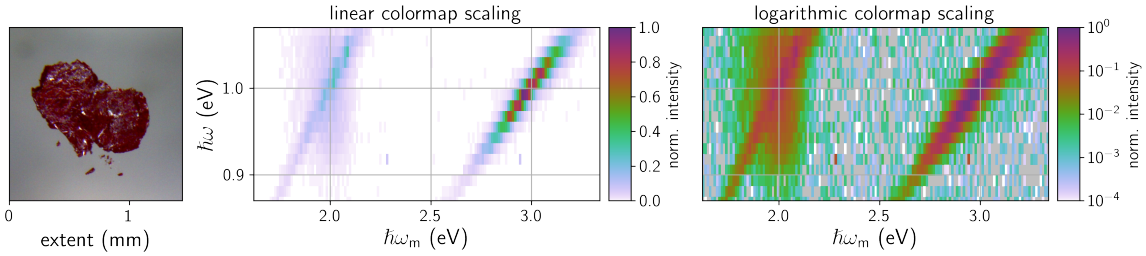

Figure 7.14: Multidimensional harmonic generation from a single crystal of $(BA)_2(EA)_2Pb_3I_{10}$ ($n = 3$). First column is the optical micrograph of the single crystal examined. Second and third column are harmonic generation measurements and have the colormap linearly and logarithmically scaled, respectively.

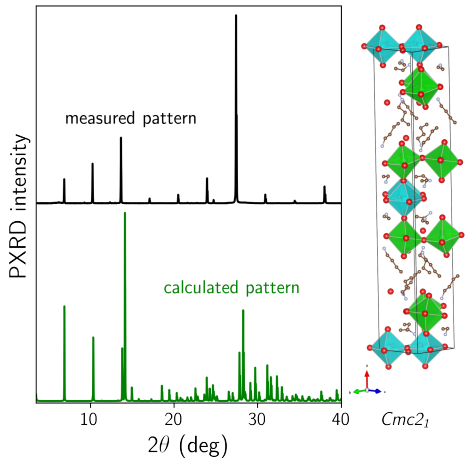

Figure 7.15: Experimental and calculated powder X-ray diffraction patterns for $(BA)_2(EA)_2Pb_3I_{10}$ ($n = 3$) crystal. The single crystal structure used to construct the calculated PXRD pattern and crystal structure diagram is from Han et al. [371].

7.13 Appendix: Discussion of $I_{\mathbf{THG}} \gg I_{\mathbf{SHG}}$

There are a few explanations as to why the measured SHG intensity could be much lower than the THG intensity:

1. SHG is merely occurring at interfaces and it therefore has a low active oscillator density compared to THG occurring in the bulk.[408, 409]
2. SHG is occurring in the bulk but is due to higher-order, non-local sources like electric quadrupoles and magnetic dipoles, while THG is caused by an electric dipole interaction.[383] Note that this explanation works for both centrosymmetric and noncentrosymmetric materials.
3. THG is resonantly enhanced or the output from SHG is selectively absorbed by the material.
4. The anharmonic potential energy surface across which electrons are driven by the applied electric field is only slightly noncentrosymmetric (the next section has a detailed discussion and derivation on this matter). The third-order centrosymmetric term (THG) therefore has a larger contribution to harmonic generation than the second-order noncentrosymmetric term (SHG).

We now address each of these possibilities. In order to determine if the air-semiconductor interface (explanation 1) or non-electric dipole sources (explanation 2) are the dominate contributions to our observed SHG, we compare our measured SHG intensities to those from a silicon wafer. Silicon is centrosymmetric but is known to support bulk SHG from non-electric-dipole sources and support surface SHG with both contributions being of similar magnitude.[383, 410] We found the SHG intensity from silicon to be three orders of magnitude less intense than the 2D perovskite SHG. Thus, as long as higher-order, nonlocal sources like electric quadruple and magnetic dipole are of similar effect-size as silicon, our measured SHG is due to a lack of inversion symmetry in the bulk of the RP perovskite samples. Interestingly, DeCrescent et al. [411] suggests that magnetic dipoles may indeed be an important contribution to the optical properties of 2D-RP perovskites. These authors observed magnetic dipole effects for BA $n = 1$ and $n = 2$, but we observe no SHG for BA $n = 2$, so the magnetic dipole contribution to SHG from our crystals is still likely small.

In order to address explanation 3, we compared the THG intensity of TPMA $n = 3$ when excited with 0.68 eV light to its SHG intensity when excited with 1.02 eV light both leading to an output at 2.04 eV. These measurements yielded THG which was a factor of 300 times more intense than SHG even though both driving lasers had the same fluence. This comparison indicates that neither absorption nor resonant enhancement effects are the primary causes of the relative weakness of SHG to THG. Instead, we believe that the SHG intensity is weak compared to the THG due to the anharmonic potential felt by the optically driven electrons being only weakly noncentrosymmetric (explanation 4). In the next section we show how the anharmonicity of a restoring potential dictates the SHG to THG ratio.

7.14 Appendix: Centrosymmetric vs. non-centrosymmetric anharmonic potentials

In this section, we show how a simple one-dimensional electron oscillator model can be used to understand how symmetry requirements can control the relative efficiency of SHG and THG. Electrons that experience an anharmonic restoring potential that is only weakly noncentrosymmetric (meaning that the potential has dominantly even-symmetry around the electron's equilibrium position) have a small SHG/THG intensity ratio. Our derivation is influenced by Boyd's discussion of how noncentrosymmetric and centrosymmetric media give different contributions to the nonlinear susceptibility.[38] Note that the model assumed throughout this section works best when all optical frequencies of interest are considerably smaller than the lowest electronic resonances of the material. For the semiconductor systems we examined, this criterion does not hold, however, the takeaway of our model, that the symmetry of the potential influences the SHG to THG ratio, still holds.

7.14.1 A solution to a linear Lorentz model

To understand the derivation surrounding an anharmonic restoring potential, we first must understand the motion of a driven electron in a harmonic restoring potential. Consider a one dimensional oscillator equation of motion for an electron in a parabolic potential given by

$$\ddot{\tilde{x}} + 2\gamma\dot{\tilde{x}} + \omega_0^2\tilde{x} = -\frac{e}{m}\tilde{E}(t), \tag{7.4}$$

in which the term 2γ defines the damping imposed on the electron with mass m, driven by an electric field, $\tilde{E}$, interacting with the electron's charge, $-e$. Note that a tilde above a term indicates that the term varies rapidly in time. In Equation 7.4 the restoring force is given by

$$\tilde{F}_{\text{restoring}} = -m\omega_0^2\tilde{x}. \tag{7.5}$$

This restoring force corresponds to a potential energy function of

$$U(\tilde{x}) = -\int \tilde{F}_{\text{restoring}} \mathrm{d}\tilde{x} \tag{7.6}$$

$$= \frac{1}{2} m\omega_0^2 \tilde{x}^2, \tag{7.7}$$

which is indeed a parabolic potential with a minima (electron equilibrium position) at the origin—this potential is what an electron Coulombically attracted to a nuclear core might feel. Observe that U satisfies

$$U(\tilde{x}) = U(-\tilde{x}), \tag{7.8}$$

which means that this particular potential is centrosymmetric.

We desire to find a solution to Equation 7.4. We suppose an electric field of the form

$$\tilde{E}(t) = E \exp(-i\omega t) + \text{c.c.}, \tag{7.9}$$

and an ansatz for the steady state solution of Equation 7.4 given by

$$\tilde{x}(t) = x(\omega) \exp(-i\omega t) + \text{c.c.}, \tag{7.10}$$

with an amplitude coefficient of

$$x(\omega) = -\frac{e}{m} \frac{E}{D(\omega)}, \tag{7.11}$$

in which

$$D(\omega) \equiv \omega_0^2 - \omega^2 - 2i\omega\gamma, \tag{7.12}$$

with c.c. meaning complex conjugate. We now find the derivatives of Equation 7.10 to ensure our

ansatz is suitable

$$\dot{\tilde{x}} = x(\omega)(-i\omega)\exp\left(-i\omega t\right) + \text{c.c.} \tag{7.13}$$

$$\ddot{\tilde{x}} = x(\omega)(-\omega^2)\exp\left(-i\omega t\right) + \text{c.c.}. \tag{7.14}$$

Substitution of the LHSs of Equation 7.13 and Equation 7.14 into Equation 7.4 yields

$$x(\omega)(-\omega^2)\exp\left(-i\omega t\right) + 2\gamma x(\omega)(-i\omega)\exp\left(-i\omega t\right) + \omega_0^2 x(\omega)\exp\left(-i\omega t\right) = -\frac{e}{m}E\exp\left(-i\omega t\right) \tag{7.15}$$

$$\implies -x(\omega)(\omega^2) + 2\gamma x(\omega)(-i\omega) + \omega_0^2 x(\omega) = -\frac{e}{m}E, \tag{7.16}$$

in which we have discarded all complex conjugates. Collecting terms yields

$$x(\omega)\left(-\omega^2 - 2i\omega\gamma + \omega_0^2\right) = -\frac{e}{m}E \tag{7.17}$$

$$\implies x(\omega) = -\frac{e}{m}\frac{E}{\omega_0^2 - \omega^2 - 2i\omega\gamma}, \tag{7.18}$$

which is equivalent to Equation 7.11 which completes the proof that Equation 7.10 is a valid solution to Equation 7.4.

7.14.2 A solution to a nonlinear Lorentz model

We now consider an anharmonic restoring force. We express the force as a low-order Taylor expansion

$$\tilde{F}_{\text{restoring}} = -m\omega_0^2\tilde{x} - ma\tilde{x}^2 + mb\tilde{x}^3, \tag{7.19}$$

with a and b defining the degree of anharmonicity. As we will soon show, a defines the degree of non-centrosymmetric anharmonicity, while b defines the degree of centrosymmetric anharmonicity. The potential energy surface is given by Equation 7.6 which upon integration yields

$$U(\tilde{x}) = \frac{1}{2}m\omega_0^2\tilde{x}^2 + \frac{1}{3}ma\tilde{x}^3 - \frac{1}{4}mb\tilde{x}^4. \tag{7.20}$$

If $a = 0$, then $U(\tilde{x}) = U(-\tilde{x})$ and the system is centrosymmetric; if $a \neq 0$, then the system is noncentrosymmetric. Figure 7.16 shows examples of how the potential energy surface can change based on the values of a and b.

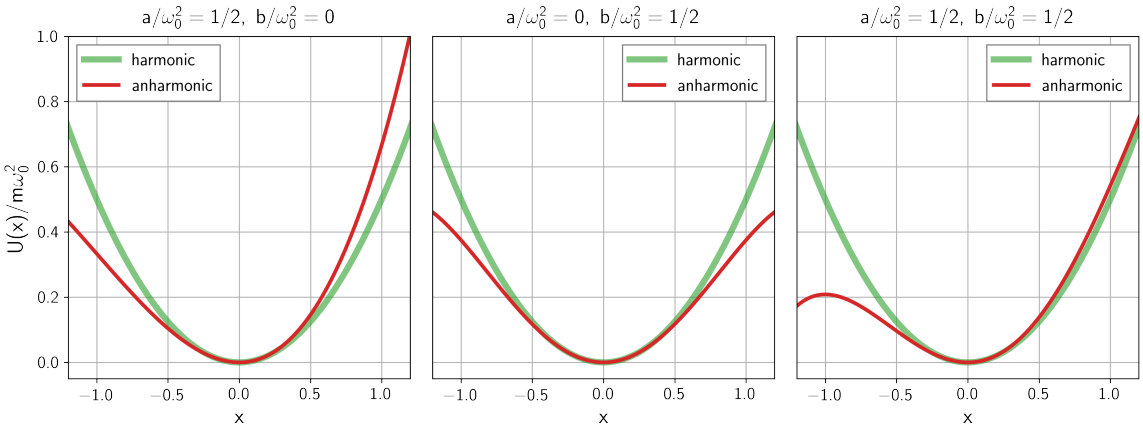

Figure 7.16: Plots of Equation 7.20 for three different combinations of a and b. The first column demonstrates a non-centrosymmetric anharmonic potential. The second column shows a centrosymmetric anharmonic potential. The third column shows an anharmonic potential with both centrosymmetric and non-centrosymmetric terms contributing to the overall form.

The equation of motion for a 1D electron oscillator with this anharmonic potential is

$$\ddot{\tilde{x}} + 2\gamma\dot{\tilde{x}} + \omega_0^2\tilde{x} + a\tilde{x}^2 - b\tilde{x}^3 = -\frac{e}{m}\tilde{E}(t). \tag{7.21}$$

The simplest applied field which will yield harmonic generation (but no other nonlinear processes) is

$$\tilde{E}(t) = E\exp(-i\omega t) + \text{c.c.}. \tag{7.22}$$

More electric fields with different frequencies could be added if difference and sum frequency generation were of interest.

We desire to find a solution to Equation 7.21, but no analytical solution exists. Instead we can find an approximate solution using a perturbative expansion. Our method is the same as used by Boyd

[38] and is analogous to the Rayleigh-Schrödinger perturbation theory in quantum mechanics.[1] We rewrite the electric field

$$\tilde{E}(t) \rightarrow \lambda \tilde{E}(t), \tag{7.23}$$

in which λ varies continuously from 0 to 1 and characterizes the strength of the electric field (we will set λ to unity at the end of the derivation). We desire a solution in the form of a power series expansion in λ:

$$\tilde{x} = \lambda \tilde{x}^{(1)} + \lambda^2 \tilde{x}^{(2)} + \lambda^3 \tilde{x}^{(3)} + \cdots . \tag{7.24}$$

A key insight of perturbation theory is that for Equation 7.24 to be a valid solution of Equation 7.21 for any value of λ, the different terms in Equation 7.21 that are proportional to different powers of λ all must satisfy Equation 7.21 separately.

We substitute Equation 7.23 and Equation 7.24 into Equation 7.21 and gather together, by powers of λ, terms up to λ^3:

$$\ddot{\tilde{x}}^{(1)} + 2\gamma \dot{\tilde{x}}^{(1)} + \omega_0^2 \tilde{x}^{(1)} = -\frac{e}{m}\tilde{E}(t) \qquad \lambda^1 \tag{7.25}$$

$$\ddot{\tilde{x}}^{(2)} + 2\gamma \dot{\tilde{x}}^{(2)} + \omega_0^2 \tilde{x}^{(2)} + a\left[\tilde{x}^{(1)}\right]^2 = 0 \qquad \lambda^2 \tag{7.26}$$

$$\dddot{\tilde{x}}^{(3)} + 2\gamma \ddot{\tilde{x}}^{(3)} + \omega_0^2 \dot{\tilde{x}}^{(3)} + a\left[\tilde{x}^{(1)} \cdot \tilde{x}^{(2)} + \tilde{x}^{(2)} \cdot \tilde{x}^{(1)}\right] + b\left[\tilde{x}^{(1)} \cdot \tilde{x}^{(1)}\right]\tilde{x}^{(1)} = 0 \qquad \lambda^3. \tag{7.27}$$

First-order solution

The solution to the lowest-order contribution, $\tilde{x}^{(1)}$ (Equation 7.25), is given by the linear Lortentz model which we previously solved as Equation 7.10

$$\tilde{x}^{(1)}(t) = -\frac{e}{m}\frac{E}{D(\omega)}\exp\left(-i\omega t\right) + \text{c.c.}. \tag{7.28}$$

[1] The reader interested in the origins of Rayleigh-Schrödinger perturbation theory can consult Schrödinger's original paper in German,[412] an English translation of the original given in Schrödinger's book collection on wave mechanics,[413] a summary in English written by Schrödinger,[414] or a modern summary with extension to nondegenerate energies.[415]

For sake of shorthand we explicitly note that

$$\tilde{x}^{(1)}(t) = x^{(1)}(\omega)\exp\left(-i\omega t\right) + \text{c.c.} \tag{7.29}$$

$$x^{(1)}(\omega) \equiv -\frac{e}{m}\frac{E}{D(\omega)}. \tag{7.30}$$

Thus, the first-order contribution scales as E with no contributions from the anharmonicity of the potential (neither a nor b are present) in the response function.

Second-order solution

Substitution of Equation 7.28 into Equation 7.26 yields

$$\ddot{\tilde{x}}^{(2)} + 2\gamma\dot{\tilde{x}}^{(2)} + \omega_0^2\tilde{x}^{(2)} = -a\left(\frac{eE}{m}\right)^2\left[\frac{\exp\left(-i2\omega t\right)}{D^2(\omega)} + \frac{\exp\left(i2\omega t\right)}{D^2(-\omega)} + \frac{2}{D(\omega)D(-\omega)}\right], \tag{7.31}$$

which contains the frequencies $\pm 2\omega$ and 0. We are interested in harmonic generation, so we seek a steady-state solution with frequencies of 2ω. Great care must be taken in deciding which frequencies are kept. In our final result, we only care about components at 2ω and 3ω, but we must ensure that terms that have components of -2ω or 0 frequency will not be needed when we move to the third order term. Inspection of Equation 7.27 demonstrates that terms which go as -2ω or 0 frequency will not be multiplied by another term that will yield frequency components of 2ω or 3ω. Hence, we select for analysis only the parts of Equation 7.31 which oscillate at 2ω:

$$\ddot{\tilde{x}}^{(2)} + 2\gamma\dot{\tilde{x}}^{(2)} + \omega_0^2\tilde{x}^{(2)} = -a\left(\frac{eE}{m}\right)^2\left[\frac{\exp\left(-i2\omega t\right)}{D^2(\omega)}\right]. \tag{7.32}$$

Our ansatz is

$$\tilde{x}^{(2)}(t) = x^{(2)}(2\omega)\exp\left(-i2\omega t\right), \tag{7.33}$$

that upon substitution into Equation 7.32 yields a solution which once again has the same form as the linear Lorentz model,

$$x^{(2)}(2\omega) = -a\left(\frac{e}{m}\right)^2 \frac{E^2}{D(2\omega)D^2(\omega)}. \tag{7.34}$$

Importantly, we see that the strength of the second-order contribution scales as aE^2—stronger electric fields or a more anharmonic potential both yield larger second-order contributions.

Third-order solution

To solve for the third-order contribution, we must substitute our solved forms of $\tilde{x}^{(1)}(t)$ and $\tilde{x}^{(2)}(t)$ back into Equation 7.27. For sake of compactness, we only keep terms which go as 2ω (no terms result) and 3ω:

$$\ddot{\tilde{x}}^{(3)} + 2\gamma\dot{\tilde{x}}^{(3)} + \omega_0^2\tilde{x}^{(3)} = -a\left[\tilde{x}^{(1)}\cdot\tilde{x}^{(2)} + \tilde{x}^{(2)}\cdot\tilde{x}^{(1)}\right] - b\left[\tilde{x}^{(1)}\cdot\tilde{x}^{(1)}\right]\tilde{x}^{(1)} \tag{7.35}$$

$$= -2a\left[x^{(1)}(\omega)x^{(2)}(2\omega)\exp\left(-i3\omega t\right)\right] - b\left\{\left[x^{(1)}(\omega)\right]^3\exp\left(-i3\omega t\right)\right\} \tag{7.36}$$

$$= \left[-2a^2\left(\frac{e}{m}\right)^3\frac{E^3}{D(2\omega)D^3(\omega)} + b\left(\frac{e}{m}\right)^3\frac{E^3}{D^3(\omega)}\right]\exp\left(-i3\omega t\right) \tag{7.37}$$

$$= \left[\frac{eE}{mD(\omega)}\right]^3\left[-\frac{2a^2}{D(2\omega)} + b\right]\exp\left(-i3\omega t\right). \tag{7.38}$$

Because we seek third harmonic generation, we impose an ansatz of

$$\tilde{x}^{(3)}(t) = x^{(3)}(3\omega)\exp\left(-i3\omega t\right), \tag{7.39}$$

in which we now solve for $x^{(3)}(3\omega)$. Inspection of Equation 7.38 yields

$$x^{(3)}(3\omega) = \left[\frac{eE}{mD(\omega)}\right]^3\left[-\frac{2a^2}{D(2\omega)} + b\right]\cdot\frac{1}{D(3\omega)}. \tag{7.40}$$

We see here that the strength of the third-order contribution scales as E^3, $2a^2$, and b; if the system is centrosymmetric, then the third-order contribution exclusively scales as bE^3.

7.14.3 Connection to susceptibility

In order to connect our results to a material's nonlinear susceptibility, we write the polarization caused by an electric field as a power series in the field strength:

$$\tilde{P}(t) = \epsilon_0 \left[\chi^{(1)} \tilde{E}(t) + \chi^{(2)} \tilde{E}^2(t) + \chi^{(3)} \tilde{E}^3(t) + \cdots \right] \tag{7.41}$$

$$\equiv \tilde{P}^{(1)}(t) + \tilde{P}^{(2)}(t) + \tilde{P}^{(3)}(t) + \cdots , \tag{7.42}$$

in which ϵ_0 is the permittivity of free space. The polarization is related to a material's dipole, μ, and therefore its charge displacement from equilibrium, x, by

$$P = N\mu = -Nex, \tag{7.43}$$

in which N is the number density of atoms. Setting $\lambda = 1$ yields a form of the displacement given in Equation 7.24 that satisfies Equation 7.41 and Equation 7.43:

$$\tilde{x} = \tilde{x}^{(1)} + \tilde{x}^{(2)} + \tilde{x}^{(3)} + \cdots . \tag{7.44}$$

Comparing Equation 7.41, Equation 7.43, and Equation 7.44 yields a relationship between the n^{th}-order susceptibility and the n^{th}-order displacement

$$-Nex^{(n)} = \epsilon_0 \chi^{(n)} E^n \tag{7.45}$$

$$\implies \chi^{(n)} = \frac{-Nex^{(n)}}{\epsilon_0 E^n}. \tag{7.46}$$

Substituting the results of our previous three sections yields

$$\boxed{\begin{aligned} \chi^{(1)} &= \left(\frac{Ne}{\epsilon_0}\right)\left(\frac{e}{m}\right)\frac{1}{D(\omega)} && (7.47)\\ \chi^{(2)} &= \left(\frac{Ne}{\epsilon_0}\right)\left(\frac{e}{m}\right)^2\frac{a}{D(2\omega)D^2(\omega)} && (7.48)\\ \chi^{(3)} &= \left(\frac{Ne}{\epsilon_0}\right)\left(\frac{e}{m}\right)^3\frac{1}{D(3\omega)D^3(\omega)}\left[\frac{2a^2}{D(2\omega)} - b\right]. && (7.49) \end{aligned}}$$

Note how $\chi^{(2)}$ is only present when $a \neq 0$; SHG will only be present when the potential energy surface experienced by the electron is non-centrosymmetric. Also, note that the magnitude of $\chi^{(3)}$ is determined by a and b, and that $\chi^{(3)}$ is nonzero even if $a = 0$, meaning that THG may be present when the potential energy surface experienced by the electron is centrosymmetric. Recalling that

$$I_{\text{SHG}} \propto \left|\chi^{(2)}\right|^2 I^2 \tag{7.50}$$

$$I_{\text{THG}} \propto \left|\chi^{(3)}\right|^2 I^3 \tag{7.51}$$

$$\implies \frac{I_{\text{SHG}}}{I_{\text{THG}}} \cong \left|\frac{\chi^{(2)}}{\chi^{(3)}}\right|^2 \cdot \frac{1}{|E|^2}, \tag{7.52}$$

we see that the relative sizes of the nonlinear susceptibilities determine the relative magnitude of SHG to THG. Taking the ratio of the $\chi^{(3)}$ (Equation 7.49) to $\chi^{(2)}$ (Equation 7.48) yields

$$\frac{\chi^{(3)}}{\chi^{(2)}} = \frac{\left(\frac{e}{m}\right)\frac{1}{D(3\omega)D(\omega)}\left[\frac{2a^2}{D(2\omega)} - b\right]}{\frac{a}{D(2\omega)}} \tag{7.53}$$

$$= \left(\frac{e}{m}\right)\frac{1}{D(3\omega)D(\omega)}\left[2a - \frac{b}{a}D(2\omega)\right], \tag{7.54}$$

in which it is clear that materials that are rigorously non-centrosymmetric but that have small values of a compared to b will have THG that is more intense than SHG. This statement is true despite THG being a higher-order process than SHG.

7.14.4 Connection to the Morse potential

A subtle yet important point is that the overall crystal symmetry of a medium dictates whether or not the medium can support dipole mediated SHG. It is not the microscopic symmetry of an individual electron's potential energy surface which determines whether the medium can support dipole mediated SHG. Instead the *macroscopic* potential energy surface experienced by a system's electron density determines a medium's SHG capabilities. Another way to rationalize this fact is that the wavelength of all radiation is much larger than the interatomic spacing of the polarizable media.

An interesting corollary to the above point is that the potential energy surface of an individual electron-atomic-core species is a poor approximation to the potential energy surface across which electrons are polarized by an intense electric field. Consider the case of an atomic gas. The potential felt by shell electrons of an atomic gas can be approximated by a Morse potential

$$U(x) = D\left[1 - \exp\left(-\beta(x - x_0)\right)\right]^2 \tag{7.55}$$

in which D is a measure of the dissociation energy and β is a measure of the potential's anharmonicity.[416] A plot of the Morse potential is shown in Figure 7.17. In what follows we will use the Morse potential to constrain the values of a and b which parametrizes our original anharmonic potential (Equation 7.20). We will find that erroniously assuming the *microscopic* potential (the Morse potential) defines the *macroscopic* potential energy surface (Equation 7.20) predicts that atomic systems will have $\frac{I_{\text{SHG}}}{I_{\text{THG}}} \gg 1$ for modest applied electric fields. Conversely it has been found that atomic gases only support odd harmonic generation (no SHG);[417, 418, 419, 420] so the Morse potential is a poor realization of the macroscopic potential over which an applied electric field generates a polarization.

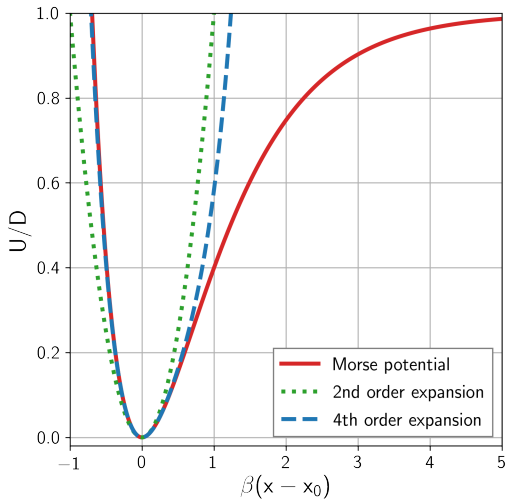

Figure 7.17: Morse potential, Equation 7.55; second-order (harmonic) approximation of the Morse potential; and fourth-order expansion, Equation 7.56, of the Morse potential. By construction, all axes are unitless.

A fourth-order Taylor expansion of Equation 7.55 around $x = 0$ yields

$$U(x) = D\beta^2 x^2 - D\beta^3 x^3 + \frac{7}{12} D\beta^4 x^4 - \mathcal{O}\left(x^5\right) \tag{7.56}$$

and a term-by-term comparison of Equation 7.56 to our original anharmonic potential (Equation 7.20) yields values of a, b, and ω_0 in terms of the Morse potential parameters

$$\omega_0^2 = \frac{2D\beta^2}{m} \tag{7.57}$$

$$a = \frac{3D\beta^3}{m} \tag{7.58}$$

$$b = \frac{7D\beta^4}{3m}. \tag{7.59}$$

Observe in Figure 7.17 how the fourth-order expansion well captures the repulsive part ($\beta(x - x_0) < 0$) of the Morse potential but only captures the attractive part for $\beta(x - x_0) \leq 0.5$—for sake of simplicity, the attractive overshoot will be considered inconsequential for the rest of our dicussion.

In order to constrain our system further, we assume a low frequency limit $\omega \ll \omega_0$ such that $D(\omega) \to \omega_0^2$. Equation 7.54 in this limit becomes

$$\frac{\chi^{(3)}}{\chi^{(2)}} = \left(\frac{e}{m}\right) \frac{1}{\omega_0^4} \left[2a - \frac{b}{a}\omega_0^2\right]. \tag{7.60}$$

Substitution of the fourth-order Morse potential parameters yields

$$\frac{\chi^{(3)}}{\chi^{(2)}} = -\frac{2e}{D\beta} \tag{7.61}$$

which upon substitution into Equation 7.52 yields

$$\frac{I_{\text{SHG}}}{I_{\text{THG}}} = \frac{D^2\beta^2}{4e^2|E|^2}. \tag{7.62}$$

We may evaluate Equation 7.62 for the case of a crystalline argon (parameters approximated from Jelinek [421]) under modestly intense excitation—see Table 7.3 for parameters. These parameters are similar to those found for a lead iodide system.[422] We find the intensity ratio is $\frac{I_{\text{SHG}}}{I_{\text{THG}}} \approx 10$.

Thus, the Morse potential does not function as a good approximation for the macroscopic potential energy surface of atomic systems (which have been observed to have no SHG). This result highlights that the local potential energy surface experienced by an electron is not the determining factor of a system's ability to support SHG.

Table 7.3: Parameters for evaluation of the SHG to THG ratio expected from a Morse potential.

$\|E\|$	1 GW/cm^2 ($\sim$0.004 V/Å)
D	15 meV
β	1.6 Å

Appendix A Transient-Transmittance Spectroscopy of a Methylammonium Lead Iodide Perovskite Thin Film

This Chapter details data originally collected by Blaise Thompson, Eric Hagee, and myself in 2016. The sample was synthesized by Yongping Fu. This data was originally intended to be modeled by Eric Hagee, however, he was unable to complete the project. The purpose of this chapter is to serve as a resting place for the ideas and representations surrounding the datasets.

A.1 Introduction

Methylammonium lead iodide perovskite, $CH_3NH_3PbI_3$ ($MAPbI_3$), is an acclaimed material for cost-effective photovoltaic applications. $MAPbI_3$ is a solution processable semiconductor with a direct optical band gap, a high optical absorption coefficient, and a long electron/hole diffusion length even in solution-processed polycrystalline thin films. Solar cell efficiencies in the astonishingly high 20-25 % range have been reported.

Since before I started graduate school, the Jin and Wright groups have shown much interest in the synthesis, characterization, and ultrafast dynamics of lead halide perovskite materials. Yongping Fu was adept at making polycrystalline $MAPbI_3$ thin films (Figure A.1a) which were sandwiched between two glass slides and sealed with paraffin. Both Matt Rowley and Eric Hagee were investigating these samples with specific interest in novel cool mechanisms of hot carriers. Between the time that Matt and Eric started thinking about hot carrier cooling in $MAPbI_3$ and now, an extraordinary amount of literature has been published about the ultrafast physics of $MAPbI_3$.

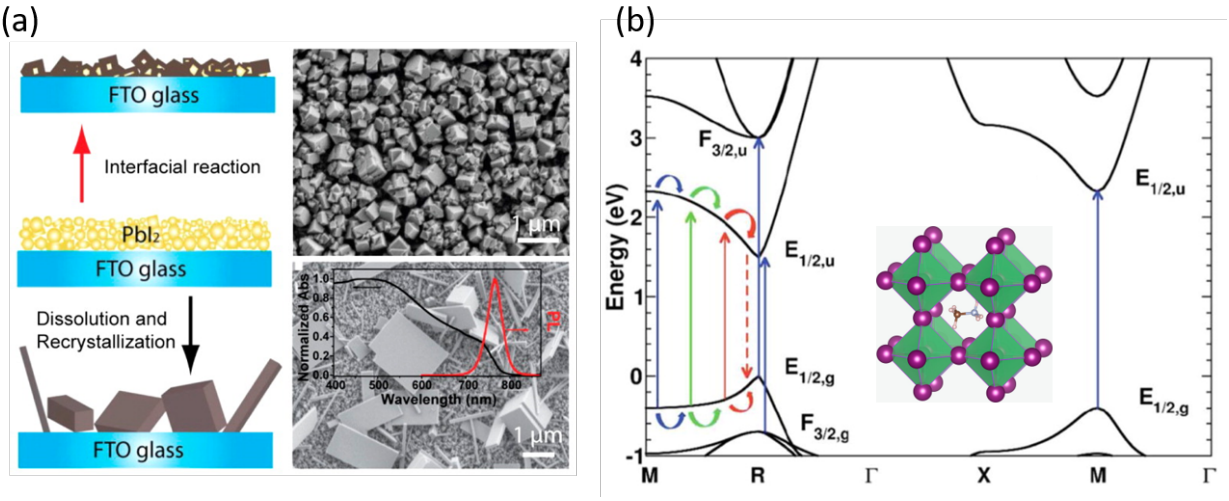

Figure A.1: Overview of $MAPbI_3$. (a) is the table of contents figure from Fu et al. [423] and shows the different grain morphology accessible by solution processing. (b) is adapted from refs.[424, 425, 426] and shows the electronic band diagram of the cubic phase of $MAPbI_3$ taking spin-orbit coupling into account; an upward energy shift of 1.4 eV has been applied to match the experimental bandgap value at R. Carrier localization and transport after optical excitation are sketched. The inset of (b) is from Eames et al. [427] and used under a CC-BY-4.0 License.

In 2016 Blaise Thompson and I collected transient transmittance (TT) data for Eric. Eric was interested in following a similar tact as Yang et al. [428] to model the data. Eric was unable to finish his project. John then tasked me with modeling the data. Immediately a slew of problems became apparent to me:

- The sample thickness (useful for Fresnel-like analysis) was never measured. The thickness could generally be calculated from a good absorption spectrum
- The absorption spectrum (Figure A.2) we have is dubious (∼0.2 OD below bandgap which is likely caused by heavy scattering of test light).
- TT measurements were accomplished at an unknown fluence with unknown beam waists. My

best guess is that pump fluence was $\sim 10\ \mu J/cm^2$.

- We do not have any fluence scaling data.
- Because we have no thickness data, poor absorption measurements, and no known fluences, we cannot calculate initial carrier density. Cooling behavior is radically different depending on initial carrier density and many important modeling variables are parametrically dependent on carrier density. These carrier densities will also vary across pump wavelengths because our OPA spectrum is not uniform (Figure A.2).
- At negative population times, we have a non-uniform offset that I do not understand—the same offset is present in Richter et al. [429]'s data.
- No SEM or AFM data characterizing the grain size. Recent work has shown that the grain size can influence whether or not reflectance artifacts needs to be taken into account.[430, 202, 203, 431]

Given these problems and that much work has already been published on hot carrier cooling in $MAPbI_3$, I eventually decided to stop working on the project.

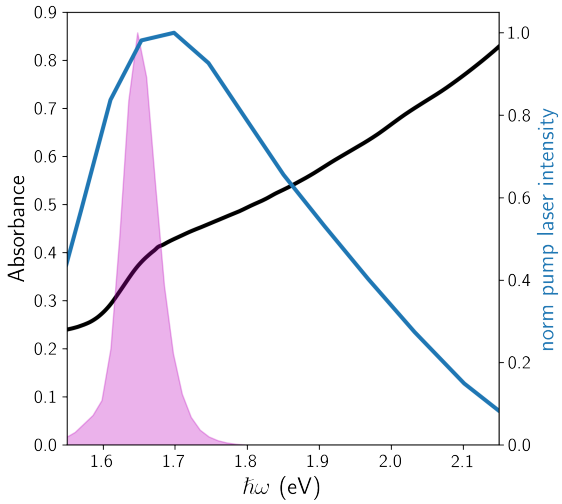

Figure A.2: Measured absorption spectrum (black) of $MAPbI_3$ film, pump laser spectrum at a specific setpoint (magenta fill), and pump laser intensity vs. setpoint spectrum (blue).

A.2 Datas

The TT data is currently most easily accessible at git.chem.wisc.edu/wright-group/MAPbI3_TT. It was acquired without accounting for reflectance artifacts. It has been smoothed, but not leveled. The data is recorded and represented as

$$signal = \frac{\Delta I}{I} = \frac{I_{\text{pump on}} - I_{\text{pump off}}}{I_{\text{pump off}}} \tag{A.1}$$

and if the universe is simple $\frac{\Delta T}{T} > 0$ corresponds to a bleach or stimulated emission while $\frac{\Delta T}{T} < 0$ corresponds to an excited state absorption.

Figure A.3 shows Delay time vs. probe frequency at different pump energies. A bleach is present at the bandedge with a uniform decrease in transmittance above the bandedge. Intriguingly, as the pump energy is increased, a low energy decrease in transmittance becomes apparent. Some of attributed this feature to a reflectance artifact,[430] while others have considered it a sign of band gap renormalization.[428] There is also a prominent 0.5 ps dynamic which is often attributed to hot carrier cooling.

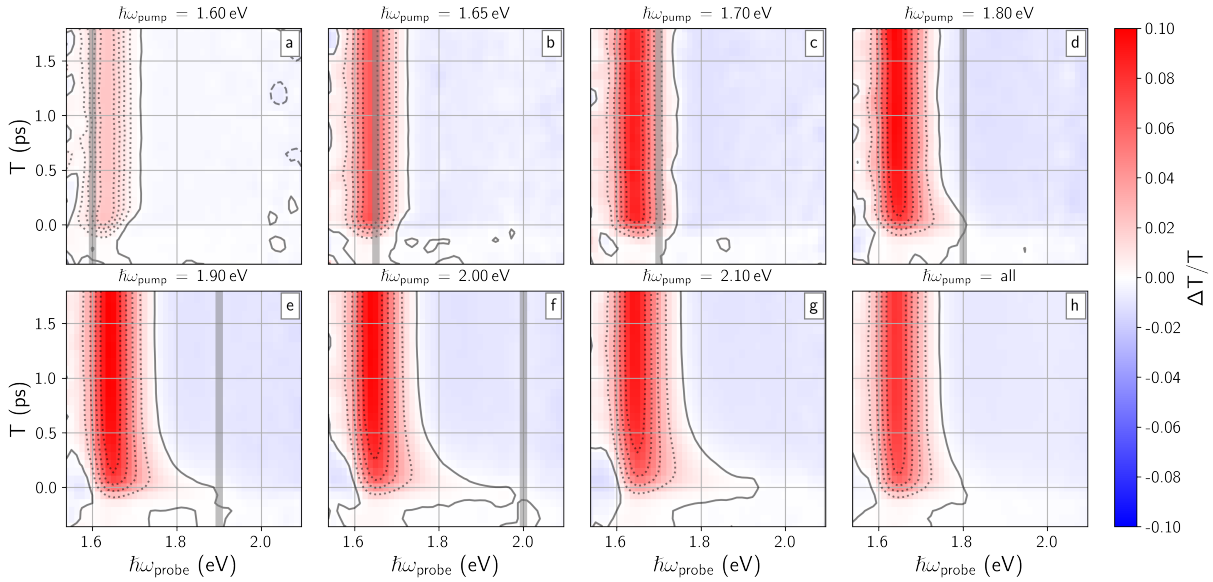

Figure A.3: Delay time vs. probe frequency slices. (a-g) Slices at different pump frequencies. (h) response integrated over all pump frequencies which is analogous to a white-light excitation.

This dataset is also intriguing when looked at as pump frequency vs. probe frequency (Figure A.5). Before and near $T = 0$ the data shows a diagonal zero-crossing which slides into a vertical node in a few hundred femtoseconds. As the pump frequency increases, the pump-induced bleach gets wider near $T = 0$. This wide lineshape at high pump frequencies (clearly shown in Figure A.4) is often fit simplistically to an exponential function and attributed to a Maxwell Boltzmann distribution.[432]

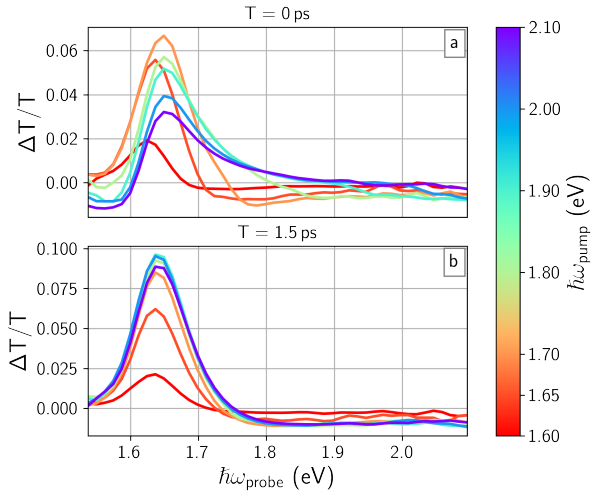

Figure A.4: One-dimensional slices through the data presented in Figure A.3 at $T = 0$ (a) and $T = 1.5$ ps (b) at different pump frequencies (indicated by colorbar).

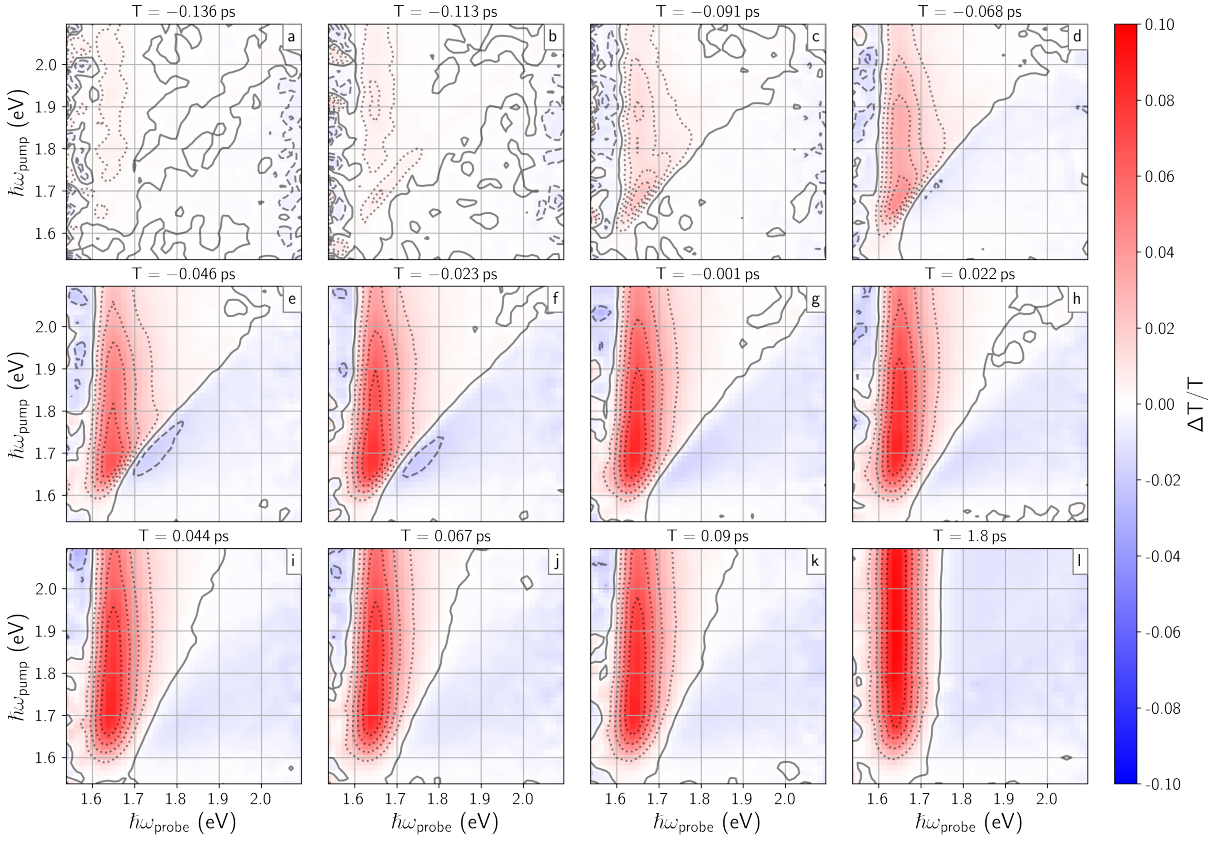

Figure A.5: Pump frequency vs. probe frequency slices.

A.3 Comparison

Richter et al. [429] accomplishes a 2D-ES experiment on a similar $MAPbI_3$ sample. Figure A.6 shows a comparison between their data (replotted with a signed colormap) and our data. Other than the decrease in transmittance at low probe frequencies but high pump frequencies, the datasets largely agree. Note that Richter et al. [429]'s broadband excitation has a significant peak at ∼1.7 and ∼1.95 eV which leads to the enhanced bleach structure.

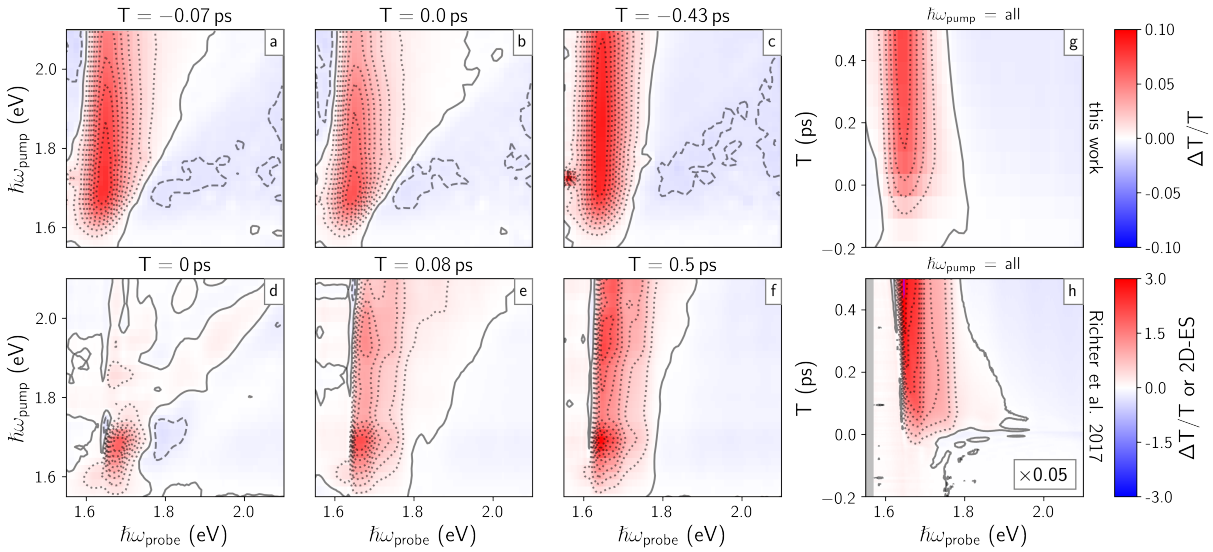

Figure A.6: Our data (top row) and comparison to 2D-ES (d-f) and broadband pump transient transmittance (h) from Richter et al. [429] (data is re-plotted after being acquired from their public repository[433]). Spot in (c) at $\hbar\omega_{\text{pump}} = 1.75$ eV and $\hbar\omega_{\text{probe}} < 1.6$ eV is due to the chopper losing its phase during the acquisition.

Appendix B Transient-Reflectance Spectroscopy of Single-Crystal Thin Films of $CsPbBr_3$ Epitaxially Grown on Metal Oxide Perovskite ($SrTiO_3$)

This Chapter details some of the work orginally presented in Chen et al. [434]. The authors are:

1. *Jie Chen*
2. *Darien J. Morrow*
3. *Yongping Fu*
4. *Weihao Zheng*
5. *Yuzhou Zhao*
6. *Lianna Dang*
7. *Matthew J. Stolt*
8. *Daniel D. Kohler*
9. *Xiaoxia Wang*
10. *Kyle J. Czech*
11. *Matthew P. Hautzinger*
12. *Shaohua Shen*
13. *Liejin Guo*
14. *Anlian Pan*
15. *John C. Wright*
16. *Song Jin*

B.1 Abstract

High-quality metal halide perovskite single crystals have low defect densities and excellent photophysical properties, yet thin films are the most sought after material geometry for optoelectronic devices. Perovskite single-crystal thin films (SCTFs) would be highly desirable for high-performance devices, but their growth remains challenging, particularly for inorganic metal halide perovskites. Herein we use transient-reflectance spectroscopy as a probe of the ultrafast surface dynamics of a cesium lead bromide perovskite ($CsPbBr_3$) continuous SCTF. The SCTF was grown via a new vapor-phase epitaxial growth technique on a traditional oxide perovskite $SrTiO_3$ (100) substrates. Our results indicate that the SCTF has a lower surface recombination velocity than a solution-phase grown bulk, $CsPbBr_3$ single crystal.

B.2 Introduction

Jie Chen, a visiting student in the Jin Group, devloped a chemical vapor deposition (CVD) method to grow smooth, single crystal, thin films of $CsPbBr_3$ perovskites on $SrTiO_3$ (100, STO) substrates. In the spring of 2017 Jie asked if I would be able to compare the ultrafast dynamics of his novel films to the more common solution-phase grown mm-sized crystals. Specifically, Jie wanted me to reproduce the surface recombination velocity measurements and analysis accomplished by Zhu et al. [435] on similar $CsPbBr_3$ samples and others on different lead halide perovskites.[436, 29] At the time I did not realize that the concept of a surface recombination velocity is considered by some to not be a useful concept because it is poorly constrained.[437, 438, 439, 440] The driving question behind this work is: what are the diffusion parameters which govern carrier diffusion in the first nanosecond of their lifetime? In order to answer this question, I elected to do transient-reflectance (TR) on two samples. One sample was CVD grown $CsPbBr_3$ on STO with a thickness of 7 μm (in this chapter, this sample will be called "slab") And the other sample was a solution grown $CsPbBr_3$ crystal (edges on the order of 2 mm, and had a roughly cubic shape with many faces) glued to a pedestal for easy rotation (in this chapter, this sample will be called "chunk").[1]

B.3 Transient-reflectance experiment

Our transient-reflectance experiment is diagramed in Figure B.1. An OPA creating 2.56 eV (485 nm) light acts as a pump and creates excited carriers. A white light supercontinuum generated in sapphire probes the photo-excited surface of our samples by reflecting off of the surface, being scanned by a monochromator and detected with a PMT (RCA 1P28, not cooled).[2] The pump beam diameter at the sample is 1.52 mm while the probe beam diameter is 0.66 mm, neither beams were dispersion corrected. The pump and the probe are both chopped in order to reject pump scatter;[164] the simplified definition of our signal is

$$\text{signal} = \frac{\Delta R}{R} = \frac{I_{\text{pump on}}(\omega) - I_{\text{pump off}}(\omega)}{I_{\text{pump off}}(\omega)} \tag{B.1}$$

in which the difference and ratio are calculated on the pixel level, *not* the shot level.[441]

The primary experimental results of this study are 2D acquisitions of delay vs. monochromator color.[3] I accomplished three such acquisitions for each sample (Figure B.2). The pump fluence for these acquisitions was 14 $\mu J/cm^2$. We observe a small shift ($\sim$20 meV) between the two samples in the zero crossing of the dispersive lineshape. This difference could be due to the Fresnel interference of the thin film, which has dramatically affected band edge TR spectra in other thin film perovskites.[436] The speckled response in the higher frequency range of the experiment is due to large relative variations of probe intensity for those colors.

I also collected delay traces with varying pump fluence (Figure B.3) for the single crystal thin film

[1] I had to pick through many crystals to find one which gave a usable specular reflection.

[2] Some of bulk crystals I looked at were such poor reflectors that the additional sensitivity of a PMT was needed compared to that of a photodiode.

[3] All TR data and my workup scripts are available on the Open Science Framework at dx.doi.org/10.17605/OSF.IO/V5KZN.

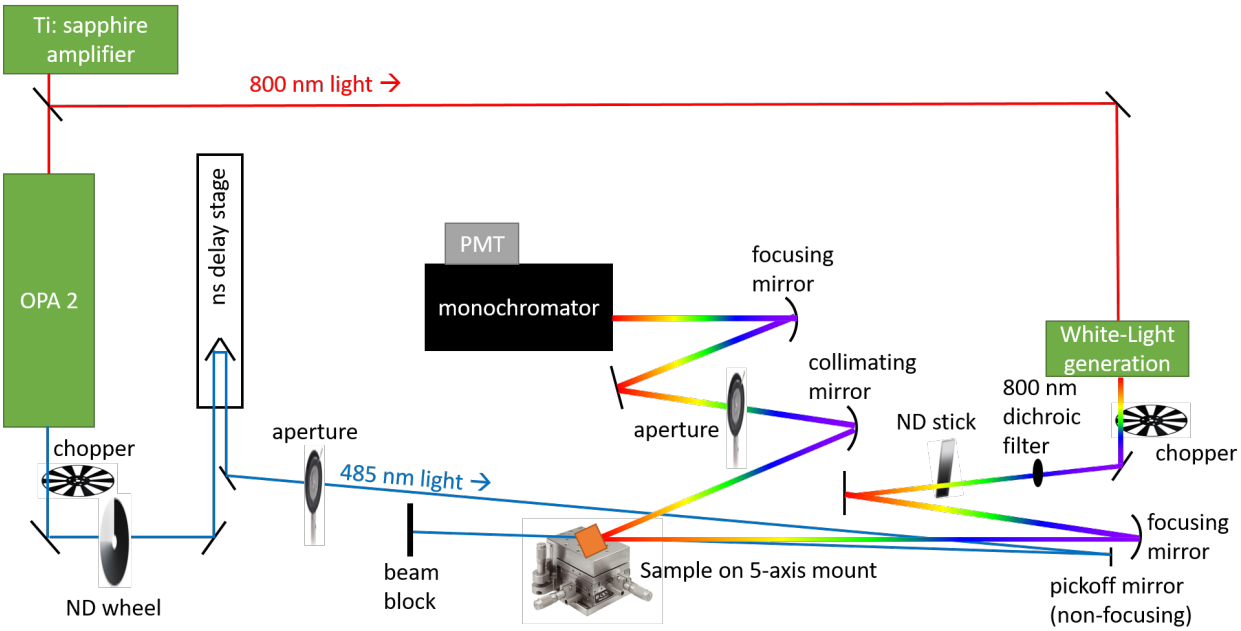

Figure B.1: Schematic of experimental setup used to perform transient reflectance experiments.

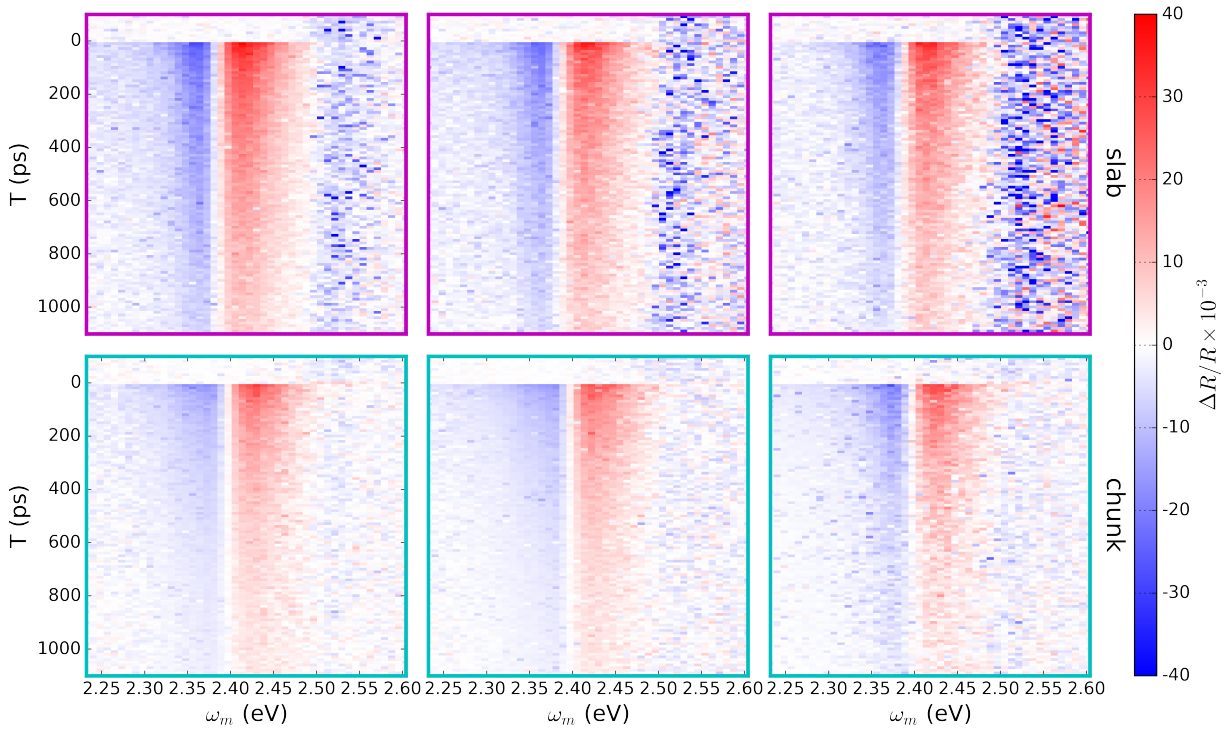

Figure B.2: Unprocessed TR data from the $CsPbBr_3$ slab (top row) and chunk (bottom row).

(slab). These data show a linear scaling of maximum response with respect to pump fluence.

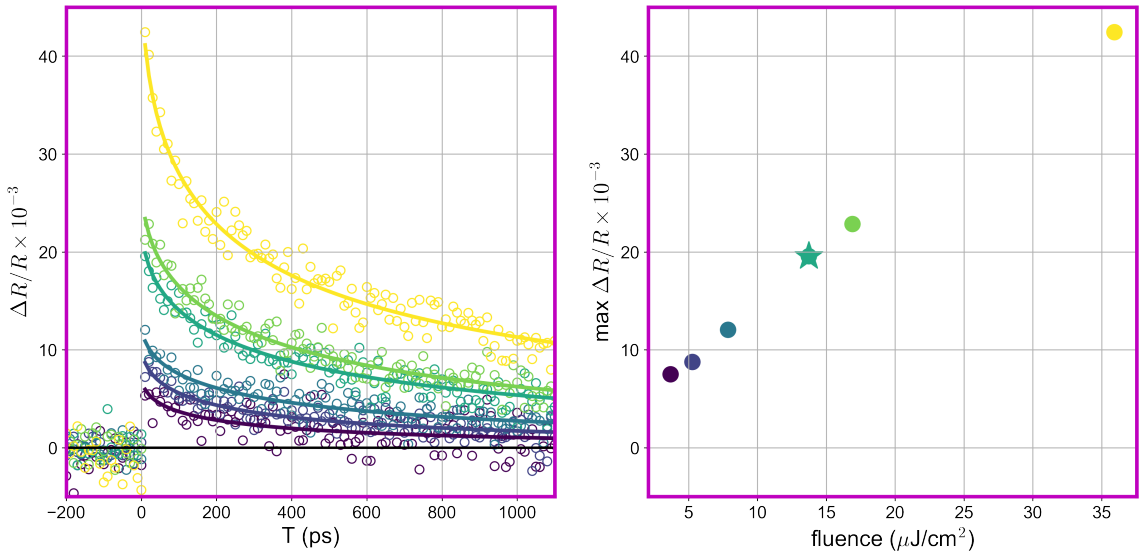

Figure B.3: (left) TR response of a $CsPbBr_3$ SCTF vs. delay for 6 different pump fluences. Solid lines are guides to the eye. (right) maximum response vs. pump fluence. The star scatter point marks the fluence at which all fitted data were acquired.

In order to suppress noise and reduce the dimensionality of the data in a model-agnostic way, I performed a singular value decomposition (SVD).[442] For both samples, the data were well described by the first singular value vector (Figure B.4). We clearly see from Figure B.4 that the chunk has faster dynamics than the slab. However, these data will need to be fit to a model to determine the values of physically relevant variables.

B.4 Diffusion and recombination modeling

At Jie's request, I fit the SVD extractions shown in Figure B.4 to a model originally developed by Hoffman et al. [443] to describe diffusion and surface recombination of semiconductors. This section details that model.

The standard model researchers use to think about carrier diffusion is derivative of Fick's second law with a single relaxation process

$$\frac{\partial N(\mathbf{r},t)}{\partial t} = \underbrace{\nabla[D(N(\mathbf{r},t))\nabla N(\mathbf{r},t)]}_{\text{diffusion}} - \underbrace{\frac{N(\mathbf{r},t)}{\tau_r(N(\mathbf{r},t))}}_{\text{relaxation}} \tag{B.2}$$

in which the diffusion coefficient, D, and relaxation coefficient, τ_r, both depend on carrier density/concentration. We then assume D and τ_r have no dependence on carrier concentration because we are in a low fluence regime. It is also implicitly presumed that D is the ambipolar diffusion

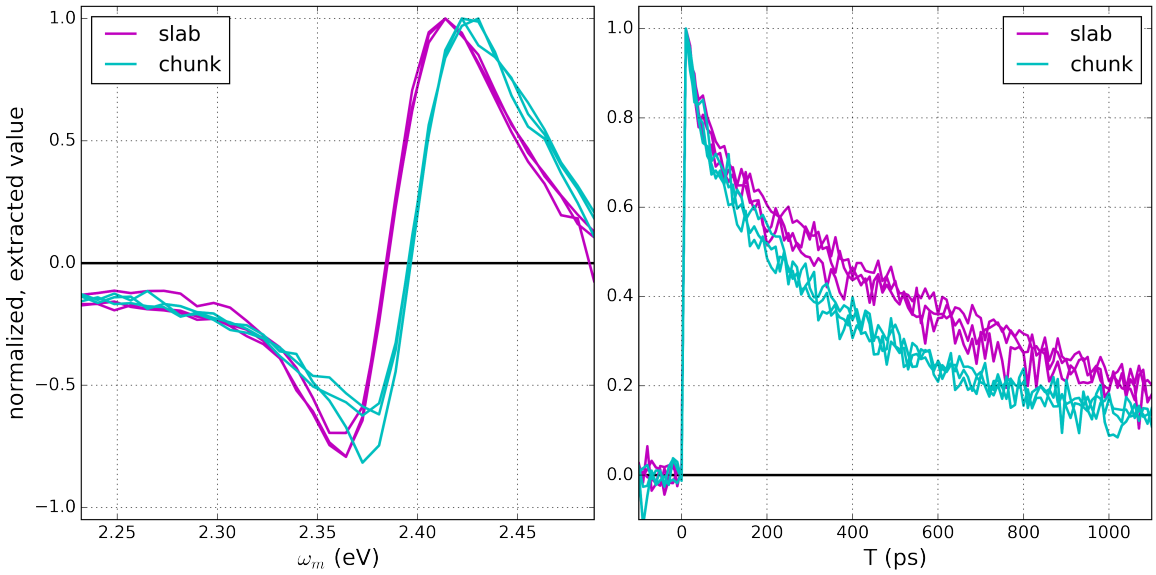

Figure B.4: First singular vectors extracted from raw data shown in Figure B.2.

coefficient—whatever diffusion happens, the material doesn't have a charge gradient build up inside of it. Equation B.2 then becomes

$$\frac{\partial N(\mathbf{r},t)}{\partial t} = \underbrace{\nabla[D\nabla N(\mathbf{r},t)]}_{\text{diffusion}} - \underbrace{\frac{N(\mathbf{r},t)}{\tau_r}}_{\text{relaxation}} \tag{B.3}$$

$$= \nabla^2 N(\mathbf{r},t) - \frac{N(\mathbf{r},t)}{\tau_r}. \tag{B.4}$$

Next we assume that carrier relaxation is much slower than diffusion and that our specific experiment only captures diffusion dynamics. The differential equation to be integrated is then

$$\frac{\partial N(\mathbf{r},t)}{\partial t} = \nabla^2 N(\mathbf{r},t) \tag{B.5}$$

This is the well known *heat equation*.[4] We must impose initial and boundary conditions onto this differential equation. The conditions are (with some simplifications):

1. All carrier diffusion happens in the z coordinate— a sufficiently uniform pumped region is

[4] I quite like a description of the dynamics imposed by this function found on Wikipedia wikipedia.org/wiki/Heat_equation: "Suppose one has a function u that describes the temperature at a given location (x, y, z). This function will change over time as heat spreads throughout space. The heat equation is used to determine the change in the function u over time. The rate of change of u is proportional to the "curvature" of u. Thus, the sharper the corner, the faster it is rounded off. Over time, the tendency is for peaks to be eroded, and valleys filled in. If u is linear in space (or has a constant gradient) at a given point, then u has reached steady-state and is unchanging at this point (assuming a constant thermal conductivity)."

being probed such that the probed region is cylindrically symmetric.

$$N(\mathbf{r}, t) \Longrightarrow N(z, t) \tag{B.6}$$

2. The initial carrier distribution is exclusively governed by Lambert's law in which uniform attenuation is presumed. Furthermore the carriers are excited by a delta function pulse in time.

$$N(z, t = 0) = N_0 \exp(-\alpha z) \tag{B.7}$$

3. At the surface, the recombination flux is proportional to the surface density of carriers, $J(t) = -SN(z = 0, t)$, with S being the *surface recombination velocity*. The spatial differential equation governing this recombination is then derived using Fick's first law, $J = -D\nabla N$, to yield

$$\left.\frac{\partial N(z,t)}{\partial z}\right|_{z=0} = \frac{S}{D} N(z = 0, t). \tag{B.8}$$

Note that, the rate at which carriers dive back into the bulk of the material is governed by the ratio of S to D. In other words, S is normalized by D.

4. There are no carriers at the backside of the material and the material is assumed to be infinitely thick (from the perspective of the carriers and time scale of the experiment):

$$N(z = \infty, t) = 0 \tag{B.9}$$

This assumption is good because the excitation depth at our pump color is around 0.2 microns while the thinnest sample we explore is 7 microns thick. The possible diffusion distance for our experimental observation window is given by $\langle r \rangle = \sqrt{Dt}$ which upon estimating D to be 1 cm^2/s and t to be 1 ns yields a distance of merely 30 nm.

Given all of the above conditions, our system will evolve as the known solution[443]

$$N(z,t) = \frac{N_0}{2} \exp\left(-\frac{z^2}{4Dt}\right) \left\{ W\left(\alpha\sqrt{Dt} - \frac{z}{2\sqrt{Dt}}\right) + W\left(\alpha\sqrt{Dt} + \frac{z}{2\sqrt{Dt}}\right) - \frac{2(S/D)}{S/D - \alpha} \left[W\left(\alpha\sqrt{Dt} + \frac{z}{2\sqrt{Dt}}\right) - W\left(\frac{S}{D}\sqrt{Dt} + \frac{z}{2\sqrt{Dt}}\right) \right] \right\} \tag{B.10}$$

in which we have followed Zhu et al. [435] in the form of the equation and

$$W(X) \equiv \exp\left(X^2\right) [1 - \operatorname{erf}(X)] \tag{B.11}$$

$$= \exp\left(X^2\right) \operatorname{erfc}(X). \tag{B.12}$$

If bulk relaxation is not negligible, a prefactor of $\exp\left(-\frac{t}{\tau_r}\right)$ should be multiplied into Equation B.10.

In order to gain intuition about the predictions of Equation B.10, consider Figure B.5. Here we see that Equation B.10 predicts a spreading out and leveling of the carrier distribution as time progresses. Importantly, when $S = 0$ (Figure B.5a), the interface always has a carrier gradient of 0. However, when $S > 0$ (Figure B.5b), carriers at the surface are rapidly removed forming an uphill gradient of the carrier concentration at the surface. The removal of carriers from the surface

causes the distribution maximum to gradually move further and further into the sample (instead of staying at the surface as is the case when $S = 0$).

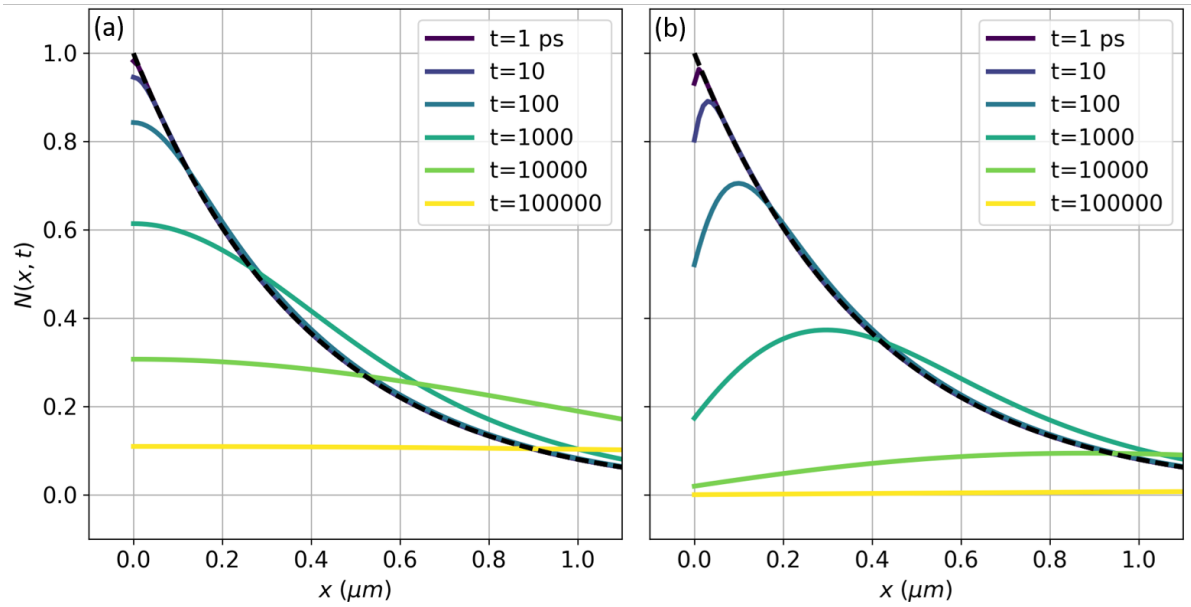

Figure B.5: Spatial dependence of carrier concentration at different times after excitation. In both panels $D = 0.4$ cm^2/s and the initial Lambertian carrier distribution is shown by the dashed, black line. In (a) $S = 0$. In (b), $S = 30000$ cm/s.

In the case where we *only* probe the surface of the photo-excited material the carrier concentration we care about is $N(z = 0, t)$. This is valid if we have a small probing depth.

$$N(z=0,t) = N_0 \left\{ W\left(\alpha\sqrt{Dt}\right) - \frac{S/D}{S/D-\alpha}\left[W\left(\alpha\sqrt{Dt}\right) - W\left(\frac{S}{D}\sqrt{Dt}\right)\right]\right\} \tag{B.13}$$

This is the equation we will be fitting. We will also be fitting a standard biexponential equation for comparison

$$\text{signal}(t) = a_1 \exp\left(-\frac{t}{\tau_1}\right) + a_2 \exp\left(-\frac{t}{\tau_2}\right) + (1 - a_1 - a_2). \tag{B.14}$$

B.5 Diffusion and recombination fitting

In order to fit our data to a surface recombination model, we must know the absorption coefficient of our material. The literature absorption coefficient for $CsPbBr_3$ at our 485 nm pump wavelength is 0.45×10^5 cm^{-1} which corresponds to a penetration depth of 0.2 μm.[444][5]

Figure B.6 represents the accomplished fits of Equation B.13 to the SVD decomposed data. In all cases, solid lines are the diffusion model while dashed lines are a biexponential relaxation model.

[5]The cited work investigated the absorption coefficient of $CsPbBr_3$ "nanocrystals"; we make a crucial assumption in presuming that our two materials share an analogous absorption spectrum.

In the top subplot, we see the three acquisitions for the slab. In the middle subplot we see the three acquisitions for the chunk. And in the bottom subplot we see the averaged experimental data and fits. The black line in the bottom subplot is generated from Zhu et al. [435] fit parameters for $CsPbBr_3$ nanoplates. The parameters associated with the averaged fits are given in Table B.1.

Table B.1: Fitting parameters. Errors for our fits are calculated as the standard deviations of the fit parameters obtained over the three acquisitions for each material. Zhu et al. [435] errors are from measuring over many samples.

Diffusion	S (cm/s)	D (cm^2/s)	S/D (cm^{-1})	
slab	15300 ± 1700	0.35 ± 0.04	44000	
chunk	30200 ± 1200	0.7 ± 0.03	43000	
$CsPbBr_3$ single crystal, Zhu et al. [435]	7700 ± 3500	1 ± 0.3	7700	
Lit: non-passivated GaAs	10^6	10-200		
Lit: Si	10^3-10^6	10-30		
Biexponential	a_1	τ_1 (ps)	a_2	τ_2 (ps)
slab	0.29 ± 0.014	65 ± 5	0.83 ± 0.05	1100 ± 150
chunk	0.23 ± 0.04	53 ± 3	0.67 ± 0.04	415 ± 20

In all cases, the diffusion model does not fit as well as the biexponential model. The diffusion model predicts too low of values for early times and too large of values for later times. Figure B.7 is a combination of the salient results of the experimental session.

The primary result of this analysis is that the slab has a surface recombination velocity which is a factor of two smaller than the chunk. If it is the case the our model is a good one, then this result implies that the slab has "better" surface properties (e.g. fewer recombination centers).

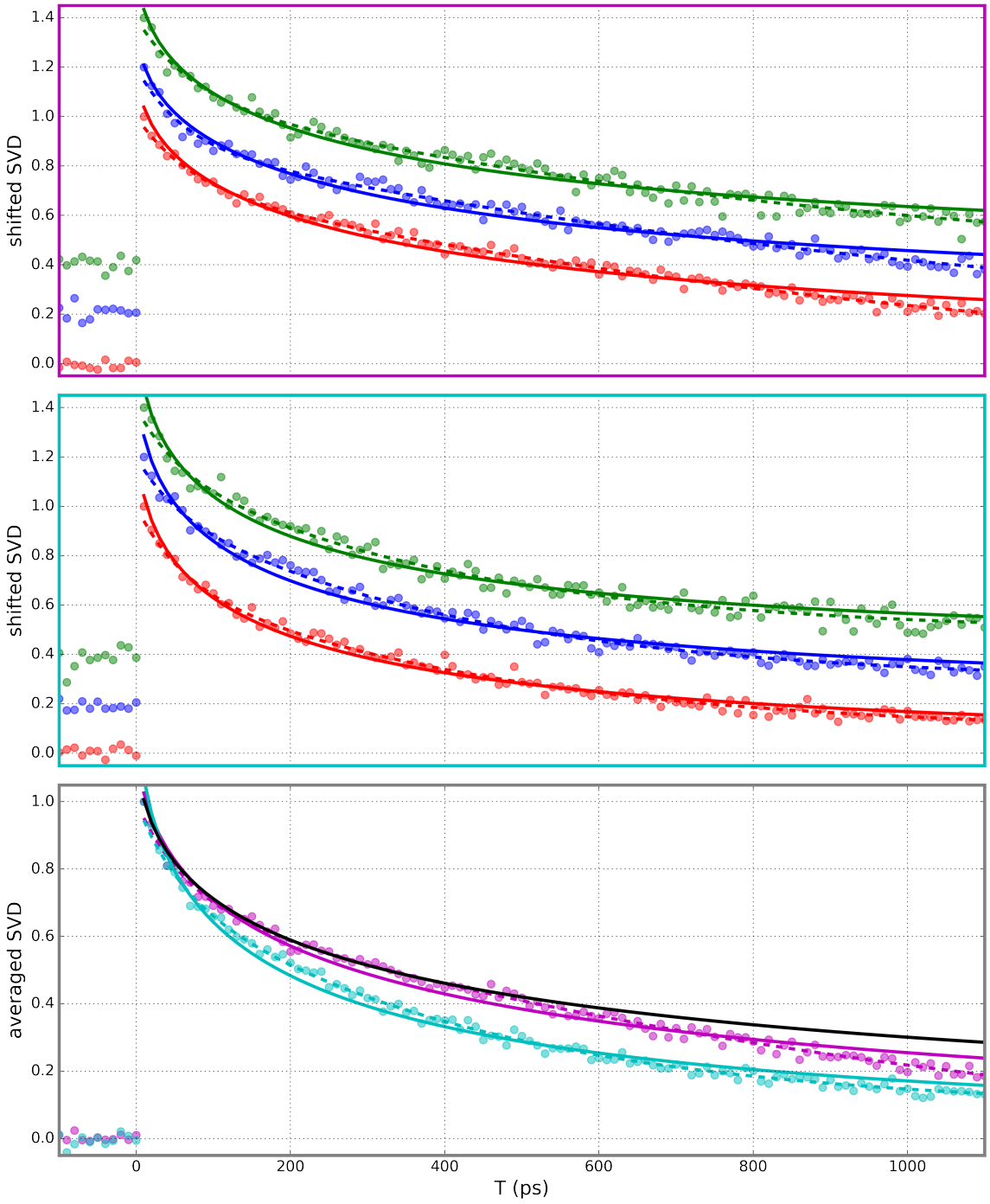

Figure B.6: Fits of SVD extracted data to Equation B.13 and Equation B.14

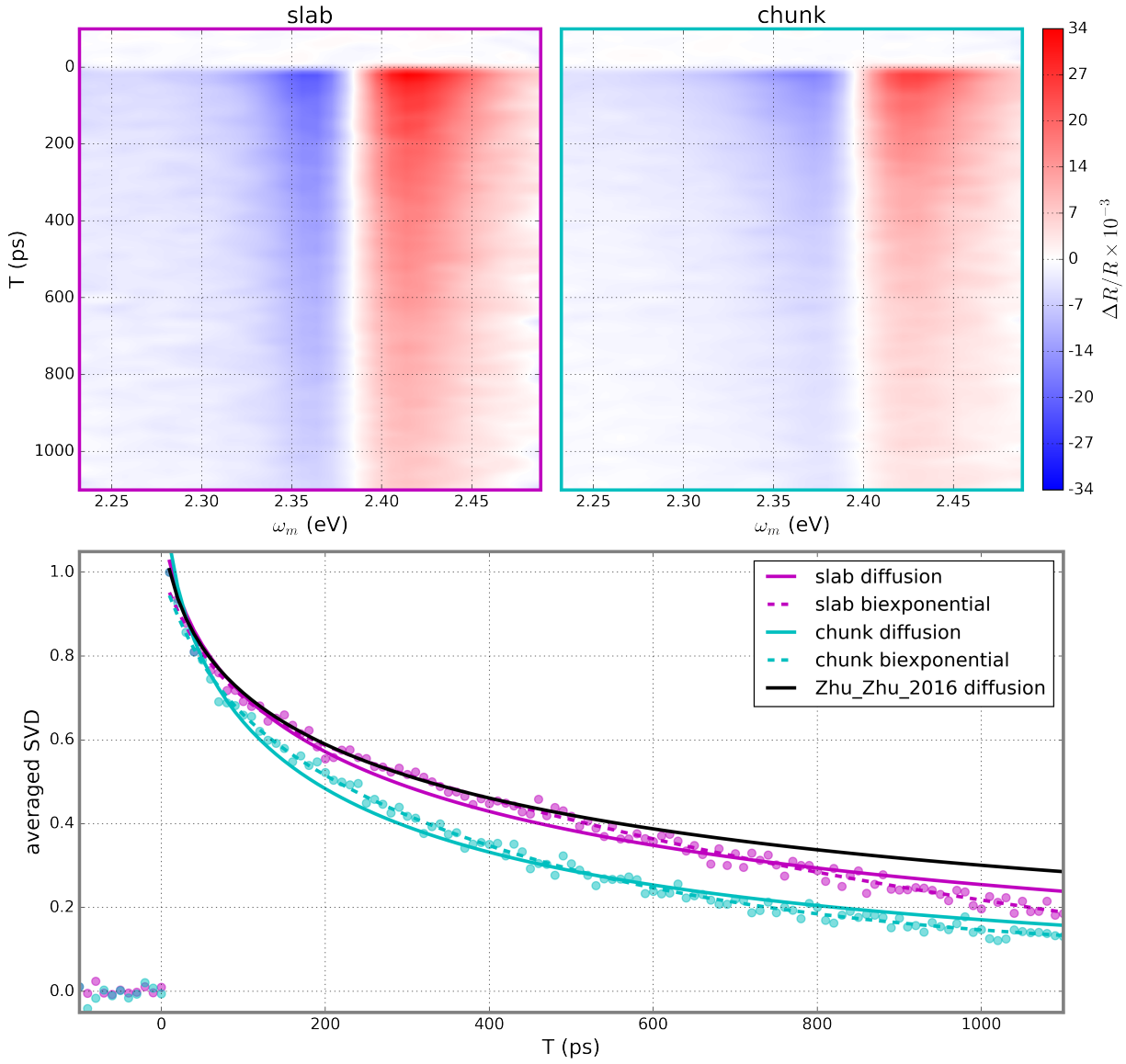

Figure B.7: 2D subplots are the average of the three acquisitions for each sample with a small bit of smoothing. The bottom subplot results from the SVD analysis fitting to models.

B.6 How well are S and D constrained?

Our measurements and model predict significantly different values for S and D compared to the values obtained by Zhu et al. [435]. Fortunately I was able to get their data and fit it. I found that drastically different values of S (even negative!) and D were consistent with their data depending on which wavelength was chosen to fit. This prompted me to see how well our data actually constrained the values of S and D. Figure B.8 shows a representation in which we set the values of S and D and then calculate the root mean square error (RMS) between the model and the data. A wide range of values for each parameter give reasonable errors, and the values are correlated in such a way that a small increase in D can be offset by a small decrease in S. Given a data set with slightly different random noise, we could have fit to a vastly different value of S and D. However, the surface recombination velocity of the two samples do differ significantly. Observe how the chunk's RMS error balloons as S values of 15000 cm/s are approached. The slab has the same behavior as S values of 30000 cm/s are approached. This entails that the two values must differ by a considerable amount.

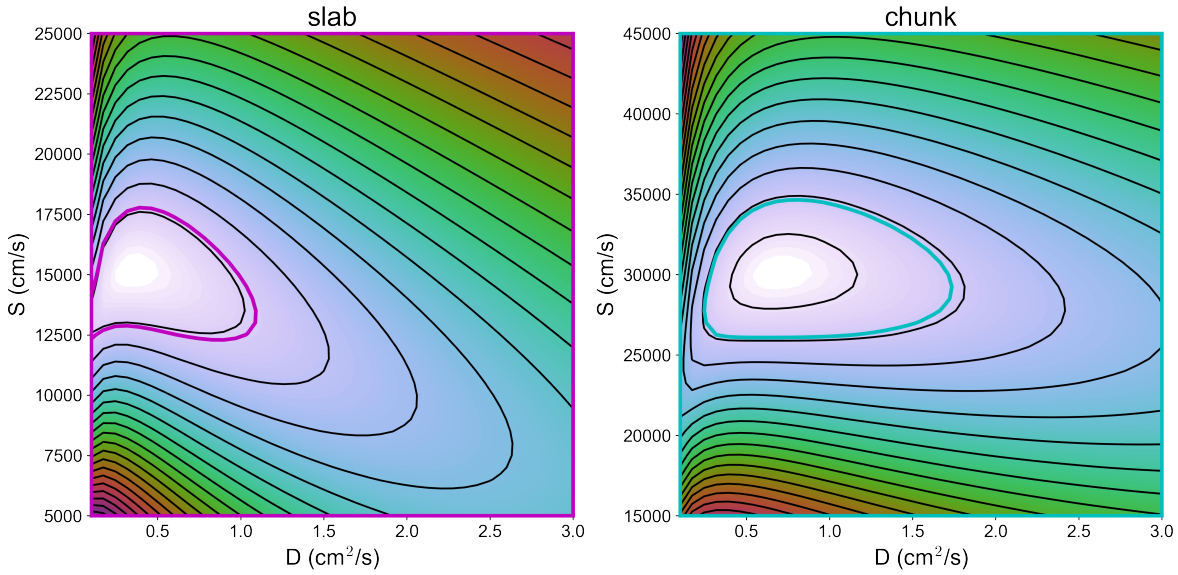

Figure B.8: Exploration of the fitting errors. Color bar is RMS value after fit. White is lowest error. The bold, colored contour line shows a 10% increase of RMS error from the minimum RMS error.

B.7 Conclusion

In the context of my graduate-school career, this was my first completed side-project pursuing a question of interest to someone in the Jin group. This project taught me a great deal about collaboration, and how collaboration is helped along by clear formulation of questions. However, this project also taught me how different scientists can view models of reality in very different ways.

It is now my personal belief that the surface recombination and Fickian diffusion model we used was not well constrained by our TR data and should not have been used. To some of my collaborators, the fact that this model had previously been used in the literature and that I was able to contort my data to it automatically entailed that it could tell us something about our universe of inquiry.

It is unnerving to me that a phenomenological biexponential fit recapitulated our data better than the recombination/diffusion model. Many material's chemists would elect to use the biexponential out of familiarity and simplicity. But which model actually holds more Truth, insight, and/or quantitative results? The model that does not constrain the data but offers mechanistic insight, or the model which perfectly fits the data but offers merely phenomenological timescales? The common view of science which values mechanistic explanations,[445, 446, 447] likely does not help us answer this question.

Appendix C Safety considerations for aligning Class 3B and Class 4 lasers

I originally wrote this guide as a list of things to mention to 1st year graduate students when discussing laser alignment and safety. The guide is divided up into three sections concerning items to consider before, during, and after alignment. The guide is adapted from the following sources:

- http://ehs.virginia.edu/Laser-Safety-Alignment.html
- https://ehs.washington.edu/system/files/resources/Laser_Alignment_Guideline.pdf

C.1 Before alignment

1. Alignment should be done only by those who have received laser safety training.
2. Make sure that all appropriate warning signs, lights and locks are operating.
3. Wear protective eyewear and clothing to the extent practicable. Use special alignment eyewear when circumstances (e.g. wavelength, power, etc.) permit their use.
4. Exclude unnecessary personnel from the laser area during alignment.
5. Remember that the user who turns on or unshutters a laser is responsible for the beam
   (a) Check personnel for eyewear appropriate for the laser and/or ensure that the beam is completely enclosed.
   (b) Know where the beam is going.
   (c) Give an audible warning to other personnel in the area.
6. Alignments are not to be performed when other lab (floor) members are not available to aid in an emergency. Consider having at least one other person present to help with the alignment (colleague or "buddy").
7. Housekeeping is paramount. The work area and optical table should be free of objects or surfaces that could reflect the laser.
   (a) Remove any jewelry, watches, rings, remove objects in shirt pockets, and remove ID badges.
   (b) Make sure any reflective surfaces in the area are blocked or covered.
   (c) Remove any unnecessary equipment, tools and combustible materials.
8. Collect needed tools (endeavor not to use reflective tools)
   - Screwdrivers
   - Viewing cards and viewing scopes
   - Beam blocks

C.2 During alignment

1. Whenever possible, use low-power visible lasers for path simulation of higher-power visible or invisible lasers. This may involve coalignment of a class 2 or 3 laser with the class 4 laser.
2. Enclose the beam as much as possible. The beam should be confined to the optical table's limit and a horizontal plane close to the table top.
3. Use a shutter or beam block to block high-power beams at their source except when actually needed during the alignment process. Beam lines which are not in use for an experiment should be blocked as far upstream as possible.
4. When aligning invisible and visible laser beams, use beam display devices such as business cards, image converter viewers, and phosphor cards to locate beams.
   - Never directly view the laser with your eye.
   - If a laser is too bright to be viewed from the face of an alignment card, try viewing it from the back of the alignment card. Remember when using a card, diffuse reflectance not specular reflectance should be viewed.
   - Another trick is to angle cards downward so any specular reflectance from the card (for instance if it has a coating) is directed away from the viewer and only diffuse reflectance is observed.
5. Perform alignment tasks that use high-power lasers, at the lowest possible power level. If the laser is Q-switched, turn off the Q-switch and use low power or CW mode.
6. Always block the beam upstream when inserting/removing anything into/from the beam path.
7. When placing a new optic, the following procedure should be followed:
   (a) Block beam upstream of new optic location
   (b) Place new optic, roughly align its poynting direction
   (c) Bolt the optic to the table and secure all thumbscrews. Never allow a laser to impinge on an unsecured optic or beam block.
   (d) Use a card to catch the beam on the beam block, remove beam block and slowly follow the beam onto the new optic.
      - Tip: place beam blocks behind optics (e.g., turning mirrors) to terminate beams that might miss mirrors during alignment.
   (e) Use a card (angled downward) to follow the beam off the new optic.
      i. Check for any unintended reflection/transmission. Be aware of the potential for errant reflections (stray beams) from components such as periscopes, polarizers, and dielectric mirrors.
      ii. Ensure the beam off of the new optic is traveling parallel to the table surface.
      iii. Slowly follow the beam with the card to ensure it is traveling in the correct direction. If it is not going in the correct direction, slowly use the degrees-of-freedom of the optic to change the poynting. Always ensure the beam is being caught by a card or block during this process.
   (f) Locate and block all stray reflections before proceeding to the next optical component or section.
   (g) Ensure beam off the new optic is caught by an appropriate block.
   (h) If the optic is to be rotated (e.g. a polarizer, wave-plate, or mixing crystal) ensure that rotation of the optic does not cause new, unintended, reflections. If so, ensure they will be caught by appropriate beam blocks.
8. Use beam blocks and/or laser protective barriers in conditions where alignment beams could

stray into areas with uninvolved personnel.
9. Never allow the beam to propagate beyond the point to which you have aligned and always be aware of the full beam path.
10. Avoid having beams cross aisle ways – if this is unavoidable ensure the accessible aisle way is appropriately marked and barricaded during laser operations.

C.3 After alignment

1. Be sure all beams and reflections are properly terminated before high-power operation.
2. Remember that whoever moves or places an optical component on an optical table (or in a beam path) is responsible for identifying and terminating each and every stray beam coming from that component (meaning reflections, diffuse or specular).
3. At alignment conclusion, normal laser hazard controls shall be restored. Controls set back in place include replacing all enclosures, covers, beam blocks, barriers and checking affected interlocks for proper operation.
4. Ensure area (and posted warnings) is returned to a state of safety which does not require laser eyewear.

Appendix D Common detector responsivities

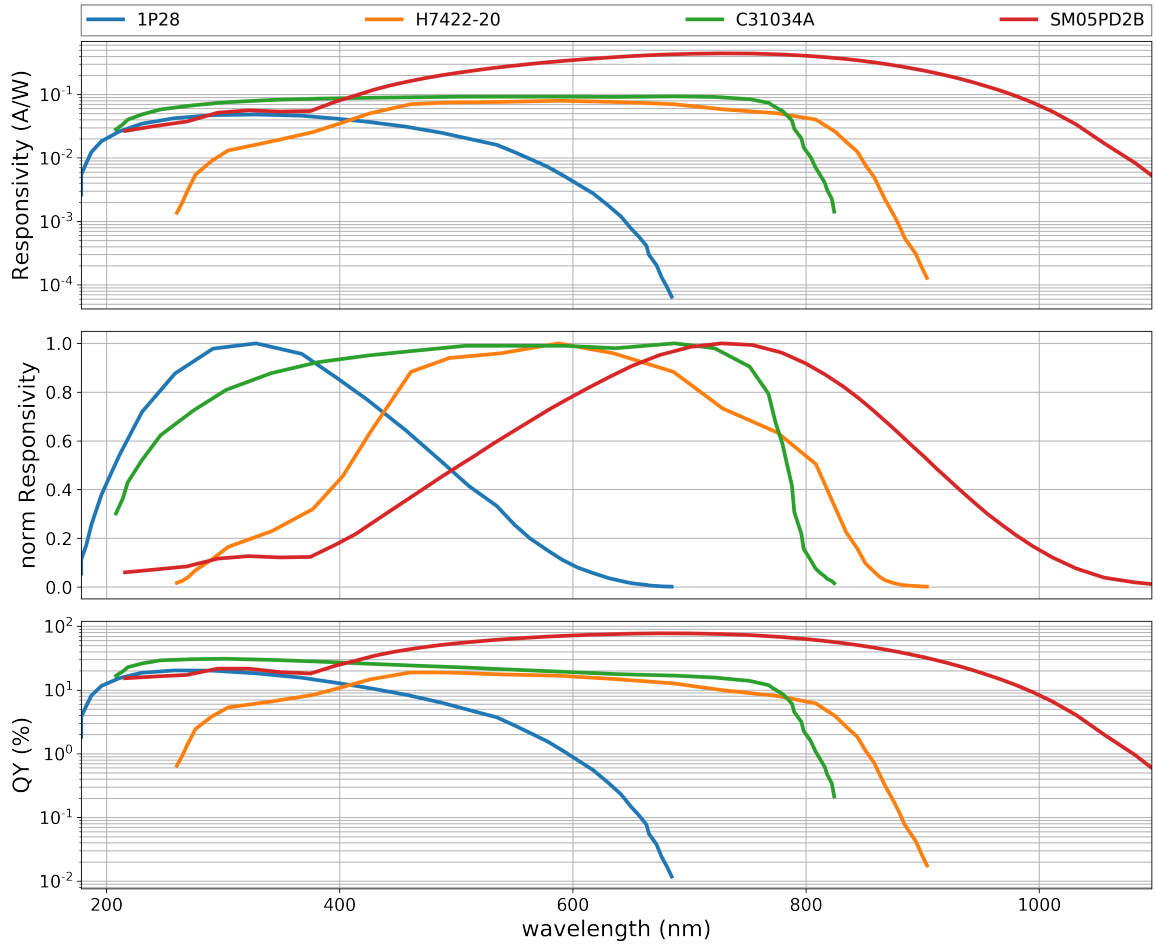

Figure D.1: Wavelength dependent response of detectors used in this dissertation. All traces are acquired from digitally tracing manufacturer spec sheets with apps.automeris.io/wpd/. "1P28" is a Hamamatsu, circular cage PMT. "H7422-20" is a Hamamatsu multialkali photocathode PMT. "C31034A" is a Burle, end-on, GaAs:Cs-0 photocathode PMT. "SM05PD2B" is a mounted, Si, anode-grounded, photodiode from Thorlabs.

Appendix E Delay stage alignment guide

Suppose that we have a delay stage we wish to align. In the ideal case, we desire to have the stage traverse its entire dynamic range without causing any shifting of the output beam spatially (especially at the down-stream sample position). Historically, the Wright Group has defined a stage to be *parallax adjusted* or *corrected for parallax* if the stage can traverse its dynamic range without the output beam walking off of the sample pinhole.[1] This appendix outlines how to align a translation stage such that parallax is no longer an issue.[2]

The standard Wright Group delay stage system involves the following components.

- a translation stage, `TS`
- a mirror, `M1`, which directs upstream light towards optics on `TS`
- a retroreflector assembly `RR` (generally a corner cube type optic) which definitionally reflects incoming light parrallel to itself such that $\vec{k}_{\mathsf{in}} = -\vec{k}_{\mathsf{out}}$ but the outgoing light can be non-collinear (shifted spatially) from the incoming light
- in many Wright Group translation stage assembly `RR` is mounted on a manual XYZ stage, `XYZ`, which is in turn mounted on `TS`
- a mirror, `M2`, which directs light output from `RR` towards other down stream optics

We define a well-aligned delay stage assembly to be one that has $\left|\vec{k}_{\mathsf{in}}\right|$ parrallel to the direction of travel of `TS`. If a delay stage is misalligned, the far-field position of the beam off of `M2` (or more generally `RR`) will change when `TS` is at different positions. We also define the *far* position of the translation stage, $\mathtt{TS}_{\mathtt{far}}$, to be one in which the stage is farthest away from `M1` and `M2`. Conversely, we define the *near* position of the translation stage, $\mathtt{TS}_{\mathtt{near}}$, to be one in which the stage is closest to `M1` and `M2`.

In order to align the delay stage the following directions should be followed:

1. Align the delay stage assembly such that the beam which travels downstream from `M2` is taking the desired final path. During this stage ensure `TS` is at $\mathtt{TS}_{\mathtt{far}}$.

[1] According to the Wikipedia article on parallax: "Parallax is a displacement or difference in the apparent position of an object viewed along two different lines of sight, and is measured by the angle or semi-angle of inclination between those two lines." https://en.wikipedia.org/wiki/Parallax The Wright Group thusly uses a slight deviation from this standard defintion. Our definition would be: "Parallax is a displacement of the position of a beam, when the beam traverses two different translation stage settings." Specifically, our definition does not deal with *apparent* displacement, but rather *actual* displacement and it is not the position of the *observer* which is changing between cases but the position of an *optic* in the beam path.

[2] Some of the ideas in this appendix originally came from a guide prepared by Dr. Daniel Kohler and kept in the old group OneNote labnotebook.

2. Place an aperture, A1, (or a mask) downstream of M2 such that the output beam is centered in the aperture. If you are using a beam that is visible to the naked eye, place a detector behind A1 and use it to readout the beam position.
3. Close A1 to cut-out about half of the beams diameter or intensity—we want to make sure we are aligning to the center of our laser's mode.
4. Move to $\texttt{TS}_{\texttt{near}}$ and change either XYZ or M2 to ensure the beam off of M2 is centered through A1. Generally, I pick either XYZ or M2 to be the degree of freedom when aligning (but not a wishy-washy both). One rule-of-thumb is if A1 is close to M2, use XYZ as the adjustment, while if A1 is far from M2 then use M2 as the adjustment.
5. Move back to $\texttt{TS}_{\texttt{far}}$ and change M1 to ensure the beam off of M2 is centered through A1.
6. Iterate through steps 4 and 5 until the beam is centered through A1 when TS is at both $\texttt{TS}_{\texttt{near}}$ and $\texttt{TS}_{\texttt{far}}$

Appendix F On adjustable periscopes

OPAs output horizontal or vertically polarized electric fields according to which tuning process is used to generate the electric field. Oftentimes, a specific experiment will require a specific polarization for each electric field which interacts at the sample. Changing the polarization state of an electric field is generally accomplished by using a combination of one or more of the following optical tools:

- quarter wave plate: converts between circular and linearly polarized light
- half wave plate: rotates the polarization direction of linearly polarized light
- linear polarizer: passes light of a given linear polarization direction while absorbing or reflecting all other polarization states
- periscope: changes height of beam and can change or keep the polarization state of the original beam

The optical elements which compose the first three methods only work effectively in specific wavelength ranges, so when experiments are conducted over many wavelength ranges, periscopes are ideal. On the `fs table`, periscopes also facilitate bringing the output of the OPAs and Spitfire to the 5 inch table standard height.

Blaise Thompson[1] led a team who designed and constructed two adjustable periscopes (picture shown in Figure F.1). These periscopes bring the output of the OPA to 5 inches while either keeping or switching the linear polarization state of the OPA output. Both polarization configurations have the same path length, so source polarization can be switched without large changes to zero delay. All of this is done with just two (switched polarization) or three (kept polarization) reflections.

F.1 Alignment strategy

While these periscopes are easy to align (given the large number of kinematic degrees of freedom), their unique design means that it is not necessarily obvious what the correct alignment strategy is. The following strategy will always converge:

1. use two apertures along the output beamline
2. in `flipped polarization` mode (two mirror configuration):
    - use the stage (green X, Y) to align near aperture
    - use the upper mirror (yellow TA, TB) to align far aperture

[1] A previous, bare-bones version of this appendix existed as an unfinished/unpublished appendix of Blaise's thesis.

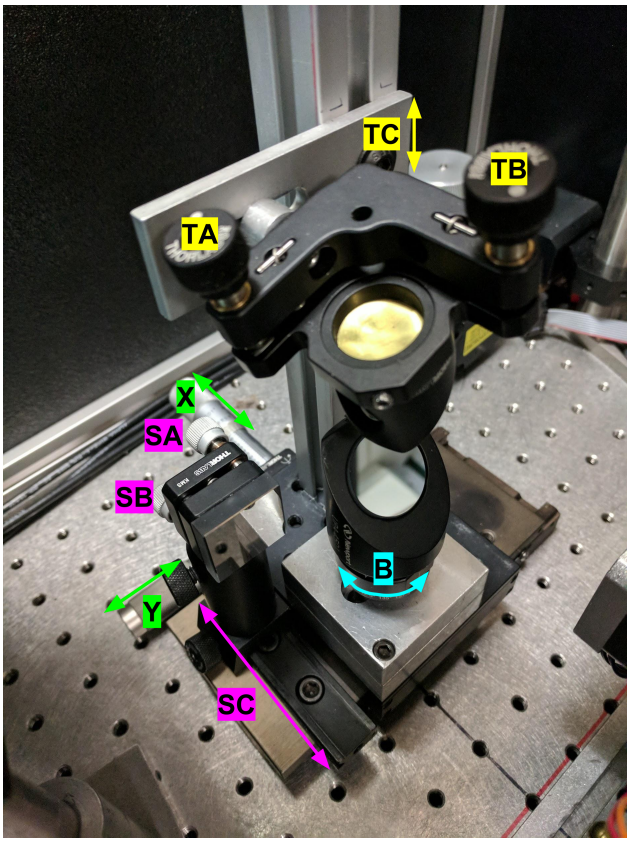

Figure F.1: Photo of adjustable periscope.

- iterate above

3. in `kept polarization` (three mirror configuration):
   - use stage X (green X) and upper mirror height (yellow TC, requires loosening of three bolts, sliding the L bracket, and then tightening the three bolts) to align near aperture
   - use lower mirror (pink SA, SB) to align far aperture
   - iterate above

The `kept polarization` alignment is derivative of the `fixed polarization` alignment. One must ensure that the `fixed polarization` is correctly aligned before moving onto aligning the `kept polarization`.

Mirror B (aqua) is magnetically mounted to switch between polarization conditions. Ensure that the lower turning mirror (pink) does not bump into mirror B (aqua) in polarization switching configuration. The lower turning mirror is on a rail (pink SC). This rail is a rough adjust for the same degree of freedom as pink SA. Adjust the rail only to ensure that the beam is roughly centered on the free aperture of the turning mirror.

F.2 Damage thresholds

The top optic of the periscope should be chosen carefully to avoid damage of itself and downstream optics. The output of signal, idler, or second-harmonic-signal from a TOPAS-C is generally much more intense than is allowed by the damage threshold of metallic mirrors. If intense OPA processes are filtered out before reaching the periscope (for instance if accomplishing DFG) then a metallic mirror may be used as the top optic of the periscope. The next section describes how the periscopes can be used to dump (transmit) a large amount of input light to a beam-dump and reflect only a small percentage of light to downstream optics. In this section we discuss damage thresholds that will need to be considered when choosing the top optic—this optic is usually the first non-LightConversion optic in the OPA output path.

Assuming 300 mW of signal output power from the OPA, 4 mm diameter, 1 kHz repetition rate, and 50 fs pulse width, the fluence out of the OPA is **2.4 mJ/cm^2** and 48 GW/cm^2 peak intensity.

The damage threshold (in fluence units) of an optic depends on at least the following parameters of the laser:[2]

1. pulsewidth of laser
2. color of laser
3. spotsize of laser on optic (damage threshold fluence increases as beam radius decreases)[449]
4. number of laser shots optic will need to interact with sequentially (more shots at a given fluence will more likely lead to damage)[450]
5. time between experiments (color centers can develop and then "heal" over the course of days)[451]

Given that laser induced damage is a complex parameter space, it is difficult to find relevant damage thresholds for the cases present on the `fs table`. Table F.1 has some typical damage thresholds. The Thorlabs thresholds are "certified values" in that you can operate the optic at the reported fluence with no damage. The values from von Conta [448] are failure values.

	ThorLabs	von Conta [448]
Fused Silica Broadband Dielectric Mirrors	0.2 J/cm^2 (800 nm, 99 fs, 1 kHz, ⌀0.166 mm)	
Ultrafast-Enhanced Silver Mirrors	0.18 J/cm^2 (800 nm, 52 fs, 1000 Pulses)	
Protected Silver Mirrors	3 J/cm^2 (1064 nm, 10 ns, 10 Hz, ⌀1.000 mm)	0.24 J/cm^2 (790 nm, 50 fs, 1 kHz, ⌀0.085 mm)
Fused Silica	7.5 J/cm^2 (810 nm, 10 ns, 10 Hz, ⌀0.133 mm)	1.5 J/cm^2 (790 nm, 50 fs, 1 kHz, ⌀0.085 mm)
Metallic Neutral Density Filters	0.025 J/cm^2 (355 nm, 10 ns, 10 Hz, ⌀0.772 mm	

Table F.1: Some damage thresholds provided by Thorlabs and von Conta [448]

We see that fused silica has an order of magnitude more damage tolerance than a silver mirror which in turn is an order of magnitude more resilient than some of our ND filters. Moreover, when the ND filter damage threshold fluence is scaled to 1 kHZ and 50 fs pulses it will be far below that which our OPAs provide—validating the need to dump light using the periscope. It appears like a standard silver mirror has a failure threshold 100 times larger than the OPA fluence present on the top mirror. However, this damage threshold does not account for month long exposures, mode hotspots, or dirty optics causing localized heating.

[2] von Conta [448] has a nice discussion on this topic

F.3 Use of a wedge in the top optic position

If filtering has not been accomplished, the periscope can *dump* (transmit) a fair portion of the incoming light by using a wedge (generally fused silica) in the top optic position. A wedge is used instead of a window to ensure back-reflections can explicitly be blocked and do not propagate with the first, desired reflection.

A downside of using a wedge to dump incoming light is that s (horizontal in the lab frame as observed by the top optic) and p (vertical in the lab frame as observed by the top optic) polarized light will have different power through-puts towards the downstream system. A Fresnel-like analysis for 45 degree incidence (see next subsection) shows that horizontally polarized light will have a maximum throughput of 8% through the periscope while vertically polarized light will have a maximum throughput of merely 0.6%. Practically, this means that signal (V) and idler (H) will have an order of magnitude different efficiencies of throughput. This problem can be mediated by using Daniel Kohler's "Brewster periscopes", which happen to be very persnickety in there align, but which do offer the ability to have a uniform throughput of vertically and horizontally polarized light and guaranteed vertically polarized light upon output.

F.3.1 Fresnel analysis

If we desire to think about the throughput of our periscope with a wedge in the top position, we need to consider the affects of different polirization states. The Fresnel equations (c.f. https://en.wikipedia.org/wiki/Fresnel_equations) give the Reflectance of s and p polarizations for light moving from medium with refractive index n_1 to a medium with refractive index n_2 and incident angle θ_i:

$$R_{\mathrm{s}} = \left|\frac{n_1\cos\theta_{\mathrm{i}} - n_2\cos\theta_{\mathrm{t}}}{n_1\cos\theta_{\mathrm{i}} + n_2\cos\theta_{\mathrm{t}}}\right|^2 = \left|\frac{n_1\cos\theta_{\mathrm{i}} - n_2\sqrt{1-\left(\frac{n_1}{n_2}\sin\theta_{\mathrm{i}}\right)^2}}{n_1\cos\theta_{\mathrm{i}} + n_2\sqrt{1-\left(\frac{n_1}{n_2}\sin\theta_{\mathrm{i}}\right)^2}}\right|^2 \tag{F.1}$$

$$R_{\mathrm{p}} = \left|\frac{n_1\cos\theta_{\mathrm{t}} - n_2\cos\theta_{\mathrm{i}}}{n_1\cos\theta_{\mathrm{t}} + n_2\cos\theta_{\mathrm{i}}}\right|^2 = \left|\frac{n_1\sqrt{1-\left(\frac{n_1}{n_2}\sin\theta_{\mathrm{i}}\right)^2} - n_2\cos\theta_{\mathrm{i}}}{n_1\sqrt{1-\left(\frac{n_1}{n_2}\sin\theta_{\mathrm{i}}\right)^2} + n_2\cos\theta_{\mathrm{i}}}\right|^2 \tag{F.2}$$

$$T_{\mathrm{s}} = 1 - R_{\mathrm{s}} \tag{F.3}$$

$$T_{\mathrm{p}} = 1 - R_{\mathrm{p}} \tag{F.4}$$

in which θ_i and θ_t are related by Snell's law: $n_1\sin(\theta_i) = n_2\sin(\theta_t)$. These equations can be used to visualize the how incident angle can drastically change the reflectance off of a surface

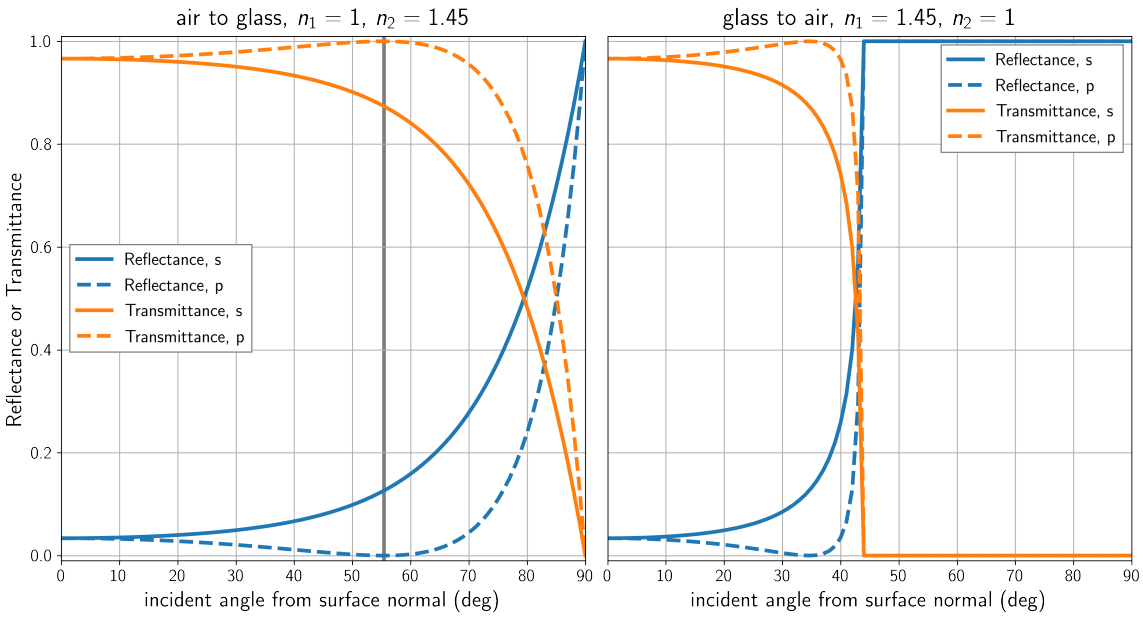

Figure F.2: Reflectance and transmittance of a homogeneous medium as a function of incident angle and polarization state. Vertical line at 55.4° denotes Brewster's angle, $\theta_B = \arctan\left(\frac{n_2}{n_1}\right)$. The abrupt discontinuity at 43.6° in the glass to air case demonstrates total internal reflection which onsets at $\theta_c = \arcsin\left(\frac{n_2}{n_1}\right)$.

Appendix G On calculating the fluence of a laser

G.1 Introduction

Oftentimes one desires to characterize the flux of a laser beam. It can be confusing to put all of the pieces together to calculate how much energy per unit area is impinged upon a sample. The purpose of this appendix is to elucidate the framework required to take values that can be measured in lab and to convert them into values useful in a model or for describing your laser to a colleague. The main result of this appendix is that a good metric for fluence (in units of Jm^{-2}) is

$$\mathcal{F} = \frac{P}{2\ln(2)\pi\nu_{\mathrm{rep}}\mathrm{HWHM}^2} \approx \frac{0.2296 \cdot P}{\nu_{\mathrm{rep}}\mathrm{HWHM}^2} \tag{G.1}$$

in which P is the power in watts of the laser, ν_{rep} is the laser's repetition rate in hertz, and HWHM is the half-width-at-half-maximum in meters of the focused laser beam at the sample position. In Section G.3.1 and Section G.3.2 this appendix describes two related ways that the HWHM of a laser can be measured using a translation stage and a razor blade. There are two "sub-appendices" to this appendix which lay out some useful function definitions and relations (Section G.5) and a result of Poynting's Theorem which we use to calculate the total power flow of a plane wave laser (Section G.6).

G.2 Gaussian beams

The complex electric field, E, of a laser beam in cylindrical coordinates within the paraxial approximation is generally described to first order by a TEM_{00} Gaussian beam.

$$\tilde{E}(z,r,t) = E(z,r)\exp\left[-i\omega t\right] + \text{c.c.} \tag{G.2}$$

$$E(z,r) = E_0\left(\frac{w_0}{w}\right)\exp\left[-i\psi\right]\exp\left[-\frac{r^2}{w^2}\right]\exp\left[ik\left(z+\frac{r^2}{2R}\right)\right] \tag{G.3}$$

$$w(z) \equiv w_0\sqrt{1+\frac{z^2}{z_R^2}} \qquad 1/e \text{ spot size} \tag{G.4}$$

$$z_R \equiv \frac{\pi w_0^2}{\lambda} \qquad \text{Rayleigh range} \tag{G.5}$$

$$R(z) \equiv z + \frac{z_R^2}{z} \qquad \text{Wavefront radius of curvature} \tag{G.6}$$

$$\psi(z) \equiv \arctan\left[\frac{z}{z_R}\right] \qquad \text{Guoy phase} \tag{G.7}$$

The electric field has angular frequency, ω, wave number, k, and wavelength, λ. $E_0 = E(0,0)$ is the electric field amplitude (and phase) at the origin at time 0, The smallest waist of this electric field is at $z = 0$ with a value of w_0. Note that the Rayleigh range customarily defines the cutoff between the "near-field" (Fresnel) and "far-field" (Fraunhofer) regions for a beam propagating out from its waist; the "confocal parameter" of a beam is thusly given by $2z_R$. The entire evolution of the beam is specified by knowing the frequency/wavelength of the field and the location/size of the beam waist.

At $z = 0$, the location of the transverse beam waist, the electric field amplitude, E_0 is rather simple.

$$E(z=0,r) = E_0\exp\left[-\frac{r^2}{w_0^2}\right] \tag{G.8}$$

The intensity of our electric field (see Section G.6 for derivation) is given by $I = \frac{1}{2}\epsilon_0 c|E|^2$. So the spatial distribution of intensity is given by

$$I(z=0,r) = \frac{1}{2}\epsilon_0 c|E_0|^2\exp\left[-\frac{2r^2}{w_0^2}\right] \tag{G.9}$$

$$= I_0\exp\left[-\frac{2r^2}{w_0^2}\right] \tag{G.10}$$

in which it is now clear that w_0 is the $1/e^2$ width on the *intensity* level. The purpose of the next section is to describe how to measure w_0.

G.3 Razor blade formalism

Generally one is not able to perform spatial measurements in cylindrical coordinates accurately.[1] So, in order to measure w_0 we transform Equation G.9 to Cartesian coordinates by $r^2 \to x^2 + y^2$

$$I(x, y, z = 0) = \frac{1}{2}\epsilon_0 c|E_0|^2 \exp\left[-\frac{2x^2}{w_0^2}\right] \exp\left[-\frac{2y^2}{w_0^2}\right]. \tag{G.11}$$

A quantity that is easily measurable in lab is the total power of a beam, P. P is time and space averaged. If our laser is pulsed with a repetition rate given by ν_{rep} and we say Equation G.11 defines the *pulse* intensity, then the power measured by our power meter will be

$$P = \nu_{\text{rep}} \iint_{-\infty}^{+\infty} I(x, y, z = z')\mathrm{d}x\mathrm{d}y \tag{G.12}$$

in which we set $z' = 0$ for convenience in our calculation, the result will be the same no matter what value is picked. Substitution of Equation G.11 into Equation G.12 yields

$$P = \nu_{\text{rep}} \iint_{-\infty}^{+\infty} \frac{1}{2}\epsilon_0 c|E_0|^2 \exp\left[-\frac{2x^2}{w_0^2}\right] \exp\left[-\frac{2y^2}{w_0^2}\right]\mathrm{d}x\mathrm{d}y \tag{G.13}$$

$$= \frac{1}{2}\nu_{\text{rep}}\epsilon_0 c|E_0|^2 \int_{-\infty}^{+\infty} \exp\left[-\frac{2x^2}{w_0^2}\right]\mathrm{d}x \int_{-\infty}^{+\infty} \exp\left[-\frac{2y^2}{w_0^2}\right]\mathrm{d}y \tag{G.14}$$

$$= \frac{\pi}{4}\nu_{\text{rep}}\epsilon_0 c|E_0|^2 w_0^2 \tag{G.15}$$

in which we used the standard Gaussian integral identity—see Section G.5. Now we can calculate the peak intensity, I_0, if we know the total power in the beam rearranging the above equation we can find

$$P = \frac{\pi}{2}\nu_{\text{rep}} w_0^2 \left(\frac{1}{2}\epsilon_0 c\,|E_0|^2\right) \tag{G.16}$$

$$I_0 = \frac{1}{2}\epsilon_0 c\,|E_0|^2 \tag{G.17}$$

$$\implies P = \frac{\pi}{2}\nu_{\text{rep}} w_0^2 I_0 \tag{G.18}$$

$$\implies I_0 = \frac{2P}{\nu_{\text{rep}} w_0^2 \pi} \tag{G.19}$$

Equation G.15 gives the *total* power in a beam. Now, if we slide a razor blade across the beam (say in the X direction) at $z = 0$ the measured power, $P(X)$, will be attenuated from P to 0. There are two common strategies for using a razor blade to measure w_0. The first strategy is to measure $P(X)$ for many different X positions of the razor blade and to fit the resultant curve to extract w_0. The second strategy is to experimentally determine the values of X that satisfy $P(X_{10\%}) = 0.1P$

[1] Some of this section is based on a lab manual section (http://www.physics.iitm.ac.in/~ph5060/manuals/Gaussianlaserbeam.pdf) hosted by the Department of Physics at the Indian Institute of Technology Madras, Chennai. I do not know who wrote that document.

and $P(X_{90\%}) = 0.9P$ (20% and 80% are sometimes used) and then relate those values to w_0. We will explicate both strategies.

G.3.1 Razor blade measurement with curve fitting

The measured power as a function of razor blade position is given by

$$P(X) = P - \frac{2P}{w_0^2\pi}\int_{-\infty}^{X}\exp\left[-\frac{2x^2}{w_0^2}\right]\mathrm{d}x\int_{-\infty}^{+\infty}\exp\left[-\frac{2y^2}{w_0^2}\right]\mathrm{d}y \tag{G.20}$$

$$= P - \frac{P}{w_0}\sqrt{\frac{2}{\pi}}\int_{-\infty}^{X}\exp\left[-\frac{2x^2}{w_0^2}\right]\mathrm{d}x. \tag{G.21}$$

Our goal is to now cast Equation G.21 into the form of the error function—see Section G.5 for a review. Consider,

$$\int_{-\infty}^{X}\exp\left[-\frac{2x^2}{w_0^2}\right]\mathrm{d}x = \int_{-\infty}^{0}\exp\left[-\frac{2x^2}{w_0^2}\right]\mathrm{d}x + \int_{0}^{X}\exp\left[-\frac{2x^2}{w_0^2}\right]\mathrm{d}x \tag{G.22}$$

$$= \sqrt{\frac{\pi}{8}}w_0 + \int_{0}^{X}\exp\left[-\frac{2x^2}{w_0^2}\right]\mathrm{d}x \tag{G.23}$$

in which we used the integral identity given by Equation G.57. We now do a change of variable s.t. $u^2 = \frac{2x^2}{w_0^2}$ and $\mathrm{d}x = \frac{w_0\mathrm{d}u}{\sqrt{2}}$. Hence,

$$\int_{-\infty}^{X}\exp\left[-\frac{2x^2}{w_0^2}\right]\mathrm{d}x = \sqrt{\frac{\pi}{8}}w_0 + \frac{w_0}{\sqrt{2}}\int_{0}^{\frac{\sqrt{2}X}{w_0}}\exp\left[-u^2\right]\mathrm{d}u \tag{G.24}$$

$$= \sqrt{\frac{\pi}{8}}w_0 + \frac{w_0\sqrt{\pi}}{2\sqrt{2}}\mathrm{erf}\left[\frac{\sqrt{2}X}{w_0}\right] \tag{G.25}$$

$$= \sqrt{\frac{\pi}{8}}w_0\left(1 + \mathrm{erf}\left[\frac{\sqrt{2}X}{w_0}\right]\right). \tag{G.26}$$

Substitution of Equation G.26 into Equation G.21 yields

$$P(X) = P - \frac{P}{w_0}\sqrt{\frac{2}{\pi}}\sqrt{\frac{\pi}{8}}w_0\left(1 + \mathrm{erf}\left[\frac{\sqrt{2}X}{w_0}\right]\right) \tag{G.27}$$

$$= P - \frac{P}{2}\left(1 + \mathrm{erf}\left[\frac{\sqrt{2}X}{w_0}\right]\right) \tag{G.28}$$

$$= \frac{P}{2}\mathrm{erfc}\left[\frac{\sqrt{2}X}{w_0}\right]. \tag{G.29}$$

Hence, if we slide a razor blade across the smallest part of the beam and measure the total transmitted power the width of the beam may be recovered by fitting a three parameter function like

$$P(X) = \frac{p_0}{2}\text{erfc}\left[\frac{\sqrt{2}\,(X - p_1)}{p_2}\right] \tag{G.30}$$

in which $p_2 = w_0$. This is the desired result.

G.3.2 Two point razor blade measurement

We now consider a two point measure of the beam waist. Consider the positions of our razor blade which makes the following equations true

$$P\left(X_{10\%}\right) = 0.1P = \frac{P}{2}\text{erfc}\left[\frac{\sqrt{2}\,(X_{10\%} - X_0)}{w_0}\right] \tag{G.31}$$

$$P\left(X_{90\%}\right) = 0.9P = \frac{P}{2}\text{erfc}\left[\frac{\sqrt{2}\,(X_{90\%} - X_0)}{w_0}\right] \tag{G.32}$$

in which X_0 has been added as an experimental offset for the zero position of the razor blade relative to the beam waist. Numerical computation shows that these equations may be true when the arguments of the complementary error functions are given by

$$\frac{\sqrt{2}\,(X_{10\%} - X_0)}{w_0} \approx 0.9062 \tag{G.33}$$

$$\frac{\sqrt{2}\,(X_{90\%} - X_0)}{w_0} \approx -0.9062 \tag{G.34}$$

$$\implies \frac{\sqrt{2}}{w_0}\left(X_{10\%} - X_{90\%}\right) \approx 0.9062 - (-0.9062) \tag{G.35}$$

$$\implies w_0 \approx 0.7803\left(X_{10\%} - X_{90\%}\right) \tag{G.36}$$

$$\implies \text{FWHM} \approx 0.9187\left(X_{10\%} - X_{90\%}\right). \tag{G.37}$$

This is the desired result. The size of a beam at its waist may be measured by merely finding at what razor blade position the beam is at 10% and 90% its initial power. If the beam is radially unsymmetrical or deviating form Gaussian behavior, this metric will become inadequate.

G.4 Fluence calculations

There are many metrics for recording the flux of a laser beam. Some common ones include

$$\text{fluence} = \mathcal{F} = \frac{\text{laser pulse energy}}{\text{effective focal spot area}} \tag{G.38}$$

$$\text{intensity} = I = \frac{\text{laser peak power}}{\text{effective focal spot area}} \tag{G.39}$$

The peak power is generally defined as

$$\text{laser peak power} = \frac{\text{laser pulse energy}}{\text{effective pulse duration}} \tag{G.40}$$

The SI units for fluence are $\mathrm{Jm^{-2}}$ but are oftentimes reported as $\mu\mathrm{J\ cm^{-2}}$. The SI units for intensity are $\mathrm{Wm^{-2}}$ but are oftentimes reported as $\mathrm{W\ cm^{-2}}$ with a prefix of T or G on the watts. In the high-harmonic generation and THz spectroscopy communities, peak electric field amplitudes are oftentimes reported instead of intensities; the units are generally $\mathrm{Vm^{-1}}$ or $\mathrm{VÅ^{-1}}$.

The problem with the above definitions of fluence and intensity is their use of an "effective focal spot area"—as far as I can tell, there is no rigidly agreed upon metric for this effective area. One way that I have calculated fluence in the past, which I now think is non-ideal, is to model the laser beam as a cylindrical "flat-top" pulse. The fluence is then

$$\mathcal{F}_{\text{flat-top}} = \frac{E_p}{\pi R^2} \tag{G.41}$$

in which R is some suitable metric of the beam waist, for this work we shall say $R = \text{HWHM} = \frac{\text{FWHM}}{2}$ and E_p is the pulse energy.

I think a more holistic way to calculate fluence is to consider the average intensity felt by a point inside of the area (volume) swept out by R. Recalling that the differential volume element is given by $\mathrm{d}V = r\mathrm{d}r\mathrm{d}\theta\mathrm{d}z$ we have the average intensity

$$I_{\text{average}} = \frac{1}{V}\int_0^R \int_0^{2\pi} \int_0^Z I\left(r,\theta,z\right) r\mathrm{d}r\mathrm{d}\theta\mathrm{d}z. \tag{G.42}$$

For a sample with no absorption and radial symmetry we have

$$I\left(r,\theta,z\right) = I_0 \exp\left[-\frac{2r^2}{w_0^2}\right] \tag{G.43}$$

were there to be absorption we would need an additional factor of $\exp\left[-\alpha z\right]$. Letting $V = \pi R^2 Z$ be a cylindrical volume we have

$$I_{\text{average}} = \frac{1}{\pi R^2 Z}\left(2\pi Z\right)\int_0^R I_0 \exp\left[-\frac{2r^2}{w_0^2}\right] r\mathrm{d}r \tag{G.44}$$

$$= \frac{2I_0}{R^2}\int_0^R \exp\left[-\frac{2r^2}{w_0^2}\right] r\mathrm{d}r \tag{G.45}$$

$$= \frac{2I_0}{R^2}\left(\frac{w_0^2}{4}\left\{1 - \exp\left[-\frac{2R^2}{w_0^2}\right]\right\}\right) \tag{G.46}$$

Letting $R = \text{HWHM}$ and evaluating the expression we get

$$I_{\text{average}} = \frac{2I_0}{\frac{w_0^2 \ln\left(2\right)}{2}}\left(\frac{w_0^2}{8}\right) \tag{G.47}$$

$$= \frac{I_0}{2\ln\left(2\right)} \approx 0.7213 \cdot I_0 \tag{G.48}$$

So the fluence using this metric will be

$$\mathcal{F}_{\text{average}} = \frac{0.7213 \cdot E_p}{\pi \text{HWHM}^2}. \tag{G.49}$$

Remember that the energy in a pulse is merely

$$E_p = \frac{P}{\nu_{\text{rep}}}. \tag{G.50}$$

We are now in the position to take values we can measure in the lab and calculate fluences! In performing these calculations we have neglected all substrate interference effects which can change the fluence actually experienced by a sample.

G.5 Gaussian and Error functions

The Normal (Gaussian) distribution has two equivalent definitions depending on if a width, σ, and non-zero mean, μ, are included

$$\phi(x) = \left[\sqrt{2\pi}\right]^{-1} \exp\left[-\frac{x^2}{2}\right] \tag{G.51}$$

$$\Phi(x) = \left[\sigma\sqrt{2\pi}\right]^{-1} \exp\left[-\frac{(x-\mu)^2}{2\sigma^2}\right]. \tag{G.52}$$

ϕ is an even function. A bit of algebra shows that the full width at half maximum, FWHM, and $1/e^2$ width, w, are given by

$$\text{FWHM} = 2\sqrt{2\ln[2]}\sigma \approx 2.355\sigma \tag{G.53}$$

$$w = 2\sigma = \frac{\text{FWHM}}{\sqrt{2\ln[2]}} \approx 0.8493 \cdot \text{FWHM}. \tag{G.54}$$

A common definite integral of the Gaussian distribution is

$$\int_{-\infty}^{\infty} \exp\left[-\left(ax^2 + bx + c\right)\right] \mathrm{d}x = \sqrt{\frac{\pi}{a}} \exp\left[\frac{b^2 - 4ac}{4a}\right] \tag{G.55}$$

$$\implies \int_{-\infty}^{\infty} \exp\left[-\frac{2x^2}{w^2}\right] \mathrm{d}x = w\sqrt{\frac{\pi}{2}}. \tag{G.56}$$

Another common definite integral is

$$\int_{-\infty}^{0} \exp\left[-ax^2\right] \mathrm{d}x = \int_{0}^{\infty} \exp\left[-ax^2\right] \mathrm{d}x = \frac{1}{2}\sqrt{\frac{\pi}{a}} \tag{G.57}$$

The error function is defined by

$$\operatorname{erf}[x] \equiv \frac{2}{\sqrt{\pi}} \int_0^x \exp\left[-t^2\right] \mathrm{d}t \tag{G.58}$$

and is an odd function. The complementary error function is defined as

$$\operatorname{erfc}[x] \equiv 1 - \operatorname{erf}[x] \tag{G.59}$$

It has some special values

$$\operatorname{erfc}[-\infty] = 2 \tag{G.60}$$
$$\operatorname{erfc}[0] = 1 \tag{G.61}$$
$$\operatorname{erfc}[\infty] = 0. \tag{G.62}$$

G.6 Power flow per unit area of an electromagnetic plane wave

Consider a plane electromagnetic wave with an x-polarized electric field

$$E(t, z) = E_0 \cos(kz - \omega t). \tag{G.63}$$

In this section we will prove that the total power flow per unit area (sometimes just called the "intensity") for this wave is

$$\langle I_{total} \rangle = \frac{1}{2} \epsilon_0 c E_0^2. \tag{G.64}$$

We first recall that in a vacuum the energy density of an electromagnetic field is given by Equation G.65, which is a direct consequence of Poynting's Theorem. In this equation the energy density of the electric field is given by Equation G.66 where as the energy density of the magnetic field is given by Equation G.67

$$U = \frac{\epsilon_0}{2} \vec{E}^2 + \frac{1}{2\mu_0} \vec{B}^2 = U_E + U_B \tag{G.65}$$
$$U_E = \frac{\epsilon_0}{2} \vec{E}^2 \tag{G.66}$$
$$U_B = \frac{1}{2\mu_0} \vec{B}^2. \tag{G.67}$$

Next, we write out a form for both the electric and magnetic fields and their squares.

$$\vec{E}(t, z) = E_0 \cos(kz - \omega t) \hat{x} \tag{G.68}$$
$$\vec{B}(t, z) = \frac{E_0}{c} \cos(kz - \omega t) \hat{y} \tag{G.69}$$
$$\vec{E}^2(t, z) = E_0^2 \cos^2(kz - \omega t) \hat{x} \tag{G.70}$$
$$\vec{B}^2(t, z) = \frac{E_0^2}{c^2} \cos^2(kz - \omega t) \hat{y} \tag{G.71}$$

We may then substitute Equation G.70) and Equation G.71 into Equation G.66 and Equation G.67 to get another expression for the energy densities (note, we disregard unit vectors here).

$$U_E = \frac{\epsilon_0 E_0^2}{2} \cos^2(kz - \omega t) \tag{G.72}$$

$$U_B = \frac{E_0^2}{2\mu_0 c^2} \cos^2(kz - \omega t) \tag{G.73}$$

Next, we desire to calculate the spatially averaged energy density, $\langle U_E \rangle$ and $\langle U_B \rangle$. We do this by picking a time value, say $t = t_0$ and then integrating over the spatial dependence of Equation G.72 and Equation G.73. But we need not integrate over the entirety of the spatial dependance, we merely need to integrate over one phase cycle, z_0 to $z_0 + 2\pi$, and then divide that by the space integrated over, $\Delta z = 2\pi$. Hence,

$$\langle U_E \rangle = \frac{1}{\Delta z} \int_{z_0}^{z_0+2\pi} (U_E(z, t = t_0))\, dz = \frac{1}{2\pi} \int_{z_0}^{z_0+2\pi} \left(\frac{\epsilon_0 E_0^2}{2} \cos^2(kz - \omega t) \right) dz \tag{G.74}$$

$$\langle U_B \rangle = \frac{1}{\Delta z} \int_{z_0}^{z_0+2\pi} (U_B(z, t = t_0))\, dz = \frac{1}{2\pi} \int_{z_0}^{z_0+2\pi} \left(\frac{E_0^2}{2\mu_0 c^2} \cos^2(kz - \omega t) \right) dz. \tag{G.75}$$

We now recall the cute math fact that $\int_n^{n+2\pi} \left(\cos^2(\theta)\right) d\theta = \pi$. Hence, Equation G.74 and Equation G.75 simplify to Equation G.76 and Equation G.77, in which we have used the fact that $c = \frac{1}{\sqrt{\mu_0 \epsilon_0}} \Rightarrow \epsilon_0 = \frac{1}{\mu_0 c^2}$.

$$\langle U_E \rangle = \frac{\pi}{2\pi} \left(\frac{\epsilon_0 E_0^2}{2} \right) = \frac{\epsilon_0 E_0^2}{4} \tag{G.76}$$

$$\langle U_B \rangle = \frac{\pi}{2\pi} \left(\frac{E_0^2}{2\mu_0 c^2} \right) = \frac{\epsilon_0 E_0^2}{4}. \tag{G.77}$$

These equations explicate the spatially averaged energy density for the electric and magnetic fields. Now, if the wave moves at a speed of c we may easily calculate the average power flow per unit area for each field, $\langle I_E \rangle$ and $\langle I_B \rangle$. We note that power is energy transfer (work) integrated over time. But, because we have already calculated an *averaged* energy density, we may merely calculate the intensity (the power through a surface area) by multiplying our average density by the speed that the wave moves through the surface. Hence,

$$\langle I_E \rangle = c \cdot \langle U_E \rangle = \frac{c\epsilon_0 E_0^2}{4} \tag{G.78}$$

$$\langle I_B \rangle = c \cdot \langle U_B \rangle = \frac{c\epsilon_0 E_0^2}{4}. \tag{G.79}$$

Finally, the total intensity (power flow per unit area) is given by the summation of all the various field's individual intensities. Hence,

$$\langle I_{total} \rangle = \langle I_E \rangle + \langle I_B \rangle = \frac{c\epsilon_0 E_0^2}{4} + \frac{c\epsilon_0 E_0^2}{4} = \frac{c\epsilon_0 E_0^2}{2} \tag{G.80}$$

This is the desired result.

Appendix H Elliott model extended to $\chi^{(2u+1)}$ for $u \in \mathbb{W}$

We desire to calculate the third order optical susceptibility expected from Wannier excitons near resonance. We extend the treatment in 3D first authored by Elliott [312] and extended to 2D by Shinada and Sugano [313] in which the imaginary component of the first order susceptibility was calculated. Our derivation is informed by Haug and Koch [316], Tanguy [314, 315], and Pedersen and Cornean [452] and makes the following assumptions and simplifications:

1. All non-resonant and forbidden transitions are disregarded.
2. All broadening of transitions is described by a phenomenological dephasing/damping rate, Γ, and accounted for by convolving the penultimum result with a complex Lorentzian.
3. Band dispersion is described by the effective mass approximation with parabolic conduction and valence bands with a bandgap of E_g and electron (hole) effective masses of m_e (m_h). The dispersions are $E_c[k] = E_g + \frac{\hbar^2 k^2}{2m_e}$ for the conduction band and $E_v[k] = -\frac{\hbar^2 k^2}{2m_h}$ for the valence band.
4. The transition dipole moment between these two bands (with no Coulomb interaction), d_{cv}, does not depend on k and is a constant.
5. The electron-hole pair is described by the Wannier equation (in relative coordinates)

$$-\left[\frac{\hbar^2 \nabla_r^2}{2m_r} + V[r]\right] \psi_\ell(r) = E_v \psi_\ell[r]$$

   in which ψ_ℓ describes the relative motion of electron and hole on a length scale greater than the lattice constant of the material, $V[r] = \frac{e^2}{\varepsilon_0 r}$ is the Coulomb potential, and $m_r^{-1} = m_e^{-1} + m_h^{-1}$ is the system's reduced mass . ψ_ℓ are given by the Laguerre polynomials.

The optical susceptibility from an electron-hole-pair near resonance with a driving field of frequency ω is

$$\chi_\Gamma^{(2u+1)}\left[\hbar\omega_u\right] = \chi^{(2u+1)}\left[\hbar\omega_u\right] * \mathcal{L}\left[\hbar\omega_u; \Gamma\right] \tag{H.1}$$

in which the output frequency is defined by $\omega_u \equiv (2u+1)\omega$ with $u \in \mathbb{Z}^+$ such that $u = 0$ corresponds to first order processes like absorption and reflection while $u = 1$ corresponds to third order processes like third harmonic generation. Within this parameterization, a third order process interacts between the same two states 4 times through the interaction series; for instance, one Louiville pathway for such an interaction series is

$$gg \to ag \to gg \to ag \to gg. \tag{H.2}$$

Equation H.1 is composed of sticks, $\chi^{(2u+1)}\left[\hbar\omega_u\right]$, convolved with a causal Lorentzian

$$\mathcal{L}\left[E;E_0,\Gamma\right] \equiv \sqrt{\frac{\Gamma}{\pi}}\frac{1}{E_0 - E - i\Gamma} \tag{H.3}$$

which satisfys the normalization condition $\int_{-\infty}^{\infty}\left|\mathcal{L}\left[E\right]\right|^2 \mathrm{d}E = 1$.

Our extension of the Elliott model starts with relating the susceptibility to transition dipoles and the probability of initially finding a conduction band electron and a valence band hole within the same unit cell

$$\chi^{(2u+1)}\left[\hbar\omega_u\right] = A\left|d_{cv}\right|^{2+2u}\sum_{\ell}\left|\psi_\ell\left[r=0\right]\right|^{2+2u} \tag{H.4}$$

in which A is a collection of proportionality constants which include system dependent values like the exciton Bohr radius. The value of $\left|\psi_\ell\left(r=0\right)\right|^{2+2u}$ will be dependent on whether the exciton state is bound ($E_\ell < 0$) or unbound ($E_\ell > 0$) and if the system is considered to be spanning two or three dimensions. Accordingly, we break up Equation H.4 and suppress functional notion for brevity

$$\chi_{\mathrm{3D}}^{(2u+1)} = A\left|d_{cv}\right|^{2+2u}\left(\zeta_{\mathrm{3D}}^{\mathrm{bound}} + \zeta_{\mathrm{3D}}^{\mathrm{unbound}}\right) \tag{H.5}$$

$$\chi_{\mathrm{2D}}^{(2u+1)} = A\left|d_{cv}\right|^{2+2u}\left(\zeta_{\mathrm{2D}}^{\mathrm{bound}} + \zeta_{\mathrm{2D}}^{\mathrm{unbound}}\right). \tag{H.6}$$

The bound exciton energies are given by[316]

$$E_\ell^{\mathrm{3D}} = -\frac{E_0}{\ell^2} \text{ with } \ell \in \mathbb{Z}^+ = \{1,2,3,\dots\} \tag{H.7}$$

$$E_\ell^{\mathrm{2D}} = -\frac{E_0}{\left(\ell+1/2\right)^2} \text{ with } \ell \in \mathbb{Z}^* = \{0,1,2,\dots\} \tag{H.8}$$

in which $E_0 = \frac{e^4 m_r}{2\varepsilon_0^2\hbar^2}$ is the exciton Rydberg energy. We note that the binding energy, E_b, is E_0 in 3D and $4E_0$ in 2D. These bound states give contributions of[316, 312, 313]

$$\zeta_{\mathrm{3D}}^{\mathrm{bound}} = \sum_{\ell=1}^{\infty}\left(\frac{4}{\ell^3}\right)^{u+1}\delta\left[\Delta + \frac{1}{\ell^2}\right] \tag{H.9}$$

$$\zeta_{\mathrm{2D}}^{\mathrm{bound}} = \sum_{\ell=0}^{\infty}\left(\frac{4}{\left(\ell+\frac{1}{2}\right)^3}\right)^{u+1}\delta\left[\Delta + \frac{1}{\left(\ell+\frac{1}{2}\right)^2}\right] \tag{H.10}$$

in which δ is the Dirac Delta Distribution and $\Delta \equiv \frac{\hbar\omega_u - E_g}{E_0}$. Note that in a system with finite temperature and disorder, few, if any, bound transitions will noticeably contribute to the susceptibility.

The unbound states of the exciton form a continuum. When $\hbar\omega_u - E_g > 0$ it is appropriate to use the continuous analog of the summation found in Equation H.4 and weight the transitions by a

density of states, ρ,

$$\rho_{3\mathrm{D}} \propto \Theta\left[\Delta\right]\sqrt{\Delta} \tag{H.11}$$

$$\rho_{2\mathrm{D}} \propto \Theta\left[\Delta\right] \tag{H.12}$$

in which Θ is the Heaviside step function. The transitions have strength scaled by the "Coulomb enhancement factor", C, which approaches unity as $E_0 \to 0$ and are given by[316, 312, 313]

$$C_{3\mathrm{D}} = \left(\frac{\exp\left[\pi/\sqrt{\Delta}\right]}{\sqrt{\Delta}\sinh\left[\pi/\sqrt{\Delta}\right]}\right)^{u+1} \tag{H.13}$$

$$C_{2\mathrm{D}} = \left(\frac{\exp\left[\pi/\sqrt{\Delta}\right]}{\cosh\left[\pi/\sqrt{\Delta}\right]}\right)^{u+1} \tag{H.14}$$

These enhancement factors take into account that the unbound electron-hole-pair is over a potential well at finite separation distance. These enhancments fall out due to $\left|\psi_\ell\left[r=0\right]\right|^2$ not being a constant for states slightly above the bandedge. Accordingly

$$\zeta_{3\mathrm{D}}^{\mathrm{unbound}} = \left(\frac{\exp\left[\pi/\sqrt{\Delta}\right]}{\sqrt{\Delta}\sinh\left[\pi/\sqrt{\Delta}\right]}\right)^{u+1} \Theta\left[\Delta\right]\sqrt{\Delta} \tag{H.15}$$

$$\zeta_{2\mathrm{D}}^{\mathrm{unbound}} = \left(\frac{\exp\left[\pi/\sqrt{\Delta}\right]}{\cosh\left[\pi/\sqrt{\Delta}\right]}\right)^{u+1} \Theta\left[\Delta\right]. \tag{H.16}$$

We may put all of the pieces together to reach the desired result

$$\chi_{3\mathrm{D}}^{(2u+1)}\left[\hbar\omega_u\right] = A\left|d_{cv}\right|^{2+2u}\left\{\sum_{\ell=1}^{\infty}\left(\frac{4}{\ell^3}\right)^{u+1}\delta\left[\Delta+\frac{1}{\ell^2}\right] + \left(\frac{\exp\left[\pi/\sqrt{\Delta}\right]}{\sqrt{\Delta}\sinh\left[\pi/\sqrt{\Delta}\right]}\right)^{u+1}\Theta\left[\Delta\right]\sqrt{\Delta}\right\} \tag{H.17}$$

$$\chi_{2\mathrm{D}}^{(2u+1)}\left[\hbar\omega_u\right] = A\left|d_{cv}\right|^{2+2u}\left\{\sum_{\ell=0}^{\infty}\left(\frac{4}{\left(\ell+\frac{1}{2}\right)^3}\right)^{u+1}\delta\left[\Delta+\frac{1}{\left(\ell+\frac{1}{2}\right)^2}\right] + \left(\frac{\exp\left[\pi/\sqrt{\Delta}\right]}{\cosh\left[\pi/\sqrt{\Delta}\right]}\right)^{u+1}\Theta\left[\Delta\right]\right\} \tag{H.18}$$

in which all frequency dependence is encoded in the unit-less Δ. When convolved with a causal Lorentzian, the delta functions of the bound states will become Lorentzians centered at values given by Equation H.7 and Equation H.8; the bound contributions will of course also be smeared.

Appendix I Enabling *ab initio* predictions of acetonitrile response for non-linear spectroscopies

I originally wrote some of this appendix as part of a final project for Prof. Qiang Cui's Electronic Structure Theory class which I took in the fall of 2016. The goal of that project was to use *ab initio* methods to calculate the DOVE spectrum of acetonitrile. I ran out of time before I could figure out how to correctly implement the *ab initio* calculations in `Gaussian09`. I had initially thought the project would be easy because I would be largely copying the theoretical structure described in Kwak et al. [453]. However, I found the derivation of DOVE intensities in Kwak et al. [453] to be severely lacking in details, so I spent most of my time attempting to understand their derivation. This appendix provides pedagogical details about Kwak et al. [453]'s derivation.

I.1 Introduction

Coherent multidimensional spectroscopy (CMDS) is the optical analog to multidimensional NMR. There are myriad of different multidimensional spectroscopies each with its strengths, weaknesses, and catchy/cringe-worthy initialism/acronym. One such spectroscopy is Doubly Vibrationally Enhanced (DOVE) infrared four wave mixing (FWM). The Wright Group pioneered this spectroscopy in 1999.[454, 455] The Wright Group then spent many years understanding and modeling the intricacies of this spectroscopy.[456, 457, 458, 459] The Cho Group worked to rigorously predict the magnitude of expected response from DOVE.[460, 453] The Klug Group has since used this spectroscopy [1] to great success to identify/quantify peptides in proteins, determine intermolecular structure, and many more feats generally reserved for 2D NMR.[461, 462, 463, 464]

The strength of DOVE, like many CMDS methods, is its intrinsic sensitivity to anharmonicities in the potential energy surface of the system of interest. DOVE's multi-dimensional nature also allows for spectral decongestion if a sample's 1D spectra is fraught with many resonances. In early experiments the multidimensional aspect of DOVE came from two tunable mid-IR lasers which were scanned over vibrational resonances.

DOVE is formally composed of three pathways as shown in Figure I.1. The difference in the pathways involves the time-ordering of excitation pulses. Canonically, DOVE is defined as having two IR pulses which are vibrationally resonant and one visible pulse which is non-resonant and causes a Raman-like transition. The phase-matching associated with DOVE which defines how the

[1] The Klug Group does not use the acronym DOVE, but instead calls it electron–vibration–vibration two–dimensional infrared spectroscopy with the intialism EVV 2D–IR

individual pulses interact with the sample is $\vec{k}_1 - \vec{k}_2 + \vec{k}_3$ for $\vec{k}_i$ being a wavevector of an excitation laser.

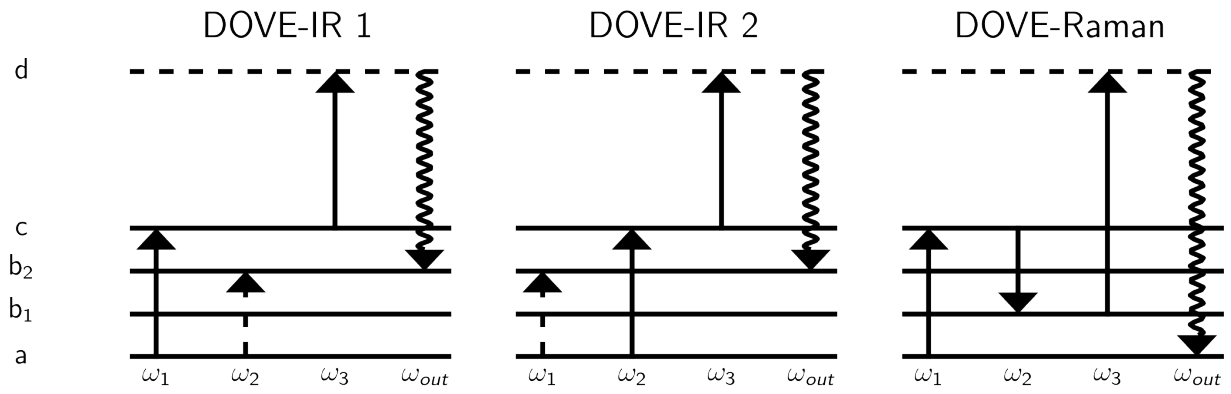

Figure I.1: Wave-mixing energy level diagrams of DOVE's three pathways. Time proceeds from left to write. Energy of the states increases from top to bottom.

The initial DOVE experiments performed by the Wright group were on neat acetonitrile with nanosecond lasers. The usage of nanosecond lasers prevents time ordering of pulses, so all pathways are present for a given experiment. The three DOVE pathways interfere on the amplitude level while signal is measured on the intensity level. Pathway interference may cause spectra to be hard to interpret. It is therefore of worth to know the relative magnitude of the individual pathways of DOVE for the system of interest.

Kwak et al. [453] demonstrated the viability of using *ab initio* methods to calculate the magnitude of each DOVE pathway. This work attempts to use their methodology to calculate a DOVE spectra of acetonitrile. This spectra will be the analog to the experimental spectra shown in Besemann et al. [457] whose main feature is from a combination band of the CC and CN stretch of acetonitrile while the diagonal feature is a CARS line from C_6D_6. The present work will not take into account the CARS line.

There are numerous ways to use *ab initio* methods to calculate the magnitude of each DOVE pathway. One way is calculate the two wavefunctions, $|i\rangle$ and $|f\rangle$, associated with *each* transition and then calculate the transition moment of the individual transitions

$$\text{Transition moment } (|i\rangle \rightarrow |f\rangle) = \langle f|\mu|i\rangle \tag{I.1}$$

in which μ is the dipole moment operator. This methodology is conceptually simple, but computationally demanding. Specifically, it would be nearly impossible to calculate the two transition moments associated with the Raman-like transitions of DOVE. For e and v representing electronic and vibrational states, respectively, these Raman-like transitions may be represented as

$$e_g v_i \xrightarrow{\text{visible laser}} e_x v_y \xrightarrow{\text{spontaneous}} e_g v_f \tag{I.2}$$

in which x and y indicate the unknown aspect of the excited electronic state that was excited to by the visible laser. The third excitation of DOVE excites the system to a non-resonant *family* of states. So if the Raman-like transition moments are to be carefully considered using this wavefunction

methodology, then the family of states must be known. TD-DFT methods could be used to calculate the wavefunction of many excited states with energies around the visible laser's frequency and then these states could be appropriately weighted by their easily calculated Franck-Condon factor.

Using TD-DFT methods for large systems could become prohibitively expensive. So the above described methods will not be used in this proof-of-concept work. In the Theory section we will derive results which will allow us to calculate transition moments for all transitions without needing to laboriously calculate excited vibrational and electron state wavefunctions. Instead, by judiciously using first order perturbation theory and expanded representations of operators we may rely merely upon the ground state potential energy surface and movements over it to describe the needed transitions.

I.2 Theory

I.2.1 Signal in the Driven Limit

DOVE FWM consists of three pathways which interfere on the amplitude level while signal is measured on the intensity level. There are two DOVE-IR and one DOVE-Raman Louiville pathways that leads to signal:

- DOVE IR 1: $aa \rightarrow ca \rightarrow cb_2 \rightarrow db_2$
- DOVE IR 2: $aa \rightarrow ab_2 \rightarrow cb_2 \rightarrow db_2$
- DOVE Raman: $aa \rightarrow ca \rightarrow b_1a \rightarrow da$.

Each pathway is represented by a density matrix, ρ. These matrices describe the oscillating coherences which define a polarization. Oscillating polarizations generate an electric field. The oscillators in a DOVE experiment conspire to generate a directional and phased electric field which is detected by the experimentalist.

Original DOVE experiments, which we are attempting to replicate *in silico*, were accomplished using nanosecond lasers. These lasers had large time bandwidths and thus small frequency bandwidths. The time bandwidth of these lasers greatly exceeded the coherence time of the excited acetonitrile transitions. In multidimensional spectroscopy lingo, these experiments were performed in the *driven limit*. In the driven limit, the defining density matrices and signal, S, of DOVE's three pathways take on the following standard form:[459]

$$\rho_{db}^{\text{IR 1}} = -\sum_{abcd} \frac{\Omega_{ac}\Omega_{ab}\Omega_{cd}}{\Delta_{ac}\Delta_{ab}\Delta_{cd}}\Lambda \tag{I.3}$$

$$\rho_{db}^{\text{IR 2}} = +\sum_{abcd} \frac{\Omega_{ab}\Omega_{ac}\Omega_{cd}}{\Delta_{ab}^{*}\Delta_{ac}\Delta_{cd}}\Lambda \tag{I.4}$$

$$\rho_{db}^{\text{Raman}} = +\sum_{abcd} \frac{\Omega_{ac}\Omega_{cb}\Omega_{bd}}{\Delta_{ca}\Delta_{ba}\Delta_{da}}\Lambda \tag{I.5}$$

$$S(\omega_1, \omega_2, \omega_3) \propto \left|\rho_{db}^{\text{IR 1}} + \rho_{db}^{\text{IR 2}} + \rho_{db}^{\text{Raman}}\right|^2. \tag{I.6}$$

The states *abcd* are not rigorously related to the states of the same name as detailed in the In-

troduction. Instead, the sum over states is a sum over all *possible* states and thus transitions. However, appreciable signal will only result from a few states due to the small frequency range over which the excitation lasers may be scanned.

In the above equations we have used many new variables:

$$\Lambda \equiv \rho_{aa} e^{i[(k_1 - k_2 + k_3)z - (\omega_1 - \omega_2 + \omega_3)t]} \tag{I.7}$$

$$\Omega_{ij} \equiv \frac{\mu_{ij} \cdot E_\ell}{2\hbar} \tag{I.8}$$

$$\mu_{ij} \equiv \langle i|\mu|j\rangle \tag{I.9}$$

Λ characterizes the population of the starting state and the frequency, ω_ℓ and wavevector, k_ℓ, terms of the three ℓ^{th} electric fields, E_ℓ. Because nanosecond lasers are in use, we may posit our electric fields to be perfectly monochromatic, infinite plane waves. Ω_{ij} is called the Rabi frequency of the ij transition; it defines the strength of the transition pumped by field the E_ℓ. μ_{ij} is the transition moment. This work will calculate these transition moments. Δ_{ij} is called a *resonance denominator* and defines the lineshape associated with a driven transition. In the driven limit, Rabi frequencies belong to a transition while a resonance denominator belongs to a particular experimental time ordering with a given set of laser frequencies. In this work we will use the standard form of the resonance denominators (shown later). For more information, the interested reader is pointed to Wright et al. [459] and references there-in.

I.2.2 Amplitude of pathways

Given that all three pathways are driven by the same three lasers, the amplitude each pathway accrues is a function of the strength of the transition moments. The same three lasers drive each pathway, so we may write a simple proportionality statement for all density matrices. In doing so we have removed all electric field dependency from our expressions.

$$\rho_{db}^{\text{IR 1}} \propto -\sum_{abcd} \frac{\mu_{ac}\mu_{ab}\mu_{cd}}{\Delta_{ac}\Delta_{ab}\Delta_{cd}} \tag{I.10}$$

$$\rho_{db}^{\text{IR 2}} \propto +\sum_{abcd} \frac{\mu_{ab}\mu_{ac}\mu_{cd}}{\Delta_{ab}^{*}\Delta_{ac}\Delta_{cd}} \tag{I.11}$$

$$\rho_{db}^{\text{Raman}} \propto +\sum_{abcd} \frac{\mu_{ac}\mu_{bc}\mu_{bd}}{\Delta_{ca}\Delta_{ba}\Delta_{da}} \tag{I.12}$$

All states in the pathways are oscillating coherences. These coherences are polarizations which create new electric fields. The transition which turns a ρ_{db} coherence into a signal is used by all three pathways.[2] We may add this transition to our density matrix expressions while still maintaining the proportionality statement. For sake of notional clarity we drop the db subscript

[2] At this point in the derivation, d and b are still unspecified states.

on the density matrices to distinguish them from the previous density matrices.

$$\rho^{\text{IR 1}} \propto -\sum_{abcdf} \frac{\mu_{ac}\mu_{ab}\mu_{cd}\mu_{df}}{\Delta_{ac}\Delta_{ab}\Delta_{cd}} \tag{I.13}$$

$$\rho^{\text{IR 2}} \propto +\sum_{abcdf} \frac{\mu_{ab}\mu_{ac}\mu_{cd}\mu_{df}}{\Delta^*_{ab}\Delta_{ac}\Delta_{cd}} \tag{I.14}$$

$$\rho^{\text{Raman}} \propto +\sum_{abcdf} \frac{\mu_{ac}\mu_{cb}\mu_{bd}\mu_{df}}{\Delta_{ca}\Delta_{ba}\Delta_{da}} \tag{I.15}$$

The Raman transition associated with each pathway is thus described by the term $\frac{\mu_{cd}\mu_{df}}{\Delta_{cd}}$ for DOVE IR and $\frac{\mu_{bd}\mu_{df}}{\Delta_{da}}$ for DOVE Raman. For a sufficiently non-resonant Raman transition the two dipole mediated transitions may be written as a single *polarizability* mediated transition. The non-resonant assumption also removes our dependency on the resonance denominator because in the far tail of a resonance the resonance contribution varies very slowly with a change in laser frequency. Our density matrices are then given by

$$\rho^{\text{IR 1}} \propto -\sum_{abcf} \frac{\mu_{ac}\mu_{ab}\alpha_{cf}}{\Delta_{ac}\Delta_{ab}} \tag{I.16}$$

$$\rho^{\text{IR 2}} \propto +\sum_{abcf} \frac{\mu_{ab}\mu_{ac}\alpha_{cf}}{\Delta^*_{ab}\Delta_{ac}} \tag{I.17}$$

$$\rho^{\text{Raman}} \propto +\sum_{abcf} \frac{\mu_{ac}\mu_{cb}\alpha_{bf}}{\Delta_{ca}\Delta_{ba}} \tag{I.18}$$

in which $\alpha_{ij} \equiv \langle i|\alpha|j\rangle$ for α being the polarizability.

We now desire to write our density matrices, not in the general case, but rather in the case appropriate for Wright et al.'s work with acetonitrile. Acetonitrile has 12 normal modes. Normal mode 3 is the CC stretch while mode 9 is the CN stretch. In standard harmonic oscillator/normal mode nomenclature the four states considered in this work are then given by:

$$\begin{array}{lll} |a\rangle & = |0_3 0_9\rangle & \text{ground state} \\ |b_1\rangle & = |1_3 0_9\rangle & \text{CC stretch} \\ |b_2\rangle & = |0_3 1_9\rangle & \text{CN stretch} \\ |c\rangle & = |1_3 1_9\rangle & \text{combination band} \end{array} \tag{I.19}$$

where the $|x_y\rangle$ nomenclature means normal mode y has x quanta of excitement/energy.

So the density matrices which are relevant to Wright et al.'s work with acetonitrile are

$$\rho^{\text{IR 1}} \propto -\frac{\mu_{ac}\mu_{ab_2}\alpha_{cf}}{\Delta_{ac}\Delta_{ab_2}} \tag{I.20}$$

$$\rho^{\text{IR 2}} \propto +\frac{\mu_{ab_2}\mu_{ac}\alpha_{cf}}{\Delta^*_{ab_2}\Delta_{ac}} \tag{I.21}$$

$$\rho^{\text{Raman}} \propto +\frac{\mu_{ac}\mu_{cb_1}\alpha_{b_1 f}}{\Delta_{ac}\Delta_{b_1 a}} \tag{I.22}$$

We now must derive expressions for the individual transition moments in the above equations.

I.2.3 Normal Mode Harmonic Oscillator Basis

In order to make our problem tractable, we write all of our states in a harmonic oscillator product basis. For instance, we may write state a as

$$|a\rangle = \prod_{j}^{n} |\nu_j^a\rangle \tag{I.23}$$

in which j is a normal mode and ν_j^a is the quanta of energy associated with mode j such that state a is defined. For acetonitrile $n = 3N - 6 = 12$. In choosing to write our states as in this HO product basis, we assume all perturbations to the normal modes of our system are not encoded in the original wave function description of our states—there is no wavefunction level coupling of states. Coupling of states will instead be later taken into account in two key ways:

1. High orders of dipole and polarizability expansion
2. Cubic potentials realized in first order perturbation theory

I.2.4 Fundamental Transition

We desire to write the transition moment of a fundamental transition in terms of easily calculated parameters. In equation form we desire to calculate $\langle b\,|\mu|\,a\rangle$ and $\langle b\,|\alpha|\,a\rangle$ for a and b differing by *one* quanta of energy in *one* mode. We start by Taylor expanding the dipole and polarizability operators around the equilibrium geometry w.r.t. normal mode coordinates, Q_j.

$$\mu = \mu^0 + \sum_j \left(\frac{\partial \mu}{\partial Q_j}\right)_0 Q_j + \frac{1}{2}\sum_{jk}\left(\frac{\partial^2}{\partial Q_j \partial Q_k}\right)_0 Q_j Q_k + \cdots \tag{I.24}$$

$$\alpha = \alpha^0 + \sum_j \left(\frac{\partial \alpha}{\partial Q_j}\right)_0 Q_j + \frac{1}{2}\sum_{jk}\left(\frac{\partial^2 \alpha}{\partial Q_j \partial Q_k}\right)_0 Q_j Q_k + \cdots \tag{I.25}$$

The zero subscripts on the partial derivatives stands for zero applied electric field. μ is technically a rank 1 tensor while α is technically a rank 2 tensor. In this section we will suppress vector/tensor notation and instead take into account the directional nature of our system latter. We may substitute this expression for μ in our transition moment integral and then simplify for $|a\rangle \neq |b\rangle$.

$$\langle b\,|\mu|\,a\rangle = \left\langle b \middle| \mu^0 + \sum_j \left(\frac{\partial \mu}{\partial Q_j}\right)_0 Q_j + \frac{1}{2}\sum_{jk}\left(\frac{\partial^2 \mu}{\partial Q_j \partial Q_k}\right)_0 Q_j Q_k + \cdots \middle| a \right\rangle \tag{I.26}$$

$$= \langle b\,|\mu^0|\,a\rangle + \left\langle b \middle| \sum_j \left(\frac{\partial \mu}{\partial Q_j}\right)_0 Q_j \middle| a \right\rangle + \frac{1}{2}\left\langle b \middle| \sum_{jk}\left(\frac{\partial^2 \mu}{\partial Q_j \partial Q_k}\right)_0 Q_j Q_k \middle| a \right\rangle + \cdots \tag{I.27}$$

$$= 0 + \sum_j \left(\frac{\partial \mu}{\partial Q_j}\right)_0 \langle b\,|Q_j|\,a\rangle + \frac{1}{2}\sum_{jk}\left(\frac{\partial^2 \mu}{\partial Q_j \partial Q_k}\right)_0 \langle b\,|Q_j Q_k|\,a\rangle + \cdots . \tag{I.28}$$

$$= \sum_j \left(\frac{\partial \mu}{\partial Q_j}\right)_0 \langle b\,|Q_j|\,a\rangle + \frac{1}{2}\sum_{jk}\left(\frac{\partial^2 \mu}{\partial Q_j \partial Q_k}\right)_0 \langle b\,|Q_j Q_k|\,a\rangle + \cdots \tag{I.29}$$

We must further express $\langle b\,|Q_j|\,a\rangle$ and $\langle b\,|Q_jQ_k|\,a\rangle$ in calculable parameters. In order to do so, we write $|a\rangle$ and $|b\rangle$ in our harmonic oscillator product basis. Because we judiciously chose this basis, we have many handy identities.

$$\langle\nu_i|Q_j|\nu_k\rangle = \begin{cases} 0, & \text{for } i \neq j \neq k \\ 1, & \text{for } i = k \neq j \\ \sqrt{\frac{\hbar}{2M_j\omega_j}}, & \text{for } i = k = j \text{ and } \nu_i = \nu_k \pm 1 \end{cases} \tag{I.30}$$

in which M_j is the reduced mass and ω_j is the frequency of normal mode j.

We are now ready to evaluate some integrals. Let us start with the $\langle b\,|Q_j|\,a\rangle$ term.

$$\sum_j^n \left(\frac{\partial\mu}{\partial Q_j}\right)_0 \langle b\,|Q_j|\,a\rangle = \sum_j^n \left(\frac{\partial\mu}{\partial Q_j}\right)_0 \left\langle \prod_i^n \nu_i^{b_i}\,|Q_j|\prod_k^n \nu_k^{a_k}\right\rangle \tag{I.31}$$

$$= \sum_j^n \left(\frac{\partial\mu}{\partial Q_j}\right)_0 \left\langle \prod_j^n \nu_j^{b_j}\,|Q_j|\prod_j^n \nu_j^{a_j}\right\rangle \tag{I.32}$$

$$= \sum_j^n \left(\frac{\partial\mu}{\partial Q_j}\right)_0 \prod_j^n \left\langle \nu_j^{b_j}\,|Q_j|\,\nu_j^{a_j}\right\rangle \tag{I.33}$$

$$= \sum_j^n \left(\frac{\partial\mu}{\partial Q_j}\right)_0 \left\langle \nu_j^{b_j}\,|Q_j|\,\nu_j^{a_j}\right\rangle \delta(b_j, a_j = b_j \pm 1) \tag{I.34}$$

$$= \sum_j^n \left(\frac{\partial\mu}{\partial Q_j}\right)_0 \sqrt{\frac{\hbar}{2M_j\omega_j}}\delta(b_j, a_j = b_j \pm 1) \tag{I.35}$$

We now turn to writing out our $\langle b\,|Q_jQ_k|\,a\rangle$ term. We note that an integral of a product of varying coordinates is merely the product of the integrals over the individual coordinates. We implicitly expand our states in the HO basis.

$$\langle b\,|Q_jQ_k|\,a\rangle = \langle b\,|Q_j|\,a\rangle\,\langle b\,|Q_k|\,a\rangle \tag{I.36}$$

$$= \left\langle \nu_j^{b_j}\,|Q_j|\,\nu_j^{a_j}\right\rangle \delta(b_j, a_j = b_j \pm 1)\left\langle \nu_k^{b_k}\,|Q_k|\,\nu_k^{a_k}\right\rangle \delta(b_k, a_k = b_k \pm 1) \tag{I.37}$$

$$= \frac{\hbar}{2\sqrt{M_jM_k\omega_j\omega_k}}\delta(b_j, a_j = b_j \pm 1)\delta(b_k, a_k = b_k \pm 1) \tag{I.38}$$

Note that this result holds under the same condition as our other result: j and k must be modes which satisfy $b_j, a_j = b_j \pm 1$ and $b_k, a_k = b_k \pm 1$. So for a single quantum transition, $\langle b\,|Q_jQ_k|\,a\rangle = 0$. It then follows:

$$\langle b\,|\mu|\,a\rangle = \sum_j \left(\frac{\partial\mu}{\partial Q_j}\right)_0 \sqrt{\frac{\hbar}{2M_j\omega_j}} + \frac{1}{2}\sum_{jk}\left(\frac{\partial^2\mu}{\partial Q_j\partial Q_k}\right)_0 \frac{\hbar}{2\sqrt{M_jM_k\omega_j\omega_k}} + \cdots \tag{I.39}$$

$$= \sum_j \left(\frac{\partial\mu}{\partial Q_j}\right)_0 \sqrt{\frac{\hbar}{2M_j\omega_j}} \text{ for a single quantum transition} \tag{I.40}$$

Because we expanded μ and α in identical ways, we get an analog for the polarizability.

$$\langle b\,|\alpha|\,a\rangle = \sum_j \left(\frac{\partial\alpha}{\partial Q_j}\right)_0 \sqrt{\frac{\hbar}{2M_j\omega_j}} + \frac{1}{2}\sum_{jk}\left(\frac{\partial^2\alpha}{\partial Q_j\partial Q_k}\right)_0 \frac{\hbar}{2\sqrt{M_jM_k\omega_j\omega_k}} + \cdots \tag{I.41}$$

$$= \sum_j \left(\frac{\partial\alpha}{\partial Q_j}\right)_0 \sqrt{\frac{\hbar}{2M_j\omega_j}} \text{ for a single quantum transition} \tag{I.42}$$

In short, we have written fundamental transition moments without actually calculating an integral. We have instead cast our problem in terms of calculated molecular parameters, specifically $\left(\frac{\partial\mu}{\partial Q_j}\right)_0$ and $\left(\frac{\partial\alpha}{\partial Q_j}\right)_0$. For j being the excited or de-excited mode.

I.2.5 Combination Band

We now must turn to calculating the transition moment associated with our combination band. The combination band transition is considered forbidden—without mode coupling the transition moment is zero. In order to get a nonzero moment, we must turn to using first order perturbation theory. We assume any perturbation is sufficiently local so it may be described merely by *adding* additional terms to our unperturbed wavefunction. We use the canonical result of first order perturbation theory.[3] H is the total system Hamiltonian.

$$H \cong H_0 + V' \tag{I.43}$$

$$\langle c| \cong {}^0\langle c| + {}'\langle c| \tag{I.44}$$

$$= {}^0\langle c| + \sum_{M\neq c} \frac{{}^0\langle c|V'|M\rangle^0}{\hbar(\omega_c - \omega_M)}{}^0\langle M| \tag{I.45}$$

$$|a\rangle \cong |a\rangle^0 + |a\rangle' \tag{I.46}$$

$$= |a\rangle^0 + \sum_{K\neq a} \frac{{}^0\langle K|V'|a\rangle^0}{-\hbar\omega_K}|K\rangle^0 \tag{I.47}$$

[3] See https://en.wikipedia.org/wiki/Perturbation_theory_(quantum_mechanics) for more info.

Here we have presumed that a is the ground state. We may now define our perturbation, V'.

$$H \equiv T + V \tag{I.48}$$
$$= T + V^\dagger + V_{vib} \tag{I.49}$$
$$= T + V^\dagger + \frac{1}{2}\sum_i \left(\frac{\partial^2 V}{\partial Q_i \partial Q_i}\right)_0 Q_i Q_i + \frac{1}{8}\sum_{ijk}\left(\frac{\partial^3 V}{\partial Q_i \partial Q_j \partial Q_k}\right)_0 Q_i Q_j Q_k + \cdots \tag{I.50}$$
$$\approx H_0 + \frac{1}{8}\sum_{ijk}\left(\frac{\partial^3 V}{\partial Q_i \partial Q_j \partial Q_k}\right)_0 Q_i Q_j Q_k \tag{I.51}$$
$$\cong H_0 + V' \tag{I.52}$$
$$\implies V' \equiv \frac{1}{8}\sum_{ijk}\left(\frac{\partial^3 V}{\partial Q_i \partial Q_j \partial Q_k}\right)_0 Q_i Q_j Q_k \tag{I.53}$$

We now consider a dipole mediated transition written in first order perturbation theory. For sake of equation size we write $\mu = \mu_0 + \mu_1 + \mu_2 + \cdots$ in which the subscripts indicate the order of the Taylor expansion as given in Equation I.24.

$$\langle c|\mu|a\rangle = {}'\langle c|\mu|a\rangle' + {}^0\langle c|\mu|a\rangle' + {}'\langle c|\mu|a\rangle^0 + {}^0\langle c|\mu|a\rangle^0 \tag{I.54}$$
$$= {}'\langle c|\mu_0+\mu_1+\mu_2|a\rangle' + {}^0\langle c|\mu_0+\mu_1+\mu_2|a\rangle' + {}'\langle c|\mu_0+\mu_1+\mu_2|a\rangle^0 + {}^0\langle c|\mu_0+\mu_1+\mu_2|a\rangle^0 \tag{I.55}$$
$$= \begin{cases} +{}'\langle c|\mu_0|a\rangle' + {}^0\langle c|\mu_0|a\rangle' + {}'\langle c|\mu_0|a\rangle^0 + {}^0\langle c|\mu_0|a\rangle^0 \\ +{}'\langle c|\mu_1|a\rangle' + {}^0\langle c|\mu_1|a\rangle' + {}'\langle c|\mu_1|a\rangle^0 + {}^0\langle c|\mu_1|a\rangle^0 \\ +{}'\langle c|\mu_2|a\rangle' + {}^0\langle c|\mu_2|a\rangle' + {}'\langle c|\mu_2|a\rangle^0 + {}^0\langle c|\mu_2|a\rangle^0 \end{cases} \tag{I.56}$$
$$= \begin{cases} +\cancelto{0}{{}'\langle c|\mu_0|a\rangle'} + \cancelto{0}{{}^0\langle c|\mu_0|a\rangle'} + \cancelto{0}{{}'\langle c|\mu_0|a\rangle^0} + \cancelto{0}{{}^0\langle c|\mu_0|a\rangle^0} \\ \quad +\cancelto{0}{{}'\langle c|\mu_1|a\rangle'} + {}^0\langle c|\mu_1|a\rangle' + {}'\langle c|\mu_1|a\rangle^0 + \cancelto{0}{{}^0\langle c|\mu_1|a\rangle^0} \\ \quad +\cancelto{0}{{}'\langle c|\mu_2|a\rangle'} + \cancelto{0}{{}^0\langle c|\mu_2|a\rangle'} + \cancelto{0}{{}'\langle c|\mu_2|a\rangle^0} + {}^0\langle c|\mu_2|a\rangle^0 \end{cases} \tag{I.57}$$
$$= {}^0\langle c|\mu_1|a\rangle' + {}'\langle c|\mu_1|a\rangle^0 + {}^0\langle c|\mu_2|a\rangle^0 \tag{I.58}$$
$$\cong \langle c|\mu|a\rangle^M + \langle c|\mu|a\rangle^E \tag{I.59}$$

In canceling out many of our integrals we noticed many handy things.[4]

1. $|c\rangle^0$ and $|a\rangle^0$ differ by two quanta in the normal mode basis. Thus if no mixing term (e.g. Q_i) is present the integral goes to zero.
2. μ_0 is the equivalent of zero raising and lowering operators, μ_1 is the equivalent of a sum over terms containing one raising and lowering operator, μ_2 is the equivalent of a sum over terms containing two raising and lowering operators.
3. $|i\rangle^0$ and $|j\rangle'$ differ in some places by merely one quanta.
4. $|i\rangle'$ and $|j\rangle'$ differ from each other by more than two quanta. This entails our maximum of two mixing terms cannot yield a nonzero value for these integrals.

[4]The author apologizes to the reader for not providing a careful explanation as to why each of the nine cases go to zero. Many are non-elementary, but the author did not have enough time to explicate all cases. So it goes... A rigorous exploration would formally write each and every term in the normal mode basis and then carefully perform the summations and multiplications. Additionally closure relations may be of great use here depending on the basis one is *actually* writing the perturbative expansion in.

We also wrote our result in terms of mechanical, M, and electrical, E, anharmonic terms. Let us hash out what each of these terms is equal to.

$$\langle c|\mu|a\rangle^M \equiv {}'\langle c|\mu^{(1)}|a\rangle^0 + {}^0\langle c|\mu^{(1)}|a\rangle' \tag{I.60}$$

$$= \sum_j \left(\frac{\partial \mu}{\partial Q_j}\right)_0 \left[{}'\langle c|Q_j|a\rangle^0 + {}^0\langle c|Q_j|a\rangle'\right] \tag{I.61}$$

$$= \sum_j \left(\frac{\partial \mu}{\partial Q_j}\right)_0 \left[\sum_{M\neq c} \frac{{}^0\langle c|V'|M\rangle^0}{\hbar(\omega_c-\omega_M)} {}^0\langle M|Q_j|a\rangle^0 + \sum_{K\neq a} \frac{{}^0\langle K|V'|a\rangle^0}{-\hbar\omega_K} {}^0\langle c|Q_j|K\rangle^0\right] \tag{I.62}$$

$$\cong \sum_j \left(\frac{\partial \mu}{\partial Q_j}\right)_0 \left[\aleph_j + \aleph_j^\dagger\right] \tag{I.63}$$

in which we have let

$$\aleph_j \equiv \sum_{M\neq c} \frac{{}^0\langle c|V'|M\rangle^0}{\hbar(\omega_c-\omega_M)} {}^0\langle M|Q_j|a\rangle^0 \tag{I.64}$$

$$\aleph_j^\dagger \equiv \sum_{K\neq a} \frac{{}^0\langle K|V'|a\rangle^0}{-\hbar\omega_K} {}^0\langle c|Q_j|K\rangle^0 \tag{I.65}$$

We now write out what V' is for the $\aleph_j$ case—$\aleph_j'$ follows in exactly the same way.

$$\aleph_j = \sum_{M\neq c} \frac{{}^0\left\langle c\left|\frac{1}{8}\sum_{i\ell k}\left(\frac{\partial^3 V}{\partial Q_i\partial Q_\ell\partial Q_k}\right)_0 Q_iQ_\ell Q_k\right|M\right\rangle^0}{\hbar(\omega_c-\omega_M)} {}^0\langle M|Q_j|a\rangle^0 \tag{I.66}$$

$$= \sum_{M\neq c} \frac{{}^0\left\langle c\left|\frac{1}{8}\sum_{ijk}\left(\frac{\partial^3 V}{\partial Q_i\partial Q_j\partial Q_k}\right)_0 Q_iQ_jQ_k\right|M\right\rangle^0}{\hbar(\omega_c-\omega_M)} {}^0\langle M|Q_j|a\rangle^0 \tag{I.67}$$

$$\cong \sum_{M\neq c}\sum_{ijk} \beth_{ijkM} {}^0\langle c|Q_iQ_jQ_k|M\rangle^0 {}^0\langle M|Q_j|a\rangle^0 \tag{I.68}$$

$$\Longrightarrow \beth_{ijkM} \equiv \frac{\frac{1}{8}\left(\frac{\partial^3 V}{\partial Q_i\partial Q_j\partial Q_k}\right)_0}{\hbar(\omega_c-\omega_M)} \tag{I.69}$$

We now expand in our harmonic oscillator, normal mode basis. We must be careful with our summations. M describes a *state* while ijk describe *modes*. The state M is composed of quanta of

energy in the set of modes which define the system.

$$\aleph_j = \sum_{M=|x_q x_r x_s\rangle \neq c} \sum_{ijk} \beth_{ijkM}{}^0 \langle 0_q 1_r 1_s | Q_i Q_j Q_k | x_q x_r x_s \rangle^{0\,0} \langle x_q x_r x_s | Q_j | 0_q 0_r 0_s \rangle^0 \tag{I.70}$$

$$= \sum_{M \neq c} \sum_{ijk} \beth_{ijkM}{}^0 \langle 1_i 0_j 1_k | Q_i Q_j Q_k | 0_i 1_j 0_k \rangle^{0\,0} \langle 0_i 1_j 0_k | Q_j | 0_i 0_i 0_k \rangle^0 \tag{I.71}$$

$$= \sum_{M \neq c} \sum_{ijk} \beth_{ijkM} \sqrt{\frac{\hbar^4}{16 M_i \omega_i M_j \omega_j M_k \omega_k M_j \omega_j}} \tag{I.72}$$

In writing the first movement we observed that our summands are non-zero only when $x_q x_r x_s = 1_j 0_k 0_i$. Our resultant term holds for ik being combination band modes, and j are the modes summed over which define the perturbative mixing of the non-perturbed state with a normal mode basis.

We now write out our 'simplified' mechanical anharmonicity term.

$$\langle c|\mu|a\rangle^M = \sum_{ijk} \left(\frac{\partial \mu}{\partial Q_j} \right)_0 \left[\beth_{ijkj} \sqrt{\frac{\hbar^4}{16 M_i \omega_i M_j \omega_j M_k \omega_k M_j \omega_j}} + \beth^\dagger_{ijkj} \sqrt{\frac{\hbar^4}{16 M_i \omega_i M_j \omega_j M_k \omega_k M_j \omega_j}} \right] \tag{I.73}$$

$$= \sum_{ijk} \left(\frac{\partial \mu}{\partial Q_j} \right)_0 \sqrt{\frac{\hbar^4}{16 M_i \omega_i M_j \omega_j M_k \omega_k M_j \omega_j}} \left[\beth_{ijkj} + \beth^\dagger_{ijkj} \right] \tag{I.74}$$

$$= \sum_{ijk} \left(\frac{\partial \mu}{\partial Q_j} \right)_0 \sqrt{\frac{\hbar^4}{16 M_i \omega_i M_j \omega_j M_k \omega_k M_j \omega_j}} \frac{1}{8} \left(\frac{\partial^3 V}{\partial Q_i \partial Q_j \partial Q_k} \right)_0 \left[\frac{1}{\hbar(\omega_c - \omega_j)} + \frac{1}{-\hbar \omega_j} \right] \tag{I.75}$$

This result is a bit cumbersome, but all of its terms are calculate-able with *ab initio* methods. We have turned a complicated integral into a sum of tensors. We do the same thing again for the electrical coupling term.

$$\langle c|\mu|a\rangle^E \equiv {}^0\langle c|\mu^{(2)}|a\rangle^0 \tag{I.76}$$

$$= \frac{1}{2} \sum_{ij} \left(\frac{\partial^2 \mu}{\partial Q_i \partial Q_j} \right)_0 {}^0\langle c|Q_i Q_j|a\rangle^0 \tag{I.77}$$

$$= \frac{1}{2} \left(\frac{\partial^2 \mu}{\partial Q_i \partial Q_j} \right)_0 {}^0\langle c|Q_i Q_j|a\rangle^0 \text{ for } \langle c| = \langle 1_i 1_j| \text{ and } |a\rangle = |0_i 0_j\rangle \tag{I.78}$$

$$= \frac{1}{2} \left(\frac{\partial^2 \mu}{\partial Q_i \partial Q_j} \right)_0 \frac{\hbar}{2\sqrt{M_i M_j \omega_i \omega_j}} \tag{I.79}$$

We may put all of our results together! For ik being the modes over which our combination band

transition happens we have

$$\langle c|\mu|a\rangle = \langle c|\mu|a\rangle^M + \langle c|\mu|a\rangle^E \tag{I.80}$$

$$= \sum_j \left(\frac{\partial \mu}{\partial Q_j}\right)_0 \sqrt{\frac{\hbar^4}{16 M_i \omega_i M_j \omega_j M_k \omega_k M_j \omega_j}} \frac{1}{8} \left(\frac{\partial^3 V}{\partial Q_i \partial Q_j \partial Q_k}\right)_0 \left[\frac{1}{\hbar(\omega_c - \omega_j)} + \frac{1}{-\hbar\omega_j}\right] + \frac{1}{2}\left(\frac{\partial^2 \mu}{\partial Q_i \partial Q_j}\right)_0 \frac{\hbar}{2\sqrt{M_i M_j \omega_i \omega_j}} \tag{I.81}$$

Let us quickly have an executive summary of what we have accomplished.

- We can write all of the integrals needed to described the DOVE pathways in terms of derivatives and other constants.
- A fundamental transition may be written in terms of first and second order dipole derivatives w.r.t. normal modes.
- A Raman transition may be written in terms of first and second order polarizability derivatives w.r.t. normal modes.
- A combination band transition is complex, but it can be written as a sum of mechanical and electrical couplings.
  - Electrical: A single second order dipole derivatives w.r.t. normal modes
  - Mechanical: A sum over normal modes of the third order derivative of the potential w.r.t. normal modes and a first order derivative of the dipole w.r.t. a normal mode.
  - In the mechanical case, all modes can contribute to the observed non-linearity! The combination band is possibly coupled into existence by all normal modes of the molecule.

I.2.6 Resonance Denominators

The resonance denominators, as stated before, define the line shape of each pathway. All the work we have done has merely defined the amplitude of the strongest feature in each pathway. We use the standard form of the resonance denominators.

$$\Delta_{ca} \equiv \omega_{ca} - \omega_1 - i\Gamma_{ca} - \delta \tag{I.82}$$

$$\Delta_{b_1 a} \equiv \omega_{b_1 a} - \omega_1 + \omega_2 - i\Gamma_{b_1 a} \tag{I.83}$$

$$\Delta_{a b_2} \equiv \omega_{a b_2} + \omega_2 + i\Gamma_{a b_2} \tag{I.84}$$

Note how the resonance denominator of DOVE Raman $\Delta_{b_1 a}$ is different from the DOVE IR's $\Delta_{a b_2}$. This is because the second transition of DOVE Raman is from a coherence that is being *driven* by the first laser interaction. The frequency of the first coherence is defined by the driving laser and not by the frequency of the actual transition. This dependency of the second transition on the first gives DOVE Raman a line shape which is elongated along the diagonal where-as the DOVE IRs have line shapes elongated in a plus-sign shape. All interesting interference and 2D frequency behavior is defined by these denominators. Taking the square magnitude of a resonance denominator generates an unnormalized Lorentzian function.

Appendix J On the modeling of white light formation in a fiber

I originally wrote some of this appendix as part of a final project for Prof. Deniz Yavuz's Applied Optics class which I took in the spring of 2016. This appendix focuses on the mathematical formalism and an integration method which may be used to model white light formation in nonlinear fibers. This appendix does not present any numerical results.

Figure J.1: White light generated in a CaF_2 window from 800 nm, 35 fs light. Photo taken in the Wright lab by Justin Earley.

J.1 Introduction

White light supercontinuum generation (WLG) was first observed by Alfano and Shapiro.[465, 466, 467] In these original works, the mechanistic cause for WLG from picosecond pulses was attributed to self-phase modulation (SPM). The exact mechanistic nature of WLCG is not currently fully understood. Generally, a complex interplay of nonlinear optical phenomena push and pull against each other to eventually generate white light. Some of these (intertwined) phenomena include:

- **Self-phase modulation (SPM)**
- **Stimulated Raman scattering (SRS)**
- **Self-steepening (SS)** [468]
- Self-focusing [469]
- Multi-photon absorption and four-wave mixing (FWM)
- Pulse splitting
- Pulse-front steepening and optical shock generation

- Free electron plasma generation

WLG is a useful phenomena in that it may function as a coherent, broadband, "flat" source for usage in all kinds of spectroscopies and technical applications.[470, 471] In the last two decades, hollow core fibers have been implemented as substrates to tune the desired properties of a fiber to offer pulse compression, dispersion, or other nonlinear effects. Some companies (e.g. NKT Photonics) now offer products which allow for WLG within a fiber when that fiber is pumped by an ultrafast laser. A strong selling point of these fibers is their ability to be operated in a single-mode configuration for a desired wavelength range.

In this appendix we desire to create a formalism which allows for numerical modeling of WLG in fibers. All properties of light (electric field) propagation through a fiber are phenomenologically defined by the tensor elements of the linear and nonlinear susceptibilities, $\chi^{(i)}$, of the fiber. These suceptibilities may be tuned by adjusting the structure and composition of a fiber

J.2 Relationship between E and P

Optical fibers are generally considered to be nonmagnetic and contain no free charges. Hence, we may use Maxwell's equations to write an equation that relates an electric field, $\mathbf{E}$, to an induced polarization, $\mathbf{P}$. This polarization may then generate its own associated electric field. These polarizations and electric fields are functions of both time and Cartesian space. Maxwell's wave equation is

$$\nabla^2\mathbf{E} - \frac{1}{c^2}\frac{\partial^2\mathbf{E}}{\partial t^2} = \mu_0\frac{\partial^2\mathbf{p}}{\partial t^2}. \tag{J.1}$$

We now assume the response of the fiber to be local and instantaneous compared to the pulse duration of our incident electric field. This assumption allows us to write out the standard Taylor expanded form of the polarization as a power series in $\mathbf{E}$

$$\mathbf{P} = \epsilon_0\left[\chi^{(1)}\mathbf{E} + \chi^{(2)}\mathbf{EE} + \chi^{(3)}\mathbf{EEE} + \cdots\right] \tag{J.2}$$

in which $\chi^{(i)}$ is the ith order susceptibility of the material. In general, $\chi^{(i)}$ are tensors of rank $i+1$. In a system like a bulk fiber which has inversion symmetry, all elements of $\chi^{(2)}$ must identically go to 0. Hence, we may rewrite Equation J.2 for a fiber

$$\mathbf{P} = \epsilon_0\left[\chi^{(1)}\mathbf{E} + \chi^{(3)}\mathbf{EEE} + \cdots\right]. \tag{J.3}$$

We now write our polarization as a sum of linear and nonlinear terms

$$\mathbf{P} = \mathbf{P}_L + \mathbf{P}_{NL} \tag{J.4}$$

$$= \epsilon_0\left[\chi^{(1)}\mathbf{E}\right] + \epsilon_0\left[\chi^{(3)}\mathbf{EEE} + \cdots\right]. \tag{J.5}$$

We now simplify Equation J.1 by making a bunch of assumptions and substitutions:[1]

[1] Boyd [38] and Washburn [472] both have excellent, careful statements of these assumptions and their implications

- We write the electric fields as $\mathbf{E} = E(\mathbf{r}, t)e^{i(k_0 z - \omega_0 t)}$.
  - All of our spectral information will then be contained in E(**r**, t).
  - If we are talking about a fiber then our wavevector becomes an effective wave vector: $k \to \beta$.
- We make the slowly varying envelope approximation (SVEA)
  - The spatial distribution associated with **E** changes slowly as a function of propagation along the z direction.
  - The pulse duration is much longer than the carrier oscillation period.
- We neglect transverse dimensions and we assume space and time are not coupled such that z and t are independent dimensions.
- We assume the medium is isotropic (this greatly simplifies χ).
- We transform to retarded spatial and time coordinates that move along with the pulse at the group velocity of the pulse.

The relationship between the electric field and the induced nonlinear polarization is then

$$\frac{\partial E(z,t)}{\partial z} = \frac{i\omega_0}{2n_0\epsilon_0 c}\left(1 + \frac{i}{\omega_0}\frac{\partial}{\partial t}\right)P_{NL} + i\tilde{D}E(z,t) \tag{J.6}$$

$$\tilde{D} \equiv \sum_{m=0}^{M}\left(\frac{i^{m-1}}{m!}\beta_m\frac{\partial}{\partial t^m}\right) \tag{J.7}$$

in which $\tilde{D}$ is the dispersion and attenuation operator which contains a term β_m that is the m'th term of the Taylor expanded effective wavevector along the propagation direction in the fiber/medium. For instance, β_0 is an attenuation term, where as β_2 is the group velocity dispersion term. This is a form of what is called the Nonlinear Schrödinger Equation (NLSE). This equation is only related in form to the regular Schrödinger Equation—it says nothing about the evolution of quantum states. Assume that all of our nonlinear polarizations are due exclusively to third order processes yields

$$\frac{\partial E(z,t)}{\partial z} = \frac{i\omega_0}{2n_0 c}\left(1 + \frac{i}{\omega_0}\frac{\partial}{\partial t}\right)\chi^{(3)}|E(z,t)|^2 E(z,t) + i\tilde{D}E(z,t). \tag{J.8}$$

J.3 The simple case of self-phase modulation

In order to understand the implications of Equation J.8 we start by implementing the case of SPM. Consider a fiber which is dispersionless, lossless, and instantaneously responds to an applied electric field. Equation J.8 then reduces to

$$\frac{\partial E(z,t)}{\partial z} = \frac{i\omega_0}{2n_0 c}\chi^{(3)}|E(z,t)|^2 E(z,t) \tag{J.9}$$

$$\frac{\partial E(z,t)}{\partial z} = i\gamma|E(z,t)|^2 E(z,t \tag{J.10}$$

in which we defined a nonlinear coefficient $\gamma \equiv \frac{\omega_0}{2n_0 c}\chi^{(3)}(\omega_0)$ (for a fiber $\gamma_f \equiv \frac{\omega_0}{2n_0 c A_{eff}}\chi^{(3)}(\omega_0)$ in which A_{eff} is the effective core area of the fiber).

We now impose an ansatz solution on this differential equation

$$E(z,t) = E(z=0,t)e^{i\gamma|E(z,t)|^2}\left[e^{i(k_0 z-\omega_0 t)} + e^{-i(k_0 z-\omega_0 t)}\right] \tag{J.11}$$

which is essentially a normal plane wave but with an intensity dependent modulation of phase velocity

$$n = n_0 + I(z,t)\cdot n_2. \tag{J.12}$$

We call this self-phase modulation (SPM).

In order to understand the implications of Equation J.11 we run the following algorithm:

1. Define an initial electric field, for instance, a Gaussian pulse of ∼100 fs FWHM.
2. Analytically propagate pulse some desired distance, z.
3. Obtain the frequency spectra of the propagated pulse by Fourier transforming the time domain electric field. $E(z,\omega) = \mathcal{F}\{E(z,t)\}$.

Results of this algorithm are shown in Figure J.2 for three different propagation distances. We see that the initially sharp pulse undergoes substantial stretching in the frequency domain, the pulse does not broaden temporally, though. After propagation through the material, the temporal front of the pulse has a lower instantaneous frequency than the back of the pulse.

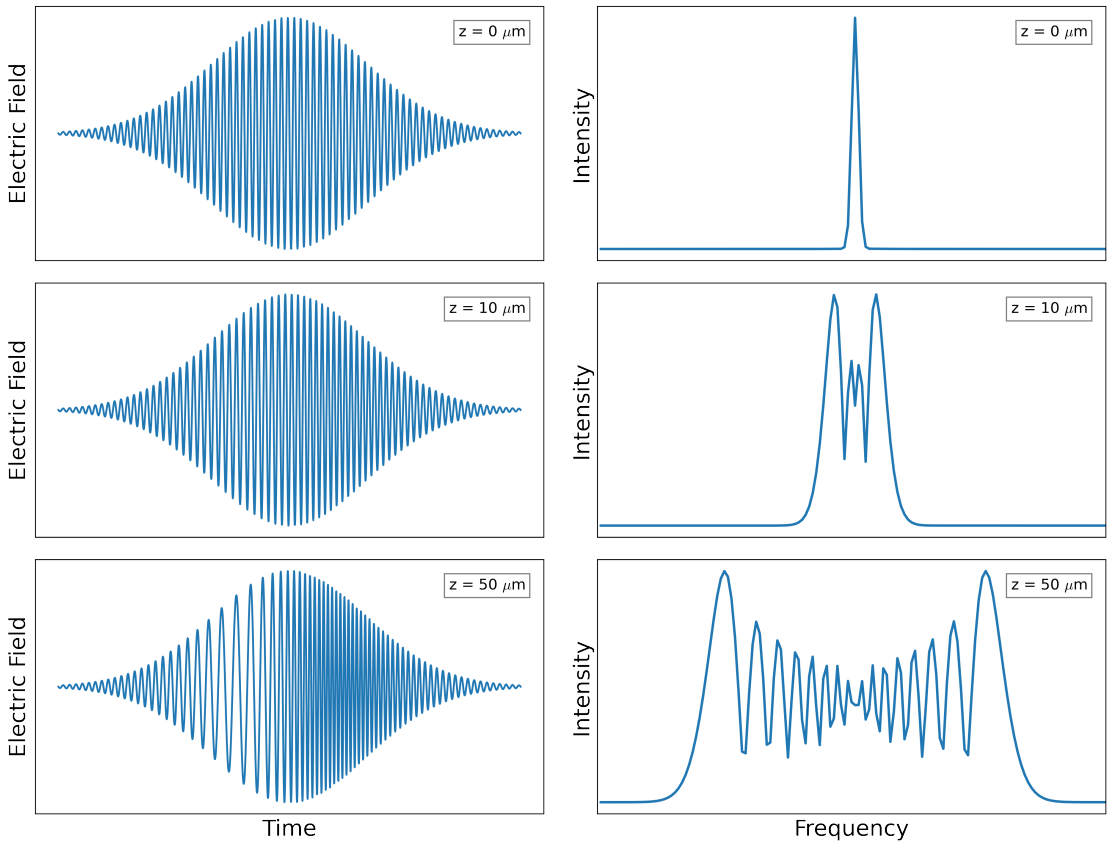

Figure J.2: Ultra-fast pulse propagating through a representative non-resonant medium.

J.4 Holistic treatment of the nonlinear Schrödinger equation

J.4.1 Theory

We now consider the nonlinear repsonse of our system in the time domain as an integral over a response function, $R(t)$. This function aids us greatly when we realize that $\chi^{(3)}$ is due mainly to high frequency electronic states and lower frequency vibrational states. We may assume that the electronic states respond instantaneously to the applied field, but we do not assume this for the vibrational states. Our response function can then be broken into a fraction, f_R, of a Raman response, $h_R(t)$ and a delta function for the electronic response

$$R(t) = (1 - f_R)\,\delta(t) + f_R h_R(t). \tag{J.13}$$

If a non-zero non-instantaneous response is present, a "Raman wave" will form. This wave will be a frequency change in either the Stokes or anti-Stokes direction which will cause energy from the fundamental mode to be transferred to another mode which is offset in frequency.

We now rewrite Equation J.8 into a form that is much more useful for numerical calculations

$$\frac{\partial E(z,t)}{\partial z} = \text{Loss} + \text{Disp} + \text{SPM} + \text{SS} + \text{SRS} \tag{J.14}$$

$$\text{Loss} = -\frac{\alpha}{2}E \tag{J.15}$$

$$\text{Disp} = -\left[\sum_{m=2} \frac{i^{m-1}}{m!}\beta_m \frac{\partial^m}{\partial t^m}\right] E \tag{J.16}$$

$$\text{SPM} = +i\gamma\,(1 - f_R)\,|E|^2\,E \tag{J.17}$$

$$\text{SS} = -\frac{\gamma}{\omega_0}\,(1 - f_R)\,\frac{\partial}{\partial t}\left(|E|^2\,E\right) \tag{J.18}$$

$$\text{SRS} = -i\gamma T_R E \frac{\partial\,|E|^2}{\partial t} \tag{J.19}$$

in which T_R is a derived quantity that is an integral over the Raman response (useful approximations in Washburn [472]) and α is an absorption coefficient. As before, in these equations, t corresponds to a retarded temporal frame of reference that travels with the pulse.

J.4.2 Numerical modeling : split-step Fourier method

The split-step Fourier method (SSF) is an numerical integration method that is widely used to numerically integrate nonlinear partial differential equations.[473, 474, 475] The alogorithm is efficient because no numerical derivatives are ever explicitly accomplished—this is in direct contrast to finite difference methods like the Crank-Nicolson method.[473] Instead all derivatives are accomplished in the Fourier domain by multiplying by $i\omega$. This method may be improved (in terms of error per time domain step) by using a symmetrized split-step Fourier method.

The basic idea

Using the SSF we split a spatial step over a distance h into two steps: one that is easy to compute in the time domain and another that is easy to compute in the frequency domain (see Figure J.3). This algorithm is looped N times in order to propagate a total distance of $h \cdot N$. The electric field calculated for the $z+h$ spatial step, $E(z+h,t)$, is fed to the algorithm to calculate the next spatial step, $z+2h$, in order to build $E(z+2h,t)$.

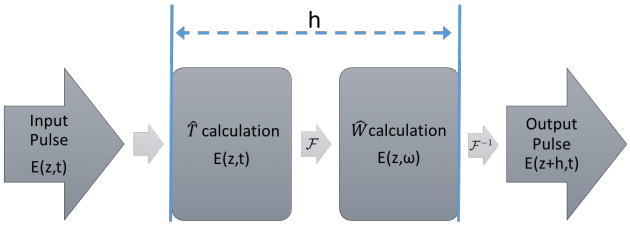

Figure J.3: Sketch of SSF Method for a single spatial step.

Mathy specifics

We write Equation J.14 as a function of a term that we will calculate in the time domain, and a term that we will calculate in the frequency domain. We represent these by the operators $\hat{T}$ and $\hat{W}$, respectively. These will operate on the electric field to give the derivative w.r.t. z

$$\frac{\partial E(z,t)}{\partial z} = \left[\hat{T} + \hat{W}\right] E(z,t). \tag{J.20}$$

For an arbitrarily small spatial step, h, the solution to this is

$$E(z+h,t) = \exp\left[h\left(\hat{T}+\hat{W}\right)\right] E(z,t) \tag{J.21}$$

$$\approx \exp\left[h\hat{W}\right] \exp\left[h\hat{T}\right] E(z,t) \tag{J.22}$$

Note that in going from Equation J.21 Equation J.22 we have assumed that $\hat{T}$ and $\hat{W}$ commute, but this is not necessarily true. We now desire to compute one part of eEquation J.22 in the time domain and the other part in the frequency domain. We use Fourier transforms to go back and forth between the domains.

$$E(z+h,t) = \mathcal{F}^{-1}\left\{\exp\left[h\cdot\hat{W}(i\omega)\right]\mathcal{F}\left\{\exp\left[h\cdot\hat{T}(t)\right]E(z,t)\right\}\right\} \tag{J.23}$$

The effects of SPM are calculated in the time domain, and all other effects are calculated in the frequency domain.

Appendix K Colophon

This document was prepared using LaTeX and typeset with the Computer Modern font created by Donald Knuth. The LaTeX Class used was originally assembled by Blaise Thompson and adapted by me.

All source files may be found at https://git.chem.wisc.edu/dmorrow3/dissertation. If using `git`, simply clone the repository by using a terminal to execute:

```
git clone https://git.chem.wisc.edu/dmorrow3/dissertation.git
```.

The entire document may be built by executing

```
python build.py latex
```

in the top-level directory of the repository.

Please contact me directly for any reason at my permanent email address: darienmorrow@gmail.com.

References

[1] Freddy T. Rabouw and Celso de Mello Donega. "Excited-State Dynamics in Colloidal Semiconductor Nanocrystals". In: *Topics in Current Chemistry* 374.5 (Aug. 2016). DOI: 10.1007/s41061-016-0060-0. URL: https://doi.org/10.1007/s41061-016-0060-0.

[2] Michael Bass, ed. *Handbook of Optics, Vol. 2: Devices, Measurements, and Properties*. 2nd ed. McGraw-Hill Professional, 1994.

[3] Manish Chhowalla, Hyeon Suk Shin, Goki Eda, Lain-Jong Li, Kian Ping Loh, and Hua Zhang. "The chemistry of two-dimensional layered transition metal dichalcogenide nanosheets". In: *Nat. Chem.* 5.4 (Mar. 2013), pp. 263–275. DOI: 10.1038/nchem.1589. URL: https://doi.org/10.1038/nchem.1589.

[4] B. Radisavljevic, A. Radenovic, J. Brivio, V. Giacometti, and A. Kis. "Single-layer MoS_2 transistors". In: *Nat. Nanotech.* 6.3 (Jan. 2011), pp. 147–150. DOI: 10.1038/nnano.2010.279. URL: https://doi.org/10.1038/nnano.2010.279.

[5] Gabriel Landolt, Sergey V Eremeev, Oleg E Tereshchenko, Stefan Muff, Bartosz Slomski, Konstantin A Kokh, Masaki Kobayashi, Thorsten Schmitt, Vladimir N Strocov, Jürg Osterwalder, Evgueni V Chulkov, and J Hugo Dil. "Bulk and surface Rashba splitting in single termination BiTeCl". In: *New J. Phys.* 15.8 (Aug. 2013), p. 085022. DOI: 10.1088/1367-2630/15/8/085022. URL: https://doi.org/10.1088/1367-2630/15/8/085022.

[6] Kin Fai Mak, Changgu Lee, James Hone, Jie Shan, and Tony F. Heinz. "Atomically Thin MoS_2: A New Direct-Gap Semiconductor". In: *Phys. Rev. Lett.* 105.13 (Sept. 2010), p. 136805. DOI: 10.1103/physrevlett.105.136805. URL: https://doi.org/10.1103/physrevlett.105.136805.

[7] A. K. Geim and I. V. Grigorieva. "Van der Waals heterostructures". In: *Nature* 499.7459 (July 2013), pp. 419–425. DOI: 10.1038/nature12385. URL: https://doi.org/10.1038/nature12385.

[8] Yuzhou Zhao and Song Jin. "Controllable Water Vapor Assisted Chemical Vapor Transport Synthesis of WS_2–MoS_2 Heterostructure". In: *ACS Materials Lett.* 2.1 (Nov. 2019), pp. 42–48. DOI: 10.1021/acsmaterialslett.9b00415. URL: https://doi.org/10.1021/acsmaterialslett.9b00415.

[9] Patrick A. Lee and N. Phuan Ong. "Philip W. Anderson (1923–2020)". In: *Science* 368.6490 (Apr. 2020), pp. 475–475. DOI: 10.1126/science.abc1042. URL: https://doi.org/10.1126/science.abc1042.

[10] P. W. Anderson. "More Is Different". In: *Science* 177.4047 (Aug. 1972), pp. 393–396. DOI: 10.1126/science.177.4047.393. URL: https://doi.org/10.1126/science.177.4047.393.

[11] Monique Combescot, Roland Combescot, and François Dubin. "Bose–Einstein condensation and indirect excitons: a review". In: *Rep. Prog. Phys.* 80.6 (Mar. 2017), p. 066501. DOI: 10.1088/1361-6633/aa50e3. URL: https://doi.org/10.1088/1361-6633/aa50e3.

[12] Alexey Chernikov, Timothy C. Berkelbach, Heather M. Hill, Albert Rigosi, Yilei Li, Ozgur Burak Aslan, David R. Reichman, Mark S. Hybertsen, and Tony F. Heinz. "Exciton Binding Energy and Nonhydrogenic Rydberg Series in Monolayer WS_2". In: *Phys. Rev. Lett.* 113.7 (Aug. 2014). DOI: 10.1103/physrevlett.113.076802. URL: https://doi.org/10.1103/physrevlett.113.076802.

[13] Archana Raja, Lutz Waldecker, Jonas Zipfel, Yeongsu Cho, Samuel Brem, Jonas D. Ziegler, Marvin Kulig, Takashi Taniguchi, Kenji Watanabe, Ermin Malic, Tony F. Heinz, Timothy C. Berkelbach, and Alexey Chernikov. "Dielectric disorder in two-dimensional materials". In: *Nat. Nanotechnol.* 14.9 (Aug. 2019), pp. 832–837. DOI: 10.1038/s41565-019-0520-0. URL: https://doi.org/10.1038/s41565-019-0520-0.

[14] Diana Y. Qiu, Felipe H. da Jornada, and Steven G. Louie. "Optical Spectrum of MoS_2: Many-Body Effects and Diversity of Exciton States". In: *Phys. Rev. Lett.* 111.21 (Nov. 2013), p. 216805. DOI: 10.1103/physrevlett.111.216805. URL: https://doi.org/10.1103/physrevlett.111.216805.

[15] Erin S. Boyle, Andrei V. Pakoulev, and John C. Wright. "Fully Coherent Triple Sum Frequency Spectroscopy of a Benzene Fermi Resonance". In: *J. Phys. Chem. A* 117.27 (July 2013), pp. 5578–5588. DOI: 10.1021/jp404713x. URL: https://doi.org/10.1021/jp404713x.

[16] Erin S. Boyle, Nathan A. Neff-Mallon, and John C. Wright. "Triply Resonant Sum Frequency Spectroscopy: Combining Advantages of Resonance Raman and 2D-IR". In: *J. Phys. Chem. A* 117.47 (Nov. 2013), pp. 12401–12408. DOI: 10.1021/jp409377a. URL: https://doi.org/10.1021/jp409377a.

[17] Erin S. Boyle, Nathan A. Neff-Mallon, Jonathan D. Handali, and John C. Wright. "Resonance IR: A Coherent Multidimensional Analogue of Resonance Raman". In: *J. Phys. Chem. A* 118.17 (May 2014), pp. 3112–3119. DOI: 10.1021/jp5018554. URL: https://doi.org/10.1021/jp5018554.

[18] Mischa Bonn, Christian Hess, James H. Miners, Tony F. Heinz, Huib J. Bakker, and Minhaeng Cho. "Novel Surface Vibrational Spectroscopy: Infrared-Infrared-Visible Sum-Frequency Generation". In: *Phys. Rev. Lett.* 86.8 (Feb. 2001), pp. 1566–1569. DOI: 10.1103/physrevlett.86.1566. URL: https://doi.org/10.1103/physrevlett.86.1566.

[19] Nathan A. Neff-Mallon and John C. Wright. "Multidimensional Spectral Fingerprints of a New Family of Coherent Analytical Spectroscopies". In: *Analytical Chemistry* 89.24 (Nov. 2017), pp. 13182–13189. DOI: 10.1021/acs.analchem.7b02917. URL: https://doi.org/10.1021/acs.analchem.7b02917.

[20] Jonathan D. Handali, Kyle F. Sunden, Blaise J. Thompson, Nathan A. Neff-Mallon, Emily M. Kaufman, Thomas C. Brunold, and John C. Wright. "Three Dimensional Triply Resonant Sum Frequency Spectroscopy Revealing Vibronic Coupling in Cobalamins: Toward a Probe of Reaction Coordinates". In: *J. Phys. Chem. A* 122.46 (Oct. 2018), pp. 9031–9042. DOI: 10.1021/acs.jpca.8b07678. URL: https://doi.org/10.1021/acs.jpca.8b07678.

[21] Maksim Grechko, Simon A. Bretschneider, Laura Vietze, Heejae Kim, and Mischa Bonn. "Vibrational Coupling between Organic and Inorganic Sublattices of Hybrid Perovskites". In: *Angew. Chem.* 57.41 (Sept. 2018), pp. 13657–13661. DOI: 10.1002/anie.201806676. URL: https://doi.org/10.1002%2Fanie.201806676.

[22] Maksim Grechko, Taisuke Hasegawa, Francesco D'Angelo, Hironobu Ito, Dmitry Turchinovich, Yuki Nagata, and Mischa Bonn. "Coupling between intra- and intermolecular motions in liquid water revealed by two-dimensional terahertz-infrared-visible spectroscopy". In: *Nat. Commun.* 9.1 (Feb. 2018), p. 885. DOI: 10.1038/s41467-018-03303-y. URL: https://doi.org/10.1038/s41467-018-03303-y.

[23] Edbert J. Sie, Timm Rohwer, Changmin Lee, and Nuh Gedik. "Time-resolved XUV ARPES with tunable 24–33 eV laser pulses at 30 meV resolution". In: *Nat. Commun.* 10.1 (Aug. 2019). DOI: 10.1038/s41467-019-11492-3. URL: https://doi.org/10.1038/s41467-019-11492-3.

[24] S. K. Sundaram and E. Mazur. "Inducing and probing non-thermal transitions in semiconductors using femtosecond laser pulses". In: *Nat. Mater.* 1.4 (Dec. 2002), pp. 217–224. DOI: 10.1038/nmat767. URL: https://doi.org/10.1038/nmat767.

[25] John Paul Callan. "Ultrafast dynamics and phase changes in solids excited by femtosecond laser pulses". PhD thesis. Harvard University, 2000. URL: https://ui.adsabs.harvard.edu/abs/2000PhDT.....75C/abstract.

[26] Florian Kanal. "Femtosecond Transient Absorption Spectroscopy—Technical Improvements and Applications to Ultrafast Molecular Phenomena". PhD thesis. University of Würzburg, 2015. URL: https://opus.bibliothek.uni-wuerzburg.de/opus4-wuerzburg/frontdoor/deliver/index/docId/11877/file/Florian_Kanal_Dissertation.pdf.

[27] Giulio Cerullo and Sandro De Silvestri. "Ultrafast optical parametric amplifiers". In: *Review of Scientific Instruments* 74.1 (Jan. 2003), pp. 1–18. DOI: 10.1063/1.1523642. URL: https://doi.org/10.1063%2F1.1523642.

[28] C Manzoni and G Cerullo. "Design criteria for ultrafast optical parametric amplifiers". In: *Journal of Optics* 18.10 (Aug. 2016), p. 103501. DOI: 10.1088/2040-8978/18/10/103501. URL: https://doi.org/10.1088/2040-8978/18/10/103501.

[29] Ye Yang, Mengjin Yang, David T. Moore, Yong Yan, Elisa M. Miller, Kai Zhu, and Matthew C. Beard. "Top and bottom surfaces limit carrier lifetime in lead iodide perovskite films". In: *Nat.Energy* 2.2 (Jan. 2017). DOI: 10.1038/nenergy.2016.207. URL: https://doi.org/10.1038/nenergy.2016.207.

[30] Julia S. Kirpich, Sean M. Gottlieb, Che-Wei Chang, Peter W. Kim, Shelley S. Martin, J. Clark Lagarias, and Delmar S. Larsen. "Reverse Photodynamics of the Noncanonical Red/Green NpR3784 Cyanobacteriochrome from Nostoc punctiforme". In: *Biochemistry* 58.18 (Apr. 2019), pp. 2307–2317. DOI: 10.1021/acs.biochem.8b01275. URL: https://doi.org/10.1021/acs.biochem.8b01275.

[31] Darien J. Morrow, Daniel D. Kohler, and John C. Wright. "Group- and phase-velocity-mismatch fringes in triple sum-frequency spectroscopy". In: *Phys. Rev. A* 96.6 (Dec. 2017), p. 063835. DOI: 10.1103/physreva.96.063835. URL: https://doi.org/10.1103/physreva.96.063835.

[32] John C. Wright. "Applications of the New Family of Coherent Multidimensional Spectroscopies for Analytical Chemistry". In: *Annu. Rev. Anal. Chem.* 10.1 (June 2017), pp. 45–70. DOI: 10.1146/annurev-anchem-061516-045349. URL: https://doi.org/10.1146/annurev-anchem-061516-045349.

[33] J. A. Armstrong, N. Bloembergen, J. Ducuing, and P. S. Pershan. "Interactions between Light Waves in a Nonlinear Dielectric". In: *Phys. Rev.* 127.6 (Sept. 1962), pp. 1918–1939. DOI: 10.1103/physrev.127.1918. URL: https://doi.org/10.1103/physrev.127.1918.

[34] N. Bloembergen. *Nonlinear Optics*. W. A. Benjamin, Inc., 1965.

[35] D. Stoker, M. F. Becker, and J. W. Keto. "Optical third-harmonic generation using ultrashort laser pulses". In: *Phys. Rev. A* 71.6 (June 2005). DOI: 10.1103/physreva.71.061802. URL: https://doi.org/10.1103/physreva.71.061802.

[36] D. S. Stoker, J. Baek, W. Wang, D. Kovar, M. F. Becker, and J. W. Keto. "Ultrafast third-harmonic generation from textured aluminum nitride–sapphire interfaces". In: *Phys. Rev. A* 73.5 (May 2006). DOI: 10.1103/physreva.73.053812. URL: https://doi.org/10.1103/physreva.73.053812.

[37] W. E. Angerer, N. Yang, A. G. Yodh, M. A. Khan, and C. J. Sun. "Ultrafast second-harmonic generation spectroscopy of GaN thin films on sapphire". In: *Phys. Rev. B* 59.4 (Jan. 1999), pp. 2932–2946. DOI: 10.1103/physrevb.59.2932. URL: https://doi.org/10.1103/physrevb.59.2932.

[38] Robert W. Boyd. *Nonlinear Optics*. 3rd ed. Academic Press, 2008.

[39] Richard S. Tasgal and Y. B. Band. "Third-harmonic generation in isotropic media by focused pulses". In: *Phys. Rev. A* 70.5 (Nov. 2004). DOI: 10.1103/physreva.70.053810. URL: https://doi.org/10.1103/physreva.70.053810.

[40] Anthony E. Siegman. *Lasers*. 1st ed. University Science Books, 1986.

[41] Arkady Major, Fumiyo Yoshino, Irkalis Nikolakakos, J. Stewart Aitchison, and Peter W. E. Smith. "Dispersion of the nonlinear refractive index in sapphire". In: *Optics Letters* 29.6 (Mar. 2004), p. 602. DOI: 10.1364/ol.29.000602. URL: https://doi.org/10.1364/ol.29.000602.

[42] P. D. Maker and R. W. Terhune. "Study of Optical Effects Due to an Induced Polarization Third Order in the Electric Field Strength". In: *Phys. Rev.* 137.3A (Feb. 1965), A801–A818. DOI: 10.1103/physrev.137.a801. URL: https://doi.org/10.1103/physrev.137.a801.

[43] Daniel D. Kohler, Blaise J. Thompson, and John C. Wright. "Frequency-domain coherent multidimensional spectroscopy when dephasing rivals pulsewidth: Disentangling material and instrument response". In: *J. Chem. Phys.* 147.8 (Aug. 2017), p. 084202. DOI: 10.1063/1.4986069. URL: https://doi.org/10.1063/1.4986069.

[44] Y. R. Shen. *The Principles of Nonlinear Optics*. 1st ed. John Wiley & Sons, 1984.

[45] P. D. Maker, R. W. Terhune, M. Nisenoff, and C. M. Savage. "Effects of Dispersion and Focusing on the Production of Optical Harmonics". In: *Phys. Rev. Lett.* 8.1 (Jan. 1962), pp. 21–22. DOI: 10.1103/physrevlett.8.21. URL: https://doi.org/10.1103/physrevlett.8.21.

[46] M. Mlejnek, E. M. Wright, J. V. Moloney, and N. Bloembergen. "Second Harmonic Generation of Femtosecond Pulses at the Boundary of a Nonlinear Dielectric". In: *Phys. Rev. Lett.* 83.15 (Oct. 1999), pp. 2934–2937. DOI: 10.1103/physrevlett.83.2934. URL: https://doi.org/10.1103/physrevlett.83.2934.

[47] Peter Trabs, Frank Noack, Aleksandr S. Aleksandrovsky, Alexandre I. Zaitsev, Nikita V. Radionov, and Valentin Petrov. "Spectral fringes in non-phase-matched SHG and refinement of dispersion relations in the VUV". In: *Opt. Express* 23.8 (Apr. 2015), p. 10091. DOI: 10.1364/oe.23.010091. URL: https://doi.org/10.1364/oe.23.010091.

[48] R. Maleck Rassoul, A. Ivanov, E. Freysz, A. Ducasse, and F. Hache. "Second-harmonic generation under phase-velocity and group-velocity mismatch: influence of cascading self-phase and cross-phase modulation". In: *Optics Letters* 22.5 (Mar. 1997), p. 268. DOI: 10.1364/ol.22.000268. URL: https://doi.org/10.1364/ol.22.000268.

[49] W. Glenn. "Second-harmonic generation by picosecond optical pulses". In: *IEEE Journal of Quantum Electronics* 5.6 (June 1969), pp. 284–290. DOI: 10.1109/jqe.1969.1081948. URL: https://doi.org/10.1109/jqe.1969.1081948.

[50] Erkin Sidick, André Knoesen, and Andrew Dienes. "Ultrashort-pulse second-harmonic generation I Transform-limited fundamental pulses". In: *J. Opt. Soc. Am. B* 12.9 (Sept. 1995), p. 1704. DOI: 10.1364/josab.12.001704. URL: https://doi.org/10.1364/josab.12.001704.

[51] Jean-Claude Diels and Wolfgang Rudolph. *Ultrashort Laser Pulse Phenomena: Fundamentals, Techniques, and Applications on a Femtosecond Time Scale*. 1st ed. Academic Press, May 1996.

[52] Irving H. Malitson. "Refraction and Dispersion of Synthetic Sapphire". In: *J. Opt. Soc. Am.* 52.12 (Dec. 1962), p. 1377. DOI: 10.1364/josa.52.001377. URL: https://doi.org/10.1364/josa.52.001377.

[53] Jamal T. Manassah. "Effects of velocity dispersion on a generated second harmonic signal". In: *Applied Optics* 27.21 (Nov. 1988), p. 4365. DOI: 10.1364/ao.27.004365. URL: https://doi.org/10.1364/ao.27.004365.

[54] L. D. Noordam, H. J. Bakker, M. P. de Boer, and H. B. van Linden van den Heuvell. "Second-harmonic generation of femtosecond pulses: observation of phase-mismatch effects". In: *Optics Letters* 15.24 (Dec. 1990), p. 1464. DOI: 10.1364/ol.15.001464. URL: https://doi.org/10.1364/ol.15.001464.

[55] Guido van Rossum et al. *Python*. [Online; accessed 2017-09-28]. 2001–. URL: http://www.python.org/.

[56] Eric Jones, Travis Oliphant, and Pearu Peterson. *SciPy: Open source scientific tools for Python*. [Online; accessed 2017-09-28]. 2001. URL: http://www.scipy.org/.

[57] Stéfan van der Walt, S Chris Colbert, and Gaël Varoquaux. "The NumPy Array: A Structure for Efficient Numerical Computation". In: *Comput. Sci. Eng.* 13.2 (Mar. 2011), pp. 22–30. DOI: 10.1109/mcse.2011.37. URL: https://doi.org/10.1109/mcse.2011.37.

[58] John D. Hunter. "Matplotlib: A 2D Graphics Environment". In: *Comput. Sci. Eng.* 9.3 (2007), pp. 90–95. DOI: 10.1109/mcse.2007.55. URL: https://doi.org/10.1109/mcse.2007.55.

[59] Keith M. Murdoch, David E. Thompson, Kent A. Meyer, and John C. Wright. "Modeling Window Contributions to Four-Wave Mixing Spectra and Measurements of Third-Order Optical Susceptibilities". In: *Appl. Spectrosc.* 54.10 (Oct. 2000), pp. 1495–1505. DOI: 10.1366/0003702001948411. URL: https://doi.org/10.1366/0003702001948411.

[60] Andreas Volkmer, Ji-Xin Cheng, and X. Sunney Xie. "Vibrational Imaging with High Sensitivity via Epidetected Coherent Anti-Stokes Raman Scattering Microscopy". In: *Phys. Rev. Lett.* 87.2 (June 2001). DOI: 10.1103/physrevlett.87.023901. URL: https://doi.org/10.1103/physrevlett.87.023901.

[61] Kyle J. Czech, Blaise J. Thompson, Schuyler Kain, Qi Ding, Melinda J. Shearer, Robert J. Hamers, Song Jin, and John C. Wright. "Measurement of Ultrafast Excitonic Dynamics of Few-Layer MoS_2 Using State-Selective Coherent Multidimensional Spectroscopy". In: *ACS Nano* 9.12 (Nov. 2015), pp. 12146–12157. DOI: 10.1021/acsnano.5b05198. URL: https://doi.org/10.1021/acsnano.5b05198.

[62] Charles C. Wang and E. L. Baardsen. "Study of Optical Third-Harmonic Generation in Reflection". In: *Phys. Rev.* 185.3 (Sept. 1969), pp. 1079–1082. DOI: 10.1103/physrev.185.1079. URL: https://doi.org/10.1103/physrev.185.1079.

[63] P.P. Bey, J.F. Guiliani, and H. Rabin. "Third-harmonic nonlinear reflection from a liquid with adjustable momentum matching". In: *Physics Letters A* 28.2 (Nov. 1968), pp. 89–90. DOI: 10.1016/0375-9601(68)90403-9. URL: https://doi.org/10.1016/0375-9601(68)90403-9.

[64] M. D. Crisp. "Propagation of Small-Area Pulses of Coherent Light through a Resonant Medium". In: *Phys. Rev. A* 1.6 (June 1970), pp. 1604–1611. DOI: 10.1103/physreva.1.1604. URL: https://doi.org/10.1103/physreva.1.1604.

[65] Roger J. Carlson and John C. Wright. "Absorption and Coherent Interference Effects in Multiply Resonant Four-Wave Mixing Spectroscopy". In: *Appl. Spectrosc.* 43.7 (Sept. 1989), pp. 1195–1208. DOI: 10.1366/0003702894203408. URL: https://doi.org/10.1366/0003702894203408.

[66] Kathryn M. Kornau, Mark A. Rickard, Nathan A. Mathew, Andrei V. Pakoulev, and John C. Wright. "Multiresonant Coherent Multidimensional Vibrational Spectroscopy of Aromatic Systems: Pyridine, a Model System". In: *J. Phys. Chem. A* 115.16 (Apr. 2011), pp. 4054–4062. DOI: 10.1021/jp1104856. URL: https://doi.org/10.1021/jp1104856.

[67] Opher Kinrot and Yehiam Prior. "Four-wave mixing in optically dense media". In: *Phys. Rev. A* 50.3 (Sept. 1994), R1999–R2002. DOI: 10.1103/physreva.50.r1999. URL: https://doi.org/10.1103/physreva.50.r1999.

[68] Darien J. Morrow, Daniel D. Kohler, Kyle J. Czech, and John C. Wright. "Communication: Multidimensional triple sum-frequency spectroscopy of MoS_2 and comparisons with absorption and second harmonic generation spectroscopies". In: *J. Chem. Phys.* 149.9 (Sept. 2018), p. 091101. DOI: 10.1063/1.5047802. URL: https://doi.org/10.1063/1.5047802.

[69] Steven T. Cundiff. "Coherent spectroscopy of semiconductors". In: *Opt. Express* 16.7 (Mar. 2008), p. 4639. DOI: 10.1364/oe.16.004639. URL: https://doi.org/10.1364/oe.16.004639.

[70] Galan Moody and Steven T. Cundiff. "Advances in multi-dimensional coherent spectroscopy of semiconductor nanostructures". In: *Advances in Physics: X* 2.3 (May 2017), pp. 641–674. DOI: 10.1080/23746149.2017.1346482. URL: https://doi.org/10.1080/23746149.2017.1346482.

[71] Jason K. Ellis, Melissa J. Lucero, and Gustavo E. Scuseria. "The indirect to direct band gap transition in multilayered MoS_2 as predicted by screened hybrid density functional theory". In: *Appl. Phys. Lett.* 99.26 (Dec. 2011), p. 261908. DOI: 10.1063/1.3672219. URL: https://doi.org/10.1063/1.3672219.

[72] Qing Hua Wang, Kourosh Kalantar-Zadeh, Andras Kis, Jonathan N. Coleman, and Michael S. Strano. "Electronics and optoelectronics of two-dimensional transition metal dichalcogenides". In: *Nature Nanotechnology* 7.11 (Nov. 2012), pp. 699–712. DOI: 10.1038/nnano.2012.193. URL: https://doi.org/10.1038/nnano.2012.193.

[73] Fengnian Xia, Han Wang, Di Xiao, Madan Dubey, and Ashwin Ramasubramaniam. "Two-dimensional material nanophotonics". In: *Nat. Photonics* 8.12 (Dec. 2014), pp. 899–907. DOI: 10.1038/nphoton.2014.271. URL: https://doi.org/10.1038/nphoton.2014.271.

[74] Kin Fai Mak and Jie Shan. "Photonics and optoelectronics of 2D semiconductor transition metal dichalcogenides". In: *Nat. Photonics* 10.4 (Apr. 2016), pp. 216–226. DOI: 10.1038/nphoton.2015.282. URL: https://doi.org/10.1038%2Fnphoton.2015.282.

[75] Alejandro Molina-Sánchez, Davide Sangalli, Kerstin Hummer, Andrea Marini, and Ludger Wirtz. "Effect of spin-orbit interaction on the optical spectra of single-layer, double-layer, and bulk MoS_2". In: *Phys. Rev. B* 88.4 (July 2013), p. 045412. DOI: 10.1103/physrevb.88.045412. URL: https://doi.org/10.1103/physrevb.88.045412.

[76] Yilei Li, Alexey Chernikov, Xian Zhang, Albert Rigosi, Heather M. Hill, Arend M. van der Zande, Daniel A. Chenet, En-Min Shih, James Hone, and Tony F. Heinz. "Measurement of the optical dielectric function of monolayer transition-metal dichalcogenides:MoS_2, $MoSe_2$, WS_2, and WSe_2". In: *Phys. Rev. B* 90.20 (Nov. 2014), p. 205422. DOI: 10.1103/physrevb.90.205422. URL: https://doi.org/10.1103/physrevb.90.205422.

[77] Keliang He, Nardeep Kumar, Liang Zhao, Zefang Wang, Kin Fai Mak, Hui Zhao, and Jie Shan. "Tightly Bound Excitons in Monolayer WSe_2". In: *Phys. Rev. Lett.* 113.2 (July 2014), p. 026803. DOI: 10.1103/physrevlett.113.026803. URL: https://doi.org/10.1103/physrevlett.113.026803.

[78] Nihit Saigal, Vasam Sugunakar, and Sandip Ghosh. "Exciton binding energy in bulk MoS_2: A reassessment". In: *Appl. Phys. Lett.* 108.13 (Mar. 2016), p. 132105. DOI: 10.1063/1.4945047. URL: https://doi.org/10.1063/1.4945047.

[79] J. Kopaczek, M. P. Polak, P. Scharoch, K. Wu, B. Chen, S. Tongay, and R. Kudrawiec. "Direct optical transitions at K- and H-point of Brillouin zone in bulk MoS_2, $MoSe_2$, WS_2, and WSe_2". In: *J. Appl. Phys.* 119.23 (June 2016), p. 235705. DOI: 10.1063/1.4954157. URL: https://doi.org/10.1063/1.4954157.

[80] L. Britnell, R. M. Ribeiro, A. Eckmann, R. Jalil, B. D. Belle, A. Mishchenko, Y.- J. Kim, R. V. Gorbachev, T. Georgiou, S. V. Morozov, A. N. Grigorenko, A. K. Geim, C. Casiraghi, A. H. C. Neto, and K. S. Novoselov. "Strong Light-Matter Interactions in Heterostructures of Atomically Thin Films". In: *Science* 340.6138 (May 2013), pp. 1311–1314. DOI: 10.1126/science.1235547. URL: https://doi.org/10.1126%2Fscience.1235547.

[81] A. Carvalho, R. M. Ribeiro, and A. H. Castro Neto. "Band nesting and the optical response of two-dimensional semiconducting transition metal dichalcogenides". In: *Phys. Rev. B* 88.11 (Sept. 2013). DOI: 10.1103/physrevb.88.115205. URL: https://doi.org/10.1103%2Fphysrevb.88.115205.

[82] Jaehun Jeong, Yoon-Ho Choi, Kwangsik Jeong, Hanbum Park, Dasol Kim, and Mann-Ho Cho. "Evolution of the broadband optical transition in large-area $MoSe_2$". In: *Phys. Rev. B* 97.7 (Feb. 2018). DOI: 10.1103/physrevb.97.075433. URL: https://doi.org/10.1103%2Fphysrevb.97.075433.

[83] Maciej Bieniek, Marek Korkusiński, Ludmiła Szulakowska, Paweł Potasz, Isil Ozfidan, and Paweł Hawrylak. "Band nesting, massive Dirac fermions, and valley Landé and Zeeman effects in transition metal dichalcogenides: A tight-binding model". In: *Phys. Rev. B* 97.8 (Feb. 2018). DOI: 10.1103/physrevb.97.085153. URL: https://doi.org/10.1103%2Fphysrevb.97.085153.

[84] N. Bloembergen and Y. R. Shen. "Quantum-Theoretical Comparison of Nonlinear Susceptibilities in Parametric Media, Lasers, and Raman Lasers". In: *Phys. Rev.* 133.1A (Jan. 1964), A37–A49. DOI: 10.1103/physrev.133.a37. URL: https://doi.org/10.1103%2Fphysrev.133.a37.

[85] Yilei Li, Yi Rao, Kin Fai Mak, Yumeng You, Shuyuan Wang, Cory R. Dean, and Tony F. Heinz. "Probing Symmetry Properties of Few-Layer MoS_2 and h-BN by Optical Second-Harmonic Generation". In: *Nano Lett.* 13.7 (June 2013), pp. 3329–3333. DOI: 10.1021/nl401561r. URL: https://doi.org/10.1021/nl401561r.

[86] Leandro M. Malard, Thonimar V. Alencar, Ana Paula M. Barboza, Kin Fai Mak, and Ana M. de Paula. "Observation of intense second harmonic generation from MoS_2 atomic crystals". In: *Phys. Rev. B* 87.20 (May 2013), p. 201401. DOI: 10.1103/physrevb.87.201401. URL: https://doi.org/10.1103/physrevb.87.201401.

[87] Nardeep Kumar, Sina Najmaei, Qiannan Cui, Frank Ceballos, Pulickel M. Ajayan, Jun Lou, and Hui Zhao. "Second harmonic microscopy of monolayer MoS_2". In: *Phys. Rev. B* 87.16 (Apr. 2013), p. 161403. DOI: 10.1103/physrevb.87.161403. URL: https://doi.org/10.1103/physrevb.87.161403.

[88] Rui Wang, Hui-Chun Chien, Jatinder Kumar, Nardeep Kumar, Hsin-Ying Chiu, and Hui Zhao. "Third-Harmonic Generation in Ultrathin Films of MoS_2". In: *ACS Appl. Mater. Interfaces* 6.1 (Dec. 2013), pp. 314–318. DOI: 10.1021/am4042542. URL: https://doi.org/10.1021/am4042542.

[89] Mads L. Trolle, Gotthard Seifert, and Thomas G. Pedersen. "Theory of excitonic second-harmonic generation in monolayer MoS_2". In: *Phys. Rev. B* 89.23 (June 2014). DOI: 10.1103/physrevb.89.235410. URL: https://doi.org/10.1103/physrevb.89.235410.

[90] M. Grüning and C. Attaccalite. "Second harmonic generation inh-BN and MoS_2 monolayers: Role of electron-hole interaction". In: *Phys. Rev. B* 89.8 (Feb. 2014). DOI: 10.1103/physrevb.89.081102. URL: https://doi.org/10.1103/physrevb.89.081102.

[91] D. J. Clark, V. Senthilkumar, C. T. Le, D. L. Weerawarne, B. Shim, J. I. Jang, J. H. Shim, J. Cho, Y. Sim, M.-J. Seong, S. H. Rhim, A. J. Freeman, K.-H. Chung, and Y. S. Kim. "Strong optical nonlinearity of CVD-grown MoS_2 monolayer as probed by wavelength-dependent second-harmonic generation". In: *Phys. Rev. B* 90.12 (Sept. 2014). DOI: 10.1103/physrevb.90.121409. URL: https://doi.org/10.1103/physrevb.90.121409.

[92] Mads L. Trolle, Yao-Chung Tsao, Kjeld Pedersen, and Thomas G. Pedersen. "Observation of excitonic resonances in the second harmonic spectrum of MoS_2". In: *Phys. Rev. B* 92.16 (Oct. 2015). DOI: 10.1103/physrevb.92.161409. URL: https://doi.org/10.1103/physrevb.92.161409.

[93] G. Wang, X. Marie, I. Gerber, T. Amand, D. Lagarde, L. Bouet, M. Vidal, A. Balocchi, and B. Urbaszek. "Giant Enhancement of the Optical Second-Harmonic Emission of WSe_2 Monolayers by Laser Excitation at Exciton Resonances". In: *Phys. Rev. Lett.* 114.9 (Mar. 2015), p. 097403. DOI: 10.1103/physrevlett.114.097403. URL: https://doi.org/10.1103/physrevlett.114.097403.

[94] Jianhui Sun, Yan-Juan Gu, Dang Yuan Lei, Shu Ping Lau, Wing-Tak Wong, Kwok-Yin Wong, and Helen Lai-Wai Chan. "Mechanistic Understanding of Excitation-Correlated Nonlinear Optical Properties in MoS_2 Nanosheets and Nanodots: The Role of Exciton Resonance". In: *ACS Photonics* 3.12 (Dec. 2016), pp. 2434–2444. DOI: 10.1021/acsphotonics.6b00682. URL: https://doi.org/10.1021/acsphotonics.6b00682.

[95] Lasse Karvonen, Antti Säynätjoki, Mikko J. Huttunen, Anton Autere, Babak Amirsolaimani, Shisheng Li, Robert A. Norwood, Nasser Peyghambarian, Harri Lipsanen, Goki Eda, Khanh Kieu, and Zhipei Sun. "Rapid visualization of grain boundaries in monolayer MoS_2 by multiphoton microscopy". In: *Nat. Commun.* 8 (June 2017), p. 15714. DOI: 10.1038/ncomms15714. URL: https://doi.org/10.1038/ncomms15714.

[96] Melinda J. Shearer, Leith Samad, Yi Zhang, Yuzhou Zhao, Alexander Puretzky, Kevin W. Eliceiri, John C. Wright, Robert J. Hamers, and Song Jin. "Complex and Noncentrosymmetric Stacking of Layered Metal Dichalcogenide Materials Created by Screw Dislocations". In: *J. Am. Chem. Soc.* 139.9 (Feb. 2017), pp. 3496–3504. DOI: 10.1021/jacs.6b12559. URL: https://doi.org/10.1021/jacs.6b12559.

[97] M. M. Glazov, L. E. Golub, G. Wang, X. Marie, T. Amand, and B. Urbaszek. "Intrinsic exciton-state mixing and nonlinear optical properties in transition metal dichalcogenide monolayers". In: *Phys. Rev. B* 95.3 (Jan. 2017). DOI: 10.1103/physrevb.95.035311. URL: https://doi.org/10.1103/physrevb.95.035311.

[98] Naveen K. Balla, Maria O'Brien, Niall McEvoy, Georg S. Duesberg, Hervé Rigneault, Sophie Brasselet, and David McCloskey. "Effects of Excitonic Resonance on Second and Third Order Nonlinear Scattering from Few-Layer MoS_2". In: *ACS Photonics* (Feb. 2018). DOI: 10.1021/acsphotonics.7b00912. URL: https://doi.org/10.1021%2Facsphotonics.7b00912.

[99] John C. Wright. "Multiresonant Coherent Multidimensional Spectroscopy". In: *Annu. Rev. Phys. Chem.* 62.1 (May 2011), pp. 209–230. DOI: 10.1146/annurev-physchem-032210-103551. URL: https://doi.org/10.1146/annurev-physchem-032210-103551.

[100] Jonathan D. Handali, Kyle F. Sunden, Emily M. Kaufman, and John C. Wright. "Interference and phase mismatch effects in coherent triple sum frequency spectroscopy". In: *Chemical Physics* 512 (June 2018), pp. 13–19. DOI: 10.1016/j.chemphys.2018.05.023. URL: https://doi.org/10.1016/j.chemphys.2018.05.023.

[101] A. Honold, L. Schultheis, J. Kuhl, and C. W. Tu. "Reflected degenerate four-wave mixing on GaAs single quantum wells". In: *Appl. Phys. Lett.* 52.25 (June 1988), pp. 2105–2107. DOI: 10.1063/1.99549. URL: https://doi.org/10.1063/1.99549.

[102] Masihhur R. Laskar, Lu Ma, Santhakumar Kannappan, Pil Sung Park, Sriram Krishnamoorthy, Digbijoy N. Nath, Wu Lu, Yiying Wu, and Siddharth Rajan. "Large area single crystal (0001) oriented MoS_2". In: *Appl. Phys. Lett.* 102.25 (June 2013), p. 252108. DOI: 10.1063/1.4811410. URL: https://doi.org/10.1063/1.4811410.

[103] Blaise J. Thompson, Kyle F. Sunden, Darien J. Morrow, and Nathan Andrew Neff-Mallon. *PyCMDS*. Mar. 2018. DOI: 10.5281/zenodo.1198911. URL: https://doi.org/10.5281/zenodo.1198911.

[104] Blaise J. Thompson, Kyle F. Sunden, Darien J. Morrow, Nathan Andrew Neff-Mallon, Kyle J. Czech, Daniel D. Kohler, and Rachel Swedin. *WrightTools*. Mar. 2018. DOI: 10.5281/zenodo.1198905. URL: https://doi.org/10.5281/zenodo.1198905.

[105] Saifeng Zhang, Ningning Dong, Niall McEvoy, Maria O'Brien, Sinéad Winters, Nina C. Berner, Chanyoung Yim, Yuanxin Li, Xiaoyan Zhang, Zhanghai Chen, Long Zhang, Georg S. Duesberg, and Jun Wang. "Direct Observation of Degenerate Two-Photon Absorption and Its Saturation in WS_2 and MoS_2 Monolayer and Few-Layer Films". In: *ACS Nano* 9.7 (July 2015), pp. 7142–7150. DOI: 10.1021/acsnano.5b03480. URL: https://doi.org/10.1021/acsnano.5b03480.

[106] J.D.E. McIntyre and D.E. Aspnes. "Differential reflection spectroscopy of very thin surface films". In: *Surface Science* 24.2 (Feb. 1971), pp. 417–434. DOI: 10.1016/0039-6028(71)90272-x. URL: https://doi.org/10.1016/0039-6028(71)90272-x.

[107] Kin Fai Mak, Matthew Y. Sfeir, Yang Wu, Chun Hung Lui, James A. Misewich, and Tony F. Heinz. "Measurement of the Optical Conductivity of Graphene". In: *Phys. Rev. Lett.* 101.19 (Nov. 2008), p. 196405. DOI: 10.1103/physrevlett.101.196405. URL: https://doi.org/10.1103/physrevlett.101.196405.

[108] J. E. Sipe and A. I. Shkrebtii. "Second-order optical response in semiconductors". In: *Phys. Rev. B* 61.8 (Feb. 2000), pp. 5337–5352. DOI: 10.1103/physrevb.61.5337. URL: https://doi.org/10.1103/physrevb.61.5337.

[109] V. M. Axt and S. Mukamel. "Nonlinear optics of semiconductor and molecular nanostructures: a common perspective". In: *Rev. Mod. Phys.* 70.1 (Jan. 1998), pp. 145–174. DOI: 10.1103/revmodphys.70.145. URL: https://doi.org/10.1103/revmodphys.70.145.

[110] Nasser Peyghambarian, Stephan W. Koch, and Andre Mysyrowicz. *Introduction to Semiconductor Optics*. Prentice Hall, 1993.

[111] Mildred Dresselhaus, Gene Dresselhaus, Stephen Cronin, and Antonio Gomes Souza Filho. *Solid State Properties*. Springer Berlin Heidelberg, 2018. DOI: 10.1007/978-3-662-55922-2. URL: https://doi.org/10.1007/978-3-662-55922-2.

[112] J. E. Padilha, H. Peelaers, A. Janotti, and C. G. Van de Walle. "Nature and evolution of the band-edge states in MoS_2: From monolayer to bulk". In: *Phys. Rev. B* 90.20 (Nov. 2014). DOI: 10.1103/physrevb.90.205420. URL: https://doi.org/10.1103/physrevb.90.205420.

[113] A. B. Kuzmenko. "Kramers–Kronig constrained variational analysis of optical spectra". In: *Review of Scientific Instruments* 76.8 (Aug. 2005), p. 083108. DOI: 10.1063/1.1979470. URL: https://doi.org/10.1063/1.1979470.

[114] Edbert J. Sie, Alex J. Frenzel, Yi-Hsien Lee, Jing Kong, and Nuh Gedik. "Intervalley biexcitons and many-body effects in monolayer MoS_2". In: *Phys. Rev. B* 92.12 (Sept. 2015), p. 125417. DOI: 10.1103/physrevb.92.125417. URL: https://doi.org/10.1103/physrevb.92.125417.

[115] Torsten Stiehm, Robert Schneider, Johannes Kern, Iris Niehues, Steffen Michaelis de Vasconcellos, and Rudolf Bratschitsch. "Supercontinuum second harmonic generation spectroscopy of atomically thin semiconductors". In: *Rev. Sci. Instrum.* 90.8 (Aug. 2019), p. 083102. DOI: 10.1063/1.5100593. URL: https://doi.org/10.1063/1.5100593.

[116] D M Roessler. "Kramers-Kronig analysis of reflection data". In: *British Journal of Applied Physics* 16.8 (Aug. 1965), pp. 1119–1123. DOI: 10.1088/0508-3443/16/8/310. URL: https://doi.org/10.1088/0508-3443/16/8/310.

[117] Hong Li, Qing Zhang, Chin Chong Ray Yap, Beng Kang Tay, Teo Hang Tong Edwin, Aurelien Olivier, and Dominique Baillargeat. "From Bulk to Monolayer MoS_2: Evolution of Raman Scattering". In: *Advanced Functional Materials* 22.7 (Jan. 2012), pp. 1385–1390. DOI: 10.1002/adfm.201102111. URL: https://doi.org/10.1002/adfm.201102111.

[118] P. A. Bertrand. "Surface-phonon dispersion of MoS_2". In: *Phys. Rev. B* 44.11 (Sept. 1991), pp. 5745–5749. DOI: 10.1103/physrevb.44.5745. URL: https://doi.org/10.1103%2Fphysrevb.44.5745.

[119] Changgu Lee, Hugen Yan, Louis E. Brus, Tony F. Heinz, James Hone, and Sunmin Ryu. "Anomalous Lattice Vibrations of Single- and Few-Layer MoS_2". In: *ACS Nano* 4.5 (Apr. 2010), pp. 2695–2700. DOI: 10.1021/nn1003937. URL: https://doi.org/10.1021/nn1003937.

[120] Hanzhe Liu, Yilei Li, Yong Sing You, Shambhu Ghimire, Tony F. Heinz, and David A. Reis. "High-harmonic generation from an atomically thin semiconductor". In: *Nat. Phys.* 13.3 (Nov. 2016), pp. 262–265. DOI: 10.1038/nphys3946. URL: https://doi.org/10.1038/nphys3946.

[121] Charles C. Kim, J. W. Garland, H. Abad, and P. M. Raccah. "Modeling the optical dielectric function of semiconductors: Extension of the critical-point parabolic-band approximation". In: *Phys. Rev. B* 45 (20 May 1992), pp. 11749–11767. DOI: 10.1103/PhysRevB.45.11749. URL: https://link.aps.org/doi/10.1103/PhysRevB.45.11749.

[122] W Y Liang and A R Beal. "A study of the optical joint density-of-states function". In: *Journal of Physics C: Solid State Physics* 9.14 (July 1976), pp. 2823–2832. DOI: 10.1088/0022-3719/9/14/020. URL: https://doi.org/10.1088%2F0022-3719%2F9%2F14%2F020.

[123] Darien J. Morrow, Daniel D. Kohler, Yuzhou Zhao, Song Jin, and John C. Wright. "Triple sum frequency pump-probe spectroscopy of transition metal dichalcogenides". In: *Phys. Rev. B* 100.23 (Dec. 2019), p. 235303. DOI: 10.1103/physrevb.100.235303. URL: https://doi.org/10.1103/physrevb.100.235303.

[124] Ronald Ulbricht, Euan Hendry, Jie Shan, Tony F. Heinz, and Mischa Bonn. "Carrier dynamics in semiconductors studied with time-resolved terahertz spectroscopy". In: *Rev. Mod. Phys.* 83.2 (June 2011), pp. 543–586. DOI: 10.1103/revmodphys.83.543. URL: https://doi.org/10.1103/revmodphys.83.543.

[125] Wei Xiong, Jennifer E. Laaser, Peerasak Paoprasert, Ryan A. Franking, Robert J. Hamers, Padma Gopalan, and Martin T. Zanni. "Transient 2D IR Spectroscopy of Charge Injection in Dye-Sensitized Nanocrystalline Thin Films". In: *J. Am. Chem. Soc.* 131.50 (Dec. 2009), pp. 18040–18041. DOI: 10.1021/ja908479r. URL: https://doi.org/10.1021/ja908479r.

[126] Daniel R. Dietze and Richard A. Mathies. "Femtosecond Stimulated Raman Spectroscopy". In: *ChemPhysChem* 17.9 (Mar. 2016), pp. 1224–1251. DOI: 10.1002/cphc.201600104. URL: https://doi.org/10.1002/cphc.201600104.

[127] Arthur E. Bragg, Wenjian Yu, Jiawang Zhou, and Timothy Magnanelli. "Ultrafast Raman Spectroscopy as a Probe of Local Structure and Dynamics in Photoexcited Conjugated Materials". In: *J. Phys. Chem. Lett.* 7.19 (Sept. 2016), pp. 3990–4000. DOI: 10.1021/acs.jpclett.6b01060. URL: https://doi.org/10.1021/acs.jpclett.6b01060.

[128] Frank Ceballos, Ming-Gang Ju, Samuel D. Lane, Xiao Cheng Zeng, and Hui Zhao. "Highly Efficient and Anomalous Charge Transfer in van der Waals Trilayer Semiconductors". In: *Nano Lett.* 17.3 (Feb. 2017), pp. 1623–1628. DOI: 10.1021/acs.nanolett.6b04815. URL: https://doi.org/10.1021/acs.nanolett.6b04815.

[129] Aritra Mandal, Jonathan D. Schultz, Yi-Lin Wu, Adam F. Coleman, Ryan M. Young, and Michael R. Wasielewski. "Transient Two-Dimensional Electronic Spectroscopy: Coherent Dynamics at Arbitrary Times along the Reaction Coordinate". In: *J. Phys. Chem. Lett.* 10.13 (June 2019), pp. 3509–3515. DOI: 10.1021/acs.jpclett.9b00826. URL: https://doi.org/10.1021/acs.jpclett.9b00826.

[130] Edbert J. Sie, Clara M. Nyby, C. D. Pemmaraju, Su Ji Park, Xiaozhe Shen, Jie Yang, Matthias C. Hoffmann, B. K. Ofori-Okai, Renkai Li, Alexander H. Reid, Stephen Weathersby, Ehren Mannebach, Nathan Finney, Daniel Rhodes, Daniel Chenet, Abhinandan Antony, Luis Balicas, James Hone, Thomas P. Devereaux, Tony F. Heinz, Xijie Wang, and Aaron M. Lindenberg. "An ultrafast symmetry switch in a Weyl semimetal". In: *Nature* 565.7737 (Jan. 2019), pp. 61–66. DOI: 10.1038/s41586-018-0809-4. URL: https://doi.org/10.1038/s41586-018-0809-4.

[131] Fang Liu, Mark E. Ziffer, Kameron R. Hansen, Jue Wang, and Xiaoyang Zhu. "Direct Determination of Band-Gap Renormalization in the Photoexcited Monolayer MoS_2". In: *Phys. Rev. Lett.* 122.24 (June 2019), p. 246803. DOI: 10.1103/physrevlett.122.246803. URL: https://doi.org/10.1103/physrevlett.122.246803.

[132] F. Langer, C. P. Schmid, S. Schlauderer, M. Gmitra, J. Fabian, P. Nagler, C. Schüller, T. Korn, P. G. Hawkins, J. T. Steiner, U. Huttner, S. W. Koch, M. Kira, and R. Huber. "Lightwave valleytronics in a monolayer of tungsten diselenide". In: *Nature* 557.7703 (May 2018), pp. 76–80. DOI: 10.1038/s41586-018-0013-6. URL: https://doi.org/10.1038/s41586-018-0013-6.

[133] Zhou Wang, Hyunwook Park, Yu Hang Lai, Junliang Xu, Cosmin I. Blaga, Fengyuan Yang, Pierre Agostini, and Louis F. DiMauro. "The roles of photo-carrier doping and driving wavelength in high harmonic generation from a semiconductor". In: *Nat. Commun.* 8.1 (Nov. 2017), p. 1686. DOI: 10.1038/s41467-017-01899-1. URL: https://doi.org/10.1038/s41467-017-01899-1.

[134] Peter C. Chen. "An Introduction to Coherent Multidimensional Spectroscopy". In: *Appl. Spectrosc.* 70.12 (Dec. 2016), pp. 1937–1951. DOI: 10.1177/0003702816669730. URL: https://doi.org/10.1177/0003702816669730.

[135] Christopher L. Smallwood and Steven T. Cundiff. "Multidimensional Coherent Spectroscopy of Semiconductors". In: *Laser Photonics Rev.* 12.12 (Nov. 2018), p. 1800171. DOI: 10.1002/lpor.201800171. URL: https://doi.org/10.1002/lpor.201800171.

[136] Steven T. Cundiff and Shaul Mukamel. "Optical multidimensional coherent spectroscopy". In: *Physics Today* 66.7 (July 2013), pp. 44–49. DOI: 10.1063/pt.3.2047. URL: https://doi.org/10.1063/pt.3.2047.

[137] Minhaeng Cho. "Coherent Two-Dimensional Optical Spectroscopy". In: *Chem. Rev.* 108.4 (Apr. 2008), pp. 1331–1418. DOI: 10.1021/cr078377b. URL: https://doi.org/10.1021/cr078377b.

[138] Minhaeng Cho, ed. *Coherent Multidimensional Spectroscopy*. Springer Singapore, 2019. DOI: 10.1007/978-981-13-9753-0. URL: https://doi.org/10.1007/978-981-13-9753-0.

[139] Jens Bredenbeck, Jan Helbing, Raymond Behrendt, Christian Renner, Luis Moroder, Josef Wachtveitl, and Peter Hamm. "Transient 2D-IR Spectroscopy: Snapshots of the Nonequilibrium Ensemble during the Picosecond Conformational Transition of a Small Peptide". In: *J. Phys. Chem. B* 107.33 (Aug. 2003), pp. 8654–8660. DOI: 10.1021/jp034552q. URL: https://doi.org/10.1021/jp034552q.

[140] Baxter Abraham, Luis G. C. Rego, and Lars Gundlach. "Electronic–Vibrational Coupling and Electron Transfer". In: *J. Phys. Chem. C* 123.39 (July 2019), pp. 23760–23772. DOI: 10.1021/acs.jpcc.9b03849. URL: https://doi.org/10.1021/acs.jpcc.9b03849.

[141] Adam M. Hanninen, Richard C. Prince, and Eric Potma. "Triple Modal Coherent Nonlinear Imaging with Vibrational Contrast". In: *IEEE J. Sel. Top. Quantum Electron.* 25.1 (2018), pp. 1–11. DOI: 10.1109/jstqe.2018.2846030. URL: https://doi.org/10.1109%2Fjstqe.2018.2846030.

[142] Adam M. Hanninen, Richard C. Prince, Raul Ramos, Maksim V. Plikus, and Eric O. Potma. "High-resolution infrared imaging of biological samples with third-order sum-frequency generation microscopy". In: *Biomed. Opt. Express* 9.10 (Sept. 2018), p. 4807. DOI: 10.1364/boe.9.004807. URL: https://doi.org/10.1364%2Fboe.9.004807.

[143] Hiroki Segawa, Masanari Okuno, Hideaki Kano, Philippe Leproux, Vincent Couderc, and Hiro-o Hamaguchi. "Label-free tetra-modal molecular imaging of living cells with CARS, SHG, THG and TSFG (coherent anti-Stokes Raman scattering, second harmonic generation, third harmonic generation and third-order sum frequency generation)". In: *Opt. Express* 20.9 (Apr. 2012), p. 9551. DOI: 10.1364/oe.20.009551. URL: https://doi.org/10.1364/oe.20.009551.

[144] Gang Wang, Alexey Chernikov, Mikhail M. Glazov, Tony F. Heinz, Xavier Marie, Thierry Amand, and Bernhard Urbaszek. "Colloquium : Excitons in atomically thin transition metal dichalcogenides". In: *Rev. Mod. Phys.* 90.2 (Apr. 2018), p. 021001. DOI: 10.1103/revmodphys.90.021001. URL: https://doi.org/10.1103/revmodphys.90.021001.

[145] Anton Autere, Henri Jussila, Yunyun Dai, Yadong Wang, Harri Lipsanen, and Zhipei Sun. "Nonlinear Optics with 2D Layered Materials". In: *Adv. Mater.* 30.24 (Mar. 2018), p. 1705963. DOI: 10.1002/adma.201705963. URL: https://doi.org/10.1002/adma.201705963.

[146] Y. M. Chang, L. Xu, and H. W. K. Tom. "Observation of Coherent Surface Optical Phonon Oscillations by Time-Resolved Surface Second-Harmonic Generation". In: *Phys. Rev. Lett.* 78.24 (June 1997), pp. 4649–4652. DOI: 10.1103/physrevlett.78.4649. URL: https://doi.org/10.1103/physrevlett.78.4649.

[147] Chunlei Guo, George Rodriguez, and Antoinette J. Taylor. "Ultrafast Dynamics of Electron Thermalization in Gold". In: *Phys. Rev. Lett.* 86.8 (Feb. 2001), pp. 1638–1641. DOI: 10.1103/physrevlett.86.1638. URL: https://doi.org/10.1103/physrevlett.86.1638.

[148] Arthur McClelland, Vasiliy Fomenko, and Eric Borguet. "Ultrafast Time-Evolution of the Nonlinear Susceptibility of Hot Carriers at the Ge(111)-GeO_2 Interface As Probed by SHG". In: *J. Phys. Chem. B* 108.12 (Mar. 2004), pp. 3789–3793. DOI: 10.1021/jp036231k. URL: https://doi.org/10.1021/jp036231k.

[149] D. Hsieh, F. Mahmood, J. W. McIver, D. R. Gardner, Y. S. Lee, and N. Gedik. "Selective Probing of Photoinduced Charge and Spin Dynamics in the Bulk and Surface of a Topological Insulator". In: *Phys. Rev. Lett.* 107.7 (Aug. 2011), p. 077401. DOI: 10.1103/physrevlett.107.077401. URL: https://doi.org/10.1103/physrevlett.107.077401.

[150] W. A. Tisdale, K. J. Williams, B. A. Timp, D. J. Norris, E. S. Aydil, and X.- Y. Zhu. "Hot-Electron Transfer from Semiconductor Nanocrystals". In: *Science* 328.5985 (June 2010), pp. 1543–1547. DOI: 10.1126/science.1185509. URL: https://doi.org/10.1126/science.1185509.

[151] H. Park, M. Gutierrez, X. Wu, W. Kim, and X.-Y. Zhu. "Optical Probe of Charge Separation at Organic/Inorganic Semiconductor Interfaces". In: *J. Phys. Chem. C* 117.21 (May 2013), pp. 10974–10979. DOI: 10.1021/jp4029408. URL: https://doi.org/10.1021/jp4029408.

[152] C. A. Nelson, J. Luo, A. K.-Y. Jen, R. B. Laghumavarapu, D. L. Huffaker, and X.-Y. Zhu. "Time-, Energy-, and Phase-Resolved Second-Harmonic Generation at Semiconductor Interfaces". In: *J. Phys. Chem. C* 118.48 (Nov. 2014), pp. 27981–27988. DOI: 10.1021/jp5094614. URL: https://doi.org/10.1021/jp5094614.

[153] Ehren M. Mannebach, Karel-Alexander N. Duerloo, Lenson A. Pellouchoud, Meng-Ju Sher, Sanghee Nah, Yi-Hong Kuo, Yifei Yu, Ann F. Marshall, Linyou Cao, Evan J. Reed, and Aaron M. Lindenberg. "Ultrafast Electronic and Structural Response of Monolayer MoS_2 under Intense Photoexcitation Conditions". In: *ACS Nano* 8.10 (Sept. 2014), pp. 10734–10742. DOI: 10.1021/nn5044542. URL: https://doi.org/10.1021/nn5044542.

[154] Justin P. Lomont, Kacie L. Rich, Michał Maj, Jia-Jung Ho, Joshua S. Ostrander, and Martin T. Zanni. "Spectroscopic Signature for Stable β-Amyloid Fibrils versus β-Sheet-Rich Oligomers". In: *J. Phys. Chem. B* 122.1 (Dec. 2017), pp. 144–153. DOI: 10.1021/acs.jpcb.7b10765. URL: https://doi.org/10.1021/acs.jpcb.7b10765.

[155] Ariel M. Alperstein, Joshua S. Ostrander, Tianqi O. Zhang, and Martin T. Zanni. "Amyloid found in human cataracts with two-dimensional infrared spectroscopy". In: *Proc. Natl. Acad. Sci. U.S.A.* 116.14 (Mar. 2019), pp. 6602–6607. DOI: 10.1073/pnas.1821534116. URL: https://doi.org/10.1073/pnas.1821534116.

[156] N. Bloembergen and P. S. Pershan. "Light Waves at the Boundary of Nonlinear Media". In: *Phys. Rev.* 128.2 (Oct. 1962), pp. 606–622. DOI: 10.1103/physrev.128.606. URL: https://doi.org/10.1103/physrev.128.606.

[157] Alireza Taghizadeh and T. G. Pedersen. "Nonlinear optical selection rules of excitons in monolayer transition metal dichalcogenides". In: *Phys. Rev. B* 99 (23 June 2019), p. 235433. DOI: 10.1103/PhysRevB.99.235433. URL: https://link.aps.org/doi/10.1103/PhysRevB.99.235433.

[158] Alireza Taghizadeh and T. G. Pedersen. "Gauge invariance of excitonic linear and nonlinear optical response". In: *Phys. Rev. B* 97 (20 May 2018), p. 205432. DOI: 10.1103/PhysRevB.97.205432. URL: https://link.aps.org/doi/10.1103/PhysRevB.97.205432.

[159] Alireza Taghizadeh, F. Hipolito, and T. G. Pedersen. "Linear and nonlinear optical response of crystals using length and velocity gauges: Effect of basis truncation". In: *Phys. Rev. B* 96 (19 Nov. 2017), p. 195413. DOI: 10.1103/PhysRevB.96.195413. URL: https://link.aps.org/doi/10.1103/PhysRevB.96.195413.

[160] Thomas Garm Pedersen. "Intraband effects in excitonic second-harmonic generation". In: *Phys. Rev. B* 92 (23 Dec. 2015), p. 235432. DOI: 10.1103/PhysRevB.92.235432. URL: https://link.aps.org/doi/10.1103/PhysRevB.92.235432.

[161] Daniel B. S. Soh, Christopher Rogers, Dodd J. Gray, Eric Chatterjee, and Hideo Mabuchi. "Optical nonlinearities of excitons in monolayer MoS_2". In: *Phys. Rev. B* 97 (16 Apr. 2018), p. 165111. DOI: 10.1103/PhysRevB.97.165111. URL: https://link.aps.org/doi/10.1103/PhysRevB.97.165111.

[162] L A Falkovsky. "Optical properties of graphene". In: *J. Phys. Conf. Ser.* 129 (Oct. 2008), p. 012004. DOI: 10.1088/1742-6596/129/1/012004. URL: http://stacks.iop.org/1742-6596/129/i=1/a=012004?key=crossref.c5ca23f0554ca37549b54a096f165e25.

[163] Andrea Splendiani, Liang Sun, Yuanbo Zhang, Tianshu Li, Jonghwan Kim, Chi-Yung Chim, Giulia Galli, and Feng Wang. "Emerging Photoluminescence in Monolayer MoS_2". In: *Nano Lett.* 10.4 (Apr. 2010), pp. 1271–1275. DOI: 10.1021/nl903868w. URL: https://doi.org/10.1021/nl903868w.

[164] Koichi Furuta, Masanori Fuyuki, and Akihide Wada. "Cross-Term Selective, Two-Pulse Correlation Measurements by Phase-Shifted Parallel Modulation for Analysis of a Multi-Photon Process". In: *Appl. Spectrosc.* 66.12 (Dec. 2012), pp. 1475–1479. DOI: 10.1366/12-06657. URL: https://doi.org/10.1366/12-06657.

[165] Darien J. Morrow. "Pump-triple sum-frequency-probe spectroscopy of transition metal dichalcogenides". In: *Open Science Framework* (2019). DOI: 10.17605/OSF.IO/UMSXC. URL: https://osf.io/umsxc/.

[166] Blaise Thompson, Kyle Sunden, Darien Morrow, Daniel Kohler, and John Wright. "Wright-Tools: a Python package for multidimensional spectroscopy". In: *J. Open Source Softw.* 4.33 (Jan. 2019), p. 1141. DOI: 10.21105/joss.01141. URL: https://doi.org/10.21105/joss.01141.

[167] Ayse Berkdemir, Humberto R. Gutiérrez, Andrés R. Botello-Méndez, Néstor Perea-López, Ana Laura Elías, Chen-Ing Chia, Bei Wang, Vincent H. Crespi, Florentino López-Urías, Jean-Christophe Charlier, Humberto Terrones, and Mauricio Terrones. "Identification of individual and few layers of WS_2 using Raman Spectroscopy". In: *Sci. Rep.* 3 (Apr. 2013), p. 1755. DOI: 10.1038/srep01755.

[168] Xiaopeng Fan, Yuzhou Zhao, Weihao Zheng, Honglai Li, Xueping Wu, Xuelu Hu, Xuehong Zhang, Xiaoli Zhu, Qinglin Zhang, Xiao Wang, Bin Yang, Jianghua Chen, Song Jin, and Anlian Pan. "Controllable Growth and Formation Mechanisms of Dislocated WS_2 Spirals". In: *Nano Lett.* 18.6 (May 2018), pp. 3885–3892. DOI: 10.1021/acs.nanolett.8b01210. URL: https://doi.org/10.1021/acs.nanolett.8b01210.

[169] Xiaopeng Fan, Ying Jiang, Xiujuan Zhuang, Hongjun Liu, Tao Xu, Weihao Zheng, Peng Fan, Honglai Li, Xueping Wu, Xiaoli Zhu, Qinglin Zhang, Hong Zhou, Wei Hu, Xiao Wang, Litao Sun, Xiangfeng Duan, and Anlian Pan. "Broken Symmetry Induced Strong Nonlinear Optical Effects in Spiral WS_2 Nanosheets". In: *ACS Nano* 11.5 (Apr. 2017), pp. 4892–4898. DOI: 10.1021/acsnano.7b01457. URL: https://doi.org/10.1021/acsnano.7b01457.

[170] Liming Zhang, Kaihui Liu, Andrew Barnabas Wong, Jonghwan Kim, Xiaoping Hong, Chong Liu, Ting Cao, Steven G. Louie, Feng Wang, and Peidong Yang. "Three-Dimensional Spirals of Atomic Layered MoS_2". In: *Nano Lett.* 14.11 (Oct. 2014), pp. 6418–6423. DOI: 10.1021/nl502961e. URL: https://doi.org/10.1021/nl502961e.

[171] Hui Zhang, Yi Wan, Yaoguang Ma, Wei Wang, Yilun Wang, and Lun Dai. "Interference effect on optical signals of monolayer MoS_2". In: *Appl. Phys. Lett.* 107.10 (2015), p. 101904. DOI: 10.1063/1.4930257. URL: https://doi.org/10.1063/1.4930257.

[172] M M Benameur, B Radisavljevic, J S Héron, S Sahoo, H Berger, and A Kis. "Visibility of dichalcogenide nanolayers". In: *Nanotechnology* 22.12 (Feb. 2011), p. 125706. DOI: 10.1088/0957-4484/22/12/125706. URL: https://doi.org/10.1088%2F0957-4484%2F22%2F12%2F125706.

[173] P. Blake, E. W. Hill, A. H. Castro Neto, K. S. Novoselov, D. Jiang, R. Yang, T. J. Booth, and A. K. Geim. "Making graphene visible". In: *Appl. Phys. Lett.* 91.6 (Aug. 2007), p. 063124. DOI: 10.1063/1.2768624. URL: https://doi.org/10.1063/1.2768624.

[174] Eva A. A. Pogna, Margherita Marsili, Domenico De Fazio, Stefano Dal Conte, Cristian Manzoni, Davide Sangalli, Duhee Yoon, Antonio Lombardo, Andrea C. Ferrari, Andrea Marini, Giulio Cerullo, and Deborah Prezzi. "Photo-Induced Bandgap Renormalization Governs the Ultrafast Response of Single-Layer MoS_2". In: *ACS Nano* 10.1 (Jan. 2016), pp. 1182–1188. DOI: 10.1021/acsnano.5b06488. URL: https://doi.org/10.1021/acsnano.5b06488.

[175] Alexey Chernikov, Claudia Ruppert, Heather M. Hill, Albert F. Rigosi, and Tony F. Heinz. "Population inversion and giant bandgap renormalization in atomically thin WS_2 layers". In: *Nat. Photonics* 9.7 (June 2015), pp. 466–470. DOI: 10.1038/nphoton.2015.104. URL: https://doi.org/10.1038/nphoton.2015.104.

[176] A. Steinhoff, M. Rösner, F. Jahnke, T. O. Wehling, and C. Gies. "Influence of Excited Carriers on the Optical and Electronic Properties of MoS_2". In: *Nano Lett.* 14.7 (June 2014), pp. 3743–3748. DOI: 10.1021/nl500595u. URL: https://doi.org/10.1021/nl500595u.

[177] L. Meckbach, T. Stroucken, and S. W. Koch. "Giant excitation induced bandgap renormalization in TMDC monolayers". In: *Appl. Phys. Lett.* 112.6 (2018), p. 061104. DOI: 10.1063/1.5017069. URL: https://doi.org/10.1063/1.5017069.

[178] Ryan E. Wood, Lawson T. Lloyd, Fauzia Mujid, Lili Wang, Marco A. Allodi, Hui Gao, Richard Mazuski, Po-Chieh Ting, Saien Xie, Jiwoong Park, and Gregory S. Engel. "Evidence for the Dominance of Carrier-Induced Band Gap Renormalization over Biexciton Formation in Cryogenic Ultrafast Experiments on MoS_2 Monolayers". In: *J. Phys. Chem. Lett.* 11.7 (Mar. 2020), pp. 2658–2666. DOI: 10.1021/acs.jpclett.0c00169. URL: https://doi.org/10.1021/acs.jpclett.0c00169.

[179] Sangwan Sim, Jusang Park, Jeong-Gyu Song, Chihun In, Yun-Shik Lee, Hyungjun Kim, and Hyunyong Choi. "Exciton dynamics in atomically thin MoS_2: Interexcitonic interaction and broadening kinetics". In: *Phys. Rev. B* 88.7 (Aug. 2013), p. 075434. DOI: 10.1103/physrevb.88.075434. URL: https://doi.org/10.1103/physrevb.88.075434.

[180] Paul D. Cunningham, Aubrey T. Hanbicki, Kathleen M. McCreary, and Berend T. Jonker. "Photoinduced Bandgap Renormalization and Exciton Binding Energy Reduction in WS_2". In: *ACS Nano* 11.12 (Dec. 2017), pp. 12601–12608. DOI: 10.1021/acsnano.7b06885. URL: https://doi.org/10.1021/acsnano.7b06885.

[181] Paul D. Cunningham, Kathleen M. McCreary, Aubrey T. Hanbicki, Marc Currie, Berend T. Jonker, and L. Michael Hayden. "Charge Trapping and Exciton Dynamics in Large-Area CVD Grown MoS_2". In: *J. Phys. Chem. C* 120.10 (Mar. 2016), pp. 5819–5826. DOI: 10.1021/acs.jpcc.6b00647. URL: https://doi.org/10.1021/acs.jpcc.6b00647.

[182] Hongyan Shi, Rusen Yan, Simone Bertolazzi, Jacopo Brivio, Bo Gao, Andras Kis, Debdeep Jena, Huili Grace Xing, and Libai Huang. "Exciton Dynamics in Suspended Monolayer and Few-Layer MoS_2 2D Crystals". In: *ACS Nano* 7.2 (Jan. 2013), pp. 1072–1080. DOI: 10.1021/nn303973r. URL: https://doi.org/10.1021/nn303973r.

[183] Pieter Schiettecatte, Pieter Geiregat, and Zeger Hens. "Ultrafast Carrier Dynamics in Few-Layer Colloidal Molybdenum Disulfide Probed by Broadband Transient Absorption Spectroscopy". In: *J. Phys. Chem. C* 123.16 (Apr. 2019), pp. 10571–10577. DOI: 10.1021/acs.jpcc.9b01494. URL: https://doi.org/10.1021/acs.jpcc.9b01494.

[184] Demetra Tsokkou, Xiaoyun Yu, Kevin Sivula, and Natalie Banerji. "The Role of Excitons and Free Charges in the Excited-State Dynamics of Solution-Processed Few-Layer MoS_2 Nanoflakes". In: *J. Phys. Chem. C* 120.40 (Oct. 2016), pp. 23286–23292. DOI: 10.1021/acs.jpcc.6b09267. URL: https://doi.org/10.1021/acs.jpcc.6b09267.

[185] Zhaogang Nie, Run Long, Linfeng Sun, Chung-Che Huang, Jun Zhang, Qihua Xiong, Daniel W. Hewak, Zexiang Shen, Oleg V. Prezhdo, and Zhi-Heng Loh. "Ultrafast Carrier Thermalization and Cooling Dynamics in Few-Layer MoS_2". In: *ACS Nano* 8.10 (Oct. 2014), pp. 10931–10940. DOI: 10.1021/nn504760x. URL: https://doi.org/10.1021/nn504760x.

[186] Nardeep Kumar, Jiaqi He, Dawei He, Yongsheng Wang, and Hui Zhao. "Charge carrier dynamics in bulk MoS_2 crystal studied by transient absorption microscopy". In: *J. Appl. Phys.* 113.13 (Apr. 2013), p. 133702. DOI: 10.1063/1.4799110. URL: https://doi.org/10.1063/1.4799110.

[187] Zhaogang Nie, Run Long, Jefri S. Teguh, Chung-Che Huang, Daniel W. Hewak, Edwin K. L. Yeow, Zexiang Shen, Oleg V. Prezhdo, and Zhi-Heng Loh. "Ultrafast Electron and Hole Relaxation Pathways in Few-Layer MoS_2". In: *J. Phys. Chem. C* 119.35 (Aug. 2015), pp. 20698–20708. DOI: 10.1021/acs.jpcc.5b05048. URL: https://doi.org/10.1021/acs.jpcc.5b05048.

[188] Frank Ceballos, Qiannan Cui, Matthew Z. Bellus, and Hui Zhao. "Exciton formation in monolayer transition metal dichalcogenides". In: *Nanoscale* 8.22 (2016), pp. 11681–11688. DOI: 10.1039/c6nr02516a. URL: https://doi.org/10.1039/c6nr02516a.

[189] Akshay Singh, Galan Moody, Sanfeng Wu, Yanwen Wu, Nirmal J. Ghimire, Jiaqiang Yan, David G. Mandrus, Xiaodong Xu, and Xiaoqin Li. "Coherent Electronic Coupling in Atomically Thin $MoSe_2$". In: *Phys. Rev. Lett.* 112.21 (May 2014), p. 216804. DOI: 10.1103/physrevlett.112.216804. URL: https://doi.org/10.1103/physrevlett.112.216804.

[190] Galan Moody, Chandriker Kavir Dass, Kai Hao, Chang-Hsiao Chen, Lain-Jong Li, Akshay Singh, Kha Tran, Genevieve Clark, Xiaodong Xu, Gunnar Berghäuser, Ermin Malic, Andreas Knorr, and Xiaoqin Li. "Intrinsic homogeneous linewidth and broadening mechanisms of excitons in monolayer transition metal dichalcogenides". In: *Nat. Commun.* 6.1 (Sept. 2015), p. 8315. DOI: 10.1038/ncomms9315. URL: https://doi.org/10.1038/ncomms9315.

[191] Akshay Singh, Galan Moody, Kha Tran, Marie E. Scott, Vincent Overbeck, Gunnar Berghäuser, John Schaibley, Edward J. Seifert, Dennis Pleskot, Nathaniel M. Gabor, Jiaqiang Yan, David G. Mandrus, Marten Richter, Ermin Malic, Xiaodong Xu, and Xiaoqin Li. "Trion formation dynamics in monolayer transition metal dichalcogenides". In: *Phys. Rev. B* 93.4 (Jan. 2016), p. 041401. DOI: 10.1103/physrevb.93.041401. URL: https://doi.org/10.1103/physrevb.93.041401.

[192] Kai Hao, Galan Moody, Fengcheng Wu, Chandriker Kavir Dass, Lixiang Xu, Chang-Hsiao Chen, Liuyang Sun, Ming-Yang Li, Lain-Jong Li, Allan H. MacDonald, and Xiaoqin Li. "Direct measurement of exciton valley coherence in monolayer WSe_2". In: *Nat. Phys.* 12.7 (Feb. 2016), pp. 677–682. DOI: 10.1038/nphys3674. URL: https://doi.org/10.1038/nphys3674.

[193] Kai Hao, Lixiang Xu, Philipp Nagler, Akshay Singh, Kha Tran, Chandriker Kavir Dass, Christian Schüller, Tobias Korn, Xiaoqin Li, and Galan Moody. "Coherent and Incoherent Coupling Dynamics between Neutral and Charged Excitons in Monolayer $MoSe_2$". In: *Nano Lett.* 16.8 (July 2016), pp. 5109–5113. DOI: 10.1021/acs.nanolett.6b02041. URL: https://doi.org/10.1021/acs.nanolett.6b02041.

[194] Kai Hao, Judith F. Specht, Philipp Nagler, Lixiang Xu, Kha Tran, Akshay Singh, Chandriker Kavir Dass, Christian Schüller, Tobias Korn, Marten Richter, Andreas Knorr, Xiaoqin Li, and Galan Moody. "Neutral and charged inter-valley biexcitons in monolayer $MoSe_2$". In:

Nat. Commun. 8.1 (June 2017), p. 15552. DOI: 10.1038/ncomms15552. URL: https://doi.org/10.1038/ncomms15552.

[195] Liang Guo, Meng Wu, Ting Cao, Daniele M. Monahan, Yi-Hsien Lee, Steven G. Louie, and Graham R. Fleming. "Exchange-driven intravalley mixing of excitons in monolayer transition metal dichalcogenides". In: *Nat. Phys.* 15.3 (Dec. 2018), pp. 228–232. DOI: 10.1038/s41567-018-0362-y. URL: https://doi.org/10.1038%2Fs41567-018-0362-y.

[196] Fahad Mahmood, Zhanybek Alpichshev, Yi-Hsien Lee, Jing Kong, and Nuh Gedik. "Observation of Exciton–Exciton Interaction Mediated Valley Depolarization in Monolayer $MoSe_2$". In: *Nano Lett.* 18.1 (Dec. 2017), pp. 223–228. DOI: 10.1021/acs.nanolett.7b03953. URL: https://doi.org/10.1021%2Facs.nanolett.7b03953.

[197] Luyi Yang, Nikolai A. Sinitsyn, Weibing Chen, Jiangtan Yuan, Jing Zhang, Jun Lou, and Scott A. Crooker. "Long-lived nanosecond spin relaxation and spin coherence of electrons in monolayer MoS_2 and WS_2". In: *Nat. Phys.* 11.10 (Aug. 2015), pp. 830–834. DOI: 10.1038/nphys3419. URL: https://doi.org/10.1038%2Fnphys3419.

[198] Galan Moody, John Schaibley, and Xiaodong Xu. "Exciton dynamics in monolayer transition metal dichalcogenides". In: *J. Opt. Soc. Am. B* 33.7 (Apr. 2016), p. C39. DOI: 10.1364/josab.33.000c39. URL: https://doi.org/10.1364/josab.33.000c39.

[199] S. Schmitt-Rink, D. S. Chemla, and D. A. B. Miller. "Theory of transient excitonic optical nonlinearities in semiconductor quantum-well structures". In: *Phys. Rev. B* 32.10 (Nov. 1985), pp. 6601–6609. DOI: 10.1103/physrevb.32.6601. URL: https://doi.org/10.1103/physrevb.32.6601.

[200] Paul W. Juodawlkis and Stephen E. Ralph. "Hole-induced transient bandgap renormalization: A mechanism for photo-induced absorption in defect-engineered semiconductors". In: *Appl. Phys. Lett.* 76.13 (Mar. 2000), pp. 1722–1724. DOI: 10.1063/1.126147. URL: https://doi.org/10.1063/1.126147.

[201] Gary Mak and Henry M. van Driel. "Femtosecond transmission spectroscopy at the direct band edge of germanium". In: *Phys. Rev. B* 49.23 (June 1994), pp. 16817–16820. DOI: 10.1103/physrevb.49.16817. URL: https://doi.org/10.1103/physrevb.49.16817.

[202] Junxue Liu, Jing Leng, Shiping Wang, Jun Zhang, and Shengye Jin. "Artifacts in Transient Absorption Measurements of Perovskite Films Induced by Transient Reflection from Morphological Microstructures". In: *J. Phys. Chem. Lett.* 10.1 (Jan. 2019), pp. 97–101. DOI: 10.1021/acs.jpclett.8b03704. URL: https://doi.org/10.1021/acs.jpclett.8b03704.

[203] Tufan Ghosh, Sigalit Aharon, Adva Shpatz, Lioz Etgar, and Sanford Ruhman. "Reflectivity Effects on Pump–Probe Spectra of Lead Halide Perovskites: Comparing Thin Films versus Nanocrystals". In: *ACS Nano* 12.6 (May 2018), pp. 5719–5725. DOI: 10.1021/acsnano.8b01570. URL: https://doi.org/10.1021/acsnano.8b01570.

[204] Hugo Anders. *Thin Films in Optics*. The Focal Press, June 1967.

[205] S. Bikorimana, P. Lama, A. Walser, R. Dorsinville, S. Anghel, A. Mitioglu, A. Micu, and L. Kulyuk. "Nonlinear optical responses in two-dimensional transition metal dichalcogenide multilayer: WS_2, WSe_2, MoS_2 and $Mo_{0.5}W_{0.5}S_2$". In: *Opt. Express* 24.18 (Aug. 2016), p. 20685. DOI: 10.1364/oe.24.020685. URL: https://doi.org/10.1364/oe.24.020685.

[206] Ziliang Ye, Ting Cao, Kevin O'Brien, Hanyu Zhu, Xiaobo Yin, Yuan Wang, Steven G. Louie, and Xiang Zhang. "Probing excitonic dark states in single-layer tungsten disulphide". In: *Nature* 513.7517 (Aug. 2014), pp. 214–218. DOI: 10.1038/nature13734. URL: https://doi.org/10.1038/nature13734.

[207] Timothy C. Berkelbach, Mark S. Hybertsen, and David R. Reichman. "Bright and dark singlet excitons via linear and two-photon spectroscopy in monolayer transition-metal dichalcogenides". In: *Phys. Rev. B* 92.8 (Aug. 2015), p. 085413. DOI: 10.1103/physrevb.92.085413. URL: https://doi.org/10.1103%2Fphysrevb.92.085413.

[208] Ningning Dong, Yuanxin Li, Saifeng Zhang, Niall McEvoy, Riley Gatensby, Georg S. Duesberg, and Jun Wang. "Saturation of Two-Photon Absorption in Layered Transition Metal Dichalcogenides: Experiment and Theory". In: *ACS Photonics* 5.4 (Feb. 2018), pp. 1558–1565. DOI: 10.1021/acsphotonics.8b00010. URL: https://doi.org/10.1021%2Facsphotonics.8b00010.

[209] Qiannan Cui, Yuanyuan Li, Jianhua Chang, Hui Zhao, and Chunxiang Xu. "Temporally Resolving Synchronous Degenerate and Nondegenerate Two-Photon Absorption in 2D Semiconducting Monolayers". In: *Laser Photonics Rev.* 13.2 (Dec. 2018), p. 1800225. DOI: 10.1002/lpor.201800225. URL: https://doi.org/10.1002%2Flpor.201800225.

[210] Tim Völzer, Matthias Lütgens, Franziska Fennel, and Stefan Lochbrunner. "Recombination dynamics of optically excited charge carriers in bulk MoS_2". In: *J. Phys. B* 50.19 (Sept. 2017), p. 194003. DOI: 10.1088/1361-6455/aa89df. URL: https://doi.org/10.1088/1361-6455/aa89df.

[211] Arend M. van der Zande, Pinshane Y. Huang, Daniel A. Chenet, Timothy C. Berkelbach, YuMeng You, Gwan-Hyoung Lee, Tony F. Heinz, David R. Reichman, David A. Muller, and James C. Hone. "Grains and grain boundaries in highly crystalline monolayer molybdenum disulphide". In: *Nat. Mater.* 12.6 (May 2013), pp. 554–561. DOI: 10.1038/nmat3633. URL: https://doi.org/10.1038%2Fnmat3633.

[212] Wu Zhou, Xiaolong Zou, Sina Najmaei, Zheng Liu, Yumeng Shi, Jing Kong, Jun Lou, Pulickel M. Ajayan, Boris I. Yakobson, and Juan-Carlos Idrobo. "Intrinsic Structural Defects in Monolayer Molybdenum Disulfide". In: *Nano Lett.* 13.6 (May 2013), pp. 2615–2622. DOI: 10.1021/nl4007479. URL: https://doi.org/10.1021%2Fnl4007479.

[213] Zhi Gen Yu, Yong-Wei Zhang, and Boris I. Yakobson. "An Anomalous Formation Pathway for Dislocation-Sulfur Vacancy Complexes in Polycrystalline Monolayer MoS_2". In: *Nano Lett.* 15.10 (Oct. 2015), pp. 6855–6861. DOI: 10.1021/acs.nanolett.5b02769. URL: https://doi.org/10.1021%2Facs.nanolett.5b02769.

[214] Jinhua Hong, Zhixin Hu, Matt Probert, Kun Li, Danhui Lv, Xinan Yang, Lin Gu, Nannan Mao, Qingliang Feng, Liming Xie, Jin Zhang, Dianzhong Wu, Zhiyong Zhang, Chuanhong Jin, Wei Ji, Xixiang Zhang, Jun Yuan, and Ze Zhang. "Exploring atomic defects in molybdenum disulphide monolayers". In: *Nat. Commun.* 6.1 (Feb. 2015), p. 6293. DOI: 10.1038/ncomms7293. URL: https://doi.org/10.1038%2Fncomms7293.

[215] Hao Qiu, Tao Xu, Zilu Wang, Wei Ren, Haiyan Nan, Zhenhua Ni, Qian Chen, Shijun Yuan, Feng Miao, Fengqi Song, Gen Long, Yi Shi, Litao Sun, Jinlan Wang, and Xinran Wang. "Hopping transport through defect-induced localized states in molybdenum disulphide". In: *Nat. Commun.* 4.1 (Oct. 2013), p. 2642. DOI: 10.1038/ncomms3642. URL: https://doi.org/10.1038%2Fncomms3642.

[216] Chih-Pin Lu, Guohong Li, Jinhai Mao, Li-Min Wang, and Eva Y. Andrei. "Bandgap, Mid-Gap States, and Gating Effects in MoS_2". In: *Nano Lett.* 14.8 (July 2014), pp. 4628–4633. DOI: 10.1021/nl501659n. URL: https://doi.org/10.1021/nl501659n.

[217] P. A. Franken, A. E. Hill, C. W. Peters, and G. Weinreich. "Generation of Optical Harmonics". In: *Phys. Rev. Lett.* 7.4 (Aug. 1961), pp. 118–119. DOI: 10.1103/physrevlett.7.118. URL: https://doi.org/10.1103%2Fphysrevlett.7.118.

[218] Kyle L. Seyler, John R. Schaibley, Pu Gong, Pasqual Rivera, Aaron M. Jones, Sanfeng Wu, Jiaqiang Yan, David G. Mandrus, Wang Yao, and Xiaodong Xu. "Electrical control of second-harmonic generation in a WSe_2 monolayer transistor". In: *Nat. Nanotechnol.* 10.5 (Apr. 2015), pp. 407–411. DOI: 10.1038/nnano.2015.73. URL: https://doi.org/10.1038/nnano.2015.73.

[219] Carlo Sirtori, Federico Capasso, Deborah L. Sivco, A. L. Hutchinson, and Alfred Y. Cho. "Resonant Stark tuning of second-order susceptibility in coupled quantum wells". In: *Appl. Phys. Lett.* 60.2 (Jan. 1992), pp. 151–153. DOI: 10.1063/1.106999. URL: https://doi.org/10.1063/1.106999.

[220] M. Lafrentz, D. Brunne, B. Kaminski, V. V. Pavlov, A. V. Rodina, R. V. Pisarev, D. R. Yakovlev, A. Bakin, and M. Bayer. "Magneto-Stark Effect of Excitons as the Origin of Second Harmonic Generation in ZnO". In: *Phys. Rev. Lett.* 110.11 (Mar. 2013), p. 116402. DOI: 10.1103/physrevlett.110.116402. URL: https://doi.org/10.1103/physrevlett.110.116402.

[221] D. Brunne, M. Lafrentz, V. V. Pavlov, R. V. Pisarev, A. V. Rodina, D. R. Yakovlev, and M. Bayer. "Electric field effect on optical harmonic generation at the exciton resonances in GaAs". In: *Phys. Rev. B* 92.8 (Aug. 2015), p. 085202. DOI: 10.1103/physrevb.92.085202. URL: https://doi.org/10.1103/physrevb.92.085202.

[222] Zhipei Sun, Amos Martinez, and Feng Wang. "Optical modulators with 2D layered materials". In: *Nat. Photonics* 10.4 (Mar. 2016), pp. 227–238. DOI: 10.1038/nphoton.2016.15. URL: https://doi.org/10.1038/nphoton.2016.15.

[223] Brian A. Ruzicka, Lalani K. Werake, Guowei Xu, Jacob B. Khurgin, E. Ya. Sherman, Judy Z. Wu, and Hui Zhao. "Second-Harmonic Generation Induced by Electric Currents in GaAs". In: *Phys. Rev. Lett.* 108.7 (Feb. 2012), p. 077403. DOI: 10.1103/physrevlett.108.077403. URL: https://doi.org/10.1103/physrevlett.108.077403.

[224] S. H. Autler and C. H. Townes. "Stark Effect in Rapidly Varying Fields". In: *Phys. Rev.* 100.2 (Oct. 1955), pp. 703–722. DOI: 10.1103/physrev.100.703. URL: https://doi.org/10.1103/physrev.100.703.

[225] J.S. Bakos. "AC stark effect and multiphoton processes in atoms". In: *Phys. Rep.* 31.3 (July 1977), pp. 209–235. DOI: 10.1016/0370-1573(77)90016-3. URL: https://doi.org/10.1016/0370-1573(77)90016-3.

[226] Benjamin J. Sussman. "Five ways to the nonresonant dynamic Stark effect". In: *Am. J. Phys.* 79.5 (May 2011), pp. 477–484. DOI: 10.1119/1.3553018. URL: https://doi.org/10.1119/1.3553018.

[227] N. Peyghambarian, S. W. Koch, M. Lindberg, B. Fluegel, and M. Joffre. "Dynamic Stark effect of exciton and continuum states in CdS". In: *Phys. Rev. Lett.* 62.10 (Mar. 1989), pp. 1185–1188. DOI: 10.1103/physrevlett.62.1185. URL: https://doi.org/10.1103/physrevlett.62.1185.

[228] W. H. Knox, D. S. Chemla, D. A. B. Miller, J. B. Stark, and S. Schmitt-Rink. "Femtosecond ac Stark effect in semiconductor quantum wells: Extreme low- and high-intensity limits". In: *Phys. Rev. Lett.* 62.10 (Mar. 1989), pp. 1189–1192. DOI: 10.1103/physrevlett.62.1189. URL: https://doi.org/10.1103/physrevlett.62.1189.

[229] R. Binder, S. W. Koch, M. Lindberg, N. Peyghambarian, and W. Schäfer. "Ultrafast adiabatic following in semiconductors". In: *Phys. Rev. Lett.* 65.7 (Aug. 1990), pp. 899–902. DOI: 10.1103/physrevlett.65.899. URL: https://doi.org/10.1103/physrevlett.65.899.

[230] Martin Holthaus and Daniel W. Hone. "ac Stark effects and harmonic generation in periodic potentials". In: *Phys. Rev. B* 49.23 (June 1994), pp. 16605–16608. DOI: 10.1103/physrevb.49.16605. URL: https://doi.org/10.1103/physrevb.49.16605.

[231] Edbert J. Sie, James W. McIver, Yi-Hsien Lee, Liang Fu, Jing Kong, and Nuh Gedik. "Valley-selective optical Stark effect in monolayer WS_2". In: *Nat. Mater.* 14.3 (Dec. 2014), pp. 290–294. DOI: 10.1038/nmat4156. URL: https://doi.org/10.1038/nmat4156.

[232] Edbert J. Sie, Chun Hung Lui, Yi-Hsien Lee, Jing Kong, and Nuh Gedik. "Observation of Intervalley Biexcitonic Optical Stark Effect in Monolayer WS_2". In: *Nano Lett.* 16.12 (Nov. 2016), pp. 7421–7426. DOI: 10.1021/acs.nanolett.6b02998. URL: https://doi.org/10.1021/acs.nanolett.6b02998.

[233] Edbert J. Sie, Chun Hung Lui, Yi-Hsien Lee, Liang Fu, Jing Kong, and Nuh Gedik. "Large, valley-exclusive Bloch-Siegert shift in monolayer WS_2". In: *Science* 355.6329 (Mar. 2017), pp. 1066–1069. DOI: 10.1126/science.aal2241. URL: https://doi.org/10.1126/science.aal2241.

[234] Jonghwan Kim, Xiaoping Hong, Chenhao Jin, Su-Fei Shi, Chih-Yuan S. Chang, Ming-Hui Chiu, Lain-Jong Li, and Feng Wang. "Ultrafast generation of pseudo-magnetic field for valley excitons in WSe_2 monolayers". In: *Science* 346.6214 (Dec. 2014), pp. 1205–1208. DOI: 10.1126/science.1258122. URL: https://doi.org/10.1126/science.1258122.

[235] Chaw-Keong Yong, Jason Horng, Yuxia Shen, Hui Cai, Alex Wang, Chan-Shan Yang, Chung-Kuan Lin, Shilong Zhao, Kenji Watanabe, Takashi Taniguchi, Sefaattin Tongay, and Feng Wang. "Biexcitonic optical Stark effects in monolayer molybdenum diselenide". In: *Nat. Phys.* 14.11 (July 2018), pp. 1092–1096. DOI: 10.1038/s41567-018-0216-7. URL: https://doi.org/10.1038/s41567-018-0216-7.

[236] Chaw-Keong Yong, M. Iqbal Bakti Utama, Chin Shen Ong, Ting Cao, Emma C. Regan, Jason Horng, Yuxia Shen, Hui Cai, Kenji Watanabe, Takashi Taniguchi, Sefaattin Tongay, Hui Deng, Alex Zettl, Steven G. Louie, and Feng Wang. "Valley-dependent exciton fine structure and Autler–Townes doublets from Berry phases in monolayer $MoSe_2$". In: *Nat. Mater.* 18.10 (Aug. 2019), pp. 1065–1070. DOI: 10.1038/s41563-019-0447-8. URL: https://doi.org/10.1038/s41563-019-0447-8.

[237] Trevor LaMountain, Hadallia Bergeron, Itamar Balla, Teodor K. Stanev, Mark C. Hersam, and Nathaniel P. Stern. "Valley-selective optical Stark effect probed by Kerr rotation". In: *Phys. Rev. B* 97.4 (Jan. 2018), p. 045307. DOI: 10.1103/physrevb.97.045307. URL: https://doi.org/10.1103/physrevb.97.045307.

[238] Paul D. Cunningham, Aubrey T. Hanbicki, Thomas L. Reinecke, Kathleen M. McCreary, and Berend T. Jonker. "Resonant optical Stark effect in monolayer WS_2". In: *Nat. Commun.* 10.1 (Dec. 2019), p. 5539. DOI: 10.1038/s41467-019-13501-x. URL: https://doi.org/10.1038/s41467-019-13501-x.

[239] Kai-Qiang Lin, Sebastian Bange, and John M. Lupton. "Quantum interference in second-harmonic generation from monolayer WSe_2". In: *Nat. Phys.* 15.3 (Jan. 2019), pp. 242–246. DOI: 10.1038/s41567-018-0384-5. URL: https://doi.org/10.1038/s41567-018-0384-5.

[240] Kai Wang, Rodrigo A. Muniz, J. E. Sipe, and S. T. Cundiff. "Quantum Interference Control of Photocurrents in Semiconductors by Nonlinear Optical Absorption Processes". In: *Phys. Rev. Lett.* 123.6 (Aug. 2019), p. 067402. DOI: 10.1103/physrevlett.123.067402. URL: https://doi.org/10.1103/physrevlett.123.067402.

[241] Perry T. Mahon, Rodrigo A. Muniz, and J. E. Sipe. "Quantum interference control of localized carrier distributions in the Brillouin zone". In: *Phys. Rev. B* 100.7 (Aug. 2019), p. 075203. DOI: 10.1103/physrevb.100.075203. URL: https://doi.org/10.1103/physrevb.100.075203.

[242] Rodrigo A. Muniz, Cuauhtémoc Salazar, Kai Wang, S. T. Cundiff, and J. E. Sipe. "Quantum interference control of carriers and currents in zinc blende semiconductors based on nonlinear absorption processes". In: *Phys. Rev. B* 100.7 (Aug. 2019), p. 075202. DOI: 10.1103/physrevb.100.075202. URL: https://doi.org/10.1103/physrevb.100.075202.

[243] Ye Yang, Mengjin Yang, Kai Zhu, Justin C. Johnson, Joseph J. Berry, Jao van de Lagemaat, and Matthew C. Beard. "Large polarization-dependent exciton optical Stark effect in lead iodide perovskites". In: *Nat.Commun.* 7.1 (Aug. 2016), p. 12613. DOI: 10.1038/ncomms12613. URL: https://doi.org/10.1038/ncomms12613.

[244] Andrew H. Proppe, Grant W. Walters, Abdullah Y. Alsalloum, Ayan A. Zhumekenov, Edoardo Mosconi, Shana O. Kelley, Filippo De Angelis, Lyudmyla Adamska, Paolo Umari, Osman M. Bakr, and Edward H. Sargent. "Transition Dipole Moments of n = 1, 2, and 3 Perovskite Quantum Wells from the Optical Stark Effect and Many-Body Perturbation Theory". In: *J. Phys. Chem. Lett.* 11.3 (Jan. 2020), pp. 716–723. DOI: 10.1021/acs.jpclett.9b03349. URL: https://doi.org/10.1021/acs.jpclett.9b03349.

[245] Duckhwan Lee and Andreas C. Albrecht. "A Unified View of Raman, Resonance Raman, and Fluorescence Spectroscopy (and their Analogues in Two-Photon Absorption)". In: *Advances in Infrared and Raman Spectroscopies*. Vol. 12. 1985, pp. 179–213.

[246] Shaul Mukamel. *Principles of Nonlinear Optical Spectroscopy*. Oxford University Press, 1999.

[247] Maxim F. Gelin, Dassia Egorova, and Wolfgang Domcke. "Efficient method for the calculation of time- and frequency-resolved four-wave mixing signals and its application to photon-echo spectroscopy". In: *J. Chem. Phys.* 123.16 (Oct. 2005), p. 164112. DOI: 10.1063/1.2062188. URL: https://doi.org/10.1063/1.2062188.

[248] Blaise Thompson, Kyle Sunden, and Daniel Kohler. *WrightSim*. Version v0.1.0p0. Apr. 2020. DOI: 10.5281/zenodo.3774515. URL: https://doi.org/10.5281/zenodo.3774515.

[249] Shambhu Ghimire and David A. Reis. "High-harmonic generation from solids". In: *Nat. Phys.* 15.1 (Jan. 2019), pp. 10–16. DOI: 10.1038/s41567-018-0315-5. URL: http://dx.doi.org/10.1038/s41567-018-0315-5.

[250] O. Blum, P. Harshman, T. K. Gustafson, and P. L. Kelley. "Application of radiative renormalization to strong-field resonant nonlinear optical interactions". In: *Phys. Rev. A* 47.6 (June 1993), pp. 5165–5179. DOI: 10.1103/physreva.47.5165. URL: https://doi.org/10.1103/physreva.47.5165.

[251] Pauli Virtanen, Ralf Gommers, Travis E. Oliphant, Matt Haberland, Tyler Reddy, David Cournapeau, Evgeni Burovski, Pearu Peterson, Warren Weckesser, Jonathan Bright, Stéfan J. van der Walt, Matthew Brett, Joshua Wilson, K. Jarrod Millman, Nikolay Mayorov, Andrew R. J. Nelson, Eric Jones, Robert Kern, Eric Larson, C J Carey, İlhan Polat, Yu Feng, Eric W. Moore, Jake VanderPlas, Denis Laxalde, Josef Perktold, Robert Cimrman, Ian Henriksen, E. A. Quintero, Charles R. Harris, Anne M. Archibald, Antônio H. Ribeiro, Fabian Pedregosa, and Paul van Mulbregt. "SciPy 1.0: fundamental algorithms for scientific computing in Python". In: *Nat. Methods* (Feb. 2020). DOI: 10.1038/s41592-019-0686-2. URL: https://doi.org/10.1038/s41592-019-0686-2.

[252] C Cohen-Tannoudji and S Reynaud. "Dressed-atom description of resonance fluorescence and absorption spectra of a multi-level atom in an intense laser beam". In: *J. Phys. B* 10.3 (Feb. 1977), pp. 345–363. DOI: 10.1088/0022-3700/10/3/005. URL: https://doi.org/10.1088/0022-3700/10/3/005.

[253] E.T. Jaynes and F.W. Cummings. "Comparison of quantum and semiclassical radiation theories with application to the beam maser". In: *Proc. IEEE* 51.1 (1963), pp. 89–109. DOI: 10.1109/proc.1963.1664. URL: https://doi.org/10.1109/proc.1963.1664.

[254] B. R. Mollow. "Power Spectrum of Light Scattered by Two-Level Systems". In: *Phy. Rev.* 188.5 (Dec. 1969), pp. 1969–1975. DOI: 10.1103/physrev.188.1969. URL: https://doi.org/10.1103/physrev.188.1969.

[255] Peter Hamm and Martin Zanni. *Concepts and Methods of 2D Infrared Spectroscopy*. Cambridge University Press, 2011.

[256] C.H. Brito Cruz, J.P. Gordon, P.C. Becker, R.L. Fork, and C.V. Shank. "Dynamics of spectral hole burning". In: *IEEE J. Quantum Electron.* 24.2 (Feb. 1988), pp. 261–269. DOI: 10.1109/3.122. URL: https://doi.org/10.1109/3.122.

[257] C. Sieh, T. Meier, F. Jahnke, A. Knorr, S. W. Koch, P. Brick, M. Hübner, C. Ell, J. Prineas, G. Khitrova, and H. M. Gibbs. "Coulomb Memory Signatures in the Excitonic Optical Stark Effect". In: *Phys. Rev. Lett.* 82 (15 Apr. 1999), pp. 3112–3115. DOI: 10.1103/PhysRevLett.82.3112. URL: https://link.aps.org/doi/10.1103/PhysRevLett.82.3112.

[258] M. Lindberg and S. W. Koch. "Theory of coherent transients in semiconductor pump–probe spectroscopy". In: *J. Opt. Soc. Am. B* 5.1 (Jan. 1988), pp. 139–146. DOI: 10.1364/JOSAB.5.000139. URL: http://josab.osa.org/abstract.cfm?URI=josab-5-1-139.

[259] J. P. Sokoloff, M. Joffre, B. Fluegel, D. Hulin, M. Lindberg, S. W. Koch, A. Migus, A. Antonetti, and N. Peyghambarian. "Transient oscillations in the vicinity of excitons and in the band of semiconductors". In: *Phys. Rev. B* 38.11 (Oct. 1988), pp. 7615–7621. DOI: 10.1103/physrevb.38.7615. URL: https://doi.org/10.1103/physrevb.38.7615.

[260] M. Joffre, D. Hulin, A. Migus, A. Antonetti, C. Benoit à la Guillaume, N. Peyghambarian, M. Lindberg, and S. W. Koch. "Coherent effects in pump–probe spectroscopy of excitons". In: *Opt. Lett.* 13.4 (Apr. 1988), pp. 276–278. DOI: 10.1364/OL.13.000276. URL: http://ol.osa.org/abstract.cfm?URI=ol-13-4-276.

[261] Kyle Sunden, Blaise Thompson, and John Wright. "WrightSim: Using PyCUDA to Simulate Multidimensional Spectra". In: *Proceedings of the 17th Python in Science Conference*. SciPy, 2018. DOI: 10.25080/majora-4af1f417-00c. URL: https://doi.org/10.25080/majora-4af1f417-00c.

[262] Timothy C. Berkelbach and David R. Reichman. "Optical and Excitonic Properties of Atomically Thin Transition-Metal Dichalcogenides". In: *Annu. Rev. Condens. Matter Phys.* 9.1 (Mar. 2018), pp. 379–396. DOI: 10.1146/annurev-conmatphys-033117-054009. URL: https://doi.org/10.1146/annurev-conmatphys-033117-054009.

[263] Zefang Wang, Daniel A. Rhodes, Kenji Watanabe, Takashi Taniguchi, James C. Hone, Jie Shan, and Kin Fai Mak. "Evidence of high-temperature exciton condensation in two-dimensional atomic double layers". In: *Nature* 574.7776 (Oct. 2019), pp. 76–80. DOI: 10.1038/s41586-019-1591-7. URL: https://doi.org/10.1038/s41586-019-1591-7.

[264] Eunice Y. Paik, Long Zhang, G. William Burg, Rahul Gogna, Emanuel Tutuc, and Hui Deng. "Interlayer exciton laser of extended spatial coherence in atomically thin heterostructures". In: *Nature* 576.7785 (Nov. 2019), pp. 80–84. DOI: 10.1038/s41586-019-1779-x. URL: https://doi.org/10.1038/s41586-019-1779-x.

[265] Chenhao Jin, Emma C. Regan, Aiming Yan, M. Iqbal Bakti Utama, Danqing Wang, Sihan Zhao, Ying Qin, Sijie Yang, Zhiren Zheng, Shenyang Shi, Kenji Watanabe, Takashi Taniguchi, Sefaattin Tongay, Alex Zettl, and Feng Wang. "Observation of moiré excitons in WSe_2/WS_2 heterostructure superlattices". In: *Nature* 567.7746 (Feb. 2019), pp. 76–80. DOI: 10.1038/s41586-019-0976-y. URL: https://doi.org/10.1038/s41586-019-0976-y.

[266] Kyle L. Seyler, Pasqual Rivera, Hongyi Yu, Nathan P. Wilson, Essance L. Ray, David G. Mandrus, Jiaqiang Yan, Wang Yao, and Xiaodong Xu. "Signatures of moiré-trapped valley excitons in $MoSe_2/WSe_2$ heterobilayers". In: *Nature* 567.7746 (Feb. 2019), pp. 66–70. DOI: 10.1038/s41586-019-0957-1. URL: https://doi.org/10.1038/s41586-019-0957-1.

[267] Evgeny M. Alexeev, David A. Ruiz-Tijerina, Mark Danovich, Matthew J. Hamer, Daniel J. Terry, Pramoda K. Nayak, Seongjoon Ahn, Sangyeon Pak, Juwon Lee, Jung Inn Sohn, Maciej R. Molas, Maciej Koperski, Kenji Watanabe, Takashi Taniguchi, Kostya S. Novoselov, Roman V. Gorbachev, Hyeon Suk Shin, Vladimir I. Fal'ko, and Alexander I. Tartakovskii. "Resonantly hybridized excitons in moiré superlattices in van der Waals heterostructures". In: *Nature* 567.7746 (Mar. 2019), pp. 81–86. DOI: 10.1038/s41586-019-0986-9. URL: https://doi.org/10.1038/s41586-019-0986-9.

[268] Kha Tran, Galan Moody, Fengcheng Wu, Xiaobo Lu, Junho Choi, Kyounghwan Kim, Amritesh Rai, Daniel A. Sanchez, Jiamin Quan, Akshay Singh, Jacob Embley, André Zepeda, Marshall Campbell, Travis Autry, Takashi Taniguchi, Kenji Watanabe, Nanshu Lu, Sanjay K. Banerjee, Kevin L. Silverman, Suenne Kim, Emanuel Tutuc, Li Yang, Allan H. MacDonald, and Xiaoqin Li. "Evidence for moiré excitons in van der Waals heterostructures". In: *Nature* 567.7746 (Feb. 2019), pp. 71–75. DOI: 10.1038/s41586-019-0975-z. URL: https://doi.org/10.1038/s41586-019-0975-z.

[269] Emma C. Regan, Danqing Wang, Chenhao Jin, M. Iqbal Bakti Utama, Beini Gao, Xin Wei, Sihan Zhao, Wenyu Zhao, Zuocheng Zhang, Kentaro Yumigeta, Mark Blei, Johan D. Carlström, Kenji Watanabe, Takashi Taniguchi, Sefaattin Tongay, Michael Crommie, Alex Zettl, and Feng Wang. "Mott and generalized Wigner crystal states in WSe_2/WS_2 moiré superlattices". In: *Nature* 579.7799 (Mar. 2020), pp. 359–363. DOI: 10.1038/s41586-020-2092-4. URL: https://doi.org/10.1038/s41586-020-2092-4.

[270] Yanhao Tang, Lizhong Li, Tingxin Li, Yang Xu, Song Liu, Katayun Barmak, Kenji Watanabe, Takashi Taniguchi, Allan H. MacDonald, Jie Shan, and Kin Fai Mak. "Simulation of Hubbard model physics in WSe_2/WS_2 moiré superlattices". In: *Nature* 579.7799 (Mar.

2020), pp. 353–358. DOI: 10.1038/s41586-020-2085-3. URL: https://doi.org/10.1038/s41586-020-2085-3.

[271] Chenhao Jin, Eric Yue Ma, Ouri Karni, Emma C. Regan, Feng Wang, and Tony F. Heinz. "Ultrafast dynamics in van der Waals heterostructures". In: *Nat. Nanotechnol.* 13.11 (Nov. 2018), pp. 994–1003. DOI: 10.1038/s41565-018-0298-5. URL: https://doi.org/10.1038%2Fs41565-018-0298-5.

[272] Pasqual Rivera, Hongyi Yu, Kyle L. Seyler, Nathan P. Wilson, Wang Yao, and Xiaodong Xu. "Interlayer valley excitons in heterobilayers of transition metal dichalcogenides". In: *Nat. Nanotechnol.* 13.11 (Aug. 2018), pp. 1004–1015. DOI: 10.1038/s41565-018-0193-0. URL: https://doi.org/10.1038%2Fs41565-018-0193-0.

[273] Xiaoping Hong, Jonghwan Kim, Su-Fei Shi, Yu Zhang, Chenhao Jin, Yinghui Sun, Sefaattin Tongay, Junqiao Wu, Yanfeng Zhang, and Feng Wang. "Ultrafast charge transfer in atomically thin MoS_2/WS_2 heterostructures". In: *Nat. Nanotechnol.* 9.August (2014), pp. 682–686. DOI: 10.1038/nnano.2014.167. URL: http://www.nature.com/doifinder/10.1038/nnano.2014.167.

[274] P. Merkl, F. Mooshammer, P. Steinleitner, A. Girnghuber, K.-Q. Lin, P. Nagler, J. Holler, C. Schüller, J. M. Lupton, T. Korn, S. Ovesen, S. Brem, E. Malic, and R. Huber. "Ultrafast transition between exciton phases in van der Waals heterostructures". In: *Nat. Mater.* 18.7 (Apr. 2019), pp. 691–696. DOI: 10.1038/s41563-019-0337-0. URL: https://doi.org/10.1038/s41563-019-0337-0.

[275] Luis A. Jauregui, Andrew Y. Joe, Kateryna Pistunova, Dominik S. Wild, Alexander A. High, You Zhou, Giovanni Scuri, Kristiaan De Greve, Andrey Sushko, Che-Hang Yu, Takashi Taniguchi, Kenji Watanabe, Daniel J. Needleman, Mikhail D. Lukin, Hongkun Park, and Philip Kim. "Electrical control of interlayer exciton dynamics in atomically thin heterostructures". In: *Science* 366.6467 (Nov. 2019), pp. 870–875. DOI: 10.1126/science.aaw4194. URL: https://doi.org/10.1126/science.aaw4194.

[276] Han Wang, Junhyeok Bang, Yiyang Sun, Liangbo Liang, Damien West, Vincent Meunier, and Shengbai Zhang. "The role of collective motion in the ultrafast charge transfer in van der Waals heterostructures". In: *Nat. Commun.* 7.May (2016), pp. 1–9. DOI: 10.1038/ncomms11504. URL: http://www.nature.com/doifinder/10.1038/ncomms11504.

[277] Run Long and Oleg V. Prezhdo. "Quantum Coherence Facilitates Efficient Charge Separation at a $MoS_2/MoSe_2$ van der Waals Junction". In: *Nano Lett.* 16.3 (2016), pp. 1996–2003. DOI: 10.1021/acs.nanolett.5b05264.

[278] Peymon Zereshki, Yaqing Wei, Run Long, and Hui Zhao. "Layer-Coupled States Facilitate Ultrafast Charge Transfer in a Transition Metal Dichalcogenide Trilayer Heterostructure". In: *J. Phys. Chem. Lett.* 9.20 (Sept. 2018), pp. 5970–5978. DOI: 10.1021/acs.jpclett.8b02622. URL: https://doi.org/10.1021/acs.jpclett.8b02622.

[279] Yong Wang, Zhan Wang, Wang Yao, Gui-Bin Liu, and Hongyi Yu. "Interlayer coupling in commensurate and incommensurate bilayer structures of transition-metal dichalcogenides". In: *Phys. Rev. B* 95.11 (Mar. 2017), p. 115429. DOI: 10.1103/physrevb.95.115429. URL: https://doi.org/10.1103/physrevb.95.115429.

[280] Lingling Wu, Yuzhong Chen, Hongzhi Zhou, and Haiming Zhu. "Ultrafast Energy Transfer of Both Bright and Dark Excitons in 2D van der Waals Heterostructures Beyond Dipolar Coupling". In: *ACS Nano* 13.2 (Feb. 2019), pp. 2341–2348. DOI: 10.1021/acsnano.8b09059. URL: https://doi.org/10.1021/acsnano.8b09059.

[281] Qijing Zheng, Yu Xie, Zhenggang Lan, Oleg V. Prezhdo, Wissam A. Saidi, and Jin Zhao. "Phonon-coupled ultrafast interlayer charge oscillation at van der Waals heterostructure interfaces". In: *Phys. Rev. B* 97.20 (May 2018), p. 205417. DOI: 10.1103/physrevb.97.205417. URL: https://doi.org/10.1103/physrevb.97.205417.

[282] Prasana K. Sahoo, Shahriar Memaran, Yan Xin, Luis Balicas, and Humberto R. Gutiérrez. "One-pot growth of two-dimensional lateral heterostructures via sequential edge-epitaxy". In: *Nature* 553.7686 (Jan. 2018), pp. 63–67. DOI: 10.1038/nature25155. URL: https://doi.org/10.1038%2Fnature25155.

[283] M.-Y. Li, Y. Shi, C.-C. Cheng, L.-S. Lu, Y.-C. Lin, H.-L. Tang, M.-L. Tsai, C.-W. Chu, K.-H. Wei, J.-H. He, W.-H. Chang, K. Suenaga, and L.-J. Li. "Epitaxial growth of a monolayer WSe_2-MoS_2 lateral p-n junction with an atomically sharp interface". In: *Science* 349.6247 (July 2015), pp. 524–528. DOI: 10.1126/science.aab4097. URL: https://doi.org/10.1126%2Fscience.aab4097.

[284] Yongji Gong, Junhao Lin, Xingli Wang, Gang Shi, Sidong Lei, Zhong Lin, Xiaolong Zou, Gonglan Ye, Robert Vajtai, Boris I. Yakobson, Humberto Terrones, Mauricio Terrones, Beng Kang Tay, Jun Lou, Sokrates T. Pantelides, Zheng Liu, Wu Zhou, and Pulickel M. Ajayan. "Vertical and in-plane heterostructures from WS_2/MoS_2 monolayers". In: *Nat. Mater.* 13.12 (Sept. 2014), pp. 1135–1142. DOI: 10.1038/nmat4091. URL: https://doi.org/10.1038%2Fnmat4091.

[285] Chunming Huang, Sanfeng Wu, Ana M. Sanchez, Jonathan J. P. Peters, Richard Beanland, Jason S. Ross, Pasqual Rivera, Wang Yao, David H. Cobden, and Xiaodong Xu. "Lateral heterojunctions within monolayer $MoSe_2$–WSe_2 semiconductors". In: *Nat. Mater.* 13.12 (Aug. 2014), pp. 1096–1101. DOI: 10.1038/nmat4064. URL: https://doi.org/10.1038%2Fnmat4064.

[286] Zhengwei Zhang, Peng Chen, Xidong Duan, Ketao Zang, Jun Luo, and Xiangfeng Duan. "Robust epitaxial growth of two-dimensional heterostructures, multiheterostructures, and superlattices". In: *Science* 357.6353 (Aug. 2017), pp. 788–792. DOI: 10.1126/science.aan6814. URL: https://doi.org/10.1126%2Fscience.aan6814.

[287] Saien Xie, Lijie Tu, Yimo Han, Lujie Huang, Kibum Kang, Ka Un Lao, Preeti Poddar, Chibeom Park, David A. Muller, Robert A. DiStasio, and Jiwoong Park. "Coherent, atomically thin transition-metal dichalcogenide superlattices with engineered strain". In: *Science* 359.6380 (Mar. 2018), pp. 1131–1136. DOI: 10.1126/science.aao5360. URL: https://doi.org/10.1126%2Fscience.aao5360.

[288] Biyuan Zheng, Chao Ma, Dong Li, Jianyue Lan, Zhe Zhang, Xingxia Sun, Weihao Zheng, Tiefeng Yang, Chenguang Zhu, Gang Ouyang, Gengzhao Xu, Xiaoli Zhu, Xiao Wang, and Anlian Pan. "Band Alignment Engineering in Two-Dimensional Lateral Heterostructures". In: *J. Am. Chem. Soc.* 140.36 (Aug. 2018), pp. 11193–11197. DOI: 10.1021/jacs.8b07401. URL: https://doi.org/10.1021%2Fjacs.8b07401.

[289] Chendong Zhang, Ming-Yang Li, Jerry Tersoff, Yimo Han, Yushan Su, Lain-Jong Li, David A. Muller, and Chih-Kang Shih. "Strain distributions and their influence on electronic structures of WSe_2–MoS_2 laterally strained heterojunctions". In: *Nat. Nanotechnol.* 13.2 (Jan. 2018), pp. 152–158. DOI: 10.1038/s41565-017-0022-x. URL: https://doi.org/10.1038%2Fs41565-017-0022-x.

[290] Eunhye Koo, Yonggeun Lee, Youngho Song, Minsuk Park, and Sang-Yong Ju. "Growth Order-Dependent Strain Variations of Lateral Transition Metal Dichalcogenide Heterostructures". In: *ACS Appl. Electron. Mater.* 1.1 (Jan. 2019), pp. 113–121. DOI: 10.1021/acsaelm.8b00051. URL: https://doi.org/10.1021%2Facsaelm.8b00051.

[291] Xin-Quan Zhang, Chin-Hao Lin, Yu-Wen Tseng, Kuan-Hua Huang, and Yi-Hsien Lee. "Synthesis of Lateral Heterostructures of Semiconducting Atomic Layers". In: *Nano Lett.* 15.1 (Dec. 2014), pp. 410–415. DOI: 10.1021/nl503744f. URL: https://doi.org/10.1021%2Fnl503744f.

[292] Kun Chen, Xi Wan, Weiguang Xie, Jinxiu Wen, Zhiwen Kang, Xiaoliang Zeng, Huanjun Chen, and Jianbin Xu. "Lateral Built-In Potential of Monolayer MoS_2-WS_2 In-Plane Heterostructures by a Shortcut Growth Strategy". In: *Adv. Mater.* 27.41 (Sept. 2015), pp. 6431–6437. DOI: 10.1002/adma.201502375. URL: https://doi.org/10.1002%2Fadma.201502375.

[293] Tao Chen, Degong Ding, Jia Shi, Guang Wang, Liangzhi Kou, Xiaoming Zheng, Xibiao Ren, Xinfeng Liu, Chuanhong Jin, Jianxin Zhong, and Guolin Hao. "Lateral and Vertical $MoSe_2$–MoS_2 Heterostructures via Epitaxial Growth: Triggered by High-Temperature Annealing and Precursor Concentration". In: *J. Phys. Chem. Lett.* 10.17 (July 2019), pp. 5027–5035. DOI: 10.1021/acs.jpclett.9b01961. URL: https://doi.org/10.1021%2Facs.jpclett.9b01961.

[294] Oscar Ávalos-Ovando, Diego Mastrogiuseppe, and Sergio E. Ulloa. "Lateral interfaces of transition metal dichalcogenides: A stable tunable one-dimensional physics platform". In: *Phys. Rev. B* 99.3 (Jan. 2019), p. 035107. DOI: 10.1103/physrevb.99.035107. URL: https://doi.org/10.1103%2Fphysrevb.99.035107.

[295] Zhenfa Zheng, Qijing Zheng, and Jin Zhao. "Ultrafast electron transfer dynamics in lateral transition-metal dichalcogenide heterostructures". In: *Electron. Struct.* 1.3 (Sept. 2019), p. 034001. DOI: 10.1088/2516-1075/ab3b28. URL: https://doi.org/10.1088/2516-1075/ab3b28.

[296] Xu Zhang, Jesús Grajal, Jose Luis Vazquez-Roy, Ujwal Radhakrishna, Xiaoxue Wang, Winston Chern, Lin Zhou, Yuxuan Lin, Pin-Chun Shen, Xiang Ji, Xi Ling, Ahmad Zubair, Yuhao Zhang, Han Wang, Madan Dubey, Jing Kong, Mildred Dresselhaus, and Tomás Palacios. "Two-dimensional MoS_2-enabled flexible rectenna for Wi-Fi-band wireless energy harvesting". In: *Nature* 566.7744 (Jan. 2019), pp. 368–372. DOI: 10.1038/s41586-019-0892-1. URL: https://doi.org/10.1038%2Fs41586-019-0892-1.

[297] Meng-Lin Tsai, Ming-Yang Li, José Ramón Durán Retamal, Kai-Tak Lam, Yung-Chang Lin, Kazu Suenaga, Lih-Juann Chen, Gengchiau Liang, Lain-Jong Li, and Jr-Hau He. "Single Atomically Sharp Lateral Monolayer p-n Heterojunction Solar Cells with Extraordinarily High Power Conversion Efficiency". In: *Adv. Mater.* 29.32 (June 2017), p. 1701168. DOI: 10.1002/adma.201701168. URL: https://doi.org/10.1002%2Fadma.201701168.

[298] Matthew Z. Bellus, Masoud Mahjouri-Samani, Samuel D. Lane, Akinola D. Oyedele, Xufan Li, Alexander A. Puretzky, David Geohegan, Kai Xiao, and Hui Zhao. "Photocarrier Transfer across Monolayer MoS_2–$MoSe_2$ Lateral Heterojunctions". In: *ACS Nano* 12.7 (June 2018), pp. 7086–7092. DOI: 10.1021/acsnano.8b02843. URL: https://doi.org/10.1021%2Facsnano.8b02843.

[299] Kun Ye, Lixuan Liu, Yujie Liu, Anmin Nie, Kun Zhai, Jianyong Xiang, Bochong Wang, Fusheng Wen, Congpu Mu, Zhisheng Zhao, Yongji Gong, Zhongyuan Liu, and Yongjun Tian. "Lateral Bilayer MoS_2–WS_2 Heterostructure Photodetectors with High Responsivity and Detectivity". In: *Adv. Opt. Mater.* 7.20 (July 2019), p. 1900815. DOI: 10.1002/adom.201900815. URL: https://doi.org/10.1002%2Fadom.201900815.

[300] Heather M Hill, Albert F Rigosi, Kwang Taeg Rim, George W. Flynn, and Tony F. Heinz. "Band alignment in MoS_2/WS_2 transition metal dichalcogenide heterostructures probed by scanning tunneling microscopy and spectroscopy". In: *Nano Lett.* 16.8 (2016), pp. 4831–4837. DOI: 10.1021/acs.nanolett.6b01007. URL: http://pubs.acs.org/doi/abs/10.1021/acs.nanolett.6b01007.

[301] Daniel D. Kohler, Blaise J. Thompson, and John C. Wright. "Resonant Third-Order Susceptibility of PbSe Quantum Dots Determined by Standard Dilution and Transient Grating Spectroscopy". In: *J. Phys. Chem. C* 122.31 (July 2018), pp. 18086–18093. DOI: 10.1021/acs.jpcc.8b04462. URL: https://doi.org/10.1021/acs.jpcc.8b04462.

[302] E. J. Sie, A. Steinhoff, C. Gies, C. H. Lui, Q. Ma, M. Rösner, G. Schönhoff, F. Jahnke, T. O. Wehling, Y.-H. Lee, J. Kong, P. Jarillo-Herrero, and N. Gedik. "Observation of Exciton Redshift–Blueshift Crossover in Monolayer WS_2". In: *Nano Lett.* 17.7 (June 2017), pp. 4210–4216. DOI: 10.1021/acs.nanolett.7b01034. URL: https://doi.org/10.1021/acs.nanolett.7b01034.

[303] Paul D. Cunningham, Kathleen M. McCreary, and Berend T. Jonker. "Auger Recombination in Chemical Vapor Deposition-Grown Monolayer WS_2". In: *J. Phys. Chem. Lett.* 7.24 (Dec. 2016), pp. 5242–5246. DOI: 10.1021/acs.jpclett.6b02413. URL: https://doi.org/10.1021/acs.jpclett.6b02413.

[304] Long Yuan, Ti Wang, Tong Zhu, Mingwei Zhou, and Libai Huang. "Exciton Dynamics, Transport, and Annihilation in Atomically Thin Two-Dimensional Semiconductors". In: *J. Phys. Chem. Lett.* 8.14 (July 2017), pp. 3371–3379. DOI: 10.1021/acs.jpclett.7b00885. URL: https://doi.org/10.1021/acs.jpclett.7b00885.

[305] Yumeng You, Xiao-Xiao Zhang, Timothy C. Berkelbach, Mark S. Hybertsen, David R. Reichman, and Tony F. Heinz. "Observation of biexcitons in monolayer WSe_2". In: *Nat. Phys.* 11.6 (May 2015), pp. 477–481. DOI: 10.1038/nphys3324. URL: https://doi.org/10.1038%2Fnphys3324.

[306] Dezheng Sun, Yi Rao, Georg A. Reider, Gugang Chen, Yumeng You, Louis Brézin, Avetik R. Harutyunyan, and Tony F. Heinz. "Observation of Rapid Exciton–Exciton Annihilation in Monolayer Molybdenum Disulfide". In: *Nano Lett.* 14.10 (Sept. 2014), pp. 5625–5629. DOI: 10.1021/nl5021975. URL: https://doi.org/10.1021/nl5021975.

[307] Alexey Chernikov, Arend M. van der Zande, Heather M. Hill, Albert F. Rigosi, Ajanth Velauthapillai, James Hone, and Tony F. Heinz. "Electrical Tuning of Exciton Binding Energies in Monolayer WS_2". In: *Phys. Rev. Lett.* 115.12 (Sept. 2015), p. 126802. DOI: 10.1103/physrevlett.115.126802. URL: https://doi.org/10.1103/physrevlett.115.126802.

[308] Claudia Ruppert, Alexey Chernikov, Heather M. Hill, Albert F. Rigosi, and Tony F. Heinz. "The Role of Electronic and Phononic Excitation in the Optical Response of Monolayer WS_2 after Ultrafast Excitation". In: *Nano Lett.* 17.2 (Jan. 2017), pp. 644–651. DOI: 10.1021/acs.nanolett.6b03513. URL: https://doi.org/10.1021/acs.nanolett.6b03513.

[309] Darien J. Morrow. "Ultrafast, multidimensional pump-probe spectroscopy of atomically thin WS2-MoS2 lateral heterostructures". In: *Open Science Framework* (2020). DOI: 10.17605/OSF.IO/PQE9B. URL: https://osf.io/pqe9b/.

[310] A Castellanos-Gomez, N Agraït, and G Rubio-Bollinger. "Optical identification of atomically thin dichalcogenide crystals". In: *Appl. Phys. Lett.* 96.21 (May 2010), p. 213116. DOI: 10.1063/1.3442495. URL: https://doi.org/10.1063/1.3442495.

[311] S. Roddaro, P. Pingue, V. Piazza, V. Pellegrini, and F. Beltram. "The Optical Visibility of Graphene: Interference Colors of Ultrathin Graphite on SiO2". In: *Nano Lett.* 7.9 (Sept. 2007), pp. 2707–2710. DOI: 10.1021/nl0711581. URL: https://doi.org/10.1021/nl0711581.

[312] R. J. Elliott. "Intensity of Optical Absorption by Excitons". In: *Phys. Rev.* 108.6 (Dec. 1957), pp. 1384–1389. DOI: 10.1103/physrev.108.1384. URL: https://doi.org/10.1103/physrev.108.1384.

[313] Masaki Shinada and Satoru Sugano. "Interband Optical Transitions in Extremely Anisotropic Semiconductors. I. Bound and Unbound Exciton Absorption". In: *J. Phys. Soc. Jpn.* 21.10 (Oct. 1966), pp. 1936–1946. DOI: 10.1143/jpsj.21.1936. URL: https://doi.org/10.1143/jpsj.21.1936.

[314] Christian Tanguy. "Optical Dispersion by Wannier Excitons". In: *Phys. Rev. Lett* 75.22 (Nov. 1995), pp. 4090–4093. DOI: 10.1103/physrevlett.75.4090. URL: https://doi.org/10.1103/physrevlett.75.4090.

[315] Christian Tanguy. "Complex dielectric constant of two-dimensional Wannier excitons". In: *Solid State Communications* 98.1 (Apr. 1996), pp. 65–68. DOI: 10.1016/0038-1098(95)00750-4. URL: https://doi.org/10.1016/0038-1098(95)00750-4.

[316] Hartmut Haug and Stephan W Koch. *Quantum Theory of the Optical and Electronic Properties of Semiconductors*. WORLD SCIENTIFIC, Jan. 2009. DOI: 10.1142/7184. URL: https://doi.org/10.1142/7184.

[317] Heather M. Hill, Albert F. Rigosi, Cyrielle Roquelet, Alexey Chernikov, Timothy C. Berkelbach, David R. Reichman, Mark S. Hybertsen, Louis E. Brus, and Tony F. Heinz. "Observation of Excitonic Rydberg States in Monolayer MoS_2 and WS_2 by Photoluminescence Excitation Spectroscopy". In: *Nano Lett.* 15.5 (Apr. 2015), pp. 2992–2997. DOI: 10.1021/nl504868p. URL: https://doi.org/10.1021%2Fnl504868p.

[318] A.T. Hanbicki, M. Currie, G. Kioseoglou, A.L. Friedman, and B.T. Jonker. "Measurement of high exciton binding energy in the monolayer transition-metal dichalcogenides WS_2 and WSe_2". In: *Solid State Communications* 203 (Feb. 2015), pp. 16–20. DOI: 10.1016/j.ssc.2014.11.005. URL: https://doi.org/10.1016/j.ssc.2014.11.005.

[319] I. H. Malitson. "Interspecimen Comparison of the Refractive Index of Fused Silica". In: *J. Opt. Soc. Am.* 55.10 (Oct. 1965), p. 1205. DOI: 10.1364/josa.55.001205. URL: https://doi.org/10.1364/josa.55.001205.

[320] Edward D. Palik. *Handbook of Optical Constants of Solids*. Academic Press, 1985.

[321] Rui Wang, Brian A. Ruzicka, Nardeep Kumar, Matthew Z. Bellus, Hsin-Ying Chiu, and Hui Zhao. "Ultrafast and spatially resolved studies of charge carriers in atomically thin molybdenum disulfide". In: *Phys. Rev. B* 86.4 (July 2012), p. 045406. DOI: 10.1103/physrevb.86.045406. URL: https://doi.org/10.1103/physrevb.86.045406.

[322] Jue Wang, Jenny Ardelean, Yusong Bai, Alexander Steinhoff, Matthias Florian, Frank Jahnke, Xiaodong Xu, Mackillo Kira, James Hone, and X.-Y. Zhu. "Optical generation of high carrier densities in 2D semiconductor heterobilayers". In: *Sci. Adv.* 5.9 (Sept. 2019), eaax0145. DOI: 10.1126/sciadv.aax0145. URL: https://doi.org/10.1126/sciadv.aax0145.

[323] Junpei Zhang, Linhua Yao, Nan Zhou, Hongwei Dai, Hui Cheng, Mingshan Wang, Luman Zhang, Xiaodie Chen, Xia Wang, Tianyou Zhai, and Junbo Han. "Multiphoton Excitation and Defect-Enhanced Fast Carrier Relaxation in Few-Layered MoS_2 Crystals". In: *J. Phys. Chem. C* 123.17 (Apr. 2019), pp. 11216–11223. DOI: 10.1021/acs.jpcc.9b00619. URL: https://doi.org/10.1021/acs.jpcc.9b00619.

[324] Jichen Dong, Leining Zhang, and Feng Ding. "Kinetics of Graphene and 2D Materials Growth". In: *Adv. Mater.* 31.9 (Oct. 2018), p. 1801583. DOI: 10.1002/adma.201801583. URL: https://doi.org/10.1002%2Fadma.201801583.

[325] Haiyan Nan, Zilu Wang, Wenhui Wang, Zheng Liang, Yan Lu, Qian Chen, Daowei He, Pingheng Tan, Feng Miao, Xinran Wang, Jinlan Wang, and Zhenhua Ni. "Strong Photoluminescence Enhancement of MoS_2 through Defect Engineering and Oxygen Bonding". In: *ACS Nano* 8.6 (May 2014), pp. 5738–5745. DOI: 10.1021/nn500532f. URL: https://doi.org/10.1021/nn500532f.

[326] Humberto R. Gutiérrez, Nestor Perea-López, Ana Laura Elías, Ayse Berkdemir, Bei Wang, Ruitao Lv, Florentino López-Urías, Vincent H. Crespi, Humberto Terrones, and Mauricio Terrones. "Extraordinary Room-Temperature Photoluminescence in Triangular WS_2 Monolayers". In: *Nano Lett.* 13.8 (Dec. 2012), pp. 3447–3454. DOI: 10.1021/nl3026357. URL: https://doi.org/10.1021/nl3026357.

[327] Yung-Chang Lin, Shisheng Li, Hannu-Pekka Komsa, Li-Jen Chang, Arkady V. Krasheninnikov, Goki Eda, and Kazu Suenaga. "Revealing the Atomic Defects of WS_2 Governing Its Distinct Optical Emissions". In: *Adv. Funct. Mater.* 28.4 (Nov. 2017), p. 1704210. DOI: 10.1002/adfm.201704210. URL: https://doi.org/10.1002/adfm.201704210.

[328] Ouri Karni, Elyse Barré, Sze Cheung Lau, Roland Gillen, Eric Yue Ma, Bumho Kim, Kenji Watanabe, Takashi Taniguchi, Janina Maultzsch, Katayun Barmak, Ralph H. Page, and Tony F. Heinz. "Infrared Interlayer Exciton Emission in MoS_2/WSe_2 Heterostructures". In: *Phys. Rev. Lett.* 123.24 (Dec. 2019). DOI: 10.1103/physrevlett.123.247402. URL: https://doi.org/10.1103/physrevlett.123.247402.

[329] Kyoung-Duck Park, Omar Khatib, Vasily Kravtsov, Genevieve Clark, Xiaodong Xu, and Markus B. Raschke. "Hybrid Tip-Enhanced Nanospectroscopy and Nanoimaging of Monolayer WSe_2 with Local Strain Control". In: *Nano Letters* 16.4 (Mar. 2016), pp. 2621–2627. DOI: 10.1021/acs.nanolett.6b00238. URL: https://doi.org/10.1021/acs.nanolett.6b00238.

[330] S. Schmitt-Rink, D. S. Chemla, and H. Haug. "Nonequilibrium theory of the optical Stark effect and spectral hole burning in semiconductors". In: *Phys. Rev. B* 37.2 (Jan. 1988), pp. 941–955. DOI: 10.1103/physrevb.37.941. URL: https://doi.org/10.1103/physrevb.37.941.

[331] Peng Yao, Dawei He, Peymon Zereshki, Yongsheng Wang, and Hui Zhao. "Nonlinear optical effect of interlayer charge transfer in a van der Waals heterostructure". In: *Appl. Phys. Lett.* 115.26 (Dec. 2019), p. 263103. DOI: 10.1063/1.5131165. URL: https://doi.org/10.1063/1.5131165.

[332] J. Qi, M. S. Yeganeh, I. Koltover, A. G. Yodh, and W. M. Theis. "Depletion-electric-field-induced changes in second-harmonic generation from GaAs". In: *Phys. Rev. Lett.* 71.4 (July 1993), pp. 633–636. DOI: 10.1103/physrevlett.71.633. URL: https://doi.org/10.1103/physrevlett.71.633.

[333] O. A. Aktsipetrov, A. A. Fedyanin, V. N. Golovkina, and T. V. Murzina. "Optical second-harmonic generation induced by a dc electric field at the Si–SiO_2 interface". In: *Opt. Lett.* 19.18 (Sept. 1994), p. 1450. DOI: 10.1364/ol.19.001450. URL: https://doi.org/10.1364/ol.19.001450.

[334] Huakang Yu, Deep Talukdar, Weigao Xu, Jacob B. Khurgin, and Qihua Xiong. "Charge-Induced Second-Harmonic Generation in Bilayer WSe_2". In: *Nano Lett.* 15.8 (July 2015), pp. 5653–5657. DOI: 10.1021/acs.nanolett.5b02547. URL: https://doi.org/10.1021/acs.nanolett.5b02547.

[335] Marvin Kulig, Jonas Zipfel, Philipp Nagler, Sofia Blanter, Christian Schüller, Tobias Korn, Nicola Paradiso, Mikhail M. Glazov, and Alexey Chernikov. "Exciton Diffusion and Halo Effects in Monolayer Semiconductors". In: *Phys. Rev. Lett.* 120.20 (May 2018), p. 207401. DOI: 10.1103/physrevlett.120.207401. URL: https://doi.org/10.1103/physrevlett.120.207401.

[336] Andrew C. Jones, Nicholas M. Kearns, Jia-Jung Ho, Jessica T. Flach, and Martin T. Zanni. "Impact of non-equilibrium molecular packings on singlet fission in microcrystals observed using 2D white-light microscopy". In: *Nat. Chem.* 12.1 (Dec. 2019), pp. 40–47. DOI: 10.1038/s41557-019-0368-9. URL: https://doi.org/10.1038%2Fs41557-019-0368-9.

[337] Andrew C. Jones, Nicholas M. Kearns, Miriam Bohlmann Kunz, Jessica T. Flach, and Martin T. Zanni. "Multidimensional Spectroscopy on the Microscale: Development of a Multimodal Imaging System Incorporating 2D White-Light Spectroscopy, Broadband Transient Absorption, and Atomic Force Microscopy". In: *J. Phys. Chem. A* 123.50 (Nov. 2019), pp. 10824–10836. DOI: 10.1021/acs.jpca.9b09099. URL: https://doi.org/10.1021%2Facs.jpca.9b09099.

[338] Geoffrey Piland and Erik M. Grumstrup. "High-Repetition Rate Broadband Pump–Probe Microscopy". In: *J. Phys. Chem. A* 123.40 (June 2019), pp. 8709–8716. DOI: 10.1021/acs.jpca.9b03858. URL: https://doi.org/10.1021/acs.jpca.9b03858.

[339] Christoph Schnedermann, Jooyoung Sung, Raj Pandya, Sachin Dev Verma, Richard Y. S. Chen, Nicolas Gauriot, Hope M. Bretscher, Philipp Kukura, and Akshay Rao. "Ultrafast Tracking of Exciton and Charge Carrier Transport in Optoelectronic Materials on the Nanometer Scale". In: *J. Phys. Chem. Lett.* 10.21 (Oct. 2019), pp. 6727–6733. DOI: 10.1021/acs.jpclett.9b02437. URL: https://doi.org/10.1021/acs.jpclett.9b02437.

[340] Milan Delor, Hannah L. Weaver, QinQin Yu, and Naomi S. Ginsberg. "Imaging material functionality through three-dimensional nanoscale tracking of energy flow". In: *Nat. Mater.* 19.1 (Oct. 2019), pp. 56–62. DOI: 10.1038/s41563-019-0498-x. URL: https://doi.org/10.1038/s41563-019-0498-x.

[341] D. J. Clark, C. T. Le, V. Senthilkumar, F. Ullah, H.-Y. Cho, Y. Sim, M.-J. Seong, K.-H. Chung, Y. S. Kim, and J. I. Jang. "Near bandgap second-order nonlinear optical characteristics of MoS_2 monolayer transferred on transparent substrates". In: *Appl. Phys. Lett.* 107.13 (Sept. 2015), p. 131113. DOI: 10.1063/1.4932134. URL: https://doi.org/10.1063/1.4932134.

[342] Keith T. Butler, Jarvist M. Frost, and Aron Walsh. "Ferroelectric materials for solar energy conversion: photoferroics revisited". In: *Energy Environ. Sci.* 8.3 (2015), pp. 838–848. DOI: 10.1039/c4ee03523b. URL: https://doi.org/10.1039/c4ee03523b.

[343] Charles Paillard, Xiaofei Bai, Ingrid C. Infante, Maël Guennou, Grégory Geneste, Marin Alexe, Jens Kreisel, and Brahim Dkhil. "Photovoltaics with Ferroelectrics: Current Status and Beyond". In: *Adv. Mater.* 28.26 (May 2016), pp. 5153–5168. DOI: 10.1002/adma.201505215. URL: https://doi.org/10.1002%2Fadma.201505215.

[344] Yongping Fu, Haiming Zhu, Jie Chen, Matthew P. Hautzinger, X.-Y. Zhu, and Song Jin. "Metal halide perovskite nanostructures for optoelectronic applications and the study of physical properties". In: *Nat. Rev. Mater.* 4.3 (Feb. 2019), pp. 169–188. DOI: 10.1038/s41578-019-0080-9. URL: https://doi.org/10.1038%2Fs41578-019-0080-9.

[345] Yixin Zhao and Kai Zhu. "Organic–inorganic hybrid lead halide perovskites for optoelectronic and electronic applications". In: *Chem. Soc. Rev.* 45.3 (2016), pp. 655–689. DOI: 10.1039/c4cs00458b. URL: https://doi.org/10.1039%2Fc4cs00458b.

[346] Bayrammurad Saparov and David B. Mitzi. "Organic–Inorganic Perovskites: Structural Versatility for Functional Materials Design". In: *Chem. Rev.* 116.7 (Apr. 2016), pp. 4558–4596. DOI: 10.1021/acs.chemrev.5b00715. URL: https://doi.org/10.1021%2Facs.chemrev.5b00715.

[347] Yevgeny Rakita, Omri Bar-Elli, Elena Meirzadeh, Hadar Kaslasi, Yagel Peleg, Gary Hodes, Igor Lubomirsky, Dan Oron, David Ehre, and David Cahen. "Tetragonal $CH_3NH_3PbI_3$ is ferroelectric". In: *Proc. Natl. Acad. Sci. U.S.A.* 114.28 (June 2017), E5504–E5512. DOI: 10.1073/pnas.1702429114. URL: https://doi.org/10.1073%2Fpnas.1702429114.

[348] Holger Röhm, Tobias Leonhard, Alexander D. Schulz, Susanne Wagner, Michael J. Hoffmann, and Alexander Colsmann. "Ferroelectric Properties of Perovskite Thin Films and Their Implications for Solar Energy Conversion". In: *Adv. Mater.* 31.26 (Feb. 2019), p. 1806661. DOI: 10.1002/adma.201806661. URL: https://doi.org/10.1002/adma.201806661.

[349] Zhen Fan, Juanxiu Xiao, Kuan Sun, Lei Chen, Yating Hu, Jianyong Ouyang, Khuong P. Ong, Kaiyang Zeng, and John Wang. "Ferroelectricity of $CH_3NH_3PbI_3$ Perovskite". In: *J. Phys. Chem. Lett.* 6.7 (Mar. 2015), pp. 1155–1161. DOI: 10.1021/acs.jpclett.5b00389. URL: https://doi.org/10.1021%2Facs.jpclett.5b00389.

[350] Hui-Seon Kim, Sung Kyun Kim, Byeong Jo Kim, Kyung-Sik Shin, Manoj Kumar Gupta, Hyun Suk Jung, Sang-Woo Kim, and Nam-Gyu Park. "Ferroelectric Polarization in $CH_3NH_3PbI_3$ Perovskite". In: *J. Phys. Chem. Lett.* 6.9 (Apr. 2015), pp. 1729–1735. DOI: 10.1021/acs.jpclett.5b00695. URL: https://doi.org/10.1021%2Facs.jpclett.5b00695.

[351] Sharada G, Pratibha Mahale, Bhushan P. Kore, Somdutta Mukherjee, Mysore S. Pavan, Chandan De, Somnath Ghara, A. Sundaresan, Anshu Pandey, Tayur N. Guru Row, and D. D. Sarma. "Is $CH_3NH_3PbI_3$ Polar?" In: *J. Phys. Chem. Lett.* 7.13 (June 2016), pp. 2412–2419. DOI: 10.1021/acs.jpclett.6b00803. URL: https://doi.org/10.1021%2Facs.jpclett.6b00803.

[352] Zhang-Ran Gao, Xiao-Fan Sun, Yu-Ying Wu, Yi-Zhang Wu, Hong-Ling Cai, and X. S. Wu. "Ferroelectricity of the Orthorhombic and Tetragonal MAPbBr3 Single Crystal". In: *J. Phys. Chem. Lett.* 10.10 (May 2019), pp. 2522–2527. DOI: 10.1021/acs.jpclett.9b00776. URL: https://doi.org/10.1021%2Facs.jpclett.9b00776.

[353] Yevgeny Rakita, Elena Meirzadeh, Tatyana Bendikov, Vyacheslav Kalchenko, Igor Lubomirsky, Gary Hodes, David Ehre, and David Cahen. "CH3NH3PbBr3 is not pyroelectric, excluding ferroelectric-enhanced photovoltaic performance". In: *APL Materials* 4.5 (May 2016), p. 051101. DOI: 10.1063/1.4949760. URL: https://doi.org/10.1063%2F1.4949760.

[354] Peiqi Wang, Jinjin Zhao, Liyu Wei, Qingfeng Zhu, Shuhong Xie, Jinxi Liu, Xiangjian Meng, and Jiangyu Li. "Photo-induced ferroelectric switching in perovskite $CH_3NH_3PbI_3$ films". In: *Nanoscale* 9.11 (2017), pp. 3806–3817. DOI: 10.1039/c6nr09310h. URL: https://doi.org/10.1039%2Fc6nr09310h.

[355] Hsin-Wei Chen, Nobuya Sakai, Masashi Ikegami, and Tsutomu Miyasaka. "Emergence of Hysteresis and Transient Ferroelectric Response in Organo-Lead Halide Perovskite Solar Cells". In: *J. Phys. Chem. Lett.* 6.1 (Dec. 2014), pp. 164–169. DOI: 10.1021/jz502429u. URL: https://doi.org/10.1021%2Fjz502429u.

[356] J. Beilsten-Edmands, G. E. Eperon, R. D. Johnson, H. J. Snaith, and P. G. Radaelli. "Non-ferroelectric nature of the conductance hysteresis in $CH_3NH_3PbI_3$ perovskite-based photovoltaic devices". In: *Appl. Phys. Lett.* 106.17 (Apr. 2015), p. 173502. DOI: 10.1063/1.4919109. URL: https://doi.org/10.1063%2F1.4919109.

[357] Lingling Mao, Constantinos C. Stoumpos, and Mercouri G. Kanatzidis. "Two-Dimensional Hybrid Halide Perovskites: Principles and Promises". In: *J. Am. Chem. Soc.* 141.3 (Nov. 2018), pp. 1171–1190. DOI: 10.1021/jacs.8b10851. URL: https://doi.org/10.1021/jacs.8b10851.

[358] Ian C. Smith, Eric T. Hoke, Diego Solis-Ibarra, Michael D. McGehee, and Hemamala I. Karunadasa. "A Layered Hybrid Perovskite Solar-Cell Absorber with Enhanced Moisture Stability". In: *Angew. Chem* 53.42 (Sept. 2014), pp. 11232–11235. DOI: 10.1002/anie.201406466. URL: https://doi.org/10.1002/anie.201406466.

[359] Hsinhan Tsai, Wanyi Nie, Jean-Christophe Blancon, Constantinos C. Stoumpos, Reza Asadpour, Boris Harutyunyan, Amanda J. Neukirch, Rafael Verduzco, Jared J. Crochet, Sergei Tretiak, Laurent Pedesseau, Jacky Even, Muhammad A. Alam, Gautam Gupta, Jun Lou, Pulickel M. Ajayan, Michael J. Bedzyk, Mercouri G. Kanatzidis, and Aditya D. Mohite. "High-efficiency two-dimensional Ruddlesden–Popper perovskite solar cells". In: *Nature* 536.7616 (July 2016), pp. 312–316. DOI: 10.1038/nature18306. URL: https://doi.org/10.1038/nature18306.

[360] Duyen H. Cao, Constantinos C. Stoumpos, Omar K. Farha, Joseph T. Hupp, and Mercouri G. Kanatzidis. "2D Homologous Perovskites as Light-Absorbing Materials for Solar Cell Applications". In: *J. Am. Chem. Soc.* 137.24 (June 2015), pp. 7843–7850. DOI: 10.1021/jacs.5b03796. URL: https://doi.org/10.1021/jacs.5b03796.

[361] Constantinos C. Stoumpos, Duyen H. Cao, Daniel J. Clark, Joshua Young, James M. Rondinelli, Joon I. Jang, Joseph T. Hupp, and Mercouri G. Kanatzidis. "Ruddlesden–Popper Hybrid Lead Iodide Perovskite 2D Homologous Semiconductors". In: *Chem. Mater.* 28.8 (Apr. 2016), pp. 2852–2867. DOI: 10.1021/acs.chemmater.6b00847. URL: https://doi.org/10.1021%2Facs.chemmater.6b00847.

[362] Xu-Hui Zhu, Nicolas Mercier, Amédée Riou, Philippe Blanchard, and Pierre Frère. "$(C_4H_3SCH_2NH_3)_2(CH_3N$ non-centrosymmetrical crystal structure of a bilayer hybrid perovskite". In: *Chem. Commun.* 18 (2002), pp. 2160–2161. DOI: 10.1039/b205543k. URL: https://doi.org/10.1039%2Fb205543k.

[363] Hongtao Lai, Bin Kan, Tingting Liu, Nan Zheng, Zengqi Xie, Tong Zhou, Xiangjian Wan, Xiaodan Zhang, Yongsheng Liu, and Yongsheng Chen. "Two-Dimensional Ruddlesden–Popper Perovskite with Nanorod-like Morphology for Solar Cells with Efficiency Exceeding 15%". In: *J. Am. Chem. Soc.* 140.37 (Aug. 2018), pp. 11639–11646. DOI: 10.1021/jacs.8b04604. URL: https://doi.org/10.1021%2Fjacs.8b04604.

[364] J.-C. Blancon, A. V. Stier, H. Tsai, W. Nie, C. C. Stoumpos, B. Traoré, L. Pedesseau, M. Kepenekian, F. Katsutani, G. T. Noe, J. Kono, S. Tretiak, S. A. Crooker, C. Katan, M. G. Kanatzidis, J. J. Crochet, J. Even, and A. D. Mohite. "Scaling law for excitons in 2D perovskite quantum wells". In: *Nat. Commun.* 9.1 (June 2018). DOI: 10.1038/s41467-018-04659-x. URL: https://doi.org/10.1038/s41467-018-04659-x.

[365] Ke-zhao Du, Qing Tu, Xu Zhang, Qiwei Han, Jie Liu, Stefan Zauscher, and David B. Mitzi. "Two-Dimensional Lead(II) Halide-Based Hybrid Perovskites Templated by Acene Alkylamines: Crystal Structures, Optical Properties, and Piezoelectricity". In: *Inorg. Chem.* 56.15 (July 2017), pp. 9291–9302. DOI: 10.1021/acs.inorgchem.7b01094. URL: https://doi.org/10.1021/acs.inorgchem.7b01094.

[366] Yongping Fu, Matthew P. Hautzinger, Ziyu Luo, Feifan Wang, Dongxu Pan, Michael M. Aristov, Ilia A. Guzei, Anlian Pan, Xiaoyang Zhu, and Song Jin. "Incorporating Large A Cations into Lead Iodide Perovskite Cages: Relaxed Goldschmidt Tolerance Factor and Impact on Exciton–Phonon Interaction". In: *ACS Cent. Sci.* 5.8 (July 2019), pp. 1377–1386. DOI: 10.1021/acscentsci.9b00367. URL: https://doi.org/10.1021/acscentsci.9b00367.

[367] Tanja Schmitt, Sean Bourelle, Nathaniel Tye, Giancarlo Soavi, Andrew D. Bond, Sascha Feldmann, Boubacar Traore, Claudine Katan, Jacky Even, Siân E. Dutton, and Felix Deschler. "Control of Crystal Symmetry Breaking with Halogen-Substituted Benzylammonium in Layered Hybrid Metal-Halide Perovskites". In: *J. Am. Chem. Soc.* (Mar. 2020). DOI: 10.1021/jacs.9b11809. URL: https://doi.org/10.1021/jacs.9b11809.

[368] Sasa Wang, Xitao Liu, Lina Li, Chengmin Ji, Zhihua Sun, Zhenyue Wu, Maochun Hong, and Junhua Luo. "An Unprecedented Biaxial Trilayered Hybrid Perovskite Ferroelectric with Directionally Tunable Photovoltaic Effects". In: *J. Am. Chem. Soc.* 141.19 (May 2019), pp. 7693–7697. DOI: 10.1021/jacs.9b02558. URL: https://doi.org/10.1021%2Fjacs.9b02558.

[369] Lina Li, Xiaoying Shang, Sasa Wang, Ningning Dong, Chengmin Ji, Xueyuan Chen, Sangen Zhao, Jun Wang, Zhihua Sun, Maochun Hong, and Junhua Luo. "Bilayered Hybrid Perovskite Ferroelectric with Giant Two-Photon Absorption". In: *J. Am. Chem. Soc.* 140.22 (May 2018), pp. 6806–6809. DOI: 10.1021/jacs.8b04014. URL: https://doi.org/10.1021%2Fjacs.8b04014.

[370] Zhenyue Wu, Chengmin Ji, Lina Li, Jintao Kong, Zhihua Sun, Sangen Zhao, Sasa Wang, Maochun Hong, and Junhua Luo. "Alloying n -Butylamine into $CsPbBr_3$ To Give a Two-Dimensional Bilayered Perovskite Ferroelectric Material". In: *Angew. Chem.* 57.27 (May 2018), pp. 8140–8143. DOI: 10.1002/anie.201803716. URL: https://doi.org/10.1002/anie.201803716.

[371] Shiguo Han, Xitao Liu, Yi Liu, Zhiyun Xu, Yaobin Li, Maochun Hong, Junhua Luo, and Zhihua Sun. "High-Temperature Antiferroelectric of Lead Iodide Hybrid Perovskites". In: *J. Am. Chem. Soc.* 141.32 (July 2019), pp. 12470–12474. DOI: 10.1021/jacs.9b05124. URL: https://doi.org/10.1021/jacs.9b05124.

[372] Wei-Qiang Liao, Yi Zhang, Chun-Li Hu, Jiang-Gao Mao, Heng-Yun Ye, Peng-Fei Li, Songping D. Huang, and Ren-Gen Xiong. "A lead-halide perovskite molecular ferroelectric semiconductor". In: *Nat. Commun.* 6.1 (May 2015). DOI: 10.1038/ncomms8338. URL: https://doi.org/10.1038/ncomms8338.

[373] Jialiang Xu, Xinyue Li, Jianbo Xiong, Chunqing Yuan, Sergey Semin, Theo Rasing, and Xian-He Bu. "Halide Perovskites for Nonlinear Optics". In: *Adv. Mater.* (Mar. 2019), p. 1806736. DOI: 10.1002/adma.201806736. URL: https://doi.org/10.1002/adma.201806736.

[374] Chunqing Yuan, Xinyue Li, Sergey Semin, Yaqing Feng, Theo Rasing, and Jialiang Xu. "Chiral Lead Halide Perovskite Nanowires for Second-Order Nonlinear Optics". In: *Nano Lett.* 18.9 (Aug. 2018), pp. 5411–5417. DOI: 10.1021/acs.nanolett.8b01616. URL: https://doi.org/10.1021/acs.nanolett.8b01616.

[375] Wen-Juan Wei, Xing-Xing Jiang, Li-Yuan Dong, Wei-Wei Liu, Xiao-Bo Han, Yan Qin, Kai Li, Wei Li, Zhe-Shuai Lin, Xian-He Bu, and Pei-Xiang Lu. "Regulating Second-Harmonic Generation by van der Waals Interactions in Two-dimensional Lead Halide Perovskite Nanosheets". In: *J. Am. Chem. Soc.* 141.23 (May 2019), pp. 9134–9139. DOI: 10.1021/jacs.9b01874. URL: https://doi.org/10.1021/jacs.9b01874.

[376] Ibrahim Abdelwahab, Gustavo Grinblat, Kai Leng, Yi Li, Xiao Chi, Andrivo Rusydi, Stefan A. Maier, and Kian Ping Loh. "Highly Enhanced Third-Harmonic Generation in 2D Perovskites at Excitonic Resonances". In: *ACS Nano* 12.1 (Dec. 2017), pp. 644–650. DOI: 10.1021/acsnano.7b07698. URL: https://doi.org/10.1021%2Facsnano.7b07698.

[377] F. O. Saouma, C. C. Stoumpos, J. Wong, M. G. Kanatzidis, and J. I. Jang. "Selective enhancement of optical nonlinearity in two-dimensional organic-inorganic lead iodide perovskites". In: *Nat. Commun.* 8.1 (Sept. 2017). DOI: 10.1038/s41467-017-00788-x. URL: https://doi.org/10.1038%2Fs41467-017-00788-x.

[378] Hideki Hirori, Peiyu Xia, Yasushi Shinohara, Tomohito Otobe, Yasuyuki Sanari, Hirokazu Tahara, Nobuhisa Ishii, Jiro Itatani, Kenichi L. Ishikawa, Tomoko Aharen, Masashi Ozaki, Atsushi Wakamiya, and Yoshihiko Kanemitsu. "High-order harmonic generation from hybrid organic–inorganic perovskite thin films". In: *APL Mater.* 7.4 (Apr. 2019), p. 041107. DOI: 10.1063/1.5090935. URL: https://doi.org/10.1063/1.5090935.

[379] D. J. Clark, C. C. Stoumpos, F. O. Saouma, M. G. Kanatzidis, and J. I. Jang. "Polarization-selective three-photon absorption and subsequent photoluminescence inCsPbBr3single crystal at room temperature". In: *Phys. Rev. B* 93.19 (May 2016). DOI: 10.1103/physrevb.93.195202. URL: https://doi.org/10.1103%2Fphysrevb.93.195202.

[380] Wenjie Chen, Shuai Zhang, Minghao Zhou, Tonghan Zhao, Xujin Qin, Xinfeng Liu, Minghua Liu, and Pengfei Duan. "Two-Photon Absorption-Based Upconverted Circularly Polarized Luminescence Generated in Chiral Perovskite Nanocrystals". In: *J. Phys. Chem. Lett.* 10.12 (May 2019), pp. 3290–3295. DOI: 10.1021/acs.jpclett.9b01224. URL: https://doi.org/10.1021%2Facs.jpclett.9b01224.

[381] Yasuhiro Yamada, Takumi Yamada, Le Quang Phuong, Naoki Maruyama, Hidetaka Nishimura, Atsushi Wakamiya, Yasujiro Murata, and Yoshihiko Kanemitsu. "Dynamic Optical Properties of $CH_3NH_3PbI_3$ Single Crystals As Revealed by One- and Two-Photon Excited Photoluminescence Measurements". In: *J. Am. Chem. Soc.* 137.33 (Aug. 2015), pp. 10456–10459. DOI: 10.1021/jacs.5b04503. URL: https://doi.org/10.1021/jacs.5b04503.

[382] Zhixing Gan, Xiaoming Wen, Weijian Chen, Chunhua Zhou, Shuang Yang, Guiyuan Cao, Kenneth P. Ghiggino, Hua Zhang, and Baohua Jia. "The Dominant Energy Transport Pathway in Halide Perovskites: Photon Recycling or Carrier Diffusion?" In: *Adv. Energy Mater.* 9.20 (Apr. 2019), p. 1900185. DOI: 10.1002/aenm.201900185. URL: https://doi.org/10.1002/aenm.201900185.

[383] N. Bloembergen, R. K. Chang, S. S. Jha, and C. H. Lee. "Optical Second-Harmonic Generation in Reflection from Media with Inversion Symmetry". In: *Phys. Rev.* 174.3 (Oct. 1968), pp. 813–822. DOI: 10.1103/physrev.174.813. URL: https://doi.org/10.1103/physrev.174.813.

[384] Sharada Govinda, Bhushan P. Kore, Pratibha Mahale, Anshu Pandey, and D. D. Sarma. "Can SHG Measurements Determine the Polarity of Hybrid Lead Halide Perovskites?" In: *ACS Energy Lett.* 3.8 (July 2018), pp. 1887–1891. DOI: 10.1021/acsenergylett.8b00999. URL: https://doi.org/10.1021%2Facsenergylett.8b00999.

[385] Andrew P. Shreve, Nerine J. Cherepy, and Richard A. Mathies. "Effective Rejection of Fluorescence Interference in Raman Spectroscopy Using a Shifted Excitation Difference Technique". In: *Appl. Spectrosc.* 46.4 (Apr. 1992), pp. 707–711. DOI: 10.1366/0003702924125122. URL: https://doi.org/10.1366/0003702924125122.

[386] Kajari Bera, Siu Yi Kwang, Alyssa A. Cassabaum, Christopher C. Rich, and Renee R. Frontiera. "Facile Background Discrimination in Femtosecond Stimulated Raman Spectroscopy Using a Dual-Frequency Raman Pump Technique". In: *J. Phys. Chem. A* 123.37 (Sept. 2019), pp. 7932–7939. DOI: 10.1021/acs.jpca.9b02473. URL: https://doi.org/10.1021/acs.jpca.9b02473.

[387] Robert W. Boyd. "Order-of-magnitude estimates of the nonlinear optical susceptibility". In: *J. Mod. Opt.* 46.3 (Mar. 1999), pp. 367–378. DOI: 10.1080/09500349908231277. URL: https://doi.org/10.1080/09500349908231277.

[388] J. Calabrese, N. L. Jones, R. L. Harlow, N. Herron, D. L. Thorn, and Y. Wang. "Preparation and characterization of layered lead halide compounds". In: *J. Am. Chem. Soc.* 113.6 (Mar. 1991), pp. 2328–2330. DOI: 10.1021/ja00006a076. URL: https://doi.org/10.1021/ja00006a076.

[389] Dane W. deQuilettes, Kyle Frohna, David Emin, Thomas Kirchartz, Vladimir Bulovic, David S. Ginger, and Samuel D. Stranks. "Charge-Carrier Recombination in Halide Perovskites". In: *Chem. Rev.* 119.20 (Sept. 2019), pp. 11007–11019. DOI: 10.1021/acs.chemrev.9b00169. URL: https://doi.org/10.1021/acs.chemrev.9b00169.

[390] J.-C. Blancon, H. Tsai, W. Nie, C. C. Stoumpos, L. Pedesseau, C. Katan, M. Kepenekian, C. M. M. Soe, K. Appavoo, M. Y. Sfeir, S. Tretiak, P. M. Ajayan, M. G. Kanatzidis, J. Even, J. J. Crochet, and A. D. Mohite. "Extremely efficient internal exciton dissociation through edge states in layered 2D perovskites". In: *Science* 355.6331 (Mar. 2017), pp. 1288–1292. DOI: 10.1126/science.aal4211. URL: https://doi.org/10.1126/science.aal4211.

[391] Enzheng Shi, Shibin Deng, Biao Yuan, Yao Gao, Akriti, Long Yuan, Chelsea S. Davis, Dmitry Zemlyanov, Yi Yu, Libai Huang, and Letian Dou. "Extrinsic and Dynamic Edge States of Two-Dimensional Lead Halide Perovskites". In: *ACS Nano* (Feb. 2019). DOI: 10.1021/acsnano.8b07631. URL: https://doi.org/10.1021/acsnano.8b07631.

[392] Hee Joon Jung, Constantinos C. Stompus, Mercouri G. Kanatzidis, and Vinayak P. Dravid. "Self-Passivation of 2D Ruddlesden–Popper Perovskite by Polytypic Surface PbI_2 Encapsulation". In: *Nano Lett.* 19.9 (Aug. 2019), pp. 6109–6117. DOI: 10.1021/acs.nanolett.9b02069. URL: https://doi.org/10.1021/acs.nanolett.9b02069.

[393] Félix Thouin, David A. Valverde-Chávez, Claudio Quarti, Daniele Cortecchia, Ilaria Bargigia, David Beljonne, Annamaria Petrozza, Carlos Silva, and Ajay Ram Srimath Kandada. "Phonon coherences reveal the polaronic character of excitons in two-dimensional lead halide perovskites". In: *Nat. Mater.* 18.4 (Jan. 2019), pp. 349–356. DOI: 10.1038/s41563-018-0262-7. URL: https://doi.org/10.1038/s41563-018-0262-7.

[394] Stefanie Neutzner, Félix Thouin, Daniele Cortecchia, Annamaria Petrozza, Carlos Silva, and Ajay Ram Srimath Kandada. "Exciton-polaron spectral structures in two-dimensional hybrid lead-halide perovskites". In: *Phys. Rev. Materials* 2.6 (June 2018). DOI: 10.1103/physrevmaterials.2.064605. URL: https://doi.org/10.1103/physrevmaterials.2.064605.

[395] Félix Thouin, Stefanie Neutzner, Daniele Cortecchia, Vlad Alexandru Dragomir, Cesare Soci, Teddy Salim, Yeng Ming Lam, Richard Leonelli, Annamaria Petrozza, Ajay Ram Srimath Kandada, and Carlos Silva. "Stable biexcitons in two-dimensional metal-halide perovskites with strong dynamic lattice disorder". In: *Phys. Rev. Materials* 2.3 (Mar. 2018). DOI: 10.1103/physrevmaterials.2.034001. URL: https://doi.org/10.1103/physrevmaterials.2.034001.

[396] Watcharaphol Paritmongkol, Nabeel S. Dahod, Alexia Stollmann, Nannan Mao, Charles Settens, Shao-Liang Zheng, and William A. Tisdale. "Synthetic Variation and Structural Trends in Layered Two-Dimensional Alkylammonium Lead Halide Perovskites". In: *Chem. Mater.* 31.15 (July 2019), pp. 5592–5607. DOI: 10.1021/acs.chemmater.9b01318. URL: https://doi.org/10.1021/acs.chemmater.9b01318.

[397] Xihan Chen, Haipeng Lu, Zhen Li, Yaxin Zhai, Paul F. Ndione, Joseph J. Berry, Kai Zhu, Ye Yang, and Matthew C. Beard. "Impact of Layer Thickness on the Charge Carrier and Spin Coherence Lifetime in Two-Dimensional Layered Perovskite Single Crystals". In: *ACS Energy Lett.* 3.9 (Aug. 2018), pp. 2273–2279. DOI: 10.1021/acsenergylett.8b01315. URL: https://doi.org/10.1021/acsenergylett.8b01315.

[398] Yongping Fu, Xinyi Jiang, Xiaotong Li, Boubacar Traore, Ioannis Spanopoulos, Claudine Katan, Jacky Even, Mercouri G. Kanatzidis, and Elad Harel. "Cation Engineering in Two-Dimensional Ruddlesden–Popper Lead Iodide Perovskites with Mixed Large A-Site Cations in the Cages". In: *J. Am. Chem. Soc.* 142.8 (Feb. 2020), pp. 4008–4021. DOI: 10.1021/jacs.9b13587. URL: https://doi.org/10.1021/jacs.9b13587.

[399] *Bruker-AXS. APEX3*. Version 2016.5-0. 2016.

[400] Lennard Krause, Regine Herbst-Irmer, George M. Sheldrick, and Dietmar Stalke. "Comparison of silver and molybdenum microfocus X-ray sources for single-crystal structure determination". In: *J. Appl. Cryst.* 48.1 (Jan. 2015), pp. 3–10. DOI: 10.1107/s1600576714022985. URL: https://doi.org/10.1107/s1600576714022985.

[401] George M. Sheldrick. *The SHELX homepage*. http://shelx.uni-ac.gwdg.de/SHELX/. 2013.

[402] George M. Sheldrick. *XPREP*. Version 2013/1. 2013.

[403] George M. Sheldrick. "SHELXT– Integrated space-group and crystal-structure determination". In: *Acta Cryst. A* 71.1 (Jan. 2015), pp. 3–8. DOI: 10.1107/s2053273314026370. URL: https://doi.org/10.1107/s2053273314026370.

[404] George M. Sheldrick. "Crystal structure refinement with SHELXL". In: *Acta Cryst. C* 71.1 (Jan. 2015), pp. 3–8. DOI: 10.1107/s2053229614024218. URL: https://doi.org/10.1107/s2053229614024218.

[405] Oleg V. Dolomanov, Luc J. Bourhis, Richard J. Gildea, Judith A. K. Howard, and Horst Puschmann. "OLEX2: a complete structure solution, refinement and analysis program". In: *J. Appl. Cryst.* 42.2 (Jan. 2009), pp. 339–341. DOI: 10.1107/s0021889808042726. URL: https://doi.org/10.1107/s0021889808042726.

[406] Ilia A. Guzei. *Programs* Gn. University of Wisconsin-Madison, Madison, Wisconsin, USA. 2007-2013.

[407] Ilia A. Guzei. "An idealized molecular geometry library for refinement of poorly behaved molecular fragments with constraints". In: *J. Appl. Cryst.* 47.2 (Mar. 2014), pp. 806–809. DOI: 10.1107/s1600576714004427. URL: https://doi.org/10.1107/s1600576714004427.

[408] Y. R. Shen. "Surface properties probed by second-harmonic and sum-frequency generation". In: *Nature* 337.6207 (Feb. 1989), pp. 519–525. DOI: 10.1038/337519a0. URL: https://doi.org/10.1038/337519a0.

[409] Victor Mizrahi and J. E. Sipe. "Phenomenological treatment of surface second-harmonic generation". In: *J. Opt. Soc. Am. B* 5.3 (Mar. 1988), p. 660. DOI: 10.1364/josab.5.000660. URL: https://doi.org/10.1364/josab.5.000660.

[410] H. W. K. Tom, T. F. Heinz, and Y. R. Shen. "Second-Harmonic Reflection from Silicon Surfaces and Its Relation to Structural Symmetry". In: *Phys. Rev. Lett.* 51.21 (Nov. 1983), pp. 1983–1986. DOI: 10.1103/physrevlett.51.1983. URL: https://doi.org/10.1103/physrevlett.51.1983.

[411] Ryan A. DeCrescent, Naveen R. Venkatesan, Clayton J. Dahlman, Rhys M. Kennard, Xie Zhang, Wenhao Li, Xinhong Du, Michael L. Chabinyc, Rashid Zia, and Jon A. Schuller. "Bright magnetic dipole radiation from two-dimensional lead-halide perovskites". In: *Sci. Adv.* 6.6 (Feb. 2020), eaay4900. DOI: 10.1126/sciadv.aay4900. URL: https://doi.org/10.1126/sciadv.aay4900.

[412] E. Schrödinger. "Quantisierung als Eigenwertproblem". In: *Ann. Phys.* 385.13 (1926), pp. 437–490. DOI: 10.1002/andp.19263851302. URL: https://doi.org/10.1002/andp.19263851302.

[413] Erwin Schrödinger. *Collected Papers on Wave Mechanics*. American Mathematical Society, Nov. 2003.

[414] E. Schrödinger. "An Undulatory Theory of the Mechanics of Atoms and Molecules". In: *Phys. Rev.* 28.6 (Dec. 1926), pp. 1049–1070. DOI: 10.1103/physrev.28.1049. URL: https://doi.org/10.1103/physrev.28.1049.

[415] Joseph O. Hirschfelder. "Formal Rayleigh-Schrödinger perturbation theory for both degenerate and non-degenerate energy states". In: *Int. J. Quantum Chem.* 3.5 (Sept. 1969), pp. 731–748. DOI: 10.1002/qua.560030517. URL: https://doi.org/10.1002/qua.560030517.

[416] Philip M. Morse. "Diatomic Molecules According to the Wave Mechanics. II. Vibrational Levels". In: *Phys. Rev.* 34.1 (July 1929), pp. 57–64. DOI: 10.1103/physrev.34.57. URL: https://doi.org/10.1103/physrev.34.57.

[417] Anne L'Huillier and Ph. Balcou. "High-order harmonic generation in rare gases with a 1-ps 1053-nm laser". In: *Phys. Rev. Lett.* 70.6 (Feb. 1993), pp. 774–777. DOI: 10.1103/physrevlett.70.774. URL: https://doi.org/10.1103/physrevlett.70.774.

[418] X. F. Li, A. L'Huillier, M. Ferray, L. A. Lompré, and G. Mainfray. "Multiple-harmonic generation in rare gases at high laser intensity". In: *Phys. Rev. A* 39.11 (June 1989), pp. 5751–5761. DOI: 10.1103/physreva.39.5751. URL: https://doi.org/10.1103/physreva.39.5751.

[419] G. H. C. New and J. F. Ward. "Optical Third-Harmonic Generation in Gases". In: *Phys. Rev. Lett.* 19.10 (Sept. 1967), pp. 556–559. DOI: 10.1103/physrevlett.19.556. URL: https://doi.org/10.1103/physrevlett.19.556.

[420] G. Vampa, T. J. Hammond, N. Thiré, B. E. Schmidt, F. Légaré, C. R. McDonald, T. Brabec, and P. B. Corkum. "Linking high harmonics from gases and solids". In: *Nature* 522.7557 (June 2015), pp. 462–464. DOI: 10.1038/nature14517. URL: https://doi.org/10.1038/nature14517.

[421] G. E. Jelinek. "Properties of Crystalline Argon, Krypton, and Xenon Based upon the Born and Huang Method of Homogeneous Deformations. I. Zero-Pressure Thermal and Elastic Data". In: *Phys. Rev. B* 3.8 (Apr. 1971), pp. 2716–2724. DOI: 10.1103/physrevb.3.2716. URL: https://doi.org/10.1103/physrevb.3.2716.

[422] Jiaxun Liu, Anthony E. Phillips, David A. Keen, and Martin T. Dove. "Thermal Disorder and Bond Anharmonicity in Cesium Lead Iodide Studied by Neutron Total Scattering and the Reverse Monte Carlo Method". In: *J. Phys. Chem. C* 123.24 (May 2019), pp. 14934–14940. DOI: 10.1021/acs.jpcc.9b02936. URL: https://doi.org/10.1021/acs.jpcc.9b02936.

[423] Yongping Fu, Fei Meng, Matthew B. Rowley, Blaise J. Thompson, Melinda J. Shearer, Dewei Ma, Robert J. Hamers, John C. Wright, and Song Jin. "Solution Growth of Single Crystal Methylammonium Lead Halide Perovskite Nanostructures for Optoelectronic and Photovoltaic Applications". In: *J. Am. Chem. Soc.* 137.17 (Apr. 2015), pp. 5810–5818. DOI: 10.1021/jacs.5b02651. URL: https://doi.org/10.1021/jacs.5b02651.

[424] Jacky Even, Laurent Pedesseau, and Claudine Katan. "Analysis of Multivalley and Multibandgap Absorption and Enhancement of Free Carriers Related to Exciton Screening in Hybrid Perovskites". In: *J. Phys. Chem. C* 118.22 (May 2014), pp. 11566–11572. DOI: 10.1021/jp503337a. URL: https://doi.org/10.1021/jp503337a.

[425] Jacky Even, Laurent Pedesseau, Claudine Katan, Mikaël Kepenekian, Jean-Sébastien Lauret, Daniel Sapori, and Emmanuelle Deleporte. "Solid-State Physics Perspective on Hybrid Perovskite Semiconductors". In: *J. Phys. Chem. C* 119.19 (Apr. 2015), pp. 10161–10177. DOI: 10.1021/acs.jpcc.5b00695. URL: https://doi.org/10.1021/acs.jpcc.5b00695.

[426] Martin A. Green, Yajie Jiang, Arman Mahboubi Soufiani, and Anita Ho-Baillie. "Optical Properties of Photovoltaic Organic–Inorganic Lead Halide Perovskites". In: *J. Phys. Chem. Lett.* 6.23 (Nov. 2015), pp. 4774–4785. DOI: 10.1021/acs.jpclett.5b01865. URL: https://doi.org/10.1021/acs.jpclett.5b01865.

[427] Christopher Eames, Jarvist M. Frost, Piers R. F. Barnes, Brian C. O'Regan, Aron Walsh, and M. Saiful Islam. "Ionic transport in hybrid lead iodide perovskite solar cells". In: *Nat. Commun.* 6.1 (June 2015). DOI: 10.1038/ncomms8497. URL: https://doi.org/10.1038/ncomms8497.

[428] Ye Yang, David P. Ostrowski, Ryan M. France, Kai Zhu, Jao van de Lagemaat, Joseph M. Luther, and Matthew C. Beard. "Observation of a hot-phonon bottleneck in lead-iodide perovskites". In: *Nature Photon.* 10.1 (Oct. 2015), pp. 53–59. DOI: 10.1038/nphoton.2015.213. URL: https://doi.org/10.1038/nphoton.2015.213.

[429] Johannes M. Richter, Federico Branchi, Franco Valduga de Almeida Camargo, Baodan Zhao, Richard H. Friend, Giulio Cerullo, and Felix Deschler. "Ultrafast carrier thermalization in lead iodide perovskite probed with two-dimensional electronic spectroscopy". In: *Nat. Commun.* 8.1 (Aug. 2017). DOI: 10.1038/s41467-017-00546-z. URL: https://doi.org/10.1038/s41467-017-00546-z.

[430] Michael B. Price, Justinas Butkus, Tom C. Jellicoe, Aditya Sadhanala, Anouk Briane, Jonathan E. Halpert, Katharina Broch, Justin M. Hodgkiss, Richard H. Friend, and Felix Deschler. "Hot-carrier cooling and photoinduced refractive index changes in organic–inorganic lead halide perovskites". In: *Nat. Commun.* 6.1 (Sept. 2015). DOI: 10.1038/ncomms9420. URL: https://doi.org/10.1038/ncomms9420.

[431] Ronnie R. Tamming, Justinas Butkus, Michael B. Price, Parth Vashishtha, Shyamal K. K. Prasad, Jonathan E. Halpert, Kai Chen, and Justin M. Hodgkiss. "Ultrafast Spectrally Resolved Photoinduced Complex Refractive Index Changes in CsPbBr3 Perovskites". In: *ACS Photon.* 6.2 (Jan. 2019), pp. 345–350. DOI: 10.1021/acsphotonics.9b00091. URL: https://doi.org/10.1021/acsphotonics.9b00091.

[432] Jia Wei Melvin Lim, David Giovanni, Marcello Righetto, Minjun Feng, Subodh Gautam Mhaisalkar, Nripan Mathews, and Tze Chien Sum. "Hot Carriers in Halide Perovskites: How Hot Truly?" In: *J. Phys. Chem. Lett.* 11.7 (Mar. 2020), pp. 2743–2750. DOI: 10.1021/acs.jpclett.0c00504. URL: https://doi.org/10.1021/acs.jpclett.0c00504.

[433] Johannes Richter, F Branchi, F Valduga De Almeida Camargo, Baodan Zhao, Richard Friend, G Cerullo, and Felix Deschler. *Research data supporting: "Ultrafast carrier thermalization in lead iodide perovskite probed with two-dimensional electronic spectroscopy"*. 2017. DOI: 10.17863/CAM.11883. URL: https://www.repository.cam.ac.uk/handle/1810/265669.

[434] Jie Chen, Darien J. Morrow, Yongping Fu, Weihao Zheng, Yuzhou Zhao, Lianna Dang, Matthew J. Stolt, Daniel D. Kohler, Xiaoxia Wang, Kyle J. Czech, Matthew P. Hautzinger, Shaohua Shen, Liejin Guo, Anlian Pan, John C. Wright, and Song Jin. "Single-Crystal Thin Films of Cesium Lead Bromide Perovskite Epitaxially Grown on Metal Oxide Perovskite ($SrTiO_3$)". In: *J. Am. Chem. Soc.* 139.38 (Sept. 2017), pp. 13525–13532. DOI: 10.1021/jacs.7b07506. URL: https://doi.org/10.1021/jacs.7b07506.

[435] Haiming Zhu, M. Tuan Trinh, Jue Wang, Yongping Fu, Prakriti P. Joshi, Kiyoshi Miyata, Song Jin, and X.-Y. Zhu. "Organic Cations Might Not Be Essential to the Remarkable Properties of Band Edge Carriers in Lead Halide Perovskites". In: *Adv. Mater.* 29.1 (Oct. 2016), p. 1603072. DOI: 10.1002/adma.201603072. URL: https://doi.org/10.1002/adma.201603072.

[436] Ye Yang, Yong Yan, Mengjin Yang, Sukgeun Choi, Kai Zhu, Joseph M. Luther, and Matthew C. Beard. "Low surface recombination velocity in solution-grown CH3NH3PbBr3 perovskite single crystal". In: *Nat. Commun.* 6.1 (Aug. 2015). DOI: 10.1038/ncomms8961. URL: https://doi.org/10.1038/ncomms8961.

[437] Boguslawa Adamowicz and Hideki Hasegawa. "Computer Analysis of Surface Recombination Process at Si and Compound Semiconductor Surfaces and Behavior of Surface Recombination Velocity". In: *Jpn. J. Appl. Phys.* 37.Part 1, No. 3B (Mar. 1998), pp. 1631–1637. DOI: 10.1143/jjap.37.1631. URL: https://doi.org/10.1143/jjap.37.1631.

[438] X. Correig, J. Calderer, E. Blasco, and R. Alcubilla. "Comments on the use of the surface recombination velocity concept". In: *Solid State Electron.* 33.5 (May 1990), pp. 477–484. DOI: 10.1016/0038-1101(90)90230-c. URL: https://doi.org/10.1016/0038-1101(90)90230-c.

[439] Patrick De Visschere. "Comment on G.J. Rees "surface recombination velocity—a useful concept?"". In: *Solid State Electron.* 29.11 (Nov. 1986), pp. 1161–1165. DOI: 10.1016/0038-1101(86)90059-6. URL: https://doi.org/10.1016/0038-1101(86)90059-6.

[440] G.J. Rees. "Surface recombination velocity—A useful concept?" In: *Solid State Electron.* 28.5 (May 1985), pp. 517–519. DOI: 10.1016/0038-1101(85)90116-9. URL: https://doi.org/10.1016/0038-1101(85)90116-9.

[441] Johanna Brazard, Laurie A. Bizimana, and Daniel B. Turner. "Accurate convergence of transient-absorption spectra using pulsed lasers". In: *Rev. Sci. Inst.* 86.5 (May 2015), p. 053106. DOI: 10.1063/1.4921479. URL: https://doi.org/10.1063/1.4921479.

[442] E.R. Henry and J. Hofrichter. "[8] Singular value decomposition: Application to analysis of experimental data". In: *Methods in Enzymology*. Elsevier, 1992, pp. 129–192. DOI: 10.1016/0076-6879(92)10010-b. URL: https://doi.org/10.1016/0076-6879(92)10010-b.

[443] C. A. Hoffman, K. Jarašiūnas, H. J. Gerritsen, and A. V. Nurmikko. "Measurement of surface recombination velocity in semiconductors by diffraction from picosecond transient free-carrier gratings". In: *Appl. Phys. Lett.* 33.6 (Sept. 1978), pp. 536–539. DOI: 10.1063/1.90428. URL: https://doi.org/10.1063/1.90428.

[444] Jonathan De Roo, Maria Ibáñez, Pieter Geiregat, Georgian Nedelcu, Willem Walravens, Jorick Maes, Jose C. Martins, Isabel Van Driessche, Maksym V. Kovalenko, and Zeger Hens. "Highly Dynamic Ligand Binding and Light Absorption Coefficient of Cesium Lead Bromide Perovskite Nanocrystals". In: *ACS Nano* 10.2 (Jan. 2016), pp. 2071–2081. DOI: 10.1021/acsnano.5b06295. URL: https://doi.org/10.1021/acsnano.5b06295.

[445] Philip Kitcher. "Explanatory Unification". In: *Philos. Sci.* 48.4 (Dec. 1981), pp. 507–531. DOI: 10.1086/289019. URL: https://doi.org/10.1086/289019.

[446] Michael Friedman. "Explanation and Scientific Understanding". In: *J. Philos.* 71.1 (Jan. 1974), p. 5. DOI: 10.2307/2024924. URL: https://doi.org/10.2307/2024924.

[447] Peter Machamer, Lindley Darden, and Carl F. Craver. "Thinking about Mechanisms". In: *Philos. Sci.* 67.1 (Mar. 2000), pp. 1–25. DOI: 10.1086/392759. URL: https://doi.org/10.1086/392759.

[448] Aaron von Conta. "Characterization of the laser induced damage threshold of mirrors in the ultra short pulse regime". BACHELOR THESIS. MA thesis. The address of the publisher: Hochschule München, July 1993.

[449] S. Martin, A. Hertwig, M. Lenzner, J. Krüger, and W. Kautek. "Spot-size dependence of the ablation threshold in dielectrics for femtosecond laser pulses". In: *Appl. Phys. A* 77.7 (Dec. 2003), pp. 883–884. DOI: 10.1007/s00339-003-2213-6. URL: https://doi.org/10.1007/s00339-003-2213-6.

[450] Mark Mero. "On the damage behavior of dielectric films when illuminated with multiple femtosecond laser pulses". In: *Opt. Eng.* 44.5 (May 2005), p. 051107. DOI: 10.1117/1.1905343. URL: https://doi.org/10.1117/1.1905343.

[451] A. Hertwig, S. Martin, J. Krüger, and W. Kautek. "Surface damage and color centers generated by femtosecond pulses in borosilicate glass and silica". In: *Appl. Phys. A* 79.4-6 (Sept. 2004), pp. 1075–1077. DOI: 10.1007/s00339-004-2634-x. URL: https://doi.org/10.1007/s00339-004-2634-x.

[452] T. G Pedersen and H. D Cornean. "Optical second harmonic generation from Wannier excitons". In: *Europhysics Letters (EPL)* 78.2 (Apr. 2007), p. 27005. DOI: 10.1209/0295-5075/78/27005. URL: https://doi.org/10.1209/0295-5075/78/27005.

[453] Kyungwon Kwak, Sangyob Cha, Minhaeng Cho, and John C. Wright. "Vibrational interactions of acetonitrile: Doubly vibrationally resonant IR–IR–visible four-wave-mixing spectroscopy". In: *J. Chem. Phys.* 117.12 (Sept. 2002), pp. 5675–5687. DOI: 10.1063/1.1501129. URL: https://doi.org/10.1063/1.1501129.

[454] Wei Zhao and John C. Wright. "Measurement of $\chi(3)$ for Doubly Vibrationally Enhanced Four Wave Mixing Spectroscopy". In: *Phys. Rev. Lett.* 83.10 (Sept. 1999), pp. 1950–1953. DOI: 10.1103/physrevlett.83.1950. URL: https://doi.org/10.1103/physrevlett.83.1950.

[455] Wei Zhao and John C. Wright. "Spectral Simplification in Vibrational Spectroscopy Using Doubly Vibrationally Enhanced Infrared Four Wave Mixing". In: *J. Am. Chem. Soc.* 121.47 (Dec. 1999), pp. 10994–10998. DOI: 10.1021/ja9926414. URL: https://doi.org/10.1021/ja9926414.

[456] Wei Zhao, Keith M. Murdoch, Daniel M. Besemann, Nicholas J. Condon, Kent A. Meyer, and John C. Wright. "Nonlinear Two-Dimensional Vibrational Spectroscopy". In: *Appl. Spectrosc.* 54.7 (July 2000), pp. 1000–1004. URL: http://as.osa.org/abstract.cfm?URI=as-54-7-1000.

[457] Daniel M. Besemann, Nicholas J. Condon, Keith M. Murdoch, Wei Zhao, Kent A. Meyer, and John C. Wright. "Interference, dephasing, and vibrational coupling effects between coherence pathways in doubly vibrationally enhanced nonlinear spectroscopies". In: *Chem. Phys.* 266.2-3 (May 2001), pp. 177–195. DOI: 10.1016/s0301-0104(01)00227-0. URL: https://doi.org/10.1016/s0301-0104(01)00227-0.

[458] Kent A. Meyer and John C. Wright. "Interference, Dephasing, and Coherent Control in Time-Resolved Frequency Domain Two-Dimensional Vibrational Spectra". In: *J. Phys. Chem. A* 107.41 (Sept. 2003), pp. 8388–8395. DOI: 10.1021/jp035146+. URL: https://doi.org/10.1021/jp035146+.

[459] John C. Wright, Nicholas J. Condon, Keith M. Murdoch, Daniel M. Besemann, and Kent A. Meyer. "Quantitative Modeling of Nonlinear Processes in Coherent Two-Dimensional Vibrational Spectroscopy†". In: *J. Phys. Chem. A* 107.40 (Oct. 2003), pp. 8166–8176. DOI: 10.1021/jp034018i. URL: https://doi.org/10.1021/jp034018i.

[460] Minhaeng Cho. "Theoretical description of two-dimensional vibrational spectroscopy by infrared-infrared-visible sum frequency generation". In: *Phys. Rev. A* 61.2 (Jan. 2000). DOI: 10.1103/physreva.61.023406. URL: https://doi.org/10.1103/physreva.61.023406.

[461] Frédéric Fournier, Elizabeth M. Gardner, Darek A. Kedra, Paul M. Donaldson, Rui Guo, Sarah A. Butcher, Ian R. Gould, Keith R. Willison, and David R. Klug. "Protein identification and quantification by two-dimensional infrared spectroscopy: Implications for an all-optical proteomic platform". In: *Proc. Natl. Acad. Sci. U.S.A.* 105.40 (Oct. 2008), pp. 15352–15357. DOI: 10.1073/pnas.0805127105. URL: https://doi.org/10.1073/pnas.0805127105.

[462] Rui Guo, Frederic Fournier, Paul M. Donaldson, Elizabeth M. Gardner, Ian R. Gould, and David R. Klug. "Detection of complex formation and determination of intermolecular geometry through electrical anharmonic coupling of molecular vibrations using electron-vibration–vibration two-dimensional infrared spectroscopy". In: *Phys. Chem. Chem. Phys.* 11.38 (2009), p. 8417. DOI: 10.1039/b910804a. URL: https://doi.org/10.1039/b910804a.

[463] Rui Guo, Margherita Miele, Elizabeth M. Gardner, Frederic Fournier, Kathryn M. Kornau, Ian R. Gould, and David R. Klug. "Potential for the detection of molecular complexes and determination of interaction geometry by 2DIR: Application to protein sciences". In: *Faraday Discuss.* 150 (2011), p. 161. DOI: 10.1039/c1fd00007a. URL: https://doi.org/10.1039/c1fd00007a.

[464] Hugh Sowley, ZhiQiang Liu, Julia Davies, Robert Peach, Rui Guo, Sophie Sim, FengQin Long, Geoffrey Holdgate, Keith Willison, Wei Zhuang, and David R. Klug. "Detection of Drug Binding to a Target Protein Using EVV 2DIR Spectroscopy". In: *J. Phys. Chem. B* 123.17 (Mar. 2019), pp. 3598–3606. DOI: 10.1021/acs.jpcb.9b00501. URL: https://doi.org/10.1021/acs.jpcb.9b00501.

[465] R. R. Alfano and S. L. Shapiro. "Emission in the Region 4000 to 7000 Å Via Four-Photon Coupling in Glass". In: *Phys. Rev. Lett.* 24.11 (Mar. 1970), pp. 584–587. DOI: 10.1103/physrevlett.24.584. URL: https://doi.org/10.1103/physrevlett.24.584.

[466] R. R. Alfano and S. L. Shapiro. "Observation of Self-Phase Modulation and Small-Scale Filaments in Crystals and Glasses". In: *Phys. Rev. Lett.* 24.11 (Mar. 1970), pp. 592–594. DOI: 10.1103/physrevlett.24.592. URL: https://doi.org/10.1103/physrevlett.24.592.

[467] Robert R. Alfano, ed. *The Supercontinuum Laser Source*. Springer-Verlag, 2006. DOI: 10.1007/b106776. URL: https://doi.org/10.1007/b106776.

[468] F. DeMartini, C. H. Townes, T. K. Gustafson, and P. L. Kelley. "Self-Steepening of Light Pulses". In: *Phys. Rev.* 164.2 (Dec. 1967), pp. 312–323. DOI: 10.1103/physrev.164.312. URL: https://doi.org/10.1103/physrev.164.312.

[469] P. L. Kelley. "Self-Focusing of Optical Beams". In: *Phys. Rev. Lett.* 15.26 (Dec. 1965), pp. 1005–1008. DOI: 10.1103/physrevlett.15.1005. URL: https://doi.org/10.1103/physrevlett.15.1005.

[470] Maximilian Bradler. "Bulk continuum generation: The ultimate tool for laser applications and spectroscopy—From new insights to ultrafast amplifiers and spectrometers". PhD thesis. Ludwig Maximilian University of Munich, July 2014. URL: https://edoc.ub.uni-muenchen.de/17456/1/Bradler_Maximilian.pdf.

[471] Nicholas M. Kearns, Andrew C. Jones, Miriam Bohlmann Kunz, Ryan T. Allen, Jessica T. Flach, and Martin T. Zanni. "Two-Dimensional White-Light Spectroscopy Using Supercontinuum from an All-Normal Dispersion Photonic Crystal Fiber Pumped by a 70 MHz Yb Fiber Oscillator". In: *J. Phys. Chem. A* 123.13 (Mar. 2019), pp. 3046–3055. DOI: 10.1021/acs.jpca.9b02206. URL: https://doi.org/10.1021/acs.jpca.9b02206.

[472] Brian Richard Washburn. "Dispersion and nonlinearities associated with supercontinuum generation in microstructure fibers". PhD thesis. Georgia Institute of Technology, Apr. 2002.

[473] Thiab R Taha and Mark I Ablowitz. "Analytical and numerical aspects of certain nonlinear evolution equations. II. Numerical, nonlinear Schrödinger equation". In: *J. Comput. Phys.* 55.2 (Aug. 1984), pp. 203–230. DOI: 10.1016/0021-9991(84)90003-2. URL: https://doi.org/10.1016/0021-9991(84)90003-2.

[474] J. A. C. Weideman and B. M. Herbst. "Split-Step Methods for the Solution of the Nonlinear Schrödinger Equation". In: *SIAM J. Numer. Anal.* 23.3 (June 1986), pp. 485–507. DOI: 10.1137/0723033. URL: https://doi.org/10.1137/0723033.

[475] Stéphane Balac and Fabrice Mahé. "An Embedded Split-Step method for solving the nonlinear Schrödinger equation in optics". In: *J. Comput. Phys.* 280 (Jan. 2015), pp. 295–305. DOI: 10.1016/j.jcp.2014.09.018. URL: https://doi.org/10.1016/j.jcp.2014.09.018.